Bhaumik Breakthrough of the Year Award launches p. 1145

Policy reform for pathogen research oversight p. 1170

Monopoles hopping on a fractal cluster pp. 1177 & 1218

Science

$15
16 DECEMBER 2022
science.org

AAAS

The transformational potential of 5G in health care

In early 2020, in an effort to protect medical personnel from COVID-19, a field hospital staffed entirely by robots opened in Hongshan Sports Center in Wuhan, China. The robots took temperatures, delivered meals, and disinfected the facility. However, the true hero of this story of health care automation is the telecommunications breakthrough that made it possible: a 5G network.

5G technology provided the speed, reliability, and bandwidth that allowed these robots to perform such intricate tasks. But, more importantly, this innovation suggests how 5G networks could transform all critical components of health care, including telehealth, the transfer of large medical files, instrument-assisted examinations, remote real-time monitoring, telesurgery, and vaccine distribution, as well as providing patients with ongoing treatment information, education, and support. To cite one example: Researchers at Tsinghua University in Beijing used an application developed by Beijing PINS Medical Company Limited to remotely update and adjust the deep brain stimulation (DBS) systems in patients during the initial COVID-19 outbreak (see sidebar).

Democratizing medical access

Health care is poised to evolve into a hybrid medical practice of live face-to-face clinical care and telemedicine-based care that will relieve strain on health care systems and prepare for future pandemics. In China, health care accessibility is unevenly distributed, with rural regions generally more disadvantaged. Telemedicine can address this inequity, bringing services to remote areas of the country, even aiding in remote emergency rescues, such as traffic accidents and natural disasters. The advent of 5G technology means that a Parkinson's disease patient in a remote region of China who requests deep brain stimulation treatment does not need to travel to the nearest city, which could be hundreds of miles away, explains Jian-Guo Zhang, director of the Department of Functional Neurosurgery at Beijing Tiantan Hospital. "Now patients can receive DBS programming while at home."

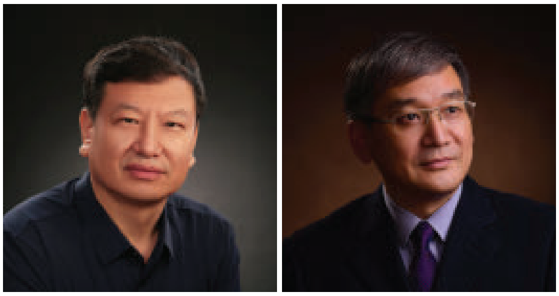

Left, Jian-Guo Zhang; **Right**, Wen-Bin Zhang

"Before the 5G era, signal speed and communication instability restricted the use of telemedicine and remote consultation, and the efficiency and security of data transmission did not meet the necessary high standards," says Wen-Bin Zhang, professor of neurosurgery at the Affiliated Brain Hospital of Nanjing Medical University.

With its ultra-high speed, ultra-low time delay, and ultra-dense connectivity, the next generation of wireless communication technology has the potential to accelerate advances in remote diagnosis and treatment. "With 5G technology, doctors can obtain real-time imaging and field data with which to enhance the accuracy of remote diagnosis and treatment," Wen-Bin Zhang says.

Democratizing health care

The 5G technology in health care is bringing many social and economic benefits, observes Wen-Bin Zhang. Many human and material resources can be saved, reducing the pressure on the health care system and freeing resources that can be allocated more efficiently and evenly. It is also saving money by offering affordable services to more people, promoting health checkups, and providing early intervention in diseases.

The coronavirus pandemic has brought telemedicine into many people's lives and catalyzed industrial advances. The deep integration of telemedicine is becoming increasingly crucial in bolstering remote prevention, diagnosis, and treatment of diseases. 5G-powered telemedicine will promote the development of smart medical care by integrating 5G technology with artificial intelligence, cloud computing, vision, control, sensing, and virtual reality technology.

According to Jian-Guo Zhang, most hospitals will soon use 5G telemedicine. "This solves the problem of uneven resource distribution and spares people from having to travel long distances to receive adequate care."

SPONSORED BY PINS

Forward to the future

Beijing PINS Medical Company Limited has invested in telemedicine technology since 2014 and developed a postoperative program to remotely control neuromodulation surgeries. Now, in collaboration with Tsinghua University, China Mobile, Beijing Tiantan Hospital, and Beijing Union Medical College Hospital, it has started a test project with 5G-supported deep brain stimulation (DBS) telemedicine to treat neuropsychiatric/neurodegenerative diseases such as Parkinson's disease and myodystonia. "The availability of the 5G network makes Parkinson's disease diagnosis, deep brain stimulation device use, and postoperative programming more accessible and fairer for all," Jian-Guo Zhang says.

IMAGE: © TIPPAPATT/SHUTTERSTOCK.COM; PHOTOS: PROVIDED BY PINS

Advertorial

Going greener with lab consumables

At Eppendorf, sustainability lies at the heart of its corporate philosophy, and that philosophy has informed its development of novel biobased lab tubes.

Programs for making scientific labs more sustainable exist in facilities around the world, from the U.S. National Institutes of Health to the United Kingdom's Royal Society of Chemistry. The extensive use of plastic-based lab consumables offers a crucial opportunity to improve the sustainability of scientific research, because most—in fact, nearly all—of these items depend on raw materials created from petroleum products. "For at least the past 2 years, we've seen increasing interest from scientists in improving the sustainability of lab consumables," says Jan-Hendrik Bebermeier, global marketing manager at Eppendorf, headquartered in Hamburg, Germany.

The leaders at Eppendorf see sustainability in a holistic way, encompassing as many of its practices as possible. For example, Eppendorf's German headquarters and production facilities, as well as its UK- and U.S.-based production facilities, rely on 100% green external power sources, such as wind energy. By 2028, Eppendorf plans to be carbon neutral in their own operations.

"We have a dedicated team of experts establishing and further developing our sustainability approach," says Florian König, innovation manager consumables at Eppendorf. Recently, the company extended its sustainability philosophy to address the use of predominantly petroleum-based plastic lab products.

Minimizing petroleum in lab tubes

At ACHEMA 2022 in Frankfurt, Germany, the company launched Eppendorf Tubes BioBased, which are made from 90% renewable and reused raw materials, according to the ISCC (International Sustainability and Carbon Certification) mass-balance approach. Feedstock sources can be used cooking oil and residues, which are waste products from the food industry. Given that many lab consumables cannot be easily recycled due to contamination, making tubes from renewable, recycled materials is the next-best option. These screw cap tubes are available for volumes of 5, 15, 25, and 50 mL.

These tubes could also be made from what König calls first-generation biobased material, which is not recycled. As König says, "From my point of view, that would be a second-best choice, because we would directly use plants—that could potentially be used for nutritional products—as input material for products." Using recycled biobased raw materials instead, he explains, "is one of the best measures we can take to reduce the CO_2 footprint of our products."

In fact, Eppendorf confirmed the greenhouse-gas benefits. The company conducted a product carbon-footprint screening analysis, and the development of these tubes grew out of that. "I'm responsible for a lifecycle assessment of some of these products, and we're comparing fossil-based products directly to biobased ones," König says. "So, we will be able to communicate in a transparent way the real improvement that customers can achieve when they switch from one product to another." And customers can feel confident in these conclusions because the analyses are conducted and monitored by independent, third-party companies.

PHOTOS: COMPLIMENTS OF EPPENDORF

Educating the audience

The challenge of switching from petroleum-based raw materials to biobased materials is not predominantly a technological one, since the plastic granulate that Eppendorf uses is comparable to material from fossil fuel–based sources. Rather, effort is needed to establish new processes that comply with ISCC standards.

"The challenge is more or less the core message to our users," says Bebermeier. "The characteristics of this biobased plastic granulate are identical to those of the petroleum-based ones. But scientists are understandably skeptical."

In making a switch to biobased lab tubes, even the most environmentally minded scientist needs a high-performing product. Eppendorf wouldn't do it any other way. "When we develop new products in this way, our customers can be sure that they're getting the same top quality they've come to expect from us," says Brigitte Klose, global marketing manager consumables at Eppendorf.

So, from a performance perspective, Eppendorf Tubes BioBased work just like other consumables made by the company. "The different source has no impact on the day-to-day work," Bebermeier says. "This is the same tube."

Eppendorf can even prove the equivalence between tubes made from biobased or petroleum-based raw materials. "We have done our testing, and we are working on a number of qualifications and reports to demonstrate to our customers that these tubes have the same high-quality performance and purity," says König.

When asked about the reception from scientists at ACHEMA 2022, Klose says, "They liked the idea very much." She adds, "Scientists asked a lot of questions about these new products, and they were very interested to take the message back to their laboratories and convince the lab managers to switch."

Completing the circle

Eppendorf's efforts in running on renewable energy and making tubes from recycled, biobased raw materials are only the beginning. For one thing, the company will extend its use of greener feedstocks for other consumables. Based on the reaction of scientists to Eppendorf Tubes BioBased, Klose says, "I think the interest in other products—like other tubes, plates, and pipette tips—will grow."

To support that growth, though, Eppendorf's experts see a need to inform the industry. "The challenge we have in the market at the moment is that there are so many different plastic materials being called 'sustainable,' and there are some misunderstandings," Klose explains. "When we launched our Eppendorf Tubes BioBased, for example, we found that the terms 'biobased' and 'biodegradable' can be confused." Just because a product is biobased doesn't mean that it will biodegrade. As Bebermeier notes, "The action of acids and bases required for being biodegradable are not acceptable in a lab tube, where acids and bases cannot be allowed to interact with the plastic."

Still, Eppendorf strives to complete the sustainability circle. "We don't only focus on production with the special biobased granulate. We always strive to reduce, reuse, and recycle," Klose says. For instance, she adds, "'Reduce' means having a close look at each product in terms of saving materials." Each of these processes promises to make lab consumables and the entire industry more sustainable.

Eppendorf Tubes BioBased and future consumables made from biobased raw materials already incorporate an element of reuse; now, Eppendorf is exploring where it might recycle its biobased consumables. As König says, "A bit further down the road, we are looking at interesting ideas to close the cycle." For example, he describes talking with people about turning Eppendorf's lab waste into new material that can be used again. As he puts it, "It's the start of a process, an ongoing journey, and we are really trying to accelerate this by actively looking at each component of our resources and how we can proactively improve them." Eppendorf may be recycling its products, but it is not recycling ideas. Instead, it is coming up with novel ways to balance meeting the needs of a growing research industry with being a good steward of the environment.

Sponsored by

eppendorf

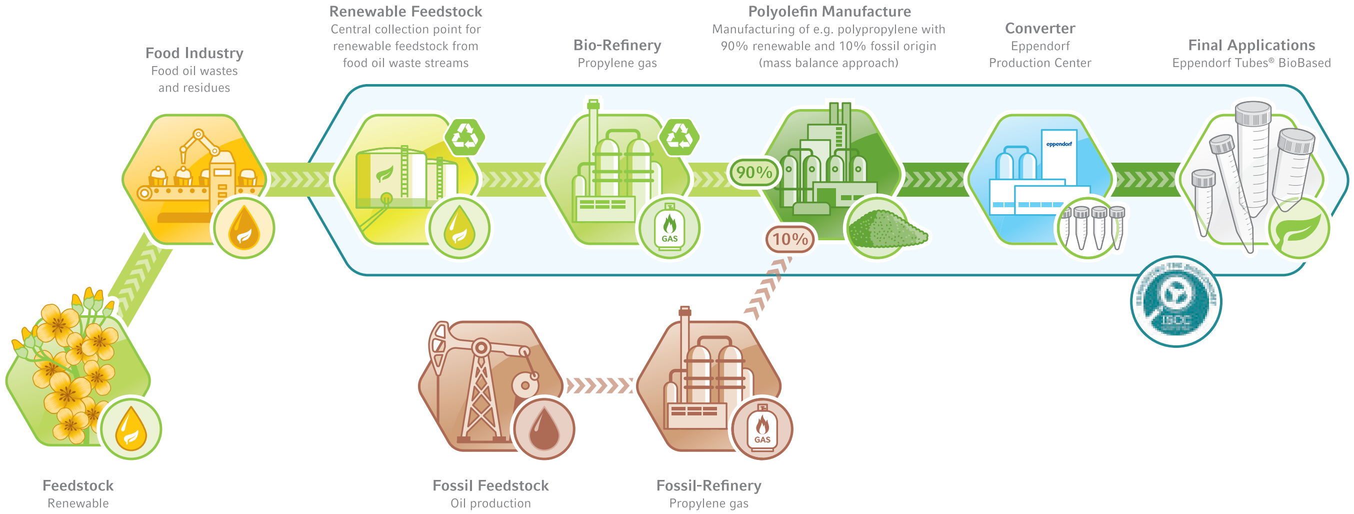

CONTENTS

16 DECEMBER 2022 • VOLUME 378 • ISSUE 6625

SPECIAL SECTION

Breakthrough of the Year

WINNER

RUNNERS-UP

ON THE COVER

For the technological feat of its construction and launch and its vast promise for exploring the universe, JWST is *Science*'s 2022 Breakthrough of the Year. In this illustration, one of its early images—showing the vast, star-forming clouds known as the Pillars of Creation—is depicted on the gold-plated segments that make up the space telescope's 6.5-meter mirror. See page 1145.

*Image: (Illustration) C. Bickel/*Science*; (Pillars of Creation) NASA; ESA; CSA; STSCI; Joseph Depasquale, Anton M. Koekemoer, and Alyssa Pagan/ STSCI*

SEE ALSO VIDEO PODCAST

NEWS

IN BRIEF

IN DEPTH

INSIGHTS

POLICY FORUM

PERSPECTIVES

PHOTO: NASA; ESA; CSA; STSCI; JOSEPH DEPASQUALE, ANTON M. KOEKEMOER, AND ALYSSA PAGAN/STSCI

BOOKS *ET AL.*

LETTERS

RESEARCH

IN BRIEF

RESEARCH ARTICLES


1242

REPORTS


1178

DEPARTMENTS

CREDITS: (ILLUSTRATION) ROBERT NEUBECKER; (PHOTO) NURPHO/AP IMAGES

SCIENCE (ISSN 0036-8075) is published weekly on Friday, except last week in December, by the American Association for the Advancement of Science, 1200 New York Avenue, NW, Washington, DC 20005. Periodicals mail postage (publication No. 484460) paid at Washington, DC, and additional mailing offices. Copyright © 2022 by the American Association for the Advancement of Science. The title SCIENCE is a registered trademark of the AAAS. Domestic individual membership, including subscription (12 months): $165 ($74 allocated to subscription). Domestic institutional subscription (51 issues): $2212; Foreign postage extra: Air assist delivery: $98. First class, airmail, student, and emeritus rates on request. Canadian rates with GST available upon request, GST #125488122. Publications Mail Agreement Number 1069624. **Printed in the U.S.A.**
Change of address: Allow 4 weeks, giving old and new addresses and 8-digit account number. **Postmaster:** Send change of address to AAAS, P.O. Box 96178, Washington, DC 20090–6178. **Single-copy sales:** $15 each plus shipping and handling available from backissues.science.org; bulk rate on request. **Authorization to reproduce** material for internal or personal use under circumstances not falling within the fair use provisions of the Copyright Act can be obtained through the Copyright Clearance Center (CCC), www.copyright.com. The identification code for *Science* is 0036-8075. *Science* is indexed in the *Reader's Guide to Periodical Literature* and in several specialized indexes.

AAAS | Science

The Mani L. Bhaumik
BREAKTHROUGH OF THE YEAR
Award

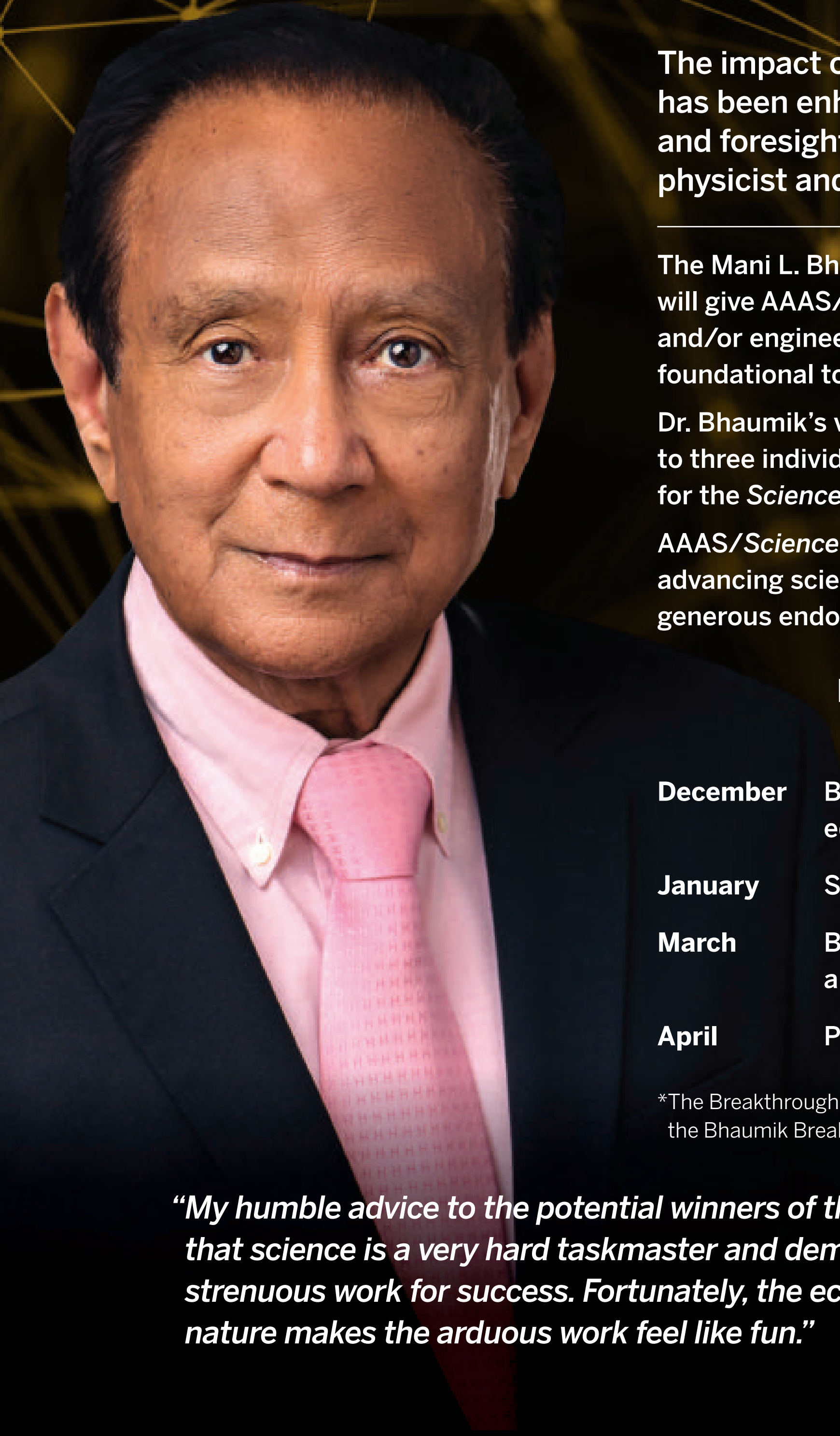

The impact of *Science*'s annual Breakthrough of the Year has been enhanced forevermore due to the generosity and foresight of Dr. Mani L. Bhaumik, a renowned physicist and philanthropist.

The Mani L. Bhaumik Breakthrough of the Year Award endowment will give AAAS/*Science* the opportunity to recognize the scientists and/or engineers whose leading research and activities are foundational to the Breakthrough of the Year.

Dr. Bhaumik's visionary gift will fund a $250,000 cash prize to up to three individuals. It will also provide sustained annual support for the *Science* journals.

AAAS/*Science* is thankful for Dr. Bhaumik's dedication to advancing science and serving society and is honored by his generous endowment.

Mani L. Bhaumik Breakthrough of the Year Award Timeline*

December	Breakthrough of the Year announced, *Science* editor-in-chief forms an award selection committee
January	Selection committee convenes
March	Bhaumik Breakthrough of the Year Award winner(s) announced
April	Public celebration at AAAS

*The Breakthrough of the Year is chosen by *Science*'s news and editorial staff before the Bhaumik Breakthrough of the Year Award selection committee is convened.

> *"My humble advice to the potential winners of the award would be for them to realize that science is a very hard taskmaster and demands dedication with unremitting strenuous work for success. Fortunately, the ecstasy of revealing the secrets of nature makes the arduous work feel like fun."*
>
> — Mani L. Bhaumik

EDITORIAL

Hard, not easy

In a speech at Rice University in September 1962, US President John F. Kennedy announced plans for human spaceflight to the Moon by saying, "We choose to go to the Moon in this decade and do the other things, not because they are easy, but because they are hard." These words marked a time when trust in and respect for science were high, and when big questions about the workings of nature were both humbling and inspiring. And although the goals of NASA's Apollo program were not principally to do science, it inspired a generation of scientists. The ensuing years have seen this enthusiasm decline because of failings within as well as outside the world of science, as science is often ridiculed whenever findings lead to political debates. But the successful launch of a remarkable new space telescope this year has rekindled a sense of awe and wonder at the magnificence of the Universe and the thrill of human achievement.

> "...a remarkable new space telescope... has rekindled a sense of awe and wonder..."

Science's Breakthrough of the Year is the successful launch and deployment of the James Webb Space Telescope (JWST). In the coming weeks, through a process separate from the discussions to choose the Breakthrough, *Science* will convene a committee to award a follow-up cash prize for the first time. The Bhaumik Breakthrough of the Year award will recognize three scientists who contributed to this year's Breakthrough.

JWST is a massive human achievement. A staggering number of operations had to go just right to bring the images home from space, including a honeycomb array of highly smooth mirrors that unfolds in space, a fabric sunshield, and cryocoolers that chill the instruments to near absolute zero. The accomplishment of deploying JWST alone is one to celebrate. It is reminiscent of the triumph of the Apollo missions: As Kennedy said, "That goal will serve to organize and measure the best of our energies and skills."

JWST holds substantial scientific promise. Its massive mirror will allow observations of events and objects at sufficient distances to reveal the Universe when it was less than a billion years old. JWST will also probe the atmospheres and climates of exoplanets, providing a glimpse into the potential of other planets to harbor life. It's hard to imagine a more exciting look into the beauty of nature than understanding how the Universe formed and whether life exists elsewhere.

Unfortunately, the name of JWST has tarnished the story. James Webb was a former NASA administrator who presided over some of the agency's biggest accomplishments. But he served at a time when a program was initiated to fire LGBTQ+ employees on the basis of their sexual orientation, and he stated to Congress that these individuals were "unsuited" for employment at NASA. NASA has tried to justify its decision to keep the name by providing evidence that Webb did not know that LGBTQ+ employees were purged from its staff. This is a distinction without a difference. The point is that Webb's name is a reminder of the so-called "Lavender Scare" and the homophobia in NASA and the scientific enterprise.

Natalie Batalha—a leader of the exoplanet program for JWST—told journalist Natalie Wolchover that she decided to become an astronomer after reading the autobiography of astronaut Sally Ride, the first American woman in space. How can JWST inspire future scientists when its name is associated with homophobia? Leading societies such as the Royal Astronomical Society and American Astronomical Society have decided to call the telescope JWST without spelling out the name. But every time this convention is explained, it will be a reminder of the exclusion that too many scientists experience every day.

When the first image taken by the telescope was released to the public, it was an event reminiscent of the Apollo Moon landing. Once again, a great human achievement brought to Earth something marvelous. It is a reminder of the power of inspiration and what societies can accomplish when motivated to generate knowledge. And it is a reminder of how great science requires great humility. Politicians and pundits often make up whatever suits their political goals about science, but scientists recognize how little we understand about the Universe. As Kennedy said, "The greater our knowledge increases, the greater our ignorance unfolds."

–H. Holden Thorp

H. Holden Thorp
Editor-in-Chief,
Science journals.
hthorp@aaas.org;
@hholdenthorp

PHOTO: CAMERON DAVIDSON

10.1126/science.adg2577

Science AAAS

Editor-in-Chief Holden Thorp, hthorp@aaas.org

Executive Editor Valda Vinson

Editor, Research Jake S. Yeston **Editor, Insights** Lisa D. Chong **Managing Editor** Lauren Kmec

DEPUTY EDITORS Gemma Alderton (UK),Stella M. Hurtley (UK), Phillip D. Szuromi, Sacha Vignieri **SR. EDITORS** Caroline Ash (UK), Michael A. Funk, Brent Grocholski, Pamela J. Hines, Di Jiang, Priscilla N. Kelly, Marc S. Lavine (Canada), Mattia Maroso, Yevgeniya Nusinovich, Ian S. Osborne (UK), L. Bryan Ray, Seth Thomas Scanlon (UK), H. Jesse Smith, Keith T. Smith (UK), Jelena Stajic, Peter Stern (UK), Valerie B. Thompson, Brad Wible **ASSOCIATE EDITORS** Bianca Lopez, Madeleine Seale (UK), Corinne Simonti, Yury V. Suleymanov, Ekeoma Uzogara **LETTERS EDITOR** Jennifer Sills **LEAD CONTENT PRODUCTION EDITORS** Chris Filiatreau, Harry Jach **SR. CONTENT PRODUCTION EDITOR** Amelia Beyna **CONTENT PRODUCTION EDITORS** Julia Haber-Katris, Nida Masiulis, Abigail Shashikanth, Suzanne M. White **SR. EDITORIAL MANAGERS** Carolyn Kyle, Beverly Shields **SR. PROGRAM ASSOCIATE** Maryrose Madrid **EDITORIAL ASSOCIATE** Joi S. Granger **SR. EDITORIAL COORDINATORS** Aneera Dobbins, Jeffrey Hearn, Lisa Johnson, Jerry Richardson, Hilary Stewart (UK), Alice Whaley (UK), Anita Wynn **EDITORIAL COORDINATORS** Maura Byrne, Alexander Kief, Ronmel Navas, Isabel Schnaidt, Qiyam Stewart, Brian White **RESEARCH & DATA ANALYST** Jessica L. Slater **ADMINISTRATIVE COORDINATOR** Karalee P. Rogers **ASI DIRECTOR, OPERATIONS** Janet Clements (UK) **ASI SR. OFFICE ADMINISTRATOR** Jessica Waldock (UK)

News Editor Tim Appenzeller

NEWS MANAGING EDITOR John Travis **INTERNATIONAL EDITOR** Martin Enserink **DEPUTY NEWS EDITORS** Shraddha Chakradhar, Elizabeth Culotta, Lila Guterman, David Grimm, Eric Hand (Europe), David Malakoff **SR. CORRESPONDENTS** Daniel Clery (UK), Jon Cohen, Jeffrey Mervis, Elizabeth Pennisi **ASSOCIATE EDITORS** Jeffrey Brainard, Michael Price, Kelly Servick **NEWS REPORTERS** Adrian Cho, Jennifer Couzin-Frankel, Jocelyn Kaiser, Rodrigo Pérez Ortega (Mexico City), Robert F. Service, Erik Stokstad, Paul Voosen, Meredith Wadman **INTERNS** Zack Savitsky, Viviana Flores, Katherine Irving **CONTRIBUTING CORRESPONDENTS** Warren Cornwall, Andrew Curry (Berlin), Ann Gibbons, Sam Kean, Eli Kintisch, Kai Kupferschmidt (Berlin), Andrew Lawler, Mitch Leslie, Eliot Marshall, Virginia Morell, Dennis Normile (Tokyo), Elisabeth Pain (Careers), Charles Piller, Gabriel Popkin, Michael Price, Joshua Sokol, Richard Stone, Emily Underwood, Gretchen Vogel (Berlin), Lizzie Wade (Mexico City) **CAREERS** Rachel Bernstein (Editor), Katie Langin (Associate Editor) **COPY EDITORS** Julia Cole (Senior Copy Editor), Morgan Everett, Cyra Master (Copy Chief) **ADMINISTRATIVE SUPPORT** Meagan Weiland

Creative Director Beth Rakouskas

DESIGN MANAGING EDITOR Chrystal Smith **GRAPHICS MANAGING EDITOR** Chris Bickel **PHOTOGRAPHY MANAGING EDITOR** Emily Petersen **MULTIMEDIA MANAGING PRODUCER** Kevin McLean **WEB CONTENT STRATEGY MANAGER** Kara Estelle-Powers **DESIGN EDITOR** Marcy Atarod **DESIGNER** Christina Aycock **SENIOR SCIENTIFIC ILLUSTRATOR** Valerie Altounian **SCIENTIFIC ILLUSTRATORS** Austin Fisher, Kellie Holoski, Ashley Mastin **INTERACTIVE GRAPHICS EDITOR** Kelly Franklin **SENIOR GRAPHICS SPECIALISTS** Holly Bishop, Nathalie Cary **SENIOR PHOTO EDITOR** Charles Borst **SENIOR PODCAST PRODUCER** Sarah Crespi **VIDEO PRODUCER** Meagan Cantwell **SOCIAL MEDIA STRATEGIST** Jessica Hubbard **SOCIAL MEDIA PRODUCER** Sabrina Jenkins **WEB DESIGNER** Jennie Pajerowski

Chief Executive Officer and Executive Publisher Sudip Parikh

Publisher, Science Family of Journals Bill Moran

DIRECTOR, BUSINESS SYSTEMS AND FINANCIAL ANALYSIS Randy Yi **DIRECTOR, BUSINESS OPERATIONS & ANALYSIS** Eric Knott **DIRECTOR OF ANALYTICS** Enrique Gonzales **MANAGER, BUSINESS OPERATIONS** Jessica Tierney **MANAGER, BUSINESS ANALYSIS** Cory Lipman **BUSINESS ANALYSTS** Kurt Ennis, Maggie Clark **FINANCIAL ANALYST** Isacco Fusi **BUSINESS OPERATIONS ADMINISTRATOR** Taylor Fisher **SENIOR PRODUCTION MANAGER** Jason Hillman **SENIOR MANAGER, PUBLISHING AND CONTENT SYSTEMS** Marcus Spiegler **CONTENT OPERATIONS MANAGER** Rebecca Doshi **SENIOR CONTENT & PUBLISHING SYSTEMS SPECIALIST** Jacob Hedrick **SENIOR PRODUCTION SPECIALIST** Kristin Wowk **PRODUCTION SPECIALISTS** Kelsey Cartelli, Audrey Diggs **DIGITAL PRODUCTION MANAGER** Lisa Stanford **CONTENT SPECIALIST** Kimberley Oster **ADVERTISING PRODUCTION OPERATIONS MANAGER** Deborah Tompkins **DESIGNER, CUSTOM PUBLISHING** Jeremy Huntsinger **SR. TRAFFIC ASSOCIATE** Christine Hall **SPECIAL PROJECTS ASSOCIATE** Sarah Dhere

ASSOCIATE DIRECTOR, BUSINESS DEVELOPMENT Justin Sawyers **GLOBAL MARKETING MANAGER** Allison Pritchard **DIGITAL MARKETING MANAGER** Aimee Aponte **JOURNALS MARKETING MANAGER** Shawana Arnold **MARKETING ASSOCIATES** Aaron Helmbrecht, Ashley Hylton, Mike Romano, Lorena Chirinos Rodriguez, Jenna Voris **SENIOR DESIGNER** Kim Huynh

DIRECTOR AND SENIOR EDITOR, CUSTOM PUBLISHING Sean Sanders **ASSISTANT EDITOR, CUSTOM PUBLISHING** Jackie Oberst **PROJECT MANAGER** Melissa Collins

DIRECTOR, PRODUCT & PUBLISHING DEVELOPMENT Chris Reid **DIRECTOR, BUSINESS STRATEGY AND PORTFOLIO MANAGEMENT** Sarah Whalen **ASSOCIATE DIRECTOR, PRODUCT MANAGMENT** Kris Bishop **PRODUCT DEVELOPMENT MANAGER** Scott Chernoff **PUBLISHING TECHNOLOGY MANAGER** Michael Di Natale **SR. PRODUCT ASSOCIATE** Robert Koepke **PRODUCT ASSOCIATE** Caroline Breul, Anne Mason **SPJ ASSOCIATE MANAGER** Samantha Bruno Fuller **SPJ ASSOCIATE** Casey Buchta

MARKETING MANAGER Kess Knight **BUSINESS DEVELOPMENT MANAGER** Rasmus Andersen **SENIOR INSTITUTIONAL LICENSING MANAGER** Ryan Rexroth **INSTITUTIONAL LICENSING MANAGER** Marco Castellan, Claudia Paulsen-Young **SENIOR MANAGER, INSTITUTIONAL LICENSING OPERATIONS** Judy Lillibridge **SENIOR OPERATIONS ANALYST** Lana Guz **SYSTEMS & OPERATIONS ANALYST** Ben Teincuff **FULFILLMENT ANALYST** Aminta Reyes

DIRECTOR, GLOBAL SALES Tracy Holmes **US EAST COAST AND MID WEST SALES** Stephanie O'Connor **US MID WEST, MID ATLANTIC AND SOUTH EAST SALES** Chris Hoag **US WEST COAST SALES** Lynne Stickrod **ASSOCIATE DIRECTOR, ROW** Roger Goncalves **SALES REP, ROW** Sarah Lelarge **SALES ADMIN ASSISTANT, ROW** Victoria Glasbey **DIRECTOR OF GLOBAL COLLABORATION AND ACADEMIC PUBLISHING RELATIONS, ASIA** Xiaoying Chu **ASSOCIATE DIRECTOR, INTERNATIONAL COLLABORATION** Grace Yao **SALES MANAGER** Danny Zhao **MARKETING MANAGER** Kilo Lan **ASCA CORPORATION, JAPAN** Rie Rambelli (Tokyo), Miyuki Tani (Osaka)

DIRECTOR, COPYRIGHT, LICENSING AND SPECIAL PROJECTS Emilie David **RIGHTS AND PERMISSIONS ASSOCIATE** Elizabeth Sandler **LICENSING ASSOCIATE** Virginia Warren **CONTRACT SUPPORT SPECIALIST** Michael Wheeler

MAIN HEADQUARTERS
Science/AAAS
1200 New York Ave. NW
Washington, DC 20005

SCIENCE INTERNATIONAL
Clarendon House
Clarendon Road
Cambridge, CB2 8FH, UK

SCIENCE CHINA
Room 1004, Culture Square
No. 59 Zhongguancun St.
Haidian District, Beijing, 100872

SCIENCE JAPAN
ASCA Corporation
Sibaura TY Bldg. 4F, 1-14-5
Shibaura Minato-ku
Tokyo, 108-0073 Japan

EDITORIAL
science_editors@aaas.org

NEWS
science_news@aaas.org

INFORMATION FOR AUTHORS
science.org/authors/science-information-authors

REPRINTS AND PERMISSIONS
science.org/help/reprints-and-permissions

MEDIA CONTACTS
scipak@aaas.org

MULTIMEDIA CONTACTS
SciencePodcast@aaas.org
ScienceVideo@aaas.org

INSTITUTIONAL SALES AND SITE LICENSES
science.org/librarian

PRODUCT ADVERTISING & CUSTOM PUBLISHING
advertising.science.org/products-services
science_advertising@aaas.org

CLASSIFIED ADVERTISING
advertising.science.org/science-careers
advertise@sciencecareers.org

JOB POSTING CUSTOMER SERVICE
employers.sciencecareers.org
support@sciencecareers.org

MEMBERSHIP AND INDIVIDUAL SUBSCRIPTIONS
science.org/subscriptions

MEMBER BENEFITS
aaas.org/membership/benefits

EDITORIAL

Monitor biodiversity for action

This week, Montreal, Canada, is at the epicenter of international negotiations for biodiversity. Thousands of people from around the world are attending the 15th Conference of the Parties to the United Nations Convention on Biological Diversity (COP15) to witness the negotiation of a new Global Biodiversity Framework. Its goals and targets replace the previous framework—the Aichi Biodiversity Targets—that failed to bring about the transformative change needed to reverse the alarming trends in biodiversity loss.

The current draft Global Biodiversity Framework is built upon four goals and 22 targets designed to galvanize immediate society-wide action by governments, nongovernmental organizations, businesses, local communities, and Indigenous peoples. The goals address the urgent need to protect and restore biodiversity, sustain the benefits that people derive from healthy ecosystems, ensure that these benefits are shared equitably, and mobilize all forms of enabling conditions, including knowledge and sufficient financial resources. The targets accompanying the goals focus measurable actions for all life on land, in fresh waters, and in the oceans.

At the heart of the Global Biodiversity Framework is a new and vital piece—a monitoring framework that proposes a suite of indicators by which the Parties can measure progress toward both national and global targets. Much like a satellite-navigation system, the monitoring framework alerts when Parties are not on track and suggests alternative pathways to adjust a country's direction and journey. Approximately 40 headline indicators have been proposed to measure progress across all targets; examples for protecting and restoring biodiversity include the Red List Index, the Species Habitat Index, and the percentage of degraded or converted ecosystems that are under restoration.

> "...it is perhaps surprising that the selection of indicators has been a source of disagreement..."

Given their importance, it is perhaps surprising that the selection of indicators has been a source of disagreement during negotiations over the past year. There are three reasons for this tension. Countries differ greatly in their capacity to generate and use data, and to calculate the indicators and update them over time. This has resulted in a highly uneven global picture of biodiversity loss. A recent estimate indicates that global datasets cover less than 7% of the world's surface at 5-km resolution, and less than 1% for most species at higher resolutions. This knowledge gap can be filled over time if infrastructure and expert knowledge are available to implement the monitoring framework—a subject that is part of the negotiation process. International organizations such as the UN Environment Programme World Conservation Monitoring Centre and the Group on Earth Observations Biodiversity Observation Network (GEO BON) are offering support to countries. International financial support for monitoring will be needed to ensure that biodiversity observations are possible for all countries.

Another key issue is data sovereignty. Countries must have confidence in the data used to update the indicators. This is best achieved if national datasets that are validated by experts are used along with global data. In the absence of adequate access to and sharing of data, the negotiation can only center on a minimum set of indicators that all countries can calculate with the available data.

There is also a risk that the framework will be too flexible. Parties may pick and choose indicators to show progress on certain facets of the Global Biodiversity Framework targets, while ignoring others. At this time, there is no consensus on which aspects of the monitoring framework are essential and must be employed by all Parties to provide a global picture of progress.

These issues of data availability, international disparities regarding data production and access, and sovereignty have prevented the Parties from reaching a consensus on quantitative targets and SMART (specific, measurable, achievable, relevant, and time-bound) indicators. This raises the specter of a Global Biodiversity Framework with low ambition that emerges from COP15. These problems are not unsolvable but require the international community and national governments to work together to invest in new or existing biodiversity monitoring systems that help all Parties. If the Parties of COP15 can agree on a global biodiversity observing system that links national monitoring networks, analogous to the Global Climate Observing System in place for climate tracking, then a path will be initiated for boosting the production and sharing of biodiversity data worldwide. Over time, this will allow all countries to implement an ambitious monitoring framework that supports the decisions and actions needed to achieve the vision of the Global Biodiversity Framework.

–Andrew Gonzalez and Maria Cecilia Londoño

Andrew Gonzalez is a co-chair of GEO BON and a professor in the Department of Biology at McGill University, Montreal, Canada. andrew.gonzalez@mcgill.ca

Maria Cecilia Londoño is a co-chair of GEO BON and a researcher at the Alexander von Humboldt Biological Resources Research Institute in Bogota, Colombia. mlondono@humboldt.org.co

Published online 8 December 2022; 10.1126/science.adg1506

As ice melts, biodiversity is lost

Team sampling the rivers draining the roof of our planet (Himalayas, Nepal).

Glaciers are melting fast. Yet rising sea levels are not the only existential threat created by glacier water—glacier-fed streams maintain some of the largest river networks on this planet and are a source of drinking water for millions of people in the lowlands. But Tom Battin, professor of environmental sciences at the Ecole Polytechnique Fédérale de Lausanne (EPFL), wonders, "What else do we lose besides water?" The Vanishing Glaciers project he leads involves an international team of researchers from Switzerland, Luxembourg, the United States, and Saudi Arabia, and aims to answer this question. Supported by the NOMIS Foundation, Battin's team has cruised the roof of the planet, reaching the highest peaks with flowing waters to "unlock the secrets of the microbial life that flows from glaciers."

Hidden life

Secluded in the icy waters of glacier-fed streams are richly biodiverse, yet little-understood communities of microorganisms. These communities drive essential biogeochemical cycles playing a crucial role in the survival of surrounding ecosystems. "This unseen biodiversity is vital for the biodiversity that we do see," says Battin.

Ecosystems of microorganisms are the base of the food chain feeding larger organisms such as insects, fish, birds, and amphibians. Microorganisms are decomposers and act as filters for the water. "So often we have neglected the relevance of what we can't see," says Leïla Ezzat, an aquatic ecologist and postdoc at EPFL, who is one of the scientists behind the Vanishing Glaciers project. "Yet microbes support all life on Earth."

Despite its vital role, glacier biodiversity is tremendously understudied, says Scott Hotaling, assistant professor at Utah State University, who did not participate in the Vanishing Glaciers project. "People tend to think that nothing lives in a glacier, but that couldn't be further from the truth. A huge amount of untapped biodiversity on the planet is completely unknown because we just aren't looking."

Microorganisms are the planet's most ancient, abundant, and prosperous forms of life. Microbial metabolism has orchestrated primary biogeochemical cycles on Earth for more than 3 billion years. Microbial life has survived global glaciations, such as those that occurred 600 to 700 million years ago when the Earth was a snowball and glacial meltwaters dominated the continental landscapes. Today, microorganisms are still the most populous forms of life found in glacier-fed streams, which are one of the most extreme environments on the planet, having temperatures nearing the freezing point, high hydraulic stress, high UV radiation, and limited nutrients.

A first global census

The Vanishing Glaciers project aspires to conduct the first global census of microbial life in glacier-fed streams by sampling glacial meltwaters across the globe and combining cutting-edge 'omics methods with phylogeny to better understand what makes these microbial communities thrive, how they differ across space, and what their future looks like given a rapidly warming climate and receding cryosphere. "We want to uncover some of the characteristics and strategies that microorganisms have evolved to become such a successful mode of life in the extreme ecosystems of glacier-fed streams," says Battin.

The current climate crisis is causing glaciers to shrink into icy remnant islands constrained to the Earth's peaks. "We are about to lose an abundance of microscopic diversity before our eyes without noticing it and without understanding its fundamental role for downstream ecosystems," says Ezzat, who works on the global biogeography of glacier-fed stream microbes. As glaciers retreat, streams

CREDIT: PHOTOS BY MARTINA SCHÖN, MATTEO TOLOSANO, VINCENT DE STAERCKE, AND MIKE STYLLAS

become murky and lose velocity, creating a hostile environment for microorganisms adapted to the cold and turbulent meltwater of glaciers. The habitat of these microorganisms is changing—and that leads to a loss of microbial diversity. "We are heading towards an ecosystem that is more and more homogeneous," says Sophie Cauvy-Fraunié, an expert in hydroecology at France's National Research Institute for Agriculture, Food and Environment (INRAE).

Hundreds of thousands of glacier-fed streams are vanishing worldwide; with them, a unique microbiome we still know very little about is disappearing. Many species researchers haven't yet discovered might already be endangered. "Glacier biodiversity research has been exceptionally data-poor. But the Vanishing Glaciers project has changed that," says Hotaling. "It's exactly the kind of thing that we need to have happen."

Cruising uncharted waters

So, what is this unseen microbial biodiversity? And what's its fate? Finding answers to these fundamental questions requires a gargantuan scientific effort and a multidisciplinary team.

When Mike Styllas, a geologist at EPFL and a mountaineer with 20 years of experience, joined the Vanishing Glaciers project in 2018, he was convinced it would be an experience like no other. "The idea immediately seduced me," he says. Styllas, the project's expedition leader, guided a team of experts up the planet's highest peaks to collect glacier water samples. Together with Martina Schön, Matteo Tolosano, and Vincent De Staercke, he climbed 11 major mountain ranges, from the European Alps to the Andes to the Himalayas. "We traveled across five continents. We visited 14 countries. We sampled 170 glaciers across the Earth. We hiked a total distance of over 1,800 kilometers [1,118 miles] flat and more than 85 kilometers [52.8 miles] in elevation." The physical fatigue was no joke. In the Himalayas, for example, the climbers spent almost 2 months at an altitude of between 4,000 and 5,000 meters (16,400 feet) until they could collect all the samples they needed. "Cruising the roof of our planet is a major endeavour," marvels Battin.

The material the team hunted for was microbial biofilm, that is, communities of microorganisms such as viruses, bacteria, archaea, fungi, algae, protozoa, and other higher organisms attached to rock surfaces. They also gathered many environmental samples and even collected satellite imagery of the glaciers that feed the streams.

The climbers then shipped the samples to their colleagues at the EPFL laboratory, from where subsets were shared with their collaborators at Paul Wilmes's laboratory at the University of Luxembourg, Daniele Daffonchio's laboratory at King Abdullah University of Science and Technology, and Robert Spencer's laboratory at Florida State University. "That is where the scientific journey through uncharted waters began, because very few people have had the chance to collect samples from those ecosystems," says Battin.


Expedition team in Ecuador (left to right: Martina Schön, Matteo Tolosano, Mike Styllas, and Vincent de Staercke).


Mike Styllas collecting samples from a glacier-fed stream in Ecuador.


Porters and local mountain guides were central to the success of the Vanishing Glaciers project.

"To answer fundamental research questions, enable discoveries, and advance human progress, we must engage innovative, unconventional approaches," says Markus Reinhard, managing director of the NOMIS Foundation. "The Vanishing Glaciers project is indeed traversing an uncharted path, and its interdisciplinary, collaborative approach is leading to insights that could change our understanding of the world." NOMIS is dedicated to enabling insight-driven, high-risk collaborative science. By supporting pioneering researchers who use radically different approaches, apply new expertise, or engage novel perspectives, NOMIS seeks to "create a spark" in the world of science.

Through the Vanishing Glaciers project, Battin has built a team at EPFL and a worldwide network of scientists with expertise in molecular biology, ecology, theoretical ecology, biogeochemistry, glaciology, geology, and computer and data science.

The multidisciplinary team of scientists analyzed microbial biomass, extracellular enzymatic activity, respiration, and production. DNA sequencing gave them a glimpse into the evolutionary process that led the glacier microbiome to prosper and what its fate might be as the planet warms. "Genomic and phylogenetic studies will allow us to look back in time as well as peek into the future," says Battin. "Now we can guess how the microorganisms in glacier-fed streams may have looked in ancient times and what their communities may look like in the future as the glaciers shrink."

The researchers reconstructed the phylogenetic tree of microbes from glacier-fed streams by working at the interface between evolution and ecology. Phylogenetic techniques offer a glance at the evolutionary history of the microbes, whereas genomic sequencing enables an understanding of the genomics underpinning the ecological success of these microbes.

One known phenomenon caused by climate change, for example, is the "greening" of some glacier-fed streams due to algae blooming. "We know these streams will only become greener in the future. What we want to discover now are the consequences of this greening for the carbon cycling in these ecosystems," says Battin.

The researchers could also study the chemistry of the water and the mineral composition of the rocks using water and sediment samples. Aerial footage obtained with a drone, combined with satellite images, gave them a quantitative appreciation of the glaciers' size.

"They have done really in-depth work using cutting-edge tools to understand not just what microbes there are, but also what they are doing functionally, what cryptic diversity and morphology they have. Not just what the water temperature is, but also what the water chemistry and flow are," says Hotaling. "It's such a powerful amount of complementary data. It's a very holistic study."

Both Hotaling and Cauvy-Fraunié agree that the main strength of the Vanishing Glaciers project is the vast amount of data collected from many sites across the

PHOTO: PHOTO PROVIDED BY NOMIS

World map showing the locations of the major mountain ranges where the Vanishing Glaciers project sampled the glacier-fed stream microbiome.

globe using the same protocols, which overcomes the limitations of meta-analyses on heterogeneous data. "This is apples-to-apples data," Hotaling says.

Styllas concurs, adding, "This project has been an unprecedented physical and mental effort to decode the biogeochemical and genetic signatures of microbes inhabiting some of our planet's coldest aquatic environments before they disappear."

An enriching experience for all

Organizing the logistics behind every expedition meant obtaining all the appropriate permits from local governments and Indigenous groups before the research team could begin their journey, dealing with customs restrictions when shipping samples back to EPFL, and following border restrictions due to the pandemic.

To overcome such difficulties, they established collaborations with universities in each country they visited. Battin and his team trained local graduate students and researchers, taught them their methods, took them on expeditions, and let them use their equipment. This approach had a dual effect. On the one hand, local researchers helped the Vanishing Glaciers project team with fieldwork and logistics, such as obtaining permits, finding a local mountain guide, helping with language barriers, or simply storing samples in their freezers. On the other hand, collaborators had the opportunity to be part of the project, explore rather unreachable glaciers, and coauthor publications.

> **“Genomic and phylogenetic studies will allow us to look back in time as well as peek into the future.”**
>
> **—Tom Battin**

"We relied on local partners because they had the knowledge we did not have," says Battin. "But the networks we built brought mutual benefits." The Vanishing Glaciers project researchers ran seminars at the Russian Academy of Sciences and the ASIAQ Greenland Survey, for instance. "In Uganda, I taught school kids about glaciers in Africa, how they respond to climate change, and how all this affects microbial life," says Battin. "An opportunity to learn about this invisible life they would otherwise not have."

"One of the NOMIS Foundation's most important objectives is to enable transformational and interdisciplinary research and discoveries through collaboration. Nurturing connections—across research disciplines as well as geographies and institutions—is essential if we are to accelerate innovation and discovery," says Reinhard.

Rosemary Nalwanga is an environmental microbiologist at the College of Natural Sciences at Makerere University, Uganda. She has known about Uganda's glaciers in the Rwenzori Mountains all her life. Yet, it wasn't until Battin visited Makerere University to talk about the Vanishing Glaciers project and organize an expedition to sample Ugandan glaciers that she had the chance to explore the mightiness and greatness of the Rwenzori Mountains. "The expedition was very exciting and eye-opening for me," says Nalwanga. "I could undertake so many scientific studies. The Rwenzori Mountains have various physical–chemical, floral, and fauna features at different altitudes, which can be key benchmarks for climate change."

"This project has been a unique opportunity to build community within the field and raise interest in glacier biodiversity. Without the partnership with the NOMIS Foundation, this would not have been possible," says Battin.

Battin's team has done an excellent job of generating enthusiasm and support for the project among their peers, says Hotaling. "The Vanishing Glaciers project represents a nice example of how science, which is typically very competitive, can proceed in a way that 'lifts all boats,'" he says. "I believe my own glacier biodiversity research will be better because this project happened."

The Vanishing Glaciers project's success is due to massive collaborative efforts that brought together people from diverse cultures and scientific backgrounds, each with their own skills, knowledge, and talents. "This project undoubtedly paves the way forward for future studies aiming at better understanding and predicting the consequences of global warming on river biodiversity," says Ezzat. "We hope it will raise awareness among policymakers and governments on the pervasive effects of global warming on aquatic ecosystem biodiversity."

"Vanishing Glaciers has, through the team's ingenuity, diverse expertise, openness, and perseverance, proved itself a groundbreaking research endeavor—one that will transform our perception of life on Earth," says Reinhard.

About the Project

bit.ly/vanishing-glaciers

Sponsored by

NOMIS
FOUNDATION
Creating the Spark

NEWS

Edited by
Jeffrey Brainard

CONSERVATION

Life can thrive in a partially logged forest, study finds

Forest plants and animals can thrive in selectively logged areas, calling into question their designation as degraded ecosystems, a study in Malaysia has found. An international team of researchers studied differences among an intact old forest, partly logged forest areas, and sites cleared for oil palm plantations, all of them in Sabah state on northern Borneo. The scientists used data—gathered over 12 years by the Stability of Altered Forest Ecosystems project, one of the world's largest ecological studies—about local plant productivity, animal populations, and what they ate. In each plot, the team calculated how photosynthetic energy flows through the ecosystem, a measure of its vitality and resilience. The selective logging created open space that fostered plant growth, which led to a 2.5-fold increase in consumption of vegetation by animals compared with the old-growth forest, the researchers report this week in *Nature*. The diversity of birds and mammals stayed roughly the same. In the monoculture palm plantations, animals consumed as much as in the old-growth forest, but their species diversity plummeted. The research was funded primarily by the U.K. Natural Environment Research Council.

Old-growth rainforest on Borneo is logged to make room for oil palm plantations.

Wellcome head moves to WHO

LEADERSHIP | Jeremy Farrar, director of the Wellcome Trust since 2013, will become the new chief scientist at the World Health Organization in early 2023. At Wellcome, Farrar oversaw one of the world's biggest nongovernmental science funders, expanding its portfolio from basic research into areas including mental health, the health impacts of climate change, and infectious diseases, including groundbreaking clinical trials for vaccines and treatments during the devastating Ebola outbreak in West Africa. Before leading Wellcome, Farrar, a trained neurologist, spent nearly 2 decades heading a Wellcome-funded infectious disease research group in Ho Chi Minh City, Vietnam.

Museum head pushes for diversity

PUBLIC ENGAGEMENT | The American Museum of Natural History last week named as its new president biochemist Sean Decatur, who will be the first African American to lead the institution. "It matters," says Decatur, now president of Kenyon College. "It's important for an institution to reflect the broader diversity of the community it serves." In April 2023, he will succeed lawyer Ellen Futter, the first woman to lead the 153-year-old institution. The 54-year-old Decatur sees expanding its dual roles in research and education as the logical next step in a career spent at liberal arts colleges.

California postdocs ratify deal

LABOR RELATIONS | Postdoctoral researchers and non–tenure-track staff scientists in the University of California system ended their nearly monthlong strike on 9 December after voting to ratify new contracts. The terms guarantee that postdocs' minimum salary will rise to $71,490 by October 2026. The pact also improves

PHOTO: TRISTAN SAVATIER/GETTY IMAGES

> “If your infection spreads … don’t feel guilty. Infection will be a common phenomenon in the future, it is inevitable.”
>
> **Feng Zijian of the Chinese Preventive Medicine Association**, quoted by the Sina Finance website, speaking to university students after China relaxed zero-COVID controls.

benefits such as family leave and child care subsidies. Staff scientists would receive raises of up to 4.5% each year over the contract’s 5-year term. Graduate student researchers and teaching assistants, who make up 36,000 of the 48,000 workers who began the strike—the largest of its kind in the United States—remain on the picket line to press their case that their existing salaries don’t provide a living wage in California. Sacramento Mayor Darrell Steinberg was brought in this week to mediate what the university described as a “negotiation gridlock.”

Zantac lawsuits fail over science

PRODUCT LIABILITY | Thousands of consumers who sued makers of the popular heartburn drug Zantac, alleging it caused them to develop cancer, failed to present a reliable scientific basis for their claims, a U.S. District Court judge in Florida said when she dismissed their lawsuits last week. In 2020, the Food and Drug Administration requested recalls of the product after research found its original active ingredient, ranitidine, could over time and in certain storage conditions develop unsafe levels of an impurity, the compound N-Nitrosodimethylamine, categorized as a probable human carcinogen. (Zantac’s makers switched out the compound that year.) But Judge Robin Rosenberg said experts hired by the plaintiffs did not establish that ranitidine causes cancer. The pharmaceutical giants GSK, Pfizer, and Sanofi, which have made Zantac, were among the defendants in the more than 50,000 claims covered by her ruling. The decision does not directly affect thousands more such lawsuits in state courts.

Portal speeds access to U.S. data

STATISTICS | Researchers can now use a single website to request access to more than 1000 restricted data sets maintained by 16 U.S. agencies. The Standard Application Process was launched on 8 December at researchdata.gov. It is expected to make it faster and easier for scientists to analyze U.S. education, health, labor, housing, and demographic trends from data sets otherwise inaccessible to the public because they involve national security, intellectual property, or personal privacy. Researchers still must be vetted before being granted access. But those seeking data from multiple agencies won’t have to re-enter basic information about themselves and their research teams, and reviewers vetting the application will apply the same criteria regardless of which agency holds the data set. Nick Hart of the Data Foundation says he welcomes the one-stop shopping. But he calls for more improvements, including a publicly accessible catalog of all federal data now being collected, to satisfy a 2018 law promoting evidence-based policymaking through better use of federal data.

Methane studies need beefing up

CLIMATE SCIENCE | Belching cows emit much of the methane emitted in the United States, but research on how to lessen this source of greenhouse gas is underfunded, a report suggests. Agricultural lands provide roughly one-tenth of all U.S. climate-altering emissions, and 28% of this agricultural portion comes from methane created by feed fermenting in the multichambered stomachs of cattle, sheep, and goats. But research to reduce livestock emissions—by supplementing their feed with red seaweed, for example—has received just $2 million of the $241 million that U.S. federal agencies spend each year for agricultural research to mitigate the effects of climate change, according to an analysis released this week by the Breakthrough Institute, a nonprofit environmental think tank. The report found that between 2017 and 2021, most agricultural R&D funding on climate went to studying carbon sequestration by soils and crops.

Perlemoen abalone, newly listed as endangered in the wild, are farm raised in South Africa.

PHOTO: PETER CHADWICK/SCIENCE SOURCE

CONSERVATION

Many abalone species may face extinction

Facing numerous risks, 20 species of abalone—shellfish highly prized as seafood—have been added to the International Union for Conservation of Nature’s (IUCN’s) Red List of species threatened with extinction. Abalone are marine snails that can live for several decades and grow up to 30 centimeters long. For the first time, researchers consulting for IUCN reviewed the conservation status of all 54 species and identified overharvesting, including poaching, as a key threat. For example, criminal networks have pushed populations of South Africa’s perlemoen abalone (*Haliotis midae*) to the brink. Marine heat waves linked to climate change have hammered other species. Diseases, such as withering syndrome, are also hitting some species, including the critically endangered black abalone (*H. cracherodii*) in California and Mexico. Consumers should buy farmed or sustainably harvested abalone, says Howard Peters of the University of York, who led the review team.

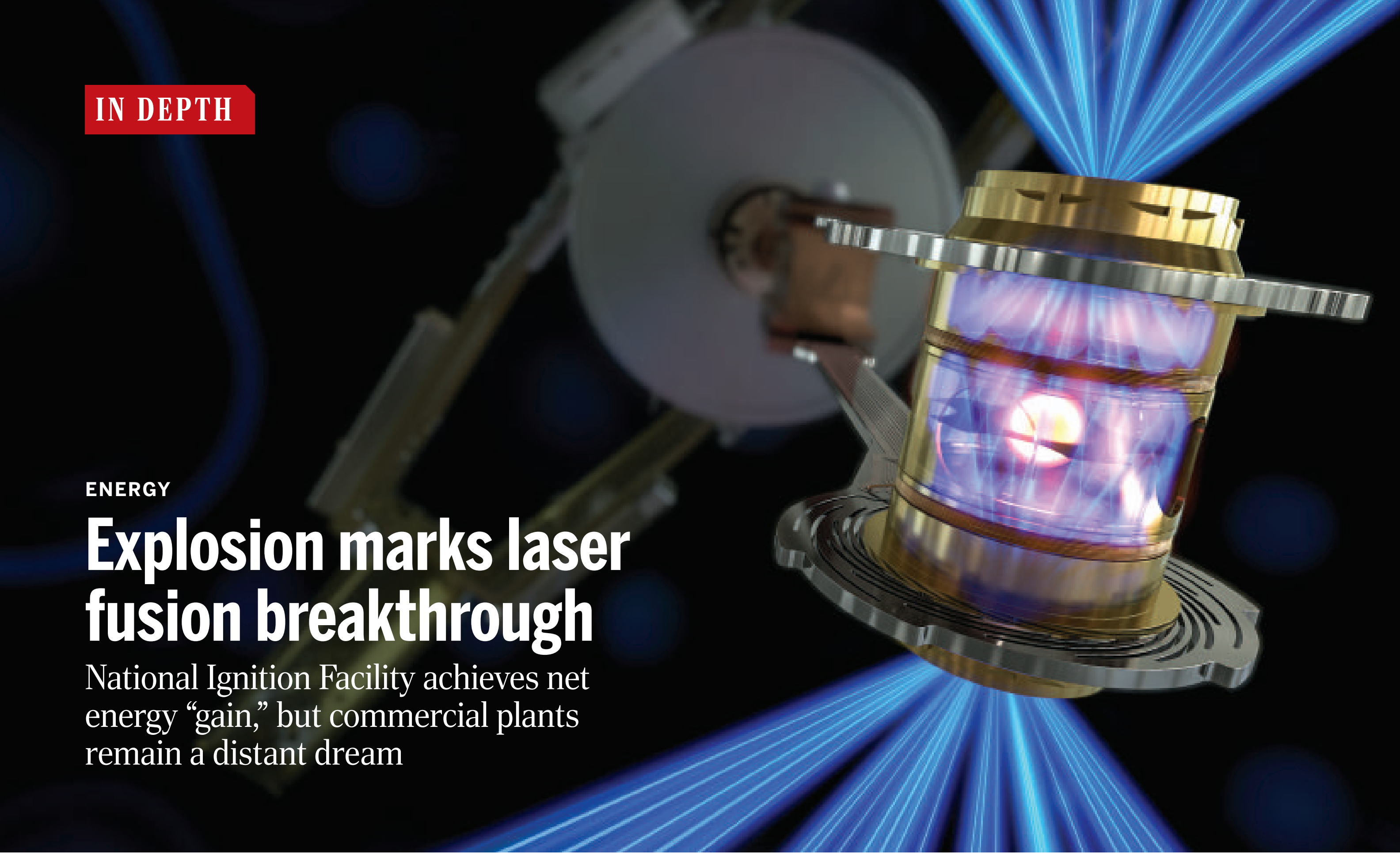

ENERGY

Explosion marks laser fusion breakthrough

National Ignition Facility achieves net energy "gain," but commercial plants remain a distant dream

At Lawrence Livermore National Laboratory, 192 laser beams heat a tiny gold can, which emits x-rays that implode a fuel capsule at its center (artist's conception).

By **Daniel Clery**

More energy out than in. For 7 decades, fusion scientists have chased this elusive goal, known as energy gain. At 1 a.m. on 5 December, researchers at the National Ignition Facility (NIF) in California finally did it, focusing 2.05 megajoules of laser light onto a tiny capsule of fusion fuel and sparking an explosion that produced 3.15 MJ of energy—the equivalent of about three sticks of dynamite.

"This is extremely exciting, it's a major breakthrough," says Anne White, a plasma physicist at the Massachusetts Institute of Technology, who was not involved in the work. Mark Herrmann, who leads NIF as the program director for weapons physics and design at Lawrence Livermore National Laboratory, says it feels "wonderful," adding: "I'm so proud of the team."

The result, announced this week by officials at the U.S. Department of Energy (DOE), represents a shot in the arm for fusion researchers, who have long been criticized for overpromising and underdelivering. Fusion holds the tantalizing promise of plentiful, carbon-free energy, without many of the radioactive headaches of fission-driven nuclear power. But getting hydrogen ions to fuse into helium and release energy requires temperatures of millions of degrees Celsius—conditions that are hard to achieve and sustain. The NIF result shows it is possible, at least for a fraction of a second. "Three megajoules is a hell of a lot of energy. It shows something is working," says plasma physicist Steven Rose of Imperial College London.

Despite the fanfare, fusion power stations are still a distant dream. NIF was never designed to produce power commercially. Its primary function is to create miniature thermonuclear explosions and provide data to ensure the U.S. arsenal of nuclear weapons is safe and reliable. Many researchers believe furnacelike tokamaks are a better design for commercial power because they can sustain longer fusion "burns." In a tokamak, microwaves and particle beams heat the fuel and magnetic fields trap it. "The challenge is to make it robust and simple," White says.

> **"The physics phenomenon has been demonstrated."**
>
> **Riccardo Betti**, University of Rochester

However, the leading tokamak device, the ITER reactor under construction in France, is anything but simple. It is vastly overbudget, long overdue, and will not generate energy until the late 2030s at the earliest. With NIF's new success, proponents of such laser-based "inertial fusion energy" will be pushing for funding to see whether they can compete with the tokamaks.

The $3.5 billion NIF began its "ignition" campaign in 2010. Its laser, housed in a building the size of three U.S. football fields, delivers a powerful, nanoseconds-long infrared pulse split into 192 beams that are converted to ultraviolet light. The beams are focused on the target—a gold can the size of a pencil eraser containing a peppercorn-size fuel capsule. Heated to millions of degrees, the gold emits x-rays that vaporize the diamond shell of the capsule. The blasted diamond implodes the fuel, compressing and heating it.

If the compression is symmetrical enough, fusion reactions in a central hot spot propagate smoothly outward through the fuel, with the heat from fusion sparking more burning. That self-sustaining burn defines ignition, and NIF scientists declared they had achieved it after a shot in August 2021 produced 70% of the input laser energy. But DOE's National Nuclear

PHOTO: NATIONAL IGNITION FACILITY/LAWRENCE LIVERMORE NATIONAL LABORATORY

Security Administration set NIF's goal as an energy gain greater than one—the threshold it passed last week.

Going that extra mile wasn't easy. After the August 2021 shot, the NIF team found it couldn't repeat it. Using a smooth diamond capsule turned out to be key: The one from August 2021 had been the smoothest and roundest to date. "We had to learn how to make the capsules better," Herrmann says. The team also made the capsule slightly thicker, which provided more momentum for the implosion but required a longer, more powerful laser pulse. So they tweaked the laser to squeeze out more juice, upping the energy from 1.9 MJ to 2.05 MJ.

A shot in September produced 1.2 MJ, showing the NIF researchers they were on the right track, but the symmetry was poor: The fuel was squashed into a pancake rather than a tight ball. By adjusting the energy among the laser's 192 beams, they were able to get a more spherical implosion, and last week they finally hit the jackpot. "The physics phenomenon has been demonstrated," says Riccardo Betti of the Laboratory for Laser Energetics at the University of Rochester.

If gain means producing more output energy than input electricity, however, NIF fell far short. Its lasers are inefficient, requiring hundreds of megajoules of electricity to produce the 2 MJ of laser light and 3 MJ of fusion energy. Moreover, a power plant based on NIF would need to raise the repetition rate from one shot per day to about 10 per second. One million capsules a day would need to be made, filled, positioned, blasted, and cleared away—a huge engineering challenge.

The NIF scheme has another inefficiency, Betti says. It relies on "indirect drive," in which the laser blasts the gold can to generate the x-rays that actually spark fusion. Only about 1% of the laser energy gets into the fuel, he says. He favors "direct drive," an approach pursued by his lab, where laser beams fire directly onto a fuel capsule and deposit 5% of their energy.

A program to develop inertial fusion energy could explore the two approaches, but DOE has never funded one. In 2020, the agency's Fusion Energy Sciences Advisory Committee recommended it should, in a report co-authored by Betti and White. "We need a new paradigm," Betti says, but "there is no clear path how to do it."

Now that NIF has cracked the nut, researchers hope laser fusion will gain credibility and more funding may flow. After the long slog to get here, Betti is savoring the moment. "This is a very important first step," he says, joking, "We've done it now, so I can retire." ■

SCIENTIFIC INTEGRITY

Paleontologist accused of fraud in paper on dino-killing asteroid

A former collaborator claims Robert DePalma fabricated data so he could scoop her on a high-profile study

By **Michael Price**

In June 2021, paleontologist Melanie During submitted a manuscript to *Nature* that she suspected might create a minor scientific sensation. Based on the chemical isotope signatures and bone growth patterns found in fossilized fish collected at Tanis, a fossil site in North Dakota, During had concluded the asteroid that ended the dinosaur era 65 million years ago struck Earth when it was spring in the Northern Hemisphere.

But During, a Ph.D. candidate at Uppsala University (UU), received a shock of her own in December 2021, while her paper was still under review. Her former collaborator Robert DePalma, whom she had listed as second author on the study, published a paper in *Scientific Reports* reaching essentially the same conclusion, based on an entirely separate data set. During, whose paper was accepted by *Nature* shortly afterward and published in February, suspects that DePalma, a Ph.D. student at the University of Manchester, wanted to scoop her—and made up the data to stake his claim.

Robert DePalma published a paper in 2021 showing the asteroid that ended the dinosaur era struck in spring.

After trying to discuss the matter with *Scientific Reports* editors for nearly a year, During and her supervisor, UU paleontologist Per Ahlberg, recently shared their concerns with *Science*. On 3 December, During also posted a statement on the journal feedback website PubPeer saying, "we are compelled to ask whether the data [in the DePalma paper] may be fabricated, created to fit an already known conclusion." (She later posted the statement on the OSF Preprints server as well.) And on 9 December, During and Ahlberg filed a complaint with the University of Manchester alleging potential research misconduct against DePalma and his supervisor there, Phillip Manning.

The plotted line graphs and figures in DePalma's paper contain numerous irregularities, During and Ahlberg claim—including missing and duplicated data points and nonsensical error bars—suggesting they were manually constructed, rather than produced by data analysis software. DePalma has not made public the raw, machine-produced data underlying his analyses; During and Ahlberg question whether they exist.

DePalma vehemently denies any wrongdoing. "We absolutely would not, and have not ever, fabricated data and/or samples to fit this or another team's results," he wrote in an email to *Science*. He says the work described in *Scientific Reports* began long before During became interested in the topic and was published after extended discussions over a joint paper went nowhere. "Ultimately, both studies, which appeared in print within weeks of each other, were complementary and mutually reinforcing," he says. The raw data are missing, he says, because the scientist who ran the analyses died years prior to the paper's publication and DePalma has been unable to recover them.

Several independent scientists consulted by *Science* agreed DePalma's paper contains suspicious irregularities, as well as typos, unresolved proofreader's notes, and several basic notation errors, and most were surprised it was published in the first place. Although they stopped short of saying the irregularities clearly point to fraud, most—but not all—said DePalma's team must come up with the raw data to clear itself.

"Something is fishy here," says Mauricio Barbi, a high energy physicist at the University of Regina who specializes in applying physics methods to paleontology. "If they can provide the raw data, it's just a sloppy paper. If not, well, fraud is on the table."

PHOTO: TAYLOR MICKAL/NASA

"The bottom line is that this case will just involve bluster and smoke-blowing until the authors produce a primary record of their lab work," adds John Eiler, a geochemist and isotope analysis expert at the California Institute of Technology. But two independent scientists who reviewed the data shortly after the paper's publication say they have no reason to distrust them.

On 9 December—3 days after *Science* first reported about the case online—*Scientific Reports* added an editor's note to DePalma's paper acknowledging the questions about its reliability. "Appropriate editorial action will be taken once this matter is resolved," the note said. Chief Editor Rafal Marszalek declined to share details.

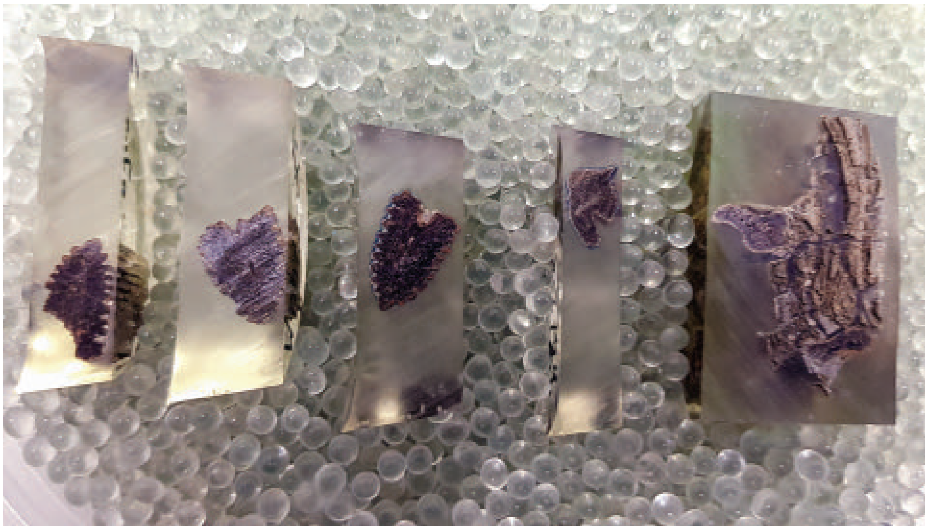

This paddlefish fossil from Tanis contained bits of glassy debris deposited shortly after the asteroid impact.

DURING SPENT 10 DAYS with DePalma at Tanis in 2017, when she was a master's student at the Free University of Amsterdam. DePalma, then a graduate student at the University of Kansas, Lawrence, holds the lease to the site, which is on private land, and controls access to it.

Part of the phenomenally fossil-rich Hell Creek Formation, Tanis sat on the shore of the ancient Western Interior Seaway some 65 million years ago. When the dino-killing asteroid struck Earth, shock waves would have caused a massive water surge in the shallows, researchers say, depositing sedimentary layers that entombed plants and animals killed in the event. "This was the most phenomenal site I've ever worked on," During says. "There was a fossil everywhere I turned."

After she returned to Amsterdam, DePalma sent her the samples she had dug up, mostly sturgeon fossils, as well as a partial paddlefish fossil he had excavated himself. During obtained extremely high-resolution x-ray images of the fossils at the European Synchrotron Radiation Facility that revealed tiny bits of glass called spherules—remnants of the shower of molten rock that would have been thrown from the impact site and rained down around the world.

The fact that spherules were found in the fishes' gills suggested the animals died in the minutes to hours after the impact. But the fossils also held clues to the season of the catastrophe, During found. A thin layer of bone cells on sturgeons' fins thickens each spring and thins in the fall, providing a kind of seasonal metronome; the x-rays revealed these layers were just beginning to thicken when the animals met their end, pointing to a springtime impact. And mass spectrometry revealed the paddlefish's fin bones had elevated levels of carbon-13, an isotope that is more abundant in modern paddlefish—and presumably their closely related ancient relatives—during spring, when they eat more zooplankton rich in carbon-13.

During described the findings in her 2018 master's thesis, a copy of which she shared with DePalma in February 2019. That same year, she began to prepare a journal article. During says she made repeated attempts to discuss authorship with DePalma, but he declined to join her paper. Still, when During submitted her manuscript to *Nature* on 22 June 2021, she listed DePalma as the study's second author.

DePalma characterizes their interactions differently. He says his team came up with the idea of using fossils' isotopic signals to hunt for evidence of the asteroid impact's season long before During came to Tanis. After his team learned about During's plan to submit a paper, DePalma says, one of his colleagues "strongly advised" her that the paper must "at minimum" acknowledge the team's earlier work and include DePalma's name as a co-author. DePalma says his team also invited During's team to join DePalma's ongoing study. "During the long process of discussing these options … they decided to submit their paper," he says.

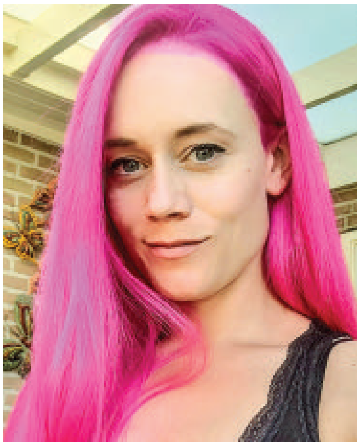

Melanie During suspects Robert DePalma made up data so he could scoop her.

DePalma submitted his own paper to *Scientific Reports* in late August 2021, with an entirely different team of authors, including Manning. "No part of During's paper had any bearing on the content of our study," DePalma says. *Science* asked other coauthors on the paper, including Manning, for comment, but none responded.

WHEN DE PALMA'S PAPER was published just over 3 months later, During says she soon noticed irregularities in the figures, and she was concerned the authors had not published their raw data. Ahlberg shared her concerns. At his suggestion, she wrote a formal letter to *Scientific Reports*. She also removed DePalma as an author from her own manuscript, then under review at *Nature*.

In a 6 January letter to the journal editor handling his manuscript, which he forwarded to *Science*, DePalma acknowledged he plotted the line graphs in his paper by hand instead of with graphing software, as is the norm in the field. He says he did so because the isotopic data had been supplied as a "non-digital data set" by a collaborator, archaeologist Curtis McKinney of Miami Dade College, who died in 2017. DePalma also acknowledged that the "manual transcription process" resulted in some "regrettable" instances in which data points drifted from the correct values, but "none of these examples changed the overall geometry of the plotted lines or affected their interpretation."

Miami Dade does not have an operational mass spectrometer, suggesting McKinney would have had to perform the isotope analyses underlying the paper at another facility. But McKinney's former department chair, Pablo Sacasa, says he is not aware of McKinney ever collaborating with laboratories at other institutions.

PHOTOS: MELANIE DURING

Asked where McKinney conducted his isotopic analyses, DePalma did not provide an answer. He did send *Science* a document containing what he says are McKinney's data. It features what appear to be scanned printouts of manually typed tables containing the isotopic data from the fish fossils. The data set "is viable for research work and remains within normal tolerances for usage," DePalma says, adding that its credibility had been verified by two outside researchers, paleontologist Neil Landman at the American Museum of Natural History and geochemist Kirk Cochran at Stony Brook University.

Both Landman and Cochran confirmed to *Science* they had reviewed the data supplied by DePalma in January, apparently following *Scientific Reports*'s request for clarification on the issues raised by During and Ahlberg. Cochran acknowledges that raw data produced by the mass spectrometer named in the paper's methods section would look different, but he says the format of the isotopic data does not appear unusual. "'Raw machine data' are seldom supplied to end users (myself included) who contract for isotope analyses from a lab that does them." Although the raw data should have been in DePalma's manuscript, "the 'bottom line' is that I have no reason to distrust the basic data or in any way believe that it was 'fabricated.'"

Eiler remains suspicious. If the data were generated in a stable isotope lab, "that lab had a desktop computer that recorded results," he says, and they should still be available. Barbi is similarly unimpressed. "They seem to have left the raw data out of the manuscript deliberately," he says, "which leads me to question the credibility of data." "There is a simple way for the DePalma team to address these concerns, and that is to publish the raw data output from their stable isotope analyses," adds University of Edinburgh paleontologist Steve Brusatte.

During and Ahlberg say they didn't get a formal response from *Scientific Reports* until 2 December, when the editor handling DePalma's paper informed them in an email that their concerns remain under investigation. The response did not satisfy During and Ahlberg, who want the paper retracted.

Eiler agrees. "If I were the editor, I would retract the paper unless [the raw data] were produced posthaste," he says. It is "certainly within the rights of the journal editors to request the source data," adds Mike Rossner, an independent scientist who investigates claims of biomedical image data manipulation. "And, if they are not forthcoming, there are numerous precedents for the retraction of scholarly articles on that basis alone." ■

MICROBIOLOGY

Exercise-crazy mice have their gut microbes to thank

Signal from bacteria may have same effect in people

By **Elizabeth Pennisi**

Willpower might be key to getting off the couch to exercise, but bacteria may lend a helping hand. Studies in mice reported this week in *Nature* suggest microbes in the gut may be behind differences in the desire to work out. A research team has homed in on specific microbial molecules that stimulate a rodent's desire to run—and keep running. By revealing exactly how these molecules talk to the brain, this group has set the stage for finding out whether similar signals help keep humans active.

The work "establishes just how critical the microbiome is for exercise and goes incredibly deep in providing a new gut-brain [connection]," says Aleksandar Kostic, a microbiologist at Harvard Medical School who is co-founder of FitBiomics, a company developing probiotics to improve fitness. Kostic, who wasn't involved in the research, and others speculate that exercise-inducing commands from the microbes might one day be packaged into pills people could take.

> **"So many different layers of discovery are rarely found in one paper."**
>
> **Sarkis Mazmanian**, California Institute of Technology

To explore why some people like to exercise and others don't, University of Pennsylvania microbiologist Christoph Thaiss studied mice bred to have a lot of genetic and behavioral variation. His team found more than a fivefold difference in how far the mice ran on wheels in their cages—some covered more than 30 kilometers in 48 hours, whereas others rarely moved in their wheels.

The active and lazy mice didn't show any significant differences in their genetics or biochemistry. But the researchers did notice one clue: When treated with antibiotics, mice that were normally highly energetic tended to exercise less. Follow-up studies showed the antibiotic treatment affected the brains of the formerly active mice. The activity of certain brain genes declined, along with levels of dopamine, a neurotransmitter that has been linked to "runner's high"—that sense of well-being that comes with prolonged exercise.

The team also found that "germ-free" mice, which lack gut bacteria, become more active when given some of the gut microbes from vigorous mice. It appears those bacteria send a signal that interferes with an enzyme responsible for breaking down dopamine in the brain, causing the neurotransmitter to build up in the brain's reward center.

By studying other mice bred to lack certain nerve cells and by chemically blocking the activity of nerves that relay messages from the gut to the brain, the team determined the dopamine-enhancing signal reaches the brain via nerves in the spine. By stimulating those nerves, the team was able to send that pro-exercise command even in mice lacking gut bacteria.

In the lab, Thaiss and colleagues dissected out these spinal nerves and exposed them to subsets of gut bacteria as well as substances the microbes produce. When they gave one set of these molecules, fatty acid amides, to mice whose gut microbes had been wiped out with antibiotics, dopamine levels surged in the animals' brains as they exercised. When a different bacterium was endowed with genes for making fatty acid amides and fed to germ-free mice, the mice again got a dopamine boost.

Microbiome researchers call the work a tour de force. "So many different layers of discovery are rarely found in one paper," says Sarkis Mazmanian, a microbiologist at the California Institute of Technology.

Will the finding hold in people? "I would be extremely cautious in extrapolating how these results are related to human physiology," says Juleen Zierath, a physiologist at the Karolinska Institute. Researchers note that rodents' muscle structure and biochemistry differ from people's—as do their activity patterns. And rodents don't make New Year's resolutions.

Still, studies have found that marathoners have high levels of a particular gut microbe, suggesting an exercise connection in people. And much work has demonstrated the key role dopamine plays in motivating overall behavior. As Kostic puts it, "This reward system is such a central facet of physiology that it's something that's almost certainly true in other mammals"—including humans. ■

Aid workers check a COVAX vaccine shipment after its arrival in Khartoum, Sudan, on 11 February.

COVID-19

Pandemic vaccine equity plan may soon start winding down

COVAX distributed 1.84 billion vaccine doses, but many came too late. Can the world do better next time?

By **Gretchen Vogel**

COVAX, the unprecedented global effort to distribute COVID-19 vaccines more fairly, is set to wind down over the next 2 years. On 8 December, the board of Gavi, the Vaccine Alliance—a key partner in the project—voted "in principle" to phase out much of its support for COVID-19 vaccines in middle-income countries starting in 2024, and to incorporate COVID-19 vaccinations into its regular vaccine programs for the poorest countries—if they still want them.

The decision isn't final, but critics of COVAX—many from poorer countries—would not mourn its demise. The effort has delivered some 1.84 billion vaccine doses to 146 countries, but many, if not most, arrived too late to have a big impact. "COVAX was completely useless for developing countries," says Claudia Patricia Vaca González, an expert on access to medicines at the National University of Colombia, Bogotá. "It was a failure and we should admit it," says Christian Happi, a molecular biologist at Redeemer's University in Ede, Nigeria.

Others have a more positive take. "Gavi and COVAX were in my mind transformational and inspirational in their aims," says Lawrence Gostin, an expert on global health law at Georgetown University. "It got a lot of shots in a lot of arms." Still, "I totally understand Gavi's reasoning," Gostin adds. Demand for COVID-19 vaccines dropped sharply after the pandemic ebbed, and Gavi wants to refocus on campaigns that have lagged during the crisis, including vaccination against the cancer-causing human papillomavirus, and ensuring no child fails to receive routine childhood vaccinations.

The COVID-19 Vaccines Global Access Facility, as COVAX is officially called, was formed in April 2020 as an alliance between Gavi, the World Health Organization (WHO), UNICEF, and the Coalition for Epidemic Preparedness Innovations. Its initial goal was to secure roughly 2 billion doses, enough to vaccinate 20% of the populations of low- and middle-income countries. That, leaders calculated, would be enough to cover health care workers and high-risk groups. (WHO later set a goal of fully vaccinating 70% of the population in developing countries by the middle of this year, but many experts say that was never really feasible—or necessary, given that young people are less likely to develop serious disease from COVID-19 and many developing countries have a median age below 20.) The plan was to pool resources and buy vaccines in bulk for both rich and poor countries. Participating countries would receive doses based on their population instead of their purchasing power.

But early in the pandemic, wealthy countries—including some COVAX members—bought up huge quantities of vaccines for themselves, at higher prices, leaving COVAX at the back of the line. "COVAX was built on the status quo of market dynamics: Whoever pays the most is first in line," says Victorine de Milliano, a policy adviser for the Doctors Without Borders Access Campaign. "COVAX missed out."

The initiative suffered another major setback in the spring of 2021 when India banned the export of vaccines in the middle of its deadly Delta wave. One of COVAX's main suppliers, the Serum Institute of India, suspended its delivery of 1.1 billion doses to COVAX. When COVAX did ship vaccines, they arrived unpredictably, making it difficult for recipient governments to plan effective vaccination campaigns.

By mid-November 2021, when most Western countries had fully vaccinated 70% of their populations or more and started to administer booster shots, COVAX had still only distributed about 500 million doses. Less than 2% of COVAX country populations were fully vaccinated with doses supplied by the program and 18 countries had not received any vaccines at all. (A Gavi spokesperson notes some successes, however: Some 81% of health care workers in COVAX-recipient countries are now fully vaccinated, and only eight countries still have vaccination rates below 10%.)

Meanwhile, demand for the vaccine has plummeted. Several big COVID-19 waves have come and gone, and the Omicron variants that started circulating early this year seemed to cause less severe disease.

With that in mind, a Gavi spokesperson says, the board moved to adopt a "planning framework" that focuses on seasonal boosting of high-risk groups rather than trying to cover entire populations. Starting in 2024, 37 middle-income countries would no longer receive free vaccines or extra support for their distribution. They would still be able to purchase vaccines through COVAX, however, and would receive a one-time sum to boost their ability to purchase and distribute them. Another 54 of the poorest countries would remain eligible for free vaccines and distribution support.

Last week's decision drew fire from some

PHOTO: EBRAHIM HAMID/AFP VIA GETTY IMAGES

observers, who say Gavi did not consult the affected countries. From the start of COVAX, "the countries that were going to benefit were not included in the decision-making. And now, in the wrap-up, they are again not included," de Milliano says. "It is very condescending for Gavi to think that they know better than the countries themselves," Happi says. (A WHO report about COVAX released in October acknowledged that low- and medium-income country governments "were insufficiently included" in planning, which hobbled the response.)

Gavi leaders emphasize that the board will discuss the topic further when it meets again in June 2023. In the meantime, Gavi will ask for input from affected countries, collect more data on the state of the pandemic, and assess how much difference vaccines can make in populations now that the virus has already swept through, says John-Arne Røttingen, a global health expert at the Norwegian Ministry of Foreign Affairs and a Gavi board member.

There's widespread agreement the world needs to do better the next time a pandemic requires a global vaccination drive. That will require a "major rethink," Vaca González says. "We can't just say, 'OK, we did our best. We didn't really achieve our goal, but let's wind it down,'" Gostin says. "We should have a COVAX 2.0 that goes beyond COVID and provides a far more robust way to ensure equitable access."

Making developing countries less dependent on donors is crucial, he and others say. Happi says a robust system "should support countries to produce the vaccine themselves rather than create a situation where there are donors on one end and recipients on the other."

WHO is taking some steps in that direction. In 2021, it established a hub in South Africa for transferring messenger RNA vaccine technology to companies in low- and middle-income countries. And at last week's meeting, the Gavi board voted to support "the development of a regionally diversified vaccine manufacturing ecosystem," including helping countries and companies decide which vaccines to make. It also is considering setting up a specific fund to purchase vaccines manufactured in Africa.

Making vaccines where they are needed is the way forward, says Gostin, who thinks it's unrealistic to expect wealthy countries not to put their own populations first. "Vaccine nationalism is a fact of life." Vaca González agrees. She says COVAX's basic premise—buying vaccines developed in wealthy countries from large pharmaceutical firms—was flawed from the start: "That was the original sin of COVAX." ■

PHOTO: RAWPIXEL/GETTY IMAGES

BIOMEDICAL RESEARCH

Sequencing projects will screen 200,000 newborns for disease

U.K. and New York City efforts face cost and ethical issues

By **Jocelyn Kaiser**

The once-futuristic idea of sequencing every newborn child's DNA to screen for genes that could shape their future health is being put to two major tests. The United Kingdom this week announced plans to sequence the genomes of 100,000 newborns for about 200 rare genetic diseases starting next year. In New York City, a similar project already underway will screen 100,000 babies.

The goal is to catch treatable diseases that standard newborn screening cannot detect. If sequencing delivers an early warning of a problem, the baby could receive care that averts permanent disability or even death.

Genome sequencing can reveal whether newborns carry any of hundreds of genetic diseases.

But sequencing the full genomes of newborns raises a host of ethical questions, including who will get access to the data, and whether it will needlessly worry parents by revealing genes that may never cause serious illness. "We're really cognizant of the complexity of the questions," says Richard Scott, chief medical officer for Genomics England, the government-funded company running the U.K. project. At the same time, he says, "There's a really pressing need" to detect more childhood diseases.

In many countries, a drop of blood from every newborn's heel is screened, using mostly biochemical tests, for up to several dozen genetic diseases. They range from metabolic disorders that can be treated with a special diet to muscle diseases that have drug treatments. Whole-genome sequencing, which is much costlier—up to $1000—but is getting cheaper, could detect many more disorders, such as thyroid conditions that can cause brain damage.

Genomics England's $129 million Newborn Genomes Programme will invite expecting parents in England who are receiving care through the National Health Service (NHS) to sign up starting in late 2023. The aim is to enroll 100,000 newborns over 2 years. To avoid raising the alarm about gene variants whose risk is uncertain or that only cause disease in adulthood, parents will only receive results for 200 treatable diseases caused by well-studied genetic variants that are almost certain to cause symptoms before age 5.

The project expects to spot at least 500 newborns with genetic disease. If such testing were used across the United Kingdom, researchers estimate it would find some 3000 babies per year with these diseases.

The project has public support, but some experts argue the money would be better spent on expanding standard U.K. screening, which now covers just nine diseases. Others say following up on the screening results will tax an already overstretched NHS. "It seems like the economics is the big unanswered question," says bioethicist Josephine Johnston of the Hastings Center.

The New York City project, launched in September, is led by Columbia University geneticist Wendy Chung and supported by two firms. The 4-year effort will sequence DNA from 100,000 newborns for about 160 treatable diseases. Parents can opt to add 100 neurodevelopmental disorders that can't be cured, but for which speech and physical therapy could help. Chung says her team consulted with "every voice I could think of" to ensure the project was ethically designed. So far, about 75% of 600 couples approached at New York-Presbyterian hospitals want to enroll, and most opt for the longer disease list.

Both studies, which will also track the care given to babies with problems, aim to help policymakers decide whether newborn sequencing should become routine. The vast reach of the U.K. health service "gives us the real strength to ask those questions," Scott says. In the United States, with its fractured health care system, such answers may be harder to get, Chung acknowledges. ■

2022 BREAKTHROUGH OF THE YEAR

GOLDEN EYE

A new space telescope makes a spectacular debut after a troubled gestation

By **Daniel Clery**

On 11 July, in a live broadcast from the White House, U.S. President Joe Biden unveiled the first image from what he called a "miraculous" new space telescope. Along with millions of people around the world, he marveled at a crush of thousands of galaxies, some seen as they were 13 billion years ago. "It's hard to even fathom," Biden said.

Not many telescopes get introduced by the president, but JWST, the gold-plated wunderkind of astronomy built by NASA with the help of the European and Canadian space agencies, deserves that honor. It is the most complex science mission ever put into space and at $10 billion the most expensive. And it did not come easy. Its construction on Earth took 20 years and faced multiple setbacks. New perils came during the telescope's monthlong, 1.5-million-kilometer journey into space, as its giant sunshield unfurled and its golden mirror blossomed. Engineers ticked off a total of 344 critical steps—any one of which could have doomed the mission had they gone wrong.

The first data and images beamed back to Earth by JWST suggest it was all worthwhile. They are "beautiful" and "mind-blowing," according to astronomers who have spoken with *Science*. It was like putting on infrared glasses, one said, and seeing the universe anew.

Because of the controversy surrounding the telescope's name (see p. 1145), *Science* now refers to it as JWST.

But those images only hint at what is to come. With the largest mirror ever flown in space and a suite of instruments sensitive to infrared light, JWST will peer further into the past than any predecessor, including the much smaller Hubble Space Telescope. It can reveal exquisite detail in closer objects and parse the atmospheres of alien worlds. Although papers started to pop up on preprint servers such as arXiv within days of data being released, firm results are still scarce. But few doubt the telescope will revolutionize our picture of the cosmos, and so we name JWST *Science*'s 2022 Breakthrough of the Year.

Space telescopes see the universe undistorted by Earth's atmosphere, whose shifting air causes stars to scintillate, or twinkle, and whose gas molecules block many wavelengths entirely, including much of the in-

IMAGE: NASA; ESA; CSA; STSCI; JOSEPH DEPASQUALE, ALYSSA PAGAN, AND ANTON M. KOEKEMOER/STSCI

JWST captures the birth of a star, only visible in the infrared light the telescope is designed to capture. (The image has been recolored.)

frared. The Hubble telescope showed the immense power of a mirror in space. Its data have fueled more than 22,000 papers.

But even before Hubble got off the ground in 1990, astronomers began to plan its successor. Next time, they wanted a telescope with infrared eyes. The earliest stars and galaxies in the universe, hot and newly formed, shine brightest at ultraviolet and visible wavelengths. But in the billions of years it took that light to travel across space to reach Earth, the universe itself expanded, stretching the light to longer—infrared—wavelengths. As a result, infrared light provides the best view of those early times.

Astronomers also wanted to capture enough light from the far reaches of the universe to separate it out into a spectrum of its constituent colors, which reveal what an object is made of and how it's moving. The spectrum of starlight passing through the atmosphere of an exoplanet, for example, carries the fingerprints of gases in the planet's atmosphere and hints as to whether conditions are favorable to life.

To do all that, astronomers drew up plans for a telescope with a huge mirror—JWST's is 6.5 meters across, nearly three times the width of Hubble's. That was too big to fit inside a rocket, so it had to be able to fold up for launch. Another challenge was keeping the whole telescope cold, to prevent its own warm glow from spoiling the infrared observations. So engineers devised an unfolding multilayered sunshield to keep it at an icy –233°C and a mechanical cryocooler to chill one instrument to –266°C. They also chose to make the mirror from toxic beryllium, rather than the usual glass, because it is light and performs better in the extreme cold.

The expense and complexity of these innovations nearly doomed the mission. Delays and costs mounted, leading the U.S. Congress to threaten the project with cancellation in 2011. Astronomers lobbied hard for JWST's survival, however, and lawmakers relented, setting a firm deadline and cost ceiling. NASA kept to those limits, for a while.

All those travails were forgotten on 25 December 2021 when a European Ariane 5 rocket deposited JWST in space. The telescope opened its solar arrays, and set off for a gravitational balance point far from the noise and warmth of the Sun and Earth. Over the next several months, engineers and astronomers watched nervously as the tennis court–size sunshield unfurled, mirror sections swung into place, and starlight passed through its instruments for the first time.

JWST began to collect data for scientists on 21 June, and NASA released the first images and spectra on 12 July. Within days researchers began to find galaxies more distant than any previously documented. Hubble's deepest images took more than 100 hours of observing, and the most distant galaxy it found was shining when the universe was just 3% of its current age of 13.8 billion years. But in just a dozen hours, JWST revealed a galaxy that pushed the record back another 50 million years and another galaxy possibly 100 million years earlier still. These ages are rough estimates and are only now beginning to be confirmed, but they show JWST can peer deep into the universe's galactic nursery.

Already, that nursery is looking crowded. JWST's initial glimpses revealed many more galaxies than researchers expected, shining more brightly. Broader surveys are now underway to see whether the crowding is an anomaly—a localized cluster of galaxies—or an artifact due to a telescope calibration issue or more recent galaxies shrouded in dust that reddens them and makes them look older. But if JWST shows that this era, soon after the universe's birth, is as bustling and bright as it appears, theorists will have to rewrite their accounts of the universe's early history to explain how so many galaxies could form so fast.

In September, JWST gave another taste of things to come when it focused on a planet orbiting another star, a young giant seven times the mass of Jupiter called HIP 65426 b. Most exoplanets are lost in the overwhelming brightness of the parent star, and only about 20 have been caught on camera to date. But by using an optical mask to block out the star's glare, JWST imaged HIP 65426 b at four different wavelengths. Capturing the planet's own glow will provide important clues to how planetary systems form. With JWST's sharp vision, researchers are looking forward to imaging smaller exoplanets, down to the size of Saturn or even Neptune.

And last month, the telescope captured the spectrum of starlight that filtered through an exoplanet's atmosphere—an extremely challenging task for other telescopes. The spectrum showed that WASP-39 b, a Saturn-mass planet orbiting close to a star 700 light-years from Earth, is shrouded by gases including water vapor, sodium, potassium, and carbon monoxide, as well as patchy clouds.

Earlier observations had hinted at some of these gases, but JWST picked up two others never previously detected around an exoplanet: carbon dioxide and sulfur dioxide. The sulfur dioxide signature was so strong that astronomers concluded ultraviolet light from the star is driving the formation of the gas, in the same way the Sun creates ozone in our atmosphere. It's the first evidence of photochemistry around an exoplanet and hints that as JWST continues to probe exoplanet atmospheres, it will deliver new surprises about these alien worlds.

As data continue to pour in from JWST and thousands of astronomers around the world work to mold them into concrete results, the pace of discoveries will accelerate. And they should keep coming for a good while. JWST's journey used far less fuel than expected, so the telescope has enough to hold it steady at its celestial vantage point well into the 2040s. For those riding the first wave, it's a time of wonders. As one astronomer said: "Every day I open up arXiv and there are fireworks in there." ■

VIDEO AND PODCAST
Interviews with JWST scientists and more: science.org/boty2022

A surprisingly massive microbe

The discovery of a giant bacterium with complex innards shook biology this year. Microbes are supposed to be microscopic, but this one, tentatively dubbed *Thiomargarita magnifica*, can be 5000 times bigger than many bacterial cells—as long as a pushpin. The single, threadlike cells were first spotted on the surfaces of dying leaves in a mangrove swamp in the French Antilles.

Bacteria need to be tiny, researchers thought, because they lack the internal transport systems found in other cells and depend on diffusion to move nutrients and wastes. Diffusing molecules can't travel very far, limiting how big a bacterium can be—or so the thinking went. Textbooks also say bacteria typically lack internal compartments, but *T. magnifica* has several, researchers reported in February.

One is a water-filled sac that may have allowed the microbe to become a macrobe. It pushes all the cell's proteins and other components against the outer cell envelope, putting them in range of oxygen, sulfur, and other essential molecules diffusing in and out of the cell. By adding customized amino acid building blocks to the bacteria and tracing their incorporation into proteins, the researchers demonstrated that protein production takes place near the periphery of the cell. A few other bacteria, including one no bigger than a poppy seed found off the Namibian coast in 1999, have similar structures.

The long, threadlike cells of *Thiomargarita magnifica* challenge traditional definitions of bacteria.

Other features appear to be unique to *T. magnifica*. The DNA of virtually all other known bacteria floats freely in their cells, but *T. magnifica* packages its huge 12-million-base genome into membranous sacs the researchers call pepins, along with the molecular machinery for making proteins. And whereas most bacteria produce the energy molecule ATP in their cell envelope, *T. magnifica* has a whole network of internal membranes that also make ATP, enabling it to produce enough fuel for such a large cell.

These structures shake up the traditional division of life into eukaryotes and prokaryotes. Eukaryotes include plants, animals, and other organisms with complex cells that segregate their components into membrane-lined compartments called organelles. Prokaryotes include bacteria and other single-celled organisms that lack organelles and have sometimes been characterized as simply "bags of proteins." *T. magnifica* seems to represent something in between—perhaps mirroring transitional forms that evolved billions of years ago. —*Elizabeth Pennisi*

PHOTOS: (TOP TO BOTTOM) COSTFOTO/FUTURE PUBLISHING/GETTY IMAGES; TOMÁŠ TYML

By making seasonal replanting unnecessary, perennial rice could save farmers weeks of hard work each year.

Perennial rice promises easier farming

The world's major food crops—rice, wheat, corn—must be planted anew for every harvest. That's a lot of work for farmers and can contribute to environmental problems such as soil erosion. Perennial grains that survive and produce year after year could ease the burden, but breeding plants that are long-lived and productive enough has been a challenge. This year, researchers in China showed perennial rice can meet those benchmarks and save farmers many weeks of backbreaking labor.

Called Perennial Rice 23 (PR23), the variety was created years ago by crossing a commercial variety of Asian rice with a perennial wild rice that grows in Africa. Improving its yield and quality took more than 2 decades. Finally, in 2018, researchers at Yunnan University and other institutions released PR23 to farmers in China, enlisting them in a large-scale experiment to find out how many times the rice can be harvested and measure the yield and other benefits.

PR23 yielded just as much grain as regular, seasonally planted rice, the team reported last month in *Nature Sustainability*. In the first year, planting and cultivation cost about the same. But in the second year, farmers could eliminate a major task: transplanting young rice seedlings into a paddy, grueling work often done by women and children. Skipping this step, thanks to the perennial rice, reduced the amount of work per hectare by as much as 77 person-days each season, and helped lower farmers' costs by half. Soil nutrients also increased in the fields containing perennial rice. By the fifth year, however, yields dropped so much the perennial rice needed to be replanted.

More and more farmers are cultivating PR23, thanks to technical assistance from Yunnan University and government promotion. More than 15,000 hectares were planted in southern China last year, a fourfold increase from 2020. PR23 and similar varieties are being tested in Africa as well. Perennial rice could also reduce soil erosion in the terraced uplands of Southeast Asia. But plant breeders still need to develop a strain adapted to that environment's drier and less fertile soil. Researchers also worry about long-term impacts. One concern is that weeds and pathogens will accumulate in the unplowed fields, requiring more herbicide than conventional rice does. Another question is whether the rice emits more nitrous oxide—a potent greenhouse gas. But as cultivation spreads, the costs and benefits of perennial rice should come into focus. *—Erik Stokstad*

Black Death's legacy detected in the genes of Europeans

Ever since the Black Death killed one-third to one-half of the people living in Europe 700 years ago, researchers have wondered how the deadly plague left its mark on survivors. Such a devastating pandemic must have acted as a potent selective force, favoring people with particularly effective immune defenses. But detecting its legacy has been impossible in living people because our immune genes change frequently in response to new pathogens.

This year, researchers harnessed tools for studying ancient DNA to look at differences in immune genes in the very people who lived and died during the plague—and identified a dramatic effect. The team analyzed ancient DNA from the bones of more than 500 people buried before, during, and after the Black Death in London and Denmark. In October, they reported in *Nature* that survivors were much more likely to carry gene variants that boosted their immune response to *Yersinia pestis*, the flea-borne bacterium that causes the plague.

An astonishing 245 gene variants rose or fell in frequency after the Black Death in London; four of them also changed in ancient DNA from people in Denmark. One gene in particular stood out: *ERAP2*. It encodes a protein called endoplasmic reticulum aminopeptidase 2, which has been shown to help immune cells recognize and fight threatening viruses.

The team found two variants of *ERAP2* that differ by just one letter in the genetic code. One produces a full-size protein, the other a truncated version. People who inherited two copies of the variant encoding the full-size protein were twice as likely to have survived the plague as those who inherited two copies of the other variant. The researchers also cultured immune cells from 25 modern-day British people in the lab, and found that cells with the full-size, protective version of *ERAP2* produced more immune system proteins called cytokines when exposed to *Y. pestis*.

Ancient DNA from 14th century bones buried in a London cemetery recorded changes in immune genes.

The fast spread of this protective gene variant in Europe during the century after the Black Death is the strongest example yet of natural selection on the human genome. The protective variant of *ERAP2* is still found in 45% of British people today. Its persistence suggests it continued to be favored by natural selection until recently—probably because the plague was endemic in Europe and Asia until the early 19th century. But this protection may have a price: The same variant also confers a higher risk of developing autoimmune diseases, such as Crohn's disease and rheumatoid arthritis.
—Ann Gibbons

PHOTO: MUSEUM OF LONDON ARCHAEOLOGY

DNA from soil revealed a unique plant and animal community in Greenland 2 million years ago.

ILLUSTRATION: BETH ZAIKEN/BETHZAIKEN.COM

Ancient ecosystem reconstructed from 2-million-year-old DNA

Until recently, DNA's shelf life was pegged at about 1 million years. Genetic material much older than that presumedly would be too badly degraded to read. This year, scientists wound back the clock further than they once thought possible, extracting tiny DNA snippets at least 2 million years old from frozen soil in an Arctic desert.

The study, hailed as a tour de force, demonstrates the power of environmental DNA, or eDNA, to reconstruct lost worlds: in this case, a coastal forest unlike any in existence today that flourished during a warm climate episode at the tip of northern Greenland. DNA fragments in 41 organic-rich samples from a thick layer of sediment heaped at the mouth of a fjord revealed a lush forest of poplars, thujas, and other conifers; black geese and horseshoe crabs; and mammals such as reindeer, lemmings—and mastodons. No one had expected the range of this extinct relative of elephants to extend that far north.

What preserved the DNA over the ages was not only the natural icebox of permafrost, but also grains of quartz and clay, especially smectite, whose charged surfaces bound and protected the DNA. The team spent years honing techniques for prizing DNA snippets from the minerals and then decoding them with high-throughput sequencing.

The findings raise the prospect of extracting eDNA at other high Arctic sites, where fossils are scarce. But the further back in time paleogeneticists delve, the harder it will be to identify some species—especially those in dead-end lineages whose genomes likely bear scant resemblance to contemporary species.

Profiling eDNA from ancient sediments could pay off by revealing genetic adaptations that allowed plants and animals to thrive in the far north at temperatures warmer than today's. More controversially, novel gene sequences might even be plucked out of ancient genomes and, using CRISPR gene editing, stitched into present-day life forms—to help crops germinate earlier, for example. The prospect of resurrecting ancient genes is bound to make many scientists uncomfortable—but proponents argue the looming climate crisis demands drastic interventions.

—Richard Stone

RSV vaccines near the finish line

Large scale clinical trials of two vaccines against respiratory syncytial virus (RSV) have finally proved they can safely protect the two groups hardest hit by this common infection: infants and the elderly. Both vaccines prevented severe disease in people over age 60 without causing serious side effects. One also protected infants for 6 months when given to their mothers late in pregnancy, so they could pass the antibodies to their fetuses.

RSV usually only causes mild, coldlike symptoms, but in babies the virus can inflame small airways in the lungs, and in the elderly, it can worsen existing lung and heart conditions. RSV vaccine development was derailed for decades after a clinical trial of an experimental candidate more than 50 years ago killed two children and hospitalized 80% of those who received it. Scientists subsequently figured out the key reason: Made from a chemically inactivated version of the entire virus, the vaccine only elicited relatively weak antibodies, which not only failed to stop the virus, but, through little-understood mechanisms, helped RSV damage airways.

The new vaccines avoid this problem by relying on a key advance made by Barney Graham and co-workers at the National Institute of Allergy and Infectious Diseases in 2013. A viral surface protein used in the vaccines changes its shape after it docks onto a cellular receptor and the virus fuses with the cell, establishing an infection. Led by Graham, who is now at the Morehouse School of Medicine, the team figured out how to lock the protein into its prefusion state. As a result, vaccination triggers far higher levels of potent antibodies.

The good news from this year's trials, run by GSK and Pfizer, vindicated that strategy. More results will come soon: Janssen Pharmaceuticals and Bavarian Nordic have efficacy trials underway of their own RSV vaccines for older adults. Both vaccines performed well in the earlier phases of development.

Developers remain skittish because of past disappointments: GSK in February stopped its maternal RSV vaccine after unspecified "safety signals" surfaced in clinical trials. But none of the other studies has reported red flags to date, and several of the candidate vaccines could receive approval from regulators around the world next year. *—Jon Cohen*

Vaccines against RSV could help keep infants out of intensive care units.

PHOTOS: (LEFT TO RIGHT) MARIJAN MURAT/PICTURE ALLIANCE/GETTY IMAGES; NASA/JOHNS HOPKINS APL

Asteroid deflected

For thousands—if not millions—of years, a little moon named Dimorphos made laps around a larger asteroid, millions of kilometers from Earth. On 26 September, NASA smacked into it with a spacecraft, forever altering its orbit—and demonstrating a strategy that might one day save humanity.

When the fridge-size Double Asteroid Redirection Test (DART) satellite barreled into the 160-meter-wide Dimorphos at 6 kilometers per second, scientists celebrated the first-ever mock trial of a planetary defense mission. NASA's goal was to knock Dimorphos slightly closer to its partner, shortening its orbital period and demonstrating a strategy for thwarting real threats, should future Earth-bound asteroids be detected.

For years leading up to the big event, scientists ran computer simulations and blasted small-scale replicas of asteroids with projectiles to forecast how much momentum would be transferred. Predictions varied widely, depending in part on whether the target was a monolithic rock or a gravity-bound heap of rubble.

In the minutes leading up to the final collision, DART's onboard cameras streamed images of Dimorphos (above), which the ever-closer view revealed to be an egg-shaped rubble pile. Two weeks after the impact, scientists compiled observations to confirm that the moon's nearly 12-hour orbit had shortened by 32 minutes—a change more than 26 times larger than NASA had set as its goal. The collision was a one-off, but it gives scientists a crucial data point for the momentum models they would use to design any future asteroid-deflection missions.

So far, however, astronomers have only detected about 40% of the estimated 25,000 near-Earth asteroids large enough to decimate a large city and common enough to pose a threat. The Near-Earth Object Surveyor, a long-anticipated space-based infrared telescope, would help locate more of these bodies, but it has faced repeated funding cuts and delays from NASA. DART's bull's-eye has shown what's possible, but a capable planetary defense system will also require more intelligence about the threat. *—Zack Savitsky*

Artist Jason Allen's prize-winning work, *Théâtre D'opéra Spatial*, was created using text-to-image artificial intelligence.

United States passes landmark climate law

For decades, U.S. scientists have led the world in documenting the risks of climate change, and U.S. diplomats have cast global warming as a dire threat in international fora. Those warnings rang hollow, though, because unlike many wealthy countries, the world's second largest producer of greenhouse gases had never passed a law to substantially reduce those emissions. This summer, attempts to pass such a bill appeared doomed to fail yet again.

Then, in a legislative instant, it all changed when a key senator suddenly dropped his opposition. The climate provisions of the so-called Inflation Reduction Act (IRA) amount to the biggest step the United States has ever taken to slow global warming. The legislation provides $369 billion over 10 years to support electricity from renewable sources and nuclear power, while also spurring a wholesale move to electric vehicles and research into ways to reduce industrial emissions. Several independent research groups have calculated it should put the United States on track to cut its greenhouse gas emissions by 40% from 2005 levels by decade's end.

New U.S. climate legislation will subsidize renewable energy sources, including solar.

Yet the IRA alone is not enough for the United States to meet its commitment under the 2016 Paris agreement to cut emissions by 50% by 2030. For that to happen, analysts say, individual states will have to increase their clean energy generation. The Environmental Protection Agency will also have to issue, and enforce, long-expected greenhouse gas regulations for electric utilities—and future presidents and the courts will need to sustain them. Some climate activists have also criticized the IRA for its incentives for capturing carbon from smokestacks and its provisions to allow continued oil and gas drilling in the Gulf of Mexico. Those measures won the support needed to pass the bill, but critics see them as perpetuating a fossil fuel industry in no need of lifelines.

Meanwhile, a world that has already warmed 1.2°C since preindustrial times has little time left before the global average surpasses 1.5°C, the threshold of "dangerous climate warming" set in international negotiations. Emissions are expected to rise again this year globally, rather than falling as needed, and many climate scientists believe the world is certain to overshoot 1.5°C. Although the IRA is a step in the right direction, activists say, humanity needs much more action—and soon. *—Paul Voosen*

IMAGES: (TOP TO BOTTOM) © 2022 JASON M. ALLEN; PAUL HENNESSY/SOPA IMAGES/LIGHTROCKET/GETTY IMAGES

AI gets creative

Artificial intelligence (AI) is making inroads in areas once considered uniquely human, including artistic expression and scientific discovery. The machines' encroachment was slow at first, but this year it turned into a landgrab.

The most visually stunning evidence—inescapable on social media—came from so-called text-to-image models. They use machine learning to analyze pairings of text and images online, finding patterns that allow them to create new images based on new text. Last year, the research lab OpenAI presented a software system called DALL-E that when asked for "an armchair in the shape of an avocado" could spit out several charming examples. This spring, OpenAI released a large upgrade, DALL-E 2. It implemented a machine-learning technique called diffusion, in which images emerge from "noise," guided by context or text descriptions. The method can efficiently generate realistic and alluring pictures. Several diffusion models became available for public use this year, and an artist using one won a fine art competition, stirring both curiosity and acrimony. At the same time, Meta, Google, and others released diffusion models that can conjure videos.

Machine learning is also showing off its creativity in science, math, and programming. *Science*'s 2021 Breakthrough of the Year honored AI tools that predict the 3D structure of proteins from the sequence of their amino acid building blocks. Expanding on that work, researchers have now used AI to design entirely novel proteins that could be used in vaccines, building materials, or nanomachines. One technique, called "hallucination," starts with random sequences and mutates them toward sequences that other AI tools are confident will fold up into stable proteins.

Meanwhile, DeepMind announced a tool called AlphaTensor, an algorithm that designs more efficient algorithms for multiplying blocks of numbers called matrices—an operation useful for computer graphics, physics simulations, and machine learning itself. It found shortcuts that human mathematicians had overlooked for decades. The company also presented AlphaCode, a system that writes programs to solve numerical problems (such as calculating how many binary strings of a given length don't have consecutive zeroes). It uses a model trained on previous programs and their descriptions to produce many candidate programs, then picks the best prospects. Pitted against human programmers, AlphaCode places in the middle of the pack.

Aside from philosophical debates about whether these feats of silicon count as real creativity, they raise practical and ethical dilemmas. Some observers worry the artificial coders and artists will violate copyright, perpetuate stereotypes, spread misinformation, or eliminate jobs. But there's no doubt humans will harness these tools to extend our own creativity, much as we did in the past with looms, cameras, and other once-unsettling inventions. *—Matthew Hutson*

Virus fingered as cause of multiple sclerosis

Drawing on a vast trove of military medical records, researchers this year showed a common herpes virus is an essential player in multiple sclerosis (MS), a disease in which the immune system attacks neurons. The findings may lead to new ways to treat or prevent the mysterious disorder, which causes mild symptoms—including blurred vision, fatigue, and numbness—in some of its 2.8 million sufferers around the world, but gradually leaves others unable to speak or walk.

A leading suspect in MS has long been Epstein-Barr virus, which infects most people in childhood, then lies dormant in certain white blood cells. Transmitted mainly through saliva, the virus can lead to infectious mononucleosis, or "kissing disease," in newly infected teens and young adults. Nearly all people with MS have antibodies to Epstein-Barr virus, but so do 95% of healthy adults, making it difficult to nail down the virus as a cause.

To firm up the link, epidemiologists trawled 20 years of medical records for more than 10 million U.S. military recruits and analyzed some of their stored blood samples. Of 801 soldiers who developed MS, all but one had previously tested positive for Epstein-Barr virus. And among soldiers who were initially negative, a subsequent infection raised MS risk 32-fold, the team reported in January in *Science*. That exceeds the increase in lung cancer risk caused by smoking.

Other researchers identified a possible mechanism, reporting in *Nature* just days later that the hibernating virus may awaken and cause nerve damage through so-called molecular mimicry. One of Epstein-Barr's proteins resembles a protein made in the brain and spinal cord, which apparently tricks the immune system into attacking the sheathing around nerve cells that's essential for conducting electrical signals. About 20% to 25% of MS patients sampled had antibodies in their blood that bind both proteins.

These discoveries are spurring efforts to develop drugs to treat MS by targeting the virus. And if one of the Epstein-Barr vaccines now in clinical trials proves effective and is given to children worldwide, someday MS could even go the way of polio and be virtually wiped out. *—Jocelyn Kaiser*

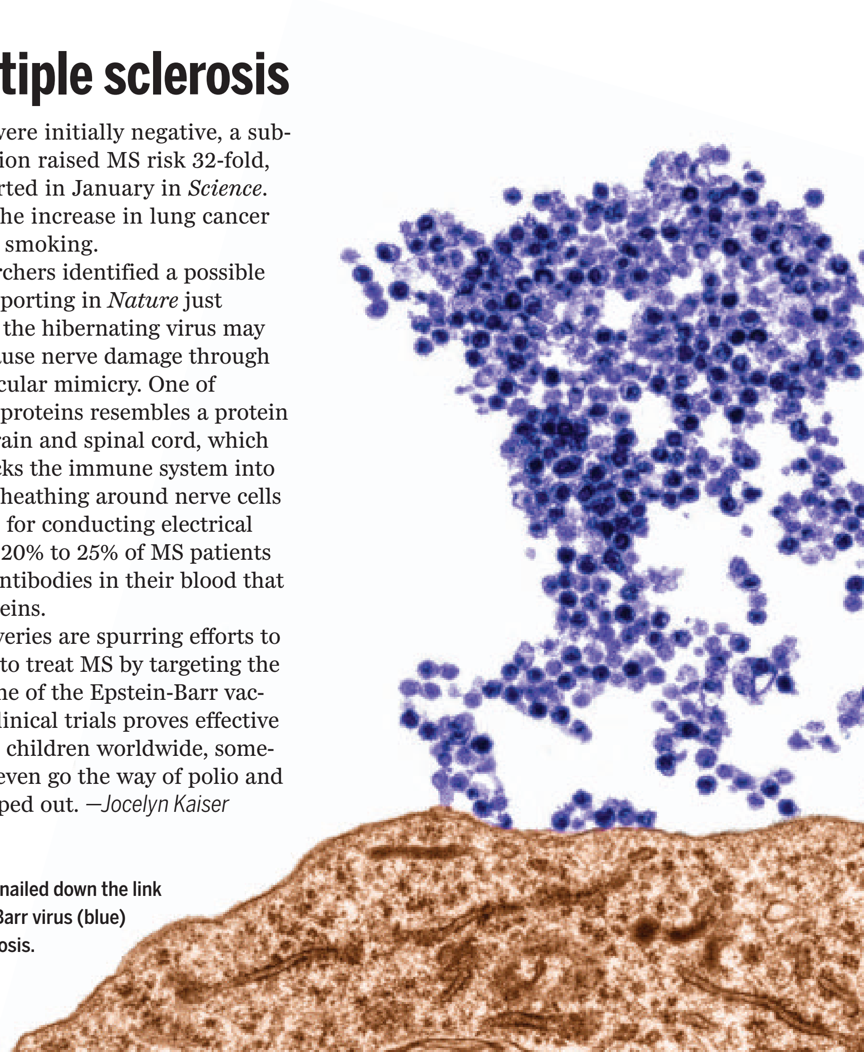

New research has nailed down the link between Epstein-Barr virus (blue) and multiple sclerosis.

PHOTO: STEVE GSCHMEISSNER/SCIENCE SOURCE

BREAKDOWNS OF THE YEAR

What went wrong in the world of science

People took to the streets in Beijing and other cities last month to protest China's strict zero-COVID policies.

PHOTO: KEVIN FRAYER/GETTY IMAGES

Zero COVID no longer works

At first, zero COVID was a success. But with time, China's strict lockdown policy strained its economy, frustrated its citizens, and arguably did more harm than good to public health. This month the government belatedly started relaxing restrictions without formally ending the zero-COVID strategy.

China's lockdown of Wuhan, the pandemic's epicenter, contained the virus for 76 days in early 2020 until the city's outbreak burned out. Life in Wuhan returned to nearly normal. New Zealand, Australia, Singapore, and Taiwan all adopted zero-COVID policies modified to suit their own legal and cultural norms and used them to buy time until vaccines arrived. Those countries then relaxed controls and transitioned to living with the virus.

China, however, despite having its own (less effective) vaccines, made zero COVID a goal in itself. To sniff out infections that are mostly asymptomatic, masses of citizens got tested every other day. They faced quarantine if positive and their apartment blocks were locked down. As the highly transmissible Omicron variant drove infection numbers to levels not seen since the Wuhan outbreak, the lockdowns grew more frequent and economically damaging. China's gross domestic product growth, a robust 8% in 2021, is projected to slump to 3% this year.

China's people have lost patience. On 14 November, residents of Guangzhou defied a lockdown and poured into the streets, toppling the barriers intended to keep them home. After 10 people died in a high-rise apartment building fire in Urumqi on 24 November, deaths many blamed on an ongoing lockdown, pent-up frustration erupted in cities throughout China. Protesters demanded the end of zero COVID and the end of mass testing; some even called on President Xi Jinping to step down. Now, authorities are hurriedly rolling back restrictions, despite an ongoing Omicron surge.

Ending zero COVID carries risks of its own, as China is still ill-prepared to live with the virus. Just 66% of those over age 80 are fully vaccinated and only 40% have gotten boosters, leaving them vulnerable to the expected wave of infections. China missed its chance to plan and execute a more orderly transition from zero COVID.

—Dennis Normile

War boosts CO_2 emissions

The Ukraine war roiled global energy markets, driving up prices and scrambling plans for cutting greenhouse gas emissions.

In Europe, steep cuts of natural gas imports from Russia upended plans to use gas as a lower carbon substitute for coal while economies transition to renewable sources such as wind and solar. Now, Germany and Austria say they will delay closing some coal-fired power plants—and even reopen shuttered stations—in order to keep the lights on. That could increase their carbon emissions by up to 20% over the next 2 years, researchers say. Europe is also seeking to import more liquefied natural gas from the United States and the Middle East, which could mean more leaks of methane, a potent warming gas, from wells, pipelines, and storage tanks.

But the crisis could ultimately end up speeding the transition to cleaner energy. It has highlighted the "unsustainability of the current global energy system," the International Energy Agency (IEA) said in October, and prompted many nations to "accelerate structural changes." Those changes—including major investments in renewables by the United States, Europe, Japan, and South Korea—will increase global spending on clean energy by at least 50% over the next decade, analysts estimate. IEA forecasts the crisis-driven uptick in coal use will be temporary as alternatives take hold.

Climate advocates hope such rosy scenarios come true. But forecasting global energy markets, they note, has proved hazardous.

—David Malakoff

Science ties fray

Escalating tensions severely bent—but didn't always break—superpower science collaborations this year.

Within weeks of Russia's invasion of Ukraine on 24 February, most major research funders in Europe announced they were severing relations with the Russian government, although some existing projects would be allowed to finish. The European Space Agency (ESA) suspended work on ExoMars, a nearly finished Mars rover mission that depended on Russian help. (ESA now has a plan to fly the rover without Russia, but much delayed.) And CERN, Europe's particle physics laboratory, said it would no longer welcome scientists from Russia and its ally Belarus after pacts with those nations expire in 2024. In June, the United States followed suit, saying it would "wind down" most science projects with Russia, including Arctic research.

Collaborations between China and Western nations also frayed. In the United States, concerns that China is stealing the fruits of federally funded research led Congress to place new limits on the ability of government-supported scientists to work with Chinese institutions. In Europe, similar fears prompted some universities to back away from projects with Chinese partners. In August, China suspended work with the United States on an array of issues, including climate research, to protest a visit to Taiwan by a high-ranking member of Congress.

Yet superpower leaders still seem open to at least some scientific cooperation. Despite the Ukraine war, Russia continues to contribute to the ITER fusion reactor under construction in France and launch crew and supplies to the International Space Station. And in November, after a lengthy meeting aimed at defusing tensions, U.S. and Chinese leaders announced they would resume their paused work on climate and other issues. Such cooperation, each side said, is in the best interests of the world as a whole. *—David Malakoff*

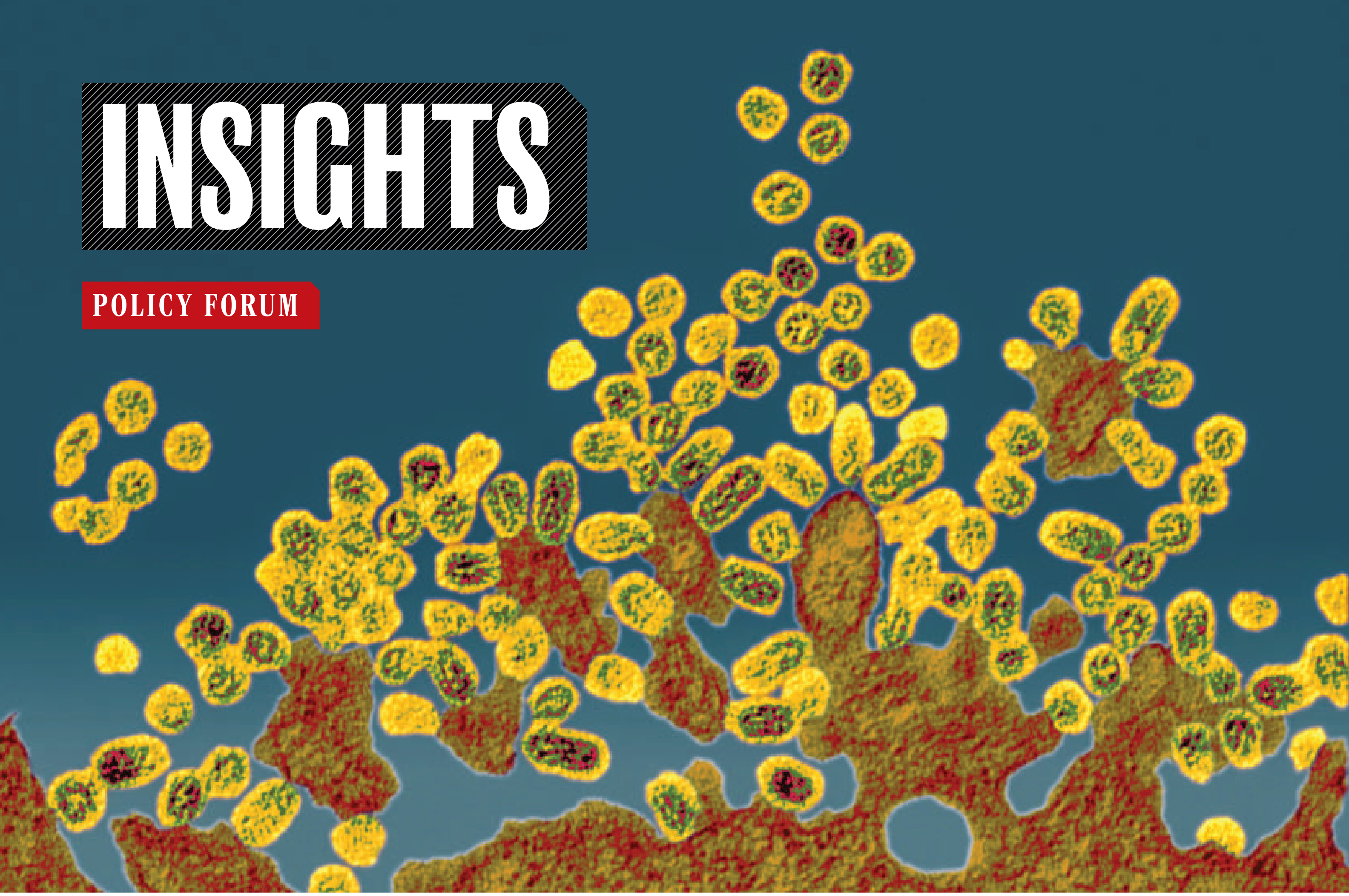

PHOTO: DR. KLAUS BOLLER/SCIENCE SOURCE

BIOSECURITY

Strengthen oversight of risky research on pathogens

Policy reset and convergence on governance are needed

By **Jaspreet Pannu**[1,2], **Megan J. Palmer**[3,4], **Anita Cicero**[1], **David A. Relman**[2,4,5,6], **Marc Lipsitch**[7], **Tom Inglesby**[1]

Life sciences research offers immense benefits and is crucial for advancements in medicine, public health, agriculture, and management of the environment. But a recent guidance framework by the World Health Organization (WHO) reminds us of the continued lack of awareness and governance structures in many countries for life sciences research that may cause harm through accident or misapplication (*1*). Robust risk management would enable the full realization and equitable distribution of potential benefits from the life sciences and associated technologies, and reassure the public (*1*). International guidelines and standards of conduct are needed (*2*), along with effective oversight institutions and leadership (*3*). The US government (USG) has played a prominent role to date and is now reviewing its biosecurity policies. We identify substantial gaps and suggest approaches to address them so as to improve US policies and usefully influence policies globally.

At the start of 2022, the National Institutes of Health (NIH) and the White House launched a review of two important US biosecurity policy frameworks, one for the oversight of "dual-use research of concern" (DURC), which outlines life sciences research that may be misapplied to pose a substantial biosecurity threat (*4*), and one for the oversight of work involving enhanced potential pandemic pathogens (ePPPs) (*5*). These policies were first established in 2012 and 2017, respectively, and were attempts to balance the benefits and risks posed by research that falls into these categories. With the passage of time, it has become clear that there are shortcomings that need to be addressed. Biotechnology has advanced with remarkable speed and impact—so have the needs and demands for benefits, along with concerns about risks.

With respect to current US policy, roles and responsibilities are inconsistent, and scope is limited. Local research institutions assess projects for the possibility of DURC, referring the work to NIH only if they view this as needed. By contrast, ePPP policy places responsibility for review with USG departments and agencies. Local institutions have no stated role, and only the Department of Health and Human Services (HHS) has enacted an ePPP policy. Both frameworks apply only to USG-funded research. This current situation probably arose from early concern by USG about overreach and the possible dampening effects on US efforts to develop defenses against naturally occurring pandemics and biological threats of deliberate origin.

It is vital to get these policies right, not only for the US, but to inspire policy development in other countries with growing

This transmission electron micrograph shows the H1N1 strain of swine influenza virus particles (yellow) and a host cell (brown).

life science and biotechnology sectors. Few countries have policies that fully manage these issues. Some have published guidance that addresses key elements. For example, Canada requires life science research institutions to establish dual-use policies that have been approved by the Public Health Agency of Canada. The German National Academy of Sciences (Leopoldina) has encouraged institutions to create dual-use oversight committees; many German institutions now have such committees, even though no law requires it. The WHO, too, in its recently published framework, provides valuable guidance on the kinds of interventions and policies that might diminish the risks associated with some life sciences research. Yet, many countries have not offered interventions or policies on these issues. Some have biosafety measures aimed at mitigating accidental harms but lack biosecurity oversight aimed at mitigating intentional misuse. A minority of countries have policies that articulate a clear role for their national government (*6*). And fewer still have policies that directly address research on PPPs.

The pandemic has dramatized the terrible impact of a highly transmissible virus. It has also dramatized the terrible inequities in the allocation and delivery of countermeasures around the world, and the disparate costs paid by different communities. If ePPP research were to cause a pandemic, it would affect everyone, not just the country that funded or approved that research. Thus, there could be a moral and ethical argument that no country should undertake research that can be reasonably anticipated to increase the risk of a pandemic, without approval by other countries, especially by those least able to prepare for and respond to pandemics. As dozens of scientists, policy researchers, and public health experts (including the authors) stated recently, “the USG [and scientific community] has an extraordinary obligation to ensure [that] USG funding or approval is not given to work that may cause an epidemic or pandemic, as well as to provide international leadership in this realm” (*7*).

POLICY RESET

Resetting US policy on these issues is a pressing need, as is international convergence around strong, effective governance of this area of science. Among the needed revisions for US policy, several bear highlighting.

Expand the scope of pathogens to be governed

The existing ePPP framework defines a potential pandemic pathogen as one that is both highly transmissible and highly virulent, because the initial priority was to ensure that the most serious risks were addressed first. But COVID-19 has shown that with a sufficient level of transmissibility, even a pathogen with modest virulence—an infection-fatality ratio of less than 1% (as compared to Ebola Sudan, for example, which has had an average case-fatality ratio above 50%)—can cause extensive global mortality, collapse of health systems, and widespread economic shock. The ePPP framework should be modified to make explicit that work reasonably anticipated to confer efficient human transmissibility on any pathogen, including those of even modest virulence, requires careful review.

Although an experiment that selects for new routes or modes of transmission or tropism for particular cells might be reasonably expected to increase a virus’s transmissibility in humans, the degree of increase is difficult to predict with current methods. Even pathogens with transmissibility modestly above the threshold of a basic reproduction number of 1 can cause outbreaks in specific populations, resulting in substantial disruption. Indeed, the past four influenza pandemics have had estimated reproductive numbers below 2 (*8*). Limited predictive ability combined with the destructive potential of modestly transmissible viruses should serve as a warning about the potential impact of engineering any degree of increased transmissibility. Although the existing HHS Framework provides criteria for funding approval and other questions that government reviewers need to address in the risk–benefit assessment, there is no concomitant guidance aimed at or communicated to research institutions or investigators; updated policy should include concrete guidance for these entities and individuals.

Similarly, the DURC framework should apply to all human pathogens, not just the 15 agents that are currently stipulated. It should also include animal and plant pathogens because of possible increased risks of epizootics or epiphytotics, with attendant risks to human health owing to diminished food security. The focus on the original 15 agents presumably was intended to place greatest attention on pathogens of highest risk while limiting the burdens of oversight for research deemed less risky. The original policy called for a revisiting of the scope. Emphasis should now be placed on the anticipated results of any research on a pathogen or research that could generate a pandemic: Will the reasonably anticipated product be an agent whose transmissibility and virulence may cause it to spread unchecked by available countermeasures, leading to substantial morbidity?

Expanding the scope of these frameworks does not necessarily mean preventing this work from occurring; it means requiring research proposals to go through independent, government-led risk–benefit assessment to determine whether the work should proceed and under what conditions. To be clear, transformative advances against pathogens can be achieved without increasing the chances of the next pandemic at the same time. HHS and NIH have not yet published the current costs and numbers of personnel required for implementing the DURC and ePPP frameworks, but clearly, an expanded oversight program will require additional resources to be effective and efficient.

Examine risks and benefits in rigorous detail

Nearly all life sciences research can be performed in ways that pose minimal risk to society. However, the narrow category of work subsumed under the ePPP and DURC frameworks may pose substantial risks. Therefore, it is essential that these risks, as well as the associated benefits, be examined in detail before funding or approval decisions are made. There is no easy, algorithmic process for weighing benefits against risks, and no off-the-shelf tool that has been evaluated for this specific application. Such assessments will require careful judgments by independent experts. Under current practice, benefits are sometimes asserted without much explanation, timeframe, or supporting evidence; for example, claims are made that a project with substantial risk is important for vaccine development but without supporting evidence. The risk–benefit calculus should be more specific and standardized.

On the risk side, the USG should make clear that the ePPP and DURC review processes must evaluate the risk and potential consequences of accidents, and the potential for deliberate theft of an isolate or insider diversion, as well as the risk that information from the research could be used in ways leading to accidents or deliberate harm. Relevant information would include genome sequences of ePPPs and compu-

---

[1]Center for Health Security, Johns Hopkins Bloomberg School of Public Health, Baltimore, MD, USA. [2]Department of Medicine, Stanford University School of Medicine, Stanford, CA, USA. [3]Department of Bioengineering, Stanford University, Stanford, CA, USA. [4]Center for International Security and Cooperation, Freeman Spogli Institute for International Studies, Stanford University, Stanford, CA, USA. [5]Department of Microbiology and Immunology, Stanford University School of Medicine, Stanford, CA, USA. [6]Infectious Diseases Section, Veterans Affairs Palo Alto Health Care System, Palo Alto, CA, USA. [7]Center for Communicable Disease Dynamics, Departments of Epidemiology and Immunology and Infectious Diseases, Harvard T.H. Chan School of Public Health, Boston, MA, USA. Email: relman@stanford.edu

tational methods for designing ePPPs. For example, a growing number of practitioners can, with increasing ease, create and engineer viruses on the basis of sequence information, reflecting new scientific conditions not adequately addressed by current policy. When the results of an accident or deliberate misuse could lead to epidemic or pandemic consequences, critical questions asked in the ePPP framework should include the following: Will the benefits of this research directly result in new approaches that could diminish the potential consequences or harms of this pathogen? How critical is the information that would be gained by the proposed experiments, and are there safer ways of attaining comparable information?

Although there are costs to rigorous reviews, such reviews should be supported and structured so that they can be improved over time, and the review process itself can inspire new lines of inquiry and technical innovations for mitigating risks. Examples of experiments and approaches with acceptable risk–benefit ratios could provide useful guidance, much like case law. Dedicated research programs can provide tools and empirical data to support more effective risk–benefit analyses. Publishing the deliberations and outcome of each review would enable learning from prior assessments and provide needed implementation guidance to researchers and institutions. So far, local DURC review has been inconsistent across institutions, nonstandardized, and hindered by disincentives for investigator reporting of risks (*9*).

Incorporate transparency into the review process

Assessments of risks and benefits should be made available to the public. Currently, research institutions and funders are reluctant to share information even when permitted because of concerns over reputational risk; both requirements and incentives will be vital to normalize these processes, establish trust, and enable cross-organizational learning. The deliberations of the USG entity deciding on approval of any ePPP research should also be made public, especially any dissenting opinions and recusals.

Reset the review process

Many types of expertise are needed for a proper review, including experts in natural science, engineering, biosafety, biosecurity, public health, vaccine and therapeutics development, and bioethics. The USG should seek nongovernmental expertise for the review process—currently, the HHS process involves only governmental experts, and the identity of these individuals is not publicly available. Clinical and public health experts are needed, because in the event of a pandemic resulting from the work, these experts would understand what would be needed for response. Individuals whose agency might be funding or participating in the proposed work have a conflict of interest. It is important for the content and the optics of the process that they recuse themselves from decision-making. The names of the individuals involved in the review, the content of the review, and the final decisions should be made public.

Review of proposed experiments now is required only at the point when a new proposal is being considered for funding by HHS. For many good reasons, scientists change their plans after funding has been approved for their original proposal. There is a need, therefore, for a mechanism to review ePPP experiments conceived after a grant proposal is funded, but before they are performed. Others have called for the same (*10*).

Expand reach to all USG agencies and to any institution performing this work

Currently, the required review of ePPP work is limited to experiments funded by HHS, which includes NIH. The policy should be revised so that all agencies that fund work related to the enhancement of potential pandemic pathogens should have that work evaluated under the ePPP framework, including, as applicable, the Department of Defense, Department of Agriculture, and others. In addition, currently neither ePPP nor DURC policies apply to non–federally funded research, leaving the USG and the rest of us in the dark about such work—despite a 2016 National Science Advisory Board for Biosecurity (NSABB) recommendation that all ePPP work be subject to oversight, regardless of funding source (*11*). The USG should use this opportunity to develop new policies and/or legislation to close these gaps in governance. Publishers and research institutions will have a role to play in this regime, as they do for human subjects research. Similar to the policies governing human subjects research, publishers should require that reports of research involving ePPP and/or DURC have been carefully reviewed under the appropriate government oversight framework or that the work has been determined by government not to fall in these categories or require review (*12*). Such policies of publishers of preprints and journals would provide incentives for countries around the world to establish review systems.

Although USG, the US National Academies of Sciences, Engineering, and Medicine, and NSABB have engaged other nations in DURC, we encourage the USG, especially the Department of State, perhaps in partnership with the NSABB, to expand its efforts to promote the importance of governance frameworks for such research.

Humanity is at a critical moment in the worldwide evolution of powerful experimental capabilities in the life sciences, motivated and humbled by an ongoing pandemic, faced with the distinct possibility of both substantial harm and good from continued work on pathogens. The current policy revision process is an unusual opportunity for addressing serious gaps and challenges. If the US is successful in this policy revision effort, it could serve to create substantial momentum for important change elsewhere in the world. ■

REFERENCES AND NOTES

1. World Health Organization, *Global Guidance Framework for the Responsible Use of the Life Sciences: Mitigating Biorisks and Governing Dual-Use Research* (World Health Organization, 2022).
2. Johns Hopkins Center for Health Security, *The Tianjin Biosecurity Guidelines for Codes of Conduct for Scientists*, The Interacademy Partnership (2021); https://www.interacademies.org/publication/tianjin-biosecurity-guidelines-codes-conduct-scientists.
3. M. J. Palmer, F. Fukuyama, D. A. Relman, *Science* **350**, 1471 (2015).
4. United States Government Policy for Oversight of Life Sciences Dual Use Research of Concern, Department of Health and Human Services, (2012); https://www.phe.gov/s3/dualuse/Documents/us-policy-durc-032812.pdf.
5. Framework for Guiding Funding Decisions about Proposed Research Involving Enhanced Potential Pandemic Pathogens (P3CO), Department of Health and Human Services (2017); https://www.phe.gov/s3/dualuse/Pages/ResearchReview-PPP.aspx.
6. S. Salloch, *BMC Med. Ethics* **19**, 53 (2018).
7. Johns Hopkins Center for Health Security, "Group of Scientists, Public Health Experts, Policy Researchers Propose Strengthening of US Government's Enhanced Potential Pandemic Pathogen Framework and Dual Use Research of Concern Policies," Johns Hopkins Center for Health Security (2022); https://www.centerforhealthsecurity.org/news/center-news/2022-07-08-ePPP-sign-on-letter.html.
8. M. Biggerstaff, S. Cauchemez, C. Reed, M. Gambhir, L. Finelli, *BMC Infect. Dis*. **14**, 480 (2014).
9. S. Evans, D. Greene, C. Hoffmann, S. Lunte, Stakeholder Engagement Workshop on the Implementation of the United States Government Policy for Institutional Oversight of Life Sciences Dual Use Research of Concern: Workshop Report (2 November 2021); https://doi.org/10.2139/ssrn.3955051.
10. E. M. Davidson, R. Frothingham, R. Cook-Deegan, *Science* **316**, 1432 (2007).
11. U.S. Government Gain-of-function Deliberative Process, NSABB Recommendations for the Evaluation and Oversight of Proposed Gain-of-Function Research, National Institutes of Health Office of Science Policy (2016); https://osp.od.nih.gov/biotechnology/gain-of-function-research.
12. T. V. Inglesby, M. Lipsitch, *MSphere* **5**, e00990 (2020).

ACKNOWLEDGMENTS

D.A.R. received support from the Thomas C. and Joan M. Merigan Endowment at Stanford University. J.P., M.J.P., A.C., D.A.R., M.L., and T.I. received support from Open Philanthropy. M.L. is the director for Science at the Center for Forecasting and Outbreak Analytics, US Centers for Disease Control and Prevention, under an Intergovernmental Personnel Agreement. He is also an Honorary Faculty member at the Wellcome Sanger Institute and an External Faculty member at the Broad Institute. M.L. has received institutional funding from Pfizer, the Waking Up Foundation, and the FTX Foundation unrelated to this work. He has received honoraria from Bristol Myers Squibb and Sanofi Pasteur, and consulting fees from Merck and Janssen. The opinions expressed here are those of the authors and do not necessarily reflect those of any institution or government agency.

10.1126/science.adf6020

CELL BIOLOGY

The endosome as engineer

Endosomes use lipid signaling to shape organelles according to nutrient levels

By **Maria Clara Zanellati** *and* **Sarah Cohen**

A hallmark of eukaryotic cells is that they are compartmentalized into membrane-bound organelles. This allows for the spatial separation of biochemically incompatible processes. Nevertheless, organelles must work together for the cell to function. There has been increasing interest in organelle communication at membrane contact sites—where two organelles are anchored in close apposition by “tether” proteins (*1*). These contact sites allow the exchange of materials and information between cellular compartments (*2*). Intriguingly, organelles can also influence one another’s abundance and morphology. Most studies have focused on the role of the endoplasmic reticulum (ER) in shaping other organelles (*3*). However, on page 1188 of this issue, Jang *et al*. (*4*) show that the endosome can reengineer ER shape in response to changing nutrient levels, which in turn affects the morphology and function of additional organelles.

Membrane contact sites mediate the exchange of lipids, ions, and proteins between organelles (*2*). The first hint that organelles can influence one another’s morphology came from movies showing ER tubules wrapped around mitochondria at sites where the mitochondria divided (*5*). Mitochondria undergo constant fusion and fission. Fission can be associated with mitochondrial biogenesis needed for cell proliferation, or it can be a mechanism to degrade damaged pieces of mitochondria (*6*). Although cytoplasmic proteins were known to affect mitochondrial fission, it was surprising to discover that the ER regulates this process. The ER also mediates fission of endosomes, which is required for endocytic cargo sorting. Because the ER is the largest source of membrane in the cell and a major site of protein and lipid synthesis, the ER can act as a central node to convey environmental cues and exert effects on the growth and division of other organelles. However, more recently it has become clear that the ER is not the only organelle that influences the morphology and function of its neighbors. Lysosomes can also influence mitochondrial division at membrane contact sites, as can the Golgi apparatus (*7*–*9*).

Jang *et al.* investigated the function of myotubularin 1 (MTM1), an endosomal phosphatidylinositol (3,4,5)-trisphosphate [PI(3)P] phosphatase that is mutated in patients with X-linked centronuclear myopathy (XLCNM). This disorder can be fatal and is characterized by myofiber hypotrophy and mitochondrial deficits and disorganization of the sarcoplasmic reticulum (the ER in muscle) (*10*, *11*).

Jang *et al.* confirmed that MTM1 loss of function causes an increase in ER tubules in XLCNM patient-derived myoblasts and that this is dependent on the accumulation of PI(3)P in endosome membranes. Inspired by previous studies showing that PI(3)P modulates nutrient sensing (*12*) and cell survival (*13*), they found that upon nutrient starvation of wild-type cells, endosomal PI(3)P levels declined and peripheral ER tubules morphologically converted to sheets. However, this response did not arise in human HeLa cells lacking MTM1, where the PI(3)P levels remained elevated. Spatial proteomics revealed that MTM1 is recruited to early endosomes upon starvation, which resulted in PI(3)P hydrolysis. Forcing the recruitment of catalytically active MTM1 to early endosomes was sufficient to boost conversion of ER tubules to sheets in fed cells, mimicking the starvation response. Jang *et al.* also showed that two ER proteins, ER ribosome-binding protein 1 (RRBP1) and kinectin 1 (KTN1), harbor lysine-rich regions that preferentially bind PI(3)P. Overall, these findings show that during starvation, MTM1 is recruited to early endosomes where it hydrolyzes PI(3)P. This reduces binding of RRBP1 and KTN1 to endosomal PI(3)P, releasing endosome-ER contacts. Without endosomes pulling the peripheral ER into tubules, these membrane domains are converted to sheets (see the figure).

Changing organelle morphology

In a fed state, PI(3)P levels are high in endosome membranes, which facilitates binding of ER proteins RRBP1 and KTN1. This pulls the ER along microtubules to form ER tubules, which mediate mitochondrial fission and promote lipid droplet biogenesis. In nutrient deprivation, MTM1 is recruited to early endosomes, where it hydrolyzes PI(3)P. This releases the endosome-ER connection, resulting in ER sheet morphology, decreased mitochondrial fission, and reduced lipid droplet biogenesis.

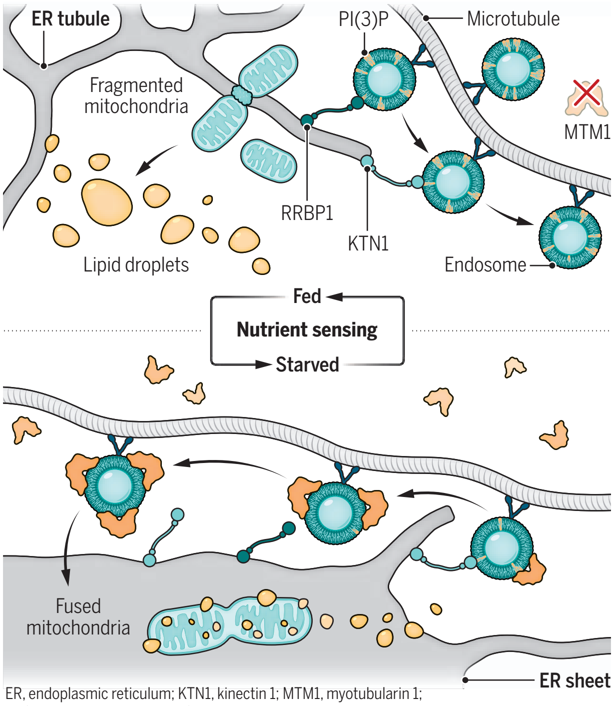

ER, endoplasmic reticulum; KTN1, kinectin 1; MTM1, myotubularin 1; PI(3)P, phosphatidylinositol (3,4,5)-trisphosphate; RRBP1, ribosome-binding protein 1.

Previous studies showed that tubular ER promotes mitochondrial fission and regulates lipid droplet biogenesis (*5*, *14*). Under fed conditions, mitochondrial fusion and fission events are highly dynamic, whereas during starvation, mitochondria fuse into tubular networks. This protects mitochondria from degradation by mitophagy and enables a metabolic shift to fatty acid oxidation (*6*). In starved XLCNM patient-derived myoblasts and in HeLa cells lacking MTM1, Jang *et al.* observed reduced mitochondrial tubular networks and exacerbated mitochondrial fission. The defective mitochondrial morphology in cells lacking MTM1 was rescued by depleting RRBP1 and KTN1, which converted ER tubules to sheets. The incompetence

---

Department of Cell Biology and Physiology, University of North Carolina at Chapel Hill, Chapel Hill, NC, USA. Email: sarahcoh@med.unc.edu

GRAPHIC: A. MASTIN/*SCIENCE*

of cells lacking MTM1 to rewire mitochondrial morphology under limited nutrient availability reduces their viability. Thus, this work identifies an endosome-ER-mitochondrion axis whereby MTM1 activity on endosomes modulates ER morphology by reducing membrane contact sites, which in turn affects mitochondrial morphology and the cellular response to starvation.

It remains unknown how MTM1 and endosomal PI(3)P levels are regulated by nutrient status. It is also unknown how this endosome-ER-mitochondrion axis intersects with autophagy. In the cell types studied by Jang *et al.*, autophagy was not altered by MTM1 loss of function. However, it has previously been reported that MTM1-deficient mice have impaired autophagy in skeletal muscle (*15*). Because autophagosomes can arise from ER or mitochondrial membranes, it is possible that the changes to the structure and function of these organelles induced by MTM1 mutations could have downstream effects on autophagy. It is also unknown whether MTM1-induced changes in ER morphology could affect other organelles. Jang *et al.* report increased lipid droplet biogenesis during starvation when MTM1 is absent. Presumably this is because lipid droplets originate from tubular ER microdomains, as do peroxisomes (*14*), suggesting that peroxisomes could similarly be affected. In addition to modulating mitochondrial fission, ER tubules regulate endosome fission. Thus, endosomal effects on ER morphology could feed back onto the morphology of endosomes themselves. The ER is a central hub of organelle communication. However, endosomal signaling lipids have been identified as an important mechanism for engineering ER shape, which relays nutrient information to distant mitochondria and lipid droplets. ■

REFERENCES AND NOTES

1. E. Dolgin, *Nature* **567**, 162 (2019).
2. W. A. Prinz, A. Toulmay, T. Balla, *Nat. Rev. Mol. Cell Biol.* **21**, 7 (2020).
3. H. Wu *et al.*, *Science* **361**, 912 (2018).
4. W. Jang *et al.*, *Science* **378**, 1188 (2022).
5. J. R. Friedman *et al.*, *Science* **334**, 358 (2011).
6. L. Pernas, L. Scorrano, *Annu. Rev. Physiol.* **78**, 505 (2016).
7. Y. C. Wong, D. Ysselstein, D. Krainc, *Nature* **554**, 382 (2018).
8. S. Nagashima *et al.*, *Science* **367**, 1366 (2020).
9. T. Kleele *et al.*, *Nature* **593**, 435 (2021).
10. L. Al-Qusairi *et al.*, *Proc. Natl. Acad. Sci. U.S.A.* **106**, 18763 (2009).
11. L. Amoasii *et al.*, *J. Cell Sci.* **126**, 1806 (2013).
12. Z. Hong *et al.*, *J. Cell Biol.* **216**, 4217 (2017).
13. M. J. Munson *et al.*, *EMBO J.* **34**, 2272 (2015).
14. A. S. Joshi, H. Zhang, W. A. Prinz, *Nat. Cell Biol.* **19**, 876 (2017).
15. K. M. Fetalvero *et al.*, *Mol. Cell. Biol.* **33**, 98 (2013).

ACKNOWLEDGMENTS

The authors are supported by the National Institute of General Medical Sciences (award R35GM133460) and by a Chan Zuckerberg Initiative Neurodegeneration Challenge Network Collaborative Pairs Award.

10.1126/science.adf5112

ELECTRONICS

Multiple pathways to stretchable electronics

Stretchable conductors expand the interfaces with biological structures

By **Tarek Rafeedi** *and* **Darren J. Lipomi**

The aim of stretchable electronics is often to integrate complex multifunctional devices with biological structures (*1–3*). To achieve this, devices need to conform to and deform with the body's anatomy (e.g., skin, internal organs, blood vessels, and nerves) while maintaining their electronic function (e.g., monitoring changes in a biological milieu or supplying stimulus to it). On page 1222 of this issue, Zhao *et al.* (*4*) report a device that can reliably interface with biological substrates while being stretched. Their work demonstrates a platform for fabricating elastic bioelectrodes based on microcracked conductive films. The authors apply four different biocompatible materials to this platform, creating a library of biosensors and stimulators.

Solids are deemed stretchable if they considerably deform (strain) under applied force (stress) and return to their original shape when the force ceases. Further, the ability of materials to stretch while retaining their electronic function is intimately related to their structure. The mechanical and electronic properties of a certain material arise from the precise arrangement of its atoms or molecules and the types of bonds formed between them, be they metallic, covalent, electrostatic, or van der Waals. Changing the atomic spacing or bond strength through the application of mechanical stress usually affects electronic properties. Thus, the key to stretchable electronics lies in materials and device layouts that can accommodate large strain in ways that do not hinder charge transport.

Many approaches have been explored to combine conductivity and stretchability, often following the motifs of making a conductor stretchy or making an elastomer material conductive. Superimposing these properties involves engineering them such that they do not, or only minimally, interfere. There are four broad strategies that have been used to make stretchable devices for biomedical applications, two of which are used by Zhao *et al.* (see the figure).

The first approach is to incorporate a conductive filler in an insulating elastomeric carrier (*5*, *6*). Conductive fillers that have been used successfully include metallic particles (e.g., nanospheres, liquid metal droplets, and

---

Department of Nano and Chemical Engineering, University of California, San Diego, La Jolla, CA, USA. Email: dlipomi@ucsd.edu

Four approaches to stretchable electronics

There are four approaches to generating stretchable electronic materials: conductive fillers, conductive polymers, patterned interconnects, and strain-cracked films. Each approach or a combination of approaches can allow the generation of stretchable devices that have biomedical applications.

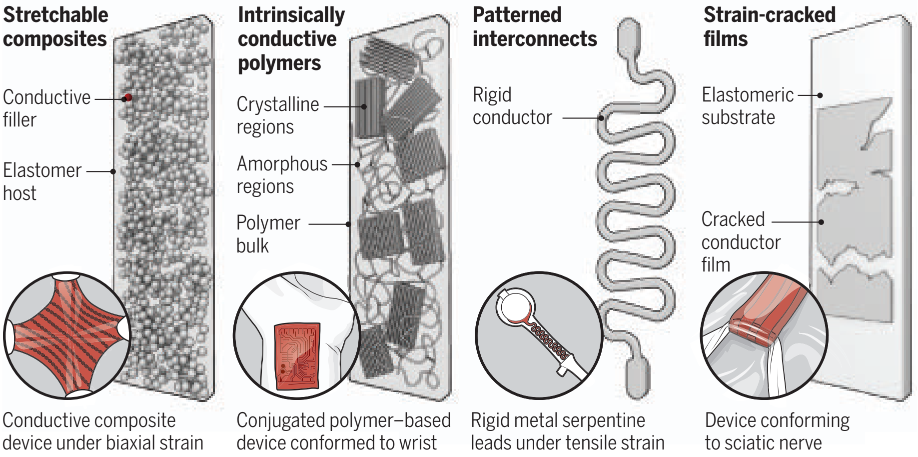

GRAPHIC: V. ALTOUNIAN/*SCIENCE*

nanowires), conductive polymers, carbon nanotubes, and graphene (*7*–*9*). A common downside of this approach is the reduced tensile strength and fracture strain limit when high amounts of filler are used. Filler particles can act as nucleation points for fracture in the host elastomer. These cracks grow with repeated stretching, leading to failure. If the filler content is lowered, however, the electrical resistance of the composite will increase and become variable with stretching. These challenges can be overcome by optimizing the filler fraction and its particle distribution and by using lower-rigidity, smaller, or folded conductors (*6*, *7*). Zhao *et al.* used this approach to compose highly stretchable, conductive substrates using silver nanowires.

The second approach is the synthesis of intrinsically conductive and stretchable polymers. A large subset of such polymers are π-conjugated polymers (CPs) (*10*). In this type of polymer, a pattern of alternating single and double covalent bonds extends along the polymer chains. This arrangement gives rise to semiconducting behavior and can be rendered conducting by oxidation or reduction. A key development in the history of CPs was the incorporation of saturated side chains, which confer solubility. Forming solutions of CPs allows for facile deposition using a variety of techniques (e.g., spin-casting, drop-casting, and blade-coating). Large deformations of CPs are generally not reversible owing to the unraveling of crystalline regions at high strains. Hence, CPs are usually deposited on an elastic substrate or are chemically cross-linked to provide a restoring force (*11*).

Another class of polymer-based conductors is ionic hydrogels. These are cross-linked polymer networks that retain an electrolyte solution. These polymers can maintain high amounts of stretchability and softness while being conductive to ions. Recent research has demonstrated the promising applications of this class of material in bioelectronic interfaces and artificial organs (*12*).

The third approach is the patterning of springlike structures (e.g., wrinkled, buckled, or serpentine configurations) using materials of intrinsically high rigidity—i.e., metals and semiconductors—onto elastomer surfaces (*1*, *3*, *13*). Generally, stretchability of the pattern is conferred by its ability to fold in on itself or protrude out of the stretching plane. Thus, the direction of stretchability is restricted by the pattern's orientation. Because the stiffness of the rigid conductor and elastomer substrate is mismatched, this approach calls for specialized methodologies and fabrication skills to design the elastomer substrate and adhere the electronics to it. Its major advantage, however, is that it can produce robust circuits that closely resemble commercially printed circuit boards.

The fourth approach, highlighted by Zhao *et al.*, is the use of microcracked films. They used a laminate of strain-fractured plates of a rigid conductor and an auxiliary conductive composite film containing vertically oriented wires. When the structure is stretched, the cracks in the rigid films expand, yet the vertically oriented wires preserve connectivity between the cracked plates. There have been other applications of this deliberate fracture and bridging strategy for conformal biological electrodes (*14*, *15*); what differentiates this work is the breadth of possible applications afforded by the range of materials used.

The main challenge in applying cracked films to stretchable devices is that electrical resistance is not invariant to strain. That is, when the material is strained, the cracks expand, leaving tortuous paths for the charge to flow, which increases the in-plane electrical resistance. To overcome this limitation, Zhao *et al.* integrate orthogonal conductive pathways using conductive fillers—making the in-plane conductivity invariant to strain. These microcracked conductors can be applied conformally to a biological substrate while maintaining a constant contact area by expanding the preformed cracks. This constant and conformal contact ensures that electrical signals from and to the electrode-anatomy interface remain intact. To demonstrate these effects, the authors report a variety of applications, including in vivo neurostimulation of a mouse sciatic nerve and in vitro electrochemical sensing of pH and select chemical compounds. They demonstrate that, in the stretched state, the bioelectrodes operate with unvarying fidelity.

The approach of Zhao *et al.* embodies the moniker of stretchable electronics, which is often used loosely and perhaps imprecisely in the field. Almost anything can be stretched, but many materials are destroyed in doing so. Their approach acknowledges the damage caused by strain and exploits it to a positive effect—creative destruction. ■

REFERENCES AND NOTES

1. N. Matsuhisa, X. Chen, Z. Bao, T. Someya, *Chem. Soc. Rev.* **48**, 2946 (2019).
2. K. Nan *et al.*, *Nat. Rev. Mater.* **7**, 908 (2022).
3. Q. Lyu, S. Gong, J. Yin, J. M. Dyson, W. Cheng, *Adv. Healthc. Mater.* **10**, 2100577 (2021).
4. Y. Zhao *et al.*, *Science* **378**, 1222 (2022).
5. S. Yao, Y. Zhu, *Adv. Mater.* **27**, 1480 (2015).
6. G. Yun *et al.*, *Small Sci.* **1**, 2000080 (2021).
7. J. Yu *et al.*, *ACS Nano* **10**, 5204 (2016).
8. T. Sekitani *et al.*, *Science* **321**, 1468 (2008).
9. Z. Ma *et al.*, *Nat. Mater.* **20**, 859 (2021).
10. T. Someya, Z. Bao, G. G. Malliaras, *Nature* **540**, 379 (2016).
11. Y. Jiang *et al.*, *Science* **375**, 1411 (2022).
12. C. Yang, Z. Suo, *Nat. Rev. Mater.* **3**, 125 (2018).
13. Y. S. Choi *et al.*, *Nat. Commun.* **11**, 5990 (2020).
14. N. Liu *et al.*, *Sci. Adv.* **3**, e1700159 (2017).
15. S. Wang *et al.*, *Sci. Adv.* **8**, eabl5511 (2022).

ACKNOWLEDGMENTS

The authors are supported in part by the Air Force Office of Scientific Research (FA9550-22-1-0454).

10.1126/science.adf2322

SYNTHETIC BIOLOGY

Engineering time-controlled immunotherapy

Designer lymphocytes expand the dynamic range of possibilities for treating disease

By **Emanuel Salazar-Cavazos** *and* **Grégoire Altan-Bonnet**

Immunotherapy harnesses the immune response to treat diseases, from cancers to autoimmune disorders. The boundaries of clinical immunotherapy for cancer have been pushed by the development of cancer-killing T cells that target tumors, therapies that block immune checkpoints to rearm cytotoxic T cells, and the optimization of engineered chimeric antigen receptor (CAR) T cells (*1*). But there remain limitations when immune functions that have evolved to clear fast-invading pathogens are repurposed to eradicate slow-growing tumors. On pages 1186 and 1227 of this issue, Allen *et al.* (*2*) and Li *et al.* (*3*), respectively, present synthetic biology-based strategies to further improve cancer immunotherapies. Rather than being limited by "natural" immunology (using leukocytes, antibodies, and cytokines), these studies expand the scope of immune responses elicited by CAR T cells against diseased tissues.

Current CAR T cell therapies involve ex vivo engineering of patient T cells to express CARs that recognize specific molecules on the surface of tumors, before they are injected into patients. However, immune responses develop over long time scales (>1 week), such that immunotherapies that are optimized for short-term cellular responses (e.g., killing of tumor cells) may not achieve long-term systemic solutions (e.g., eradication of tumors) (*4*). Indeed, postinjection interventions to increase CAR T cell activity are limited because immune perturbations and synthetic circuits that allow precise control of cell functions over time and in clinical set-

Laboratory of Integrative Cancer Immunology, Center for Cancer Research, National Cancer Institute, Bethesda, MD, USA. Email: gregoire.altan-bonnet@nih.gov

tings remain elusive. Allen *et al.* and Li *et al.* present strategies to allow control over time. Li *et al.* describe synthetic gene circuits in which cell functions (including cytokine production and CAR expression) can be activated on demand with the timed administration of a drug. Allen *et al.* introduce synthetic gene circuits that trigger the production of the cytokine interleukin-2 (IL-2), a specific growth factor for T cells, only at the time that CAR T cells are in direct contact with tumor cells.

Stepwise control of engineered T cells

Synthetic biology–based approaches could enhance the antitumor activity of chimeric antigen receptor (CAR) T cells with (**1**) synthetic Notch receptor (synNotch) circuits to recognize the tumor cells and/or (**2**) synthetic transcriptional regulators that are controlled using small-molecule inducers (drugs). This could promote the production of cytokines to drive the proliferation of CAR T cells when they reach the tumor as well as control their activity over time to give CAR T cells rest periods to prevent them from becoming exhausted.

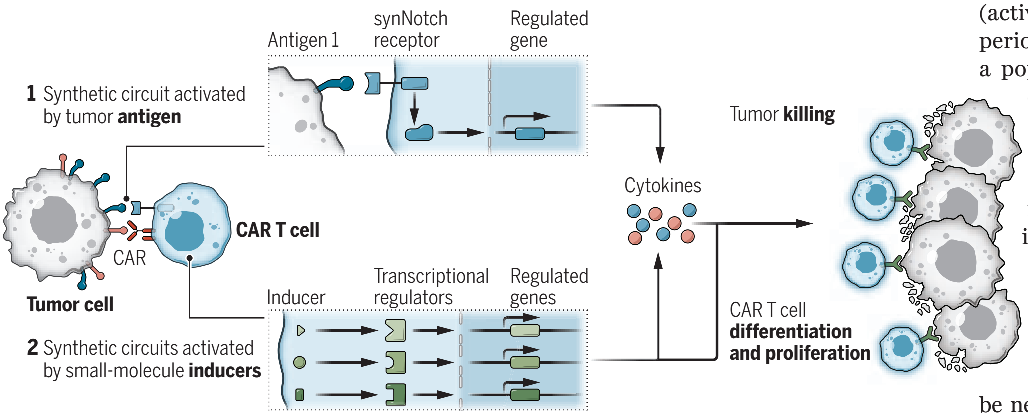

GRAPHIC: A. FISHER/*SCIENCE*

Li *et al.* engineered a set of 11 gene circuits, comprising synthetic transcriptional regulators, DNA binding motifs, and reporters. These circuits were built to be compact, minimize the risk of adverse immune responses against the synthetic gene regulators, and have minimal cross-reactivity with genes in the human genome. Some of these circuits were further engineered to allow for precise control over the timing of circuit activation and the level of gene expression through the administration of commonly used pharmaceuticals. For example, the antiviral drug grazoprevir activated the circuits by preventing the degradation of a synthetic transcriptional regulator that contains a self-cleaving protease domain. The authors quantified the dynamic ranges and kinetics of activation-deactivation for each of these circuits, which will be essential to optimize future circuit designs with timed control. As a proof of concept, they used these circuits in CAR T cells injected into mice to sequentially activate two cell functions: proliferation, through the expression of the synthetic cytokine super IL-2 (*5*) that robustly induces T cell expansion; and antitumor response, induced by the expression of the CAR. The development of these tools will allow for the exploration of dynamic immunotherapies that are fine-tuned to drive engineered immune cells into states that are ideal for effective and persistent antitumor activity.

Allen *et al.* focused on alleviating one of the main limitations of CAR T cell therapies: overcoming the immunosuppressive environment of solid tumors. Although inflammatory cytokines could help overpower immunosuppression, systemic administration of cytokines has failed to overcome this hurdle for CAR T cells. To explore whether targeting the production of cytokines at the site of the tumor would overcome CAR T cell inhibition, Allen *et al.* harnessed the recently developed synthetic Notch receptors (synNotch) (*6*), which allow the design of CAR T cells that secrete IL-2 when they come into direct contact with tumor cells. This synergistic recognition of tumor cells is engineered using a synNotch receptor that responds to a separate surface antigen that is distinct from that recognized by the CAR. Allen *et al.* demonstrated that adding this IL-2 circuit to CAR T cells allowed their infiltration into solid tumors (pancreatic cancer and melanoma) in mice and caused substantial tumor eradication. This pronounced improvement in antitumor activity was not observed when CAR T cells were engineered to produce IL-2 all the time or when the IL-2 production was downstream of CAR activation.

The combination of the two technological advances presented by Li *et al.* and Allen *et al.* will allow for an unprecedented ability to precisely control the state of therapeutic cell populations not only at the time of injection but also while the immune response is unfolding within the patient (see the figure). It is possible that these technologies can be combined to maintain CAR T cells in a proliferative and cytotoxic state, attacking the tumor cells without becoming exhausted. This proposed strategy is based on recent findings in mice that periodic resting of CAR T cells for 4 days using a drug inhibitor against Src kinases prevents CAR T cell exhaustion (*7*) and allows for greater antitumor responses than if CAR T cells are rested for 1 day or always active (*8*). In contrast to drug inhibitors, which would inhibit all CAR T cells during the resting periods, multiple populations of CAR T cells could be engineered so that their state (active versus resting) could be swapped periodically. Thus, there would always be a population of active CAR T cells. Such dynamic tuning increases antitumor functions over time and potentially improves more classical approaches of "turbocharging" tumor-infiltrating lymphocytes at the onset of the immunotherapy (*8*, *9*).

These studies multiply the number of possible interventions across time and/or in combination. Therefore, engineering approaches, machine learning, and theoretical modeling will be needed to tackle this complexity and deliver effective immunotherapies. Indeed, it is important to note that when using machine learning to determine appropriate therapies, the derived models must be interpretable (*10*–*13*) so that clinicians can understand the impact of the proposed immunotherapeutic treatments and design the next interventions that allow finely tuned dynamic control. ■

REFERENCES AND NOTES

1. Y. Zhang, Z. Zhang, *Cell. Mol. Immunol.* **17**, 807 (2020).
2. G. M. Allen *et al.*, *Science* **378**, eaba1624 (2022).
3. H.-S. Li *et al.*, *Science* **378**, 1227 (2022).
4. P. Sharma, S. Hu-Lieskovan, J. A. Wargo, A. Ribas, *Cell* **168**, 707 (2017).
5. A. M. Levin *et al.*, *Nature* **484**, 529 (2012).
6. L. Morsut *et al.*, *Cell* **164**, 780 (2016).
7. E. W. Weber *et al.*, *Science* **372**, eaba1786 (2021).
8. M. Legut *et al.*, *Nature* **603**, 728 (2022).
9. A. Schietinger, *N. Engl. J. Med.* **386**, 2334 (2022).
10. C. Rudin, *Nat. Mach. Intell.* **1**, 206 (2019).
11. S. R. Achar *et al.*, *Science* **376**, 880 (2022).
12. T. J. Rademaker, E. Bengio, P. François, *Phys. Rev. X* **9**, 031012 (2019).
13. A. Culos *et al.*, *Nat. Mach. Intell.* **2**, 619 (2020).

ACKNOWLEDGMENTS

The authors are supported by the Intramural Research Program of the National Institutes of Health, National Cancer Institute.

10.1126/science.adf5318

PHYSICS

Understanding the call of the monopole

Mysterious magnetic noise of elusive particles is finally understood

By **Felix Flicker**

Noise is often thought of as merely a hindrance to detecting a signal, but it frequently contains vital clues to otherwise hidden behavior. Recently, noise has been used to hunt for elusive particles called emergent magnetic monopoles, which are predicted to exist within crystals called spin ices (*1*). Monopoles would feature a magnetic charge that resembles the north pole of a magnet moving independently of the south pole. In 2019, the first noise measurements on monopole dynamics revealed distinctive spontaneous noise in the magnetization of spin ices (*2*). However, the noise differed from the simplest expectations for magnetization coming from moving magnetic particles. On page 1218 of this issue, Hallén *et al.* (*3*) propose that natural constraints in a spin ice restrict monopole motions to a lattice (within the spin ice crystal) that bears a fractional number of dimensions (known as a fractal). Understanding the nature of monopoles in spin ice might have important practical uses, in much the same way that understanding the nature of electrons facilitated modern electronics.

The theory of monopoles in spin ices is elegant in its simplicity. Imagine several bar magnets aligned end to end and pointed in the same direction. Flipping a single magnet gives a double north pole next to a double south pole. Flipping a neighboring magnet distances the double-north from the double-south. Subsequent magnet flips can move the double-north and double-south like independent particles. In a spin ice, this situation is believed to come about naturally, in three dimensions, on the atomic scale. However, Hallén *et al.* explain that not all flips are equal. Using a detailed model of individual atomic environments (*4*), the authors show that the possible future moves of a monopole are constrained both by where the monopoles are situated in the spin ice and where they have been. Separating double north and double south in the line of bar magnets leaves a string of flipped magnets connecting them. Similarly, "Dirac strings" weave through the spin ice. In this case, they constrain the movement of each monopole. The result is a branching tree of possibilities that grows as possible futures split and merge dynamically. The tree has the notable property that it looks the same at all scales. Furthermore, the appearance of a fractal within an ordered crystal is unprecedented.

One role monopoles could play is in the emerging field of spintronics, an alternative to electronics that uses particles' magnetic fields (spins) rather than their electric charges. Spintronic devices offer major efficiency gains and a possible route forward now that the 50-year period of exponential growth governed by Moore's law is ending. Spintronic memories are already commercially available. However, monopoles could replace many electronic devices with magnetic equivalents, in which the magnetic fields of particles are leveraged. The necessary cryogenic temperatures for such "magnetronics" need not be a hindrance in the age of cloud computing. For this to occur, however, the nature of the emergent monopoles and their dynamics must be better understood. This is where noise can help.

> **"Using noise to understand the hidden world of particles has an ancient precedent."**

Using noise to understand the hidden world of particles has an ancient precedent. Roman poet Lucretius saw evidence for the existence of atoms in the dancing patterns of dust in air (*5*). In 1905, Albert Einstein put this on a quantitative footing (*6*). He explained that the Brownian motion of pollen grains in water comes from the jostling of individual water molecules. The pollen's velocity changes randomly from moment to moment, producing a "white noise" of velocity fluctuations; in analogy to white light, any frequency is equally likely to be found. The fluctuations in the position can then be calculated by integrating over time. The result is "red noise" that decreases as the square of the frequency (analogously, removing high frequencies from white light leaves red light). Low-frequency changes in velocity move the pollen grain more than high-frequency changes because they push for longer in one direction.

The study of noise in spin ices began in 2018 when numerical simulations predicted that the noise would instead decrease as the frequency raised to a power between one and two, varying with temperature (*7*). This is called pink noise, lying between red and white. Pink noise is ubiquitous—appearing, for example, in the tide times of the Nile, heartbeat rhythms, scene lengths in films, and financial markets. Although white and red noise are well understood, no general theory of pink noise exists, and its origin and ubiquity remain major unsolved problems in physics.

Hallén *et al.* explain the origin of pink noise in the magnetization dynamics of spin ices as coming from the constrained motion of emergent magnetic monopoles. This unification of theory and experiment parallels the microscopic understanding that underpins the development of modern electronics. Yet much remains to be understood. Noise is the result of the collective motion of many monopoles. A pressing question is how to observe a single monopole. This could in principle be achieved with sufficient advances in low-temperature, atomic-scale magnetic field measurements. The development of electronic devices required a precise understanding of materials' conductive properties over a range of temperatures and driving frequencies. Practical magnetronics would require a similar understanding across the growing range of known spin ice materials. The branching possibilities understood by Hallén *et al.* also suggest an intriguing possibility of spin ices as memory storage devices. Pink noise implies that monopoles have a memory of their past, but the precise form of this memory and its relation to Dirac strings remains to be elucidated. ■

School of Physics and Astronomy, Cardiff University, Cardiff CF24 3AA, UK. Email: flicker@cardiff.ac.uk

REFERENCES AND NOTES

1. C. Castelnovo, R. Moessner, S. L. Sondhi, *Nature* **451**, 42 (2008).
2. R. Dusad *et al.*, *Nature* **571**, 234 (2019).
3. J. N. Hallén *et al.*, *Science* **378**, 1218 (2022).
4. B. Tomasello, C. Castelnovo, R. Moessner, J. Quintanilla, *Phys. Rev. Lett.* **123**, 067204 (2019).
5. T. L. Carus, *De Rerum Natura*, Book II, verses 113–140 (~60 BCE).
6. A. Einstein, *Ann. Phys.* **322**, 549 (1905).
7. F. K. K. Kirschner *et al.*, *Phys. Rev. B* **97**, 140402(R) (2018).

ACKNOWLEDGMENTS

I thank J. C. S. Davis and M. B. Weissman for helpful comments.

10.1126/science.ade2301

An operator carries a Domakha drone in Zaporizhzhia, Ukraine, on 8 November 2022.

TECHNOLOGY

Designing lethal technologies

An ethicist offers a framework for incorporating ethical and legal constraints into autonomous and AI weapons

By **Audrey Kurth Cronin**

The ongoing war in Ukraine makes it challenging to weigh ethical and moral constraints on new military technologies. Thousands of civilians are dying, the Russians are targeting civilian infrastructure, and both sides are testing novel cyber, remote, and autonomous weapons systems on the battlefield. It is tempting to conclude that restrictions on autonomous weapons systems are pointless or unrealistic. In *Law, Ethics and Emerging Military Technologies*, George Lucas presents a compelling case to think again.

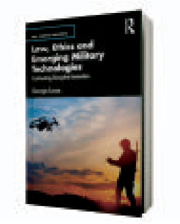

Law, Ethics and Emerging Military Technologies
George Lucas
Routledge, 2022.
232 pp.

No flighty philosophizer, Lucas takes a practical tone in his book. Having spent decades teaching and writing about military ethics at the US Naval Academy and Naval Postgraduate School, he has deep experience preparing sailors and marines to face ethical dilemmas in combat. Focusing on the use of force by states, Lucas surveys efforts to govern the use of autonomy and artificial intelligence (AI) in military weapons systems.

The book opens with a broad overview of terms and topics in the study of postmodern warfare (conflict after the Cold War), including robotics, artificial intelligence, and cyber weapons. With this strong foundation, Lucas reviews two decades of debate over lethal autonomous weapons systems, or LAWS. Proponents hold that LAWS better identify targets, spare civilians, make attacks more discriminate, and reduce overall suffering. Opponents believe that they damage human dignity, make war more likely, and could escape human control. Lucas concludes that 20 years of debate and proposed international regulation, including at the Geneva-based United Nations (UN) Convention on Certain Conventional Weapons (*1*), have yielded nothing.

Meanwhile, globally proliferated, widely produced, inexpensive systems with autonomous capabilities are already on the battlefield (*2*) and have appeared on both sides in the Ukraine war (*3*, *4*). Price, accessibility, and tactical simplicity are overtaking theoretical arguments. Autonomous weapons restrictions seem unlikelier than ever.

Lucas argues that we can reduce catastrophic risks by applying a technological solution to a technological problem, engineering autonomous systems to operate within defined limitations. Some readers will seek greater detail on how that would work. Lucas argues that engineers, industrial designers, producers, and military end users must craft systems that address this problem, lest they find themselves culpable for malfunctions, mistakes, or misuse.

Cyberwarfare is the book's next focus. Lucas believes that AI-enabled cyber operations pose three ethical problems: inadvertent escalation, where autonomous interactions spiral out of control; proliferation, where AI tools replace human beings and sophisticated cyber operations become widely accessible; and attribution, where broader participation makes it harder to identify nefarious actors. He covers a broad range of moral and legal challenges, including problems of transparency, privacy, responsibility, trust, and discrimination in targeting.

Lucas concludes with a fascinating story about the Norwegian aerospace and defense company Nammo. The Nammo M72 is a light, cheap, and portable antitank weapon easily carried and fired by one person. Nammo engineers wanted to provide it to the Ukrainians but were concerned about the safety of the human operator, who must get close to the target before the weapon can be deployed, putting themselves at risk. To solve this problem, engineers mounted the M72 on an off-the-shelf hobbyist drone, gave it AI-enhanced navigational guidance, and added target-recognition software in lieu of remote controls (*5*). Worried these changes made the Nammo M72 a lethal autonomous weapon, they consulted Lucas. "Was it legal to deploy?" they asked. Yes, he advised, the weapon's components were all legally permissible. "Was it moral to deploy?" they wondered. Although Lucas compliments the Nammo engineers for their ethical concerns, he does not render a verdict. Reportedly, Ukrainians are now using Nammo M72 shoulder-fired antitank weapons but not (yet?) the drone-mounted autonomous variant (*6*).

All in all, *Law, Ethics and Emerging Military Technologies* is an excellent contribution by a technological optimist who believes that engineers and scientists can incorporate legal and ethical constraints into machines. With this book, Lucas offers a helpful framework and urges them to do so. ■

The reviewer is director of the Center for Security, Innovation, and New Technology, American University, Washington, DC 20016, USA. Email: cronin@american.edu

REFERENCES AND NOTES

1. UN Office for Disarmament Affairs, The Convention on Certain Conventional Weapons; https://www.un.org/disarmament/the-convention-on-certain-conventional-weapons/.
2. UN Security Council, Letter from the Panel of Experts on Libya addressed to the President of the Security Council, 8 March 2021, p. 17.
3. S. Witt, "The Turkish drone that changed the nature of warfare," *The New Yorker*, 9 May 2022.
4. Z. Kallenborn, "Russia may have used a killer drone in Ukraine. Now what?," *Bulletin of the Atomic Scientists*, 15 March 2022.
5. R. Hughes, "Nammo finalises drone-mounted M72 deployment," *Janes*, 21 December 2021.
6. D. Malyasov, "Ukraine receives M72 LAW weapon systems," Defence Blog, 2 March 2022.

10.1126/science.ade9244

PHOTO: NURPHO/AP IMAGES

MATHEMATICS

The model, the modeler, and the truth

Escaping the realm of simplified systems is difficult but necessary, argues a statistician

By **James Nguyen**

Scientific models are ubiquitous. They structure much of our thought, and indeed our lives. They have acted, and continue to act, as protagonists in three of the most globally important events of my lifetime: the 2008 financial crisis, the COVID-19 pandemic, and humanity's ongoing attempts to grapple with anthropogenic climate change. It is not an overexaggeration to say that they have underpinned decisions that have affected billions of lives (not to mention the future generations whose existence may depend on these decisions). The consequences of reasoning inappropriately with models are anything but trivial.

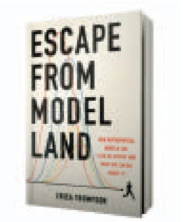

Escape from Model Land
Erica Thompson
Basic Books, 2022.
256 pp.

In her tremendous book, *Escape from Model Land*, Erica Thompson mounts a broadside against the idea that models can be naïvely interpreted as literally true descriptions of reality. The book's first three chapters introduce a philosophically rich framework by which to understand modeling endeavors. Here, readers are urged to think of models as residing in "Model Land," a realm of simplified systems. If we want to use them as guides to action, Thompson argues, we must consciously reflect on how to escape from this domain into the messy world in which we actually live. Given the limitations of models, particularly with respect to their failure to represent unquantifiable unknowns, this exit is never straightforward.

In chapter 4, Thompson explores the extent to which mathematical reasoning can aid us in this endeavor. Two exits are discussed: a quantitative one, employing statistical techniques, and a qualitative one, which requires informal expert judgment, with a particular emphasis on recognizing models' limits. One of Thompson's central arguments is that the latter needs to be put on an equal footing with the former to accurately reason with model outputs.

Next, Thompson turns to how models can aid decision-making, even in cases where their accuracy is limited. Here, readers are charmingly encouraged to consider an analogy drawn from the use of astrology in medieval courts. Models, like a court adviser's astrological predictions, can be thought of as constructive ways to systematize and communicate the thoughts of experts to decision-makers, without needing to fully capture the complexity of a given situation, she argues.

In a chapter titled "The Accountability Gap," Thompson explores the implications of understanding the modeler and the model together as a single system that is itself embedded in a wider "cognitive assemblage" of experts and models. This section deals particularly with the assignment of responsibility for model-based decisions and reiterates one of the book's recurring lessons: Because we cannot (and should not) separate the model from the modeler, and because each model provides, at best, a partial perspective that encodes the values of individual modelers, our best bet for making "good" model-based decisions is to draw on a diverse collection of models. These models, argues Thompson, should reflect values beyond those traditionally associated with individuals at elite Western universities.

The book's later chapters provide case studies devoted to the roles played by models in various high-stakes settings: Chapter 7 documents the uses and abuses of models in financial trading and banking and insurance regulation, chapter 8 focuses on models of weather and the climate, and chapter 9 turns to the epidemiological models that informed responses to the COVID-19 pandemic. The breadth of Thompson's discussion of these topics is impressive—all three are highly accessible to nonexperts; not one is dumbed down—and each chapter demonstrates incisively the pitfalls we face when we fail to recognize the limits of models and the opportunities afforded by recognizing these limits. The final chapter rounds out the discussion and offers five principles for responsible modeling that should be digested by all working modelers as well as those working with them.

There are a few instances where the book skirts some important topics rather quickly. For example, I would have welcomed a richer discussion of when the quantitative escape route is appropriate and how it can be employed beyond those simple cases where model-target divergences can be modeled as random noise. It would have also been useful to explore in more detail techniques for making "all things considered" decisions based on diverse model collections, particularly when these models disagree with one another.

Overall, however, *Escape from Model Land* is a triumph that integrates multiple areas of philosophy with a breadth of scientific expertise to motivate a genuinely humanistic account of model-based thought and action, all while providing an optimistic account of humanity's ability to integrate a diversity of perspectives for the betterment of all. ■

10.1126/science.ade9573

The reviewer is at the Department of Philosophy, Stockholm University, SE-106 91 Stockholm, Sweden. Email: james.nguyen@philosophy.su.se

ILLUSTRATION: HANNAH AGOSTA

PODCAST

Best books of 2022

An immersive tour of Earth's past, a fictional foray to a luxury space station, a sumptuous portrait of a pair of volcanologists, and a charming compendium of science-minded "spells" for kids earned our attention in 2022. This week on the podcast, *Science*'s book review editor, Valerie Thompson, discusses these and other books and films we reviewed and loved this year. https://bit.ly/3VgaEmx

10.1126/science.adg0504

LETTERS

The eruption of Mauna Loa could disrupt data collection that has taken place daily for decades.

PHOTO: ANDREW RICHARD HARA/GETTY IMAGES

Edited by **Jennifer Sills**

Editorial Expression of Concern

On 15 September, *Science* published the Research Article “Structural basis for strychnine activation of human bitter taste receptor TAS2R46” by Weixiu Xu *et al.* (*1*). The editors have been made aware that the examination of data provided after publication revealed potential discrepancies with fig. S10D. This figure was used to support a proposal of precoupling between TAS2R46 and the G protein gustducin. We are alerting readers to these concerns while the authors’ institution investigates further.

H. Holden Thorp
Editor-in-Chief

REFERENCES AND NOTES

1. W. Xu *et al.*, *Science* **377**, 1298 (2022).

Published online 22 November 2022
10.1126/science.adf8367

Give long-term datasets World Heritage status

Throughout history, people motivated by ritual or curiosity have routinely recorded their observations of the world around them. The resulting datasets document our changing planet and provide clear evidence of our role in altering the biosphere [e.g., (*1*–*7*)]. However, despite their importance, the future of many such datasets remains uncertain; one chance event or funding decision could lead to their termination. These datasets merit international recognition and support.

Some environmental datasets are so integral to our understanding of the world around us and our place in it that leaving their continuation to the vagaries of fate or government funding cycles is illogical and irresponsible. Instead, an international organization should designate universally valuable long-term environmental datasets as “World Heritage datasets,” in a process similar to the one used by the United Nations Educational, Scientific, and Cultural Organization to designate World Heritage sites. Such a designation would acknowledge that high-impact, long-term datasets that document our changing environment are a part of our cultural heritage.

World Heritage datasets should be high impact, consistent, sustained, available, and accessible. The Keeling curve data on daily atmospheric CO_2 concentrations at Mauna Loa in Hawaii, for example, has documented the impact of fossil fuel combustion on the atmosphere for 64 years (*4*, *5*). The record of cherry blossom dates in Kyoto—recorded across the centuries by imperial courts, newspapers, and scientists (*6*)—strikingly illustrates the effects of climate change on the biosphere (*1*, *2*). Data on the chemistry of precipitation and stream water at Hubbard Brook in New Hampshire (*7*), collected weekly since 1963, led to the discovery of acid rain and the passage of legislation to control it, and now documents the effectiveness of that legislation (*3*). Crucial long-term datasets like these are fragile and face threats ranging from shifts in funding priorities to volcanic eruptions (*8*).

An international organization such as the UN Environment Programme could develop the criteria and process through which World Heritage status can be awarded to environmental datasets. By establishing the value of long-term environmental records, World Heritage designation would help secure funds, ensure data longevity and accessibility, and encourage the creation of new datasets of significance for understanding global change.

Emma J. Rosi[1]*, Emily S. Bernhardt[2], Christopher T. Solomon[1], Gene E. Likens[1,3], William H. McDowell[4], Irena F. Creed[5]
[1]Cary Institute of Ecosystems Studies, Millbrook, NY 12545, USA. [2]Department of Biology, Duke University, Durham, NC 27708, USA. [3]Institute of the Environment, University of Connecticut,

Storrs, CT 06269, USA. [4]Department of Natural Resources and the Environment, University of New Hampshire, Durham, NH 03824, USA. [5]Department of Physical and Environmental Sciences, University of Toronto, Toronto, ON M1C1A4, Canada.
*Corresponding author.
Email: rosie@caryinstitute.org

REFERENCES AND NOTES

1. Y. Aono, K. Kazui, *Int. J. Climatol.* **28**, 905 (2008).
2. N. Christidis, Y. Aono, P. A. Stott, *Environ. Res. Lett.* **17**, 054051 (2022).
3. G. E. Likens, *Front. Ecol. Environ.* **8**, e1 (2010).
4. C. D. Keeling, *Tellus* **12**, 200 (1960).
5. The Keeling Curve (University of San Diego, 2022); https://keelingcurve.ucsd.edu.
6. Kyoto Cherry Blossom Full Flower Dates (Datagraver, 2022); https://www.datagraver.com/case/kyoto-cherry-blossom-full-flower-dates.
7. Ecosystem Data Visualization (2022); hbwater.org.
8. E. Shao, "Mauna Loa eruption threatens a famous climate record," *New York Times* (2022).

10.1126/science.adg0508

Support for climate policy researchers

In the past 2 years, the European Union and the United States announced plans to spend $573 and $391 billion, respectively, through 2030 on climate actions (*1*) and passed landmark legislation such as the US Inflation Reduction Act (*2*). Although unprecedented in size and scope, these combined investments of $964 billion pale in comparison to the more than $4 trillion in global clean energy investment needed annually by 2030 to stay on track for net zero greenhouse gas emissions by 2050 (*3*). To maximize the impact of this public money, efficient policies informed by independent, objective analysis will be needed. Yet scientists who commit to policy-relevant research face unique challenges that must be addressed.

Beyond infrastructure, meeting climate goals requires investing in researchers, many of whom will likely spend their entire careers analyzing clean energy technology and policy rollouts (*4*), assessing their impacts on society, and advising on needed course corrections. This community must include early-career scholars who are essential to tackling the protracted, multi-decadal challenges posed by climate change. Academia can be the wellspring for this research community, but institutions must recognize the barriers they impose on interdisciplinary, applied, policy-focused research.

Policy-relevant energy research combines a broad knowledge base, spanning engineering, social science, and physical science (*5*, *6*). Such research faces well-documented challenges in finding funding, collaborators, and knowledgeable peer reviewers and editors (*7*, *8*). It also takes time, effort, and skill to disseminate research findings to policymakers and journalists. Effectiveness usually requires deep engagement with communities and policy circles, which can introduce new risks, such as backlash from colleagues, students, and legislators.

Academic institutions can support policy-relevant researchers by providing consistency and incentives. Ensuring that funding for early-career researchers is stable should be a priority. With dependable funding, scholars can focus on activities that maximize their research's impact and advance their careers. Broadening career incentives to reflect the nature of policy-relevant research—e.g., by adding (but not mandating) policy outreach metrics alongside the usual success criteria for tenure and promotion cases—would further remove barriers.

Institutions can also facilitate connections for scientists working in these fields. Policy-focused workshops (*9*) would enhance networking and allow scholars to interact with government officials and senior researchers, fostering ideation, sharpening research questions, and providing new opportunities for collaboration. Media engagement training would better prepare them to communicate their findings. Fact-based public discourse is more important than ever, but researchers often lack the network, skills, and resources to engage effectively with journalists.

These reforms aren't without implementation challenges. Academia will need a fresh debate about how (or whether) to measure and grade policy engagement and impact and how to overcome skepticism about policy-relevant research in more traditional departments. But the gravity of the climate crisis merits a rethink. Now is the time to reevaluate academia's role.

Ryan Hanna[1]*, Eugenie Dugoua[2], Alejandro Nuñez-Jimenez[3], Destenie Nock[4,5], Stephanie Arcusa[6], Sergio Castellanos[7], Michael R. Davidson[8,9], Morgan R. Edwards[10,11], Clara Galeazzi[12], Xue Gao[13], Michelle Graff[14], Kathleen M. Kennedy[15], Eleftheria Kontou[16], Priyank Lathwal[17], Mirko Musa[18], Eric O'Rear[19], S. Sivaranjani[20], Jingjing Zhang[21], Qianru Zhu[22]

[1]Center for Energy Research, University of California San Diego, La Jolla, CA 92093, USA. [2]London School of Economics, London, UK. [3]ETH Zurich, Zurich, Switzerland. [4]Department of Engineering and Public Policy, Carnegie Mellon University, Pittsburgh, PA 15213, USA. [5]Department of Civil and Environmental Engineering, Carnegie Mellon University, Pittsburgh, PA 15213, USA. [6]Center for Negative Carbon Emissions, Arizona State University, Tempe, AZ 85287, USA. [7]Department of Civil, Architectural, and Environmental Engineering, University of Texas at Austin, Austin, TX 78712, USA. [8]School of Global Policy and Strategy, University of California San Diego, La Jolla, CA 92093, USA. [9]Jacobs School of Engineering, University of California San Diego, La Jolla, CA 92093, USA. [10]La Follette School of Public Affairs, University of Wisconsin–Madison, Madison, WI 53715, USA. [11]Nelson Institute Center for Sustainability and the Global Environment, University of Wisconsin–Madison, Madison, WI 53715, USA. [12]Centre for Energy, Environment, and Natural Resource Governance, University of Cambridge, Cambridge, UK. [13]Department of Political Science, University of Miami, Coral Gables, FL 33146, USA. [14]Maxine Goodman Levin School of Urban Affairs, Cleveland State University, Cleveland, OH 44115, USA. [15]Center for Global Sustainability, School of Public Policy, University of Maryland College Park, College Park, MD 20742, USA. [16]Department of Civil and Environmental Engineering, University of Illinois at Urbana-Champaign, Urbana, IL 61801, USA. [17]Energy and Extractives Global Practice, World Bank Group, Washington, DC 20433, USA. [18]Environmental Sciences Division, Oak Ridge National Laboratory, Oak Ridge, TN 37830, USA. [19]Rhodium Group, New York, NY 10019, USA. [20]School of Industrial Engineering, Purdue University, West Lafayette, IN 47907, USA. [21]Lawrence Berkeley National Laboratory, Berkeley, CA 94720, USA. [22]Energy Systems and Climate Analysis, Electric Power Research Institute, Palo Alto, CA 94304, USA.
*Corresponding author. Email: rehanna@ucsd.edu

REFERENCES AND NOTES

1. "Climate mainstreaming," European Commission (2021); https://ec.europa.eu/info/strategy/eu-budget/performance-and-reporting/mainstreaming/climate-mainstreaming_en.
2. "CBO scores IRA with $238 billion of deficit reduction," Committee for a Responsible Federal Budget (2022); https://www.crfb.org/blogs/cbo-scores-ira-238-billion-deficit-reduction.
3. International Energy Agency, "Net Zero by 2050: A roadmap for the global energy system" (2021).
4. R. Hanna, D. G. Victor, *Nat. Energ.* **6**, 568 (2021).
5. F. W. Geels, B. K. Sovacool, T. Schwanen, S. Sorrell, *Science* **357**, 1242 (2017).
6. B. K. Sovacool *et al.*, *Energ. Res. Soc. Sci.* **70**, 101617 (2020).
7. C. J. Hein *et al.*, *WIREs Clim. Change.* **9**, e530 (2018).
8. E. Leahey, *Eur. Rev.* **26**, S55 (2018).
9. 2022 Climate-Tech Policy "Boot Camp" for Early Career Researchers, Information Technology and Innovation Foundation (2022); https://itif.org/events/2022/06/05/2022-climate-tech-policy-boot-camp-for-early-career-researchers/.

10.1126/science.adf8956

ERRATA

Erratum for the Report "Ultrahard magnetism from mixed-valence dilanthanide complexes with metal-metal bonding," by C. A. Gould *et al.*, *Science* **378**, eadf5804 (2022). Published online 11 November 2022; 10.1126/science.adf5804

Erratum for the Research Article "Structural basis of ribosomal frameshifting during translation of the SARS-CoV-2 RNA genome," by P. R. Bhatt *et al.*, *Science* **378**, eadf3953 (2022). Published online 21 October 2022; 10.1126/science.adf3953

Your Legacy to Science

AN ESTATE GIFT TO THE
AMERICAN ASSOCIATION FOR THE ADVANCEMENT OF SCIENCE



Since 1848, our founding year, the American Association for the Advancement of Science (AAAS) has been deeply committed to advancing science, engineering and innovation around the world for the benefit of all people.

By making AAAS a beneficiary of your will, trust, retirement plan or life insurance policy, you become a member of our 1848 Society, joining Thomas Edison, Alexander Graham Bell and the many distinguished individuals whose vision led to the creation of AAAS and our world-renowned journal, *Science*, so many years ago.

Unlike many of its peers, *Science* is not for-profit. Your estate gift would provide long-term financial stability and durable annual income that will support operations and competitive innovation for years to come. **This support is vital.**

> *"As a teacher and instructor, I bear responsibility for the younger generations. If you have extra resources, concentrate them on organizations, like AAAS, that are doing work for all."*
>
> **—Prof. Elisabeth Ervin-Blankenheim, 1848 Society member**

If you intend to include AAAS in your estate plans, provide this information to your lawyer or financial adviser:

Legal Name: American Association for the Advancement of Science
Federal Tax ID Number: 53-0196568
Address: 1200 New York Avenue, NW, Washington, DC 20005

If you would like more information on making an estate gift to AAAS, cut out and return the form below or send an email to philanthropy@aaas.org. Additional details are also available online at **www.aaas.org/1848Society**.

1848
SOCIETY
AAAS

cut here ✂

Yes, I would like more information about joining the AAAS 1848 Society.

PLEASE CONTACT ME AT:

Name: ______________________________
Address: ______________________________
City: ______________ State: ________ Zip code: ____________ Country: ________
Email: ______________________ Phone: ______________________

RETURN THIS FORM TO:
AAAS Office of Philanthropy and Strategic Partnerships • 1200 New York Avenue, NW • Washington, DC 20005 USA

RESEARCH

IN *SCIENCE* JOURNALS

Edited by
Michael Funk

PHOTO: JACOB C. ZBINDEN/SCIENCE SOURCE

SKIN INFLAMMATION

Hitting the brakes on fibrosis

Tissue fibrosis is the culminating event of many human inflammatory diseases. Few antifibrotic therapies are available, and the cellular and molecular mechanisms driving fibrosis remain unclear. Using single-cell transcriptomics, Odell et al. found that skin from patients with diffuse cutaneous systemic sclerosis was enriched for dendritic cells (DCs) producing the epidermal growth factor receptor (EGFR) ligand epiregulin. DC production of epiregulin could be induced by type I interferon and promoted NOTCH-mediated extracellular matrix gene expression in fibroblasts. In mouse models of bleomycin-induced skin and lung fibrosis, an epiregulin-neutralizing antibody alleviated fibrosis. These results identify a role for epiregulin-producing DCs in maintaining fibrosis and suggest that blocking epiregulin's EGFR activity could be a promising therapeutic strategy for treating fibrotic diseases. —CO

Sci. Immunol. **7**, eabq6691 (2022).

Fluorescence microscopy image of fibroblasts, a cell type that is overstimulated in fibrotic diseases

SYNTHETIC BIOLOGY

Exploring receptor design principles

Chimeric antigen receptor T cell technology, in which cells of the immune system are modified with customized receptors, has proved effective in cancer therapy. To explore the range of cell responses that can be encoded in such receptors and to make their design more quantitative and predictive, Daniels *et al*. tested about 200 of 2400 possible combinations of 13 signaling motifs found in such receptors and used machine learning to predict other effective combinations. Using these design rules, the authors constructed receptors in human T cells with improved signaling characteristics that contributed to better tumor control in a mouse model. —LBR

Science, abq0225, this issue p. 1194

MEMBRANES

Material design maximizes performance

Zeolites are able to separate molecules with similar size and shape because of their well-defined, uniform pore size and specific adsorption properties. However, it has been a challenge to retain these features when blending a zeolite with a polymeric matrix support. Tan *et al*. developed a method to put high loadings of the aluminosilicate SSZ-39, which is known for its attraction of carbon dioxide, into a commercial polyimide selected for its compatibility with the zeolite. The resulting mixed matrix membranes were flexible and defect free, showing excellent separation of carbon dioxide that even exceeded the performance of pure zeolite membranes. —MSL

Science, ade1411, this issue p. 1189

ORGANIC CHEMISTRY

Illuminating C–N bond formation

Forming carbon–nitrogen (C–N) bonds is integral to pharmaceutical synthesis. Palladium (Pd) catalysis is an especially efficient means to this end, but alkyl amines can deactivate the catalyst by tight binding. Several recent approaches to circumventing this problem in allylic amination have focused on modifying either the amines or the Pd coordination environment. Cheung *et al*. report a distinct protocol that operates through photoinduced electron transfer to form versatile Pd(I) intermediates. This method is also compatible with more densely substituted carbon frameworks and can selectively produce just one of two mirror image products. —JSY

Science, abq1274, this issue p. 1207

QUANTUM MATERIALS

Probing the Moiré lattice

The optoelectronic properties of bilayers of two-dimensional materials exhibit a wealth of properties dependent on the twist angle. A direct probe of the transport properties and their correlation with the atomic registry has been lacking. Susarla *et al*. used cryogenic transmission electron microscopy and spectroscopy to simultaneously image the structural reconstruction and the associated spatial localization of the lowest-energy intralayer exciton in a rotationally aligned bilayer heterostructure of tungsten disulfide and tungsten diselenide. The subnanometer spatial resolution allows the real-space mapping of intralayer excitons within a Moiré unit cell and should aid in the development of materials with controlled properties. —ISO

Science, add9294, this issue p. 1235

SPIN ICE

Fractal-hopping monopoles

Spin ices have crystal lattices that consist of tetrahedra of magnetic ions. In a ground state, two of the four spins on each tetrahedron point in and two point out. When an excitation called the magnetic monopole is created, this rule is violated as the monopole moves through the crystal. Monopole dynamics are reflected in quantities such as magnetic noise, the measurements of which have shown a different frequency dependence from the one that the simplest model predicts. Hallén *et al*. solved this puzzle by realizing that the monopole motion is more restricted than previously thought and is limited to a cluster with a fractal structure (see the Perspective by Flicker). —JS

Science, add1644, this issue p. 1218;
see also ade2301, p. 1177

EVOLUTIONARY ECOLOGY

Similar but separate species

Speciation often requires a period of allopatry, when populations are separated long enough to diverge into distinct species. Sister species may occupy different niches, but whether ecological divergence occurs during or after allopatric speciation is poorly understood. Anderson and Weir used trait data on more than 1000 pairs of sister taxa, including birds, mammals, and amphibians, to model trait divergence over time. They found few examples of clear divergent adaptation, with greater support for a model of sister taxa evolving under similar selective pressures toward similar trait optima. —BEL

Science, abo7719, this issue p. 1214

CELL BIOLOGY

A path to prevent TNF cytotoxicity

Tumor necrosis factor (TNF) is a central cytokine in inflammatory reactions and is a pharmacological target in several inflammatory disorders. Recent studies demonstrated that the pathological role of TNF in these diseases can originate from its ability to trigger cell death, an outcome that is normally actively repressed in cells. Huyghe *et al*. identified an unconventional lysosomal targeting process that prevents TNF cytotoxicity by degrading the caspase-8–activating complex that forms in response to TNF binding to TNF receptor 1 (TNFR1). Abrogating this detoxification mechanism caused TNFR1-mediated embryonic lethality or an inflammatory skin disease when locally inactivated in mice. —SMH

Science, add6967, this issue p. 1201

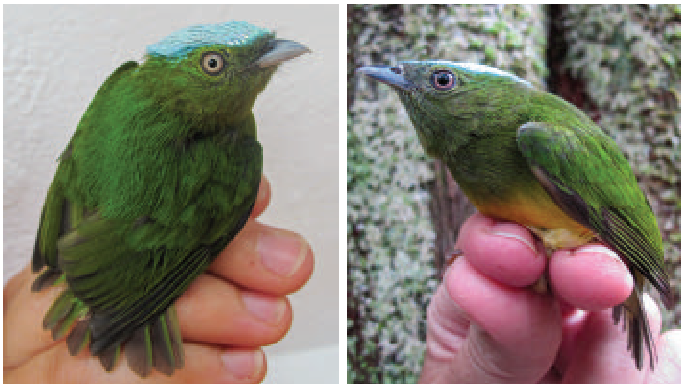

The closely related Amazonian songbirds *Lepidothrix iris* (left) and *L. nattererei* (right) evolved with similar traits despite living in different places.

IN OTHER JOURNALS

Edited by **Caroline Ash**
and **Jesse Smith**

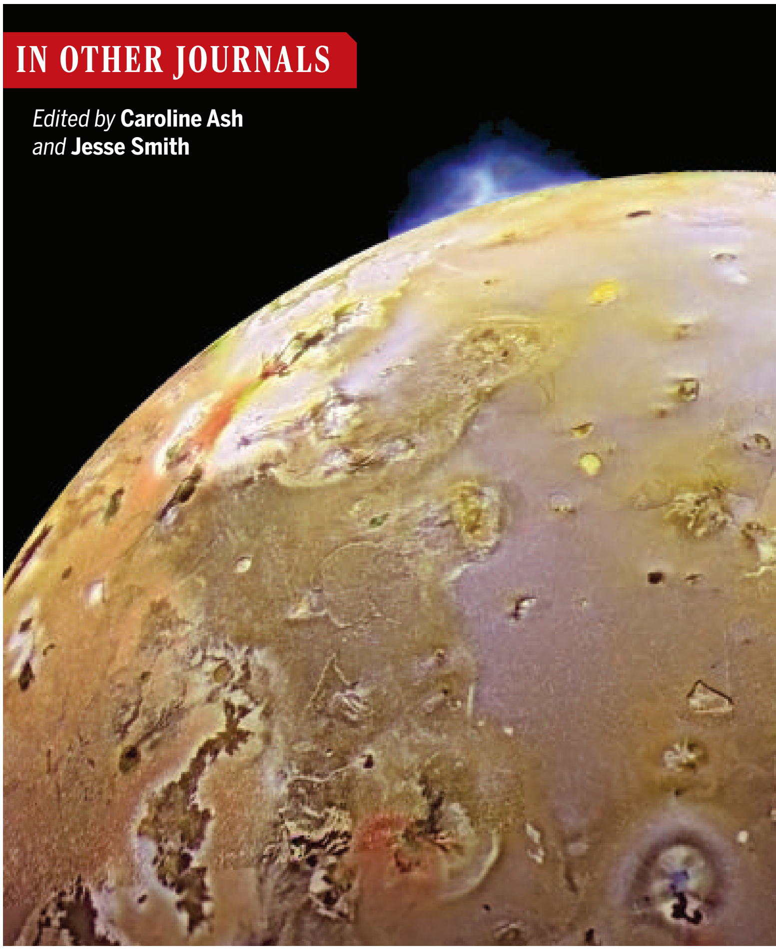

PLANT SCIENCE

Alternative crop plant dwarfing

Tall, thin stems carrying heavy grains late in the growing season are vulnerable to lodging, which is when strong winds or heavy rain flatten a field of plants. The Green Revolution of the 1960s reduced this risk with the introduction of genetic traits that shortened the average height of rice or wheat plants and increased grain yields worldwide. However, seedling growth was negatively affected and resistance to certain diseases reduced. Borrill *et al.* analyzed a plant dwarfism gene, *Reduced Height 13* (*Rht13*), that delivers its height-reducing effects later in the plant's life cycle. *Rht13* encodes a nucleotide-binding site–leucine-rich repeat (NB-LRR) protein, a member of a group of proteins often implicated in plant disease resistance. A mutation in the *Rht13* gene leaves the protein in a permanently activated state, which drives increased expression of certain disease-defense genes and results in dwarfed plants. In particular, overexpression of peroxidases might limit flexibility of cell walls, thus limiting cell elongation and overall plant height. —PJH

Proc. Natl. Acad. Sci. U.S.A.
119, e2209875119 (2022).

AQUATIC ECOLOGY

Zooplankton's nutrient limits

Energy flow through food webs is limited by consumers' ability to capture matter and energy from primary producers, which in turn depends on producer quantity and nutritional quality. In aquatic systems, studies have identified nitrogen, phosphorus, essential fatty acids, and sterols

PHOTOS: (LEFT TO RIGHT) MAYA FACCIO © 2012 THE WEIR LAB AT THE UNIVERSITY OF TORONTO AT SCARBOROUGH; NASA/JPL/DLR

PLANETARY GEOPHYSICS

Evidence for a magma ocean inside Io

Io is Jupiter's closest moon. It is on an orbit that induces strong tidal heating and makes it the most volcanically active body in the Solar System. Magnetometer data have been interpreted as indicating substantial molten material about 50 kilometers below the surface, but they cannot distinguish between a sponge-like partial melt or separate layers of solid rock and a liquid magma ocean. Miyazaki and Stevenson developed a model of the partial melt scenario, finding that such a mixture is unstable and would quickly separate into solid and liquid layers. They conclude that Io probably has a subsurface magma ocean. —KTS

Planet. Sci. J. **3**, 256 (2022).

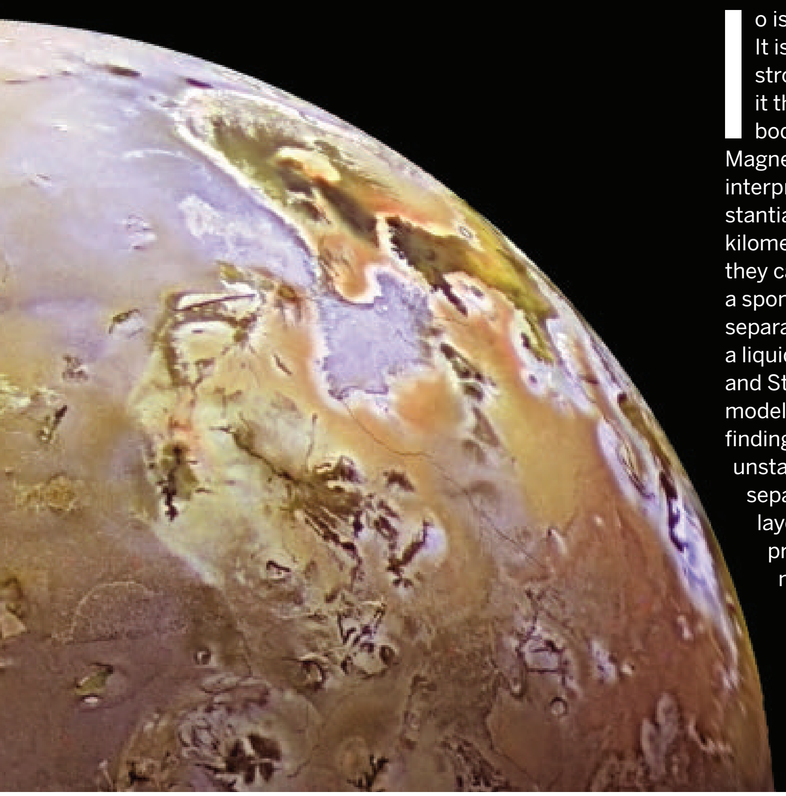

A volcanic eruption on Io, visible as the blue plume, observed by the Galileo spacecraft in 1997

as being essential nutrients for zooplankton. Thomas *et al*. performed a meta-analysis of over 100 laboratory experiments to compare the effects of these food quality indicators on zooplankton growth and reproduction. All indicators were confirmed to limit growth and reproduction, although individual fatty acids had different effects, and essential fatty acid limitation depended on phosphorus availability. The few studies that manipulated nutrients together showed strong evidence of co-limitation by multiple nutrients simultaneously. —BEL

Ecol. Lett. 10.1111/ele.14125 (2022).

CELL BIOLOGY

Leaking lysosomes and mitochondrial flux

Lysosomal damage and the leakage of lysosomal contents into the cytosol affects the function of cytoplasmic organelles. Bussi *et al.* combined high-resolution imaging, proteomics, and metabolic flux analysis to assess the effects of sterile and nonsterile lysosomal leakage in human and mouse macrophages. Nonlethal lysosomal damage led to mitochondrial protein degradation, decreased mitochondrial activity, and metabolic reprogramming in macrophages. These changes were mediated by the leakage of lysosomal proteases. Mouse lung macrophages undergoing endomembrane damage displayed impaired mitochondrial function and increased glycolytic and lipid metabolism. Finally, changes in macrophage metabolism affected host responses to *Mycobacterium tuberculosis* infection in an endomembrane damage–dependent way. —SMH

Nat. Commun. **13**, 7338 (2022).

SIGNAL TRANSDUCTION

A phase-separated osmotic stress sensor

To survive, cells need to sense osmotic stress to make compensatory responses. The protein kinase WNK1 activates survival responses, but how it senses hyperosmotic stress was unclear because the kinase is inhibited rather than activated by increased intracellular ionic strength. Instead, Boyd-Shiwarski *et al.* found that hyperosmotic stress–induced molecular crowding in the cytosol caused WNK1 to coalesce by phase separation in human cells in culture. Phase separation appears to be critical for kinase activation because the carboxyterminal region of WNK1, which is required for phase separation, can be replaced by phase-separating domains from unrelated proteins, which still allows the regulation of cell volume. —LBR

Cell **185**, 4488 (2022).

PROTEIN DEGRADERS

Understanding resistance

Small molecules that promote the proteasomal degradation of proteins show promise as therapeutics but are sensitive to mutations that disrupt protein-protein interactions. Hanzl *et al.* designed a deep mutational scanning protocol to identify functionally relevant hotspots within ubiquitin ligases and their target proteins that may lead to resistance to protein degrader therapies. Application to two commonly studied substrate receptors implicated these components in resistance but also revealed differences in mechanisms. The functional hotspots involved depended on the degrader used, likely because of distinct ternary complex structures. The authors also mapped hotspots onto data from relapsing patients and demonstrated overlap with clinical mutations. —MAF

Nat. Chem. Biol. 10.1038/s41589-022-01177-2 (2022).

ORGANIC CHEMISTRY

Closing rings at C–H bond sites

Reliable ring-closing reactions are essential to the preparation of macrocyclic pharmaceuticals. Common approaches involve condensation or olefin metathesis reactions, which constrain the end groups incorporated into the precursor. Wang *et al.* now report an alternative method that relies on successive carbon–hydrogen (C–H) bond activation steps by a rhodium catalyst: first an oxime-directed nitrene insertion reaction and then an arylation. They applied this sequence to the synthesis of a library of macrolactams, which showed preliminary activity against H1N1 influenza strains in vitro. —JSY

Chem 10.1016/j.chempr.2022.10.019 (2022).

ALSO IN *SCIENCE* JOURNALS

Edited by **Michael Funk**

BIOMATERIALS

Staying soft and conductive under strain

Most electrically conductive materials tend to be stiff and brittle, whereas human tissue is soft and compliant. It is thus a challenge to make conductive biomaterials that are sufficiently compliant but do not show a loss or distortion in performance. Zhao *et al*. used a three-layer design to couple strain-induced cracked films with a strain-isolated conductive pathway (see the Perspective by Rafeedi and Lipomi). Upon an initial prestrain to 100%, the brittle solid film on top cracks to dissipate the strain energy. However, this cracking permits a type of parallel, interconnected charge transport in which the charge carriers move between the layers to circumvent the cracks. —MSL

Science, abn5142, this issue p. 1222; see also adf2322, p. 1174

SYNTHETIC BIOLOGY

Building blocks for synthetic circuits

The promise of chimeric antigen receptor T cell therapy, in which human T cells are engineered to attack tumors, has heightened interest in cell-based therapies. Li *et al*. developed a toolkit of programmable synthetic transcription regulators that feature a compact, human protein–based design and allow transcription to be regulated by US Food & Drug Administration–approved small molecules (see the Perspective by Salazar-Cavazos and Altan-Bonnet). The authors engineered human immune cells that kill tumors when activated by the appropriate small molecule, and they also demonstrated a dual-switch system that allows sequential control of immune cell function. This platform could be adapted to design cell therapies in a variety of contexts. —VV

Science, ade0156, this issue p. 1227; see also adf5318, p. 1175

IMMUNOLOGY

Stress amps up IFN signaling

Interferon (IFN) signaling stimulates the innate immune response to infection. Boccuni *et al*. investigated the interaction between IFN signaling and stress signaling mediated by the kinase p38. In IFN-treated macrophages, coincident stress signaling synergistically increased the expression of IFN-stimulated genes. In *Listeria*-infected cultured macrophages, this boost elicited greater production of pathogen-fighting factors, but it also increased cell death. Blocking p38 signaling preserved macrophage viability without sacrificing function. —LKF

Sci. Signal. **15**, eabq5389 (2022).

MARBURG VIRUS

Fighting filoviruses

Marburg virus (MARV) outbreaks remain a major global health concern, and an effective vaccine is urgently needed. Hunegnaw *et al.* report that ChAd3-MARV, a single-shot chimpanzee adenovirus-vectored vaccine expressing the MARV glycoprotein, confers protection in nonhuman primates. Animals were protected as soon as 1 week after vaccination, and protection lasted up to 1 year, with antigen-specific antibodies serving as a predictor of protection. These results support the clinical use of ChAd3-MARV in humans. —CSM

Sci. Transl. Med. **14**, eabq6364 (2022).

SYNTHETIC BIOLOGY

Designing T cells to attack solid tumors

T cells with modified receptors that recognize tumor antigens (chimeric antigen receptor or CAR T cells) have proved effective in treating B cell malignancies, but solid tumors create an immunosuppressive microenvironment that limits their function. To overcome this limitation, Allen *et al*. enhanced engineered T cells with a second synthetic receptor that could recognize a tumor antigen and cause the T cell to secrete the cytokine interleukin-2 (see the Perspective by Salazar-Cavazos and Altan-Bonnet). Interleukin-2 promoted local proliferation of the T cells despite the tumor's immunosuppressive effects. Such engineered cells allowed effective treatment of solid tumors in mouse models. —LBR

Science, aba1624, this issue p. 1186; see also adf5318, p. 1175

CELL BIOLOGY

Alike pathways for import

Eukaryotic cells contain membrane-bounded organelles that import specific proteins from the cytosol. Organelles called peroxisomes are vital for human health because they house important metabolic enzymes. However, how enzymes are imported into peroxisomes has been mysterious, particularly because folded proteins and even protein oligomers can cross the peroxisomal membrane. Gao *et al*. found that multiple copies of a cohesive domain from the peroxisomal protein PEX13 form a dense meshwork within the membrane. Mobile import receptors can diffuse through this barrier to enter the organelle and bring bound cargo along. This mechanism resembles transport through the nuclear pore and explains how folded proteins are imported into peroxisomes. —SMH

Science, adf3971, this issue p. 1187

CELL BIOLOGY

A lipid-triggered signal in starvation

Nutrient starvation triggers changes in metabolism that are coordinated across the cell and its organelles. Jang *et al*. studied how endosomal signaling lipid turnover through MTM1, a phosphoinositide 3-phosphatase mutated in X-linked centronuclear myopathy in humans, reshapes the endoplasmic reticulum to control mitochondrial morphology and oxidative metabolism (see the Perspective by Zanellati and Cohen). A lipid-controlled organellar relay transmits nutrient-triggered changes in endosomal signaling lipid levels to mitochondria to enable metabolic rewiring. —SMH

Science, abq5209, this issue p. 1188; see also adf5112, p. 1173

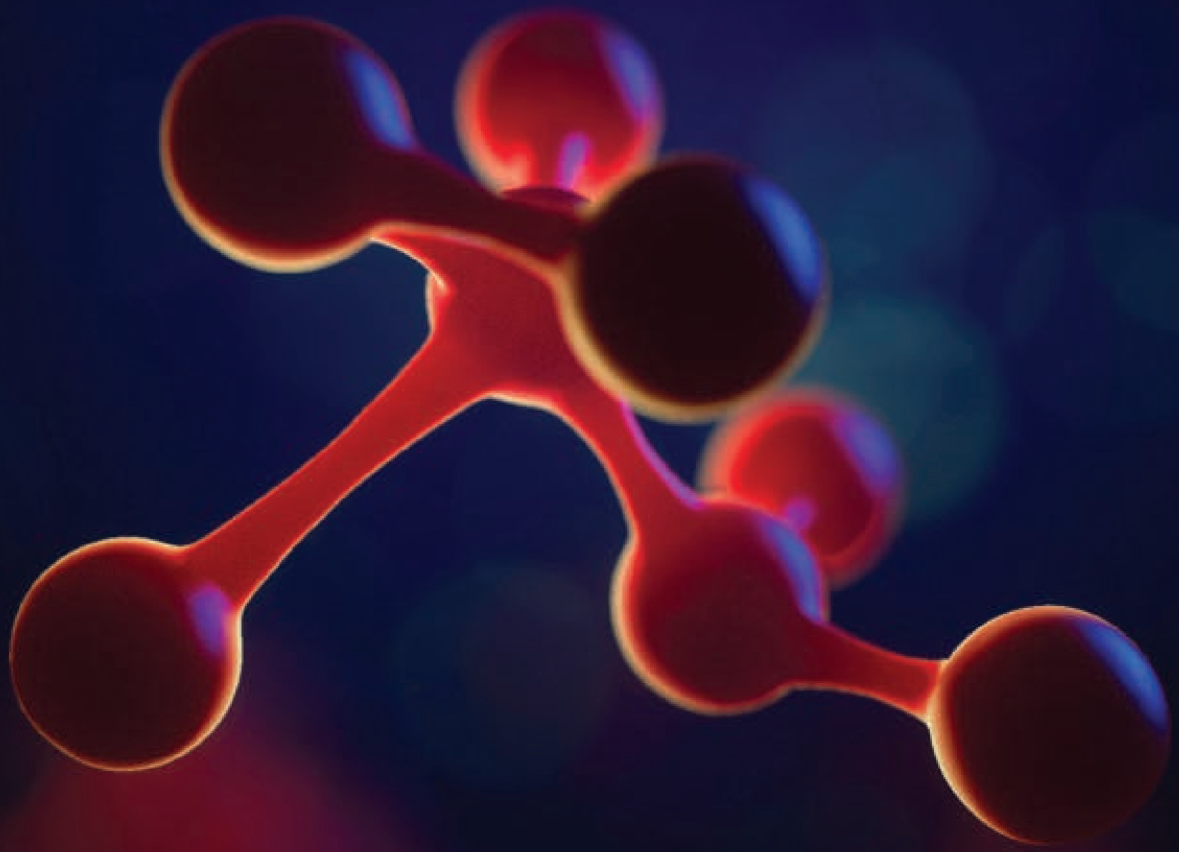

RESEARCH ARTICLE SUMMARY

SYNTHETIC BIOLOGY

Synthetic cytokine circuits that drive T cells into immune-excluded tumors

Greg M. Allen, Nicholas W. Frankel, Nishith R. Reddy, Hersh K. Bhargava, Maia A. Yoshida, Sierra R. Stark, Megan Purl, Jungmin Lee, Jacqueline L. Yee, Wei Yu, Aileen W. Li, K. Christopher Garcia, Hana El-Samad, Kole T. Roybal, Matthew H. Spitzer, Wendell A. Lim*

INTRODUCTION: Many solid tumors fail to respond to T cell therapies because their immunosuppressive microenvironment blocks T cell infiltration, activation, and proliferation. Major tumor suppression mechanisms include inhibition of T cell receptor (TCR) signaling and consumption of inflammatory cytokines. Overcoming the suppressive tumor microenvironment remains a major barrier to solid tumor immunotherapy.

RATIONALE: Supplementing T cell activity with inflammatory cytokines, such as high-dose Interleukin-2 (IL-2) has long been known to drive potent antitumor function. Systemic IL-2 treatment, however, has proven prohibitively toxic by causing severe adverse effects including capillary leak syndrome and eventually end-organ dysfunction. Cell autonomous cytokine production has the potential to overcome these toxicities by delivering cytokine locally and directly to a tumor. We engineer therapeutic T cells bearing synthetic cytokine circuits in which a tumor-specific synthetic Notch (synNotch) receptor drives IL-2 production. These tumor-targeted IL-2 delivery circuits offer a potential way to locally overcome tumor suppression while minimizing systemic IL-2 toxicity.

RESULTS: We observed that engineered synNotch→IL-2 induction circuits drove potent infiltration of chimeric antigen receptor (CAR) or TCR T cells into immune-excluded tumor models of pancreatic cancer and melanoma. This improved infiltration was associated with significantly improved tumor clearance and survival in these challenging immune-competent tumor models. Unlike systemically delivered IL-2, the local cell-based IL-2 circuit does not show toxicity as these synNotch→IL-2 circuits are not dependent on TCR/CAR activation but are still tumor-targeted.

However, the exact mechanism used to deliver IL-2 proved to be critical. CAR T cells with SynNotch-induced IL-2 circuits led to far better antitumor efficacy compared with CAR T cells engineered with constitutive IL-2 expression or TCR/CAR–induced IL-2 expression (e.g., from an nuclear factor of activated T cells (NFAT) promoter). Furthermore, we found that autocrine production of IL-2, where the same T cell expresses the CAR/TCR and synNotch→IL-2 circuit, proved to be critical. Paracrine delivery of IL-2, where a CAR T cell is supported by a separate T cell with a synNotch→IL-2 circuit, proved ineffective in the presence of competing native IL-2 consumer cells, such as host regulatory T cells or bystander T cells.

High-dimensional immune profiling shows that the IL-2 synthetic cytokine circuits act primarily on T cell populations without causing significant changes to other immune cell compartments. The tumors show significantly increased infiltration of both the CAR T cells and host bystander T cells. Nonetheless, only the antitumor CAR T cells show enhanced markers of activation, proliferation, and cytotoxicity, as well as reduced markers of exhaustion.

We hypothesize that these circuits are effective because they bypass requirements for TCR/CAR activation and provide IL-2 in a more potent autocrine configuration. These features thereby allow the engineered T cell to overcome the main modes of tumor immune suppression: inhibition of TCR signaling and competitive cytokine consumption. These engineered T cells appear to act as pioneers, triggering expansion in the tumor through their synNotch-induced IL-2 production, which then cooperatively enables the initiation of sustained CAR/TCR-mediated T cell activation and killing.

CONCLUSION: These results show that it is possible to reconfigure T cell circuits to reconstitute the key outputs required for a robust antitumor response (CAR/TCR activation and inflammatory cytokine signaling), but in a manner that bypasses the critical points of tumor immune suppression. These types of engineered local cytokine delivery circuits may thereby provide a potential general strategy for driving effective T cell activity against immune-suppressed solid tumors. ■

The list of author affiliations is available in the full article online.
*Corresponding author. Email: wendell.lim@ucsf.edu

Cite this article as G. M. Allen *et al.*, *Science* **378**, eaba1624 (2022). DOI: 10.1126/science.aba1624

S READ THE FULL ARTICLE AT
https://doi.org/10.1126/science.aba1624

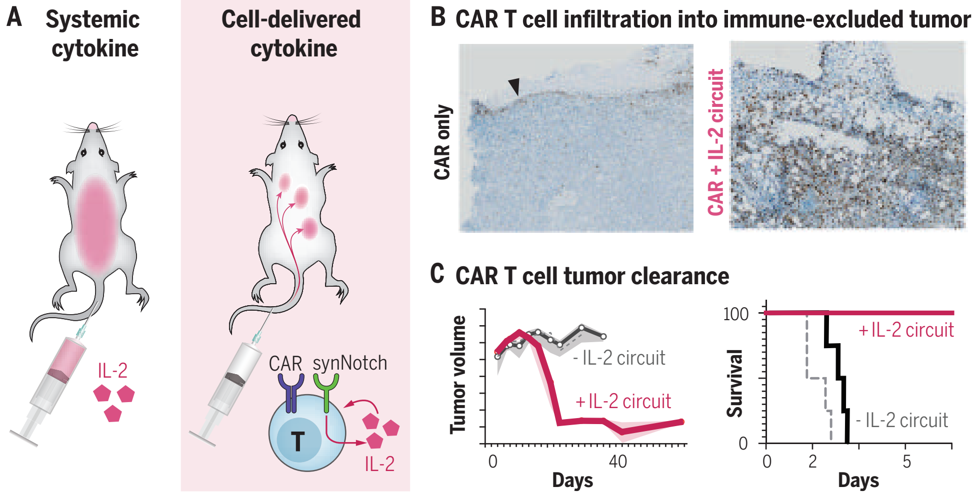

Therapeutic T cells engineered with tumor-triggered IL-2 production infiltrate and clear immune-excluded tumors. (**A**) We hypothesized that cell autonomous cytokine delivery will allow for, safer, more effective delivery of key inflammatory cytokines like IL-2. Specifically, IL-2 induction circuits that utilize synNotch to bypass requirements for CAR/TCR activation and provide IL-2 in an autocrine configuration allow CAR T cells to operate in immunosuppressive tumor micro-environments. (**B**) T cell infiltration into tumors, where addition of IL-2 induction circuit substantially improves T cell infiltration into otherwise immune-excluded tumor micro-environments. (**C**) CAR T cells with an IL-2 induction circuit (pink) are able to clear pancreatic cancer tumors that are otherwise refractory to standard CAR T cell treatments (black).

RESEARCH ARTICLE

SYNTHETIC BIOLOGY

Synthetic cytokine circuits that drive T cells into immune-excluded tumors

Greg M. Allen[1,2]†, Nicholas W. Frankel[1,3]†, Nishith R. Reddy[1,3], Hersh K. Bhargava[1,4], Maia A. Yoshida[1,3], Sierra R. Stark[1,3], Megan Purl[1,3], Jungmin Lee[1,3], Jacqueline L. Yee[5], Wei Yu[1,3], Aileen W. Li[1,3], K. Christopher Garcia[6], Hana El-Samad[1,7], Kole T. Roybal[1,5,8], Matthew H. Spitzer[5,8,9], Wendell A. Lim[1,3,7,8]*

Chimeric antigen receptor (CAR) T cells are ineffective against solid tumors with immunosuppressive microenvironments. To overcome suppression, we engineered circuits in which tumor-specific synNotch receptors locally induce production of the cytokine IL-2. These circuits potently enhance CAR T cell infiltration and clearance of immune-excluded tumors, without systemic toxicity. The most effective IL-2 induction circuit acts in an autocrine and T cell receptor (TCR)- or CAR-independent manner, bypassing suppression mechanisms including consumption of IL-2 or inhibition of TCR signaling. These engineered cells establish a foothold in the target tumors, with synthetic Notch–induced IL-2 production enabling initiation of CAR-mediated T cell expansion and cell killing. Thus, it is possible to reconstitute synthetic T cell circuits that activate the outputs ultimately required for an antitumor response, but in a manner that evades key points of tumor suppression.

Chimeric antigen receptor (CAR) T cells have demonstrated remarkable success in the treatment of B cell malignancies (*1*, *2*). Nonetheless, application of CAR or T cell receptor (TCR)-engineered T cells to solid tumors has proven far more challenging (*3*). Many solid tumors create an immune-excluded local microenvironment that blocks the infiltration, activation, or expansion of cytotoxic T cells (*4*). Within this tumor microenvironment, activation of CAR/TCR pathways are inhibited by local immunosuppressive factors and cells (*5*–*7*). While evidence suggests that local administration of high-dose inflammatory cytokines could help reverse tumor suppression (*8*), combining adoptively transferred T cells with systemic cytokine administration or engineered cytokine production has shown either systemic toxicity or poor efficacy (*9*–*11*). There is a clear need to engineer next-generation therapeutic T cells with an enhanced ability to overcome tumor suppression, without exacerbating off-target or systematic toxicity.

We have created synthetic cytokine circuits as a strategy to improve therapeutic T cell activity against immune-excluded solid tumors. Using the recently developed synthetic Notch (synNotch) receptor (*12*, *13*), we have created a bypass signaling pathway in which tumor recognition by synNotch induces local interleukin-2 (IL-2) production (Fig. 1A). The inflammatory cytokine IL-2 plays a critical role as both an output of T cell activation and as a promoter of T cell activation and expansion (*14*–*17*). Suppressive tumor microenvironments can both reduce IL-2 production and/or competitively consume IL-2 (*18*–*20*). Thus, we hypothesized that providing IL-2 in a tumor-targeted but TCR/CAR-independent manner could help bypass tumor immune suppression. Indeed, we find that certain synthetic IL-2 circuits drive highly efficient CAR T cell infiltration and tumor control in immune-excluded solid tumor models, without concomitant systemic or off-target toxicity. Immune profiling shows expansion of CAR T cells only within the tumor, with increased markers of activation and decreased markers of exhaustion. Synthetic IL-2 production likely enables infiltrating T cells to survive and initiate sustained CAR-mediated activation, expansion, and tumor killing. This type of synthetic cytokine delivery circuit could provide a powerful general approach for remodeling and overcoming immunosuppressive solid tumors.

Engineering synthetic IL-2 circuits that drive local T cell proliferation independent of T cell activation

To design a tumor-induced synthetic IL-2 circuit in T cells, we used a synNotch sensor to induce the transcription of an IL-2 transgene (Fig. 1B). In essence, synNotch receptors are chimeric receptors with a variable extracellular recognition domain, a Notch-based cleavable transmembrane domain, and an intracellular transcriptional domain (*12*, *13*). Antigen binding induces intramembrane receptor cleavage, releasing the transcriptional domain to enter the nucleus and promote expression of a target transgene.

We built a prototype circuit in primary human T cells using a synNotch receptor that recognizes the model antigen CD19, combined with a synNotch-responsive promoter driving expression of human IL-2 or an affinity-enhanced variant of IL-2 (known as super-2 or sIL-2) (*21*). As intended, stimulation of the synNotch receptor in vitro induced strong proliferation of the engineered cell population (Fig. 1C). Cells with the anti-CD19 synNotch→ sIL-2 circuit could function in a paracrine manner, driving the proliferation of co-cultured nonengineered T cells (Fig. 1D) or natural killer cells (fig. S1C) in vitro. The degree of proliferation was dependent on the type of gamma-chain cytokine payload, with significant T cell proliferation seen with production of either IL-2 or sIL-2 (fig. S1D). Production of the homeostatic cytokine IL-7 (*22*) led to T cell survival with minimal expansion whereas untethered IL-15 (*23*) had no effect. Thus, in vitro, a synNotch→ sIL-2 circuit T cell can drive its own proliferation, as well as the proliferation of other co-cultured IL-2 responsive cells.

We then tested whether the synNotch→sIL-2 circuit could drive targeted expansion of human T cells in vivo, independent of CAR or TCR activation. We established a bilateral K562 tumor model in immunocompromised Non-obese diabetic *scid* gamma (NSG) mice, where only one flank tumor expressed the synNotch target antigen, CD19 (Fig. 1E). Human primary CD8+ T cells engineered with the anti-CD19 synNotch→ sIL-2 circuit were tagged with enhanced firefly luciferase (eff-luc) and injected intravenously. Cells with the synthetic IL-2 circuit autonomously identified the target tumor (CD19$^+$/right) and locally expanded by a factor of ~100 within this tumor (Fig. 1E). By contrast, no off-target expansion was seen in the contralateral (CD19$^-$) tumor. Flow cytometry analysis of tumor infiltrating lymphocytes in the target and off-target tumor showed synNotch activation, T cell expansion, and proliferation only in the CD19+ tumor (fig. S2, A to C). The administered T cells had no CAR or TCR reactivity against tumors and thus the synthetic production of IL-2 alone did not result in killing of the K562 tumors in this immunodeficient NSG mouse model (fig. S2D).

---

[1]Cell Design Institute; University of California San Francisco, San Francisco, CA 94158, USA. [2]Department of Medicine, University of California San Francisco; San Francisco, CA 94158, USA. [3]Department of Cellular and Molecular Pharmacology, University of California San Francisco; San Francisco, CA 94158, USA. [4]Biophysics Graduate Program, University of California San Francisco; San Francisco, CA 94158, USA. [5]Department of Microbiology and Immunology, University of California San Francisco; San Francisco, CA 94158, USA. [6]Department of Molecular and Cellular Physiology and Structural Biology, Howard Hughes Medical Institute, Stanford University; Stanford, USA. [7]Department of Biochemistry and Biophysics, University of California San Francisco; San Francisco, CA 94158, USA. [8]Parker Institute for Cancer Immunotherapy, University of California San Francisco; San Francisco, CA 94158, USA. [9]Department of Otolaryngology-Head and Neck Surgery, University of California San Francisco; San Francisco, CA 94158, USA.
***Corresponding author. Email: wendell.lim@ucsf.edu**
†These authors contributed equally to this work.

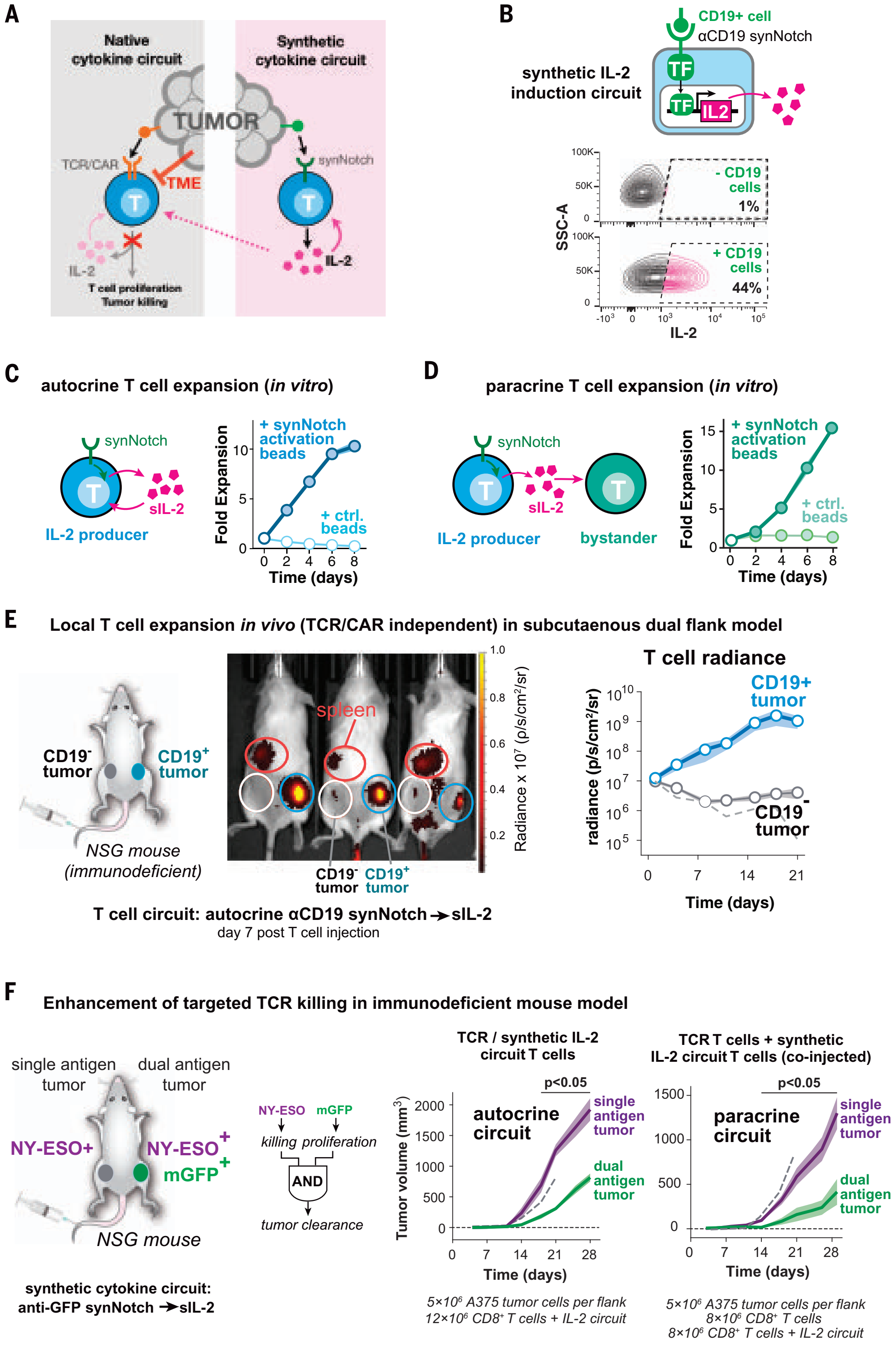

Fig. 1. Synthetic synNotch→IL-2 circuits can drive local T cell proliferation independent of TCR activation or cooperatively with T cell killing. (**A**) The tumor microenvironment (TME) acts to suppress T cell activation, including inflammatory cytokine (e.g., IL-2) production. To bypass suppression we propose engineering synthetic IL-2 circuits triggered by tumor antigens in a manner independent from TCR/CAR activation. (**B**) Synthetic IL-2 circuits were created in human primary T cells using anti-CD19 synNotch receptors to drive production of an inflammatory cytokine (super IL-2 or sIL-2). IL-2 is produced only when stimulated by A375 tumor cells bearing the cognate CD19 antigen; compare with fig. S1A. (**C**) The synthetic IL-2 circuit drives autocrine proliferation of primary human T cells in vitro only when the circuit is triggered (here, myc-tagged synNotch is activated by anti-myc antibody-coated beads). (**D**) Synthetic IL-2 circuit signals in a paracrine fashion to stimulate proliferation of a bystander population of human T cells that lack a synthetic circuit in vitro. For [(C) and (D)] the median is plotted; shading shows SEM ($n = 3$) and filled markers indicate significant expansion >1, right-tailed student's t test, $P < 0.05$. Additional replicates of autocrine and paracrine proliferation are shown in fig. S1B. (**E**) Dual flank tumor model in NSG mice to monitor T cell trafficking in vivo. Primary human T cells were engineered with synthetic anti-CD19→sIL-2 circuit and eff-luc (to track cells) and administered to mice engrafted with $CD19^+$ (right) and $CD19^-$ (left) K562 tumors. Example bioluminescence imaging shown 7 days after T cell injection. Circles indicate tumors (blue, white) and spleen (red). Plot shows quantification of T cell luminescence over time for $CD19^+$ and $CD19^-$ tumors. Dashed line shows T cells in $CD19^+$ tumors with no circuit added; shading shows SEM. (**F**) Tumor-reactive T cells, such as those bearing an anti-NY-ESO TCR, fail to produce effective cytokine and killing responses against antigen-positive tumors. We hypothesize that simultaneously engaging the TCR and a synthetic IL-2 circuit could enhance a local T cell response. In this case T cells bearing an anti–NY-ESO TCR and an anti–membrane-bound GFP (mGFP) synNotch→sIL-2 circuit could function as an AND gate that requires two antigen inputs to stimulate tumor killing, allowing more precise recognition strategies. Here a two-flank A375 tumor model in NSG mice, with NY-ESO only (left) and NY-ESO/GFP (right), was generated. Plots show tumor growth over time. Both autocrine and paracrine forms of the TCR + anti-GFP synNotch→sIL-2 cells show significantly enhanced control of only the dual antigen tumor. Error shading: SEM Dashed line indicates dual antigen tumor growth curve with no T cell treatment. NY-ESO TCR–only control and individual tumor growth curves available in fig. S4.

We also found that the anti-CD19 synNotch→sIL-2 circuit was also capable of driving T cell expansion in a paracrine (two-cell type) configuration in this NSG mouse model. We coinjected a population of bystander T cells, which did not express the sIL-2 induction circuit but expressed luciferase to distinguish them from the synNotch→sIL-2 T cells. Coinjected into mice at a 1:1 ratio, the bystander cells also specifically expanded in the targeted ($CD19^+$/right) tumor (fig. S3, A to D), where the synNotch receptor was locally activated (fig. S3E). This paracrine T cell expansion was not observed in negative control experiments using synNotch T cells that either did not produce sIL-2 or did not recognize CD19 (fig. S3F). In summary, this work represents one of the first examples in which locally targeted T cell expansion can be induced in a manner uncoupled from TCR or CAR activation.

Synthetic IL-2 circuits can enhance targeted T cell cytotoxicity in vivo

Many engineered T cell therapies show effective cytotoxicity in vitro but fail to show sufficient proliferation or persistence to achieve effective tumor control in vivo. For example, cells bearing the affinity-enhanced anti-NY-ESO-1 TCR are able to lyse A375 melanoma tumors in vitro (*24*) but have shown limited clinical benefit in patients or preclinical models (*25*). We hypothesized that the addition of a synthetic cytokine circuit producing IL-2 might enhance tumor control by NY-ESO-1 T cells. Moreover, these T cells might function as a new type of AND gate (*26*, *27*), where a therapeutic T cell exhibits enhanced specificity by requiring two antigens to be present before triggering its full cytotoxic response: the TCR antigen required for T cell activation, and the synNotch antigen required for inducing IL-2 production. In this case, we used an anti-GFP synNotch→sIL-2 synthetic cytokine circuit. By requiring the presence of both the TCR antigen (NY-ESO-1) and the synNotch antigen (in this case, membrane-tethered green fluorescent protein (GFP)) (Fig. 1F), this cellular design strategy should further minimize off-target toxicity.

We examined the efficacy of anti-NY-ESO-1 TCR human T cells in NSG mice using a bilateral tumor model of a NY-ESO-1$^+$ melanoma (A375). Only one flank tumor was co-labeled with the synNotch-targeted model antigen (membrane-tethered GFP). Anti-NY-ESO-1 TCR–expressing T cells lacking the synthetic IL-2 circuit were largely ineffective at controlling the growth of both the single (NY-ESO$^+$) and dual (NY-ESO$^+$/GFP$^+$) antigen tumors (fig. S4A). However, when mice were treated with T cells simultaneously expressing both the anti-NY-ESO-1 TCR and the anti-GFP synNotch→sIL-2 circuit, the dual-targeted NY-ESO$^+$/GFP$^+$ tumor now showed a significant reduction in tumor size (Fig. 1F). Similar tumor reduction was observed when IL-2 was provided in a paracrine configuration, by co-injection of one cell type only expressing the anti-NY-ESO-1 TCR and a second cell type only expressing the synthetic IL-2 circuit. Critically, in either the autocrine or paracrine configuration, the synthetic IL-2 circuit did not cause a reduction in the contralateral NY-ESO$^+$/GFP$^-$ tumor (lacking the synNotch ligand), highlighting the precisely targeted impact of the synthetic IL-2 circuit.

Using luciferase tracking of anti-NY-ESO-1 TCR T cells, we observed substantially increased intratumoral expansion of T cells only in tumors that were targeted by the synthetic IL-2 circuit (fig. S5A). The synthetic IL-2 circuit was only activated in the targeted double antigen positive tumor (fig. S5B), and we observed a significant increase in T cell activation markers in this targeted tumor (fig. S5C). A synthetic IL-2 circuit T cell without co-delivery of a tumor-reactive cytotoxic T cell population did not produce tumor control in these NSG mouse models (fig. S5D).

Autocrine configuration of the synthetic IL-2 circuit is required in immunocompetent tumor models

Although the above results show that synthetic synNotch→IL-2 circuits can significantly enhance T cell activity and expansion in immunodeficient mouse tumor models, we wanted to test whether they could also be effective in immunocompetent mouse models. Important factors influencing IL-2 production and consumption are likely missing in immunodeficient mouse models. Key missing factors include inhibitors of T cell activation (*28*) and the presence of competing IL-2 consumer cells (e.g., both native T cells and T regulatory cells), which could significantly lower the effectiveness of synthetically produced IL-2 within tumors (*29*, *30*). To study the effects of local IL-2 production within fully immunocompetent mouse tumor models, we rebuilt our synthetic IL-2 circuit in primary mouse T cells (Fig. 2A). Primary CD3$^+$ mouse T cells were engineered to express an anti-human-CD19 synNotch→mouse IL-2 (mIL-2) circuit. This circuit resulted in synNotch-induced proliferation of mouse T cells in vitro, as observed previously with human T cells (fig. S6A).

We then chose to deploy this IL-2 circuit in targeting the mouse pancreatic tumor model KPC (KrasLSL.G12D/+; p53R172H/+; PdxCretg/+) (*31*, *32*), as this immune-excluded tumor exhibits the challenging immunotherapy refractory features of pancreatic ductal adenocarcinoma (*33*). Like most pancreatic ductal adenocarcinomas, these cells express the tumor target antigen mesothelin (*34*). Although anti-mesothelin mouse CAR T cells show robust cytotoxicity against KPC cells in vitro (fig. S6B), they show limited to no tumor control of KPC tumors in vivo (fig. S6C). Thus, this immune competent mouse model replicates the poor in vivo therapeutic efficacy reported in early phase clinical trials of standard antimesothelin CAR T cells in pancreatic cancer (*3*), making it an ideal model for testing enhancement of the CAR T cells with synthetic IL-2 circuits. We engineered KPC tumor cells that, in addition to endogenously expressing the CAR antigen (mesothelin), also expressed a model synNotch antigen (human CD19).

We first tested CAR T cell enhancement by a paracrine synNotch→mIL-2 circuit. Anti-mesothelin CAR T cells were co-injected with a second T cell population expressing the anti-CD19 synNotch→mIL-2 circuit. Distinct from our studies in immunodeficient mice, these paracrine IL-2 circuit cells failed to improve tumor control in an immune competent context (Fig. 2B and fig. S7A). Instead, we found that in this fully immunocompetent tumor model, improved CAR T cell–mediated tumor control was only observed with the autocrine configuration of the synthetic IL-2 circuit—i.e., the cytotoxic receptor (CAR) and the synNotch→IL-2 circuit must be encapsulated within the same cell (Fig. 2C and fig. S7B). We hypothesize that the presence of competing host IL-2 consumer cells (e.g., bystander T cells and T$_{\text{regs}}$) in immune-competent models contributes to this major difference between the autocrine and paracrine circuits (i.e., paracrine circuits might be more sensitive to competing IL-2 sink cells), a model consistent with more in-depth tumor profiling data in later sections of this paper.

The autocrine synthetic IL-2 circuit anti-mesothelin CAR-T cells were extremely potent. In an even more challenging immune-competent mouse model, in which KPC tumors were engrafted orthotopically in the pancreas, complete tumor clearance was observed upon treatment (Fig. 2D): 100% of mice survived, compared with 0% with CAR-only T cells. Simply increasing the dose of anti-mesothelin CAR-T cells had a negligible effect compared to addition of the synthetic IL-2 circuit (fig. S8, A and B).

This type of autocrine IL-2 circuit also shows similar substantial therapeutic improvement in treating a different type of immune-excluded solid tumor: B16-F10 OVA intradermal melanoma tumors, treated with OT-1 TCR–expressing T cells (Fig. 2E and fig. S7C). Here again, OT-1 T cells without the cytokine circuit are ineffective in vivo in immune-competent models (despite in vitro cytotoxic activity; see fig. S6D). Only when the OT-1 TCR is co-expressed with the autocrine synNotch→IL-2 circuit do we observe effective infiltration and tumor clearance in the immune-competent model.

Comparison with other strategies of IL-2 co-delivery

Notably, this strong therapeutic improvement was not observed with other methods of co-delivering IL-2 with CAR T cells. We tested systemic co-administration of IL-2 at maximum-tolerated doses (*35*) (Fig. 3B and fig. S9B), expression of IL-2 in the CAR T cell from a constitutive promoter ("armored CAR") (Fig. 3C and fig. S9C), or expression of IL-2 from a T cell–activated promoter such as pNFAT (*36*) (Fig. 3D and fig. S9D).

Systemically injected IL-2 led to systemic toxicity without improving CAR T cell activity (fig. S10B). Constitutive production of IL-2 was

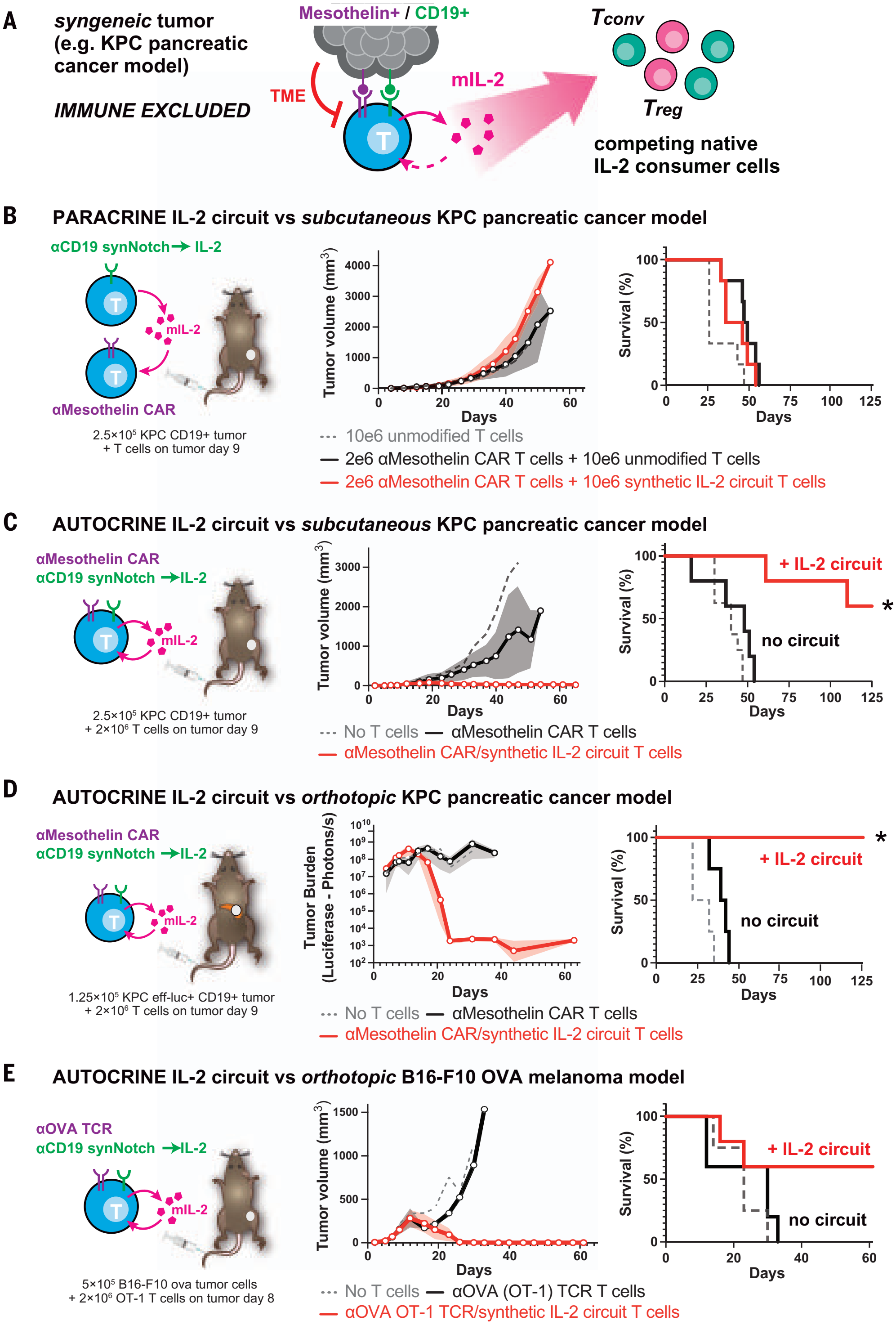

Fig. 2. Autocrine synthetic IL-2 circuits strongly improve T cell cytotoxicity against multiple models of immune-excluded syngeneic tumors. (**A**) The synthetic IL-2 circuit was recapitulated in mouse T cells producing mouse IL-2 (mIL-2) to test circuits in the presence of an intact immune system, suppressive TME, and native IL-2 consumer cells. (**B**) KPC CD19$^+$ pancreatic tumors were engrafted subcutaneously into immunocompetent C57/B16 mice and treated 9 days later with synthetic IL-2 circuit T cells and anti-mesothelin CAR T cells as a two-cell paracrine system. No tumor control was observed in this paracrine configuration, even though KPC tumors express mesothelin. (**C**) KPC CD19$^+$ pancreatic tumors were engrafted as in (B) and treated 9 days later with T cells engineered with both a synthetic IL-2 circuit and an anti-mesothelin CAR (autocrine configuration). Significant improvement in tumor control was observed (red lines) compared to anti-mesothelin CAR T cells combined with a dummy synthetic cytokine circuit (synNotch only produces BFP, black lines). (**D**) KPC CD19$^+$ pancreatic tumors were engrafted orthotopically in the pancreas tail and treated 9 days later with engineered T cells. Only with the addition of the IL-2 circuit was 100% survival observed, out to 120 days (duration of study). (**E**) B16F10 OVA CD19$^+$ melanoma tumors were engrafted orthotopically into immunocompetent C57/B16 mice and treated 8 days later with 2 × 10^6 engineered mouse CD8$^+$ OT-1 (anti-OVA) T cells. Tumor control was only observed in mice treated with T cells expressing the IL-2 circuit. For [(B) to (E)] All plots show tumor burden measured by average ± SEM of caliper or bioluminescence measurements and overall survival (n = 4 to 5 per group; *, significant difference in survival with addition of IL-2 circuit using log-rank test, $P < 0.05$). See figs. S7 and S8 for individual growth curves data.

unable to support T cell proliferation in vitro (fig. S11A) likely in part due to significant silencing of the constitutive IL-2 transgene (fig. S11B) (*37*). IL-2 can have a biphasic effect on T cell survival (*38*), partly because of promotion of activation-induced cell death (*39*) and T cell differentiation (*40*). We find that such negative effects are exacerbated by constitutive IL-2 production (fig. S11C). This suggests that when and how the IL-2 cytokine is produced is critical in determining the outcome.

Notably, despite its potent antitumor efficacy, the synNotch→IL-2 circuit showed no evidence of systemic cytokine toxicity or exacerbation of CAR T cell toxicity, as assessed by mouse survival, body weight, spleen weight, and measurements of hepatotoxicity (fig. S10). Moreover, the required recognition of two antigen inputs (CAR and synNotch antigens) should further enhance the specificity of tumor targeting [as seen by specific targeting to dual antigen tumors (fig. S7C) and reduced hepatotoxicity (fig. S10C)]. In summary, combining a tumor-reactive TCR/CAR with an autocrine synNotch→IL-2 circuit results in potent and localized antitumor enhancement.

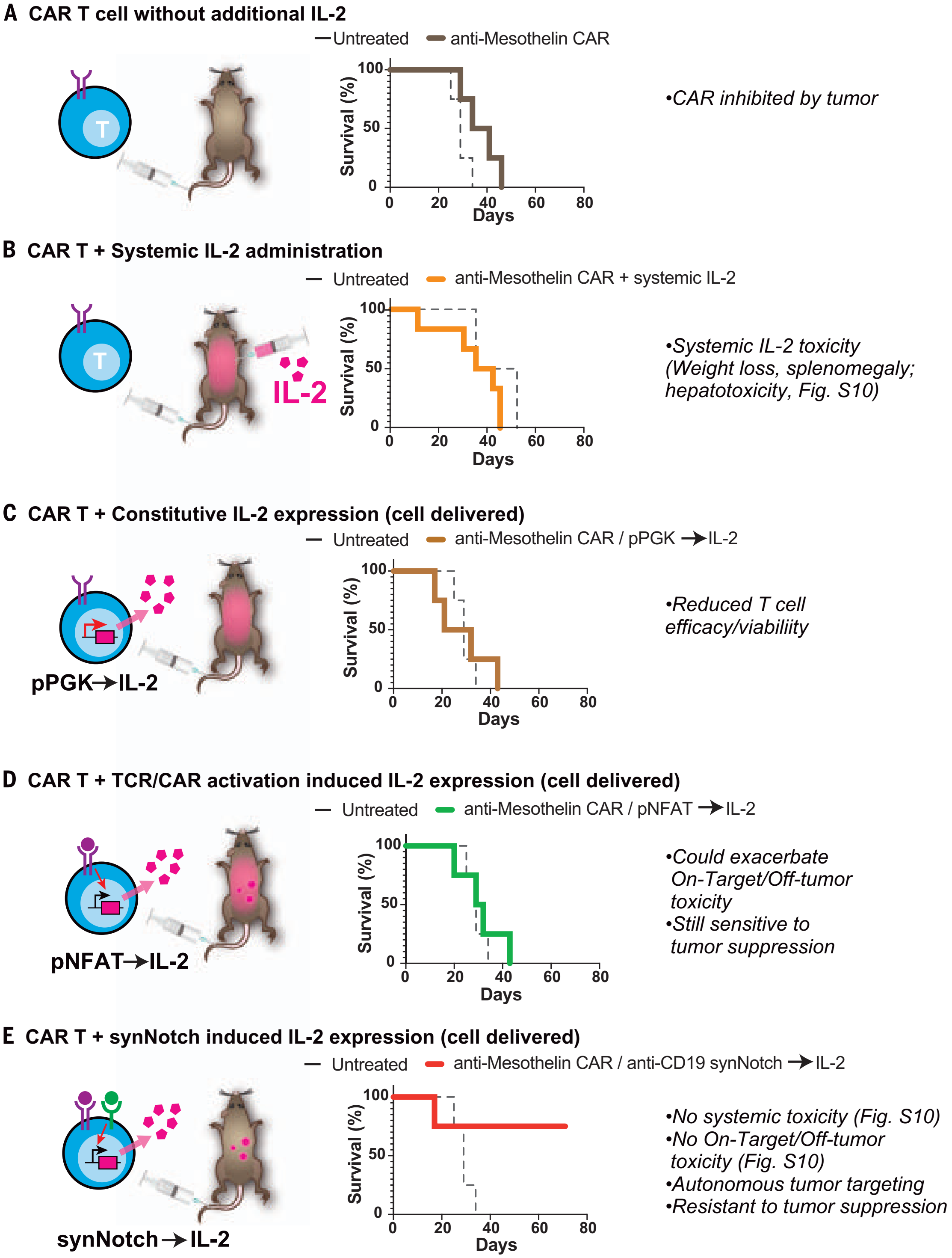

Fig. 3. Synthetic Notch–based cytokine delivery is required for effective control of KPC tumors. KPC CD19$^+$ pancreatic tumors were engrafted subcutaneously into immunocompetent C57/Bl6 mice and treated 9 days later with T cells as labeled. Plotted here is a schematic for IL-2 production as well as overall survival for each cell design compared to matched untreated mice. *n* = 4 to 5 per group. Tumor measurements for each condition are plotted in fig. S9. (**A**) 1 × 10^6 anti-mesothelin CAR T cells with no additional IL-2. (**B**) 2 × 10^6 anti-mesothelin CAR T cells with systemic IL-2 administered at a high dose (250,000 to 750,000 IU/mL) twice daily intraperitoneally for 7 days. (**C**) 1 × 10^6 anti-mesothelin CAR T cells engineered to constitutively express mIL-2 using a PGK promoter. (**D**) 1 × 10^6 anti-mesothelin CAR T cells engineered to inducibly express mIL-2 under the control of an NFAT promoter. (**E**) 1 × 10^6 anti-mesothelin CAR T cells engineered to inducibly express mIL-2 under the control of an anti-CD19 synNotch.

The synthetic IL-2 circuit drives T cell infiltration into immune-excluded tumors

To better characterize how this autocrine synthetic IL-2 circuit improves CAR T cell control of syngeneic pancreatic tumor models, we profiled the tumors in more depth during treatment. We collected KPC pancreatic tumor specimens at the beginning and partway into tumor regression (8 and 23 days after T cell treatment, respectively), and measured CD3$^+$ T cell infiltration using immunohistochemistry. Tumors treated with standard anti-mesothelin CAR T cells displayed a classic immune-excluded phenotype, with very limited T cell infiltration inside the tumor core and most T cells gathered at the tumor periphery (Fig. 4, top). By contrast, tumors treated with CAR T cells containing the synthetic autocrine IL-2 circuit showed substantially increased infiltration of T cells throughout the tumor core (Fig. 4, bottom). A similar infiltration and expansion of the CD8+ lymphocytes also seen in B16-F10 OVA melanoma tumors sampled 10 days after treatment with OT-1 T cells bearing the synthetic IL-2 circuit (fig. S12A).

To profile the tumors in more detail, we performed flow cytometry and Cytometry by time

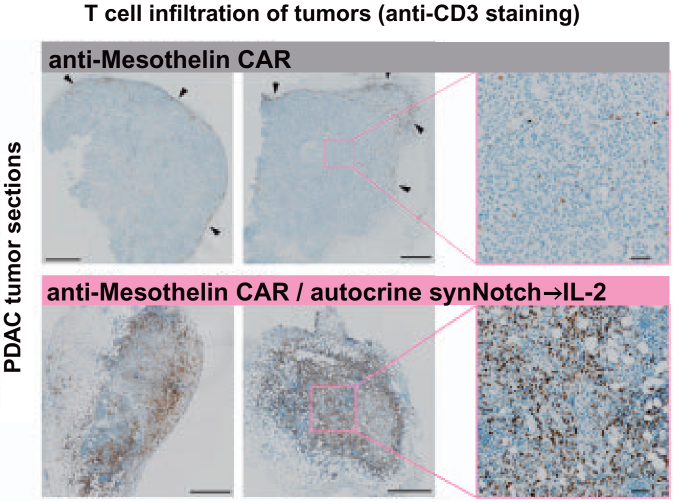

Fig. 4. The synthetic IL-2 circuit enables T cell infiltration into immune-excluded tumors. KPC $CD19^+$ tumors were engrafted subcutaneously, treated with engineered T cells, and analyzed by IHC for T cell infiltration (anti-CD3 stain). Anti-mesothelin CAR T cells (top) failed to penetrate into the tumor and only infiltrated the tumor edges (black arrows). Addition of synthetic autocrine IL-2 circuit (bottom) resulted in substantially increased T cell infiltration into tumor core. Tumors were collected 23 days (left) and 8 days (center) after T cell injection. Zoomed out scale bars are 500 μm, zoomed in are 50 μm.

of flight (CyTOF) analyses on excised and dissociated tumors. To track the endogenous (host) T cells independently from the adoptively transferred CAR T cells, we adoptively transferred congenic Thy1.1 or CD45.1 CAR T cells into Thy1.2 or CD45.2 mice, respectively, allowing us to clearly distinguish endogenous from transplanted T cells by flow cytometry.

These studies showed that the engineered autocrine T cells (expressing both CAR and the synNotch→IL-2 circuit) drove substantial intratumoral infiltration of both adoptively transferred (engineered) T cells and native host T cells (Fig. 5A and fig. S12B). By contrast parallel analysis of tumors treated with the paracrine synNotch→IL-2 circuit (CAR and synthetic cytokine circuit are expressed by two separate, co-injected cell types) showed expansion of native T cells only and no expansion of the adoptively transferred CAR T cells (Fig. 5A and fig. S13B), suggesting that in the paracrine configuration, induced IL-2 was primarily consumed by competing native T cells, leaving little available to drive expansion of the rarer CAR T cells.

Unsupervised clustering (*41*) of the CyTOF measurements (from the $CD45^+$ immune cell infiltrate in KPC tumors) identified the primary therapeutic effect of the autocrine IL-2 circuit as enrichment of the population of activated adoptively transferred CAR T cells (Fig. 5B). Little change was seen in the myeloid compartments (*42*), suggesting that synthetic IL-2 production acts primarily to drive T cell infiltration (both native and adoptive) and not by altering myeloid cell–associated immune suppression. Furthermore, the expansion of T cells was completely constrained to the tumor as no changes were seen in immune cells from isolated spleens by flow cytometry or CyTOF analysis (figs. S12A and S16), highlighting the focused local activity of the engineered cytokine circuit.

In addition to driving expansion of cytotoxic T cells in these immunologically cold tumors, the synthetic autocrine IL-2 circuit improved the phenotypes of the CAR T cells that infiltrate the tumor. CyTOF analysis showed that the synthetic autocrine IL-2 circuit up-regulated markers of T cell activation (CD25), effector activity (Granzyme B) and proliferation (Ki67). Conversely, these IL-2-enhanced T cells also showed reduced expression of markers of exhaustion (Tim3, Lag3, PD-1) (Fig. 5C and fig. S14B) (*43*). Most native T cells (non-CAR) found in the tumors, however, appear to act simply as IL-2 sinks—they did not show markers of activation, effector function, proliferation, or exhaustion (Fig. 5C and fig. S14B) but instead largely exhibited a naïve phenotype (fig. S14, C and D, and fig. S15C). The phenotype of the regulatory T cell population was mostly unchanged (figs. S14D and S15D). These findings suggest that the tumor has a significant population of native host T cells that, in bulk, compete to consume IL-2 without contributing to the antitumor response (akin to T_{reg} suppression through IL-2 consumption).

Discussion

Cell-delivered IL-2 is a powerful tool to synergize with therapeutic T cells

Cytokines such as IL-2 have long been known as powerful stimulators of antitumor immunity (*44*). However, systemic IL-2 delivery is also well known to be highly toxic, leading to a broad set of adverse effects such as capillary leak syndrome, thereby greatly limiting its therapeutic use (*45*). Most current efforts in IL-2 engineering have focused on engineering the cytokine to be more selective for tumors, but we employ a different strategy: harnessing the power of an engineered cell to identify a tumor and locally deliver IL-2 exactly where it is needed. We show that cell-mediated local cytokine (IL-2) delivery can effectively overcome immune suppression, augmenting CAR T cells to efficiently clear multiple immune-excluded tumor models (pancreatic cancer and melanoma) that are otherwise nearly completely resistant to standard CAR T cell treatment.

However, the exact manner by which the cytokine is produced is critical to its success. First, cytokine production must be dynamically regulated (inducible). Constant production of IL-2 risks exacerbating off-target toxicity. Moreover, constitutive IL-2 expression in T cells has negative effects as it leads to terminal differentiation, fails to drive autonomous proliferation, and is limited by payload silencing. Second, to bypass TCR/CAR suppression by the tumor microenvironment induction of IL-2 production must be independent of the TCR activation pathway (e.g., NFAT promoter–induced IL-2 still requires TCR/CAR activation to be triggered). We find that one powerful solution to this constraint is to engineer a synthetic signal transduction pathway that is tumor-triggered but bypasses the native CAR/TCR activation pathway (Fig. 6, A and B). Use of a synNotch receptor that detects the tumor to drive IL-2 production provides a simple and modular way to achieve this goal. The synNotch IL-2 circuit can maintain payload expression despite T cell inhibition or exhaustion (fig. S17A).

Finally, we find that simply having an immune cell that can individually produce high levels of IL-2 in the tumor is not sufficient to overcome suppression. The specific circuit architecture is critical, including exactly which cells produce IL-2. We find that an effective therapeutic response is only observed with an autocrine IL-2 circuit (i.e., the synthetic IL-2 induction pathway is contained within the same cell as the antitumor CAR/TCR).

Mechanisms underlying autocrine/paracrine circuit differences

Why does the autocrine IL-2 induction circuit perform so much better than the equivalent paracrine circuit in driving T cell infiltration of immunosuppressed tumor models? Both circuits act by the same principle of delivering high levels of IL-2 (fig. S17B) directly to the tumor. Moreover, we also ask why we only see this large difference in autocrine versus paracrine circuit efficacy in the presence of a native immune system.

It is likely that there are multiple mechanisms that contribute to the far better efficacy of the autocrine circuit (Fig. 6, C and D). These mechanisms are tightly interlinked and likely act in a highly cooperative manner, thus making

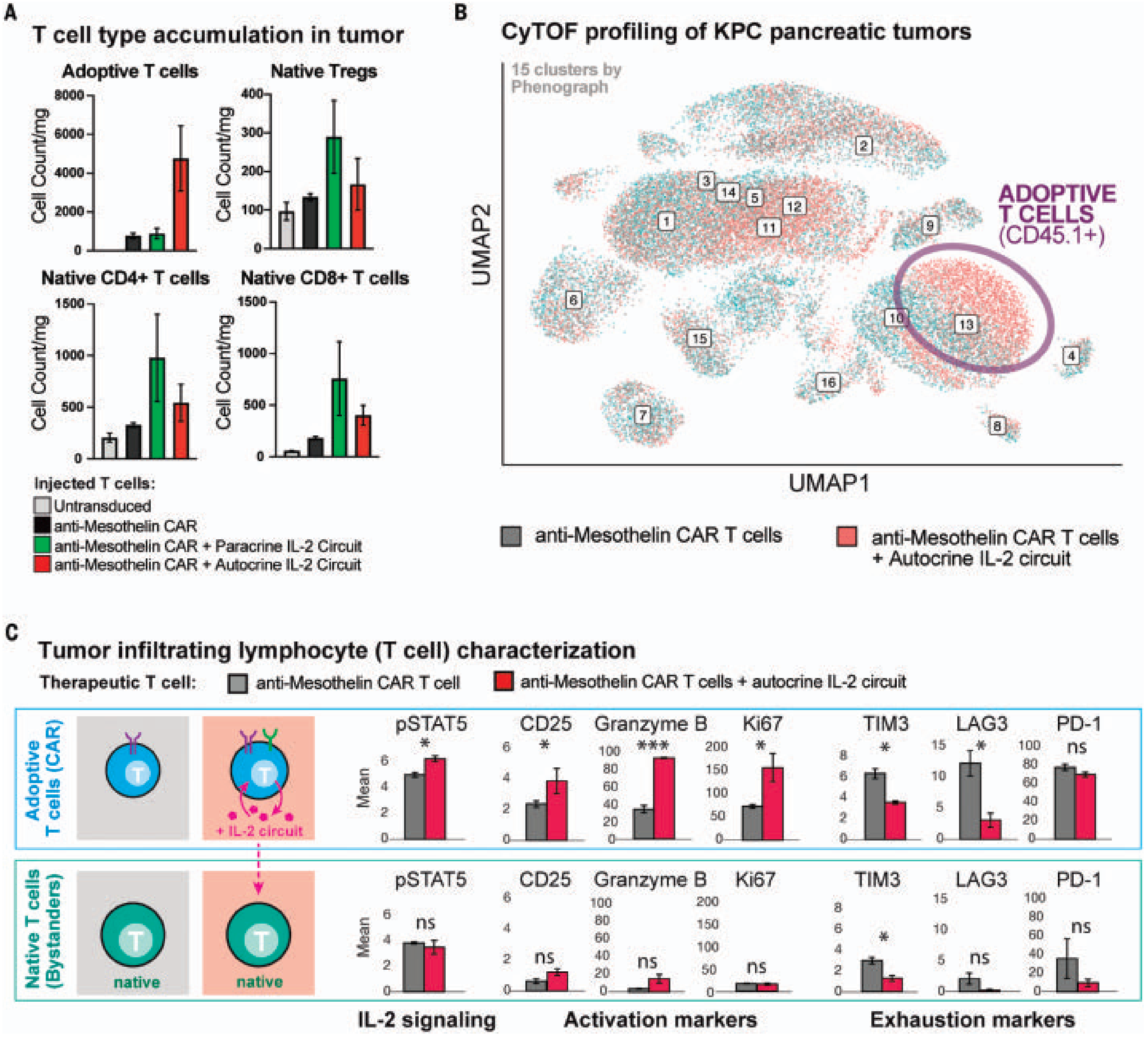

Fig. 5. Profiling of the tumor microenvironment shows expansion and activation of CAR T cells with the autocrine IL-2 circuit. (**A**) Treated KPC CD19$^+$ tumors were collected as in Fig. 4 after 9 days for analysis by CyTOF using CD45.1 as a marker of adoptively transferred T cells and CD45.2 as marker of native T cells. Native T cells and regulatory T cells (T$_{\text{regs}}$) showed expansion in tumors treated with anti-mesothelin CAR + synthetic IL-2 circuit in autocrine or paracrine configuration whereas adoptive (CAR) T cells showed far more substantial expansion only with anti-mesothelin CAR + synthetic IL-2 circuit in autocrine configuration. *n* = 3 samples per treatment, no *P* value calculated. Counts are normalized to tumor weight. (**B**) Unsupervised analysis of CyTOF data. UMAP shown for KPC tumors treated by anti-mesothelin CAR ± IL-2 circuit (autocrine). Labeled numbers indicate clusters by phenograph. Enrichment was only seen in adoptively transferred CAR T cells when the synthetic IL-2 circuit was engaged, see fig. S13 for mean marker expression for each phenograph cluster and measures of cluster enrichment. (**C**) Analysis of tumor-infiltrating lymphocytes markers in CAR T cells (CD45.1) from CyTOF data shows that CAR T cells with the synthetic IL-2 circuit in autocrine show higher expression of markers of IL-2 signaling (pSTAT5), activation (CD25), effector function (Granzyme B), and proliferation (Ki67), while showing decreased expression of markers of exhaustion (Tim3, Lag3, PD1). Matched analysis of native T cells (CD45.2) shows limited IL-2 signaling, activation, effector responses, proliferation, or exhaustion markers, with or without addition of the synthetic IL-2 circuit. Mean ± S.D. is plotted. See figs. S13 to S15, for additional data including repeat CyTOF runs. Statistical significance was tested using a two-tailed Student's *t* test. (n.s., not significant > 0.05, $^*P < 0.05$, $^{***}P < 0.001$).

it difficult to precisely pinpoint the relative contribution of each mechanism.

First, it is likely that autocrine cells have preferential access to self-produced IL-2, especially in environments with competing IL-2 sinks. Paracrine circuits must physically transfer IL-2 further through space from a producer T cell to an effector T cell. This becomes challenging in the presence of competing IL-2 consumer cells (e.g., T$_{\text{regs}}$ in immune competent models), which can greatly reduce the effective length scale of IL-2 signaling, creating gradients that drop off sharply around IL-2 sources (*46*). Here, in both the autocrine and paracrine circuit we observe an expansion of host T$_{\text{reg}}$ cells

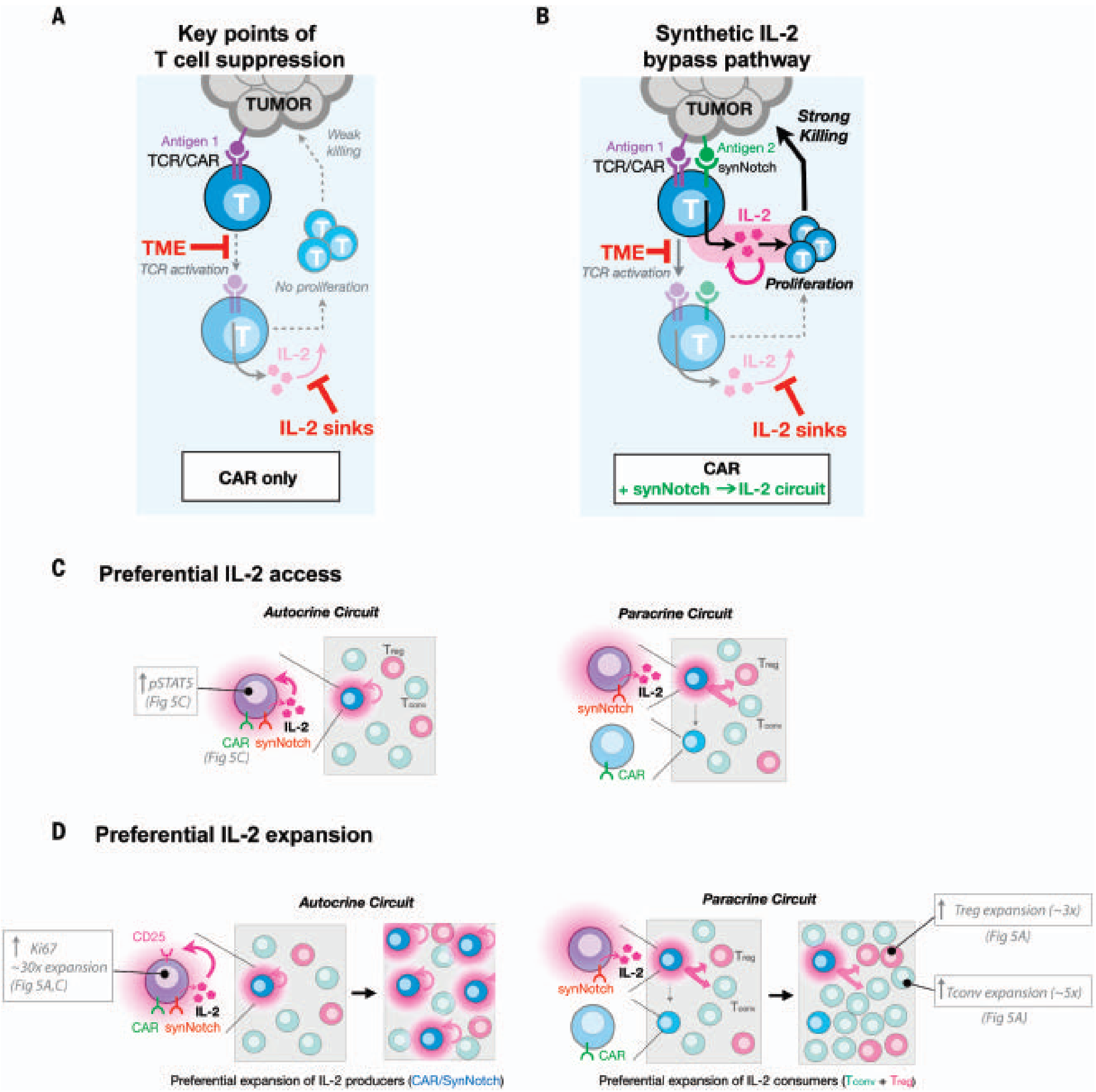

Fig. 6. Bypassing tumor immune suppression mechanisms with a synthetic IL-2 delivery circuit. (**A**) Standard CAR/TCR T cell activity in suppressive microenvironments is limited by inhibition of T cell activation, minimal production of IL-2, and consumption of IL-2 by competing native cells (sinks). Activation of both TCR and cytokine signaling, required for the full T cell response (AND gate), is blocked at these steps. (**B**) Creating a bypass channel for IL-2 production that is independent of CAR/TCR activation can overcome key suppressive steps. New circuits allow initiation of T cell activation through synergistic TCR/cytokine stimulation, leading to positive feedback, T cell activation, proliferation, and efficient killing of tumor cells. The synthetic circuit reconstitutes the key requirements for a strong T cell response in a manner that bypasses key suppressive bottlenecks. (**C**) Schematic differences between autocrine and paracrine IL-2 signaling in the presence of IL-2 consumers. An autocrine IL-2 circuit provides preferential spatial access to self-made IL-2 in comparison to a paracrine IL-2 circuit, where CAR T cells must compete with other IL-2 consumers (Tregs or T-naive cells). (**D**) An autocrine IL-2 leads to preferential expansion of IL-2 producers (through T cell activation and up-regulation of CD25), by contrast to a paracrine circuit in which IL-2 producers compete on equal or lesser footing with IL-2 consumers and are not selectively enriched limiting total IL-2 produced and failing to accumulate enough IL-2 to overcome thresholds required for T cell activation.

(Fig. 5A and fig. S15A); however, we also see a much larger expansion of naïve T cells (figs. S12B and S15A). These results suggest that host conventional T cells in the tumor can also play a significant role as IL-2 sinks, especially given their vast excess population. Although it is difficult to parse out the relative contribution of these T_{regs} versus conventional T cells as IL-2 consumers, it is not uncommon to observe the presence of large numbers of tumor-infiltrating but non–tumor-reactive T cells (*30*). Whatever their relative contribution, both of these IL-2 consumers are expected to decrease the effective signaling distance of IL-2 producers (*47*, *48*), which would strongly favor the efficacy of autocrine over paracrine IL-2 production in driving CAR T cell expansion.

Second, it is also likely that autocrine cells are capable of preferential expansion in response to the available pool of IL-2. There is a characteristic proliferative positive feedback loop that could in principle take place with T cells that can induce both IL-2 and TCR/CAR activation. T cell activation can both trigger an initially IL-2-independent proliferative response (*49*) and induce expression of the high-affinity IL-2 receptor subunit CD25 (fig. S17C), which allows T cells to outcompete other T cells for available IL-2. Because an autocrine circuit cell contains both the CAR and synNotch→IL-2 circuit, it has the capability to become both a preferred IL-2 responder (through T cell activation) and strong IL-2 producer (through synNotch activation) within a tumor. We hypothesize that these dually activated autocrine cells could thereby initiate a powerful population-level positive feedback loop that builds up even higher levels of intratumoral IL-2 as a result of preferential expansion of better IL-2 consumers/responders. This population-positive feedback would not take place in the paracrine circuit, as the IL-2 producers do not up-regulate CD25 (fig. S17C) and their IL-2 production would largely contribute to expanding competing T cells (such as T_{regs}) that act to suppress T cell–based immunity. Several pieces of evidence support this model of preferred expansion of autocrine circuit cells. First, only in the autocrine CAR T cells do we observe significantly higher expression of the proliferation marker Ki67 (Fig. 5C and fig. S14B). Second, we do not see increased tumor control with an autocrine circuit that produces the homeostatic cytokine IL-7 (fig. S17D). Further experiments will be needed to definitively evaluate the relative contributions of the multiple mechanisms discussed in this model.

Essential requirements to bypass tumor immunosuppression

Our efforts to systematically design CAR T circuits that couple IL-2 production/signaling with CAR signaling in alternative ways also elucidates the basic design principles of native T cell activation. The T cell system has evolved to severely restrict improper activation while simultaneously being able to launch a locally explosive response once triggered. Population-level positive feedback signaling using a shared cytokine (IL-2) allows this type of digital response between on and off states (*50*, *51*). In this model, T cells must not only be stimulated by the proper antigens but must also subsequently produce enough IL-2 to overcome the threshold set by competing IL-2 consumer cells present throughout the microenvironment (*52*). This control mechanism, however, provides weak points that tumors can take advantage of for immune suppression. Many tumors keep a strong T cell response in check, either by blocking T cell activation (*28*) or increasing competition for amplification factors such as IL-2.

Here we show that it is possible to still reconstitute the pathways required for a strong antitumor T cell response (i.e., rewiring the cell such that T cell activation, co-stimulation, and IL-2 signaling are still cooperatively stimulated), but in a way that now evades the major tumor suppressive mechanisms. Normally IL-2 is produced after T cell activation and acts as a critical amplifier of T cell activity. By placing IL-2 production under the control of a new TCR-independent but still tumor-targeted synthetic receptor we can now produce IL-2 immediately and consistently after tumor entry despite suppression of T cell activation. In addition, IL-2 consumers normally apply a selective pressure only allowing strongly activated effector T cells to expand (*52*). By coupling TCR/CAR activation and synNotch-driven IL-2 production in an autocrine IL-2 circuit, we can selectively expand the engineered therapeutic T cell population out of a background of competing IL-2 consumers. These rewired cells ultimately activate the same critical pathways (TCR and IL-2 pathways) as seen in native T cell responses but do so in a different temporal order and in response to different inputs allowing them to be far more effective in tumor-targeted therapy (Fig. 6). The engineered circuit maintains the explosive cell expansion necessary for robust antitumor activity but triggered in a manner that evades the major mechanisms of immunosuppression.

The power of alternatively wired immune cell circuits

In summary, we have been able to use flexible synthetic biology tools—such as the synNotch receptor system—to create new, alternative ways to rapidly establish both the TCR and IL-2 pathway activity required for an effective and sustained T cell response. The resulting bypass channel for IL-2 production allows for improved tumor control and reduced toxicity compared to alternative mechanisms of IL-2 delivery. Synthetic cytokine production circuits may represent a general solution for engineering immune cell therapies that can function more effectively in hostile tumor microenvironments, illustrating the power of customizing immune responses in highly precise but novel ways.

REFERENCES AND NOTES

1. S. J. Schuster *et al*., Tisagenlecleucel in Adult Relapsed or Refractory Diffuse Large B-Cell Lymphoma. *N. Engl. J. Med.* **380**, 45–56 (2019). doi: 10.1056/NEJMoa1804980; pmid: 30501490
2. N. C. Munshi *et al*., Idecabtagene Vicleucel in Relapsed and Refractory Multiple Myeloma. *N. Engl. J. Med.* **384**, 705–716 (2021). doi: 10.1056/NEJMoa2024850; pmid: 33626253
3. A. R. Haas *et al*., Phase I Study of Lentiviral-Transduced Chimeric Antigen Receptor-Modified T Cells Recognizing Mesothelin in Advanced Solid Cancers. *Mol. Ther.* **27**, 1919–1929 (2019). doi: 10.1016/j.ymthe.2019.07.015; pmid: 31420241
4. S. Mariathasan *et al*., TGFβ attenuates tumour response to PD-L1 blockade by contributing to exclusion of T cells. *Nature* **554**, 544–548 (2018). doi: 10.1038/nature25501; pmid: 29443960
5. A. Xia, Y. Zhang, J. Xu, T. Yin, X.-J. Lu, T Cell Dysfunction in Cancer Immunity and Immunotherapy. *Front. Immunol.* **10**, 1719 (2019). doi: 10.3389/fimmu.2019.01719; pmid: 31379886
6. A. B. Frey, N. Monu, Signaling defects in anti-tumor T cells. *Immunol. Rev.* **222**, 192–205 (2008). doi: 10.1111/j.1600-065X.2008.00606.x; pmid: 18364003
7. M. Y. Balkhi, Q. Ma, S. Ahmad, R. P. Junghans, T cell exhaustion and Interleukin 2 downregulation. *Cytokine* **71**, 339–347 (2015). doi: 10.1016/j.cyto.2014.11.024; pmid: 25516298
8. L. Tang *et al*., Enhancing T cell therapy through TCR-signaling-responsive nanoparticle drug delivery. *Nat. Biotechnol.* **36**, 707–716 (2018). doi: 10.1038/nbt.4181; pmid: 29985479
9. L. Zhang *et al*., Tumor-infiltrating lymphocytes genetically engineered with an inducible gene encoding interleukin-12 for the immunotherapy of metastatic melanoma. *Clin. Cancer Res.* **21**, 2278–2288 (2015). doi: 10.1158/1078-0432.CCR-14-2085; pmid: 25695689
10. M. B. Atkins *et al*., High-dose recombinant interleukin 2 therapy for patients with metastatic melanoma: Analysis of 270 patients treated between 1985 and 1993. *J. Clin. Oncol.* **17**, 2105–2116 (1999). doi: 10.1200/JCO.1999.17.7.2105; pmid: 10561265
11. Q. Zhang *et al*., A human orthogonal IL-2 and IL-2Rβ system enhances CAR T cell expansion and antitumor activity in a murine model of leukemia. *Sci. Transl. Med.* **13**, eabg6986 (2021). doi: 10.1126/scitranslmed.abg6986; pmid: 34936380
12. L. Morsut *et al*., Engineering Customized Cell Sensing and Response Behaviors Using Synthetic Notch Receptors. *Cell* **164**, 780–791 (2016). doi: 10.1016/j.cell.2016.01.012; pmid: 26830878
13. K. T. Roybal *et al*., Precision Tumor Recognition by T Cells With Combinatorial Antigen-Sensing Circuits. *Cell* **164**, 770–779 (2016). doi: 10.1016/j.cell.2016.01.011; pmid: 26830879
14. K. A. Smith, Interleukin-2: Inception, impact, and implications. *Science* **240**, 1169–1176 (1988). doi: 10.1126/science.3131876; pmid: 3131876
15. Z. Sun *et al*., A next-generation tumor-targeting IL-2 preferentially promotes tumor-infiltrating $CD8^+$ T-cell response and effective tumor control. *Nat. Commun.* **10**, 3874 (2019). doi: 10.1038/s41467-019-11782-w; pmid: 31462678
16. G. R. Weiss *et al*., Molecular insights on the peripheral and intratumoral effects of systemic high-dose rIL-2 (aldesleukin) administration for the treatment of metastatic melanoma. *Clin. Cancer Res.* **17**, 7440–7450 (2011). doi: 10.1158/1078-0432.CCR-11-1650; pmid: 21976537
17. M. C. Panelli *et al*., Gene-expression profiling of the response of peripheral blood mononuclear cells and melanoma metastases to systemic IL-2 administration. *Genome Biol.* **3**, RESEARCH0035 (2002). doi: 10.1186/gb-2002-3-7-research0035; pmid: 12184809
18. T. Saito *et al*., Two FOXP3(+)CD4(+) T cell subpopulations distinctly control the prognosis of colorectal cancers. *Nat. Med.* **22**, 679–684 (2016). doi: 10.1038/nm.4086; pmid: 27111280
19. M. Ahmadzadeh, S. A. Rosenberg, IL-2 administration increases CD4+ CD25(hi) Foxp3+ regulatory T cells in cancer patients. *Blood* **107**, 2409–2414 (2006). doi: 10.1182/blood-2005-06-2399; pmid: 16304057
20. K. Staveley-O'Carroll *et al*., Induction of antigen-specific T cell anergy: An early event in the course of tumor progression. *Proc. Natl. Acad. Sci. U.S.A.* **95**, 1178–1183 (1998). doi: 10.1073/pnas.95.3.1178; pmid: 9448305
21. A. M. Levin *et al*., Exploiting a natural conformational switch to engineer an interleukin-2 'superkine'. *Nature* **484**, 529–533 (2012). doi: 10.1038/nature10975; pmid: 22446627
22. D. L. Wallace *et al*., Prolonged exposure of naïve CD8+ T cells to interleukin-7 or interleukin-15 stimulates proliferation without differentiation or loss of telomere length. *Immunology* **119**, 243–253 (2006). doi: 10.1111/j.1365-2567.2006.02429.x; pmid: 17005004
23. L. V. Hurton *et al*., Tethered IL-15 augments antitumor activity and promotes a stem-cell memory subset in tumor-specific T cells. *Proc. Natl. Acad. Sci. U.S.A.* **113**, E7788–E7797 (2016). doi: 10.1073/pnas.1610544113; pmid: 27849617
24. P. F. Robbins *et al*., Single and dual amino acid substitutions in TCR CDRs can enhance antigen-specific T cell functions. *J. Immunol.* **180**, 6116–6131 (2008). doi: 10.4049/jimmunol.180.9.6116; pmid: 18424733

25. P. F. Robbins *et al*., A pilot trial using lymphocytes genetically engineered with an NY-ESO-1-reactive T-cell receptor: Long-term follow-up and correlates with response. *Clin. Cancer Res.* **21**, 1019–1027 (2015). doi: 10.1158/1078-0432.CCR-14-2708; pmid: 25538264
26. J. Z. Williams *et al*., Precise T cell recognition programs designed by transcriptionally linking multiple receptors. *Science* **370**, 1099–1104 (2020). doi: 10.1126/science.abc6270; pmid: 33243890
27. C. C. Kloss, M. Condomines, M. Cartellieri, M. Bachmann, M. Sadelain, Combinatorial antigen recognition with balanced signaling promotes selective tumor eradication by engineered T cells. *Nat. Biotechnol.* **31**, 71–75 (2013). doi: 10.1038/nbt.2459; pmid: 23242161
28. G. P. Mognol *et al*., Exhaustion-associated regulatory regions in CD8$^+$ tumor-infiltrating T cells. *Proc. Natl. Acad. Sci. U.S.A.* **114**, E2776–E2785 (2017). doi: 10.1073/pnas.1620498114; pmid: 28283662
29. T. Chinen *et al*., An essential role for the IL-2 receptor in T$_{reg}$ cell function. *Nat. Immunol.* **17**, 1322–1333 (2016). doi: 10.1038/ni.3540; pmid: 27595233
30. G. Oliveira *et al*., Phenotype, specificity and avidity of antitumour CD8$^+$ T cells in melanoma. *Nature* **596**, 119–125 (2021). doi: 10.1038/s41586-021-03704-y; pmid: 34290406
31. J. Li *et al*., Tumor Cell-Intrinsic Factors Underlie Heterogeneity of Immune Cell Infiltration and Response to Immunotherapy. *Immunity* **49**, 178–193.e7 (2018). doi: 10.1016/j.immuni.2018.06.006; pmid: 29958801
32. S. R. Hingorani *et al*., Trp53R172H and KrasG12D cooperate to promote chromosomal instability and widely metastatic pancreatic ductal adenocarcinoma in mice. *Cancer Cell* **7**, 469–483 (2005). doi: 10.1016/j.ccr.2005.04.023; pmid: 15894267
33. T. N. D. Pham *et al*., Preclinical Models of Pancreatic Ductal Adenocarcinoma and Their Utility in Immunotherapy Studies. *Cancers* **13**, 440 (2021). doi: 10.3390/cancers13030440; pmid: 33503832
34. I. M. Stromnes *et al*., T Cells Engineered against a Native Antigen Can Surmount Immunologic and Physical Barriers to Treat Pancreatic Ductal Adenocarcinoma. *Cancer Cell* **28**, 638–652 (2015). doi: 10.1016/j.ccell.2015.09.022; pmid: 26525103
35. M. K. Gately, T. D. Anderson, T. J. Hayes, Role of asialo-GM1-positive lymphoid cells in mediating the toxic effects of recombinant IL-2 in mice. *J. Immunol.* **141**, 189–200 (1988). pmid: 3259967
36. E. Hooijberg, A. Q. Bakker, J. J. Ruizendaal, H. Spits, NFAT-controlled expression of GFP permits visualization and isolation of antigen-stimulated primary human T cells. *Blood* **96**, 459–466 (2000). doi: 10.1182/blood.V96.2.459; pmid: 10887106
37. H. Yamaue *et al*., Enhanced interleukin-2 production in human tumor-infiltrating lymphocytes engineered by 3′-truncated interleukin-2 gene. *J. Immunother. Emphasis Tumor Immunol.* **16**, 262–274 (1994). doi: 10.1097/00002371-199411000-00002; pmid: 7881635
38. Y. Hart *et al*., Paradoxical signaling by a secreted molecule leads to homeostasis of cell levels. *Cell* **158**, 1022–1032 (2014). doi: 10.1016/j.cell.2014.07.033; pmid: 25171404
39. Y. Refaeli, L. Van Parijs, C. A. London, J. Tschopp, A. K. Abbas, Biochemical mechanisms of IL-2-regulated Fas-mediated T cell apoptosis. *Immunity* **8**, 615–623 (1998). doi: 10.1016/S1074-7613(00)80566-X; pmid: 9620682
40. M. E. Pipkin *et al*., Interleukin-2 and inflammation induce distinct transcriptional programs that promote the differentiation of effector cytolytic T cells. *Immunity* **32**, 79–90 (2010). doi: 10.1016/j.immuni.2009.11.012; pmid: 20096607
41. J. H. Levine *et al*., Data-Driven Phenotypic Dissection of AML Reveals Progenitor-like Cells that Correlate with Prognosis. *Cell* **162**, 184–197 (2015). doi: 10.1016/j.cell.2015.05.047; pmid: 26095251
42. M. T. Saung *et al*., Targeting myeloid-inflamed tumor with anti-CSF-1R antibody expands CD137+ effector T-cells in the murine model of pancreatic cancer. *J. Immunother. Cancer* **6**, 118 (2018). doi: 10.1186/s40425-018-0435-6; pmid: 30424804
43. Y. Liu *et al*., IL-2 regulates tumor-reactive CD8$^+$ T cell exhaustion by activating the aryl hydrocarbon receptor. *Nat. Immunol.* **22**, 358–369 (2021). doi: 10.1038/s41590-020-00850-9; pmid: 33432230
44. S. A. Rosenberg, IL-2: The first effective immunotherapy for human cancer. *J. Immunol.* **192**, 5451–5458 (2014). doi: 10.4049/jimmunol.1490019; pmid: 24907378
45. R. S. Cotran *et al*., Endothelial activation during interleukin 2 immunotherapy. A possible mechanism for the vascular leak syndrome. *J. Immunol.* **140** 1883–1888 (1988). doi: 10.4049/jimmunol.140.6.1883; pmid: 3279124
46. A. Oyler-Yaniv *et al*., A Tunable Diffusion-Consumption Mechanism of Cytokine Propagation Enables Plasticity in Cell-to-Cell Communication in the Immune System. *Immunity* **46**, 609–620 (2017). doi: 10.1016/j.immuni.2017.03.011; pmid: 28389069
47. K. Thurley, D. Gerecht, E. Friedmann, T. Höfer, Three-Dimensional Gradients of Cytokine Signaling between T Cells. *PLOS Comput. Biol.* **11**, e1004206 (2015). doi: 10.1371/journal.pcbi.1004206; pmid: 25923703
48. H. S. Wong *et al*., A local regulatory T cell feedback circuit maintains immune homeostasis by pruning self-activated T cells. *Cell* **184**, 3981–3997.e22 (2021). doi: 10.1016/j.cell.2021.05.028; pmid: 34157301
49. W. N. D'Souza, L. Lefrançois, IL-2 is not required for the initiation of CD8 T cell cycling but sustains expansion. *J. Immunol.* **171**, 5727–5735 (2003). doi: 10.4049/jimmunol.171.11.5727; pmid: 14634080
50. D. Busse *et al*., Competing feedback loops shape IL-2 signaling between helper and regulatory T lymphocytes in cellular microenvironments. *Proc. Natl. Acad. Sci. U.S.A.* **107**, 3058–3063 (2010). doi: 10.1073/pnas.0812851107; pmid: 20133667
51. F. Fuhrmann *et al*., Adequate immune response ensured by binary IL-2 and graded CD25 expression in a murine transfer model. *eLife* **5**, e20616 (2016). doi: 10.7554/eLife.20616; pmid: 28035902
52. T. Höfer, O. Krichevsky, G. Altan-Bonnet, Competition for IL-2 between Regulatory and Effector T Cells to Chisel Immune Responses. *Front. Immunol.* **3**, 268 (2012). doi: 10.3389/fimmu.2012.00268; pmid: 22973270

ACKNOWLEDGMENTS

We thank H. Jiang, E. Collisson, R. Almeida, M.P. Lopez, M. Broeker, Y. Tonai, A. DeGuzman, N. Blizzard, and members of the Lim Laboratory and Cell Design Institute for assistance and advice. We acknowledge the PFCC (RRID:SCR_018206) supported in part by Grant NIH P30 DK063720 and by the NIH S10 Instrumentation Grant S10 1S10OD018040-01. **Funding:** This work was supported by the following: Jane Coffin Childs Fellowship (to G.M.A.), NIH K08CA259610 (to G.M.A.), NIH/NIGMS F32 GM120843 (to N.W.F.), Howard Hughes Medical Institute (to W.A.L.), NIH U54CA244438 (to W.A.L.), NIH R01CA249018 (to W.A.L.), NIH UC4DK116264 (to W.A.L.), NIH U01CA265697 (to W.A.L.) **Author contributions:** Conceptualization: G.M.A., N.W.F., K.C.G., H.E.S., K.T.R., M.S., and W.A.L. Methodology: G.M.A., N.W.F., M.A.Y., H.B., J.Y., and M.S. Investigation: G.M.A., N.W.F., M.A.Y., S.R.S., N.R.R., H.B., M.P., J.L., W.Y., and A.L. Visualization: G.M.A., W.A.L., N.W.F., M.A.Y., N.R.R., and H.B. Funding acquisition: G.M.A. and W.A.L. Project administration: G.M.A. and W.A.L. Supervision: G.M.A., W.A.L., M.S. Writing – G.M.A., N.W.F., W.A.L., N.R.R., H.B. **Competing interests:** W.A.L. holds equity in Gilead Sciences and Intellia Therapeutics, is an adviser for Allogene Therapeutics, and has filed patents related to this work. **Data and materials availability:** All data are available in the manuscript or supplementary materials. Reagents are available from the corresponding author upon reasonable request. Plasmids from this paper will be made available on Addgene.

SUPPLEMENTARY MATERIALS

science.org/doi/10.1126/science.aba1624
Materials and Methods
Figs. S1 to S17
Reference (*53*)
MDAR Reproducibility Checklist

Submitted 9 November 2019; resubmitted 19 May 2022
Accepted 21 October 2022
10.1126/science.aba1624

RESEARCH ARTICLE SUMMARY

CELL BIOLOGY

Protein import into peroxisomes occurs through a nuclear pore–like phase

Yuan Gao†, Michael L. Skowyra†, Peiqiang Feng, Tom A. Rapoport*

INTRODUCTION: Peroxisomes are organelles that are enclosed by a single membrane and exist in nearly all eukaryotic cells. They perform important functions related to lipid metabolism and redox homeostasis, among others. Peroxisomes are also vital for human health; inborn defects in peroxisome biogenesis cause devastating and often life-threatening disorders such as the Zellweger spectrum. Peroxisomal enzymes are made in the cytosol, where they are recognized by PEX5 and related mobile receptors and are shuttled by the receptors into the organelle. How the receptors move proteins across the peroxisomal membrane has been a long-standing question, particularly because peroxisomes can mysteriously import folded or even oligomeric proteins. This property fundamentally differs from the way in which proteins are imported into the endoplasmic reticulum or mitochondria.

RATIONALE: Protein translocation into peroxisomes requires a number of components embedded in the peroxisomal membrane—notably PEX13. We recognized that PEX13 contains an extensive unstructured region that is enriched in the amino acids tyrosine (Y) and glycine (G). This tyrosine- and glycine-rich YG domain resembles the phenylalanine (F)– and glycine-rich FG domains of nucleoporins that reside in nuclear pores. FG domains form a meshwork inside nuclear pores that restricts passage of soluble molecules yet allows nuclear transport receptors to diffuse through and bring cargo along. By analogy to FG domains, we hypothesized that the YG domain of PEX13 might form a similarly selective phase on peroxisomes, through which import receptors could move folded proteins across the peroxisomal membrane.

RESULTS: We show that the YG domain is found in PEX13 proteins from all classes of eukaryotic organisms. Our analysis reveals that this domain is distinguished by the presence of repeated aromatic amino acids, predominantly tyrosines, which are separated from one another by short flexible linkers composed mostly of glycines and serines. The tyrosine residues are essential for peroxisomal protein import in the yeast *Saccharomyces cerevisiae*. YG domains from different organisms vary extensively in their amino acid sequence and in the number of tyrosines, yet despite this diversity, the domains are functionally interchangeable in yeast. The YG domain is followed by a long amphipathic helix that we show is also conserved across eukaryotic organisms and required for peroxisomal import.

Using disulfide-mediated cross-linking, we demonstrate that YG domains from multiple PEX13 molecules associate with one another in the membrane of yeast peroxisomes. This interaction leads to the formation of a dense meshwork, which excludes large soluble material such as proteases and bulky molecules but remains permeable to small molecules that are less than 2 kD in size. The formation of the meshwork and its barrier properties depend on the aromatic residues within the YG domain. Using protease-protection and cysteine-modification experiments, we further show that PEX13 resides in the peroxisomal membrane in two opposite orientations, an unusual feature among membrane proteins. PEX13 molecules of both orientations associate with one another, an interaction that involves the proteins' YG domains.

Crucially, we find that the purified YG domain forms a hydrogel that is held together by the domain's tyrosine residues. The import receptor PEX5 fused to green fluorescent protein (GFP) can selectively partition into the hydrogel, whereas GFP alone does not. The entry of PEX5 into the hydrogel requires conserved aromatic WXXXF/Y motifs (where W is tryptophan and X denotes any residue) in the receptor's flexible N-terminal region. Furthermore, PEX5 can also bring cargo proteins into the YG hydrogel. Delivery of cargo into the gel requires the presence of WXXXF/Y motifs in the receptor.

CONCLUSION: Our results with intact yeast membranes and synthetic hydrogels reveal that peroxisomal import resembles transport through the nuclear pore. A dense meshwork—a selective phase—is suspended within the peroxisomal membrane by multiple PEX13 molecules of opposite orientations. This meshwork provides an aqueous conduit across the membrane into the peroxisomal lumen. The walls of the proposed conduit might be assembled from the protein's conserved amphipathic helix. Peroxisomal import receptors such as PEX5 can diffuse through the meshwork and bring cargo along, using their WXXXF/Y motifs to locally dissolve the cohesive interactions holding the meshwork together. This mechanism explains how folded and oligomeric proteins are imported into peroxisomes and represents a previously unidentified principle by which proteins cross membranes. ■

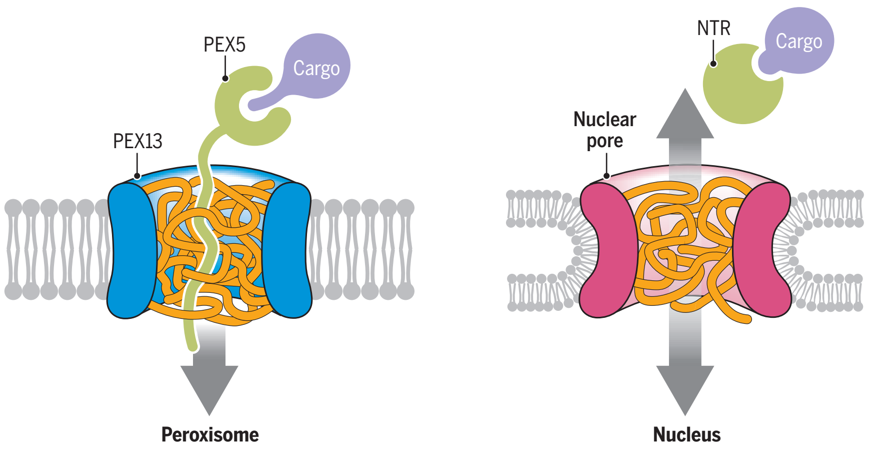

Peroxisomal protein import resembles nuclear transport. A dense meshwork is formed in the peroxisome's membrane by the YG domain of multiple copies of the peroxisomal protein PEX13. This meshwork functions as a conduit through which the import receptor PEX5 can selectively diffuse and deliver bound cargo into the peroxisome. The process is similar to how a nuclear transport receptor (NTR) moves through the FG meshwork inside a nuclear pore.

The list of author affiliations is available in the full article online.
*Corresponding author. Email: tom_rapoport@hms.harvard.edu
†These authors contributed equally to this work.
Cite this article as Y. Gao *et al*., *Science* **378**, eadf3971 (2022). DOI: 10.1126/science.adf3971

READ THE FULL ARTICLE AT
https://doi.org/10.1126/science.adf3971

RESEARCH ARTICLE

CELL BIOLOGY

Protein import into peroxisomes occurs through a nuclear pore–like phase

Yuan Gao[1,2]†, Michael L. Skowyra[1,2]†, Peiqiang Feng[1,2], Tom A. Rapoport[1,2]*

Peroxisomes are ubiquitous organelles whose dysfunction causes fatal human diseases. Most peroxisomal proteins are imported from the cytosol in a folded state by the soluble receptor PEX5. How folded cargo crosses the membrane is unknown. Here, we show that peroxisomal import is similar to nuclear transport. The peroxisomal membrane protein PEX13 contains a conserved tyrosine (Y)– and glycine (G)–rich YG domain, which forms a selective phase resembling that formed by phenylalanine-glycine (FG) repeats within nuclear pores. PEX13 resides in the membrane in two orientations that oligomerize and suspend the YG meshwork within the lipid bilayer. Purified YG domains form hydrogels into which PEX5 selectively partitions, by using conserved aromatic amino acid motifs, bringing cargo along. The YG meshwork thus forms an aqueous conduit through which PEX5 delivers folded proteins into peroxisomes.

Peroxisomes are organelles enclosed by a single membrane and are found in most eukaryotic cells (*1*). They provide vital functions, including fatty acid oxidation (*2*) and detoxification of reactive oxygen species (*3*). Peroxisomes are essential for human health: Various debilitating and often fatal disorders, notably the Zellweger spectrum, arise from the defective import of enzymes into the peroxisomal lumen, otherwise known as the matrix (*4*).

Matrix proteins are made in the cytosol and then imported into peroxisomes. Most contain a type 1 peroxisome targeting signal (PTS1) at their C terminus, which comprises the amino acid sequence Ser-Lys-Leu (SKL) or variants of it (*5*). The PTS1 is recognized in the cytosol by the soluble receptor PEX5 through the receptor's tetratricopeptide repeat (TPR) domain (*6*). PEX5 also contains a flexible N-terminal region that includes several aromatic motifs conforming to the amino acid sequence WXXXF/Y (where W is Trp, X denotes any residue, F is Phe, and Y is Tyr) (*7*). Some matrix proteins contain an alternative N-terminal signal called PTS2, whose recognition requires the adapter PEX7 (*8*). In humans, PEX7 binds a short motif in PEX5, whereas in many fungi, PEX7 associates with PEX5 paralogs that lack a TPR domain but retain the unstructured N-terminal region with its characteristic WXXXF/Y motifs (*9*).

PEX5 is recruited to peroxisomes by the membrane proteins PEX13 and PEX14 (and PEX17 in yeast) (*7*). Recruitment requires the receptor's WXXXF/Y motifs (*10*) and is followed by translocation of the cargo-bound receptor completely into the matrix (*10*–*12*). To return to the cytosol, PEX5 is ubiquitinated by the PEX2-PEX10-PEX12 ubiquitin ligase complex (*13*) and pulled out through a pore in the ligase complex (*14*) by a hexameric adenosine triphosphatase (ATPase) consisting of alternating copies of PEX1 and PEX6 (*15*). Deubiquitination in the cytosol resets PEX5 for a new import cycle (*16*, *17*).

How PEX5 crosses the peroxisomal membrane to deliver cargo into the lumen has been a long-standing question. Particularly mysterious is the receptor's ability to import folded or oligomeric proteins (*18*), or even gold beads (*19*). Thus, translocation into peroxisomes fundamentally differs from that into the endoplasmic reticulum (ER) or mitochondria, which can only import proteins in an unfolded conformation (*20*, *21*). It is also puzzling that translocation across the peroxisomal membrane does not require nucleotide hydrolysis (*22*), even though import occurs against a concentration gradient of the cargo (*23*).

Translocation into peroxisomes is thought to be mediated by PEX13 or PEX14. Although PEX14 has historically been favored (*24*), the protein lacks obvious features that could form an aqueous conduit for moving hydrophilic proteins across the membrane (*25*). In addition, PEX14 may be dispensable for import in some organisms (*26*, *27*). PEX13, by contrast, is essential for import in all organisms that have been tested (*28*, *29*). Curiously, PEX13 contains an unstructured N-terminal region of unknown function that is required for import (*30*) and is enriched in the amino acids tyrosine and glycine (*31*). We noted that this tyrosine- and glycine-rich YG domain resembles the phenylalanine- and glycine-rich FG domains of nucleoporins, which reside within the nuclear pore and form a meshwork that restricts the entry of large molecules into the nucleus (*32*). This meshwork is locally broken by nuclear transport receptors (NTRs), allowing them to rapidly diffuse through nuclear pores along with bound cargo (*33*).

Here, we show that the YG domain of PEX13 forms a similarly selective phase on peroxisomes. Our results lead to a model whereby the YG phase is locally disrupted by aromatic residues in the receptor's WXXXF/Y motifs, allowing PEX5 to diffuse across the membrane into the matrix and carry cargo along. This mechanism explains how folded and oligomeric proteins are imported into peroxisomes.

The YG domain of PEX13 is conserved and essential for peroxisomal import

The YG domain is found in PEX13 homologs from species representative of all eukaryotic clades (Fig. 1A). The domain is characterized by a preponderance of aromatic amino acids, predominantly tyrosine, but phenylalanines also occur in some organisms (Fig. 1A and fig. S1A). The number and position of the aromatic residues vary (Fig. 1A). The aromatic residues are separated by short linkers of about four amino acids (fig. S1B), which are enriched in small residues, notably glycine and serine, and lack charged residues (Fig. 1A and fig. S1A). These properties are generally similar to those of cohesive nucleoporin FG-repeat domains (fig. S1C), except that the linkers between FG repeats are longer (fig. S1D).

The YG domain is followed by a long amphipathic helix (AH) (Fig. 1A and fig. S2), which has clearly defined hydrophobic and hydrophilic surfaces (fig. S3). Whether the AH consists of a straight helical segment or has a kink in the middle is unclear (fig. S3). Downstream of the AH, most PEX13 homologs contain a canonical transmembrane segment (TM) and an SH3 domain that binds PEX5 (*28*) (Fig. 1A and fig. S2), although these are absent in some plants (*34*) (fig. S2). Thus, only the YG domain and the AH are strictly conserved.

The YG domain is necessary for peroxisomal import, which we measured in the yeast *Saccharomyces cerevisiae* using an engineered pathway that generates a pigment when import is impaired (*35*). When all 14 tyrosines in the YG domain were mutated to serines, import was abolished (Fig. 1B), whereas converting all of the tyrosines into phenylalanines caused only a modest defect (Fig. 1B). Thus, the residues' aromaticity is critical. A minimum of 11 tyrosines seems to be required in yeast (fig. S4A), but their position can be varied. The YG domain could also be replaced by the analogous domain from other organisms (Fig. 1C), albeit with variable efficiency, indicating that the domain's function is conserved despite its sequence diversity.

---

[1]Department of Cell Biology, Harvard Medical School, Boston, MA 02115, USA. [2]Howard Hughes Medical Institute, Harvard Medical School, Boston, MA 02115, USA.
***Corresponding author. Email: tom_rapoport@hms.harvard.edu**
†These authors contributed equally to this work.

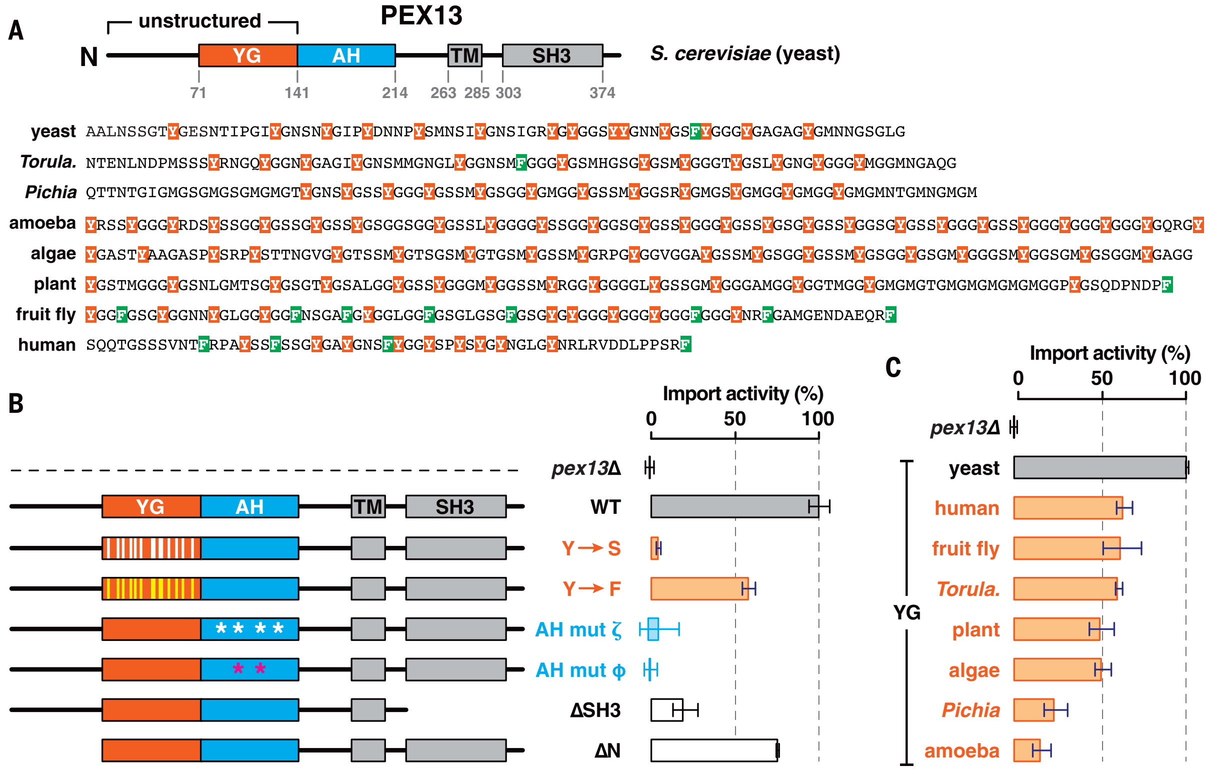

Fig. 1. The YG domain of PEX13 is required for peroxisomal protein import. (**A**) The domain organization of PEX13 from *S. cerevisiae* (yeast) is shown at the top. Numbers denote amino acid coordinates. Sequences of the YG domain in PEX13 homologs from organisms representing the indicated eukaryotic clades (*Torula*., *Torulaspora*) are shown at the bottom. (**B**) Peroxisomal protein import activity (mean ± SE of three experiments) in yeast cells expressing the indicated PEX13 mutants compared with wild-type (WT) cells and a PEX13 knockout strain (*pex13*Δ). Y→S and Y→F denote conversion of all tyrosines (positions indicated by vertical bars) in the YG domain into serines or phenylalanines, respectively. AH mut ζ and φ denote conversion of four hydrophilic residues in the AH into alanine or two hydrophobic residues into glutamate, respectively. (**C**) Import activity in yeast cells expressing PEX13 chimeras with YG domains from the indicated organisms. Single-letter abbreviations for the amino acid residues are as follows: A, Ala; C, Cys; D, Asp; E, Glu; F, Phe; G, Gly; H, His; I, Ile; K, Lys; L, Leu; M, Met; N, Asn; P, Pro; Q, Gln; R, Arg; S, Ser; T, Thr; V, Val; W, Trp; and Y, Tyr.

Taken together, these data demonstrate that the YG domain is a universal and essential feature of PEX13.

Import was also abolished by point mutations in either the hydrophilic face (mut ζ) or the hydrophobic face (mut φ) of the AH (Fig. 1B), revealing that the AH is likewise essential. Whereas loss of the SH3 domain (ΔSH3) reduced import (Fig. 1B) as reported previously (*36*), deleting the flexible region that precedes the YG domain (ΔN) had no effect (Fig. 1B), indicating that this region is dispensable. We confirmed that all mutants were similarly expressed (fig. S4, A to C).

YG domains of multiple PEX13 molecules interact on peroxisomes

To determine whether YG domains form a nuclear pore–like phase on peroxisomes, we first tested whether these domains associate with one another in the peroxisomal membrane. Individual cysteines were introduced at either of two positions (residue 104 or 131) in the YG domain of FLAG-tagged yeast PEX13 (which lacks natural cysteines) (Fig. 2A), without affecting import activity (fig. S5A). Formation of disulfide-linked dimers was then assessed using an oxidizing agent (Fig. 2A). Both positions indeed yielded efficient dimerization (>70%) (Fig. 2B, top). Dimers were disulfide-linked because the corresponding bands disappeared upon reduction with dithiothreitol (DTT) (Fig. 2B, bottom). Dimerization was also sensitive to detergent (Fig. 2B, lanes 4 and 8), suggesting that the interaction requires an intact membrane. These results thus show that the YG domains of individual PEX13 molecules interact in the peroxisomal membrane.

The interaction between YG domains is indeed multivalent and does not involve just two molecules. When two cysteines were introduced into the YG domain (at positions 104 and 131), a ladder of disulfide-linked bands was observed (Fig. 2C, right). Some cross-linking occurred even without oxidant (lane 4), suggesting that the interaction is highly favored. The largest cross-linked species reveal that more than eight PEX13 molecules interact through their YG domains. Cross-linking was greatly reduced after converting all tyrosines in the YG domain into serines (Fig. 2D, compare lanes 3 and 6 and corresponding quantification). Cross-linking was unaffected by the absence of other import components, including PEX2, PEX5, PEX14, or PEX17 (fig. S4D), suggesting that PEX13 forms oligomers by itself. This conclusion agrees with previous studies showing that PEX13 forms oligomers independently of other import components (*37*, *38*). Our analysis demonstrates that multiple PEX13 molecules associate with one another on peroxisomes through their YG domains, analogously to how nucleoporin FG domains interact within the nuclear pore.

The YG domain is inaccessible to large molecules

We next asked whether the interaction between YG domains restricts access to soluble material, similar to the FG meshwork inside nuclear pores that excludes large proteins and other molecules. A 3C protease–cleavage site was inserted at different positions in the YG domain of FLAG-tagged PEX13 or outside this domain near the N terminus (Fig. 3A, scheme). The resulting constructs replaced endogenous PEX13 in yeast and were fully active (fig. S5B). When membranes isolated from the corresponding

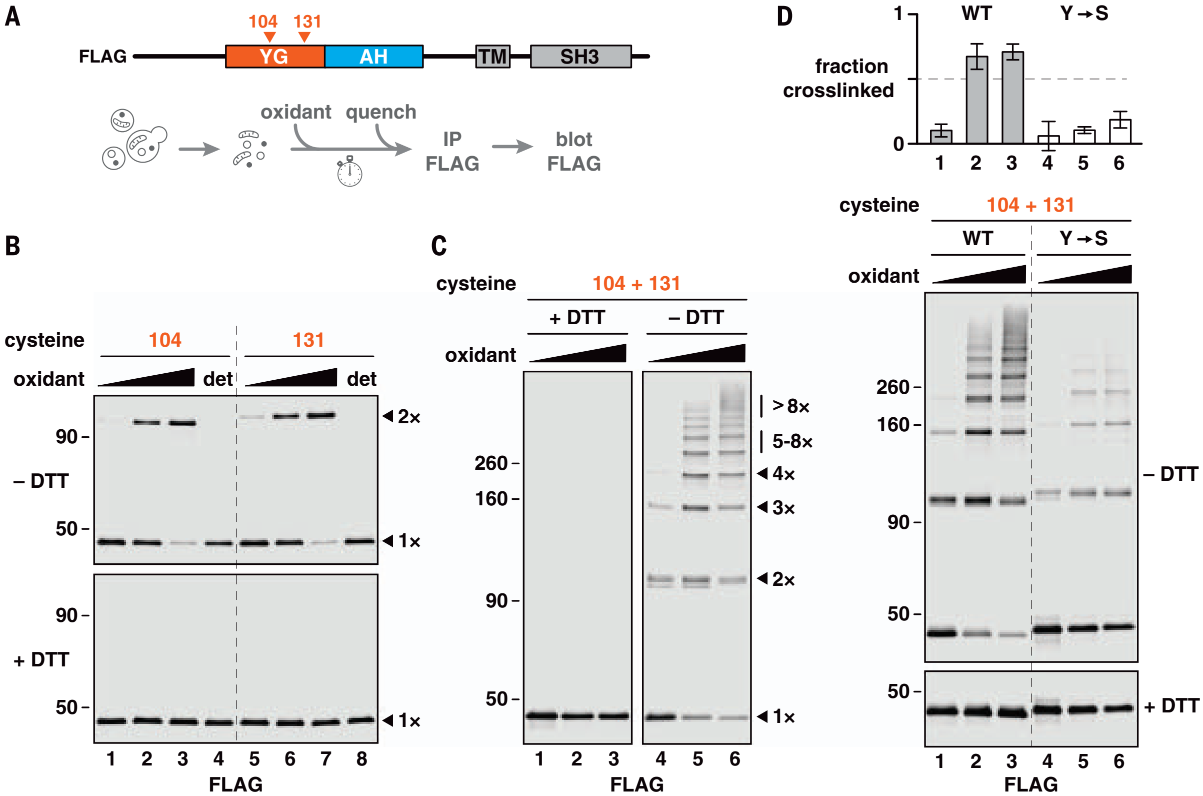

Fig. 2. The YG domain of PEX13 forms oligomers in the peroxisomal membrane. (**A**) Scheme for the experiments shown in (B) to (D). To test whether YG domains associate with one another, cysteines were introduced at the indicated positions in the YG domain of FLAG-tagged yeast PEX13 (which lacks native cysteines), and the resulting constructs were expressed in yeast. Intact membranes from the corresponding strains were treated with Aldrithiol-4 (oxidant), unreacted cysteines were then quenched with NEM, and the proteins were immunoprecipitated (IP) and analyzed by immunoblotting (blot). (**B**) As described in (A), using PEX13 proteins containing individual cysteines at the indicated positions. Reactions were performed in the presence of 0, 50, or 200 μM oxidant with or without detergent (det) and resolved by nonreducing (−DTT) or reducing (+DTT) SDS–polyacrylamide gel electrophoresis (SDS-PAGE) before immunoblotting. Monomers (1×) and disulfide-linked dimers (2×) are indicated on the right. Numbers along the left side specify relative molecular weights (in kD). (**C**) Same as in (B), but with PEX13 containing two cysteines. The number of disulfide-linked molecules is indicated on the right (1× to 8×). (**D**) Same as in (C), but comparing PEX13 with tyrosines (WT) or serines (Y→S) in the YG domain. Cross-linking efficiency is plotted at the top (mean ± SE of three experiments).

strains were treated with the protease, the constructs with N-terminal cleavage sites were readily digested (Fig. 3A, lanes 2 and 6), consistent with the reported cytosolic accessibility of the N terminus (*39*). By contrast, sites in the YG domain were much more resistant to cleavage (lanes 10 and 14) unless detergent was added (lanes 11 and 15). No cleavage occurred at any site when the protease was preinactivated by *N*-ethylmaleimide (NEM; lanes marked by skull and crossbones). These data thus show that the YG domain is not easily accessed by the 30-kD 3C protease.

To confirm this result, we probed the accessibility of the YG domain to cysteine-reactive polyethylene glycol (PEGmal). Individual cysteines were introduced throughout FLAG-tagged PEX13 in yeast (Fig. 3B, scheme), and membranes from the corresponding strains were treated with different sizes of PEGmal. Cysteines near the N terminus were readily modified by all sizes of PEGmal (Fig. 3B, upper two blots) as expected. By contrast, cysteines in the YG domain were barely modified by the two largest PEGmal reagents (5 and 10 kD) unless detergent was included (lanes 1 to 6 in the two middle blots). This resistance to modification depended on size, because the two smallest forms of PEGmal (0.8 and 2 kD) efficiently modified either cysteine (lanes 7 to 12 in the two middle blots). As a control, we tested the accessibility of a cysteine in the TM, which was not modified by PEGmal of any size (bottom blot).

Converting all tyrosines in the YG domain to serines (Y→S) increased accessibility to 10-kD PEGmal (Fig. 3C), consistent with this mutant's reduced self-association (Fig. 2D). Converting all tyrosines to phenylalanines (Y→F) instead improved the resistance to modification (Fig. 3C), again highlighting the importance of the aromatic residues in cementing the interaction between PEX13 molecules. The absence of PEX5 (*pex5*Δ) had no effect on accessibility (Fig. 3C), suggesting that active import may not be necessary for the YG domain's exclusion properties. Taken together, our results reveal that multiple YG domains form a meshwork in the peroxisomal membrane, which excludes large molecules but not small ones, similarly to the FG meshwork in nuclear pores.

To confirm this conclusion, we introduced single cysteines on either side of the transmembrane segment of the peroxisomal membrane protein PEX14 (which also lacks native cysteines) and examined their accessibility to different sizes of PEGmal as above (fig. S6A). The C terminus of PEX14 faces the cytosol (*10*, *39*), and accordingly, a cysteine located near the C terminus (position 242) was readily modified by all sizes of PEGmal in the absence of detergent (fig. S6B, upper blot). By contrast, a cysteine located near the N terminus (position 65), which is oriented toward the lumen (*10*, *39*), was modified only by the smallest PEGmal tested (fig. S6B, lower blot). In the presence of detergent, both cysteines were indiscriminately modified by all sizes of the reagent. These results thus confirm that the peroxisomal membrane is permeable to small molecules, as suggested before (*35*, *40*), and are

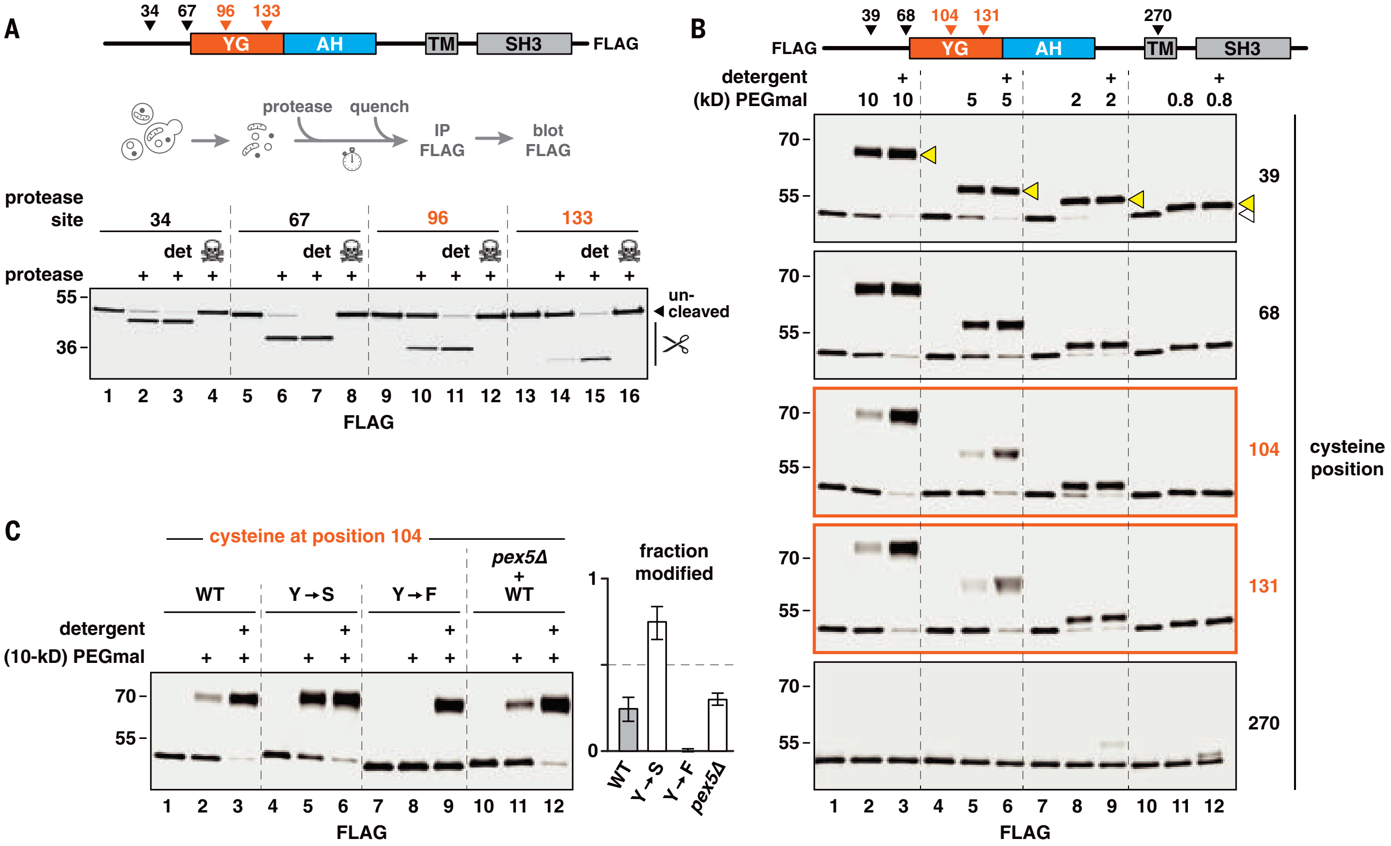

Fig. 3. The YG domain is poorly accessible to large molecules. (**A**) To test accessibility of the YG domain to proteins, a 3C protease–cleavage site was introduced into FLAG-tagged yeast PEX13 at the indicated positions, and the resulting constructs were expressed in yeast. Intact membranes from each strain were first treated with the protease with or without detergent (det) and then quenched with NEM to inactivate the protease. Where indicated (skull and crossbones), NEM was added before the protease. Scissors designate the cleaved forms. (**B**) Same as in (A), except that accessibility of the YG domain to differently sized molecules was assessed by introducing individual cysteines into FLAG-tagged PEX13 at the positions shown. Membranes from the corresponding strains were treated with different sizes (in kD) of cysteine-reactive PEGmal and then quenched with excess cysteine. Covalent modification of the proteins was visualized by immunoblotting. Modified and unmodified forms of the protein are designated by yellow and white triangles, respectively, in the top blot. (**C**) Same as in (B), but with PEX13 containing a cysteine at position 104 and tyrosines in the YG domain (WT), or tyrosines mutated to serines (Y→S) or phenylalanines (Y→F). Where indicated, membranes were isolated from a strain lacking PEX5 (*pex5*Δ). Modification was performed with 10-kD PEGmal. Modification efficiency is plotted on the right (mean ± SE of four experiments).

consistent with a dense meshwork of limited porosity residing in the membrane.

PEX13 adopts two orientations in the peroxisomal membrane

The YG meshwork must be suspended within the peroxisomal membrane to form a conduit for cargo. To determine how the YG meshwork is formed, we examined the membrane topology of PEX13. The N terminus of the protein was fused to a 3C protease–cleavage site preceded by a streptavidin-binding peptide (SBP) tag, and the C terminus was fused to a tobacco etch virus (TEV) protease–cleavage site followed by a FLAG tag (Fig. 4A, upper scheme). The construct was expressed from the endogenous locus in yeast and supported peroxisomal protein import (fig. S5B).

We first ascertained the orientation of the C terminus. Membranes were treated with TEV protease, and PEX13 was then immunoprecipitated by the N-terminal SBP tag (Fig. 4A). Interestingly, only half of the PEX13 population was cleaved (lane 2; quantification in fig. S7A). The resistant pool was protected by the membrane, because it could be cleaved in the presence of detergent (Fig. 4A, lane 3). No cleavage occurred when the protease was preinactivated by NEM (lane 4). These data thus suggest that PEX13 resides in the membrane in two orientations: one whose C terminus faces the cytosol and another whose C terminus faces the lumen (Fig. 4A, bottom scheme). The interaction between YG domains in the membrane might thus be mediated by PEX13 molecules of both orientations (see below).

To infer the orientation of the N terminus, membranes were treated with 3C protease, and PEX13 was then immunoprecipitated by the C-terminal FLAG tag (Fig. 4A). In contrast to the C terminus, more than 50% of the molecules had their N termini accessible to the protease (lane 6), and the exact proportion varied between experiments (fig. S7A). The remaining pool was again cleaved in detergent (Fig. 4A, lane 7). The N terminus might thus not be fixed in one specific orientation but may instead be free to move between the cytosol and the lumen (Fig. 4A, bottom scheme). Notably, these results agree with the cytosolic accessibility of the N terminus that was reported above (Fig. 3, A and B).

Controls were performed with PEX14 (Fig. 4B) and PEX17 (fig. S7B), which are conventional single-pass membrane proteins whose N termini face the lumen and C termini face the cytosol (*10*, *25*, *39*). Using analogously tagged constructs that supported peroxisomal import (fig. S5B), we found that the C termini of both proteins were fully cleaved in the absence of detergent, whereas their N termini

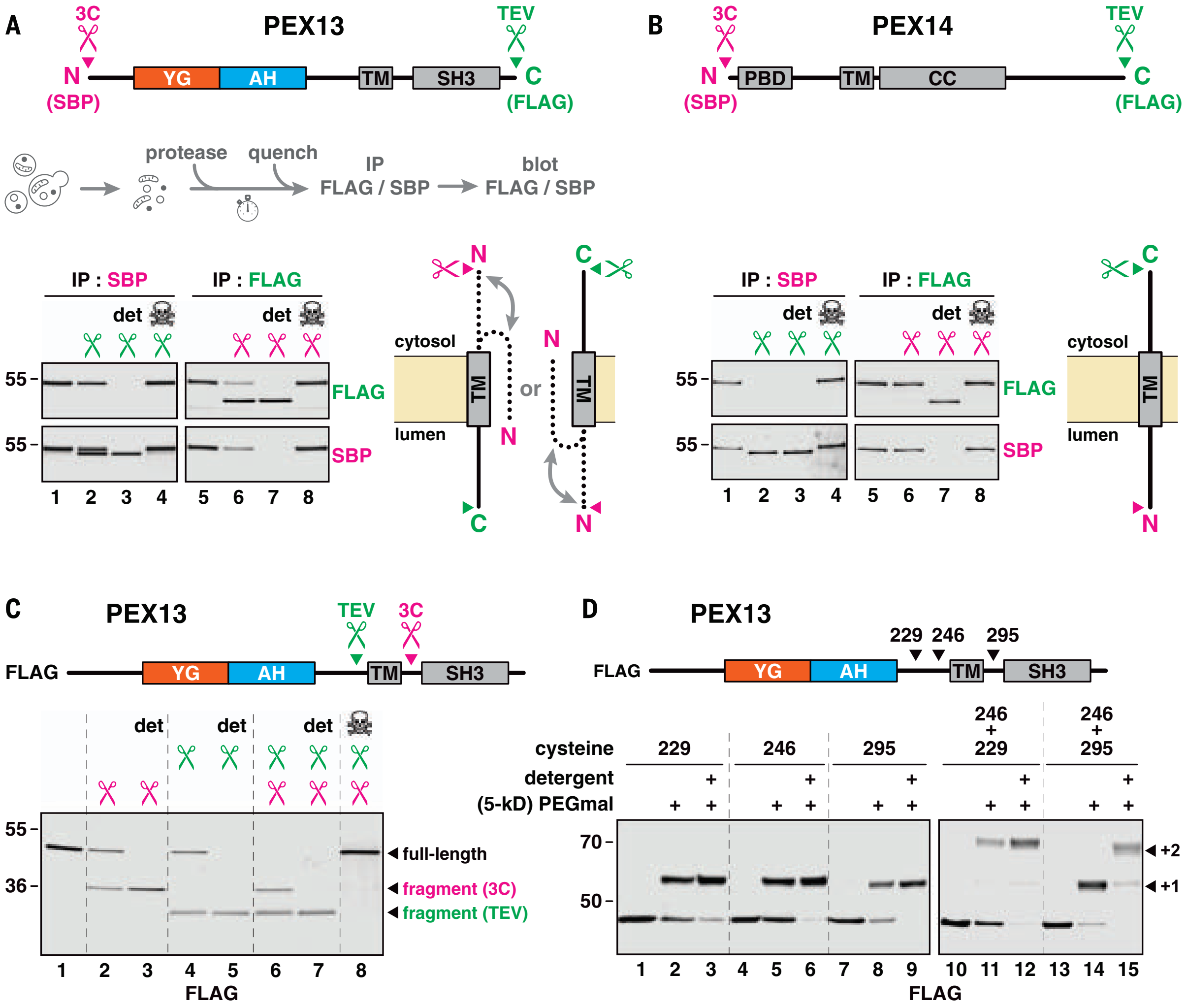

Fig. 4. PEX13 adopts two transmembrane orientations. (**A**) Membrane topology determined by protease protection. The indicated protease-cleavage sites (scissors) and epitope tags were introduced into PEX13 in yeast. Membranes containing this protein were treated with protease with or without detergent (det), the reactions were quenched with NEM, and PEX13 was immunoprecipitated (IP); cleavage was visualized by immunoblotting (see scheme). Where indicated (skull and crossbones), NEM was added before the proteases. The position of the C terminus is deduced from cleavage with TEV protease and immunoprecipitation by the N-terminal SBP tag, and the position of the N terminus is deduced from cleavage with 3C protease and immunoprecipitation by the C-terminal FLAG tag. The two inferred orientations of PEX13 are depicted on the right; the N terminus can face either side, whereas the C terminus is fixed in one of two orientations. (**B**) Same as in (A), but for PEX14. PBD, PEX5-binding domain; TM, transmembrane segment; CC, coiled-coil oligomerization domain. (**C**) Same as in (A), but with protease sites flanking the TM and a FLAG tag as shown. (**D**) TM orientation determined by modification of flanking cysteines with membrane-impermeable PEGmal. One or two cysteines were introduced into FLAG-tagged PEX13, as indicated. Membranes were treated with 5-kD PEGmal and then quenched with excess cysteine; single (+1) or double (+2) modification was visualized by immunoblotting.

were completely protected unless detergent was included (Fig. 4B and fig. S7B). The topologies of PEX14 and PEX17 thus agree with previous reports.

The dual topology of PEX13 is supported by two observed orientations of the protein's TM. We incorporated 3C protease– and TEV protease–cleavage sites on either side of the TM and added a FLAG tag to the N terminus for immunodetection (Fig. 4C, scheme). The resulting construct allowed peroxisomal import (fig. S5B). Again, half of the molecules were accessible to either protease in the absence of detergent (Fig. 4C, lanes 2 and 4), whereas the entire population was cleaved when detergent was included (lanes 3 and 5). Notably, addition of both proteases produced both cleavage products (lanes 6 to 8), consistent with two orientations of the protein in the membrane.

We confirmed the dual topology of PEX13 by PEGmal accessibility. Single cysteines were introduced on either side of the TM (Fig. 4D, scheme) without affecting import (fig. S5A), and membranes from the corresponding strains were treated with 5-kD PEGmal. Regardless of whether the cysteine resided upstream (position 229 or 246) or downstream (position 295) of the TM, about half of the molecules showed the increase in molecular weight that was expected from cysteine modification (Fig. 4D, left blot). All molecules were modified in detergent. With two cysteines on the same side of the TM (positions 229 and 246), half of the PEX13 molecules were modified on both cysteines, whereas the other half were not modified at all (Fig. 4D, right blot), as expected. By contrast, with two cysteines on opposite sides (positions 246 and 295), essentially all PEX13 molecules were modified but only on one or the other cysteine. These results confirm that the TM of PEX13 spans the membrane in two possible orientations.

Fig. 5. The two orientations of PEX13 are bridged by the YG domain. (**A**) To test whether the two orientations of PEX13 associate with each other, a single cysteine and a 3C protease–cleavage site were incorporated into FLAG-tagged yeast PEX13 as shown. An SBP tag was included at the C terminus to enhance the size shift after proteolytic cleavage. The resulting construct was integrated into yeast. Intact membranes from the corresponding strain were treated with the protease to reveal the protein's two orientations, oxidized with Aldrithiol-4 to induce disulfide-bridge formation, and quenched to inactivate the protease and oxidant. (**B**) Disulfide-linked dimers were visualized by reducing (+DTT) or nonreducing (–DTT) SDS-PAGE and immunoblotting for the FLAG tag. Where indicated, detergent (det) was included during protease cleavage. Cleaved (scissors) and uncleaved (∅) species are marked on the right. The topologies of the three observed dimers (numbered) are depicted below.

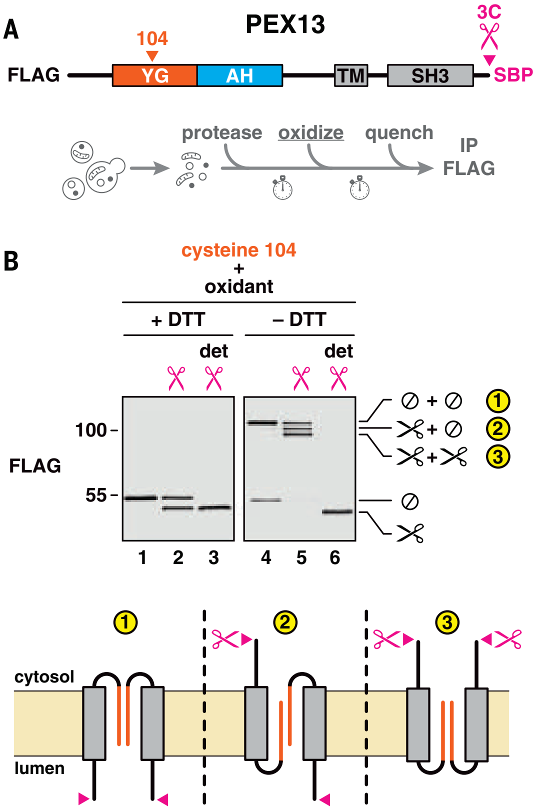

The dual topology does not require formation of the YG meshwork, because both orientations were retained after mutating all tyrosines in the YG domain into serines (fig. S8A). Both orientations were also retained in the absence of PEX2, PEX5, PEX8, PEX14, or PEX17 (fig. S8B), indicating that other import components are dispensable. By contrast, in the absence of PEX3, all PEX13 molecules became accessible to the proteases and the abundance of PEX13 was also reduced (fig. S8C). This observation agrees with previous reports of PEX13 being destabilized in the absence of PEX3 (*41*, *42*) and with the proposed role of PEX3 in peroxisomal membrane protein insertion (*43*).

The YG domain bridges both orientations of PEX13

We next asked whether the two orientations of PEX13 associate with each other, allowing the YG domains of these molecules to interact within the membrane. We introduced a single cysteine into the YG domain and tested whether disulfide-linked dimers would form between the two orientations. To discern both orientations, the C terminus was fused to a 3C protease–cleavage site followed by an SBP tag (to enhance the size shift), and an N-terminal FLAG tag was added for immunodetection (Fig. 5A). Cleavage by the protease produced two bands of equal intensity in a reducing gel (Fig. 5B, left blot), corresponding to the two orientations of the C terminus. Under oxidizing conditions, however, three disulfide-linked bands were seen after cleavage (right blot), corresponding to PEX13 dimers in which the two molecules have the same or opposite topologies (Fig. 5B, scheme). These results establish that both orientations of PEX13 directly interact with each other through their YG domains and thereby explain how the YG meshwork is localized to the plane of the membrane.

YG domains form hydrogels

Given that the nucleoporin FG meshwork can be reconstituted as a hydrogel (*44*) whose permeation properties mimic transport through the nuclear pore (*45*), we wondered whether the YG domain of PEX13 might behave similarly. After screening expression of YG domains from different organisms, we found that the entire unstructured N-terminal region (including the YG domain) from *Arabidopsis thaliana* PEX13 (Fig. 6A) expressed well in bacteria and could be purified under denaturing conditions using a His tag. Notably, the YG domain from this species could complement the yeast YG domain in peroxisomal import (Fig. 1C). After proteolytic removal of the tag (fig. S9) and concentration to 40 mg/ml (2 mM) in the presence of denaturant, the fragment indeed formed a rigid, translucent gel after several hours (Fig. 6B, left photograph). Higher concentrations could not be reached because the fragment gelled spontaneously, even when denaturant was included to retard gelation. A more dilute solution at 4 mg/ml (0.2 mM) also formed a hydrogel but after several days.

The YG domain is necessary and sufficient for gelation. When all tyrosines in the YG domain were mutated to serines (Y→S; Fig. 6A), a solution of the corresponding purified fragment never formed a gel and remained fluid (Fig. 6B, middle photograph). Furthermore, the isolated YG domain (without the upstream flexible segment; Fig. 6A) gelled as readily as the full-length fragment (Fig. 6B, right photograph). Interestingly, the gels liquified after heating to >50°C and resolidified after cooling to room temperature; this cycle could be repeated many times. The purified protein thus behaves like gelatin, even though the amino acid compositions of the two proteins are very different. This reversible thermosensitivity differs from that of the FG domain of the nucleoporin NUP98, whose phase separation is more favorable at higher temperatures (*46*). The difference might be due to hydrogen bonds between tyrosine hydroxyl groups contributing to the cohesion of the YG hydrogel.

PEX5 partitions into YG hydrogels

We next examined the permeation properties of the YG hydrogels. Small drops of the N-terminal fragment were gelled at 40 mg/ml in a glass-bottomed dish, and the influx of fluorescently labeled PEX5 or other proteins was imaged on a microscope (Fig. 7A). When buffer containing full-length PEX5 fused to green fluorescent protein (PEX5-GFP; Fig. 7B) was added, the fusion protein rapidly accumulated at the gel edge and then moved inward (Fig. 7C) at a rate of ~16 nm/s (fig. S10). PEX5-GFP was depleted from the buffer just outside the gel, indicating that the rate of entry into the gel is limited only by diffusion. Fluorescence behind the front was essentially constant in the gel, indicating that PEX5-binding sites in this region became saturated. After 30 min of permeation, the concentration of PEX5-GFP inside the gel was ~20-fold greater than the protein's concentration in the buffer (Fig. 7D). Although GFP alone could also enter the gel, it showed no enrichment (Fig. 7, C and D). Thus, PEX5 efficiently and specifically partitions into the YG hydrogel, analogously to how NTRs partition into hydrogels formed from nucleoporin FG domains.

Admission of PEX5 into YG hydrogels requires the receptor's unstructured N terminus. When just the N-terminal region of PEX5 (including all WXXXF/Y motifs) was fused to GFP (Fig. 7B), the resulting fusion protein permeated the gel as rapidly as the full-length version (Fig. 7C) and became similarly enriched (Fig. 7D). By contrast, a fusion between the cargo-binding TPR domain and GFP (Fig. 7B) accumulated to a much lower extent (Fig. 7, C and D). Entry into the gel was driven by the receptor's WXXXF/Y motifs, because ablating

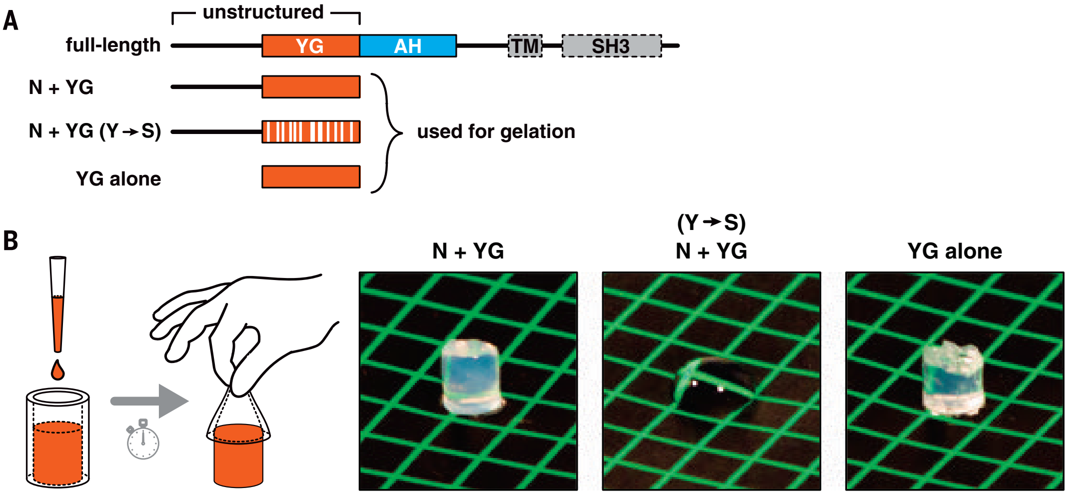

Fig. 6. The YG domain of PEX13 forms hydrogels. (**A**) Scheme depicts the domain organization of *A. thaliana* PEX13, which lacks a TM and an SH3 domain (enclosed by dashed lines). The fragments indicated below were expressed in *Escherichia coli* and purified. Y→S denotes conversion of all tyrosines in the YG domain into serines. (**B**) Concentrated solutions (40 mg/ml) of the three purified fragments were pipetted into silicone tubing and allowed to gel and then squeezed out of the tubing onto a colored surface and photographed. If gelation had occurred, the solution retained the shape of the tubing; otherwise, the solution remained fluid. Note that the YG domain is necessary and sufficient for gelation.

all of the motifs (Fig. 7B) abolished the accumulation of the N-terminal fusion protein inside the gel (Fig. 7, C and D).

PEX5 could also drag cargo into the YG hydrogels. GFP fused to a PTS1 import signal (GFP-SKL) showed no enrichment inside the gel on its own but accumulated ~10-fold in the presence of full-length PEX5 (Fig. 7, E to G). The lower partitioning coefficient likely reflects the modest affinity between the import signal and the receptor's TPR domain (*47*). The permeation rate was comparable to that of the linear PEX5-GFP fusion (fig. S10). Partitioning of cargo required the receptor's WXXXF/Y motifs, because full-length PEX5 that lacked all of the motifs (Fig. 7E) was unable to drag GFP-SKL into the gel (Fig. 7, F and G). Although the TPR domain is necessary for the interaction with the import signal, the domain is dispensable for the actual partitioning. Indeed, GFP that lacked the import signal was completely inert in the presence of full-length PEX5 but could be efficiently brought into the gel by a construct consisting of the receptor's N-terminal region fused to a GFP nanobody (PEX5-GNB; Fig. 7, E and F). In this case, GFP was enriched ~30-fold inside the gel (Fig. 7G), consistent with the higher affinity of the nanobody for the fluorescent protein (*48*). These results demonstrate that the YG domain of PEX13 forms hydrogels which selectively admit PEX5 and PEX5•cargo complexes.

Discussion

Our results with intact yeast membranes and synthetic hydrogels reveal the existence of a nuclear pore–like conduit on peroxisomes (Fig. 8A). This conduit consists of a dense meshwork—a selective phase—assembled from the YG domains of multiple PEX13 molecules that sit in the membrane in opposite orientations. Similarly to the meshwork formed by cohesive nucleoporin FG domains inside nuclear pores, the YG phase restricts passage of large soluble molecules. The YG phase can be selectively traversed by the import receptor PEX5, allowing bound cargo to move across the peroxisomal membrane. This mechanism thus allows folded and oligomeric proteins to be imported into peroxisomes, analogously to how folded cargo is moved into and out of the nucleus.

The use of tyrosines to form a selective phase is not unprecedented. For example, the protein FUS relies on tyrosine repeats to form hydrogels in vitro and to phase-separate into stress granules in vivo (*49*). Nucleoporin FG domains with tyrosines in place of phenylalanines also retain their ability to form hydrogels (*44*). Although these gels no longer accommodate NTRs, they do allow the entry of proteins engineered to bind the modified phase (*50*).

The permeation rate of PEX5 into the peroxisomal YG hydrogels (~16 nm/s) implies that cargo would traverse the 4-nm peroxisomal membrane in less than a second, which seems physiologically reasonable, although translocation rates in vivo are not known. PEX5 presumably enters the YG phase by locally dissolving the meshwork, relying predominantly on the WXXXF/Y motifs in its flexible N-terminal region (Fig. 8B). Entry of PEX5 into the YG phase might be regulated by cargo binding, because the association of the receptor with peroxisomes has been reported to rely on the presence of cargo (*51*). The interaction between PEX5 and the YG phase must be weak and transient, allowing the receptor to rapidly bind and dissociate to diffuse through the meshwork. The receptor's TPR domain also has some affinity for the YG phase and would therefore enhance diffusion, which might be relevant for translocation of larger cargo. However, only the WXXXF/Y motifs are strictly conserved among peroxisomal import receptors (*1*), suggesting that they are sufficient to drive import both of PTS1 and PTS2 proteins.

The proposed mechanism implies that peroxisomal import receptors can diffuse through the YG phase in either direction, similarly to how NTRs move bidirectionally through the nuclear pore. Whereas the directionality of nuclear transport is enforced by the Ran•GTP/GDP gradient (GTP, guanosine triphosphate; GDP, guanosine diphosphate), peroxisomal import may be driven instead by the highly favorable interaction between the receptors' WXXXF/Y motifs and the lumenal domain of the membrane protein PEX14 (*52*). This interaction might help pull PEX5 out of the YG phase on the lumenal side and would also prevent retrograde diffusion of the receptor back into the cytosol (Fig. 8A). The interaction is likely potentiated by avidity, because import receptors frequently have several WXXXF/Y motifs (*53*), and PEX14 is known to form oligomers that associate with PEX13 (*25*, *54*, *55*). Sustained import would thus require unliganded PEX14, which could only be generated by continual retrieval of PEX5 from the lumen by ATP-dependent recycling (Fig. 8A). This model explains why import, per se, is independent of nucleotide hydrolysis and yet occurs against

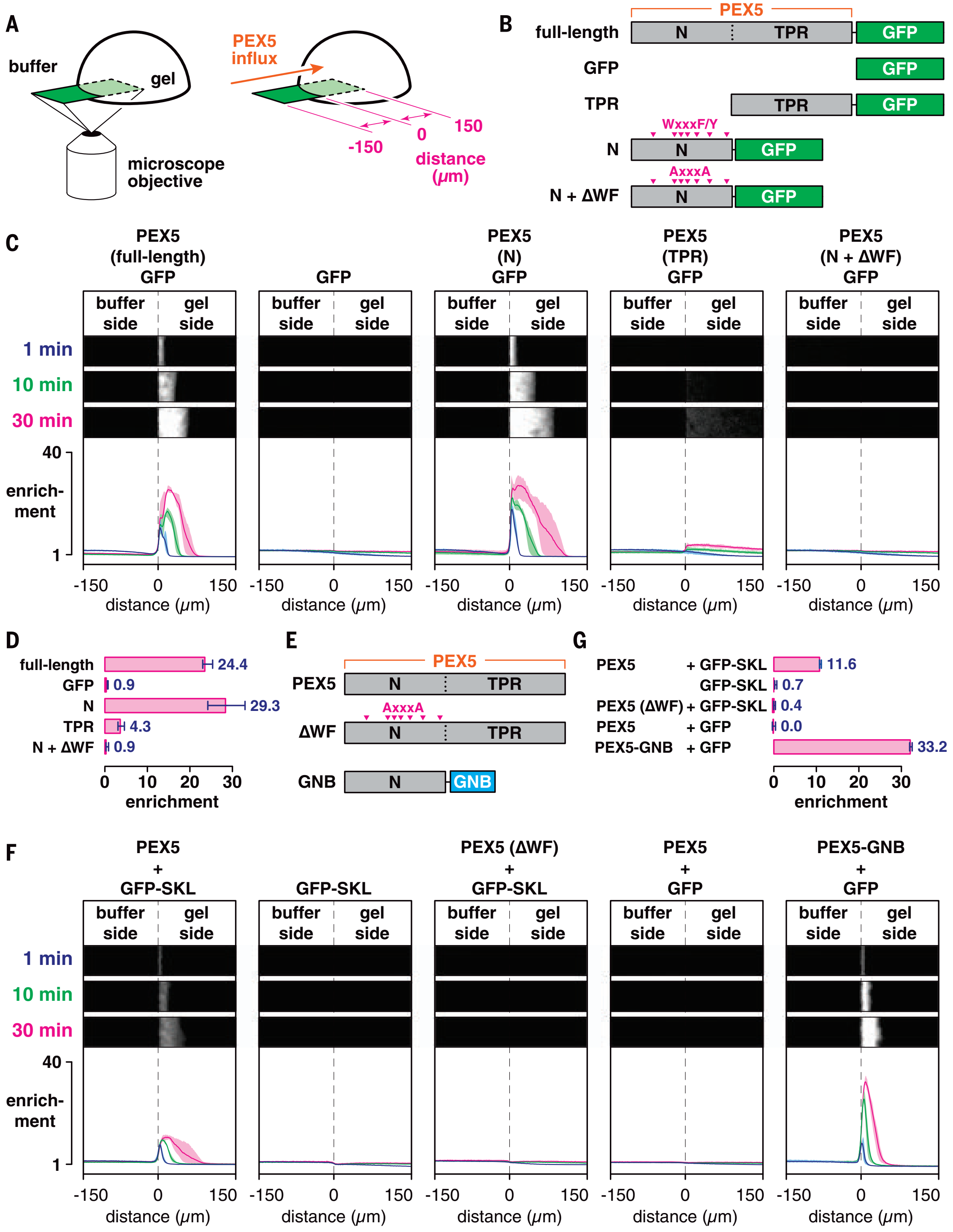

Fig. 7. The import receptor PEX5 selectively enters YG hydrogels and brings cargo along. (**A**) YG-hydrogel droplets (40 mg/ml) were prepared in glass-bottomed dishes; permeation of the gels by fluorescently labeled PEX5 or other proteins was imaged by point-scanning confocal microscopy. (**B**) Scheme depicting the PEX5 fragments that were fused to GFP. PEX5's N-terminal region contains several WXXXF/Y motifs (magenta arrows), which were mutated to AXXXA in the N + ΔWF mutant. (**C**) YG-hydrogel droplets were bathed in buffer containing the indicated GFP-fusion proteins (or GFP alone), and the interface between the buffer and gel was imaged over time. Shown are three selected time points; the fold enrichment of each protein, relative to buffer, across the imaged field is plotted below (mean ± the range of three experiments). (**D**) Mean enrichment (± the range of three experiments) of the indicated proteins inside the gel compared to buffer after 30 min of imaging as in (C). (**E**) Nonfluorescent PEX5 variants used for experiments with fluorescent cargo. GNB, anti-GFP nanobody. (**F**) Same as in (C) except with the indicated PEX5 variants, and GFP with or without the PEX5-binding SKL signal. (**G**) Mean enrichment (± the range of three experiments) of GFP or GFP-SKL after 30 min of imaging as in (F).

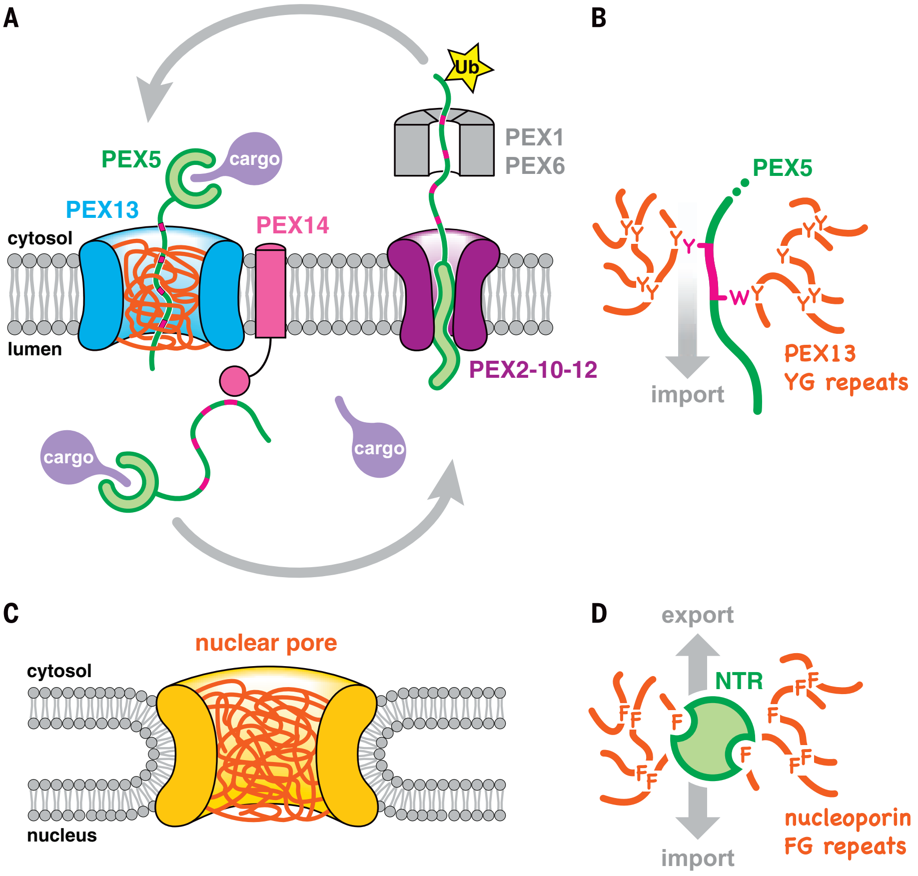

Fig. 8. Model of peroxisomal matrix protein import. (**A**) PEX13 molecules form a conduit (blue) in the peroxisomal membrane filled with a meshwork (orange) of their YG domains. PEX5 crosses this barrier with bound cargo, using WXXXF/Y motifs (magenta) in its flexible N-terminal region. The interaction between the WXXXF/Y motifs and the lumenal domain of PEX14 retains the receptor inside the organelle. To return to the cytosol, PEX5 is monoubiquitinated (Ub) by the PEX2-10-12 ubiquitin ligase complex and pulled out by the PEX1-PEX6 ATPase. Unfolding of PEX5 during export enables cargo to be released in the lumen (*10*). After refolding in the cytosol, and having Ub removed by deubiquitinases, PEX5 can begin another import cycle. (**B**) PEX5 partitions into the YG meshwork as an extended polypeptide, whose WXXXF/Y motifs locally disrupt the cohesive tyrosine interactions that hold the meshwork together. (**C**) Diagram illustrating the scaffold (yellow) of the nuclear pore complex, filled with a meshwork of nucleoporin FG domains (orange). Note how the nuclear pore is suspended outside the bilayer instead of being embedded in it like the peroxisomal pore. (**D**) NTRs use hydrophobic pockets and patches in folded domains to partition into the FG meshwork and diffuse through the nuclear pore.

the concentration gradient of the cargo: The energy derives from PEX5 export, because new receptor molecules can only enter the lumen once the previously imported ones have been retrieved. Notably, the proposed model does not contradict a possible role of PEX14 in recruiting cargo to peroxisomes (*39*).

The YG meshwork is suspended in the peroxisomal membrane by PEX13 molecules of opposite orientations. Such dual topology is unusual (*56*) and may be generated by random insertion of PEX13 directly into the peroxisomal membrane, likely with the involvement of PEX3. The dual topology facilitates assembly of the meshwork by allowing the YG domains to meet and associate within the plane of the membrane. The location of the YG meshwork directly in the lipid bilayer contrasts with the nucleoporin FG meshwork, which forms outside the nuclear membrane in the aqueous central channel of the nuclear pore complex (compare Fig. 8, A and C). Our hydrogel experiments demonstrate that the N-terminal region preceding the YG domain can be accommodated in the YG meshwork. This observation explains why the N terminus of PEX13 can cross the membrane and become accessible to proteases and modification reagents while the C terminus remains fixed in the membrane in one of the two orientations. Notably, the two orientations reconcile previously conflicting observations regarding the topology of the C terminus (*39*). The population of PEX13 with its PEX5-binding SH3 domain exposed to the cytosol could help recruit PEX5 to the organelle.

We suspect that the membrane-spanning walls that encircle the YG meshwork are formed by the long AH of PEX13. The AH is the only feature of PEX13, besides the YG domain, that is strictly conserved. Our data show that the AH is also essential for import. Given its length (>60 residues) and dual topology, we surmise that alternating orientations of the AH assemble in a tilted manner into a pore-like structure in the peroxisomal membrane (fig. S11A), with their hydrophilic face oriented toward the aqueous YG phase in the middle and their hydrophobic face toward the lipids on the outside (fig. S11B). The diameter of this structure must be at least 9 nm (the size of the largest cargo reported to enter yeast peroxisomes) (*19*) but considerably smaller than the nuclear pore (~40 nm in yeast) (*57*). Indeed, PEX13 has been observed to form nanometer-sized clusters in the peroxisomal membrane by super-resolution microscopy (*58*), which are potentially consistent with such a conduit. By analogy to the nuclear pore, the concentration of YG domains inside the conduit must be very high (≥200 mg/ml). Our inability to reach such high concentrations in vitro likely explains why our YG hydrogels incompletely exclude inert material.

The similarity between peroxisomal import and nuclear transport raises the question of how proteins are targeted to the correct compartment. A possible answer is that NTRs have evolved to bind the phenylalanine-rich motifs of FG nucleoporins and exhibit low affinity for tyrosine (*44*). The peroxisomal meshwork might also be denser than the nuclear pore phase, given the shorter distance between aromatic residues in YG domains compared with nucleoporin FG domains. Whereas peroxisomal import receptors bind the YG phase using unstructured segments (Fig. 8B), NTRs bind nucleoporin FG domains using large folded domains (*59*) (Fig. 8D). NTRs could thus be sterically impeded from penetrating the denser peroxisomal meshwork and would also have a lower affinity for the YG phase. PEX5 might not be impeded from traversing the nuclear pore, however, because it does leak into nuclei and maintains its steady-state nuclear exclusion only through continuous CRM1-mediated export (*60*). A similar export pathway does not exist in peroxisomes, which might therefore require a denser permeability barrier to exclude foreign proteins. Nevertheless, the barrier is likely not so tight as to exclude small molecules (*35*, *40*). The limited permeability of the peroxisomal membrane might explain why a nuclear pore–like import mechanism, by which a folded protein crosses the membrane, can be accommodated. By contrast, other organelles (such as the ER and mitochondria) need a mechanism that maintains a tighter seal during protein translocation and thus require imported proteins to be unfolded.

Materials and methods

All reagents were obtained from MilliporeSigma unless specified otherwise. Buffers were prepared in ultrapure water. RT denotes room temperature.

Plasmid construction

The coding sequence of each recombinant protein was codon-optimized for *Escherichia coli* and inserted into plasmid pET-28b(+) by Gibson Assembly (from New England BioLabs). PEX5 proteins and cargo were produced as fusions containing N-terminal glutathione-*S*-transferase (GST). A 3C protease–cleavage site was introduced between the GST and the recombinant protein, preceded by the amino acid sequence GSD. The sequence coding for full-length, wild-type PEX5 corresponds to isoform X3 of the *Xenopus laevis* PEX5.S gene (GenBank accession no. XP_018082765.1). The fragment corresponding to the N-terminal region spans amino acids 1 to 268, whereas the fragment corresponding to the cargo-binding TPR domain spans amino acids 260 to 579. WXXXF/Y motifs in the N-terminal region were converted to AXXXA by mutagenesis. GFP fusions to PEX5 or to the fragments reported in the text were generated by inserting the sequence encoding monomeric enhanced GFP (mEGFP) downstream of each protein, separated by either a GGSGGS linker (for full-length PEX5 or the TPR domain) or a GS linker (for the N-terminal region). GFP-SKL was assembled by fusing a modified peroxisomal targeting signal from *Photinus pyralis* (firefly) luciferase (i.e., the amino acid sequence YKGLKSKL) (*47*) to the C terminus of mEGFP, preceded by a glycine. GFP alone corresponds to mEGFP without the targeting signal. The plasmid encoding the N-terminal region of PEX5 fused to an anti-GFP nanobody was described previously (*10*).

Fragments encoding the YG domain of PEX13 were produced as fusions to an N-terminal 14× polyhistidine (14×His) tag corresponding to the amino acid sequence SKHHHHSGHHHTGHHHHSGSHHHTGS. A TEV protease–cleavage site was introduced between the 14×His tag and the recombinant protein. The fragment encompassing the entire unstructured N terminus of PEX13 corresponds to amino acids 1 to 193 of PEX13 from *A. thaliana* (GenBank accession no. NP_187412.1); the YG domain alone corresponds to amino acids 76 to 193. Tyrosines within the YG domain were mutated to serines by mutagenesis. All constructs additionally included a single engineered cysteine at the C terminus for covalent derivatization.

Constructs designed for gene deletion and gene expression cassette integration in *S. cerevisiae* (yeast) were assembled by restriction-enzyme cloning or Gibson Assembly. The coding sequence of yeast PEX13 (UniProt accession no. P80667) represents the wild type. Conventional sequences for FLAG and SBP epitope tags, as well as cleavage sites for 3C and TEV proteases, were incorporated into PEX13 at the positions indicated in the text. Constructs containing a C-terminal TEV protease-cleavage site additionally included a diserine linker between the cleavage site and the PEX13 coding sequence. All cysteine point mutations reported in the text were made by mutagenesis, as well as mutations in the hydrophilic face (mut ζ: Q150A, E153A, Q164A, and E167A) or the hydrophobic face (mut φ: L155E and L166E) of the AH in PEX13. Conversion of tyrosines in the YG domain of PEX13 (amino acids 71, 81, 86, 90, 95, 101, 108, 110, 114, 115, 119, 123, 127, and 133) into either serines or phenylalanines was performed by de novo gene synthesis (by Integrated DNA Technologies).

To replace the YG domain (amino acids 70 to 134) of yeast PEX13, the sequences of YG domains from the following organisms were used: *Homo sapiens* (human; amino acids 67 to 121, UniProt accession no. Q92968); *Drosophila melanogaster* (fruit fly; amino acids 70 to 133, UniProt accession no. Q7JRD4); *A. thaliana* (plant; amino acids 79 to 187, UniProt accession no. Q9SRR0); *Pichia pastoris* (amino acids 25 to 114, UniProt accession no. C4R2I6); *Torulaspora delbrueckii* (amino acids 59 to 135, UniProt accession no. G8ZRC9); *Dictyostelium discoideum* (amoeba; amino acids 99 to 214, UniProt accession no. Q54CL3); and *Chlamydomonas reinhardtii* (algae; amino acids 70 to 194, UniProt accession no. A0A2K3CZW8).

All constructs were verified by sequencing.

Yeast strains and culture conditions

All yeast strains reported in this study were derived from the *S. cerevisiae* parental strain UTL7A (*MAT*a, *ura3-52*, *trp1*, *leu2-3/112*). Strains were maintained on yeast extract–peptone-dextrose (YPD) medium (1% w/v yeast extract, 2% w/v peptone, 2% w/v dextrose) with or without the antibiotics hygromycin (250 µg/ml; from Fisher, no. 10687010), geneticin (200 µg/ml; from Fisher, no. 10131035), or nourseothricin (100 µg/ml; from Jena Bioscience, no. AB-101), as appropriate. Genomic deletions and insertions were performed by homologous recombination using lithium acetate–based transformation (*61*).

The UTL7A strain was first derivatized by integrating the expression cassette for the violacein biosynthetic pathway (see below) at the *leu2* locus. Briefly, the plasmid pWCD1401 (*35*) was linearized by the restriction enzyme *Not*I, and the excised 11.5-kb fragment was purified by agarose gel electrophoresis and used to transform exponentially growing UTL7A cells. Clones were selected on synthetic defined (SD) medium containing 2% w/v glucose and 6.7 g/liter yeast nitrogen base without amino acids (from BD Difco) and supplemented with an amino acid mixture lacking leucine (from Sunrise Science). Correct integration of the cassette was confirmed by polymerase chain reaction (PCR), and the resulting violacein-positive (Vio$^+$) strain was used to generate all subsequent strains and corresponds to the wild type.

All gene deletions used the *natMX* nourseothricin-resistance cassette as the selective marker. The cassette was amplified from plasmid pFA6A-*natMX* (from Addgene, no. 19343) by PCR, using primers that introduced 60–base pair (bp) overhangs corresponding to the 5′ and 3′ untranslated regions immediately upstream and downstream of each gene's open reading frame, respectively. Clones were selected on YPD medium containing nourseothricin (100 µg/ml), and replacement of each reading frame by the *natMX* cassette was confirmed by PCR.

To generate strains expressing mutant or epitope-tagged versions of the peroxisomal proteins described in the text, the *natMX* marker in the corresponding knockout strain was replaced with each mutant's coding sequence, using either the *hygMX* hygromycin-resistance or the *kanMX* geneticin-resistance cassette as the selective marker. Briefly, the relevant coding sequence was PCR-amplified either from plasmid pFA6A-*hygMX* (from Addgene, no. 19342) or pFA6A-*kanMX* (from Addgene, no. 39296), together with the corresponding antibiotic resistance marker, using primers that introduced 60-bp overhangs as above. Clones were selected on YPD medium containing hygromycin (250 µg/ml) or geneticin (200 µg/ml), as appropriate, and correct insertion of the mutant reading frame was validated by PCR.

Peroxisomal matrix protein import assay

A modified violacein biosynthetic pathway (*35*) was used to quantitatively measure peroxisomal matrix protein import activity in *S. cerevisiae* cells. Briefly, an expression cassette encoding three enzymes (VioA, VioB, and VioE), which together produce a green pigment, was integrated into the genome along with a leucine auxotrophic marker as described above. The first two enzymes (VioA and VioB) reside in the cytosol, whereas the third enzyme (VioE) contains a peroxisome targeting signal and is sequestered inside peroxisomes when import is functional. Only when import is compromised does VioE accumulate in the cytosol and the green pigment is made. Pigment production is inversely proportional to import efficiency (*35*).

To measure pigment production, strains were cultured overnight in YPD medium at 30°C with shaking. The next morning, cultures were diluted 150-fold in 3 ml of freshly prepared synthetic defined (SD) medium lacking leucine and cultured at 30°C for a further

48 hours. Cells were collected by centrifugation and resuspended in 300 μl of glacial acetic acid (from Fisher). The cell suspension was transferred to 1.5-ml microfuge tubes and incubated for 10 min at 95°C and then mixed by inversion and incubated for a further 10 min. Debris were sedimented by centrifugation at 8000*g* for 5 min at RT, and the resulting supernatants were transferred to a 96-well, round-bottom black-walled plate (from Corning, no. 3792). Fluorescence of each solution was measured with a Bio-Tek Synergy Neo2 microplate reader, using excitation and emission bands of 535 ± 5 and 585 ± 5 nm, respectively. To calculate relative import activity, the fluorescence reading from each strain was normalized to the average reading from wild-type cells (set to 100%) and *pex13*Δ cells (set to 0%) by linear interpolation.

Disulfide-mediated cross-linking

Yeast cells expressing FLAG-tagged PEX13 with introduced cysteines were cultured overnight in YPD medium at 30°C. Cells were collected by centrifugation, washed once with water, and resuspended in cold lysis buffer (20 mM HEPES•KOH pH 6.8 at RT, 150 mM potassium acetate, 5 mM magnesium acetate, 250 mM sorbitol, and 1 mM EDTA) supplemented with 1 mM phenylmethylsulfonyl fluoride (PMSF) and a protease inhibitor cocktail (from Bimake, no. B14001) according to the manufacturer's instructions. The cell suspension was transferred to 2-ml screw-capped tubes (from Sarstedt, no. 726994005) on ice and mixed with 0.5-mm prechilled glass beads, and the cells were lysed by bead-beating on a Biospec Products Mini-Beadbeater-16 (no. 607) for four 30-s cycles with 2-min cooling on ice in between. The cell lysate was clarified by low-speed centrifugation at 2000*g* for 5 min at 4°C to remove intact cells and cellular debris, and the resulting supernatant was recentrifuged at 20,000*g* for 10 min at 4°C to sediment heavy membranes, including peroxisomes. The final pellet was gently resuspended in assay buffer (20 mM HEPES•NaOH pH 7.2, 50 mM NaCl, 250 mM sucrose, and 1 mM EDTA) by pipeting followed by mixing on a rotator at 4°C for 15 min.

The homogeneous membrane suspension was treated with or without the oxidizing agent 4,4′-dithiodipyridine (Aldrithiol-4; from Millipore-Sigma, no. 143057), at the concentrations indicated in the text, for 30 min at 30°C with gentle agitation. Where indicated, 0.5% w/v of *n*-dodecyl-β-D-maltoside (DDM; from Anatrace, no. D310) was added before the oxidant to solubilize the membranes. Unreacted cysteines were quenched with 10 mM NEM at 30°C for 5 min. Membranes were then solubilized by shaking for 1 hour at 4°C with 0.5% w/v DDM, and the solubilisate was clarified by centrifugation at 20,000*g* for 10 min at 4°C. PEX13 was immunoprecipitated from the resulting supernatant using anti-FLAG M2 agarose beads (no. A2220) and eluted by heating in Laemmli buffer as described below.

Protease protection

Homogeneous membrane suspensions from yeast cells expressing PEX13 with protease-cleavage sites (and FLAG or SBP epitope tags) were prepared as described above. Suspensions were mixed with 2 μM homemade 3C protease, 2 μM homemade TEV protease, or both proteases together, as indicated in the text, and incubated for 16 hours at 4°C. Where specified, 10 mM NEM was included in the reactions to preinactivate the proteases. All reactions were ultimately quenched with 10 mM NEM, and the membranes were solubilized with 0.5% w/v DDM for 1 hour at 4°C with shaking. The solubilisate was clarified by centrifugation at 20,000*g* for 10 min at 4°C, and PEX13 was then immunoprecipitated from the resulting supernatant using either anti-FLAG M2 agarose or streptavidin agarose beads (from ThermoFisher, no. 20353), as indicated in the text. Precipitated material was eluted with 0.4 mg/ml 3×FLAG peptide (from Bimake, no. B23112) or 4 mM biotin, as appropriate, in assay buffer containing 0.05% w/v DDM, before being prepared for SDS-PAGE.

For the experiment shown in Fig. 5B, the membrane suspension was first digested with 3C protease as described above and then treated with 200 μM Aldrithiol-4 for 30 min at 30°C to promote disulfide-bond formation. Reactions were quenched with NEM and processed for SDS-PAGE.

PEGmal modification

Homogeneous membrane suspensions from yeast cells expressing FLAG-tagged PEX13 with introduced cysteines were prepared as described above. Suspensions were incubated for 90 min at 4°C and gentle agitation with 2 mM methoxypolyethylene glycol maleimide (PEGmal) of the following sizes (all from Millipore-Sigma), as specified in the text: 10-kD (no. 712469), 5-kD (no. 63187), 2-kD (no. JKA3124), and 0.8-kD (no. 712558). Where indicated, 0.5% w/v DDM was added before PEGmal to solubilize the membranes. Unreacted PEGmal was quenched with 10 mM cysteine, and PEX13 was immunoprecipitated with anti-FLAG M2 agarose and prepared for SDS-PAGE as described above.

Electrophoresis and immunoblotting

Unless specified otherwise, samples were heated in Laemmli buffer (from Bio-Rad, no. 1610747) for 5 min at 95°C, with or without 50 mM DTT (from GoldBio), and electrophoretically resolved under denaturing conditions on 4-20% TGX precast polyacrylamide gels (from Bio-Rad). For Coomassie-blue staining, gels were first fixed in 50% v/v methanol and 10% v/v acetic acid for 30 min at RT, then incubated for a further 30 min in 50% v/v methanol, 10% v/v acetic acid, and 0.001% w/v Coomassie Brilliant Blue R-250 (from Bio-Rad), and finally destained overnight in 10% v/v acetic acid before being washed into water. For immunoblotting, proteins were transferred overnight onto nitrocellulose membranes (from Bio-Rad, no. 1620112). Membranes were blotted in TBST buffer (20 mM Tris•NaOH pH 7.5, 150 mM NaCl, and 0.1% v/v Tween 20) containing 3% w/v non-fat milk solids (from Apex, no. 20241) using antibodies against the FLAG epitope (no. F7425) or the SBP tag (no. MAB10764), and fluorescently labeled secondary antibodies IRDye 800CW or IRDye 680CW (from LI-COR Biosciences), as appropriate. Blots were imaged on a LI-COR Odyssey M imaging system.

Determination of expression levels

To validate expression of FLAG-tagged PEX13 constructs reported in this study, membranes from the relevant strains were first solubilized in 0.5% w/v DDM as described above, followed by immunoprecipitation using anti-FLAG M2 beads before processing for SDS-PAGE.

Bioinformatic analysis

The amino acid composition of the YG domain of PEX13 versus nucleoporin FG domains was calculated by the ProtParam tool on the ExPASy server (*62*), using the sequences of PEX13, NUP62, and NUP98 homologs from the organisms shown in table S1. The number of amino acids between consecutive aromatic residues (i.e., the spacer length) in YG domains versus nucleoporin FG domains was calculated using a custom script and the sequences of PEX13, NUP62, and NUP98 homologs from the organisms listed in table S1. Because FG repeats consist not only of individual FG motifs but also of FXFG motifs (where "X" denotes any amino acid), such tandem motifs were considered as single aromatic clusters for calculating the spacer length.

Protein purification

Recombinant proteins were produced in *E. coli* BL21 Rosetta 2(DE3) cells (from Novagen) by induction with isopropyl β-D-1-thiogalactopyranoside (IPTG; from GoldBio, no. I2481C50). All PEX5 proteins and cargo were expressed and purified by glutathione-affinity and size-exclusion chromatographies as described previously (*10*). Briefly, the proteins were eluted from the glutathione resin by proteolytic removal of their GST tag, gel-filtered into 40 mM HEPES•KOH pH 7.8 at RT, 100 mM KCl, 250 mM sucrose, 1 mM $MgCl_2$, and 1 mM DTT, and concentrated to 100 μM before snap-freezing in single-use aliquots.

PEX13 fragments containing the YG domain were purified under denaturing conditions. Bacteria transformed with the desired plasmid were cultured in baffled flasks on an orbital shaker at 37°C in 2×YT medium (from Fisher) containing 50 μg/ml kanamycin and 34 μg/ml chloramphenicol. On reaching an optical density (OD) of 0.6, the cultures were cooled at RT for 30 min and then supplemented with 1 mM IPTG and incubated with shaking at 30°C for an additional 6 hours. Cells were collected by centrifugation at 4000*g*, rinsed in phosphate-buffered saline, and frozen. Cell pellets were resuspended in freshly prepared lysis buffer (8 M urea, 100 mM sodium phosphate, 10 mM HEPES•NaOH, 10 mM imidazole, 5 mM DTT, and pH adjusted to 8.0 at RT just before use), incubated for 30 min at RT, and then homogenized by sonication. The cell lysate was clarified by centrifugation at 15,000*g* for 30 min at 20°C, and the resulting supernatant incubated with nickel-charged nitriloacetic acid (Ni-NTA; from ThermoFisher) resin for 1 hour at RT with agitation. Beads were washed with an excess of lysis buffer and then with an excess of gelation buffer (2 M urea, 50 mM HEPES•NaOH, and 1 mM EDTA, pH adjusted to 8.0 at RT just before use) supplemented with 1 mM tris(2-carboxyethyl)phosphine (TCEP; from GoldBio). Bound protein was eluted with 500 mM imidazole in gelation buffer, supplemented with homemade 6×His-tagged TEV protease, and dialyzed overnight at RT against gelation buffer containing TCEP. The dialyzed solution was clarified by centrifugation and passed over additional nickel resin to remove the released 14×His tag and TEV protease. The final flow-through served as the starting point for gelation.

Preparation and photography of YG hydrogels

To initiate gelation, each recombinant fragment (dissolved in 2 M urea, 50 mM HEPES•NaOH pH 8.0 at RT, 1 mM TCEP, and 1 mM EDTA), was concentrated to 2 mM on a centrifugal filter device (from Amicon) at 40°C. The resulting solutions were promptly injected into short pieces of Tygon S3 silicone tubing (from Saint-Gobain) that had been plugged at one end with hot-melt adhesive and incubated at RT for several days to complete gelation. The contents of each piece of tubing were then squeezed out onto a colored grid and photographed using a Canon EF 75-300 mm f/4-5.6 III zoom lens and a Canon EOS 20D digital single-lens reflex (DSLR) camera configured to maximize spatial resolution and minimize digital noise.

YG-hydrogel permeation assay

A solution of the unstructured N-terminal region (including the YG domain) from *A. thaliana* PEX13 was concentrated to 2 mM in gelation buffer as described above. Two-microliter drops were promptly spotted on the bottom of multiple wells of a 96-well glass-bottom plate (from Cellvis, no. P96-1.5H-N) and allowed to set for several hours at RT. The resulting gel droplets were equilibrated overnight in excess assay buffer (25 mM HEPES•KOH pH 7.8 at RT, 130 mM KCl), and imaged on a Leica SP8 X point-scanning confocal system, using a DMI6000 inverted microscope and a 20× 0.70 NA HC Plan Apochromat CS air objective. The objective was centered on the boundary between the buffer and gel, and focus was maintained 5 μm above the glass surface by the Leica Adaptive Focus Control (AFC) system. Six initial frames were acquired at a rate of two frames per minute, and then a solution of fluorescently labeled protein (as indicated in the text) in assay buffer was added and the acquisition continued for a further 30 min. All proteins were used at a final concentration of 500 nM. Images were acquired in Leica LAS X software using a pixel size of 1.14 μm^2, scan speed of 100 Hz, and pinhole dilated to 1 Airy unit. Fluorescence was excited using a 490-nm bandlet selected from a white-light laser by an acousto-optic tunable filter (AOTF), and a 500- to 700-nm emission band was collected by a hybrid pixel detector (HyD) operating in standard mode without gating and gain set to 100. Imaging parameters were configured to maximize the signal-to-noise ratio while avoiding saturation. All samples intended to be compared were imaged under identical acquisition settings.

Image analysis

All analysis was performed in ImageJ (63) on the original, unmodified image data using routine functions. For images of immunoblots, band intensities were measured by densitometry. Fluorescence images of YG hydrogels were first background-subtracted and corrected for experimental variations in fluorophore concentration. To estimate the background, six successive images of the buffer-gel interface were acquired before addition of fluorescently labeled protein and then averaged. The resulting matrix was subtracted, pixel by pixel, from all frames of the time course acquired after addition of fluorescently labeled protein. Background-subtracted time courses were then normalized by mean fluorescence intensity in the buffer. To measure the protein concentration across the buffer-gel interface over time, a rectangular selection 60 μm by 300 μm was centered on the gel edge, and the mean fluorescence intensity across this field was measured at all time points using the plot profile function in ImageJ. The intensities were then normalized to the maximum value for each experimental cohort. To calculate the fold enrichment of each protein inside the gel, the mean intensity was measured inside a 15-μm arc that followed the inner contour of the gel edge at the 30-min time point. This value was then divided by the mean intensity in the buffer 150 μm away from the edge. To calculate permeation rates, the total area inside the gel occupied by the relevant permeating species at each time point was identified by intensity-based thresholding. The resulting displacement values were plotted as a function of time and fitted to straight lines whose slope corresponded to the permeation rate.

Data plotting and statistical analysis

All experiments were independently performed at least three times. Data were plotted in GraphPad Prism (v. 9.3.1), and, where indicated, statistical significance was calculated using Student's two-tailed unpaired *t* test. Fits to mathematical models were performed by nonlinear least squares regression in Prism.

Image processing for publication and figure assembly

All images intended to be compared were processed identically. Fluorescence micrographs were first background-subtracted and corrected as described above and then linearly contrast-stretched in ImageJ to the same bit range. Digitized images of immunoblots and stained gels were contrast-stretched to reveal relevant bands but avoid clipping of the background. Digital photographs of YG hydrogels were processed using the Camera Raw plugin (v. 14.5.0.1177) in Adobe Photoshop (v. 23.5.1). Helical wheel diagrams were prepared using HeliQuest (64). Secondary structure predictions were performed with AlphaFold (65). Figures were assembled for publication in Adobe Illustrator (v. 25.4.1).

REFERENCES AND NOTES

1. R. L. M. Jansen, C. Santana-Molina, M. van den Noort, D. P. Devos, I. J. van der Klei, Comparative genomics of peroxisome biogenesis proteins: Making sense of the PEX proteins. *Front. Cell Dev. Biol.* **9**, 654163 (2021). doi: 10.3389/fcell.2021.654163; pmid: 34095119
2. I. J. Lodhi, C. F. Semenkovich, Peroxisomes: A nexus for lipid metabolism and cellular signaling. *Cell Metab.* **19**, 380–392 (2014). doi: 10.1016/j.cmet.2014.01.002; pmid: 24508507
3. C. Lismont, I. Revenco, M. Fransen, Peroxisomal hydrogen peroxide metabolism and signaling in health and disease. *Int. J. Mol. Sci.* **20**, 3673 (2019). doi: 10.3390/ijms20153673; pmid: 31357514
4. Y. Fujiki, Peroxisome biogenesis and human peroxisome-deficiency disorders. *Proc. Jpn. Acad. Ser. B Phys. Biol. Sci.* **92**, 463–477 (2016). doi: 10.2183/pjab.92.463; pmid: 27941306
5. C. Brocard, A. Hartig, Peroxisome targeting signal 1: Is it really a simple tripeptide? *Biochim. Biophys. Acta* **1763**, 1565–1573 (2006). doi: 10.1016/j.bbamcr.2006.08.022; pmid: 17007944
6. G. J. Gatto Jr., B. V. Geisbrecht, S. J. Gould, J. M. Berg, Peroxisomal targeting signal-1 recognition by the TPR domains of human PEX5. *Nat. Struct. Biol.* **7**, 1091–1095 (2000). doi: 10.1038/81930; pmid: 11101887
7. V. C. Kalel, R. Erdmann, Unraveling of the structure and function of peroxisomal protein import machineries. *Subcell. Biochem.* **89**, 299–321 (2018). doi: 10.1007/978-981-13-2233-4_13; pmid: 30378029
8. D. Pan, T. Nakatsu, H. Kato, Crystal structure of peroxisomal targeting signal-2 bound to its receptor complex Pex7p-Pex21p. *Nat. Struct. Mol. Biol.* **20**, 987–993 (2013). doi: 10.1038/nsmb.2618; pmid: 23812376
9. M. Kunze, The type-2 peroxisomal targeting signal. *Biochim. Biophys. Acta Mol. Cell Res.* **1867**, 118609 (2020). doi: 10.1016/j.bbamcr.2019.118609; pmid: 31751594
10. M. L. Skowyra, T. A. Rapoport, PEX5 translocation into and out of peroxisomes drives matrix protein import. *Mol. Cell* **82**, 3209–3225.e7 (2022). doi: 10.1016/j.molcel.2022.07.004; pmid: 35931083

11. V. Dammai, S. Subramani, The human peroxisomal targeting signal receptor, Pex5p, is translocated into the peroxisomal matrix and recycled to the cytosol. *Cell* **105**, 187–196 (2001). doi: 10.1016/S0092-8674(01)00310-5; pmid: 11336669
12. J. W. Zhang, P. B. Lazarow, PEB1 (PAS7) in *Saccharomyces cerevisiae* encodes a hydrophilic, intra-peroxisomal protein that is a member of the WD repeat family and is essential for the import of thiolase into peroxisomes. *J. Cell Biol.* **129**, 65–80 (1995). doi: 10.1083/jcb.129.1.65; pmid: 7535304
13. P. Feng, M. L. Skowyra, T. A. Rapoport, Structure and function of the peroxisomal ubiquitin ligase complex. *Biochem. Soc. Trans.* **2022**, BST20221393 (2022). doi: 10.1042/BST20221393; pmid: 36421406
14. P. Feng *et al.*, A peroxisomal ubiquitin ligase complex forms a retrotranslocation channel. *Nature* **607**, 374–380 (2022). doi: 10.1038/s41586-022-04903-x; pmid: 35768507
15. N. B. Blok *et al.*, Unique double-ring structure of the peroxisomal Pex1/Pex6 ATPase complex revealed by cryo-electron microscopy. *Proc. Natl. Acad. Sci. U.S.A.* **112**, E4017–E4025 (2015). doi: 10.1073/pnas.1500257112; pmid: 26170309
16. M. O. Debelyy *et al.*, Ubp15p, a ubiquitin hydrolase associated with the peroxisomal export machinery. *J. Biol. Chem.* **286**, 28223–28234 (2011). doi: 10.1074/jbc.M111.238600; pmid: 21665945
17. C. P. Grou *et al.*, Identification of ubiquitin-specific protease 9X (USP9X) as a deubiquitinase acting on ubiquitin-peroxin 5 (PEX5) thioester conjugate. *J. Biol. Chem.* **287**, 12815–12827 (2012). doi: 10.1074/jbc.M112.340158; pmid: 22371489
18. S. Léon, J. M. Goodman, S. Subramani, Uniqueness of the mechanism of protein import into the peroxisome matrix: Transport of folded, co-factor-bound and oligomeric proteins by shuttling receptors. *Biochim. Biophys. Acta* **1763**, 1552–1564 (2006). doi: 10.1016/j.bbamcr.2006.08.037; pmid: 17011644
19. P. A. Walton, P. E. Hill, S. Subramani, Import of stably folded proteins into peroxisomes. *Mol. Biol. Cell* **6**, 675–683 (1995). doi: 10.1091/mbc.6.6.675; pmid: 7579687
20. N. Wiedemann, N. Pfanner, Mitochondrial machineries for protein import and assembly. *Annu. Rev. Biochem.* **86**, 685–714 (2017). doi: 10.1146/annurev-biochem-060815-014352; pmid: 28301740
21. T. A. Rapoport, L. Li, E. Park, Structural and mechanistic insights into protein translocation. *Annu. Rev. Cell Dev. Biol.* **33**, 369–390 (2017). doi: 10.1146/annurev-cellbio-100616-060439; pmid: 28564553
22. N. Miyata, Y. Fujiki, Shuttling mechanism of peroxisome targeting signal type 1 receptor Pex5: ATP-independent import and ATP-dependent export. *Mol. Cell. Biol.* **25**, 10822–10832 (2005). doi: 10.1128/MCB.25.24.10822-10832.2005; pmid: 16314507
23. P. Ozimek, M. Veenhuis, I. J. van der Klei, Alcohol oxidase: A complex peroxisomal, oligomeric flavoprotein. *FEMS Yeast Res.* **5**, 975–983 (2005). doi: 10.1016/j.femsyr.2005.06.005; pmid: 16169288
24. M. Meinecke *et al.*, The peroxisomal importomer constitutes a large and highly dynamic pore. *Nat. Cell Biol.* **12**, 273–277 (2010). doi: 10.1038/ncb2027; pmid: 20154681
25. P. Lill *et al.*, Towards the molecular architecture of the peroxisomal receptor docking complex. *Proc. Natl. Acad. Sci. U.S.A.* **117**, 33216–33224 (2020). doi: 10.1073/pnas.2009502117; pmid: 33323485
26. M. Monroe-Augustus *et al.*, Matrix proteins are inefficiently imported into *Arabidopsis* peroxisomes lacking the receptor-docking peroxin PEX14. *Plant Mol. Biol.* **77**, 1–15 (2011). doi: 10.1007/s11103-011-9782-0; pmid: 21553312
27. F. A. Salomons, J. A. Kiel, K. N. Faber, M. Veenhuis, I. J. van der Klei, Overproduction of Pex5p stimulates import of alcohol oxidase and dihydroxyacetone synthase in a *Hansenula polymorpha pex14* null mutant. *J. Biol. Chem.* **275**, 12603–12611 (2000). doi: 10.1074/jbc.275.17.12603 pmid: 10777551
28. C. Williams, B. Distel, Pex13p: Docking or cargo handling protein? *Biochim. Biophys. Acta* **1763**, 1585–1591 (2006). doi: 10.1016/j.bbamcr.2006.09.007; pmid: 17056133
29. Y.-T. Kao, K. L. Gonzalez, B. Bartel, Peroxisome function, biogenesis, and dynamics in plants. *Plant Physiol.* **176**, 162–177 (2018). doi: 10.1104/pp.17.01050; pmid: 29021223
30. K. Stein, A. Schell-Steven, R. Erdmann, H. Rottensteiner, Interactions of Pex7p and Pex18p/Pex21p with the peroxisomal docking machinery: Implications for the first steps in PTS2 protein import. *Mol. Cell. Biol.* **22**, 6056–6069 (2002). doi: 10.1128/MCB.22.17.6056-6069.2002; pmid: 12167700
31. A. Brennand, D. J. Rigden, P. A. M. Michels, Trypanosomes contain two highly different isoforms of peroxin PEX13 involved in glycosome biogenesis. *FEBS Lett.* **586**, 1765–1771 (2012). doi: 10.1016/j.febslet.2012.05.019; pmid: 22641036
32. H. B. Schmidt, D. Görlich, Transport selectivity of nuclear pores, phase separation, and membraneless organelles. *Trends Biochem. Sci.* **41**, 46–61 (2016). doi: 10.1016/j.tibs.2015.11.001; pmid: 26705895
33. K. Ribbeck, D. Görlich, The permeability barrier of nuclear pore complexes appears to operate via hydrophobic exclusion. *EMBO J.* **21**, 2664–2671 (2002). doi: 10.1093/emboj/21.11.2664; pmid: 12032079
34. A. Boisson-Dernier, S. Frietsch, T.-H. Kim, M. B. Dizon, J. I. Schroeder, The peroxin loss-of-function mutation abstinence by mutual consent disrupts male-female gametophyte recognition. *Curr. Biol.* **18**, 63–68 (2008). doi: 10.1016/j.cub.2007.11.067; pmid: 18160292
35. W. C. DeLoache, Z. N. Russ, J. E. Dueber, Towards repurposing the yeast peroxisome for compartmentalizing heterologous metabolic pathways. *Nat. Commun.* **7**, 11152 (2016). doi: 10.1038/ncomms11152; pmid: 27025684
36. Y. Elgersma *et al.*, The SH3 domain of the *Saccharomyces cerevisiae* peroxisomal membrane protein Pex13p functions as a docking site for Pex5p, a mobile receptor for the import PTS1-containing proteins. *J. Cell Biol.* **135**, 97–109 (1996). doi: 10.1083/jcb.135.1.97; pmid: 8858166
37. B. Agne *et al.*, Pex8p: An intraperoxisomal organizer of the peroxisomal import machinery. *Mol. Cell* **11**, 635–646 (2003). doi: 10.1016/S1097-2765(03)00062-5; pmid: 12667447
38. C. Krause, H. Rosewich, A. Woehler, J. Gärtner, Functional analysis of PEX13 mutation in a Zellweger syndrome spectrum patient reveals novel homooligomerization of PEX13 and its role in human peroxisome biogenesis. *Hum. Mol. Genet.* **22**, 3844–3857 (2013). doi: 10.1093/hmg/ddt238; pmid: 23716570
39. A. Barros-Barbosa *et al.*, Membrane topologies of PEX13 and PEX14 provide new insights on the mechanism of protein import into peroxisomes. *FEBS J.* **286**, 205–222 (2019). doi: 10.1111/febs.14697; pmid: 30414318
40. V. D. Antonenkov, R. T. Sormunen, J. K. Hiltunen, The rat liver peroxisomal membrane forms a permeability barrier for cofactors but not for small metabolites in vitro. *J. Cell Sci.* **117**, 5633–5642 (2004). doi: 10.1242/jcs.01485; pmid: 15509867
41. R. Zimmermann *et al.*, Quantitative proteomics and differential protein abundance analysis after the depletion of PEX3 from human cells identifies additional aspects of protein targeting to the ER. *Int. J. Mol. Sci.* **22**, 13028 (2021). doi: 10.3390/ijms222313028; pmid: 34884833
42. J. P. Wróblewska *et al.*, *Saccharomyces cerevisiae* cells lacking Pex3 contain membrane vesicles that harbor a subset of peroxisomal membrane proteins. *Biochim. Biophys. Acta Mol. Cell Res.* **1864**, 1656–1667 (2017). doi: 10.1016/j.bbamcr.2017.05.021; pmid: 28552664
43. R. L. M. Jansen, I. J. van der Klei, The peroxisome biogenesis factors Pex3 and Pex19: Multitasking proteins with disputed functions. *FEBS Lett.* **593**, 457–474 (2019). doi: 10.1002/1873-3468.13340; pmid: 30776093
44. S. Frey, R. P. Richter, D. Görlich, FG-rich repeats of nuclear pore proteins form a three-dimensional meshwork with hydrogel-like properties. *Science* **314**, 815–817 (2006). doi: 10.1126/science.1132516; pmid: 17082456
45. S. Frey, D. Görlich, A saturated FG-repeat hydrogel can reproduce the permeability properties of nuclear pore complexes. *Cell* **130**, 512–523 (2007). doi: 10.1016/j.cell.2007.06.024; pmid: 17693259
46. S. C. Ng, D. Görlich, A simple thermodynamic description of phase separation of Nup98 FG domains. bioRxiv 2022.07.26.501556 [Preprint] (2022); doi: 10.1101/2022.07.26.501556
47. E. L. Maynard, G. J. Gatto Jr., J. M. Berg, Pex5p binding affinities for canonical and noncanonical PTS1 peptides. *Proteins* **55**, 856–861 (2004). doi: 10.1002/prot.20112; pmid: 15146484
48. A. Kirchhofer *et al.*, Modulation of protein properties in living cells using nanobodies. *Nat. Struct. Mol. Biol.* **17**, 133–138 (2010). doi: 10.1038/nsmb.1727; pmid: 20010839
49. M. Kato *et al.*, Cell-free formation of RNA granules: Low complexity sequence domains form dynamic fibers within hydrogels. *Cell* **149**, 753–767 (2012). doi: 10.1016/j.cell.2012.04.017; pmid: 22579281
50. S. C. Ng *et al.*, Barrier-properties of Nup98 FG phases ruled by FG motif identity and inter-FG spacer length. bioRxiv 2022.10.14.512266 [Preprint] (2022); doi: 10.1101/2022.10.14.512266
51. A. M. Gouveia, C. P. Guimarães, M. E. Oliveira, C. Sá-Miranda, J. E. Azevedo, Insertion of Pex5p into the peroxisomal membrane is cargo protein-dependent. *J. Biol. Chem.* **278**, 4389–4392 (2003). doi: 10.1074/jbc.C200650200; pmid: 12502712
52. J. Saidowsky *et al.*, The di-aromatic pentapeptide repeats of the human peroxisome import receptor PEX5 are separate high affinity binding sites for the peroxisomal membrane protein PEX14. *J. Biol. Chem.* **276**, 34524–34529 (2001). doi: 10.1074/jbc.M104647200; pmid: 11438541
53. L. Emmanouilidis, M. Gopalswamy, D. M. Passon, M. Wilmanns, M. Sattler, Structural biology of the import pathways of peroxisomal matrix proteins. *Biochim. Biophys. Acta* **1863**, 804–813 (2016). doi: 10.1016/j.bbamcr.2015.09.034; pmid: 26450166
54. R. Itoh, Y. Fujiki, Functional domains and dynamic assembly of the peroxin Pex14p, the entry site of matrix proteins. *J. Biol. Chem.* **281**, 10196–10205 (2006). doi: 10.1074/jbc.M600158200; pmid: 16459329
55. A. Schell-Steven *et al.*, Identification of a novel, intraperoxisomal pex14-binding site in pex13: Association of pex13 with the docking complex is essential for peroxisomal matrix protein import. *Mol. Cell. Biol.* **25**, 3007–3018 (2005). doi: 10.1128/MCB.25.8.3007-3018.2005; pmid: 15798189
56. E. Granseth, "Dual-topology: One sequence, two topologies" in *Structural Bioinformatics of Membrane Proteins*, D. Frishman, Ed. (Springer, 2010), pp. 137–150. doi: 10.1007/978-3-7091-0045-5_8
57. C. W. Akey *et al.*, Comprehensive structure and functional adaptations of the yeast nuclear pore complex. *Cell* **185**, 361–378.e25 (2022). doi: 10.1016/j.cell.2021.12.015; pmid: 34982960
58. L. P. Crowe, C. L. Wilkinson, K. R. Nicholson, M. T. Morris, *Trypanosoma brucei* Pex13.2 is an accessory peroxin that functions in the import of peroxisome targeting sequence type 2 proteins and localizes to subdomains of the glycosome. *MSphere* **5**, e00744-19 (2020). doi: 10.1128/mSphere.00744-19; pmid: 32075879
59. I. V. Aramburu, E. A. Lemke, Floppy but not sloppy: Interaction mechanism of FG-nucleoporins and nuclear transport receptors. *Semin. Cell Dev. Biol.* **68**, 34–41 (2017). doi: 10.1016/j.semcdb.2017.06.026; pmid: 28669824
60. K. Kırlı *et al.*, A deep proteomics perspective on CRM1-mediated nuclear export and nucleocytoplasmic partitioning. *eLife* **4**, e11466 (2015). doi: 10.7554/eLife.11466; pmid: 26673895
61. R. D. Gietz, R. H. Schiestl, High-efficiency yeast transformation using the LiAc/SS carrier DNA/PEG method. *Nat. Protoc.* **2**, 31–34 (2007). doi: 10.1038/nprot.2007.13; pmid: 17401334
62. M. R. Wilkins *et al.*, Protein identification and analysis tools in the ExPASy server. *Methods Mol. Biol.* **112**, 531–552 (1999). pmid: 10027275
63. C. A. Schneider, W. S. Rasband, K. W. Eliceiri, NIH Image to ImageJ: 25 years of image analysis. *Nat. Methods* **9**, 671–675 (2012). doi: 10.1038/nmeth.2089; pmid: 22930834
64. R. Gautier, D. Douguet, B. Antonny, G. Drin, HELIQUEST: A web server to screen sequences with specific α-helical properties. *Bioinformatics* **24**, 2101–2102 (2008). doi: 10.1093/bioinformatics/btn392; pmid: 18662927
65. J. Jumper *et al.*, Highly accurate protein structure prediction with AlphaFold. *Nature* **596**, 583–589 (2021). doi: 10.1038/s41586-021-03819-2; pmid: 34265844
66. Y. Gao, M. L. Skowyra, P. Feng, T. A. Rapoport, Protein import into peroxisomes occurs through a nuclear pore–like phase, Version 2, Mendeley Data (2022); https://doi.org/10.17632/tskn79gd9p.2.

ACKNOWLEDGMENTS

We thank R. Erdmann (Ruhr-University Bochum) for the *S. cerevisiae* wild-type strain UTL7A, B. Gardner (University of California, Santa Barbara) for plasmid pWCD1401 encoding the violacein biosynthetic pathway, and J. Jia for the thermosensitivity analysis. We are also grateful to D. Görlich (Max Planck Institute, Göttingen), S. Shao (Harvard Medical School), and members of the Rapoport lab for insightful discussions and helpful comments on the manuscript. Imaging was performed with the help of M. Lowe Ocaña at the Neurobiology Imaging Facility at Harvard Medical School. **Funding:** This work was funded by National Institutes of

Health grant R01GM052586 (T.A.R.), the Howard Hughes Medical Institute (HHMI) (T.A.R.), HHMI-sponsored Helen Hay Whitney Foundation fellowship award F-1255 (M.L.S.), and HHMI-sponsored Damon Runyon Cancer Research Foundation fellowship award 2354-19 (Y.G.). **Author contributions:** Y.G. performed the experiments in yeast and with peroxisomal membranes. M.L.S. performed the experiments with hydrogels in vitro. M.L.S. noted the similarity of PEX13's YG domain with the FG-repeat domain of nucleoporins. P.F. assisted with the experiments. All authors were involved in the experimental design. M.L.S. and T.A.R. wrote a draft of the manuscript with edits from all authors. T.A.R. supervised the project. **Competing interests:** The authors declare that they have no competing interests. **Data and materials availability:** All data are available in the main text or the supplementary materials; the original unmodified image data are available from Mendeley Data (*66*). Reagents generated by this study are available from the corresponding author with a completed materials transfer agreement.

SUPPLEMENTARY MATERIALS

science.org/doi/10.1126/science.adf3971
Figs. S1 to S11
Table S1
MDAR Reproducibility Checklist

Submitted 18 October 2022; accepted 15 November 2022
10.1126/science.adf3971

RESEARCH ARTICLE SUMMARY

CELL BIOLOGY

Endosomal lipid signaling reshapes the endoplasmic reticulum to control mitochondrial function

Wonyul Jang, Dmytro Puchkov, Paula Samsó, YongTian Liang, Michal Nadler-Holly, Stephan J. Sigrist, Ulrich Kintscher, Fan Liu, Kamel Mamchaoui, Vincent Mouly, Volker Haucke*

INTRODUCTION: Cells need to react appropriately to nutritional cues. Defects in the rewiring of metabolism in response to alterations in nutrient supply have been linked to human diseases ranging from diabetes to muscle atrophy. Starvation represses anabolic pathways and facilitates catabolic ones, such as the degradation of macromolecules by autophagy and endolysosomes. Starvation also promotes the β-oxidation of fatty acids in mitochondria to produce adenosine triphosphate (ATP). Within cells, organelles including lysosomes and mitochondria undergo changes in shape and dynamics. These processes are often regulated by phosphoinositide lipids. Phosphoinositides are also involved in the formation of membrane contacts between organelles and in the response of cells and tissues to growth and nutrient signals. How the adaptive changes that protect mammalian cells and tissues from starvation-induced damage are coordinated on a cell-wide scale is unknown.

RATIONALE: Endolysosomal membrane dynamics and function are controlled by phosphoinositide signaling lipids, most notably by the synthesis and turnover of phosphatidylinositol 3-phosphate [PI(3)P]. Patients carrying mutations in the gene encoding the lipid phosphatase MTM1, an enzyme that mediates endosomal PI(3)P turnover, suffer from X-linked centronuclear myopathy (XLCNM), a severe neuromuscular disease characterized by muscle atrophy, disorganization of mitochondria, and defects in the organization of the muscle endoplasmic reticulum (ER). Given that PI(3)P is a hallmark of endosomes, we hypothesized that the control of early endosomal PI(3)P by MTM1 might serve to orchestrate adaptive changes in the dynamics of the ER and mitochondria in response to altering nutrient supply.

RESULTS: Working with XLCNM patient–derived myoblasts and engineered cell lines, we found that nutrient starvation (for example, lack of amino acids) induced the hydrolysis of PI(3)P by endosomal recruitment of MTM1. Concomitantly, tubular ER membranes were observed to be converted into ER sheets by live super-resolution light microscopy. Mechanistically, loss of early endosomal PI(3)P upon starvation was found to reduce membrane contacts between peripheral ER tubules and early endosomes. These contacts function as physical tethers that may transmit pulling forces from highly motile peripheral endosomes to the tubular ER. Using proximity labeling proteomic and functional cell biological experiments we demonstrated that the ER–endosome contacts were mediated by binding of the related ER membrane proteins RRBP1 and kinectin 1 to PI(3)P on endosomes. To study the role of starvation-induced reshaping of tubular ER membranes into sheets on mitochondrial form and function, we combined live imaging with three-dimensional focused ion beam milling scanning electron microscopy (FIB-SEM) and proteomic analysis. We found that starvation-induced ER reshaping by MTM1 reduced the rate of mitochondrial fission and promoted the formation of a hyperfused mitochondrial network. Genetic manipulations that resulted in ER sheet expansion caused the formation of an enlarged mitochondrial network even in fed cells. Conversely, impaired ER reshaping and reduced mitochondrial network formation were observed in starved myoblasts from XLCNM patients. Mitochondrial network formation appeared to be critical for the delivery of fatty acids from lipid droplets to mitochondria and for oxidative ATP production to sustain energy supply in nutrient-deprived cells.

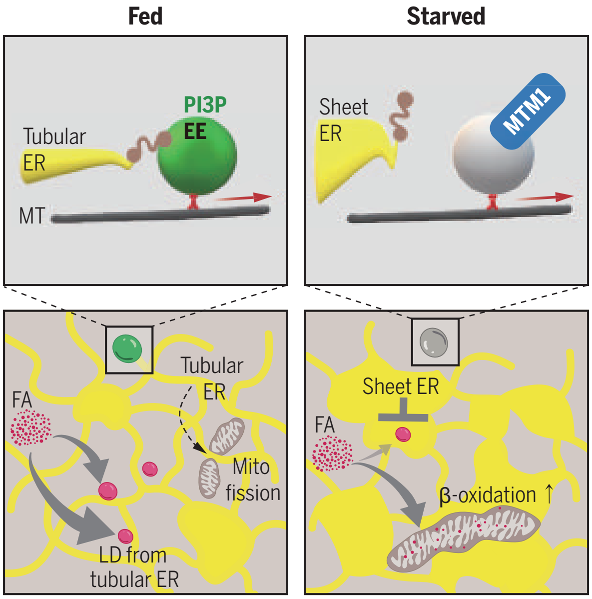

Role of MTM1-mediated endosomal PI(3)P signaling in mitochondrial metabolic rewiring through reshaping of the ER in response to starvation. In fed cells, early endosomes form contacts with ER tubules. Tubular ER membranes facilitate mitochondrial fission and serve as a source for lipid droplet formation. Nutrient starvation–induced hydrolysis of endosomal PI(3)P by MTM1 reduces membrane contacts between the tubular ER and early endosomes. The resulting loss of peripheral ER tubules induces mitochondrial network formation and the delivery of fatty acids to mitochondria to sustain cellular energy supply. EE, early endosome; MT, microtubule; FA, fatty acid; LD, lipid droplet.

CONCLUSION: Our data unravel a crucial role for early endosomal lipid signaling in controlling ER morphology and, thereby, mitochondrial form and function to orchestrate the adaptive response of cells to alterations in nutrient (e.g., amino acid) supply. This mechanism operates independent of autophagy, a cellular self-eating process typically induced by prolonged starvation. Rather, it resembles an organellar conveyor belt, in which the tubular ER serves as a membrane conduit that transmits nutrient-triggered changes in endosomal PI(3)P levels to metabolic organelles to enable metabolic rewiring. How early endosomal PI(3)P levels and MTM1 function are controlled by cellular nutrient status is currently unknown. Defects in ER shape, mitochondrial morphogenesis, and cellular ATP depletion caused by loss of MTM1 function can explain the observed myofiber hypotrophy and defective ER organization in animal models of XLCNM and in human patients who often appear undernourished. We therefore hypothesize that dysregulated organelle remodeling may underlie XLCNM caused by *MTM1* mutations in humans. ■

The list of author affiliations is available in the full article online.
*Corresponding author. Email: haucke@fmp-berlin.de
Cite this article as W. Jang *et al.*, *Science* **378**, eabq5209 (2022). DOI: 10.1126/science.abq5209

READ THE FULL ARTICLE AT
https://doi.org/10.1126/science.abq5209

RESEARCH ARTICLE

CELL BIOLOGY

Endosomal lipid signaling reshapes the endoplasmic reticulum to control mitochondrial function

Wonyul Jang[1], Dmytro Puchkov[1], Paula Samsó[1], YongTian Liang[2], Michal Nadler-Holly[1], Stephan J. Sigrist[2], Ulrich Kintscher[3], Fan Liu[1,3], Kamel Mamchaoui[4], Vincent Mouly[4], Volker Haucke[1,2,3]*

Cells respond to fluctuating nutrient supply by adaptive changes in organelle dynamics and in metabolism. How such changes are orchestrated on a cell-wide scale is unknown. We show that endosomal signaling lipid turnover by MTM1, a phosphatidylinositol 3-phosphate [PI(3)P] 3-phosphatase mutated in X-linked centronuclear myopathy in humans, controls mitochondrial morphology and function by reshaping the endoplasmic reticulum (ER). Starvation-induced endosomal recruitment of MTM1 impairs PI(3)P-dependent contact formation between tubular ER membranes and early endosomes, resulting in the conversion of ER tubules into sheets, the inhibition of mitochondrial fission, and sustained oxidative metabolism. Our results unravel an important role for early endosomal lipid signaling in controlling ER shape and, thereby, mitochondrial form and function to enable cells to adapt to fluctuating nutrient environments.

The ability of cells to react appropriately to nutritional cues is of fundamental importance for cell physiology, and defects in the cellular response to altered nutrient supply have been linked to human diseases ranging from diabetes to muscle atrophy (*1*–*4*). Among the early changes elicited by nutrient stress are the suppression of anabolic programs such as protein translation (*5*, *6*) and the concomitant induction of catabolic processes involving the proteasome, autophagy [e.g., lipophagy, reticulophagy (*7*)], endolysosomal turnover of proteins (*6*, *8*), and increased mitochondrial β-oxidation of fatty acids (*9*). How these adaptive responses that protect mammalian cells and tissues from starvation-induced damage and the induction of apoptotic cell death are coordinated is unknown. Endolysosomal membrane dynamics and function are controlled by the spatiotemporally regulated synthesis and turnover of phosphatidylinositol 3-phosphate [PI(3)P] and related signaling lipids by phosphatidylinositol (PI) 3-kinases and 3-phosphatases (*10*, *11*). MTM1, the founding member of the myotubularin family of PI 3-phosphatases, is crucially involved in PI(3)P homeostasis on endosomes (*12*–*15*). Patients carrying mutations in the *MTM1* gene suffer from X-linked centronuclear myopathy (XLCNM), a severe, often fatal disease characterized by muscle weakness due to myofiber atrophy, disorganization of mitochondria, and structural defects in the organization of the sarcoplasmic reticulum, a specialized form of the endoplasmic reticulum (ER) found in muscle tissue that is important for excitation-contraction coupling (*16*, *17*). How XLCNM-linked mutations in endosomal MTM1 cause such pleiotropic defects in the organization of the ER and other organelles has remained elusive but may relate to a thus far unexplored function of endosomes in orchestrating adaptive changes in organelle dynamics.

Results

Nutrient-regulated reshaping of the ER is controlled by endosomal MTM1

To address the question how XLCNM-linked mutations in endosomal MTM1 cause defects in ER organization, we analyzed ER morphology (*18*) in myoblast cell lines from healthy controls or XLCNM patients (table S1) (*19*–*21*) suffering from pronounced or complete loss of MTM1 protein (fig. S1A) and a resulting increase in PI(3)P levels (*15*). The ER membrane is composed of interconnected uniform flat cisternal sheets, fenestrated sheets with nanoholes (*22*, *23*), and peripheral dynamic narrow tubules (~30 to 60 nm in diameter). ER sheets and peripheral ER tubules were initially characterized by confocal light microscopy (*24*) and have recently been resolved at the nanoscale by super-resolution imaging (*22*, *25*). We determined the morphology of the peripheral ER by semiautomated image analysis of cells expressing mEmerald- or Halo-tagged versions of the ER membrane protein Sec61β or cells stained for the ER marker calreticulin (fig. S1B). This analysis revealed a prominent accumulation of tubular versus sheet ER in myoblasts from XLCNM patients compared with cells from healthy controls (Fig. 1, A and B). Accumulation of tubular ER in XLCNM myoblasts was confirmed by time-gated stimulated emission depletion (gSTED) nanoscopy imaging at 50-nm resolution [consistent with (*22*)] (Fig. 1A). Depletion of MTM1 in healthy controls phenocopied XLCNM myoblasts with respect to the accumulation of tubular ER and the concomitant reduction in sheet ER (Fig. 1C and fig. S1C). These data suggest that the defects in ER morphology observed in XLCNM patient myoblasts are a consequence of MTM1 loss of function and are consistent with earlier in vivo data indicating a possible role for MTM1 in the control of ER morphology (*17*).

A hallmark of MTM1 loss is the accumulation of its substrate lipid PI(3)P (*15*). We reasoned that the observed defects in ER shape in XLCNM myoblasts are a consequence of elevated PI(3)P levels and, thus, might be rescued by pharmacological inhibition of PI(3)P synthesis. Consistently, specific inhibition of the endosomal PI 3-kinase VPS34 in the presence of VPS34-IN1 or reexpression of active MTM1 sufficed to restore normal ER morphology in XLCNM patient myoblasts (Fig. 1D and fig. S1, D and E). An elevated ER sheet-to-tubule ratio was also observed in VPS34-IN1–treated human HeLa cells imaged by confocal light microscopy or gSTED nanoscopy at steady state (Fig. 1E and fig. S1, F and G). In contrast, depletion of phosphatidylinositol 3,5-bisphosphate [PI(3,5)P$_2$], another potential MTM1 substrate lipid (*26*), did not affect ER shape (fig. S1, F and H). Previous data show that PI(3)P is involved in the cellular response to altered nutrient supply (*27*–*29*). We therefore tested whether PI(3)P metabolism might be regulated by nutrients. We found endosomal PI(3)P levels to decline upon cellular nutrient deprivation [consistent with (*29*)] (Fig. 1F and fig. S1I), and this was accompanied by progressive ER sheet expansion in live or fixed cells imaged by super-resolution STED or confocal microscopy (Fig. 1, G and H; fig. S1, J and K; and Movies 1 and 2). The levels of major ER-shaping proteins remained unaltered (fig. S3, J and K). ER sheet expansion was also observed in cells treated with the potent catalytic mechanistic target of rapamycin (mTOR) inhibitor Torin 1 (fig. S1L), which is often used to mimic conditions of starvation. Further analysis revealed that deprivation of amino acids (glutamine in particular), rather than growth factors and glucose, was responsible for ER reshaping during starvation (Fig. 1I and fig. S1M). In contrast, amino acid replenishment failed to rescue the starvation-induced reduction in cell area (fig. S1, N and O), suggesting that ER shape and cell size are controlled by distinct mechanisms.

To probe whether reduced PI(3)P levels causally underlie the starvation-induced remodeling of ER membranes, we depleted cells of MTM1, a condition under which PI(3)P accumulates (*15*), by RNA interference or

---

[1]Leibniz-Forschungsinstitut für Molekulare Pharmakologie (FMP), 13125 Berlin, Germany. [2]Department of Biology, Chemistry, and Pharmacy, Freie Universität Berlin, 14195 Berlin, Germany. [3]Charité-Universitätsmedizin Berlin, 10117 Berlin, Germany. [4]Centre de Recherche en Myologie, Institut de Myologie, Inserm, Sorbonne Université, 75013 Paris, France.
***Corresponding author. Email: haucke@fmp-berlin.de**

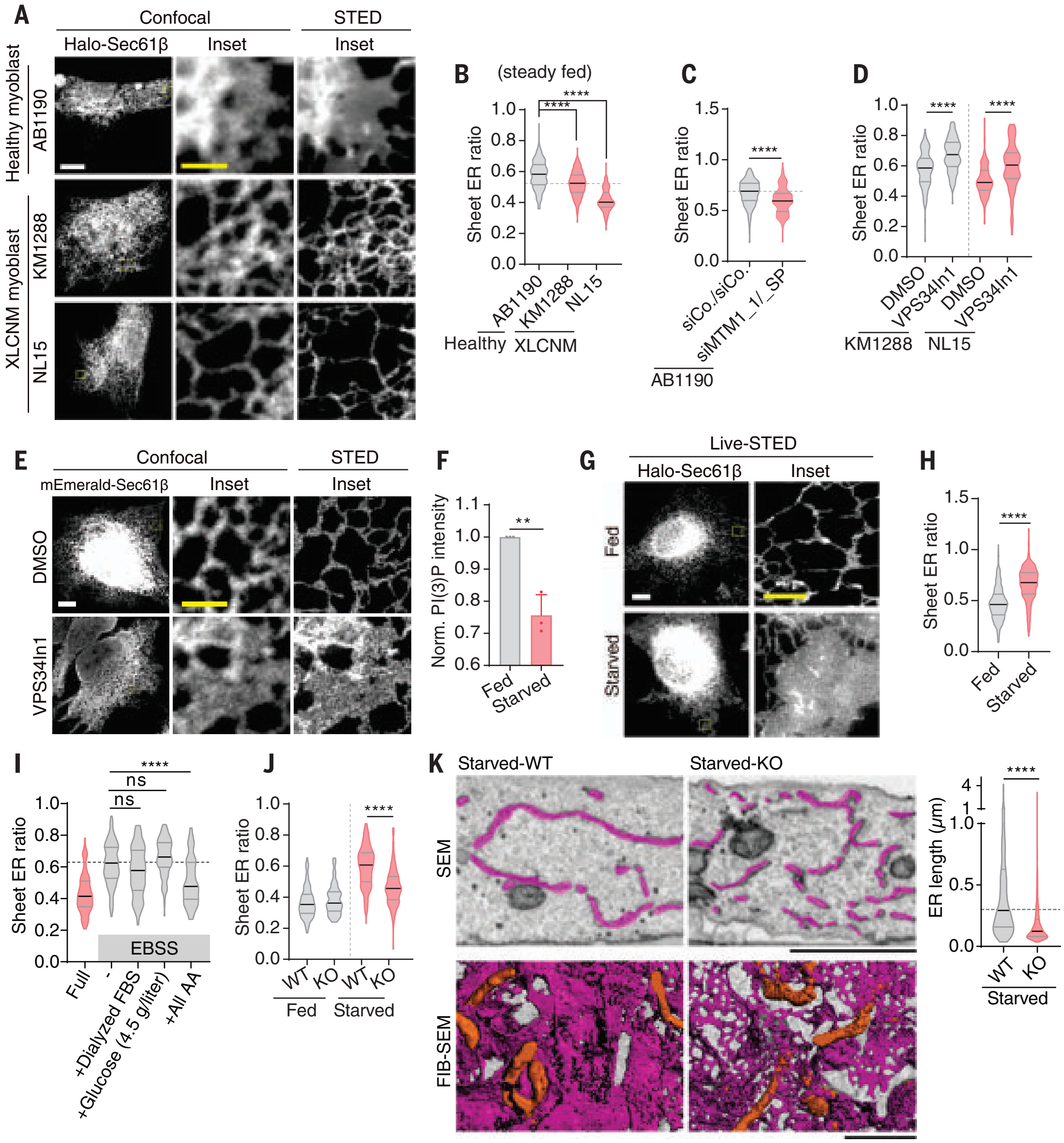

Fig. 1. Nutrient-regulated reshaping of the ER is controlled by endosomal MTM1. (**A**) Confocal and STED live images of Halo-Sec61β in fed myoblasts from healthy and XLCNM patients. (**B**) Ratio of sheet/total ER area stained for calreticulin. AB1190 (*n* = 206), KM1288 (*n* = 222), NL15 (*n* = 102). (**C**) Ratio of sheet/total ER area in fed healthy (AB1190) myoblasts at steady-state treated with control (siCo/siCo) or MTM1 siRNA (siMTM1_1/_SP). siCo/siCo (*n* = 181), siMTM1_1/_SP (*n* = 167). (**D**) Ratio of sheet/total ER area in XLCNM patient myoblasts treated with DMSO (control) or VPS34-IN1 (5 μM, 2 hours). KM1288, DMSO (*n* = 113), VPS34-IN1 (*n* = 148); NL15, DMSO (*n* = 80), VPS34-IN1 (*n* = 86). (**E**) Confocal and STED images of DMSO or VPS34-IN1-treated (5 μM, 2 hours) HeLa cells expressing mEmerald-Sec61β. (**F**) PI(3)P levels in fed (*n* = 820) or starved (EBSS 2 hours; *n* = 725) HeLa cells. (**G**) STED images of fed or starved live HeLa cells stably expressing Halo-Sec61β. See Movies 1 and 2. (**H**) Ratio of sheet/total ER area in fed or starved (EBSS 2 hours) HeLa cells stained for calreticulin. Fed (*n* = 312), Starved (*n* = 320). (**I**) Ratio of sheet/total ER area of HeLa cells expressing mEmerald-Sec61β exposed to different nutrients (2 hours). Full (*n* = 128), − (i.e., EBSS only, *n* = 148), +Dialyzed FBS (*n* = 160), +Glucose (4.5 g/liter) (*n* = 111), all amino acids (+ All AA, *n* = 171). (**J**) Ratio of sheet/total ER area in fed or starved HeLa WT or MTM1 KO cells. Fed WT (*n* = 136), KO (*n* = 123); Starved WT (*n* = 156), KO (*n* = 207). (**K**) (Top left) Electron microscopy images of starved WT or MTM1 KO HeLa cells. Purple, ER cisternal cross sections. (Right) Length of ER cross sections (# of objects: WT = 1018, KO = 1070) from three cells. (Bottom left) 3D FIB-SEM analysis. 3D reconstruction of ER (purple) and mitochondria (brown). ER sheets are fenestrated in starved KO cells. See fig. S2G and movie S1. Scale bars: 10 μm (white), 2 μm (yellow), and 1 μm (black). *n*, total number of cells analyzed from two (H) or three [(B) to (D), (F), (I), and (J)] independent experiments. One-way ANOVA with Dunnett's multiple comparisons test (B); two-tailed Mann-Whitney test [(C), (D), (H), (J), and (K)]; two-tailed unpaired *t* test (F); Kruskal-Wallis test with two-sided Dunn's multiple comparison test (I). $^{**}P \leq 0.01$, $^{****}P \leq 0.0001$. Data are median ± interquartile range [(B) to (D), and (H) to (K)] or mean ± SD (F).

CRISPR-Cas9–mediated knockout (KO). Loss of MTM1 potently antagonized the starvation-induced conversion of peripheral ER tubules into sheets (Fig. 1J and fig. S2, A to E), a phenotype that was rescued by reexpression of catalytically active mCherry-MTM1 (fig. S2F). Further ultrastructural analysis by three-dimensional (3D) focused ion beam scanning electron microscopy (FIB-SEM) showed that even the perinuclear ER, which appeared as flat uniform sheets in starved wild-type (WT) cells, was highly fenestrated in starved cells lacking MTM1 (Fig. 1K, FIB-SEM; fig. S2G; and movie S1). The total ER volume fraction was unaltered (fig. S2H). Accumulation of highly fenestrated sheet ER and ER tubules in MTM1 KO cells was further evidenced by the reduced average length of ER profiles determined by SEM analysis of 2D cross sections (Fig. 1K, SEM).

We also tested whether other members of the myotubularin family of MTM1-related phosphatases affect ER shape. On the basis of their mRNA expression levels in HeLa cells, we analyzed four myotubularin-related proteins (MTMRs) and found that, of these four, only MTMR1, the family member most closely related to MTM1, affected ER shape (fig. S2, I to K). These data suggest a close functional relationship between endosomal PI(3)P and ER morphology, in particular the presence of ER tubules in cells. Increased levels of endosomal PI(3)P caused by MTM1 loss of function prevent the starvation-induced remodeling of ER membranes, and

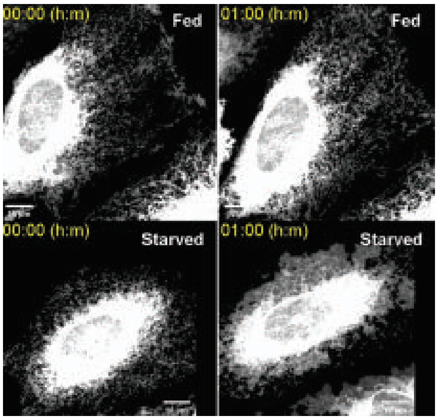

Movie 1. Live imaging of ER dynamics in fed or starved cells. Live-cell spinning disk confocal imaging of fed or starved HeLa cells expressing mEmerald-Sec61β. Videos were acquired at 1 frame/5 min for 150 min and correspond to fig. S1K.

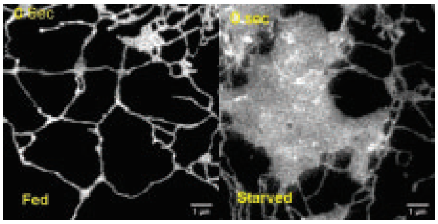

Movie 2. Live STED imaging of tubular or sheet ER from fed or starved HeLa cells expressing Halo-Sec61 β. Live-cell STED imaging of starved HeLa cells expressing Halo-Sec61β. Videos were acquired at 1 frame/3 s for 30 s and are related to Fig. 1G.

this may underlie the structural defects in ER morphology found in muscle cells and tissue from XLCNM patients (*16*, *17*, *30*, *31*).

Starvation-induced PI(3)P hydrolysis by MTM1 at ER–early endosome contacts mediates ER reshaping

We next sought to understand how PI(3)P hydrolysis by MTM1 mediates the starvation-induced conversion of peripheral ER tubules into flat uniform sheets. As the ER is subject to turnover by means of autophagy (*32*), we probed whether blockade of autophagosome formation interferes with starvation-induced ER sheet expansion. However, ER sheet expansion in starved cells was unaffected by pharmacological or genetic inhibition of autophagy in the presence of VPS34-IN1 (*15*) or knockdown of the essential autophagy factor ATG5 (fig. S3, A to D). Moreover, loss of MTM1, that is, a condition in which starvation-induced ER sheet expansion is perturbed, did not alter the ability of starved cells to form microtubule-associated protein 1 light chain 3 (LC3)–positive autophagosomes (fig. S3, E and F), the overall levels of the autophagy marker LC3-II (fig. S3G), or the subcellular localization and activation of transcription factor EB (TFEB), a master regulator of autophagy gene expression (*33*) (fig. S3, L and M). MTM1 KO cells displayed slightly reduced levels of the sheet-localized ER-phagy receptor FAM134B under fed and starved conditions (fig. S3, H and I). Reduced levels of FAM134B have been shown to result in sheet ER expansion (*32*), a phenotype opposite to the expansion of the tubular ER observed in MTM1 KO cells (Fig. 1). The starvation-induced increase in the sheet ER ratio thus appears to be independent of FAM134B-mediated ER-phagy. Although mechanistic target of rapamycin complex 1 (mTORC1) activity was elevated in fed MTM1 KO cells [consistent with observations in MTM1 KO mice (*34*)], loss of MTM1 did not affect suppression of mTORC1 activity in starved cells (fig. S3N). Finally, lumenal ER calcium levels were not significantly altered (fig. S3O), and no signs of an ER stress response were detected in MTM1 KO cells (fig. S3P). We conclude that PI(3)P hydrolysis by MTM1 in starved cells controls ER shape independently of autophagy, the ER stress response, and ER calcium homeostasis.

Given that PI(3)P is a hallmark of early endosomes (*10*, *35*) and that the ER makes extensive contacts with other organelles including the plasma membrane (*36*), endosomes, lysosomes, and mitochondria (*37*), we hypothesized that MTM1 specifically acts on peripheral early endosomes in starved cells and thereby controls ER morphology (Fig. 2A), for example, through membrane contacts. To test this, we generated a cell line stably expressing a chimera between the early endosomal protein Rab5A and the biotinylating enzyme ascorbate peroxidase 2 (APEX2) (*38*) under the control of a doxycycline-inducible promoter (fig. S4A). Proximity labeling and affinity capture revealed a prominent starvation-induced enrichment of endogenous MTM1 on early endosomes, while early endosomal antigen 1 (EEA1), a PI(3)P-binding scaffold protein, was depleted in early endosomes (Fig. 2B and fig. S4B). Nutrient starvation thus induces the recruitment of MTM1 to Rab5-containing early endosomes, likely resulting in PI(3)P hydrolysis and ER sheet expansion. We further probed this model by a chemical genetic approach that capitalizes on the FRB/FKBP system, which enables the artificial tethering of organelles via rapalog-induced heterodimerization of chimeras between FK506-binding protein (FKBP) and the FKBP-rapamycin binding (FRB) domain of mTOR (*39*). We found that acute rapalog-induced recruitment of active FKBP-MTM1 to early endosomes tagged with FRB-Rab5A resulted in massive ER tubule-to-sheet conversion in fed cells (Fig. 2C and fig. S4C), phenocopying starvation-induced PI(3)P depletion. Recruitment of active MTM1 to lysosomes (fig. S4, D and E) or early endosomal recruitment of catalytically inactive mutant MTM1 (CS) did not affect ER shape (Fig. 2C). We conclude that recruitment of catalytically active MTM1 to early endosomes drives ER sheet expansion to mount the cellular response to nutrient starvation.

The role of endosomal MTM1 in controlling ER shape might depend on the formation of hitherto molecularly undefined membrane contacts between the tubular ER and highly motile early endosomes that could provide a force that aids in keeping ER tubules under tension. In support of this hypothesis, we observed PI(3)P and the early endosome marker Rab5A to tightly colocalize with the tubular ER network in the cell periphery (Fig. 2D). Moreover, tracking early endosomes and the ER network in live cells by high-speed spinning disk confocal imaging showed that forming ER tubules are tightly associated with motile early endosomes (Fig. 2E and Movie 3), a conclusion further supported by the close association of ER tubules with early endosomes marked by internalized bovine serum albumin–gold (BSA-gold) in electron micrographs (Fig. 2F). Hence, the large population of peripheral early endosomes may serve to promote ER tubules. Consistently, we found that acute depletion of early endosomes from the cell periphery by rapalog-induced endosomal recruitment of the microtubule minus end–directed dynein adaptor BICD2 caused a near complete loss of the tubular ER network and a concomitant accumulation of perinuclear sheet ER (Fig. 2, G and H; fig. S4F; and movie S2).

We reasoned that MTM1-mediated hydrolysis of PI(3)P at early endosomes during starvation may control ER shape either by (i) controlling early endosome motility or (ii) altering the number or stability of hitherto unknown physical contacts between early endosomes and the ER (fig. S4G). As early endosome motility was unaffected by nutrient starvation (fig. S4, H and I), we followed the alternative hypothesis that nutrient regulation of early endosomal PI(3)P controls membrane contact sites between early endosomes and the ER and, thereby, ER shape. To monitor such contacts, we determined the fractional overlap between the peripheral ER and early endosomes by multicolor STED microscopy (fig. S4J). Starvation reduced the fractional overlap of the ER with early endosomes (Fig. 2I). The total contact area between the ER and early endosomes marked by internalized BSA-gold was also found to be significantly reduced in starved cells analyzed by electron microscopy (Fig. 2J). To confirm these findings by another independent approach, we generated a stable cell line that coexpresses equimolar ratios of an ER membrane targeting domain (ERM) fused

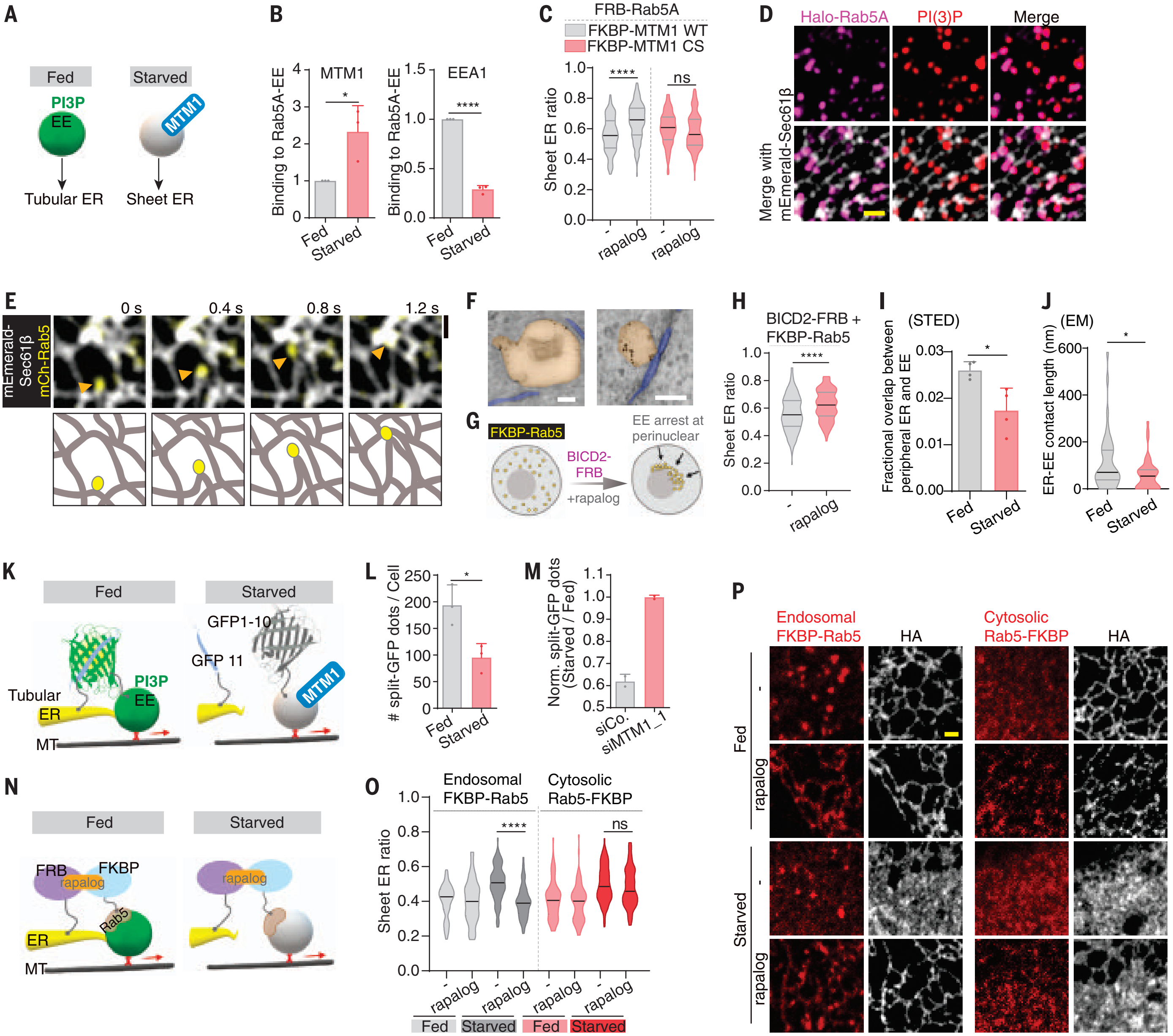

Fig. 2. Starvation-induced PI(3)P hydrolysis by MTM1 at ER–early endosome contacts mediates ER reshaping. (**A**) PI(3)P-positive early endosomes (EE) may control the tubular ER. (**B**) Starvation-induced recruitment of MTM1 to EE. EE-associated MTM1 (left) and EEA1 (right) in fed versus starved HeLa cells. *n* = 3 independent experiments. (**C**) Ratio of sheet/total ER in HeLa cells coexpressing FRB-iRFP-Rab5A and mRFP-FKBP-MTM1 WT (wild-type) or CS (inactive mutant) ± rapalog. FKBP-MTM1 WT – (*n* = 162), rapalog (*n* = 265), FKBP-MTM1 CS – (*n* = 138), rapalog (*n* = 187). (**D**) Confocal images of HeLa cells stably coexpressing Halo-Rab5A (EE) and mEmerald-Sec61β (ER) and stained for PI(3)P. (**E**) Time-lapse confocal images of HeLa cells coexpressing mEmerald- Sec61β (ER) and mCherry-Rab5 (EE). Yellow arrowheads mark motile EE. (**F**) Electron micrographs illustrating tubular ER (blue) contacts with EE (orange) marked by internalized BSA-gold. (**G**) Rapalog-induced acute depletion of EE from the periphery. See movie S2. (**H**) Ratio of sheet/total ER in mock- (*n* = 177) versus rapalog-treated (*n* = 141) HeLa cells as in (G). (**I**) Fractional overlap between the peripheral ER and EE in fed or starved cells determined by STED microscopy. Fed = 118 ROIs; Starved = 166 ROIs (40 to 50 cells from four experiments). (**J**) Morphometric analysis of contact length (nanometers) between ER and BSA-gold labeled EE in fed (42 endosomes) versus starved cells (43 endosomes). (**K**) Reconstitution of split-GFP fluorescence by ER-EE contacts. (**L**) Normalized number of ER/EE contacts in fed (*n* = 238) versus starved (*n* = 257) HeLa cells. (**M**) Rescue of ER/EE contacts in starved MTM1-depleted HeLa cells. siCo Fed (*n* = 123), Starved (*n* = 77), siMTM1_1 Fed (*n* = 111), Starved (*n* = 85). (**N**) ERM-FRB•rapalog•FKBP-Rab5A ER/EE synthetic tether. (**O**) Ratio of sheet/total ER in fed or starved cells from (N). Endosomal FKBP Rab5 Fed – (*n* = 68), rapalog (*n* = 70), Starved – (*n* = 92), rapalog (*n* = 86); Cytosolic Rab5-FKBP Fed – (*n* = 97), rapalog (*n* = 90), Starved – (*n* = 104), rapalog (*n* = 120). (**P**) Confocal images from (O) stained for HA to mark the ER, gray. Scale bars: 2 μm (yellow), 1 μm (black), and 100 nm (white). *n*, number of cells analyzed from two [(M) and (O)] or three [(C), (H), and (L)] independent experiments. Two-tailed unpaired *t* test [(B), (C), (I), (L), and (O);] two-tailed Mann-Whitney test [(H) and (J)]; $*P \leq 0.05$, $****P \leq 0.0001$; ns, nonsignificant. Data are mean ± SD [(B), (I), (L), and (M)] or median ± interquartile range [(C), (H), (J), and (O)].

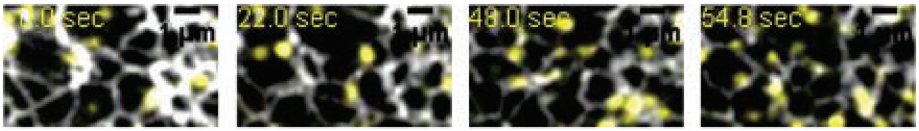

Movie 3. Live imaging of early endosome motility and the tubular ER. Live-cell high-speed spinning disk confocal imaging of fed HeLa cells expressing mEmerald-Sec61β (labeled gray) and mCherry-Rab5 (labeled yellow). Videos were acquired at 1 frame/0.4 s for 1 min and correspond to Fig. 2E.

to GFP^{11} (*40*) along with a GFP$^{1\text{-}10}$-Rab5A chimera under the control of a doxycycline-inducible promoter (fig. S4, K and L). Formation of membrane contacts between early endosomes and the ER in fed cells reconstitutes GFP fluorescence (Fig. 2K). ER–early endosome membrane contacts were greatly reduced in starved cells (Fig. 2L and fig. S4M), and this effect was reverted completely by depletion of MTM1 (Fig. 2M). These data suggest that MTM1-mediated hydrolysis of PI(3)P at early endosomes reduces the contacts between these organelles and the ER (Fig. 2K). We directly tested this model by examining the effects of semisynthetic tethering of early endosomes to the ER using chemical genetics. Acute rapalog-induced formation of ER–early endosome tethers mediated by ERM-FRB•rapalog•FKBP-Rab5A potently suppressed starvation-induced ER tubule-to-sheet conversion (Fig. 2, N to P; fig. S5B; and movie S3) but had no effect on early endosome motility (fig. S5A). In contrast, soluble, nonlipidated Rab5A (Rab5-mRFP-FKBP) or cytosolic mRFP-FKBP had no effect on ER shape (Fig. 2O and fig. S5, B and C). Extending the length of the semisynthetic tether well beyond the typical distance of 20 to 30 nm observed for organelle contacts in vivo (*36*, *37*) did not affect its ability to prevent starvation-induced ER reshaping (fig. S5, D and E), suggesting that the exertion of a physical pulling force is critical for the regulation of ER shape by membrane contacts with early endosomes. Furthermore, the capability of ERM-FRB•rapalog•FKBP-Rab5A tethers to prevent starvation-induced ER tubule-to-sheet conversion was unaffected by depletion of PI(3)P, indicating that PI(3)P acts upstream of ER–early endosome membrane contact site formation (fig. S5, F and G). Other organelles—late endosomes and lysosomes, in particular—have also been shown to form numerous contacts with the ER (*41*, *42*). Early endosomes display an even distribution throughout cells and into the periphery where the tubular ER is located and outnumber lysosomes by up to an order of magnitude. In contrast, most lysosomes are concentrated in the perinuclear area at steady state (fig. S6, A to D). As a consequence, the total number of membrane contacts between the ER and early endosomes greatly exceeds that of the ER with lysosomes (fig. S6, E to H), in spite of the high relative fraction of lysosomes in touch with the ER (*42*, *43*). Redistribution of lysosomes to the perinuclear area either through acute rapalog-induced dynein adaptor recruitment or depletion of PI(3,5)P$_2$ did not affect ER shape (fig. S6, I to L; fig. S1H; and movie S4). Sustained loss of the lysosomal kinesin adaptor Arl8b, a protein essential for lysosome dispersion, only marginally increased the sheet ER fraction [fig. S6, M to O; see also (*44*)], whereas depletion of the ER-lysosome contact site protein protrudin (*41*) was without effect. Hence, the tubular ER is largely controlled by its membrane contacts with early endosomes (as demonstrated in this study) and a smaller contribution from lysosomes, possibly dependent on cell type or conditions (*44*). Taken together, our findings unravel a crucial role for MTM1-mediated PI(3)P hydrolysis in the reduction of membrane contacts between the ER and early endosomes to reshape the ER in response to changing nutrient levels.

Contacts formed by ER membrane protein–mediated recognition of early endosomal PI(3)P controls the tubular ER

To identify the molecular machinery that tethers ER tubules to early endosomes in fed cells, we capitalized on the observation that in WT but not in MTM1 KO cells ER–early endosome contacts are reduced under conditions of nutrient starvation (Fig. 3A). Starved WT or MTM1 KO HeLa cells inducibly expressing APEX2-Rab5A were subjected to combined proximity labeling and affinity purification–mass spectrometry to probe the molecular environment of Rab5A-containing early endosomes. Subsequent biochemical fractionation to enrich for ER membrane proteins (fig. S7, A to C, and table S2) and comparison with previously identified ER surface proteins (*45*) identified several putative ER transmembrane proteins that might serve as early endosome tethers (fig. S7D). Analysis of the phenotypic consequences of cellular depletion of these factors revealed that only loss of ER ribosome-binding protein 1 (RRBP1) promoted ER tubule-to-sheet conversion in fed cells (fig. S7E). RRBP1 is localized exclusively to ER membranes (Fig. 3, B and C) and has been associated with changes in ER morphology, although no consensus regarding its precise function exists (*46*–*48*). ER tubule-to-sheet conversion was exacerbated by concomitant loss of RRBP1 and its close paralog kinectin 1 (KTN1) (Fig. 3D and fig. S8, A to C). Moreover, loss of RRBP1 and KTN1 potently reduced the number of ER–early endosome membrane contacts in fed cells (Fig. 3E), suggesting that RRBP1 and KTN1 regulate ER shape by acting as tethers for early endosomes. KTN1 and RRBP1 harbor functionally uncharacterized lysine-rich regions (LR1, -2, and -3) in their cytoplasmic domains (Fig. 3F and fig. S8, A and B) that could conceivably attach to PI(3)P. Notably, KTN1 was found to be in contact with PI(3)P-enriched early endosomes by spatiotemporally resolved interaction proteomics using 2xFYVE-APEX as a probe (*49*). We found recombinant RRBP1-LR1-3 (fig. S8D) to bind to PI(3)P with preference over both PI(4)P and PI(3,4)P$_2$ (Fig. 3, G and H). These data suggest that RRBP1 might recognize PI(3)P on early endosomes to form tethers with the ER. Consistent with this model, we observed that expression of a mini-RRBP1 truncation protein variant harboring only the lysine-rich cytoplasmic domain fused to its ER transmembrane anchor sufficed to restore a normal tubular ER network in HeLa cells depleted of endogenous RRBP1 and KTN1 (Fig. 3I, WT). Deletion of lysine-rich regions 1 or 3 or of the transmembrane anchor rendered truncated mini-RRBP1 inactive (Fig. 3I and fig. S8, E and F). These data suggest that RRBP1 and KTN1 mediate recognition of early endosomal PI 3-phosphates and, possibly, additional factors, to facilitate contact site formation between the ER and early endosomes, which control the tubular ER network in human cells.

MTM1-dependent ER reshaping is required for mitochondrial network formation during starvation

Several mechanisms have been shown to contribute to mitochondrial morphogenesis, including membrane contacts between mitochondria and lysosomes (*50*), late Golgi-derived vesicles (*51*), and the tubular ER (*37*, *52*). The tubular ER also directly promotes mitochondrial fission (*53*) and acts as a donor organelle for the formation of lipid droplets (LDs) (*54*, *55*) that serve as an energy reservoir in fed cells and tissues. Under conditions of starvation (e.g., deprivation of glutamine and other amino acids), mitochondria undergo hyperfusion into tubular networks to protect themselves from mitophagy (*56*) and to enable efficient utilization of fatty acids (*57*).

On the basis of these prior works, we hypothesized that the MTM1-mediated starvation-induced reshaping of the tubular ER into sheets (Fig. 1) might serve to enable cells to metabolically adapt to altering nutrient environments, for example, by altering mitochondrial organization. To test this hypothesis, we examined the effect of MTM1 loss on mitochondrial morphology and respiratory function. We found mitochondria to become hyperfused in starved WT but not in MTM1 KO cells or in WT cells depleted of endogenous

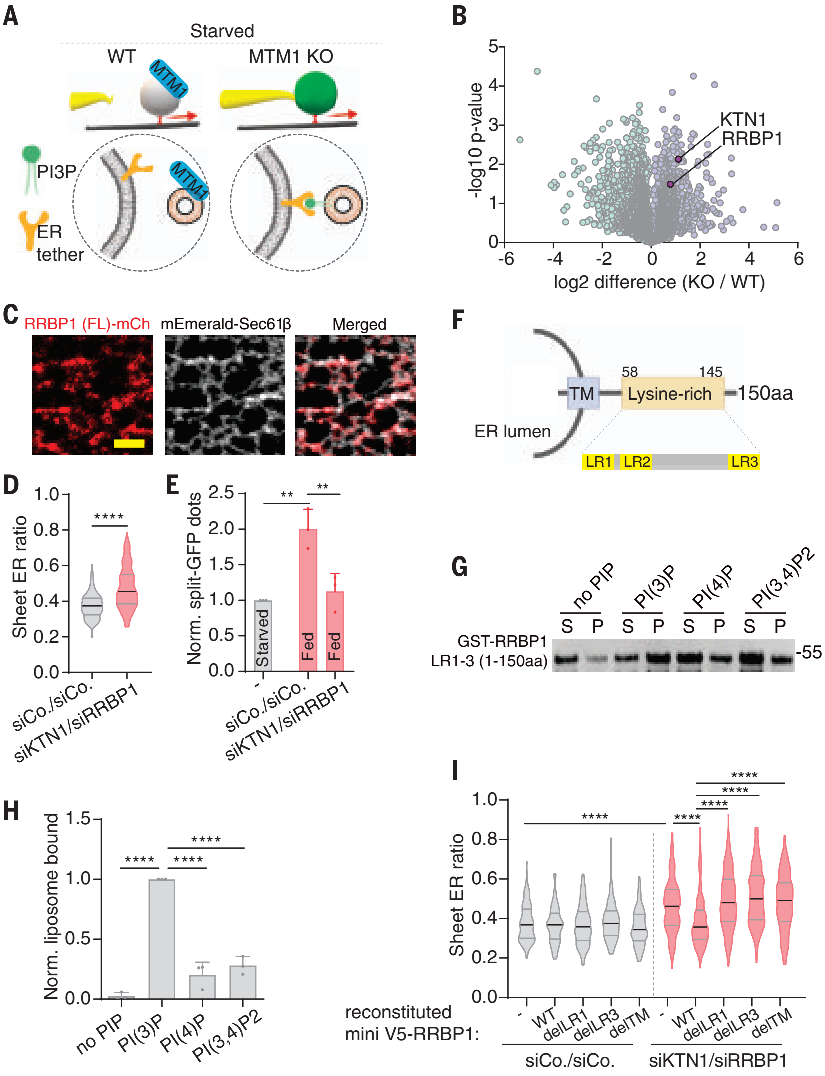

Fig. 3. Membrane contacts formed by ER ribosome-binding protein 1 and kinectin 1–mediated recognition of early endosomal PI(3)P control the tubular ER. (**A**) Starvation-induced dissociation of ER–early endosome (EE) contacts in WT but not in MTM1 KO cells. (**B**) Volcano plot of proximity biotinylated interactome of APEX2-Rab5A isolated from ER membranes of starved MTM1 KO versus WT HeLa cells. Dark purple: RRBP1 and KTN1. (**C**) Confocal images of HeLa cells coexpressing mEmerald-Sec61β (ER) and RRBP1 full length (FL)–mCherry. (**D**) Ratio of sheet/total ER in fed HeLa cells treated with control (siCo/siCo = 174) or KTN1+RRBP1 siRNAs (siKTN1/siRRBP1 = 221). (**E**) Normalized number of ER/EE contacts in control or KTN1/RRBP1-depleted fed HeLa cells. n = 3 independent experiments. (**F**) Schematic illustrating truncated mini-RRBP1 (amino acids 1 to 150). TM, transmembrane anchor; LR1-3, cytoplasmic lysine-rich regions 1 to 3. (**G**) GST-RRBP1-LR1-3 binds to PI(3)P liposomes. Supernatant (S) and liposomal pellet (P) fractions were analyzed by immunoblotting for GST. No PIP, liposomes lacking phosphoinositides. (**H**) Quantified data as in (G) from n = 3 independent experiments. (**I**) Ratio of sheet/total ER in control (siCo/siCo) or KTN1/RRBP1-depleted stable doxycycline-inducible HeLa cells expressing the indicated truncated RRBP1 protein (“mini-RRBP1”) variants [see (F)]. WT, wild-type V5-tagged mini-RRBP1; delLR1, mutant RRBP1 lacking lysine-rich region 1; delLR3, mutant RRBP1 lacking lysine-rich region 3; delTM, mutant RRBP1 lacking its transmembrane domain. siCo/siCo – (n = 111), WT (n = 129), delLR1 (n = 102), delLR3 (n = 120), delTM (n = 130); siKTN1/siRRBP1 – (n = 274), WT (n = 271), delLR1 (n = 326), delLR3 (n = 263), delTM (n = 288). Scale bars: 2 μm (yellow). n indicates the total number of cells analyzed from three independent experiments. Two-tailed Mann-Whitney test (D); one-way ANOVA with Tukey’s multiple comparisons (E); one-way ANOVA with Dunnett’s multiple comparisons test (H); Kruskal-Wallis test with two-sided Dunn’s multiple comparison test (I). $^{**}P \leq 0.01$, $^{****}P \leq 0.0001$. Data are median ± interquartile range [(D) and (I)]; data are mean ± SD [(E) and (H)].

MTM1 (Fig. 4, A and B, and fig. S9A). Further ultrastructural analysis by 3D FIB-SEM revealed the formation of an extensive cell-wide network of hyperfused mitochondria in starved WT cells. In contrast, starved MTM1 KO cells displayed an accumulation of small spherical mitochondria suggestive of exacerbated mitochondrial fission and defects in cristae morphology (Fig. 4, C to E, and fig. S9, B to D), whereas the total mitochondrial volume fraction was unchanged (Fig. 4F). Reduced mitochondrial network formation and defective ER reshaping were also observed in starved XLCNM patient–derived myoblasts (fig. S9, G and H). Defective mitochondrial morphogenesis was not a consequence of the altered expression of mitochondrial fusion- or fission-related proteins (*58*) such as mitofusin 1/2, OPA1 (*59*), and DRP1 or its hyperactive form (pS616-DRP1) in MTM1 KO cells (fig. S3, J and K). Moreover, acute rapalog-induced formation of ER–early endosome tethers to inhibit loss of ER tubules prevented the starvation-induced formation of a hyperfused mitochondrial network in WT cells (Fig. 4G and fig. S9, E and F), thereby phenocopying MTM1 loss. Conversely, reducing membrane contacts between the ER and early endosomes by depletion of RRBP1 and KTN1 led to the formation of hyperfused mitochondrial networks and expansion of the sheet ER in MTM1 KO cells (fig. S9, I to K). RRBP1 and KTN1 therefore act downstream of MTM1-mediated PI(3)P hydrolysis.

If reshaping of the tubular ER into sheets causally underlies the formation of a hyperfused mitochondrial network, one would expect experimental manipulations that reshape the ER to affect mitochondrial morphology. Consistently, we found that cellular depletion of either Rab10, a factor required for maintenance of the tubular ER (*60*); RRBP1 and KTN1; or the tubular ER-shaping protein reticulon 4 (*61*)—conditions that result in ER sheet expansion (fig. S10, A, C, D, and F)—cause the formation of an enlarged mitochondrial network in fed cells (fig. S10, B, C, E, and F). Mitochondrial hyperfusion was further induced by overexpression of the ER sheet–inducing membrane protein Climp63 (*46*) (fig. S10, G and H). Finally, we observed increased rates of mitochondrial fission in starved MTM1 KO cells (fig. S10, I to K, and movie S5), that is, conditions under which ER tubules accumulate. Collectively, these findings establish that the starvation-induced conversion of ER tubules to sheets by MTM1-mediated hydrolysis of PI(3)P at ER–early endosome contacts facilitates the formation of a functional mitochondrial network.

Defective ER morphogenesis in absence of endosomal MTM1 impairs mitochondrial metabolic rewiring during starvation

To probe the physiological consequences of defective mitochondrial morphogenesis, we monitored mitochondrial oxygen consumption and mitochondria-driven adenosine triphosphate (ATP) production in WT and MTM1 KO

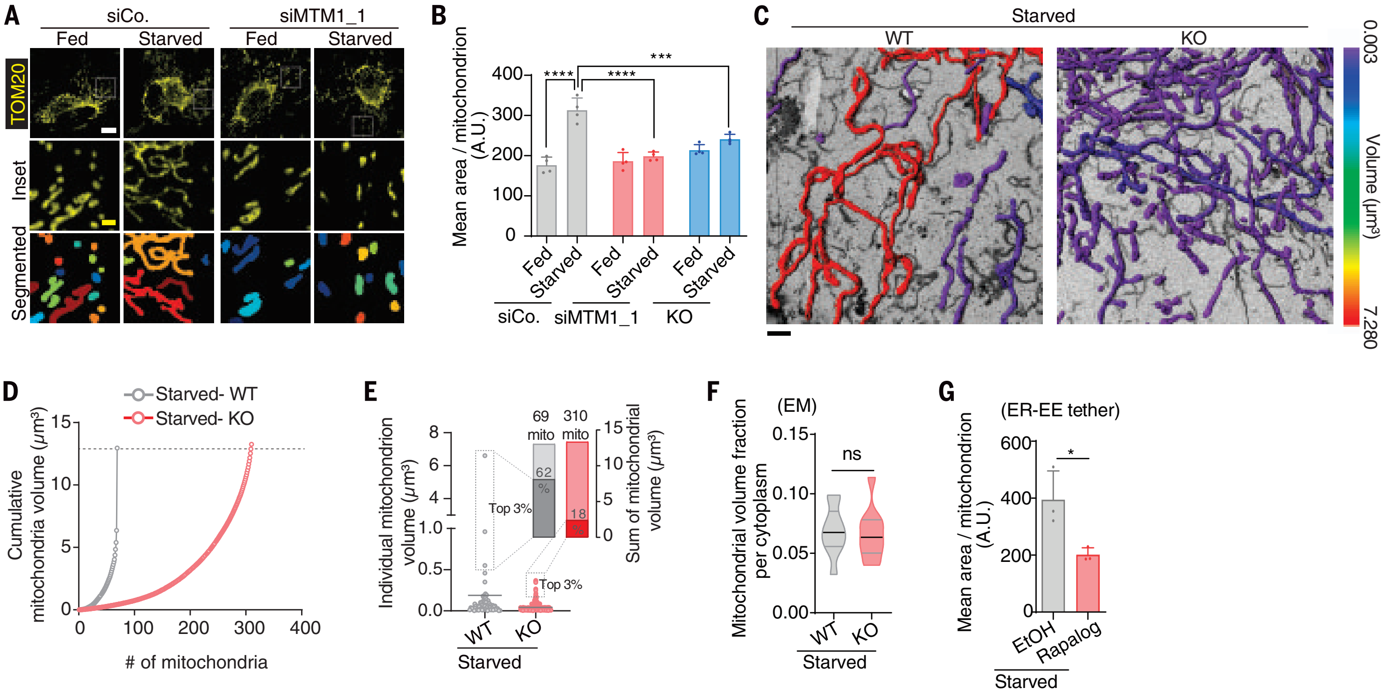

Fig. 4. MTM1-dependent ER reshaping is required for mitochondrial network formation during starvation. (**A**) Confocal images of mitochondria (TOM20) in fed or starved control (siCo) and MTM1-depleted (siMTM1_1) HeLa cells. (Bottom) Segmented mitochondria in ROI (yellow, 15 μm by 15 μm). (**B**) Mean area of individual mitochondrion per ROI from fed or starved WT or MTM1 KD or KO HeLa cells. siCo Fed = 345 ROIs, Starved = 418 ROIs; siMTM1_1 Fed = 354 ROIs, Starved = 440 ROIs; KO Fed = 343 ROIs, Starved = 322 ROIs from four independent experiments. Each ROI represents a single cell. (**C**) 3D rendering of mitochondria by FIB-SEM in starved WT and MTM1 KO HeLa cells. Heat bar reflects individual mitochondrial volumes. Images are representative of three cells. (**D**) Cumulative plot of mitochondrial volume distribution in starved WT versus MTM1 KO cells derived from FIB-SEM. (**E**) 3D volumes of individual mitochondria as in (C) were plotted. (Inset) The largest 3% of mitochondria occupied 62% of the total mitochondrial volume in WT (gray) but only 18% in KO (red) cells. The total volume of mitochondria in WT cells (69 mito = 12.95 μm^3) versus KO cells (310 mito = 13.25 μm^3) was unchanged. (**F**) Mitochondrial volume fraction in starved WT and MTM1 KO HeLa cells (n = 10) analyzed by stereological analysis of thin-sectioned electron micrographs. (**G**) Artificial ER–early endosome tethering prevents mitochondrial hyperfusion. Mean area of individual mitochondria per ROI from starved HeLa cells ± rapalog (Fig. 2N). EtOH = 251 ROIs, rapalog = 250 ROIs from three independent experiments. Each ROI represents a single cell. Scale bars: 10 μm (white), 2 μm (yellow), 1 μm (black). One-way ANOVA with Tukey's multiple comparisons (B); two-tailed unpaired t test [(F) and (G)]; $*P \leq 0.05$, $***P \leq 0.001$, $****P \leq 0.0001$; ns, nonsignificant. Data are mean ± SD [(B) and (G)] or median ± interquartile range (F).

cells using Seahorse technology. Starved MTM1 KO cells displayed severely reduced basal as well as maximal oxygen consumption rates resulting in significantly impaired mitochondrial ATP synthesis (Fig. 5, A and B, and fig. S11, A and B). As a consequence, starved MTM1 KO cells suffered from a pronounced reduction of total cellular ATP (Fig. 5C). Similar results were observed in cells, in which the ER was artificially tethered to early endosomes (Fig. 5D). No significant differences in mitochondrial basal oxygen consumption or mitochondrial ATP synthesis were detected in fed MTM1 KO cells, whereas the maximal oxygen consumption rate was marginally decreased (fig. S11, C to E). The mitochondrial membrane potential was unaffected by MTM1 loss, irrespective of the nutritional status of the cells (fig. S11F). As defective mitochondrial morphogenesis and cellular ATP depletion are associated with reduced cell viability, we probed whether MTM1 KO cells might be poised to undergo apoptosis under conditions of limited nutrient availability. Starved MTM1 KO cells indeed suffered from increased levels of cleaved caspase 3 and poly(ADP ribose) polymerase (PARP), common indicators of apoptotic cell death (fig. S11, G to I). However, defective mitochondrial morphogenesis in MTM1 KO cells was not a secondary consequence of increased apoptosis, as treatment of KO cells with the pan-caspase inhibitor Z-VAD-FMK effectively blocked apoptosis (fig. S11J) but failed to rescue defects in mitochondrial morphology (fig. S11K). We note that similar apoptotic phenotypes have been reported in starved OPA1 and mitofusin 1/2 KO cells defective in mitochondrial fusion (*62*).

These results indicate that MTM1-mediated reshaping of the tubular ER into sheets is required for the formation of a functional mitochondrial network and mitochondria-driven ATP production in starved cells. Previous work has shown that the effective transfer and utilization of fatty acids (FAs), a major substrate for mitochondrial ATP synthesis via β-oxidation, in starved cells requires mitochondria to be organized into a highly tubulated hyperfused network (*56*, *57*), although the exact underlying molecular mechanism is unclear. We therefore hypothesized that impaired mitochondrial ATP production in MTM1 KO cells might be a consequence of defective FA trafficking. We directly tested this by monitoring the fate of FAs in WT and MTM1 KO cells under different nutrient conditions. Depending on metabolic state, cytosolic FAs can be metabolized in mitochondria (e.g., during starvation) or stored in LDs (*54*, *57*, *63*), which exclusively form from the tubular ER (*55*, *64*). Consistently, we found that in WT cells, the number of LDs intermittently declined at the onset of starvation (≤2 hours), likely as a result of increased mitochondrial β-oxidation of FAs and blocked LD formation upon loss of the tubular ER, before eventually rising (Fig. 5E and fig. S11, L to N) owing to autophagy-promoted lipid buildup during sustained long-term (≥6 hours) starvation (*57*). In contrast, the number and total

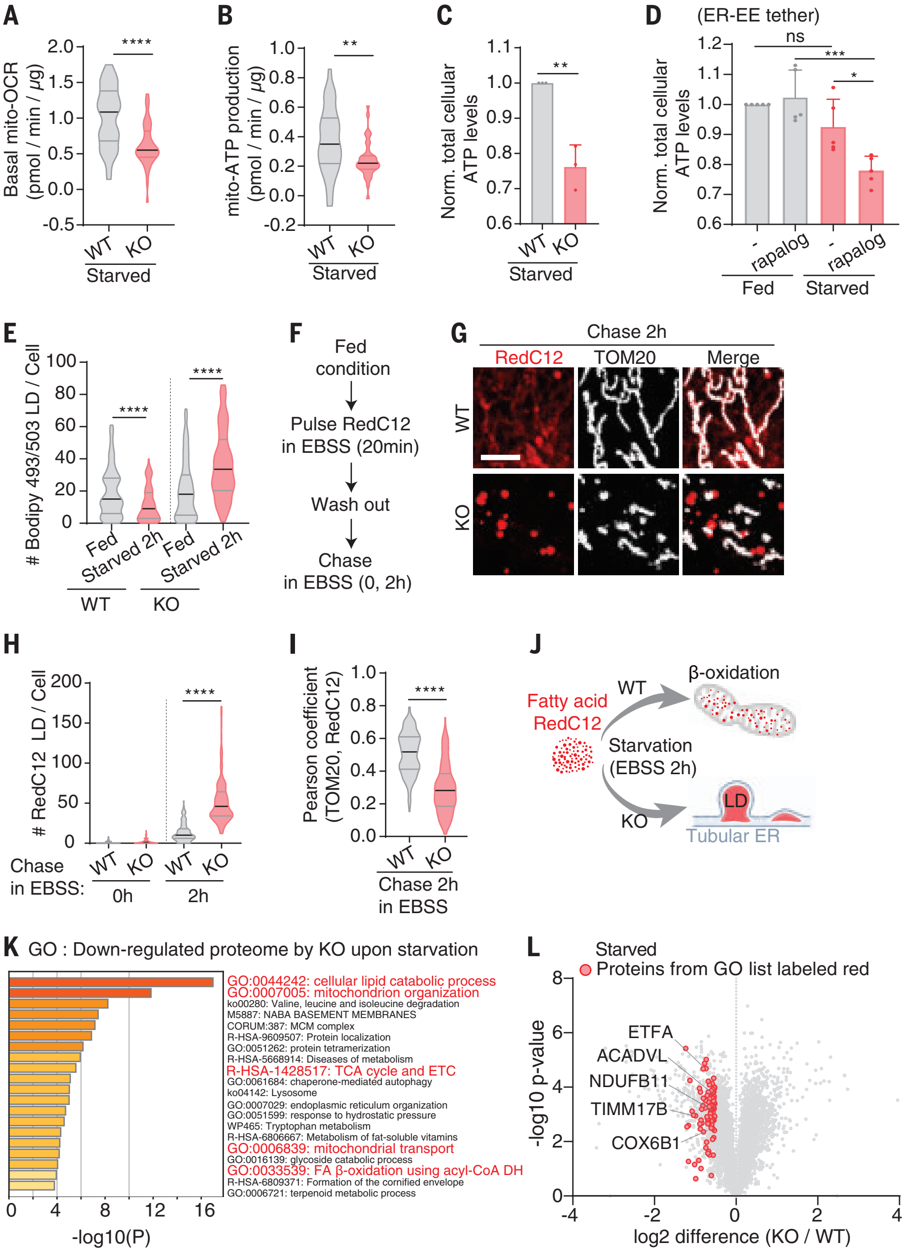

Fig. 5. Defective ER morphogenesis in absence of endosomal MTM1 impairs mitochondrial metabolic rewiring during starvation. (**A**) Basal mitochondrial oxygen consumption rate (mito-OCR) of starved WT or MTM1 KO HeLa cells. (**B**) Mitochondria-dependent ATP production of starved WT or MTM1 KO HeLa cells. (**C**) Normalized total cellular ATP levels of starved WT (set to 1) or MTM1 KO HeLa cells. *n* = 3 independent experiments. (**D**) Normalized total cellular ATP levels of fed versus starved HeLa cells ± rapalog (Fig. 2N). Data for fed cells (– rapalog) were set to 1. *n* = 5 independent experiments. (**E**) Number of BODIPY 493/503–labeled lipid droplets (LDs) in fed or starved (2 hours) WT or MTM1 KO HeLa cells. WT Fed (*n* = 157), Starved (*n* = 181); KO Fed (*n* = 153), Starved (*n* = 148). (**F**) Schematic depicting the pulse-chase assay to monitor FA mobilization. (**G**) Confocal images of WT and MTM1 KO HeLa cells pulse-labeled with RedC12 and chased for 2 hours in EBSS and stained for TOM20. (**H**) Number of RedC12-labeled LDs in WT or MTM1 KO HeLa cells chased for 0 or 2 hours in EBSS. 0h: WT (*n* = 126), KO (*n* = 112); 2h: WT (*n* = 139), KO (*n* = 118). (**I**) Pearson correlation coefficient of RedC12-labeled FAs and mitochondria (TOM20) from randomly selected 100 pixel by 100 pixel ROIs in WT or MTM1 KO cells as in (H). WT = 169 ROIs, KO = 203 ROIs from three independent experiments. (**J**) Schematic of trafficking of pulse-labeled FA RedC12 in WT and MTM1 KO cells during starvation. (**K**) Gene Ontology (GO) analysis of proteins depleted in starved MTM1 KO compared with WT HeLa cells. Terms related to fatty acid catabolism and mitochondrial function are highlighted in red. All of these proteins were unaltered in fed MTM1 KO cells. (**L**) Volcano plot of proteins depleted in starved MTM1 KO compared with WT HeLa cells. Red dots, proteins enriched from GO analysis shown in (K). Scale bars: 10 μm. *n* indicates the total number of cells analyzed from three independent experiments. Two-tailed Mann-Whitney test [(B), (E), (H), and (I)]; two-tailed unpaired *t* test [(A), (C), and (D)]; ns, nonsignificant, $*P \leq 0.05$, $**P \leq 0.01$, $***P \leq 0.001$, $****P \leq 0.0001$. Data are median ± interquartile range [(A), (B), (E), (H), and (I)] or mean ± SD [(C) and (D)].

volume of LDs increased in MTM1 KO cells at the onset of starvation (Fig. 5E and fig. S11O). LD accumulation persisted upon treatment of MTM1 KO cells with the pan-caspase inhibitor Z-VAD-FMK (fig. S11P). These results suggest that starvation-induced ER tubule-to-sheet conversion mediated by MTM1 orchestrates the reflux of FAs to mitochondria for β-oxidation while counteracting their storage in LDs. We directly probed this model by monitoring FA trafficking during early stages of starvation using the fluorescent FA analog BODIPY 558/568 C_{12} (Red C12) (Fig. 5F). Pulse-labeled Red C12 was efficiently transported to mitochondria in starved WT cells (Fig. 5G and fig. S11Q), consistent with prior data (*57*). In contrast, in starved MTM1 KO cells, Red C12 failed to accumulate in mitochondria and instead was targeted to LDs (Fig. 5, G to J). Impaired mitochondrial lipid and fatty acid catabolism was also clearly shown by the unbiased quantitative proteomic analysis of fed or starved WT and MTM1 KO cells using tandem mass tag (TMT) labeling. These analyses revealed a down-regulation of proteins involved in mitochondrial respiration and transport (Fig. 5K, fig. S11R, and tables S3 and S4), for example, mitochondrial very long-chain specific acyl–coenzyme A dehydrogenase, carnitine palmitoyltransferase 2, NADH:ubiquinone oxidoreductase, and the mitochondrial protein import factor TIMM17B (Fig. 5L), possibly as an indirect consequence of the observed structural mitochondrial defects in starved MTM1 KO cells (Fig. 4). None of these proteins were altered in KO cells under fed conditions (fig. S11S), indicative of a specific defect of MTM1 KO cells to appropriately respond to altered nutrient supply. These findings indicate that MTM1 mediates reshaping of the ER at the onset of starvation to drive the formation of a functional mitochondrial network and facilitate mitochondrial β-oxidation, which sustains ATP production. Conversely, defective ER morphogenesis in the absence of endosomal MTM1 impairs mitochondrial metabolic rewiring during starvation.

Discussion

How cells and tissues orchestrate adaptive changes in organelle dynamics and metabolism on a cell-wide scale has remained unclear.

Here we reveal a key role for early endosomal lipid signaling mediated by MTM1, a lipid phosphatase mutated in XLCNM in humans (*19*, *30*, *31*), in controlling the tubular ER and, thereby, mitochondrial morphology and metabolic function in the acute response to fluctuating nutrient conditions. This mechanism operates independent of ER-phagy, a process typically induced by prolonged starvation (*65*). We demonstrate that starvation-induced PI(3)P hydrolysis by endosomal MTM1 reduces previously undescribed membrane contacts between peripheral ER tubules and early endosomes. These contacts act as physical tethers that may transmit pulling forces from highly motile peripheral endosomes to the ER and are mediated by endosomal PI(3)P binding to RRBP1, a large ER membrane protein overexpressed in colorectal cancer (*66*), and its close paralog kinectin 1. Whether ER–early endosome membrane contacts also enable material exchange in vivo as shown for contact sites between the ER and the plasma membrane, the trans-Golgi network, or lysosomes (*37*) remains to be determined. Loss of ER tubules, possibly in conjunction with ER-independent mechanisms, drives mitochondrial network formation and, directly or indirectly, facilitates FA transfer to mitochondria to fuel β-oxidation and, thereby, mitochondrial ATP production to sustain cellular energy homeostasis. The precise relationship between mitochondrial morphogenesis, FA mobilization to mitochondria, and mitochondrial ATP production remains to be defined. Interestingly, ER sheets are favored over tubules from an energetic perspective (*67*, *68*) and, hence, should prevail under conditions of nutrient starvation when cellular energy levels are low. Consistent with this, it has recently been shown that the hepatic ER in obese mice is characterized by disorganized ER sheets and a predominance of ER tubules and accompanying defects in lipid metabolism (*69*). Our findings thus identify an organellar conveyor belt, in which the tubular ER serves as a membrane conduit that transmits nutrient-triggered changes (i.e., in glutamine and other amino acids) in early endosomal PI(3)P levels to metabolic organelles such as LDs and mitochondria [in agreement with (*56*)] to enable metabolic rewiring under conditions of limited nutrient supply and, possibly, in cancer [e.g., when RRBP1 is overexpressed (*66*)]. Defects in ER shape, mitochondrial morphogenesis, and cellular ATP depletion caused by loss of MTM1 function can explain the observed myofiber hypotrophy and defective sarcoplasmic reticulum organization in animal models of XLCNM (*16*, *17*) and in human patients who often appear undernourished (*19*, *30*, *31*). Furthermore, it is conceivable that reduced contact formation between early endosomes and ER tubules due to MTM1-mediated PI(3)P hydrolysis, in addition to its effects on ER shape and mitochondrial function, may facilitate endosomal exocytosis of β-integrins, a mechanism shown to be defective in XLCNM (*15*). How precisely early endosomal PI(3)P levels and MTM1 function are controlled by cellular nutrient status remains poorly understood. VPS34, the main PI(3)P-synthesizing enzyme on endosomes has been reported to be stimulated by fed signals (*70*), that is, conditions in which MTM1 activity is repressed.

The endosomal signaling lipid–based pathway to control oxidative cell metabolism uncovered in this work may synergize with other cellular mechanisms that impinge on the dynamics of metabolically active organelles. For example, it has been shown that the function and localization of lysosomes depend on motor proteins (*8*) as well as on their association with the ER (*41*) and are regulated by cellular nutrient status (*71*), which in turn affects nutrient signaling (*28*, *72*). Late endosomes (i.e., organelles distinct from the Rab5-positive early endosomes described here) have been shown to undergo fission at sites of contact with the ER that are molecularly and functionally distinct (*73*) from the ER–early endosome contacts identified in this study. Finally, mitochondria–lysosome contacts have been shown to regulate mitochondrial fission (*50*). Whether any of these contacts are subject to nutrient regulation and impact on cell metabolism will need to be addressed in future studies. Conceivably, lipid phosphatases including other members of the myotubularin family (*26*), many of which are linked to human disease, may play crucial physiological roles in the regulation of these and other membrane contacts.

Materials and methods

Materials

Plasmids

Plasmids used: mEmerald-Sec61β -C1 (Addgene #90992), mCh-Rab5 (Addgene #49201), ER-GCaMP6-1-150 (Addgene #86918), tdTomato-BICD2-FKBP (Addgene #64205), and mCh-Climp63 (mouse) (Addgene #136293). HA-BICD2-FRB was kindly provided by G. G. Farías. Plasmids for transient transfection (e.g., mCherry MTM1 WT, mRFP-FKBP-empty, mRFP-FKBP-MTM1 WT, mRFP-FKBP-MTM1 C375S, FRB-iRFP-Rab5A, mRFP-FKBP-Rab5A, TMEM192-3xHA-FRB, ERM-2xHA-FRB) were generated with the pcDNA3.1(+) vector and polymerase chain reaction (PCR) or ligation-based cloning. Note that ERM is the N-terminal ER membrane targeting sequence of residues 1 to 27 of ER-resident P450 oxidase 2C1. Full-length RRBP1 was amplified from pcDNA4 HisMax-V5-GFP-RRBP1 (Addgene #92150) and inserted into pcDNA3.1(+)-based mCherry expression vector with tags at its C terminus. PCR-amplified RRBP (amino acids 1–150) was inserted in pGEX4T-1 vector by ligation-based cloning. Plasmids for lentivirus transduction [e.g., mEmerald-Sec61β, mScarlet-Sec61β, 3xHA-APEX2-Rab5A, Halo-Rab5A, ERM-GFP11-p2a-GFP1-10-Rab5A, ERM-2xHA-FRB, ERM-2xHA-(EAAAK)x9-FRB, mRFP-FKBP-Rab5A, Rab5A-mRFP-FKBP, V5-RRBP1 1-150aa WT, V5-RRBP1 del PB1, V5-RRBP1 del PB3, V5-RRBP1 del TM] were generated with the pLVX-TetONE puro vector (Takara, Catalog 631849) by PCR, repetitive oligo annealing, or inverse PCR with Gibson assembly. All constructs were verified by double-stranded DNA sequencing.

Primary antibodies for immunoblots

Anti-GAPDH (glyceraldehyde-3-phosphate dehydrogenase; mouse, Sigma-Aldrich, G8795, 1:1000), anti-MTM1 (goat, Invitrogen, PA5-17972, 1:250), anti-Calnexin (rabbit, Abcam, ab75801, 1:2000), anti-calreticulin (rabbit, Thermo Fisher, PA 3-900, 1:1000), anti-Reticulon4 (Nogo) (mouse, Santa Cruz, sc-271878, 1:1000), anti-RPL26 (rabbit, Proteintech, 17619-1-AP, 1:1000), anti-RPL7 (rabbit, Proteintech, 14583-1-AP, 1:1000), anti-EEA1 (mouse, BD biosciences, 610456, 1:500), anti-Histone H1 (rabbit, Abcam, ab17729, 1:1000), anti-GST (mouse, Thermo Fisher, MA4-004, 1:1000), anti-KTN1 (rabbit, Proteintech, 19841-1-AP, 1:500), anti-RRBP1 (rabbit, Proteintech, 22015-1-AP, 1:500), anti-Clim63 (mouse, Enzo Life Sciences, ENZ-ABS669-0100, 1:2000), anti-TOM20 (mouse, Santa Cruz, sc-17764, 1:200), anti-p-DRP1 (S616) (rabbit, Cell signaling, 3455S, 1:500), anti-DRP1 (rabbit, Abcam, ab184247, 1:500), anti-MFN1 (rabbit, Proteintech, 13798-1-AP, 1:500), anti-MFN2 (rabbit, Proteintech, 12186-1-AP, 1:500), anti-OPA1 (rabbit, Proteintech, 27733-1-AP, 1:500), anti- GRP78/BIP (rabbit, Proteintech, 11587-1-AP, 1:3000), anti-CHOP (rabbit, Proteintech, 15204-1-AP, 1:500), anti-LC3-II (mouse, MBL, M152-3, 1:200), anti-Cleaved PARP(Asp214) (rabbit, Cell Signaling, 9541S, 1:1000), anti-Cleaved Caspase3(Asp175) (rabbit, Cell Signaling, 9661T, 1:250), anti-V5 (mouse, Invitrogen, P/N 46-0705, 1:1000), anti-Phospho-p70 S6 Kinase (Thr389) (rabbit, Cell signaling, 9205L, 1:500), anti-p70 S6 Kinase Antibody (rabbit, Cell Signaling, 9202L, 1:1000), anti-ATG5 (rabbit, Proteintech, 10181-2-AP, 1:1000).

Primary antibodies for immunofluorescence

Anti-calreticulin (rabbit, Thermo Fisher, PA 3-900, 1:200), anti-calreticulin (rabbit, Abcam, ab92516, 1:200), anti-Rab5A (mouse, BD biosciences, 610724, 1:100), anti-GFP (mouse, Invitrogen, A-11120, 1:500), anti-LC3-II (mouse, MBL, M152-3, 1:100), anti-HA (mouse, Santa Cruz, sc-7392, 1:500), anti-RFP (rabbit, MBL, PM005, 1:400), anti-LAMP1 (mouse, BD biosciences, 555798, 1:1000), anti-LAMP1 (rabbit, Cell signaling, 9091P, 1:300), anti-V5 (mouse, Invitrogen, P/N 46-0705, 1:200), anti-TOM20 (mouse, Santa Cruz, sc-17764, 1:500), anti-TOM20 (rabbit, Abcam, ab186734, 1:500), anti-TFEB (rabbit, Biomol, A303-673A, 1:200), Streptavidin, Alexa Fluor 647 conjugate (Thermo Fisher, S21374).

siRNAs

The small interfering RNAs (siRNAs) used were: Scrambled siControl 5′-CGUACGCGGAAUACUUCGA-3′, or Sigma MISSION Universal Negative Control (SIC001), siMTM1-1 5′-GATGCAAGACCCAGCGTAA-3′, siMTM1-2 5′-TATGAGTGGGAAACGAAATAA-3′, siMTM1-SP (ON-TARGETplus SMARTpool, Dharmacon, L-008036-00-0005), siMTMR1-1 5′-GAGATAGTGTGCAAGGATA-3′, siMTMR1-2 5′-CGCTGATACCAACAAGACAAA-3′, siMTMR2-1 5′-GGACATCGATTTCAACTAA-3′, siMTMR2-2 5′-CGGCCAAGTGTTAATGCTGTT-3′, siMTMR2-3 5′-GTAGAAAGTCTTCGGAATTTA-3′, siMTMR6-1 5′-GGACTACAAGATTTGTGAA-3′, siMTMR6-2 5′-CGGGACTACAAGATTTGTGAA-3′, siMTMR12-1 5′-CCAGGTGAACAGCTGCTTT-3′, siMTMR12-2 5′-GCAAGAGAATTAGCAAACTTA-3′, siMTMR12-3 5′- CGCTTCAAACATCAACGACAA-3′, siKTN1 (ON-TARGETplus SMARTpool, Dharmacon, L-010605-00-0005), siERLIN1 (ON-TARGETplus SMARTpool, Dharmacon, L-015639-01-0005), siERLIN2 (ON-TARGETplus SMARTpool, Dharmacon, L-017943-01-0005), siRRBP1 (ON-TARGETplus SMARTpool, Dharmacon, L-011891-02-0005), siOSBPL8 (ON-TARGETplus SMARTpool, Dharmacon, L-009508-00-0005), siITPR2 (ON-TARGETplus SMARTpool, Dharmacon, L-006208-02-0005), siARL8B (ON-TARGETplus SMARTpool, Dharmacon, L-020294-01-0005), siRTN4 (ON-TARGETplus SMARTpool, Dharmacon, L-010721-00-0005), siRab10 (ON-TARGETplus SMARTpool, Dharmacon, L-010823-00-0005), siProtrudin 5′-CTTCTTGATCCAGCTGGAGG-3′, siATG5 (ON-TARGETplus SMARTpool, Dharmacon, L-004374-00-0005).

Cell culture

HeLa, human embryonic kidney 293 T (HEK293T), and Cos7 cells were obtained from ATCC. Cells were cultured in Dulbecco's modified Eagle's medium (DMEM) high (4.5 g/liter glucose, Thermo Fisher, 41965062) containing 10% fetal bovine serum (FBS; Thermo Fisher, 10270106) and 50 units/ml penicillin, 50 mg/ml streptomycin (Thermo Fisher, 15070063). Cells were routinely tested for mycoplasm contamination. The human myoblast cell line KM1288 was derived from the deltoid muscle of a patient with XLCNM and carries a missense genomic mutation (c.205<T) in exon 4 of the *MTM1* gene (*20*). The human myoblast cell strain NL15 was derived from the quadriceps of a patient with XLCNM and carries the missense genomic mutation R241C in the *MTM1* gene (*21*). The control myoblast cell line AB1190 was derived from the paravertebral muscle of a healthy individual. AB1190 and KM1288 were immortalized as described before (*74*). Myoblasts were cultured in the homemade medium: 1 volume medium 199 (Thermo Fisher, 41150020) + 4 volumes DMEM high, supplemented with 20% FBS, Fétuin (25 μg/ml, Thermo Fisher, 10344026), human epidermal growth factor (5 ng/ml, Thermo Fisher, PHG0311), basic fibroblast growth factor (0.5 ng/ml, Thermo Fisher, PHG0026), insulin (5 μg/ml, Sigma, 91077C-1G), and dexamethasone (0.2 μg/ml, Sigma, D4902-100mg). To induce starvation, cells were washed with prewarmed Earle's balanced salt solution (EBSS; Thermo Fisher, 24010043) five times for 10 s each and then incubated in EBSS in 5% CO_2 at 37°C for 2 hours, unless indicated otherwise. This washing step is important to fully remove remaining nutrients and growth factors. For steady-state (fed) conditions, cells were incubated overnight in fresh complete DMEM medium supplemented with 10% FBS. For the experiment in fig. S1M, EBSS was supplemented, as indicated, with 5% dialyzed FBS (One Shot format, Gibco, A3382001) or insulin (final at 5 μg/ml) or glucose (final at 4.5 g/liter) or sodium pyruvate (final at 1 mM) (Gibco, 11360070) or MEM essential amino acids (50x) solution (Sigma, M5550) (final 1x dilution) or MEM solution or nonessential amino acids (100x) (Gibco, 11140050) (final 1x dilution) or L-glutamine (final at 4 mM) (Gibco, 25030081).

CRISPR-Cas9–mediated genome engineering

Guide RNAs targeting genomic human MTM1 exon 2 (sgMTM1: 5′ AGTTGATGCAGAAGCCATCC 3′) was cloned into Lenti-CRISPRv2 (Addgene plasmid # 52961). HeLa cells were transfected using FuGene-6 as a transfection reagent. Cells were t selected with puromycin (2 μg/ml) for 72 hours. Surviving cells were diluted and plated into 96-well plates with a density of 1 cell per well. Expanded colonies were screened by immunoblotting using anti-MTM1 antibodies.

Generation of doxycycline-inducible stable cell lines

Lentivirus was generated by transient transfection of HEK293T cells seeded in 10-cm cell culture plates at 80 to 90% confluency with pCMV delta R8.2 (3.5 μg), VSV-G (0.5 μg), and pLVX-TetONE puro-based constructs (4 μg) combined with 16 μl of JetPrime in 400 μl JetPrime buffer. After 16 hours of transfection, cells were replenished with 7 ml fresh DMEM. After 48 hours, the supernatant was collected, and cellular debris was removed by centrifugation (3000 rpm, 20 min). Viral supernatant (4 to 5 ml) was added to the cells with polybrene (Merck, Cat.#TR-1003-G) at 10 μg/ml. Cells were incubated with virus for 16 hours and then replenished with fresh DMEM containing puromycin (2 μg/ml) followed by selection for 2 to 3 days. After selection, cells were stabilized for 3 to 4 days in culture without puromycin. For the induction of protein expression, doxycycline (1 μg/ml) was added for 16 hours.

Transient transfection

HEK293T and HeLa cells and myoblast cells were transfected with plasmids using jetPRIME (PolyPlus, 101000001) or FuGene-6 (Promega, E2691) or ViaFect (Promega, E4981) according to the manufacturer's protocol, respectively [e.g., DNA (micrograms): reagent (microliters) ratio of 1:2]. After 18 to 24 hours of transfection, cells were further treated and analyzed. For siRNA transfection, cells were transfected with the indicated siRNA (20 nM) using jetPRIME according to the manufacturer's protocol. After 48 hours of transfection, cells were further treated and analyzed.

Dyes and pharmacological inhibitors

Dyes

TMRE (tetramethylrhodamine ethyl ester perchlorate): Cell signaling, Mitochondrial membrane potential assay kit, #13296, 200 nM). Lysotracker Red DND-99: Thermo Fisher, L7528, 1 μM for 45 min. Note that for fixed cell samples, buffer containing detergents should not be used, in order to preserve lysotracker staining. BODIPY 493/503: Thermo Fisher, D3922, 2 μM for 20 min in serum free media. No detergent-containing buffers should be used. Before treatment, cells were washed twice with serum-free media. BODIPY 558/568 C_{12}: Thermo Fisher, D3835, 1 μM for 20 min in serum-free media. Before labeling, cells were washed twice with serum-free media. For TOM20 antibody co-staining, fixed samples were permeabilized with 20 μM digitonin for 5 min.

MitoTracker Deep Red FM: Thermo Fisher, M22426, 100 nM for 30 min in full medium. CellMask Deep Red Plasma membrane Stain: Thermo Fisher, C10046, fixed cells were stained for 20 min at 1:2000 dilution. Halo-tag ligands (CA-JF646) were chemically synthesized as described in (*75*) and used at 100 nM for 10 to 16 hours.

Pharmacological inhibitors

VPS34-IN1 (Selleckchem, S7980, 1μM), apilimod (Echelon Biosciences, B-0308, 50nM), rapalog (Takara, A/C Heterodimerizer 635056, 0.5 μM), nocodazole (Sigma, M1404, 5μM), dimethyl sulfoxide (DMSO; Sigma, D2650), thapsigargin (Sigma, T9033, 3μM), Torin1 (Tocris, Cat. No. 4247, 1 μM), Z-VAD-FMK (Tocris, Cat. No. 2163, 25 μM).

RNA isolation, RT-PCR, and qRT-PCR

Total RNA was isolated using the RNeasy Plus Mini Kit (Qiagen) according to the manufacturer's instructions. Quantification of RNA yields was done with a multimode microplate reader (SPECTROstar Nano from BMG Labtech).

A reverse transcription kit (SuperScript IV; Invitrogen) was used to reverse transcribe RNA (800 ng) in a 20 μl reaction using oligo(dT) and random hexamer Primers. Reverse transcription polymerase chain reaction (RT-PCR) was performed with specific primers set against each gene with indicated cycles. For quantitative reverse transcription polymerase chain reaction (qRT-PCR), SYBR Green Master Mix (BioRad) was used according to the manufacturer's protocol with BioRad CFX Connect.

qRT-PCR primers

GAPDH Fwd: 5′-CTTCGCTCTCTGCTCCTCCT-3′; Rev: 5-GTTAAAAGCAGCCCTGGTGA-3′, MTM1 Fwd: 5′-GTTTGAGATCCTCACGAGATACG-3′; Rev:5′-GTCCATCCATCCACGTTAAACTT-3′, MTMR1 Fwd: 5′-CCTTGATGTTCCCCTTGGAGT-3′; Rev:5′-GTGCCTGTCCGTTAGAAAGAG-3′, MTMR2 Fwd: 5′-GTGGAAAGCGAAGCAAAGAAG-3′; Rev:5′-CTTGGCCGGGCATCAAATATAA-3′, MTMR3 Fwd: 5′-GACTGAACAACGCAATCCGAC-3′; Rev:5′-CCTTGAAGTTACATGCTCCCC-3′, MTMR4 Fwd: 5′-CCAAGCCAAGGATCTGTTCCC-3′; Rev:5′-GCCGGTAGTTAGAGATGGCAA-3′, MTMR5 Fwd: 5′-CGACCACACGGAGGTGTTC-3′; Rev:5′-GGTTCCCAATCACGTTCTCCA-3′, MTMR6 Fwd: 5′-GTTCCCCGGATAGCAAGCAAA-3′; Rev:5′-GTGGCTGACTACATCGACAAAT-3′, MTMR7 Fwd: 5′-TCCGCTTGGTAGATCGAGTGT-3′; Rev:5′-TTTTCCACGAATATGACATGGGT-3′, MTMR8 Fwd: 5′-TGCACTCCATCACATTGCCA-3′; Rev:5′-GGCACACAAGGTCAGAATCTAA-3′, MTMR9 Fwd: 5′-TGAAGCTCTTCGGAAGGTAGC-3′; Rev:5′-GTGGCTGACCACTTCGCATAA-3′, MTMR10 Fwd: 5′-ATCCACTTGCCTTCCAGAATACA-3′; Rev:5′-CACAAGAGCACTGCCGTTAGA-3′, MTMR11 Fwd: 5′-GCTGCTCAGAGTTGGTTTTGA-3′; Rev:5′-CCCCGAATACTGTTGGGCTT-3′, MTMR12 Fwd: 5′-GGCTCCTAAACTGCTTAAACGA-3′; Rev:5′-GTTGCCTTTGGTCCGTTCCA-3′, MTMR13 Fwd: 5′-TCATCGTGGTAGGCTATGACC-3′; Rev:5′-CCAGGCTGACAAAACAACTCA-3′, MTMR14 Fwd: 5′-GGAGTTCTCCCGGACTCAGTA-3′; Rev:5′-AACAGTAGTCTCGGCCAAACA-3′.

Immunoblot analysis

Cells were lysed with radioimmunoprecipitation assay (RIPA) buffer (50 mM Tris–Cl pH 7.5, 150 mM NaCl, 1% NP-40, 0.5% sodium deoxycholate, 0.1% SDS) containing protease and phosphatase inhibitors. Lysates were incubated for 10 min on ice before centrifugation at 17,000*g* for 10 min at 4°C. Protein concentration was measured by Bradford or bicinchoninic acid (BCA) assays. Cell lysates in Laemmli sample buffer were boiled for 10 min. Between 20 and 40 μg of protein was resolved by SDS–polyacrylamide gel electrophoresis (SDS-PAGE). Immunoblotting was done on nitrocellulose membranes. Membranes were incubated with the indicated primary antibodies at 4°C overnight. The next day, bound primary antibodies were detected by incubation with IRDye 680/800CW-conjugated or horseradish peroxidase (HRP)–conjugated secondary antibodies via the Odyssey Fc Imaging system (LI-COR Biosciences).

Light microscopy

Immunocytochemistry

Cells were seeded on Matrigel-coated coverslips (BD/Corning), fixed in 4% paraformaldehyde (PFA) for 15 to 20 min at room temperature (RT). Cells were washed three times with phosphate-buffered saline (PBS) before incubation with 3% bovine serum albumin (w/v) in 0.3% PBST (Triton X-100) for 20 min. Using the same buffer, the cells were incubated with primary antibodies for 2 hours at RT, washed three times with 0.3% PBST, and then incubated with secondary antibodies for 1 hour at RT. After washing with 0.3% PBST, cells were mounted with Hoechst 33258 (Invitrogen, H3569, 1:2000) to counter stain nuclei. Images were acquired on Zeiss 710 or 780 Laser Scanning Confocal Microscopes using ZEN.

Note for the specific staining conditions: For calreticulin staining, cells were fixed with 37°C 4% PFA for 34 min at 37°C. For Rab5A staining, cells were fixed with 37°C 4% PFA for 8 min at 37°C. For LC3-II staining, cells were permeabilized with 20 μM digitonin for 5 min at RT. After permeabilization, all subsequent procedures were done in PBS.

PI(3)P staining

Cells were fixed in 2% PFA for 15 min at RT, washed twice in PBS with 50 mM NH_4Cl, and permeabilized with 20 μM digitonin in buffer A (20 mM PIPES pH 6.8 with NaOH, 137 mM NaCl, 2.7 mM KCl) for 5 min. Note that permeabilization is critical for successful PI(3)P staining, so depending on the batch of digitonin, one might need to optimize the concentration and incubation time.

Cells were washed three times in buffer A before addition of purified GFP (or mCherry)-$2xFYVE^{Hrs}$ at 0.25 μg/ml in buffer A with 5% normal goat serum, 50 mM NH_4Cl for 1 hour. Samples were washed and decorated with antibodies against GFP or RFP in buffer A with 5% normal goat serum, 50 mM NH_4Cl for 2 hours. Cells were washed three times in buffer A, incubated for 1 hour with secondary antibodies in buffer A with 5% normal goat serum, 50 mM NH_4Cl. Samples were washed three times with buffer A, cells were postfixed for 5 min in 2% PFA, washed three times in PBS, and mounted with Hoechst 33258. Fluorescent sum intensity was measured from individual cells and normalized to the level of PI(3)P detected in fed cells set to 1.

Live-cell imaging

Cells (6×10^3 to 8×10^3) were seeded on Matrigel-coated 8-well chamber slides (ibidi, 80827). The next day, live-cell imaging was carried out using Nikon-CSU Yokogawa Spinning disk (CSU-X1) microscope equipped with an EMCCD Camera (Andor AU-888) at 37°C in the presence of 5% CO_2. Images were acquired using Nikon Elements.

Image analysis and quantification

Acquired images were first segmented to resolve individual cells by manually drawing each cell boundary using the Fiji freehand selection tools combined with Clear Outside option. Individual cell image files were saved in the input folder and batch processed in CellProfiler [v4.1.3 (76)] or in Fiji. CellProfiler pipeline modules used in this study were posted at https://cellprofiler.org/published-pipelines.

Sheet-to-tubular ER ratio

Total ER (calreticulin or mEmerald-Sec61β) segmentation was done using a three-class Otsu threshold followed by conversion into binary images. ER area was then measured using the MeasureObjectSizeShape module in CellProfiler. From the same image, sheet ER was segmented in a similar manner except using the Minimum Cross-Entropy threshold. Depending on signal-to-noise ratio and image quality, threshold settings (e.g., Threshold smoothing scale, correction factor) were adjusted using the IdentifyObjects module in CellProfiler. Sheet ER area was then divided by total ER area using CalculateMath module in the same pipeline of CellProfiler. Calculated sheet ER area/total ER area ratio was defined as "Sheet ER ratio."

Mean area and number of mitochondria per ROI

Regions of interest (ROIs; e.g., 15 μm by 15 μm) were randomly generated from individual cells in Fiji, exported to CellProfiler, and filtered with a Gaussian filter module with 1 or 2 sigma. ROIs were then processed using the EnhanceOrSuppressFeatures module with the following options: Operation = "Enhance," Feature type = "Neurites," Enhancement method = "Tubeness," Smoothing scale = "1." After binarization, mitochondria were segmented using the Robust Background Threshold in the IdentifyObjects CellProfiler module. The number and area of individual mitochondria per ROI were calculated using MeasureObjectSizeShape module in CellProfiler.

Lysosome position

Images were processed in CellProfiler using the EnhanceOrSuppressFeatures module with the following options: Operation = "Enhance," Feature type = "Speckles," Feature size = "4-6." Lysosome were then segmented using Robust Background threshold in the IdentifyObjects module. The distance between individually identified lysosomes from the cell centroid was calculated using the RelateObjects module in CellProfiler. The standard deviation of the distance of lysosomes from the centroid define the extent of lysosomal dispersion or clustering.

Early endosome distribution

Rectangular ROIs (80 pixels by width pixels ranging from cell center to cell boundary) were randomly selected from individual cells in Fiji and processed using the EnhanceOrSuppressFeatures module with the following options: Operation = "Enhance," Feature type = "Speckles," Feature size = "4-6." A Gaussian filter with sigma = 1 or 2 was applied in CellProfiler. Early endosomes and lysosomes were segmented using two-classes Otsu and robust background thresholds using the IdentifyObjects module. To compare the partitioning of early endosomes and lysosomes between the cell center and the periphery, segmented individual objects were shrunken to a dot using the ExpandOrShrinkObjects module with the "Shrink objects to a point" option in CellProfiler and converted into binary image files. The MeasureObjectIntensityDistribution module was then used to measure the intensity distribution from each object's center to its boundary within a set of bins with the following options: Bin = "5," Measurement = "Fraction at distance." The relative intensity fraction among the five bins was calculated from the binary images in CellProfiler. This intensity value indirectly represents the fraction of endosomes per bin.

Fluorescent imaging of ER–early endosome contacts and dynamics

Tubular ER segmentation of 100 pixel by 100 pixel ROIs from the cell periphery were generated using the Minimum Cross-Entropy threshold option in the IdentifyObjects module, and the ExpandOrShrinkObjects module with Operation = "Skeletonize each object," and subsequent ExpandOrShrinkObjects module with Operation = "Expand objects by a specified number of pixels" setting with 1-pixel expansion in CellProfiler. Early endosomes and lysosomes from the same image were segmented as described above. Segmented individual objects were then shrunken to a dot using the ExpandOrShrinkObjects module with "Shrink objects to a point" option, followed by Operation = "Expand objects by a specified number of pixels" setting with 1-pixel expansion. To calculate the number of endosomes that contact the ER, the MeasureObjectNeighbors module in CellProfiler was operated with the following options: Method to determine neighbors = "Within a specified distance" setting distance = 1 pixel. If the processed tubular ER and endosomes overlapped with each other at least by 1 pixel, a contact was scored.

Split GFP ER–early endosome contact sensor

To quantitatively determine the number ER–early endosome membrane contacts by measuring the number of GFP puncta, images were blurred with a Gaussian filter (sigma = 1 or 2, depending on the signal-to-noise ratio), background was subtracted with a rolling ball radius of 50 pixels, and segmented using the Find Maxima tool with prominence = 10 in Fiji.

STED image analysis of ER–early endosome contact

ROIs (8 μm by 8 μm) were randomly generated from individual cells in Fiji, exported to CellProfiler, processed using the EnhanceOrSuppressFeatures module with the following options: Operation = "Enhance," Feature type = "Speckles," with subsequent Gaussian filter module with 1. This allowed the segmentation of early endosomes via robust background thresholds using the IdentifyObjects module. Segmented early endosomes were then converted to binary images using the ConvertObjectsToImage module. ER images were filtered with a Gaussian filter module with 1 and converted to binary images using the Threshold module. The MeasureImageOverlap module was used to analyze the fractional overlap between the ER and early endosomes.

Lipid droplets (BODIPY 493/503, Red C12)

Lipid droplet images were blurred with a Gaussian filter (sigma = 1), enhanced using the EnhanceOrSuppressFeatures module (Operation = "Enhance", Feature type = "Speckles" with size = 10), and then segmented by the three-classes Otsu threshold option in CellProfiler. Segmented objects were further filtered on the basis of their measured sizes and intensities using the FilterObjects module in CellProfiler to minimize spurious detections. To measure the volume of lipid droplets, z-stacked confocal images were analyzed using the 3D objects counter plug-in in Fiji.

Pearson coefficient

To quantitatively assess colocalization between two channels, two or three randomly chosen 100 pixel by 100 pixel ROIs from the cell periphery were blurred with a Gaussian filter (sigma = 1). Pearson's coefficients were calculated using the Coloc2 plugin in Fiji or the MeasureColocalization module with correlation option in CellProfiler.

Super-resolution microscopy

Stimulated emission depletion (STED) images were taken with either a Leica SP8 TCS STED microscope (Leica Microsystems) for fixed samples or a STEDYCON (Abberior Instruments GmbH, Göttingen) for live cell imaging. Leica SP8 TCS STED microscope was equipped with a pulsed white-light excitation laser [WLL; ~80-ps pulse width, 80 MHz repetition rate (NKT Photonics)] and a STED laser for depletion (775 nm). The system was controlled by the Leica LAS X software. For images of mEmerald-Sec61β, fixed cells were further stained for GFP-Booster nanobody conjugated to Atto647N (Chromotek, gba647n-100, 1:200). Fluorophore specific excitation (Ex.) and emission filter (EmF.) settings: Atto647N (Ex.: 640 nm; EmF.: 650 to 700 nm). Time-gated detection was set from 0.3 to 6 ns. The fluorescence emission signal was collected by hybrid detectors (HyD). Images were acquired with a HC PL APO CS2 100×/1.40 NA oil objective (Leica Microsystems) in a pixel size of 18.9 nm by 18.9 nm. STEDYCON was mounted on the Nikon Eclipse Ti research microscope equipped with a Plan APO 100x/1.45 NA oil objective (Nikon). Excitation laser with a wavelength of 640 nm was used for the Halo ligand JF647 fluorescence. The wavelength of the STED laser was 775 nm. Live cells expressing Halo-Sec61β were imaged at 37°C degree with a pixel size of 20 nm by 20 nm.

Focused ion beam milling scanning electron microscopy (FIB-SEM)

Cells were fixed with 2% glutaraldehyde (GA) in PBS, washed with 0.1 M cacodylate buffer, and embedded in Durcupan following a modified rOTO protocol with 1% (w/v) OsO4/1.5% (w/v) K3Fe(CN)6 in 0.1 M cacodylate buffer (pH 7.4); 0.2% (w/v) thiocarbohydrazide in water; 1% OsO4 in water, 1% aqueous uranyl acetate with corresponding washes in between and subsequent acetone dehydration and resin infiltration. For polymerization, coverslips were mounted onto pre-polymerized resin blocks and placed into a heating cupboard for 48 hours. After polymerization, coverslips were removed by liquid nitrogen treatment, and blocks were glued to SEM aluminum stubs with conductive silver epoxy and carbon sputter coating (≈30 nm).

Helios 5CX FIB-SEM autoslice and view workflow was used to section and image the embedded cells. FIB was run at 30 kV, 0.23 nA, and 10-nm milling step. Cross section images were scanned at 1.5 to 2 kV and 86 pA to 0.17 nA. Dwell time was 5 μs at 3.37-nm pixel resolution and ICD detection. The resulting 3D stacks were binned to isotropic 10-nm voxel resolution. Alignment, segmentation of mitochondria, and analysis of ER networks were performed using Microscopy Image Browser, 3D visualization was done using Imaris. To access how continuous or fenestrated the ER is, the length of ER cisternae was measured in several distantly positioned 2D sections from FIB-SEM stacks. Sections for measurements from each cell were randomly chosen and were at least 1 μm apart from each other.

For 2D analysis of mitochondrial cristae length, ultrathin sections of cells were collected onto carbon-coated coverslips and imaged with a Helios 5CX SEM. The length of cristae was measured using Image J and normalized per mitochondrial cross-section perimeter.

For 2D analysis of ER–early endosome membrane contacts, 5 nm BSA-gold was allowed to internalize into HeLa cells for 5 min to reach early endosomes. Cells were washed before fixation with 2% GA. Cells were processed for EM analysis as described above. Ultrathin sections mounted onto EM grids were imaged using a Zeiss 900 transmission electron microscope and ER–early endosome contact sites were measured in Fiji.

Volume fraction analysis was performed on ultrathin sections mounted on wafers and scanned with a directional back-scatter detector at 2 kV, 0.34 nA, 5-μs dwell time. A measurement grid (1 μm^2 per point) was superimposed over cellular profiles and the reference volume (cytoplasm), as well as the relative volumes of the ER, and mitochondria were estimated according to stereological principles.

APEX2 proximity labeling experiments

HeLa cells stably expressing doxycycline-inducible 3xHA-APEX2-Rab5A were pretreated with doxycycline for one day. Cells were then incubated with 500 μM phenol-biotin (Sigma, SML2135) at 37°C for 30 min. To enable efficient biotinylation, cells were treated with 1 mM hydrogen peroxide and incubated at RT for 1 min. The reaction was terminated by removing the medium and the addition of ice-cold quenching buffer (10 mM sodium azide, 10 mM sodium ascorbate, 5 mM Trolox in PBS). Cells were washed with PBS, lysed with RIPA buffer (see above section on immunoblotting), and centrifuged at 17,000*g* for 10 min at 4°C. The protein concentration of the resulting supernatant was determined using the Bradford assay. Then, 150- to 200-μg samples were saved as whole cell lysate (WCL) control, while 1000 or 1500 μg of lysates were incubated with 40 μl of Streptavidin Magnetic Beads (Thermo Fisher, 88817) overnight, nutating at 4°C. Magnetic beads were washed twice with RIPA buffer, once with 1 M KCl, once with 0.1 M Na_2CO_3, once with 2 M Urea in 10 mM Tris-HCl, pH 8.0, two times with RIPA buffer, and finally eluted with Laemmli sample buffer in the presence of 2 mM biotin. WCL and eluate samples were analyzed by SDS-PAGE gels and immunoblotting. For quantification, the band intensities of eluted endogenous MTM1 or EEA1 were normalized to the band intensity of self-biotinylated Rab5A in Streptavidin-HRP blots (Fig. 2B and fig. S4B).

ER isolation and biotinylated protein collection for liquid chromatography combined with mass spectrometry (LC-MS)

HeLa WT or MTM1 KO cell line stably expressing doxycycline-inducible 3xHA-APEX2-Rab5A were seeded in 15-cm dishes with 17 × 10^5 cells (WT = 6 dishes, KO = 3 dishes) in the presence of doxycycline for 16 hours before biotinylation. The next day, cells at ~85% confluency were treated with 500 μM phenol-biotin and hydrogen peroxide to induce biotinylation, quenched, washed once with isolation buffer (225 mM mannitol, 75 mM sucrose, 30 mM Tris-HCl pH 7.4, 0.1 mM EGTA), and, finally, scraped into 1 ml of the same buffer resulting in ~2 ml total volume. Half a milliliter of this sample was saved (WCL) as a control. The remaining 1.5 ml was homogenized using a 2 ml Dounce homogenizer (~100 to 120 strokes) on ice in the presence of protease and phosphatase inhibitors. To isolate light membranes containing the ER, the material was centrifuged twice at 600*g* for 2 min each. The pellet (F1) including nuclei and cell debris was resuspended in 150 μl RIPA buffer. The remaining supernatant was centrifuged twice at 7000*g* for 20 min each. The resulting pellet (F2) including the mitochondrial fraction was resuspended in 150 μl RIPA buffer and further fractionated by centrifugation at 20,000*g* for 60 min to pellet light ER membranes (F3). This ER-enriched membrane fraction was resuspended in150 μl RIPA buffer. Protein concentration was determined using the Bradford assay. To isolate biotinylated proteins, 130 μg of WCL or F3 fraction was rotated in the presence of Streptavidin Magnetic Beads. Eluted biotinylated proteins were reduced (5 mM dithiothreitol, 30 min at 55°C), alkylated (15 mM iodacetamide, 20 min at RT in the dark), and submitted to LC-MS analysis (samples from two independent experiments).

LC-MS analysis of affinity-purified samples

Proteins were loaded on SDS-PAGE and subjected to in-gel digestion. In brief, gel bands were excised, and protein digestion was carried out using trypsin at an enzyme-to-protein ratio of 1:100 (w/w) at 37°C overnight. LC-MS measurement was achieved by reverse phase high-performance liquid chromatography (RP-HPLC) on a Thermo Scientific Dionex UltiMate 3000 system connected to a PepMap C-18 trap-column [0.075 mm by 50 mm, 3-μm particle size, 100-Å pore size (Thermo Scientific)] and a 200 cm μPAC column was used (PharmaFluidics, Ghent, Belgium) with 750 or 350 nl/min flow rate with a 120-min gradient. Samples were analyzed on an Orbitrap Fusion mass spectrometer. MS1 scan were acquired in the Orbitrap with a range of 375 to 1500 m/z, mass resolution of 120,000, automatic gain control (AGC) target value of 4 × 10^5, and 50-ms maximum injection time. MS2 scans were acquired in the ion trap with an AGC target value of 1 × 10^4 and 35-ms maximum injection time. Precursor ions with charge states 2 to 4 were isolated with an isolation window of 1.6 m/z and 40 s dynamic exclusion. Precursor ions were fragmented using higher-energy collisional dissociation with 30% normalized collision energy. Analysis of the raw data was done with MaxQuant (MQ) software version 1.6.2.6. MaxQuant standard settings were kept as default. In the search parameters, two missed cleavage sites were included, the fixed modification was set to cysteine carbamidomethyl modification, and variable modifications to methionine oxidation and N-terminal protein acetylation. The peptide mass tolerance was set to 4.5 parts per million (ppm) for MS1 scans and 20 ppm for MS2 scans. Match between runs option was enabled. The database search was done using Andromeda against the Human UniProt/Swiss-Prot database with common contaminants. The false discovery rate (FDR) was set to 1% for both peptide and protein level. Protein quantification was done on the basis of at least two razor and unique peptides. Label-free quantification and iBAQ calculation were enabled. Statistical analysis was done on the "ProteinGroups" table with Perseus version 1.6.7.0. Proteomics data have been deposited to the ProteomeXchange Consortium via PRIDE and are available via ProteomeXchange with identifier PXD033846.

Quantitative whole-cell proteomics with TMT labeling

Fed or starved (2 hours) WT or MTM1 KO HeLa cells (one 10-cm dish at 90% confluency) collected from three independent experiments were lysed in 300 μl 8 M urea-lysis-buffer in 50 mM triethylammonium bicarbonate (TEAB)–containing protease inhibitor cocktail (Roche) and 0.5 μl Benzonase Nuclease HC (Millipore). Samples were applied to a Bioruptor Pico (Diagenode) for 10 cycles (30 s on/30 s off) at 4°C. Samples were then incubated for 30 min at 25°C. Proteins were reduced with 5 mM Tris (2-carboxyethyl)phosphin-hydrochloride (TCEP) and alkylated with 40 mM chloroacetamide (CAA) for 60 min at 37°C in the dark. Protein digestion was carried out using Lys C at an enzyme-to-protein ratio of 1:100 (w/w) at 37°C for 3 hours. After diluting to 2 M urea with 50 mM TEAB buffer, the digestion was continued with trypsin at an enzyme-to-protein ratio of 1:100 (w/w) at 37°C and overnight. Digestion was stopped by adding formic acid to a final concentration of 1%. Samples were desalted with C18 Sep-Pak cartridge (Waters) and quantified with Pierce colorimetric peptide assay (Thermo Fisher Scientific). Peptides were dried under speed vacuum and stored at −20°C.

TMT labeling

Peptides were reconstituted in 50 mM TEAB buffer to a concentration of 2.1 μg/μl. TMT 10-plex reagent (Thermo Fisher Scientific) was dissolved in 20 μl 100% acetonitrile to reach 0.2 mg. For each TMT channel, peptides (100 μg) were labeled with 0.2 mg TMT 10-plex reagent (two multiplex—10plex for fed and 10plex for starved). For the internal standard (IS), peptides from all samples were mixed to reach 100 μg total peptides and labeled with the TMT 131 channel to be able to compare between the two plexes. The labeling reaction was carried out for 60 min at RT and quenched with 55 mM Tris pH 8.0 for 15 min at RT. All TMT 10-plex labeled samples were mixed and desalted with C18 Sep-Pak cartridge (Waters). The eluted peptides from the Sep-Pak were dried under speed vacuum and stored at –20°C.

High-pH prefractionation

The mixed TMT labeled peptides were reconstituted in 10 mM NH_4OH buffer with 1% acetonitrile to reach 200 μg. The Peptides were fractionated by High-pH chromatography using a Gemini column (3 μm, C18, 110 Å, Phenomenex) on an Agilent 1260 Infinity II system. An 85-min gradient was applied, and 72 fractions were collected and pooled into 12 fractions. Fractions were dried under speed vacuum until analysis by LC-MS.

LC-MS analysis

Separation of the labeled TMT samples was achieved by RP-HPLC on a Thermo Scientific Dionex UltiMate 3000 system, as described above. Samples were analyzed on an Orbitrap Fusion Lumos mass spectrometer with FAIMS Pro device (Thermo Scientific). MS1 and MS2 scans were acquired in the Orbitrap with a mass resolution of 120,000 and 50,000, respectively, MS1 scan range was set to between 400 and 1600 m/z, standard AGC target, and maximum injection time was set to auto. Precursor ions with charge states 2 to 6 were isolated with an isolation window of 0.7 m/z and dynamic exclusion of 60 s. MS2 scans were set to custom AGC target with normalized AGC target of 250%, and maximum injection time was set to auto. Precursor ions were fragmented using higher-energy collisional dissociation with 38% normalized collision energy. Cycle time was set to 2 s. An internal stepping of CVs –50, –65, and –85 was used in all runs. Data acquisition was done with Xcalibur software 4.4 and Instrument Control Software version 3.4. Data analysis for the TMT labeled samples was done in Proteome Discoverer version 2.5. The TMT 10-plex was set as the quantification method, and the 131 mass was set as the control channel. For the Sequest HT search, the following parameters were applied: MS1 ion mass tolerance of 10 ppm and a MS2 mass tolerance of 0.02 Da. Tryptic digestion allowing two missed cleavages, minimum peptide length of 6 amino acids and maximum peptide length of 144 amino acids. The following modifications were included: cysteine carbamidomethylation (+57.021 Da) as static modification, methionine oxidation (+15.995 Da) and N-terminal acetylation (+42.011 Da) were set as dynamic modifications. In addition, TMT 6-plex (229.163 Da) was set as static modification for peptide N-terminal and for lysine residue. Strict FDR was set to 0.01, and relaxed FDR was set to 0.05. The search was performed against the Human UniProt/Swiss-Prot database. Unique and razor peptides were used for quantification, co-isolation threshold was set to 50, and average reporter S/N to 10. Data were normalized against total peptide amount, and scaling was done against the control channel average. The result "Proteins" output table was exported, and the statistical analysis was done in Perseus version 1.6.15.0. Then, Gene Ontology analysis was conducted using Metascape web tool (77) (https://metascape.org/gp/index.html#/main/step1). The proteomics data have been deposited to the ProteomeXchange Consortium via PRIDE and are available via ProteomeXchange with identifier PXD033850.

Liposome co-sedimentation assays

Powdered lipids were individually resuspended in chloroform then mixed together in a glass sample vial and slowly evaporated with a dry N_2 stream. Liposome composition was 60% phosphatidylcholine (Avanti #850375P), 19.8% phosphatidylethanolamine (Avanti #850725P), 0.2% rhodamine-phosphatidylethanolamine (Avanti #810150P), 10% cholesterol (Avanti #700000), and 10% phosphatidylinositol-3-sphosphate (Avanti #850150P) or 10% phosphatidylinositol 4-phosphate (Avanti #850151P) or 10% phosphatidylinositol 3,4-biphosphate (Avanti #850153P). The mixture was resuspended in 100 μl HEPES-buffered salt solution (20 mM Hepes-NaOH pH 7.5, 150 mM NaCl) for 40 min at 37°C, occasionally vigorously vortexed, and sonicated in a 37°C water bath five times, 45 s on, 1 min off. Liposomes (25 μl) were gently mixed with 25 μl (3 μg suspended with the same buffer) recombinant *Escherichia coli* BL21 expressed GST-RRBP1 1-150aa WT and incubated for 45 min at 25°C. Liposomes were reisolated by centrifugation at 70,000*g* for 15min at 25°C. Supernatant and pellet fractions were dissolved in Laemmli sample buffer and analyzed by SDS-PAGE.

Seahorse XFe96 analyzer

The Seahorse XFe96 sensor cartridge was hydrated, and 1×10^4 cells were seeded on 96-well plates one day before the assay. The next day, while cells were fed or starved for 100 min at 37°C incubator without CO_2, the mitochondrial stress kit (Agilent, 103015-100) compound was prepared in complete DMEM or EBSS and loaded on the cartridge (OligomycinA1: 2 μM; FCCP 1.7 μM, Rot/AA 1 μM). Assay media did not include pyruvate. After instrument calibrations, cells were transferred to the XFe96 analyzer to record oxygen consumption rate at 37°C. All values were background-subtracted (i.e., control well without cells). Finally, cells were lysed with RIPA buffer and protein contents was measured using the BCA assay for data normalization.

Luminescent ATP assay

Cells (5×10^3 to 8×10^3) were seeded in the black 96-well plate. On the next day, total cellular ATP levels of fed or starved cells were analyzed using ATPlite Luminescence Assay System (PerkinElmer, 6016943) according to the manufacturer's protocol. Luminescence was measured by TECAN Luminescence plate reader, and the value was normalized by protein concentration measured via Bradford or BCA assay.

Software

Cartoons and schematics were generated using BioRender and Adobe illustrator.

Statistics and reproducibility

Statistical analysis and graphing were carried out using Prism 8. Normality testing (D'Agostino-Pearson) was conducted to determine whether to use parametric or nonparametric statistical tests. To compare two datasets, normally distributed data were analyzed by two-tailed unpaired Student's *t* test, whereas non-normally distributed data were analyzed by two-tailed Mann-Whitney test. For the comparison of more than two normally distributed datasets, we used ordinary one-way analysis of variance (ANOVA) with either Dunnett's multiple comparisons (to compare the mean of each column with a control column) or Tukey's multiple comparisons test (to compare the mean of each column with every other column). To compare more than two non-normally distributed datasets, we used the Kruskal-Wallis test with two-sided Dunn's multiple comparison test. All statistical analyses were performed on samples drawn from at least two or three independent experiments.

REFERENCES AND NOTES

1. P. Bonaldo, M. Sandri, Cellular and molecular mechanisms of muscle atrophy. *Dis. Model. Mech.* **6**, 25–39 (2013). doi: 10.1242/dmm.010389; pmid: 23268536
2. B. H. Goodpaster, L. M. Sparks, Metabolic flexibility in health and disease. *Cell Metab.* **25**, 1027–1036 (2017). doi: 10.1016/j.cmet.2017.04.015; pmid: 28467922
3. M. Sandri *et al.*, Foxo transcription factors induce the atrophy-related ubiquitin ligase atrogin-1 and cause skeletal muscle atrophy. *Cell* **117**, 399–412 (2004). doi: 10.1016/S0092-8674(04)00400-3; pmid: 15109499
4. S. Schiaffino, K. A. Dyar, S. Ciciliot, B. Blaauw, M. Sandri, Mechanisms regulating skeletal muscle growth and atrophy. *FEBS J.* **280**, 4294–4314 (2013). doi: 10.1111/febs.12253; pmid: 23517348
5. H. An, A. Ordureau, M. Körner, J. A. Paulo, J. W. Harper, Systematic quantitative analysis of ribosome inventory during nutrient stress. *Nature* **583**, 303–309 (2020). doi: 10.1038/s41586-020-2446-y; pmid: 32612236
6. A. Efeyan, W. C. Comb, D. M. Sabatini, Nutrient-sensing mechanisms and pathways. *Nature* **517**, 302–310 (2015). doi: 10.1038/nature14190; pmid: 25592535
7. H. An *et al.*, TEX264 is an endoplasmic reticulum-resident ATG8-interacting protein critical for ER remodeling during nutrient stress. *Mol. Cell* **74**, 891–908.e10 (2019). doi: 10.1016/j.molcel.2019.03.034; pmid: 31006537
8. A. Ballabio, J. S. Bonifacino, Lysosomes as dynamic regulators of cell and organismal homeostasis. *Nat. Rev. Mol. Cell Biol.* **21**, 101–118 (2020). doi: 10.1038/s41580-019-0185-4; pmid: 31768005

9. S. M. Houten, S. Violante, F. V. Ventura, R. J. Wanders, The biochemistry and physiology of mitochondrial fatty acid β-oxidation and its genetic disorders. *Annu. Rev. Physiol.* **78**, 23–44 (2016). doi: 10.1146/annurev-physiol-021115-105045; pmid: 26474213
10. T. Balla, Phosphoinositides: Tiny lipids with giant impact on cell regulation. *Physiol. Rev.* **93**, 1019–1137 (2013). doi: 10.1152/physrev.00028.2012; pmid: 23899561
11. Y. Posor, W. Jang, V. Haucke, Phosphoinositides as membrane organizers. *Nat. Rev. Mol. Cell Biol.* **23**, 797–816 (2022). doi: 10.1038/s41580-022-00490-x; pmid: 35589852
12. C. C. Campa *et al*., Rab11 activity and PtdIns(3)P turnover removes recycling cargo from endosomes. *Nat. Chem. Biol.* **14**, 801–810 (2018). doi: 10.1038/s41589-018-0086-4; pmid: 29915378
13. C. Cao, J. M. Backer, J. Laporte, E. J. Bedrick, A. Wandinger-Ness, Sequential actions of myotubularin lipid phosphatases regulate endosomal PI(3)P and growth factor receptor trafficking. *Mol. Biol. Cell* **19**, 3334–3346 (2008). doi: 10.1091/mbc.e08-04-0367; pmid: 18524850
14. C. Cao, J. Laporte, J. M. Backer, A. Wandinger-Ness, M. P. Stein, Myotubularin lipid phosphatase binds the hVPS15/hVPS34 lipid kinase complex on endosomes. *Traffic* **8**, 1052–1067 (2007). doi: 10.1111/j.1600-0854.2007.00586.x; pmid: 17651088
15. K. Ketel *et al*., A phosphoinositide conversion mechanism for exit from endosomes. *Nature* **529**, 408–412 (2016). doi: 10.1038/nature16516; pmid: 26760201
16. L. Al-Qusairi *et al*., T-tubule disorganization and defective excitation-contraction coupling in muscle fibers lacking myotubularin lipid phosphatase. *Proc. Natl. Acad. Sci. U.S.A.* **106**, 18763–18768 (2009). doi: 10.1073/pnas.0900705106; pmid: 19846786
17. L. Amoasii *et al*., Myotubularin and PtdIns3*P* remodel the sarcoplasmic reticulum in muscle *in vivo*. *J. Cell Sci.* **126**, 1806–1819 (2013). doi: 10.1242/jcs.118505; pmid: 23444364
18. Y. Shibata, G. K. Voeltz, T. A. Rapoport, Rough sheets and smooth tubules. *Cell* **126**, 435–439 (2006). doi: 10.1016/j.cell.2006.07.019; pmid: 16901774
19. J. Laporte *et al*., Mutations in the MTM1 gene implicated in X-linked myotubular myopathy. *Hum. Mol. Genet.* **6**, 1505–1511 (1997). doi: 10.1093/hmg/6.9.1505; pmid: 9305655
20. C. R. Pierson *et al*., Modeling the human *MTM1* p.R69C mutation in murine *Mtm1* results in exon 4 skipping and a less severe myotubular myopathy phenotype. *Hum. Mol. Genet.* **21**, 811–825 (2012). doi: 10.1093/hmg/ddr512; pmid: 22068590
21. O. M. Dorchies *et al*., Normal innervation and differentiation of X-linked myotubular myopathy muscle cells in a nerve-muscle coculture system. *Neuromuscul. Disord.* **11**, 736–746 (2001). doi: 10.1016/S0960-8966(01)00221-8; pmid: 11595516
22. L. K. Schroeder *et al*., Dynamic nanoscale morphology of the ER surveyed by STED microscopy. *J. Cell Biol.* **218**, 83–96 (2019). doi: 10.1083/jcb.201809107; pmid: 30442642
23. G. E. Palade, Studies on the endoplasmic reticulum. II. Simple dispositions in cells in situ. *J. Biophys. Biochem. Cytol.* **1**, 567–582 (1955). doi: 10.1083/jcb.1.6.567; pmid: 13278367
24. G. K. Voeltz, W. A. Prinz, Y. Shibata, J. M. Rist, T. A. Rapoport, A class of membrane proteins shaping the tubular endoplasmic reticulum. *Cell* **124**, 573–586 (2006). doi: 10.1016/j.cell.2005.11.047; pmid: 16469703
25. J. Nixon-Abell *et al*., Increased spatiotemporal resolution reveals highly dynamic dense tubular matrices in the peripheral ER. *Science* **354**, aaf3928 (2016). doi: 10.1126/science.aaf3928; pmid: 27789813
26. M. A. Raess, S. Friant, B. S. Cowling, J. Laporte, WANTED - Dead or alive: Myotubularins, a large disease-associated protein family. *Adv. Biol. Regul.* **63**, 49–58 (2017). doi: 10.1016/j.jbior.2016.09.001; pmid: 27666502
27. E. L. Axe *et al*., Autophagosome formation from membrane compartments enriched in phosphatidylinositol 3-phosphate and dynamically connected to the endoplasmic reticulum. *J. Cell Biol.* **182**, 685–701 (2008). doi: 10.1083/jcb.200803137; pmid: 18725538
28. Z. Hong *et al*., PtdIns3P controls mTORC1 signaling through lysosomal positioning. *J. Cell Biol.* **216**, 4217–4233 (2017). doi: 10.1083/jcb.201611073; pmid: 29030394
29. M. J. Munson *et al*., mTOR activates the VPS34-UVRAG complex to regulate autolysosomal tubulation and cell survival. *EMBO J.* **34**, 2272–2290 (2015). doi: 10.15252/embj.201590992; pmid: 26139536
30. J. Laporte *et al*., A gene mutated in X-linked myotubular myopathy defines a new putative tyrosine phosphatase family conserved in yeast. *Nat. Genet.* **13**, 175–182 (1996). doi: 10.1038/ng0696-175; pmid: 8640223
31. M. W. Lawlor, J. J. Dowling, X-linked myotubular myopathy. *Neuromuscul. Disord.* **31**, 1004–1012 (2021). doi: 10.1016/j.nmd.2021.08.003; pmid: 34736623
32. A. Khaminets *et al*., Regulation of endoplasmic reticulum turnover by selective autophagy. *Nature* **522**, 354–358 (2015). doi: 10.1038/nature14498; pmid: 26040720
33. C. Settembre *et al*., TFEB links autophagy to lysosomal biogenesis. *Science* **332**, 1429–1433 (2011). doi: 10.1126/science.1204592; pmid: 21617040
34. K. M. Fetalvero *et al*., Defective autophagy and mTORC1 signaling in myotubularin null mice. *Mol. Cell. Biol.* **33**, 98–110 (2013). doi: 10.1128/MCB.01075-12; pmid: 23109424
35. A. L. Marat, V. Haucke, Phosphatidylinositol 3-phosphates-at the interface between cell signalling and membrane traffic. *EMBO J.* **35**, 561–579 (2016). doi: 10.15252/embj.201593564; pmid: 26888746
36. Y. Wu *et al*., Contacts between the endoplasmic reticulum and other membranes in neurons. *Proc. Natl. Acad. Sci. U.S.A.* **114**, E4859–E4867 (2017). doi: 10.1073/pnas.1701078114; pmid: 28559323
37. H. Wu, P. Carvalho, G. K. Voeltz, Here, there, and everywhere: The importance of ER membrane contact sites. *Science* **361**, eaan5835 (2018). doi: 10.1126/science.aan5835; pmid: 30072511
38. S. S. Lam *et al*., Directed evolution of APEX2 for electron microscopy and proximity labeling. *Nat. Methods* **12**, 51–54 (2015). doi: 10.1038/nmeth.3179; pmid: 25419960
39. A. Fegan, B. White, J. C. Carlson, C. R. Wagner, Chemically controlled protein assembly: Techniques and applications. *Chem. Rev.* **110**, 3315–3336 (2010). doi: 10.1021/cr8002888; pmid: 20353181
40. T. Calì, M. Brini, Quantification of organelle contact sites by split-GFP-based contact site sensors (SPLICS) in living cells. *Nat. Protoc.* **16**, 5287–5308 (2021). doi: 10.1038/s41596-021-00614-1; pmid: 34686857
41. C. Raiborg *et al*., Repeated ER-endosome contacts promote endosome translocation and neurite outgrowth. *Nature* **520**, 234–238 (2015). doi: 10.1038/nature14359; pmid: 25855459
42. A. M. Valm *et al*., Applying systems-level spectral imaging and analysis to reveal the organelle interactome. *Nature* **546**, 162–167 (2017). doi: 10.1038/nature22369; pmid: 28538724
43. A. A. Rowland, P. J. Chitwood, M. J. Phillips, G. K. Voeltz, ER contact sites define the position and timing of endosome fission. *Cell* **159**, 1027–1041 (2014). doi: 10.1016/j.cell.2014.10.023; pmid: 25416943
44. M. Lu *et al*., The structure and global distribution of the endoplasmic reticulum network are actively regulated by lysosomes. *Sci. Adv.* **6**, eabc7209 (2020). doi: 10.1126/sciadv.abc7209; pmid: 33328230
45. V. Hung *et al*., Proteomic mapping of cytosol-facing outer mitochondrial and ER membranes in living human cells by proximity biotinylation. *eLife* **6**, e24463 (2017). doi: 10.7554/eLife.24463; pmid: 28441135
46. Y. Shibata *et al*., Mechanisms determining the morphology of the peripheral ER. *Cell* **143**, 774–788 (2010). doi: 10.1016/j.cell.2010.11.007; pmid: 21111237
47. P. Zheng *et al*., ER proteins decipher the tubulin code to regulate organelle distribution. *Nature* **601**, 132–138 (2022). doi: 10.1038/s41586-021-04204-9; pmid: 34912111
48. C. S. Janota *et al*., Shielding of actin by the endoplasmic reticulum impacts nuclear positioning. *Nat. Commun.* **13**, 2763 (2022). doi: 10.1038/s41467-022-30388-3; pmid: 35589708
49. B. T. Lobingier *et al*., An approach to spatiotemporally resolve protein interaction networks in living cells. *Cell* **169**, 350–360.e12 (2017). doi: 10.1016/j.cell.2017.03.022; pmid: 28388416
50. Y. C. Wong, D. Ysselstein, D. Krainc, Mitochondria–lysosome contacts regulate mitochondrial fission via RAB7 GTP hydrolysis. *Nature* **554**, 382–386 (2018). doi: 10.1038/nature25486; pmid: 29364868
51. S. Nagashima *et al*., Golgi-derived PI(4)P-containing vesicles drive late steps of mitochondrial division. *Science* **367**, 1366–1371 (2020). doi: 10.1126/science.aax6089; pmid: 32193326
52. S. C. Lewis, L. F. Uchiyama, J. Nunnari, ER-mitochondria contacts couple mtDNA synthesis with mitochondrial division in human cells. *Science* **353**, aaf5549 (2016). doi: 10.1126/science.aaf5549; pmid: 27418514
53. J. R. Friedman *et al*., ER tubules mark sites of mitochondrial division. *Science* **334**, 358–362 (2011). doi: 10.1126/science.1207385; pmid: 21885730
54. T. C. Walther, J. Chung, R. V. Farese Jr., Lipid droplet biogenesis. *Annu. Rev. Cell Dev. Biol.* **33**, 491–510 (2017). doi: 10.1146/annurev-cellbio-100616-060608; pmid: 28793795
55. A. Santinho *et al*., Membrane curvature catalyzes lipid droplet assembly. *Curr. Biol.* **30**, 2481–2494.e6 (2020). doi: 10.1016/j.cub.2020.04.066; pmid: 32442467
56. A. S. Rambold, B. Kostelecky, N. Elia, J. Lippincott-Schwartz, Tubular network formation protects mitochondria from autophagosomal degradation during nutrient starvation. *Proc. Natl. Acad. Sci. U.S.A.* **108**, 10190–10195 (2011). doi: 10.1073/pnas.1107402108; pmid: 21646527
57. A. S. Rambold, S. Cohen, J. Lippincott-Schwartz, Fatty acid trafficking in starved cells: Regulation by lipid droplet lipolysis, autophagy, and mitochondrial fusion dynamics. *Dev. Cell* **32**, 678–692 (2015). doi: 10.1016/j.devcel.2015.01.029; pmid: 25752962
58. M. Giacomello, A. Pyakurel, C. Glytsou, L. Scorrano, The cell biology of mitochondrial membrane dynamics. *Nat. Rev. Mol. Cell Biol.* **21**, 204–224 (2020). doi: 10.1038/s41580-020-0210-7; pmid: 32071438
59. T. Wai *et al*., Imbalanced OPA1 processing and mitochondrial fragmentation cause heart failure in mice. *Science* **350**, aad0116 (2015). doi: 10.1126/science.aad0116; pmid: 26785494
60. A. R. English, G. K. Voeltz, Rab10 GTPase regulates ER dynamics and morphology. *Nat. Cell Biol.* **15**, 169–178 (2013). doi: 10.1038/ncb2647; pmid: 23263280
61. J. E. Lee, P. I. Cathey, H. Wu, R. Parker, G. K. Voeltz, Endoplasmic reticulum contact sites regulate the dynamics of membraneless organelles. *Science* **367**, eaay7108 (2020). doi: 10.1126/science.aay7108; pmid: 32001628
62. L. C. Gomes, G. Di Benedetto, L. Scorrano, During autophagy mitochondria elongate, are spared from degradation and sustain cell viability. *Nat. Cell Biol.* **13**, 589–598 (2011). doi: 10.1038/ncb2220; pmid: 21478857
63. W. M. Henne, M. L. Reese, J. M. Goodman, The assembly of lipid droplets and their roles in challenged cells. *EMBO J.* **37**, e98947 (2018). doi: 10.15252/embj.201898947; pmid: 29789390
64. M. A. Roberts, A. Segura-Roman, J. A. Olzmann, Organelle biogenesis: ER shape influences lipid droplet nucleation. *Curr. Biol.* **30**, R770–R773 (2020). doi: 10.1016/j.cub.2020.05.027; pmid: 32634419
65. J. R. Liang *et al*., A genome-wide ER-phagy screen highlights key roles of mitochondrial metabolism and ER-resident UFMylation. *Cell* **180**, 1160–1177.e20 (2020). doi: 10.1016/j.cell.2020.02.017; pmid: 32160526
66. Y. Pan *et al*., Endoplasmic reticulum ribosome-binding protein 1, RRBP1, promotes progression of colorectal cancer and predicts an unfavourable prognosis. *Br. J. Cancer* **113**, 763–772 (2015). doi: 10.1038/bjc.2015.260; pmid: 26196185
67. A. H. Bahrami, G. Hummer, Formation and stability of lipid membrane nanotubes. *ACS Nano* **11**, 9558–9565 (2017). doi: 10.1021/acsnano.7b05542; pmid: 28873296
68. T. Shemesh *et al*., A model for the generation and interconversion of ER morphologies. *Proc. Natl. Acad. Sci. U.S.A.* **111**, E5243–E5251 (2014). doi: 10.1073/pnas.1419997111; pmid: 25404289
69. G. Parlakgül *et al*., Regulation of liver subcellular architecture controls metabolic homeostasis. *Nature* **603**, 736–742 (2022). doi: 10.1038/s41586-022-04488-5; pmid: 35264794
70. D. S. Hirsch *et al*., Insulin activation of vacuolar protein sorting 34 mediates localized phosphatidylinositol 3-phosphate production at lamellipodia and activation of mTOR/S6K1. *Cell. Signal.* **26**, 1258–1268 (2014). doi: 10.1016/j.cellsig.2014.02.009; pmid: 24582588
71. V. I. Korolchuk *et al*., Lysosomal positioning coordinates cellular nutrient responses. *Nat. Cell Biol.* **13**, 453–460 (2011). doi: 10.1038/ncb2204; pmid: 21394080
72. A. L. Marat *et al*., mTORC1 activity repression by late endosomal phosphatidylinositol 3,4-bisphosphate. *Science* **356**, 968–972 (2017). doi: 10.1126/science.aaf8310; pmid: 28572395
73. M. J. Hoyer *et al*., A novel class of ER membrane proteins regulates ER-associated endosome fission. *Cell* **175**, 254–265.e14 (2018). doi: 10.1016/j.cell.2018.08.030; pmid: 30220460
74. K. Mamchaoui *et al*., Immortalized pathological human myoblasts: Towards a universal tool for the study of

neuromuscular disorders. *Skelet. Muscle* **1**, 34 (2011). doi: 10.1186/2044-5040-1-34; pmid: 22040608

75. F. Bottanelli *et al*., Two-colour live-cell nanoscale imaging of intracellular targets. *Nat. Commun.* **7**, 10778 (2016). doi: 10.1038/ncomms10778; pmid: 26940217
76. C. McQuin *et al*., CellProfiler 3.0: Next-generation image processing for biology. *PLOS Biol.* **16**, e2005970 (2018). doi: 10.1371/journal.pbio.2005970; pmid: 29969450
77. Y. Zhou *et al*., Metascape provides a biologist-oriented resource for the analysis of systems-level datasets. *Nat. Commun.* **10**, 1523 (2019). doi: 10.1038/s41467-019-09234-6; pmid: 30944313

ACKNOWLEDGMENTS

We thank members of the Haucke lab for discussion and Y. Posor for critical reading of the manuscript. We thank S. Zillmann, D. Löwe, M. Mühlbauer, and C. Schmidt for expert technical assistance and M. Lehmann, C. Schmied, and J. Eichhorst for aid with microscopy and image analysis. We also thank G. G. Farías and G. Voeltz for plasmids and protocols and the MyoLine platform of the Institute of Myology in Paris for aid in the generation of myoblast cell lines. **Funding:** This work was funded by a Leibniz-German Academic Exchange Service (DAAD) Research Fellowship (57423756) (W.J.), the Postdoctoral Fellowship Program (Nurturing Next-generation Researchers) of the National Research Foundation of Korea (NRF) (2018R1A6A3A03010583) (W.J.), and Deutsche Forschungsgemeinschaft (TRR186/ A08) (V.H.). **Author contributions:** Conceptualization: W.J. and V.H. Investigation: all cell and molecular biology: W.J.; electron microscopy: D.P. with W.J.; quantitative proteomics: W.J. with M.N.-H. and F.L.; Seahorse analysis: W.J., Y.L., S.J.S., and U.K.; XLCNM myoblast patient cells: K.M. and V.M.; CRISPR: W.J. and P.S. Funding acquisition: W.J. and V.H. Project administration: V.H. Supervision: V.H., F.L., U.K., and S.J.S. Writing – original draft: W.J. and V.H. Writing – review & editing: all authors. **Competing interests:** The authors declare no competing financial interests. **Data and materials availability:** All data are available in the main text or the supplementary materials. Proteomics data have been deposited to the ProteomeXchange Consortium via PRIDE and are available via ProteomeXchange with identifier PXD033846. Materials and reagents are available from the corresponding author upon request.

SUPPLEMENTARY MATERIALS

science.org/doi/10.1126/science.abq5209
Figs. S1 to S11
Tables S1 to S4
MDAR Reproducibility Checklist
Movies S1 to S5

Submitted 13 April 2022; resubmitted 23 September 2022
Accepted 25 October 2022
10.1126/science.abq5209

RESEARCH ARTICLES

MEMBRANES

Truly combining the advantages of polymeric and zeolite membranes for gas separations

Xiaoyu Tan[1], Sven Robijns[2], Raymond Thür[1]†, Quanli Ke[2]‡, Niels De Witte[3], Aran Lamaire[4], Yun Li[1], Imran Aslam[1], Daan Van Havere[1], Thibaut Donckels[2], Tom Van Assche[3], Veronique Van Speybroeck[4], Michiel Dusselier[2]*, Ivo Vankelecom[1]*

Mixed-matrix membranes (MMMs) have been investigated to render energy-intensive separations more efficiently by combining the selectivity and permeability performance, robustness, and nonaging properties of the filler with the easy processing, handling, and scaling up of the polymer. However, truly combining all in one single material has proven very challenging. In this work, we filled a commercial polyimide with ultrahigh loadings of a high–aspect ratio, CO_2-philic Na-SSZ-39 zeolite with a three-dimensional channel system that precisely separates gas molecules. By carefully designing both zeolite and MMM synthesis, we created a gas-percolation highway across a flexible and aging-resistant (more than 1 year) membrane. The combination of a CO_2-CH_4 mixed-gas selectivity of ~423 and a CO_2 permeability of ~8300 Barrer outperformed all existing polymer-based membranes and even most zeolite-only membranes.

Over the past decades, membrane technology has matured into an established technology for many energy-intensive separations (*1*–*3*). Compared with conventional technologies, membrane technology offers a more sustainable alternative, owing to its low energy consumption, small footprint, and modular design, making it possible to retrofit membranes in existing plants (*2*, *3*). Membranes are already in use for gas separations—for example, natural gas purification, syngas treatment, and air separation (*4*–*7*)—and are becoming part of the toolbox for CO_2 removal (*5*–*10*). Whereas conventional polymeric membranes are cheap and processable, they often suffer from aging issues or an intrinsic permeability-selectivity tradeoff, which makes it challenging to obtain high permeability together with sufficient selectivity (*11*–*16*). On the other hand, inorganic membranes prepared from zeolites or other crystalline microporous materials, such as metal-organic frameworks (MOFs), typically display better separation performances but tend to be brittle and more expensive and possess poor processability and scalability (*17*–*21*). Mixed-matrix membranes (MMMs), which consist of fillers embedded in a polymeric matrix, aim at combining the intrinsic advantages of a polymeric membrane with the filler's superior gas separation properties (*22*–*27*).

Zeolites are of particular interest for MMM development because they have well-defined, rigid pores and outstanding thermal and chemical stability. Because the intrinsically low selectivity and high permeability of rubbery polymers (such as polydimethylsiloxane) neutralize the benefits of the zeolite, rigid glassy polymers are key for the development of high-performance zeolite-filled MMMs (*28*–*32*). However, the poor adhesion between zeolites and glassy polymers typically results in nonselective interfacial voids (*31*, *32*). Consequently, obtaining high zeolite loadings (≥50 wt %) while guaranteeing a defect-free polymer-zeolite interface in combination with a highly selective zeolite and appropriate glassy polymer matrix is essential to the creation of high-performance MMMs for a variety of the most critical separation challenges. In this work, a platelet-shaped, CO_2-philic, small-pore (eight-membered ring) AEI-type zeolite (SSZ-39) (*33*–*36*), possessing a long-range ordered three-dimensional (3D)–channel system and gas-selective windows, was incorporated in a poly(3,3′-4,4′-benzophenone tetracarboxylic-dianhydride diaminophenylindane) (Matrimid 5218) polymer. Because of the combination of well-designed zeolite and MMM syntheses, we obtained a high zeolite loading with a quasi-continuous zeolite phase across a self-standing membrane.

Result and discussion

Zeolite characterization

SSZ-39 zeolites were synthesized according to modified literature recipes (*33*–*35*). X-ray diffraction (XRD) of the samples confirmed the highly crystalline, pure AEI type zeolite (fig. S9). N_2 physisorption demonstrated a micropore volume of ~0.3 cm^3/g (fig. S11), which is close to the theoretical accessible volume of the AEI framework (*37*), suggesting a nearly perfect 3D-connected channel system, which allows fast gas transport. Transmission electron microscopy (TEM) images showed platelet-shaped SSZ-39 particles (Fig. 1A) of ~150 nm thickness and ~1.8 by 1.8 μm in size (fig. S48), the average aspect ratio thus reaching ~12. The random packing of the high–aspect ratio zeolite platelets (fig. S49) results in a low bulk density of ~15 mg/cm^3 (fig. S12), and elemental analysis of the as-synthesized SSZ-39 indicated a Si/Al molar ratio of ~11 (table S3).

CO_2, CH_4, and N_2 uptake and isosteric adsorption enthalpies (Q_{st}) were determined for both calcined SSZ-39 (Na/Al ratio ≈ 0.12) and Na^+-exchanged SSZ-39 (Na-SSZ-39; Na/Al ratio ≈ 0.93) (table S3). The adsorption isotherms of CO_2, CH_4, and N_2 at 10°C are shown in Fig. 1D for a pressure range of 0 to 8 bar. The theoretical maximum CO_2 uptake of Na-SSZ-39 reached ~7.0 mmol/g (~11.0 mmol/cm^3) at 10°C, and the steric heat of adsorption for CO_2 at zero coverage was –35.1 kJ/mol, reflecting a desired strong physical adsorption for membrane applications. For both SSZ-39 and Na-SSZ-39, the gas uptake decreases in the order $CO_2 \gg CH_4 > N_2$. The isosteric adsorption enthalpy of CO_2 in Na-SSZ-39 was far larger than that of CH_4 (–21.4 kJ/mol) and N_2 (–19.4 kJ/mol) as a result of the large polarizability and quadrupole moment of CO_2 (*38*). A more negative CO_2 adsorption enthalpy was obtained on Na-SSZ-39 compared with SSZ-39 (table S19). Additionally, the pronounced difference in CO_2 adsorption in the low-pressure region of the isotherms (Fig. 1D) suggests that Na^+ exchange resulted in an increased CO_2-philicity (*38*).

To better understand these findings at a molecular level, the pure-gas and mixed-gas adsorption behaviors in Na-SSZ-39 were modeled by using grand canonical Monte Carlo (GCMC) simulations. The pure-gas adsorption simulations show a good qualitative resemblance with the experimental data (fig. S37), and the enthalpies of adsorption are in good agreement (at 2 bar, GCMC yields –31.6 kJ/mol for CO_2, –18.5 kJ/mol for CH_4, and –15.8 kJ/mol for N_2). The 3D density isosurfaces for CO_2 adsorption (Fig. 1C) show that CO_2 molecules preferentially interact with the Na^+ (especially at low CO_2 pressures), whereas the windows of Na-SSZ-39 remain open for gas transport. This tendency corroborates the enhanced CO_2-philicity through Na^+ exchange, improving CO_2 adsorption and transport in Na-SSZ-39. The Si/Al molar ratio of 11 implies that on average, one aluminum site (fully counted) and thus one sodium ion exists per cage (*37*). Furthermore,

---

[1]Centre for Membrane Separations, Adsorption, Catalysis and Spectroscopy for Sustainable Solutions (cMACS), KU Leuven, Celestijnenlaan 200F, 3001 Leuven, Belgium. [2]Center for Sustainable Catalysis and Engineering, KU Leuven, Celestijnenlaan 200F, 3001 Leuven, Belgium. [3]Department of Chemical Engineering, Vrije Universiteit Brussel, Pleinlaan 2, 1050 Brussels, Belgium. [4]Center for Molecular Modeling, Ghent University, Tech Lane Ghent Science Park, Technologiepark 46, 9052 Zwijnaarde, Belgium.
***Corresponding author. Email: ivo.vankelecom@kuleuven.be (I.V.); michiel.dusselier@kuleuven.be (M.D.)**
†Present address: Agfa-Gevaert NV, Septestraat 27, 2640 Mortsel, Belgium.
‡Present address: Institute of Catalytic Reaction Engineering, Zhejiang University of Technology, Hangzhou 310014, China.

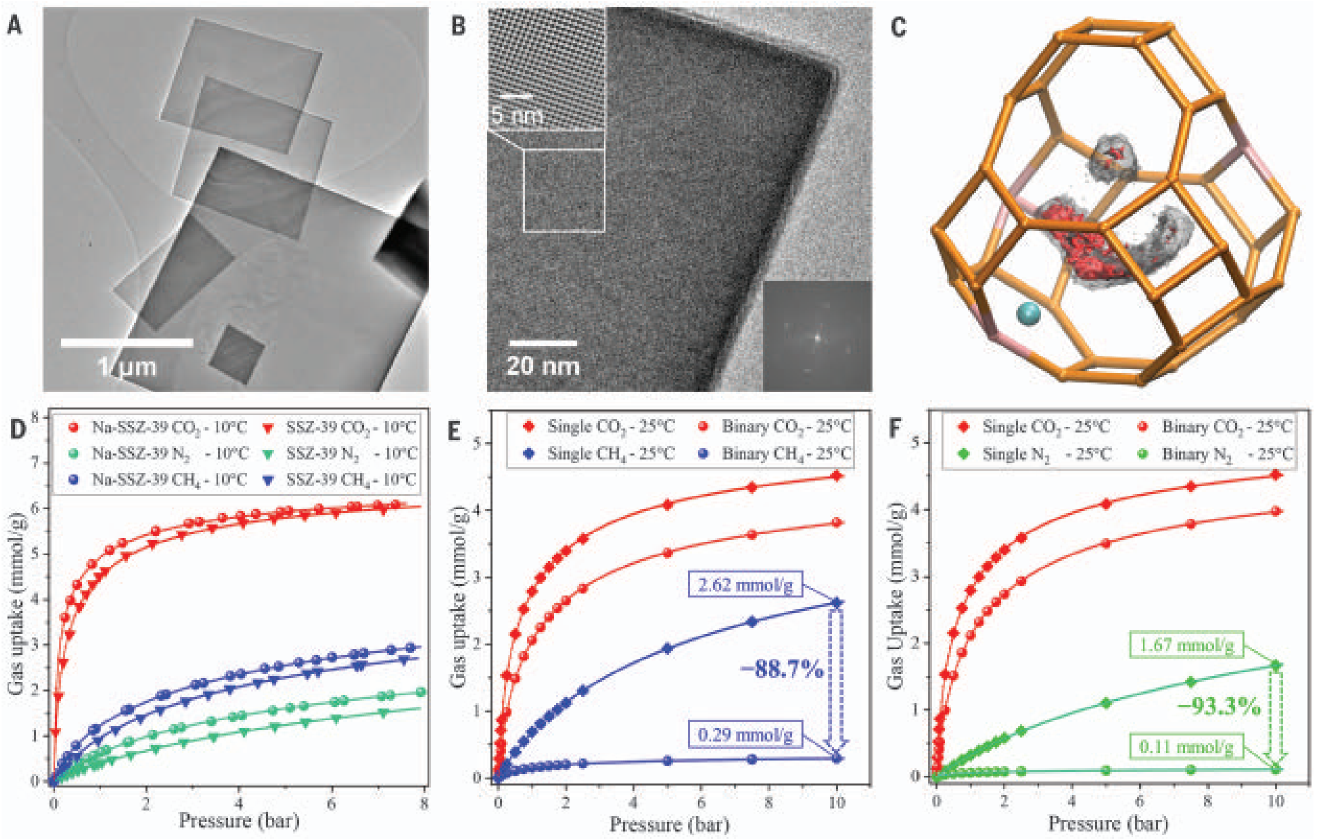

Fig. 1. SSZ-39 zeolite. (**A** and **B**). TEM images of (A) Na-SSZ-39 platelet and (B) its base-face. (Insets) (top left) A Fourier-filtered image from the selected area and (bottom right) the Fourier-transform of this image, proving that the base face refers to the [001] crystal plane of the AEI-type framework (fig. S47). (**C**) 3D density isosurface for CO$_2$ adsorption in a Na-SSZ-39 cage at 0.1 bar (red) and 1 bar (gray) under 25°C [by means of GCMC, where (3 × 1/3) Al sites are pink, Na$^+$ is cyan, and O is omitted], indicating that the Na$^+$ is a preferential adsorption site, particularly at lower pressures. At higher pressures, additional molecules are adsorbed, occupying the remaining space of the cage. (**D**) Experimental CO$_2$, CH$_4$, and N$_2$ adsorption isotherms of SZZ-39 and Na-SSZ-39 zeolites at 10°C. (**E**) Single-gas and equimolar mixed-gas CO$_2$-CH$_4$ adsorption isotherms of Na-SSZ-39 zeolite at 25°C (by means of GCMC). (**F**) Single-gas and equimolar mixed-gas CO$_2$-N$_2$ adsorption isotherms of Na-SSZ-39 zeolite at 25°C (by means of GCMC) (supplementary materials).

the CO$_2$-CH$_4$ and CO$_2$-N$_2$ mixed-gas sorption simulations demonstrate the competitive sorption of CO$_2$ at the expense of CH$_4$ and N$_2$ (movie S1). This strong competitive sorption behavior drastically reduces the uptake of CH$_4$ and N$_2$. For example, compared with the single-gas adsorption, the CH$_4$ uptake from an equimolar CO$_2$-CH$_4$ mixture was reduced by 88.7% (for N$_2$, 93.3%) at 10 bar/25°C (Fig. 1, E and F). In addition, ab initio free-energy barrier calculations [by using enhanced sampling molecular dynamics (MD) simulations] for the diffusion inside the zeolite confirmed the molecular sieving behavior of Na-SSZ-39 (fig. S41). The biggest (static) aperture of Na-SSZ-39 predicts diffusion of molecules with a diameter of 3.84 Å, which is close to the kinetic diameter of CH$_4$ (3.80 Å) but prominently larger than that of CO$_2$ (3.30 Å). Consequently, the free-energy barrier for CH$_4$ permeation through the eight-membered ring in Na-SSZ-39 is far higher than for CO$_2$ (a 18.7 kJ/mol difference). Therefore, the self-diffusion coefficient for CO$_2$ is ~1000-fold greater than for CH$_4$. Consequently, in a CO$_2$-CH$_4$ mixture, CH$_4$ is prevented from entering the zeolite by a geometric restriction supplemented by a competitive advantage in CO$_2$ adsorption. By combining the results of MD and GCMC simulations, the theoretical equimolar CO$_2$-CH$_4$ mixed-gas selectivity in Na-SSZ-39 zeolite mounted to >10,000 (at 25°C), thus pointing toward a substantial potential for further improving membrane performance on the basis of this zeolite platform (supplementary materials).

MMM characterization

Self-standing MMMs were prepared, with Na-SSZ-39 reaching extremely high loadings of up to 55 wt %. XRD confirmed the preservation of zeolite crystallinity in MMMs after all synthesis steps (fig. S13). Scanning electron microscopy (SEM) membrane cross sections (Fig. 2A) show that the zeolite platelets are positioned in the polymer matrix in a random, nonaligned packing. This homogeneous distribution of zeolite platelets at high loading was realized through a subtle and carefully optimized interplay between zeolite and casting solution during MMM synthesis. More specifically, favorable molecular interactions between zeolite and the Matrimid-chloroform solution were combined with a small density difference between zeolite and solvent (~1.55 g/cm^3 and ~1.49 g/cm^3, respectively), the high–aspect ratio of the filler, a high viscosity of the casting solution, dedicated evaporation control of the solvent, and thermal annealing. After membrane solidification, remaining interfacial defects were eliminated by means of a tuned annealing protocol, which had a profound impact on the final MMM performance (fig. S59). The 180°C annealing program resulted in slightly more permeable membranes than those of the 260°C program, but the 260°C program induced a far higher CO$_2$-CH$_4$ selectivity [for 50 wt % Na-SSZ-39 MMM, the selectivity increased from ~200 to >420 (table S5)], whereas the 350°C program resulted in fragile and brittle

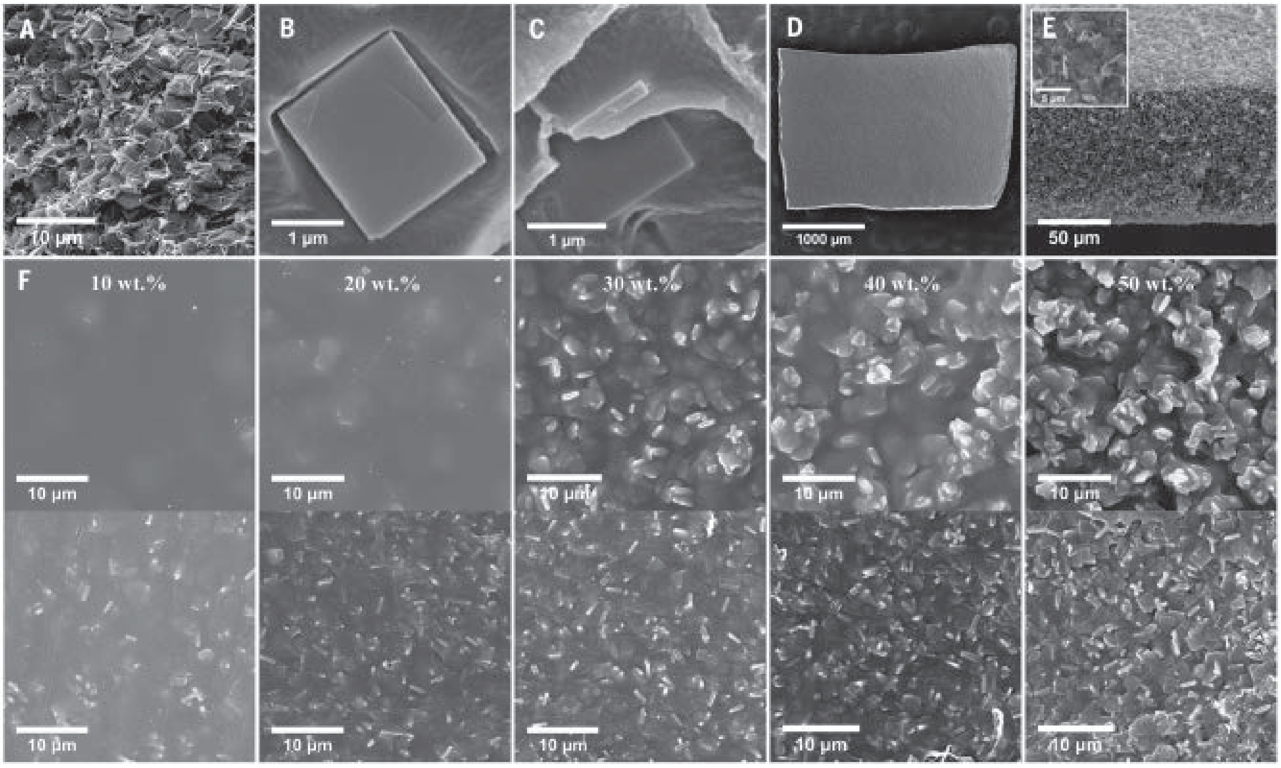

Fig. 2. SEM images of the platelet-shaped Na-SSZ-39 MMMs. (**A**) Cross section of the 40 wt % Na-SSZ-39 MMM after 260°C annealing. (**B** and **C**) Cross section of 20 wt % Na-SSZ-39 MMM (B) before and (C) after annealing. (**D**) Top view and (**E**) cross section of the 30 wt % Na-SSZ-39 MMM after 800°C oxidative treatment, burning off the polymer (figs. S51 to S53). (**F**) (Top) Top view and (bottom) bottom view of membranes with 10 to 50 wt % platelet-shaped zeolite loading (supplementary materials).

carbonized membranes. As shown in Fig. 2C, 260°C-annealed membranes did not show sieve-in-a-cage morphology, which traditionally is a major issue for zeolite MMMs (*31*). Compared with its nonannealed counterparts (Fig. 2B), a much better zeolite-polymer adhesion can be observed (figs. S54 and S55). Full removal of the polymer by means of oxidative treatment at 800°C (fig. S51) led to a stable zeolite-only film (Fig. 2, D and E, and figs. S51 to S53), confirming the high zeolite loading in a random packing. This nearly continuous zeolite phase across the MMM thus creates a “percolation highway” to allow ultrafast permeation of the selected gas molecules.

As anticipated, neither Fourier transform infrared nor Raman microspectroscopy could find evidence for a covalent interaction between polymer and zeolite after annealing (figs. S18 and S61 to S66). Differential scanning calorimetry analysis indicated very good polymer-zeolite interactions in the MMM: With the Na-SSZ-39 loading, the glass transition temperature increased from 314°C (for Matrimid) to 325°C (for annealed Na-SSZ-39 MMMs), pointing toward “wrapping” of the zeolite by the polymer and rigidification of the polymer chains at the interface (fig. S17). We performed CO_2, CH_4, and N_2 sorption experiments on the 260°C annealed Matrimid membrane and the 50 wt % Na-SSZ-39 MMM to quantify their respective gas uptake. A substantially higher gas uptake was noted for the MMM (fig. S30).

Membrane gas separation performance

The mixed-gas selectivities of Na-SSZ-39 MMMs (table S5) were clearly higher than those of their ideal-gas selectivities (table S8) because of the competitive sorption of CO_2 in the Na-SSZ-39 zeolite. For example, for the 50 wt % Na-SSZ-39 MMM, the CO_2-CH_4 ideal-gas selectivity was ~*336* (1 bar/25°C), whereas the equimolar CO_2-CH_4 mixed-gas selectivity reached >420 (2 bar/25°C—1 bar CO_2 and CH_4 partial pressures). Likewise, the CO_2-N_2 ideal-gas selectivity at 1 bar/25°C was ~32, whereas its mixed-gas selectivity at 2 bar/25°C increased to ~60. Once the stronger adsorbing CO_2 occupied the adsorption sites, the zeolite channels become partly inaccessible for the other gas, thus inhibiting permeation of CH_4 and N_2.

On the basis of the physisorption and ideal-gas permeation results, gas solubility and diffusivity values were calculated for the unfilled Matrimid membrane and 50 wt % Na-SSZ-39 MMM (table S20). With respect to the unfilled membrane, the MMM displayed a 4.6-times greater CO_2 solubility, whereas the CH_4 and N_2 solubility increased by 7.5 and 3.4 times, respectively. A 220-fold increase in CO_2 diffusivity was denoted for the MMM compared with that of the unfilled Matrimid membrane, whereas CH_4 and N_2 diffusivity only increased 14 and 148 times, respectively. The enhancement of CO_2-CH_4 diffusivity selectivity thus explains the strong improvement of the MMM gas separation capability (table S21). This results from the sharp size-sieving effect of Na-SSZ-39 for the CO_2-CH_4 pair. The increase in diffusivity selectivity for CO_2-N_2 is less pronounced because N_2 possesses a smaller kinetic diameter. The notable difference in separation factor for CO_2-CH_4 and CO_2-N_2 confirms the central role of the highly accurate size-sieving mechanism for the strong selectivities of Na-SSZ-39 MMMs.

Mixed-gas CO_2-CH_4 and CO_2-N_2 separation performances are presented in Fig. 3. For CO_2-CH_4, we observed a continuous increase in separation factor with increasing Na-SSZ-39 loading. Whereas the unfilled Matrimid membrane denotes a CO_2-CH_4 separation factor of ~45 and CO_2 permeability ~8 Barrer, we obtained the best MMM performance with the 50 wt % Na-SSZ-39 loading, which obtained a selectivity of >420 at 2 bar/25°C (~10-fold increase) at a simultaneous extreme CO_2 permeability of ~8280 Barrer (~1037-fold increase). We obtained similar results for the CO_2-N_2 separation performance in which the 50 wt %

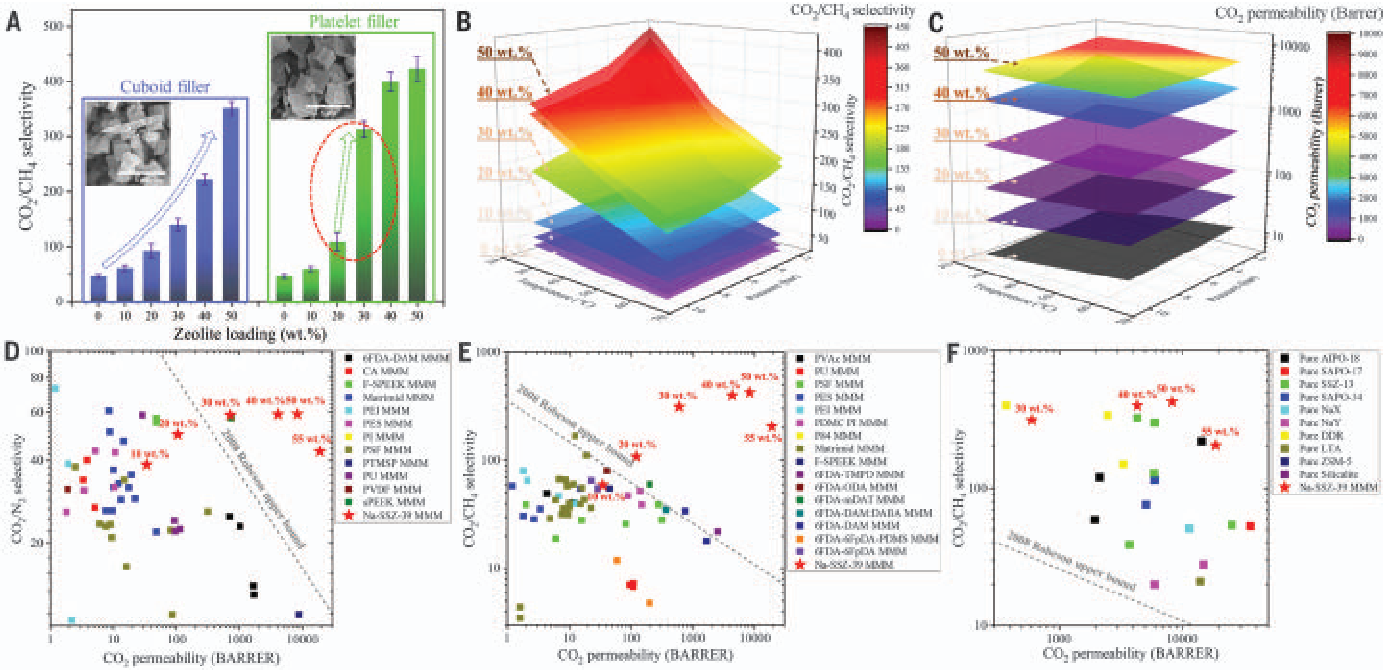

Fig. 3. The gas separation performances of Na-SSZ-39 MMMs. (**A**) The selectivity difference between cuboid-shaped and platelet-shaped Na-SSZ-39 MMMs. (Inset) SEM images show the morphology difference of two zeolites. (**B** and **C**) The temperature and pressure dependence of CO_2-CH_4 selectivity and CO_2 permeability. Nine points constitute a plane. (**D** and **E**) The performance of zeolite-filled MMMs from literature are shown in CO_2-N_2 and CO_2-CH_4 2008 Robeson plots. The red stars indicate the platelet-shaped Na-SSZ-39 MMMs. (**F**) The pure zeolite membranes from literature compared with the Na-SSZ-39 MMMs (≥30 wt %) and 2008 CO_2-CH_4 Robeson plot (full datasets are available in the supplementary materials).

MMM combined a CO_2 permeability of >8300 Barrer with a CO_2-N_2 separation factor of ~60 (versus ~8 and ~35 for unfilled Matrimid). The temperature and pressure dependency of the membrane performance are shown in Fig. 3, B and C, with different zeolite loadings. With increasing temperature, the CO_2 adsorption in the zeolite obviously decreased (fig. S27), resulting in lowered CO_2 permeability and CO_2-CH_4 selectivity. We observed similar behavior with rising feed pressure: Both CO_2 permeability and CO_2-CH_4 selectivity reduced. Because of its high CO_2-philicity, Na-SSZ-39 is already saturated with CO_2 molecules at low feed pressure. Further increased pressures thus contribute less to CO_2 permeation. For the same reason, the Na-SSZ-39 MMMs exhibit enhanced performance in feeds with lower CO_2 partial pressures (table S6). For example, the 50 wt % Na-SSZ-39 MMM gave a CO_2 permeability of >10,000 Barrer and a CO_2-CH_4 selectivity >460 for a 20 vol % CO_2/80 vol % CH_4 feed (figs. S23 and S24), which is close to the compositions of industrial feed streams, such as certain biogas and natural gas sources (*39*, *40*).

When depicted on selectivity-permeability trade-off plots, the Na-SSZ-39 MMMs already surpass the 2008 Robeson upper bound (*11*) from 30 wt % loading onward for CO_2-N_2 (Fig. 3D) and even from 20 wt % for CO_2-CH_4 (Fig. 3E). Ultimately, they realize an unprecedented jump toward the upper-right corner of the Robeson plot, ending up even beyond the performance area that is dominated by zeolite-only membranes (Fig. 3F). Outperforming most existing zeolite-only membranes can be related to the properties of the Na-SSZ-39 filler as well as the membrane morphology. Moreover, compared with the zeolite-only membranes, the Na-SSZ-39 MMMs (Fig. 4B) additionally keep their flexibility because of the presence of the polymer matrix (Fig. 4A and movie S2). Furthermore, because of the stability of the Na-SSZ-39 filler and the thermal annealing protocol, the Na-SSZ-39 MMMs (Fig. 4B) possess antiaging properties. Although the aging characteristics may vary with film thickness, the self-standing 50 wt % Na-SSZ-39 MMM shows comparable CO_2-CH_4 selectivity and CO_2 permeability even 360 days after preparation (table S5). From an application point of view in the frame of CO_2 removal, this antiaging, high-flux, and high-selectivity membrane can allow substantial reductions in both operational and capital costs because a simplified and more energy-efficient operation scheme with less recycling and milder compression and recompression stages can be applied, in combination with reduced membrane areas and less replacement (*2*, *3*).

The gas-separation performance of the Na-SSZ-39 MMMs can thus be explained by a combination of three factors.

First, the selection of the Na-SSZ-39 zeolite as membrane filler is critical. Because of its accurate molecular size-sieving effect and strong CO_2-philicity, Na-SSZ-39 possesses enormous diffusivity and solubility selectivities, thus promoting ultrahigh mixed-gas selectivity. Moreover, the noncentrosymmetric AEI-type framework allows preparation of high–aspect ratio platelets. In contrast to many high–aspect ratio porous materials that possess 1D channels perpendicular to their base face (*41*, *42*), the SSZ-39 platelet is equipped with a 3D channel system, with 3.84-Å windows in its lateral face (Fig. 1B). Therefore, regardless of the platelet's orientation inside the membrane, the SSZ-39 pore system always allows unhindered gas flow (Fig. 4, D and E).

Second, the sudden jump in CO_2-CH_4 separation factor at 20 to 30 wt % loading suggests a percolation effect (Fig. 3A); from this loading onward, gas permeation through the membrane is predominantly going through the zeolite phase. The reason for this shift in phase dominance should be sought in the practical ability to incorporate ultrahigh loadings of the high–aspect ratio filler in the polymer. This creates a membrane morphology, which consists of a quasi-continuous zeolite phase across the membrane starting from only 20 to 30 wt % loading (Fig. 4D) and allows for percolation of the gas molecules with minimal influence of the less permeable polymer phase. The top and bottom views (Fig. 2F) of the MMMs show that the zeolite platelets pile up from the bottom

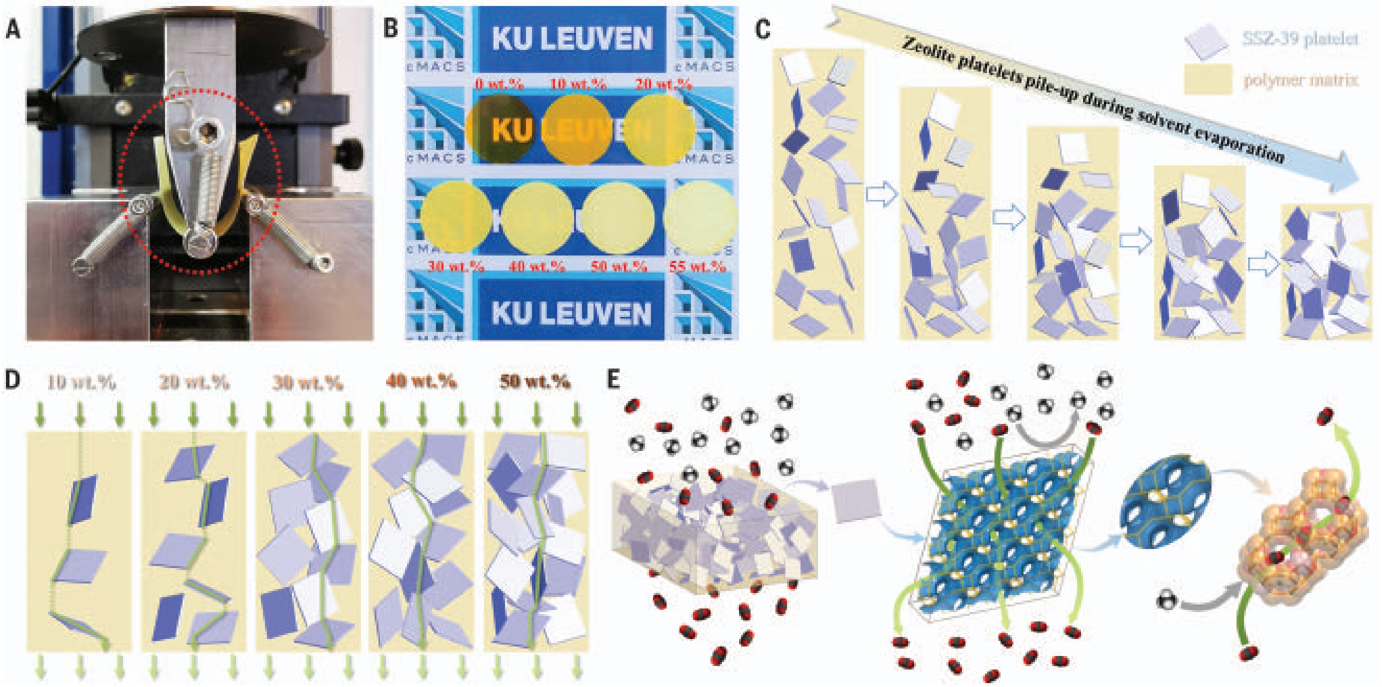

Fig. 4. Characterization and illustrations of platelet-shaped Na-SSZ-39 MMM. (**A**) The flexibility test (three-points bending) for 50 wt % Na-SSZ-39 MMM (table S4). (**B**) Visual appearance of 0 to 55 wt % Na-SSZ-39 MMMs. (**C**) Illustration of the solidification process of the platelet-shaped Na-SSZ-13 MMM, which results in a quasi-continuous zeolite phase across the membrane. (**D**) Illustration of the nonaligned zeolite platelet distribution in the polymer matrix with different zeolite loading. The preferential gas permeation pathways are indicated with the green arrows. (**E**) Schematic illustration of a MMM with (left) quasi-continuous zeolite phase and the unhindered CO_2 permeation (indicated with green arrows) through the (middle) 3D-channel system of platelet-shaped Na-SSZ-39 filler regardless of its orientation, as well as (right) the precise molecular sieving behavior that excludes CH_4 from CO_2 through the zeolite window.

and appear at the top of membrane when the zeolite loading reaches 30 wt % (Fig. 4C). In this context, the nonaligned, randomly oriented Na-SSZ-39 platelet distribution, which leads to a selective gas permeation highway, is a key driver and prerequisite for the membrane's extraordinary performance. This was also confirmed by comparing the platelet-shaped Na-SSZ-39 filler with a cuboid-shaped one [with similar properties except the aspect ratio (supplementary materials)]. As Fig. 3A shows, the sudden increment in CO_2-CH_4 selectivity was only observed for the platelet-shaped Na-SSZ-39 MMMs. Furthermore, although the cuboid-shaped Na-SSZ-39 MMMs also show great performances, the platelet-shaped Na-SSZ-39 MMMs exhibited far better CO_2-CH_4 selectivity and CO_2 permeability (tables S5 to S13), thus further confirming the morphology benefits of platelet-shaped Na-SSZ-39 MMMs.

Last, because the overall gas transport through the MMM is a net result of the properties of both zeolite and polymer, as well as of their mutual interactions, it is crucial to obtain a defect-free zeolite-polymer interface. Although rubbery polymers, such as polydimethylsiloxane (PDMS), facilitate creation of a defect-free interface (fig. S60), their intrinsically low selectivity and high permeability neutralize the beneficial contribution of the zeolite (table S15). The well-designed membrane preparation strategy minimizes the occurrence of unselective voids at the zeolite-Matrimid interface (figs. S54, S55, S58, and S59), allowing for ultrahigh zeolite loadings of >50 wt % without chemical modification of zeolite or polymer nor use of additives. Even at these high loadings, the Na-SSZ-39 MMMs still maintain desired flexibility (Fig. 4A), thus also creating excellent opportunities for module construction and upscaling.

Conclusions

We developed an ultrahigh-performance zeolite-filled MMM for CO_2 separations that shows unprecedented CO_2 removal performance, not only greater than that of any existing polymeric membrane or MMM but even surpassing that of most zeolite-only membranes. By circumventing the traditional incompatibility between zeolite filler and glassy polymer matrix, we prepared a flexible, defect-free zeolite-polyimide MMM with ultrahigh (>50 wt %) zeolite loadings. Na-SSZ-39 zeolite was discovered to be a superior filler because of its outstanding CO_2-philicity, precise molecular-sieving windows, strong competitive sorption behavior, and excellent stability, promoting strong, nonaging CO_2-separation performances. Because of the high–aspect ratio and 3D-channel system of the filler, a percolating gas permeation highway was created across the membrane, thus drastically enhancing the membrane's performance.

We used a scalable method to prepare defect-free zeolite-filled membranes with a commercially available glassy polymer, thus opening the door to developing well-processable, robust, and economical high-performance zeolite-filled MMMs for a variety of gas and liquid separations. It is especially beneficial for those zeolites that are difficult to be engineered into defect-free zeolite-only films.

REFERENCES AND NOTES

1. D. S. Sholl, R. P. Lively, *Nature* **532**, 435–437 (2016).
2. R. W. Baker, *Membrane Technology and Applications* (Wiley, ed. 3, 2012).
3. S. P. Nunes, K.-V. Peinemann, *Membrane Technology: In the Chemical Industry* (Wiley-VCH, ed. 2, 2006).
4. P. Bernardo, E. Drioli, G. Golemme, *Ind. Eng. Chem. Res.* **48**, 4638–4663 (2009).
5. R. W. Baker, B. T. Low, *Macromolecules* **47**, 6999–7013 (2014).
6. C. A. Scholes, G. W. Stevens, S. E. Kentish, *Fuel* **96**, 15–28 (2012).
7. S. Basu, A. L. Khan, A. Cano-Odena, C. Liu, I. F. J. Vankelecom, *Chem. Soc. Rev.* **39**, 750–768 (2010).
8. S. K. Simons, K. Nijmeijer, M. Wessling, *J. Membr. Sci.* **340**, 214–220 (2009).
9. G. He *et al.*, *Energy Environ. Sci.* **12**, 3305–3312 (2019).
10. M. E. Boot-Handford *et al.*, *Energy Environ. Sci.* **7**, 130–189 (2014).
11. L. M. Robeson, *J. Membr. Sci.* **320**, 390–400 (2008).
12. H. B. Park, J. Kamcev, L. M. Robeson, M. Elimelech, B. D. Freeman, *Science* **356**, eaab0530 (2017).
13. B. Comesaña-Gándara *et al.*, *Energy Environ. Sci.* **12**, 2733–2740 (2019).
14. N. Du *et al.*, *Nat. Mater.* **10**, 372–375 (2011).

15. M. Carta *et al.*, *Science* **339**, 303–307 (2013).
16. H. W. H. Lai *et al.*, *Science* **375**, 1390–1392 (2022).
17. Z. Lai *et al.*, *Science* **300**, 456–460 (2003).
18. N. Rangnekar, N. Mittal, B. Elyassi, J. Caro, M. Tsapatsis, *Chem. Soc. Rev.* **44**, 7128–7154 (2015).
19. M. Y. Jeon *et al.*, *Nature* **543**, 690–694 (2017).
20. X. Ma *et al.*, *Science* **361**, 1008–1011 (2018).
21. N. Kosinov, J. Gascon, F. Kapteijn, E. J. M. Hensen, *J. Membr. Sci.* **499**, 65–79 (2016).
22. W. J. Koros, C. Zhang, *Nat. Mater.* **16**, 289–297 (2017).
23. S. Wang *et al.*, *Energy Environ. Sci.* **9**, 1863–1890 (2016).
24. J. E. Bachman, Z. P. Smith, T. Li, T. Xu, J. R. Long, *Nat. Mater.* **15**, 845–849 (2016).
25. A. Kertik *et al.*, *Energy Environ. Sci.* **10**, 2342–2351 (2017).
26. B. Wang *et al.*, *Adv. Mater.* **32**, e1907701 (2020).
27. B. Seoane *et al.*, *Chem. Soc. Rev.* **44**, 2421–2454 (2015).
28. J. Dechnik, J. Gascon, C. J. Doonan, C. Janiak, C. J. Sumby, *Angew. Chem. Int. Ed.* **56**, 9292–9310 (2017).
29. M. Galizia *et al.*, *Macromolecules* **50**, 7809–7843 (2017).
30. I. F. Vankelecom, E. Scheppers, R. Heus, J. B. Uytterhoeven, *J. Phys. Chem.* **98**, 12390–12396 (1994).
31. R. Mahajan, R. Burns, M. Schaeffer, W. J. Koros, *J. Appl. Polym. Sci.* **86**, 881–890 (2002).
32. D. Bastani, N. Esmaeili, M. Asadollahi, *J. Ind. Eng. Chem.* **19**, 375–393 (2013).
33. S. I. Zones, Y. Nakagawa, S. T. Evans, G. S. Lee, US patent 5,958,370A (1999).
34. N. Nakazawa, S. Inagaki, Y. Kubota, *Chem. Lett.* **45**, 919–921 (2016).
35. M. Dusselier *et al.*, *Chem. Mater.* **27**, 2695–2702 (2015).
36. M. Dusselier, M. E. Davis, *Chem. Rev.* **118**, 5265–5329 (2018).
37. Ch. Baerlocher, L. B. McCusker, Database of zeolite structures (2017); http://www.iza-structure.org/databases.
38. T. D. Pham, Q. Liu, R. F. Lobo, *Langmuir* **29**, 832–839 (2013).
39. S. Faramawy, T. Zaki, A. A. E. Sakr, *J. Nat. Gas Sci. Eng.* **34**, 34–54 (2016).
40. Y. Li *et al.*, *Environ. Sci. Technol.* **53**, 11569–11579 (2019).
41. T. Rodenas *et al.*, *Nat. Mater.* **14**, 48–55 (2015).
42. S. J. Datta *et al.*, *Science* **376**, 1080–1087 (2022).

ACKNOWLEDGMENTS

We thank M. Roeffaers (KU Leuven, cMACS) for providing the Raman Spectromicroscopy measurement, M. Bastin for density measurement, and K. Yan for illustration drawing. This work was supported by the Fund for Scientific Research Flanders (FWO) and the Research Board of Ghent University (BOF). The computational resources (Stevin Supercomputer Infrastructure) and services used in this work were provided by the VSC (Flemish Supercomputer Center), funded by Ghent University, FWO, and the Flemish Government–department EWI. **Funding:** This work was supported by the Strategic Basic Research, Research Foundation–Flanders "SBOFWO" Biogas-Mambo S003721N (X.T. and I.V.); VlaioCataSPC moonrise HBC.2020.2612 (X.T. and I.V.); Research Foundation–Flanders "FWO" scholarships 1241822N, 12X7319N, and 1SB8821N (R.T., Y.L., and D.V.H.); Research Foundation–Flanders "FWO" G085220N (S.R., N.D.W., T.V.A., and M.D.); and Hercules fund AKUL/13/19 (I.V.) **Author contributions:** Conceptualization: X.T., Q.K., and I.V. Methodology: X.T., S.R., Q.K., R.T., M.D., and I.V. Investigation: X.T., S.R., Q.K., N.D.W., A.L., Y.L., I.A., D.V.H., and T.D. Visualization: X.T., S.R., A.L., and N.D.W. Funding acquisition: I.V., M.D., T.V.A., and V.V.S. Project administration: X.T. and I.V. Supervision: I.V. Writing – original draft: X.T. and R.T. Writing – review and editing: All authors. **Competing interests:** The authors declare that they have no competing interests. X.T., I.V., M.D., S.R., and R.T. submitted patent application EP22170367.1 by KU Leuven, which is based on this invention. **Data and materials availability:** All data are available in the main text or the supplementary materials.

SUPPLEMENTARY MATERIALS

science.org/doi/10.1126/science.ade1411
Materials and Methods
Supplementary Text
Figs. S1 to S66
Tables S1 to S21
References (*43–191*)
Movies S1 and S2
Data S1

Submitted 27 July 2022; accepted 16 November 2022
10.1126/science.ade1411

SYNTHETIC BIOLOGY

Decoding CAR T cell phenotype using combinatorial signaling motif libraries and machine learning

Kyle G. Daniels[1,2], Shangying Wang[3,4], Milos S. Simic[1,2], Hersh K. Bhargava[1,2], Sara Capponi[3,4], Yurie Tonai[1,2], Wei Yu[1,2], Simone Bianco[3,4]†*, Wendell A. Lim[1,2,4]*

Chimeric antigen receptor (CAR) costimulatory domains derived from native immune receptors steer the phenotypic output of therapeutic T cells. We constructed a library of CARs containing ~2300 synthetic costimulatory domains, built from combinations of 13 signaling motifs. These CARs promoted diverse human T cell fates, which were sensitive to motif combinations and configurations. Neural networks trained to decode the combinatorial grammar of CAR signaling motifs allowed extraction of key design rules. For example, non-native combinations of motifs that bind tumor necrosis factor receptor–associated factors (TRAFs) and phospholipase C gamma 1 (PLCγ1) enhanced cytotoxicity and stemness associated with effective tumor killing. Thus, libraries built from minimal building blocks of signaling, combined with machine learning, can efficiently guide engineering of receptors with desired phenotypes.

Chimeric antigen receptors (CARs) have demonstrated the power of synthetic signaling receptors as tools to reprogram immune cells to execute therapeutic functions, such as targeted killing of tumor cells (*1*). The antitumor efficacy of CARs is strongly modulated by the signaling domains that they contain. Current clinically approved CARs contain a core T cell receptor (TCR) signaling domain from CD3ζ [containing immunoreceptor tyrosine-based activation motifs (ITAMs) that recruit the kinase ZAP70] (*2*–*4*), along with a costimulatory signaling domain from either the CD28 (*5*, *6*) or 4-1BB (*7*) costimulatory immune receptors (*8*–*10*). The costimulatory domains are themselves composed of multiple signaling motifs, which are short peptides that bind to specific downstream signaling proteins, often through modular protein interaction domains [e.g., Src homology 2 (SH2), Src homology 3 (SH3), or other domains (*11*, *12*)]. Such peptide signaling motifs (referred to as linear motifs) are the fundamental building blocks that control the output of most signaling receptors. The constellation of signaling proteins recruited by a particular array of signaling motifs upon receptor stimulation is thought to shape the distinct cellular response. For example, in CARs, the 4-1BB costimulatory domain, which contains binding motifs for tumor necrosis factor receptor–associated factor (TRAF) signaling adaptor proteins, leads to increased T cell memory and persistence; the CD28 costimulatory domain, which contains binding motifs for phosphatidylinositol-3-kinase (PI3K), growth factor receptor-bound protein 2 (Grb2), and lymphocyte-specific protein tyrosine kinase (Lck), is associated with more effective T cell killing but reduced long-term T cell persistence (*13*). Thus, signaling motifs can be thought of as the "words" that are used to compose the phenotypic "sentences" communicated through signaling domains.

A major and still mostly outstanding goal in synthetic biology is to predictably generate new cell phenotypes by altering receptor composition. For example, in cancer immunotherapy, a general goal is not only to enhance T cell antitumor cytotoxicity but also to maintain a stem-like state associated with longer-term T cell persistence. Such a phenotype is associated with effective and durable tumor clearance (higher stemness is correlated with more resistance to T cell exhaustion). Libraries of costimulatory domains have been screened for improved phenotypes (*14*–*16*). However, the costimulatory domains used were from natural immune receptors (i.e., alternative preexisting sentences, to use the analogy to language). We propose that a more effective way to scan phenotypic space for synthetic receptors is to create libraries that sample new combinations of signaling motifs. Such an approach could, in principle, yield phenotypes that extend beyond those that can be generated by native receptor domains alone. Moreover, exploration of a broader range of receptor "motif space" could lead to a more systematic understanding of how different parameters of output are encoded by motif identity, combination, and order.

We recombined 13 signaling motifs (words) to create a CAR costimulatory domain library with randomized motif combinations (new

---

[1]Cell Design Institute, University of California, San Francisco, San Francisco, CA 94158, USA. [2]Department of Cellular and Molecular Pharmacology, University of California, San Francisco, San Francisco, CA 94158, USA. [3]Department of Functional Genomics and Cellular Engineering, IBM Almaden Research Center, San Jose, CA 95120, USA. [4]Center for Cellular Construction, San Francisco, CA 94158, USA.
***Corresponding author. Email: sbianco@altoslabs.com (S.B.); wendell.lim@ucsf.edu (W.A.L.)**
†Present address: Altos Labs, Redwood City, CA 94065, USA.

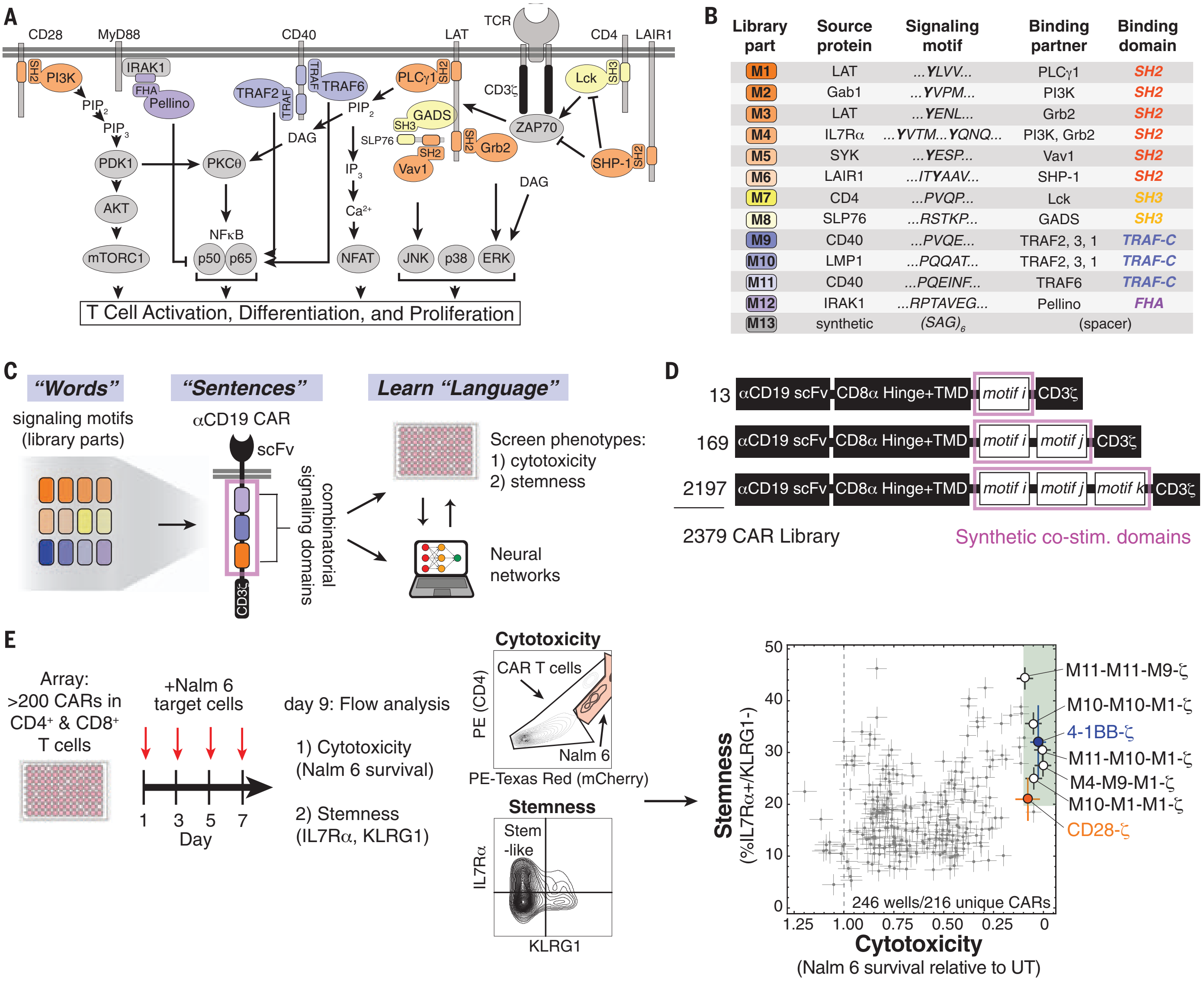

Library part	Source protein	Signaling motif	Binding partner	Binding domain
M1	LAT	*...**Y**LVV...*	PLCγ1	*SH2*
M2	Gab1	*...**Y**VPM...*	PI3K	*SH2*
M3	LAT	*...**Y**ENL...*	Grb2	*SH2*
M4	IL7Rα	*...**Y**VTM...**Y**QNQ...*	PI3K, Grb2	*SH2*
M5	SYK	*...**Y**ESP...*	Vav1	*SH2*
M6	LAIR1	*...IT**Y**AAV...*	SHP-1	*SH2*
M7	CD4	*...PVQP...*	Lck	*SH3*
M8	SLP76	*...RSTKP...*	GADS	*SH3*
M9	CD40	*...PVQE...*	TRAF2, 3, 1	*TRAF-C*
M10	LMP1	*...PQQAT...*	TRAF2, 3, 1	*TRAF-C*
M11	CD40	*...PQEINF...*	TRAF6	*TRAF-C*
M12	IRAK1	*...RPTAVEG...*	Pellino	*FHA*
M13	synthetic	$(SAG)_6$	(spacer)	

Fig. 1. CAR costimulatory domains with synthetic signaling motif combinations generate diverse cell fates with decoupled cytotoxicity and stemness. (**A**) A diverse set of proteins that function in T cell signaling are recruited by signaling motifs in the library parts. FHA, forkhead-associated domain; IP_3, inositol trisphosphate; JNK, c-Jun N-terminal kinase; mTORC1, mammalian target of rapamycin complex 1; NFAT, nuclear factor of activated T-cells; PIP_3, phosphatidylinositol 3,4,5-trisphosphate. (**B**) Description of library parts used in the combinatorial library. Each part is 16 to 18 amino acids long, including the signaling motif(s) and flanking sequence. Phospho-tyrosines are shown in bold. (**C**) New combinations of signaling motifs create distinct CAR signaling programs that control T cell phenotype. (**D**) Schematics of αCD19 CAR with variable signaling domains. (**E**) CAR T cells with various signaling motif combinations produce a broad range of cytotoxicity and stemness. $CD4^+$ and $CD8^+$ CAR T cells were pulsed four times with Nalm 6 leukemia cells and assayed for CAR T cell cytotoxicity and stemness. Errors for Nalm 6 survival and the stem-like $IL7R\alpha^+/KLRG1^-$ population in (E) were estimated by calculating the average standard deviation for seven CAR constructs with internal replicates in the array. PE, phycoerythrin; UT, untransduced.

sentences) (Fig. 1). This library of new signaling sentences produced a range of phenotypes, including combinations of phenotypes that are not observed with native signaling domains. We used neural networks to decode the language of signaling motifs, create predictive models, and extract design rules that inform the engineering of CAR signaling domains that increase cytotoxicity and stemness.

Results

A CAR library with synthetic combinations of signaling motifs generates diverse CAR T cell cytotoxicity and memory potential

To construct a combinatorial library of CAR signaling domains, we searched the Eukaryotic Linear Motif (ELM) database (*17*) and primary literature to curate a collection of 12 peptide motifs from natural signaling proteins that recruit key downstream signaling proteins that function in T cell activation. The motifs in the library recruit proteins such as phospholipase C gamma 1 (PLCγ1), TRAFs, Grb2, Grb2-related adaptor downstream of Shc (GADS), Src homology region 2 domain–containing phosphatase (SHP-1), vav guanine nucleotide exchange factor 1 (Vav1), PI3K, Lck, and Pellino protein. For example, library motif 1 is

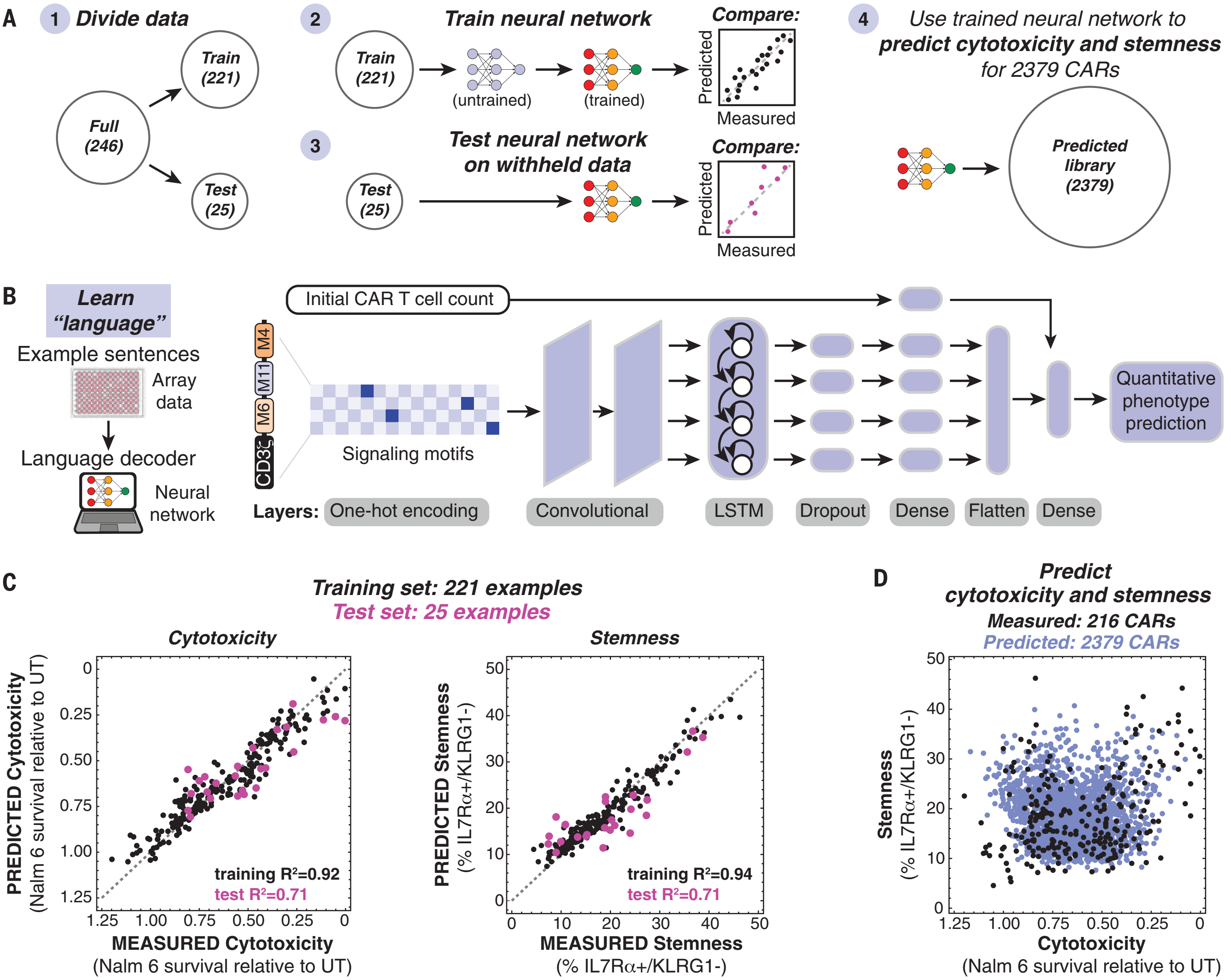

Fig. 2. Neural networks decode the combinatorial language of signaling motifs to predict cytotoxicity and stemness of motif combinations. (**A**) Array data were subdivided in datasets to train and test neural networks that were subsequently used to predict the cytotoxicity and stemness of 2379 CARs. (**B**) Schematic of the neural network used to predict CAR T cell phenotype. LSTM, long short-term memory. (**C**) Neural networks trained on array data predict the cytotoxicity and stemness of CARs in the training sets (black) and the withheld test sets (pink). The root mean squared error (RMSE) for the cytotoxicity training set is 0.07579, and the RMSE for the cytotoxicity test set is 0.1327. The RMSE for the stemness training set is 2.2038, and the RMSE for the stemness test set is 4.7941. (**D**) Trained neural networks were used to predict the cytotoxicity and stemness of 2379 CARs containing one to three variable signaling motifs. Predictions represent the mean for *n* = 10 neural networks with different hyperparameters.

derived from the linker for activation of T cells (LAT) and contains the core motif YLVV, which when tyrosine-phosphorylated, binds the N-terminal SH2 domain of PLCγ1 with high specificity (*18*) (Y, Tyr; L, Leu; V, Val). Motif 6 contains the motif ITYAAV from the leukocyte associated immunoglobulin-like receptor 1 (LAIR1), which binds the phosphatase SHP-1 through its SH2 domain (*19*) (I, Ile; T, Thr; A, Ala). In addition to the 12 signaling motifs, we included a spacer motif as the 13th component in the library. The combinatorial library was constructed within the context of an anti-CD19 CAR (containing an anti-CD19 extracellular single-chain variable fragment and a CD3ζ signaling domain). The synthetic costimulatory domains had either one, two, or three signaling motifs. The 13 motifs were randomly inserted in positions i, j, and k (Fig. 1) to yield 2379 different motif combinations (Fig. 1, B to E). To confirm that the library displayed sufficient phenotypic diversity, we first performed low-resolution pooled screens, in which we transduced a mixed population of CD4$^+$ and CD8$^+$ primary human T cells at low multiplicity of infection and activated the pool with Nalm 6 leukemia cells (CD19$^+$) for 8 to 9 days. We used fluorescence-activated cell sorting (FACS)–based sequencing enrichment assays to observe a diverse range of phenotypic outputs for T cell proliferation, formation of central memory T cells expressing receptor-type tyrosine-protein phosphatase C (CD45RA) and lacking L-selectin (CD62L), and T cell degranulation [lysosome-associated membrane glycoprotein 1 (CD107A$^+$) T cells, a proxy for cytotoxic response] (fig. S1). All T cells were activated with beads displaying CD3 and CD28 to allow for viral transduction, and subsequent activation through CARs with distinctive signaling domains led to divergent phenotypes.

To screen the library at higher resolution, we transformed bacteria with library plasmid stocks and randomly picked colonies to select

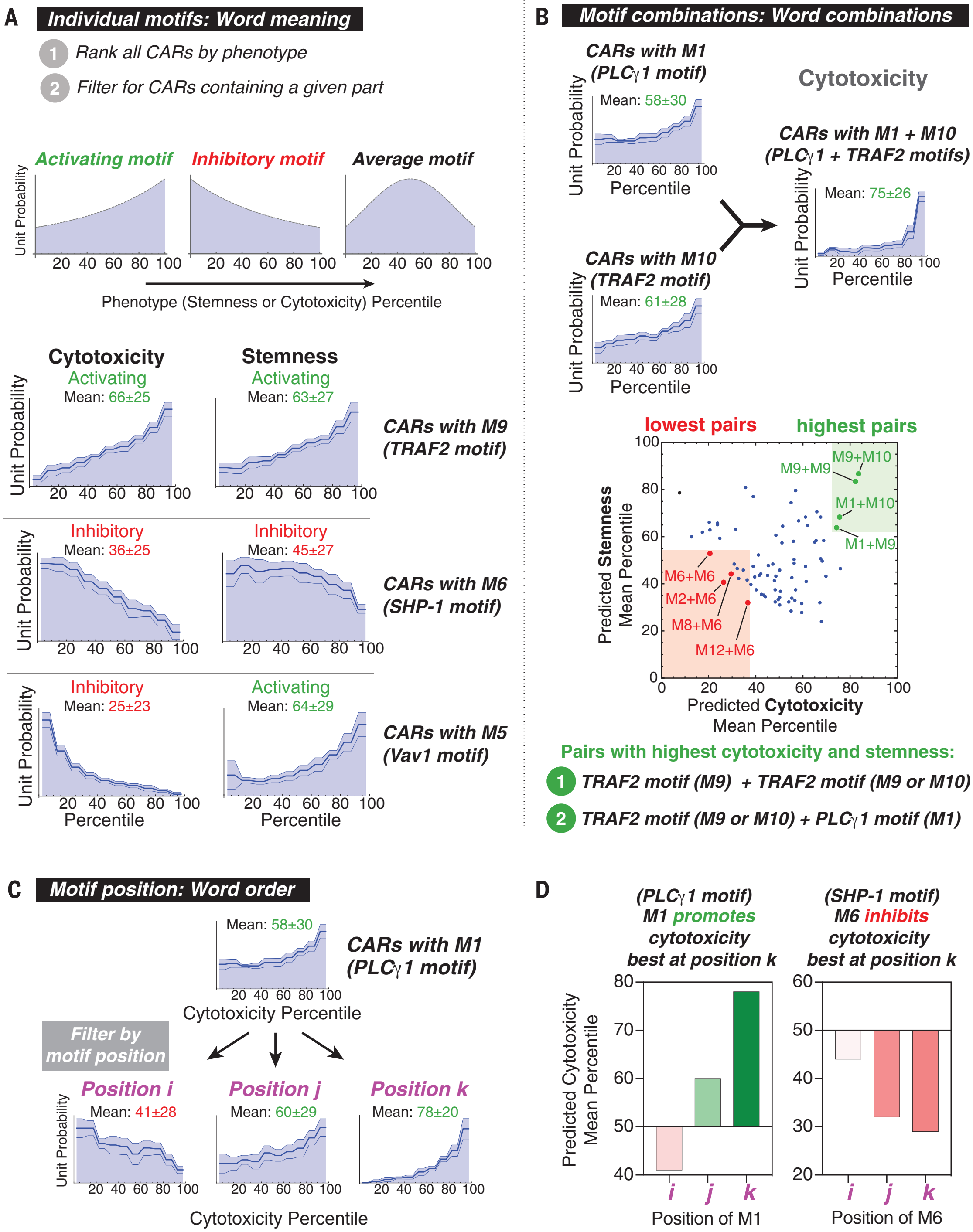

Fig. 3. Distribution analysis quantifies elements of linear motif language to extract design parameters for signaling domains. (**A**) The distribution of library parts throughout CARs in the ranked library reflects effects of signaling motifs on phenotype. Activating motifs are found in CARs with higher rank, and inhibitory motifs are found in CARs with a lower rank. The three lines within the distributions represent mean predictions ± SEM calculated from $n = 10$ neural networks. (**B**) CARs containing pairs of motifs that recruit TRAFs (M9 and M10) or PLCγ1 (M1) promote high cytotoxicity and stemness. Pairs promoting the highest and lowest cytotoxicity and stemness were determined by taking the sum of the mean percentile for each phenotype. (**C**) Cytotoxicity percentile distributions for CARs containing M1 at various positions demonstrate that effects of signaling motifs on phenotype are position dependent. (**D**) Position-dependence of signaling motifs is quantified by calculating the mean of percentile distributions. M1 is predicted to promote cytotoxicity best at position k, whereas M6 is predicted to inhibit cytotoxicity best at position k.

a subset of more than 200 CARs from the combinatorial library to characterize in an arrayed screen (Fig. 1E). An arrayed screen, in which each CAR is studied independently, was important because immune paracrine signaling could confound analysis of pooled CAR T cell screens. We activated the CD4$^+$ and CD8$^+$ CAR T cells in the arrayed screen by culturing with Nalm 6 (CD19$^+$) cells for 8 to 9 days. Four pulses of Nalm 6 cells were used to mimic longer term stimulation that can exacerbate T cell exhaustion. At the end of the coculture, we used flow cytometry to assess the cytotoxicity of the mixed CD4$^+$ and CD8$^+$ CAR T cell populations (based on Nalm 6 cell survival), stemness [interleukin-7 receptor subunit alpha (IL7Rα^+) and killer cell lectin receptor G1 (KLRG1$^-$)] (*20*–*23*), and maintenance of T cell populations with markers of central memory or naïve state (CD45RA and CD62L).

The CARs in the arrayed screen displayed a range of cytotoxicity and stemness. The total naïve and central memory population was positively correlated with cytotoxicity (fig. S2B). Stemness and the naïve population were roughly proportional across the library (fig. S2, C and D). However, cytotoxicity and stemness were uncoupled. This observation underscores the ability of unusual combinations of motifs in costimulatory domains to drive CAR T cells to varied cell fates with particular combinations of phenotypes. Several costimulatory domains produced cytotoxicity and stemness comparable to that of 4-1BB. Many of these contained motifs that recruit both TRAFs (motif 9, motif 10, motif 11) and PLCγ1 (motif 1). For example, M10-M10-M1-ζ, M10-M1-M1-ζ, M11-M10-M1-ζ, and M4-M9-M1-ζ all promoted cytotoxicity and stemness.

Neural networks predict the CAR T cell cytotoxicity and memory potential encoded by combinations of signaling motifs

The diverse cytotoxicity and stemness profiles observed in our arrayed screen are consistent with a complex relationship between signaling motif combinations and arrangement and resulting T cell phenotypes. We sought to leverage the combinatorial nature of the costimulatory domain library by using machine learning to decode the "language" of signaling motifs that relates motif combinations to cytotoxicity and stemness outputs. We separated the arrayed screen data into a training set (221 examples) and a test set (25 examples). We then used these datasets to train several machine-learning algorithms to predict cytotoxicity and stemness based on costimulatory domain identity and arrangement (Fig. 2A and fig. S3). Neural networks (Fig. 2B) were best able to recapitulate the measured phenotypes in the training data (Fig. 2C) and to effectively predict the phenotypes in the test set (Fig. 2D). For both cytotoxicity and stemness training and test sets, the neural network was able to capture much of the relationship between signaling motif composition and phenotype, with coefficient of determination (R^2) values of ~0.7 to 0.9.

The trained neural networks then allowed us to predict the CAR T cell cytotoxicity and stemness that would result from each of the 2379 motif combinations in the full combinatorial library (Fig. 2D), including those that were not part of the smaller arrayed screen. These simulated 2379 CARs sample the entire combinatorial space of the library, providing a dataset from which we extracted design rules. We analyzed (i) the overall contribution of each motif to a particular phenotype (without regard to combinatorial context), (ii) identification of pairwise motif combinations that promote particular phenotypes, and (iii) positional dependence of motifs.

Distribution analysis summarizes the effects of signaling motifs, motif combinations, and motif positions on CAR T cell phenotype

To assess the overall contribution of individual motifs, we ranked all the CARs in our library by neural network–predicted cytotoxicity and stemness and then assessed whether motifs were enriched in the strong or weak ends of the phenotypic distribution (Fig. 3A and fig. S4). If a motif is generally activating for a phenotype, then it is expected to be more common in highly ranked CARs; if a motif is inhibitory, then it is expected to be more common in poorly ranked CARs. Although the effects observed in this distribution analysis depend on other motifs in the CAR and the position of the motif in question, the distributions are informative of the overall effect that each motif has in the context of the library. An analogous distribution analysis was also done on the pooled screening proliferation data (fig. S5).

This distribution analysis highlighted several effective motifs that have activating and inhibitory roles. For example, motif M9 is the PQVE motif [from cluster of differentiation 40 (CD40)], which binds TRAF2, and is associated with T cell activation and function (*24*, *25*) (P, Pro; Q, Gln; E, Glu). Accordingly, M9 is enriched in CARs with high cytotoxicity (mean 66th percentile) and high stemness (mean: 63rd percentile), indicating that overall, it promotes both of these phenotypes. In a contrasting example, M6 (from LAIR1) recruits the phosphatase SHP-1, an inhibitor of T cell activation. Accordingly, M6 is enriched in CARs with low cytotoxicity (mean: 36th percentile) and low stemness (mean: 45th percentile), indicative of inhibition of both phenotypes. Some motifs can activate one phenotype and inhibit another: M5, which binds Vav1, is unrepresented in CARs with high cytotoxicity (mean: 25th percentile) but overrepresented in CARs with high stemness (mean: 64th percentile). Thus, Vav1 signaling appears to promote stemness while inhibiting killing. The quantified effects of all individual motifs on cytotoxicity and stemness are shown in the heatmap in fig. S4. The TRAF binding motifs (M9 and M10) are among the best at promoting both cytotoxicity and stemness.

We anticipated that phenotypes would be highly dependent on motif combinations, because different downstream signaling pathways could be either complementary, redundant, or competing. To examine motif pairs that favored particular phenotypes, we examined the occurrence of each possible pair (without regard to order) in the ranked distribution. Several specific motif pairs appear to promote both cytotoxicity and stemness when they occur in combination within a costimulatory domain. For example, M1 (PLCγ1) and M10 (TRAF) were each activating with respect to cytotoxicity (means: 58th and 60th percentiles), but the M1+M10 motif pair was even more strongly activating (mean: 75th percentile). The predicted mean cytotoxicity and stemness percentiles for all 144 pairs of motifs M1 to M12 are shown in Fig. 3B. The motif pairs M1+M10, M1+M9, M9+M9, and M9+M10 were best at promoting cytotoxicity and stemness. These pairs all demonstrate that TRAF-binding motifs (M9 and M10) work well in tandem, as well as in combination with the motif that recruits PLCγ1 (M1), whose signaling activates nuclear factor kappa B (NFκB). Thus, these pathways may serve complementary roles in these phenotypes. A number of motif pairs strongly inhibited cytotoxicity and stemness. All four motif pairs with the lowest cytotoxicity and stemness contain M6, which binds the inhibitory phosphatase SHP-1.

The phenotype of CAR T cells was highly dependent on the position of a motif within the costimulatory domain (fig. S4B). For example, M1 (PLCγ1) showed strong cytotoxicity when in positions k or j and weak cytotoxicity in position i (Fig. 3, C and D). M9 (TRAF) and M10 (TRAF) showed optimal cytotoxicity and stemness when in positions i and j. This is consistent with the experimental observation that TRAF-binding parts M9 and M10 followed by M1 (in N- to C-terminal order) promote the most cytotoxicity and stemness (M1 followed by M9 or M10 does not (fig. S2E). These results indicate that shuffling motif position is an approach for calibrating phenotype.

The above distribution analysis quantifies elements of motif language, capturing the effects of motifs (word meaning), motif pairs (word combinations), and motif position (word order) on phenotype. The analysis also yields design rules that can inform combinations and arrangements of motifs that are capable of producing a desired cell fate. For example, a synthetic costimulatory domain that contains one or more TRAF binding motifs (M9 or M10) followed by a PLCγ1 (M1) motif appears to be effective at promoting both cytotoxicity and stemness (Fig. 4A). Although tandem TRAF binding motifs occur in the naturally evolved 4-1BB receptor (*26*) (fig. S6A), the combination of TRAF and PLCγ1 motifs is not found in natural characterized immune receptors. Thus, we tested whether adding PLCγ1 (M1) motifs to 4-1BB–like domains could improve phenotypes induced by CARs. Moreover, we also wanted to determine whether adding M1 might be a general strategy to improve the efficacy of other costimulatory domains, such as CD28.

Neural networks predict that the addition of M1 enhances the cytotoxicity and memory potential of 4-1BB–ζ but not CD28–ζ

We examined the neural network–predicted library to predict the effects of adding the M1 motif to CD28-like and 4-1BB–like synthetic costimulatory domains (library members whose signaling motifs shared the overall configuration of natural signaling motifs in CD28 and 4-1BB) (Fig. 4A). The 4-1BB–like costimulatory domains were predicted by the neural network model to show increased cytotoxicity and stemness, consistent with experimental observations. By contrast, addition of M1 motifs to CD28-like costimulatory domains was not predicted to enhance cytotoxicity or stemness.

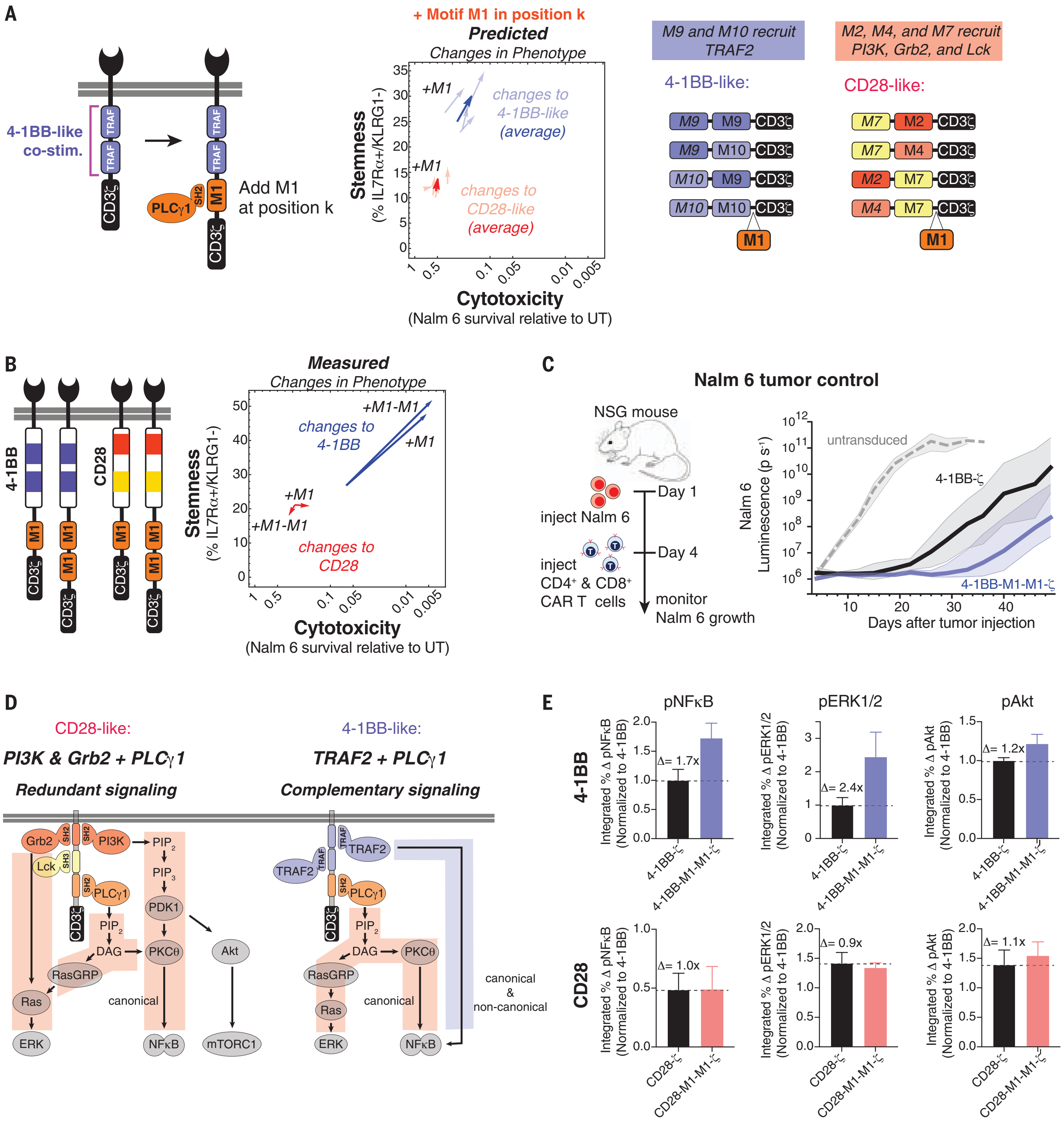

Fig. 4. Neural networks accurately predict that PLCγ1 binding motifs improve the cytotoxicity and stemness of 4-1BB–ζ but not CD28–ζ. (**A**) Library parts that share consensus signaling motifs with 4-1BB and CD28 costimulatory domains were used to predict the effect of adding M1 to 4-1BB and CD28. (**B**) Addition of one or two copies of M1 improved in vitro cytotoxicity and stemness of 4-1BB–ζ but not CD28–ζ. CAR T cell cytotoxicity and stemness were assessed after four pulses of Nalm 6 cells. Data are means of $n = 3$ to 5 replicates. (**C**) $CD4^+$ and $CD8^+$ CAR T cells were sorted for CAR expression 6 days after activation (1 day after Dynabead removal) and injected into mice 10 days later. NSG mice were injected intravenously with 0.5×10^6 Nalm 6 cells and then injected intravenously with 3×10^6 CAR^+ T cells on day 4. CAR T cells with 4-1BB–M1–M1–ζ showed improved early tumor control relative to 4-1BB–ζ. Traces in (C) are median luminescence ± SEM confidence interval. (**D**) Costimulatory PLCγ1 signaling is redundant to signaling provided by PI3K and Grb2 but complementary to TRAF signaling. (E) Addition of M1 to 4-1BB–ζ induced modest changes in Akt phosphorylation, which is not downstream of PLCγ1 signaling, relative to the changes in ERK1, ERK2 and NFκB phosphorylation, which are downstream of PLCγ1 signaling. $CD4^+$ and $CD8^+$ CAR T cells were pulsed once with Nalm 6 leukemia cells and fixed at various time points from 0 to 60 min. Phosphorylation of ERK1 and ERK2, NFκB, and Akt was assessed by flow cytometry. Data for (**E**) are means and standard deviation of $n = 3$ replicates. p, phosphorylated.

To experimentally test this, we synthesized derivatives of the 4-1BB and CD28 costimulatory domains with one or two copies of the M1 motif added to the C terminus and tested the effects of these costimulatory domains on killing of Nalm 6 and maintenance of T cell stemness (Fig. 4B). Consistent with predictions, 4-1BB showed notably enhanced cytotoxicity and stemness upon addition of M1, whereas CD28 showed almost no change. Importantly, in addition to predicted in vitro changes, the 4-1BB–M1–M1–ζ CAR construct showed improved efficacy in a Nalm 6 tumor Nod scid gamma (NSG) mouse model (Fig. 4C and fig. S6). Relative to standard 4-1BB CAR T cells, the 4-1BB–M1–M1–ζ CAR T cells delayed the growth of Nalm 6 tumor cells for an additional 2 weeks, in agreement with the predictions from the library and neural network model.

Why might a PLCγ1 motif improve T cell phenotype in combination with the 4-1BB domain (TRAF motifs) but not in the context of the CD28 domain (PI3K, Grb2, Lck motifs)? PLCγ1 catalyzes the production of diacylglycerol (DAG) from phosphatidylinositol 4,5-bisphosphate (PIP$_2$), which activates Ras guanyl-releasing protein (RasGRP) and protein kinase C theta (PKCθ), subsequently activating the extracellular signal–regulated kinases (ERK1 and ERK2) and NFκB. This signaling is similar and possibly redundant to that of PI3K and Grb2, which also activate RasGRP and PKCθ. TRAF signaling, however, does not activate RasGRP or PKCθ, such that PLCγ1 and TRAF signaling are more likely to be complementary (Fig. 4D). We experimentally characterized the 4-1BB–M1–M1–ζ CAR construct (compared with standard 4-1BB–ζ CAR) by measuring the kinetics of phosphorylation of protein kinase B (Akt), ERK1 and ERK2, and NFκB after stimulation by Nalm 6 (Fig. 4E and fig. S7A). The addition of the M1 motifs increased phosphorylation of ERK1 and ERK2 (1.7-fold) and NFκB (2.4-fold), both of which depend on activation of PLCγ1. Phosphorylation of Akt, which is not dependent on PLCγ1, showed only a 1.2-fold increase. The observed increase in activation of NFκB and ERK1 and ERK2 supports the hypothesis that PLCγ1 signaling is complementary to TRAF signaling and is consistent with the importance of NFκB activation for the maintenance of CD8$^+$ T cell memory (*27*). By contrast, no significant increase in activation of NFκB and ERK1 and ERK2 was observed for a CAR in which the PLCγ1 motif was appended to the CD28 costimulatory domain. We observed little additional activation-induced increase in PLCγ1 phosphorylation in the cells bearing the 4-1BB–M1–M1–ζ CAR (fig. S7C), suggesting that M1 may enhance signaling by altering the precise spatial organization of PLCγ1 binding sites (*28*) or by promoting PLCγ1-dependent LAT clustering (*29*).

Conclusions

We find that signaling motif libraries and machine learning can be combined to elucidate rules of CAR costimulatory signaling and to guide the design of non-natural costimulatory domains with improved phenotypes, both in vitro and in vivo. Costimulatory signaling modulates the outcome of CAR T cell activation, making costimulatory domains attractive engineering targets for customizing or improving cell therapies. Thus far, costimulatory domain engineering has mostly been limited to the addition of intact natural domains such as those from 4-1BB, CD28, or the interleukin-2 receptor beta subunit (IL2Rβ), effectively using naturally occurring signaling sentences (motif combinations). We used motifs from receptors as words to generate thousands of different signaling sentences that drove T cells to distinct cell fates, potentially yielding more diverse and nuanced phenotypic meaning. Augmenting experimental analysis of a subset of receptors with neural network analysis allowed us to explore a larger region of combinatorial motif space. In particular, we identified the non-natural combination of TRAF- and PLCγ1-binding motifs that may be useful in CAR T cell therapies. With an arrayed screen of several hundred receptors and machine learning, we identified basic elements of signaling motif language and extracted design rules that relate motif combinations to cell fate. This represents a step toward forward engineering receptors with desired properties. Similar screening approaches with other CARs and target cancer cells are needed to determine the optimal signaling domains for each CAR and tumor type. Libraries may also be of use in identifying combinations of binding, hinge, linker, transmembrane, and signaling domains that produce optimal T cell function and assessing the safety and toxicity of such combinations. Exploration of these larger libraries may benefit from machine learning owing to the size and complexity of the combinatorial space. Machine learning–augmented screens of this type might be used to engineer many other classes of receptors for biological research and cell therapy applications that involve cellular processes controlled by combinations of signaling motifs.

REFERENCES AND NOTES

1. D. M. Barrett, N. Singh, D. L. Porter, S. A. Grupp, C. H. June, *Annu. Rev. Med.* **65**, 333–347 (2014).
2. B. A. Irving, A. Weiss, *Cell* **64**, 891–901 (1991).
3. C. Romeo, B. Seed, *Cell* **64**, 1037–1046 (1991).
4. F. Letourneur, R. D. Klausner, *Proc. Natl. Acad. Sci. U.S.A.* **88**, 8905–8909 (1991).
5. A. Krause *et al.*, *J. Exp. Med.* **188**, 619–626 (1998).
6. H. M. Finney, A. D. G. Lawson, C. R. Bebbington, A. N. C. Weir, *J. Immunol.* **161**, 2791–2797 (1998).
7. C. Imai *et al.*, *Leukemia* **18**, 676–684 (2004).
8. C. A. Ramos *et al.*, *Mol. Ther.* **26**, 2727–2737 (2018).
9. G. Enblad *et al.*, *Clin. Cancer Res.* **24**, 6185–6194 (2018).
10. Y. Kagoya *et al.*, *Nat. Med.* **24**, 352–359 (2018).
11. C. A. Koch, D. Anderson, M. F. Moran, C. Ellis, T. Pawson, *Science* **252**, 668–674 (1991).
12. M. Sudol, *Oncogene* **17**, 1469–1474 (1998).
13. O. U. Kawalekar *et al.*, *Immunity* **44**, 380–390 (2016).
14. K. S. Gordon *et al.*, *Nat. Biomed. Eng.* **6**, 855–866 (2022).
15. D. B. Goodman *et al.*, *Sci. Transl. Med.* **14**, eabm1463 (2022).
16. R. Castellanos-Rueda *et al.*, *Nat. Commun.* **13**, 6555 (2022).
17. H. Dinkel *et al.*, *Nucleic Acids Res.* **40**, D242–D251 (2012).
18. J. C. D. Houtman *et al.*, *Biochemistry* **43**, 4170–4178 (2004).
19. Mj. Xu, R. Zhao, Z. J. Zhao, *J. Biol. Chem.* **275**, 17440–17446 (2000).
20. M. Borsa *et al.*, *Sci. Immunol.* **4**, eaav1730 (2019).
21. D. Herndler-Brandstetter *et al.*, *Immunity* **48**, 716–729.e8 (2018).
22. H. Wu *et al.*, *J. Immunother. Cancer* **9**, e002662 (2021).
23. E. B. M. Remmerswaal *et al.*, *Eur. J. Immunol.* **49**, 694–708 (2019).
24. S. P. Schoenberger, R. E. M. Toes, E. I. H. van der Voort, R. Offringa, C. J. M. Melief, *Nature* **393**, 480–483 (1998).
25. S. M. McWhirter *et al.*, *Proc. Natl. Acad. Sci. U.S.A.* **96**, 8408–8413 (1999).
26. H. H. Park, *Front. Immunol.* **9**, 1999 (2018).
27. K. M. Knudson *et al.*, *Proc. Natl. Acad. Sci. U.S.A.* **114**, E1659–E1667 (2017).
28. A. Basant, M. Way, *eLife* **11**, e74655 (2022).
29. L. Zeng, I. Palaia, A. Šarić, X. Su, *J. Cell Biol.* **220**, e202009154 (2021).

ACKNOWLEDGMENTS

We thank S. Levinson for sharing tumor cell lines, I. Webster of Zenysis Technologies for assistance with processing sequencing data, R. Almeida and other members of the Lim lab for helpful discussions, and W. Maestas and J. Fraser for critical reading of this manuscript. **Funding:** This work was supported by a Burroughs Wellcome Fund Postdoc Enrichment Program Fellowship to K.G.D.; a Damon Runyon Cancer Research Foundation Fellowship to K.G.D.; an IBM Exploratory Life Science program grant to S.W., S.C., and S.B.; and NSF Center for Cellular Construction grant DBI-1548297. Research reported in this publication was supported by the National Cancer Institute of the National Institutes of Health under award number U54CA244438 and R01 CA249018 to W.A.L. The content is solely the responsibility of the authors and does not necessarily represent the official views of the National Institutes of Health. **Author contributions:** K.G.D. and W.A.L. designed research. S.W., K.G.D., and S.B. designed the artificial intelligence (AI) research. K.G.D., H.K.B., M.S.S., Y.T., W.Y., and S.W. performed research. K.G.D., S.W., and W.A.L. contributed new reagents or analytic tools. K.G.D. and S.W. analyzed data. S.B., S.C., and W.A.L. contributed research guidance and supervision. K.G.D. and W.A.L. wrote the paper. All authors edited the paper. **Competing interests:** A provisional patent application has been filed by the University of California related to this work (US application number 63/279,578). W.A.L. is on the scientific advisory board for Allogene Therapeutics and is a shareholder of Gilead Sciences and Intellia Therapeutics. **Data and materials availability:** Reagents are available from the corresponding author upon request from the authors. The pHR plasmid containing the anti-CD19 CAR and plasmids containing DNA for the 13 motifs used in the combinatorial library will be available from Addgene. Array screening data are available in supplemental information. Machine-learning data analysis codes are available at https://github.com/CCCofficial/combinatorial_signaling_motif_libraries. **License information:** Copyright © 2022 the authors, some rights reserved; exclusive licensee American Association for the Advancement of Science. No claim to original US government works. https://www.science.org/about/science-licenses-journal-article-reuse

SUPPLEMENTARY MATERIALS

science.org/doi/10.1126/science.abq0225
Materials and Methods
Figs. S1 to S7
Tables S1 and S2
References (*30–32*)
MDAR Reproducibility Checklist
Data S1 to S3

Submitted 13 March 2022; accepted 18 November 2022
Published online 8 December 2022
10.1126/science.abq0225

CELL BIOLOGY

ATG9A prevents TNF cytotoxicity by an unconventional lysosomal targeting pathway

Jon Huyghe[1,2]†, Dario Priem[1,2]†, Lisette Van Hove[1,2], Barbara Gilbert[1,2], Jürgen Fritsch[3], Yasuo Uchiyama[4], Esther Hoste[1,2], Geert van Loo[1,2], Mathieu J. M. Bertrand[1,2]*

Cell death induced by tumor necrosis factor (TNF) can be beneficial during infection by helping to mount proper immune responses. However, TNF-induced death can also drive a variety of inflammatory pathologies. Protectives brakes, or cell-death checkpoints, normally repress TNF cytotoxicity to protect the organism from its potential detrimental consequences. Thus, although TNF can kill, this only occurs when one of the checkpoints is inactivated. Here, we describe a checkpoint that prevents apoptosis through the detoxification of the cytotoxic complex IIa that forms upon TNF sensing. We found that autophagy-related 9A (ATG9A) and 200kD FAK family kinase-interacting protein (FIP200) promote the degradation of this complex through a light chain 3 (LC3)–independent lysosomal targeting pathway. This detoxification mechanism was found to counteract TNF receptor 1 (TNFR1)–mediated embryonic lethality and inflammatory skin disease in mouse models.

Tumor necrosis factor (TNF) directly promotes inflammation by activating the mitogen-activated protein kinase (MAPK) and nuclear factor κB (NF-κB) signaling pathways but can also drive inflammation indirectly by triggering cell death. Accordingly, TNF-induced cell death contributes to proper immune responses during microbial infection but is also the cause of a variety of (sterile) inflammatory diseases when induced aberrantly or in excess (*1*). Cell death is, however, not the default response of TNF sensing and only proceeds when a protective brake, or cell-death checkpoint, is inactivated within the pathway. The outcome of TNF sensing is mainly regulated by the assembly of two distinct protein complexes downstream of TNF receptor 1 (TNFR1) (*2*, *3*). The membrane-bound complex I forms within seconds of TNF sensing and predominantly leads to MAPK- and NF-κB–dependent gene activation. How this complex further evolves to induce cell death is less clear but involves the assembly of a secondary cytosolic complex, Complex II, which originates from the binding of FAS-associated death domain (FADD) to the receptor-dissociated complex I components TNFR1-associated death domain (TRADD) and/or receptor-interacting protein kinase 1 (RIPK1) (*4*, *5*). Complex II functions as a cytosolic platform for the binding and activation of CASPASE-8 (CASP8), leading to the induction of extrinsic apoptosis. The complex II that assembles upon sensing of TNF alone has been renamed IIa to differentiate it from IIb, which additionally forms in conditions that trigger RIPK1 kinase activation (*6*). Two cell-death checkpoints are known to counteract apoptosis induction by these pro-death complexes. First, the NF-κB–dependent up-regulation of prosurvival genes that counteract CASP8 activation in complex IIa, such as cellular FLICE-inhibitory protein (cFLIP), protects cells from RIPK1 kinase–independent apoptosis (*5*, *7*). Second, the phosphorylation-dependent inactivation of RIPK1 by IκB kinase α (IKKα)/IKKβ, and TANK-binding kinase 1 (TBK1)/IKKε prevents complex IIb assembly and subsequent RIPK1 kinase-dependent apoptosis induction (*8*–*11*). Although both checkpoints are in place to prevent lethal CASP8 activation, a nonlethal pool of CASP8 is still activated in response to TNF and functions as a third checkpoint that prevents RIPK1 kinase–dependent necroptosis by cleaving RIPK1 and RIPK3 (*12*–*16*). We set out to elucidate how this pool of activated CASP8 can prevent necroptosis without processing apoptotic substrates and triggering cell death (fig. S1A).

ATG9A and FIP200 are part of a cell-death checkpoint that protects against TNF-induced RIPK1 kinase–independent apoptosis

To identify components of potential additional cell-death checkpoints, we performed a pooled genome-wide CRISPR-Cas9–based negative selection screen in mouse embryonic fibroblasts (MEFs). The screen was designed to identify genes that, upon deletion, switch the TNF response from survival to death (Fig. 1A). As well as identifying known prosurvival genes in the TNF pathway, which validated our experimental setup, we identified the genes encoding autophagy-related 9A (ATG9A) and 200 kD FAK family kinase-interacting protein (FIP200), both essential autophagy proteins, as two potential prosurvival genes (Fig. 1B and table S1). We confirmed their protective roles against TNF cytotoxicity in immortalized MEFs using the CRISPR-Cas9 approach (Fig. 1, C and D, and fig. S1, B and E), in primary MEFs isolated from deficient mice (fig. S1, C and D), and in human HT1080 cells (fig. S1, F and G). Reconstitution of the deficient cells with the corresponding wild-type (WT) protein completely reverted the sensitivity toward single TNF sensing (fig. S1, H and I). ATG9A and FIP200 appear to regulate the same cell-death checkpoint because the deletion of FIP200 in *Atg9a*$^{-/-}$ MEFs, or vice versa, had no additional impact on the extent of cell-death induction (Fig. 1E and fig. S1, J and K). The cell death caused by ATG9A or FIP200 deficiency demonstrated typical features of extrinsic apoptosis (Fig. 1F and fig. S1, L to O) and was independent of RIPK1 kinase activity (Fig. 1G and fig. S1, P and Q). Accordingly, no RIPK1 autophosphorylation could be observed (fig. S2A). This protective role was not observed after TNF-related apoptosis-inducing ligand (TRAIL) stimulation (fig. S1R), which suggests some specificity to the TNFR1 pathway. TNF-mediated RIPK1 kinase–independent apoptosis can occur when the NF-κB–dependent up-regulation of prosurvival genes is corrupted (*5*, *7*). However, the assembly of TNFR1 complex I and subsequent signaling to NF-κB and MAPKs were unaffected in ATG9A- and FIP200-deficient cells (fig. S2, A to D). These cells were still sensitized to TNF-induced death in the presence of the translation inhibitor cycloheximide (CHX) (Fig. 1H and fig. S2, E and H), which confirms that the prosurvival functions of ATG9A and FIP200 did not rely on gene activation and consequently on the NF-κB checkpoint. In addition to its well-characterized role in NF-κB activation (*17*), Met^1 (M1)–ubiquitination prevented RIPK1 kinase-independent apoptosis independent of gene activation. Indeed, deficiency in HOIL-1–interacting protein (HOIP) [the linear ubiquitin chain assembly complex (LUBAC) catalytic subunit] still sensitized cells to RIPK1 kinase–independent apoptosis in the presence of CHX (fig. S2, I and J). To test whether ATG9A, FIP200, and M1-ubiquitin chains contribute to the same protective brake, we inactivated ATG9A and FIP200 in cells deficient in M1-ubiquitination. The deletion of ATG9A or FIP200 did not further sensitize HOIP-deficient cells to TNF-mediated RIPK1 kinase–independent apoptosis (Fig. 1I and fig. S2, K and L), which indicates that the cytoprotective role of ATG9A and FIP200 relies on the presence of M1-ubiquitin chains. Thus, ATG9A and FIP200 collaborate in the regulation of an NF-κB–independent but M1-ubiquitination–dependent cell-death checkpoint in the TNF pathway.

The ATG9A-controlled cell-death checkpoint prevents TNF-mediated embryonic lethality independently of canonical autophagy

FIP200 and ATG9A are two core autophagy proteins that are involved in autophagy initiation

---

[1] VIB Center for Inflammation Research, 9052 Ghent, Belgium. [2] Department of Biomedical Molecular Biology, Ghent University, 9052 Ghent, Belgium. [3] Department of Infection Prevention and Infectious Diseases, University Hospital Regensburg, 93053 Regensburg, Germany. [4] Department of Cell Biology and Neuroscience, Juntendo University Graduate School of Medicine, 113-8654 Tokyo, Japan.
*Corresponding author. Email: mathieu.bertrand@irc.vib-ugent.be
†These authors contributed equally to this work.

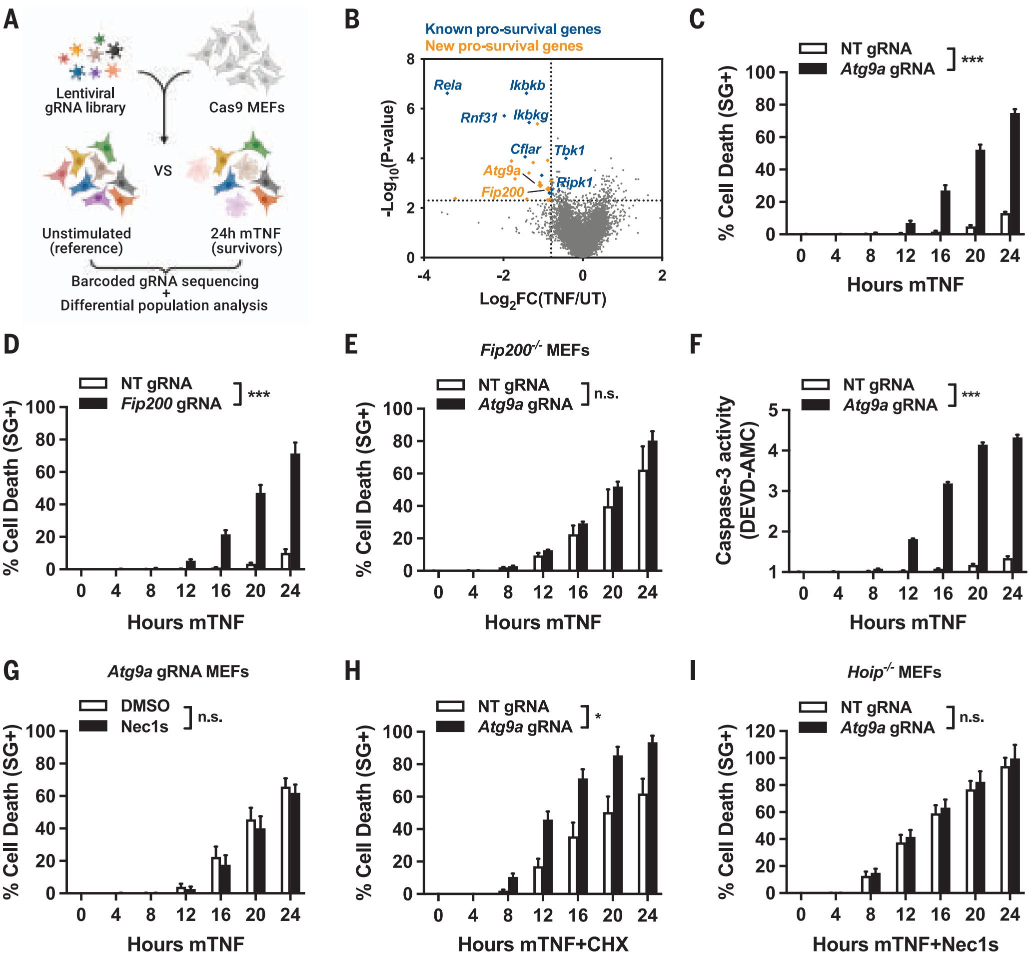

Fig. 1. ATG9A and FIP200 are part of a previously unidentified cell-death checkpoint that protects against TNF-induced RIPK1 kinase–independent apoptosis. (**A**) Schematic overview of the whole-genome CRISPR knockout screening. (**B**) Volcano plot representing screening results. (**C** and **D**) MEFs were transduced with LentiCRISPRv2 constructs targeting *Atg9a*, *Fip200* [using library-independent guide RNA (gRNA) sequences], or a nontargeting sequence (NT), and cell death was measured in function of time by SytoxGreen (SG) positivity after treating the cells with 20 ng/ml mouse TNF (mTNF). (**E**) MEFs obtained after clonal isolation of *Fip200*-specific Cas9-ribonucleoprotein (Cas9-RNP) electroporated cells (*Fip200*$^{-/-}$ MEFs) were additionally electroporated with *Atg9a*-specific or NT Cas9-RNPs. Cells were stimulated with 1 ng/ml mTNF, and cell death was measured in function of time by SG positivity. (**F**) MEFs were transduced with LentiCRISPRv2 constructs targeting *Atg9a* or NT and were treated with 20 ng/ml mTNF. Extracellular caspase activity was quantified by using a fluorescent caspase-activity probe (DEVD-AMC). (**G** and **H**) MEFs were transduced with LentiCRISPRv2 constructs targeting *Atg9a* or NT. Cells were pretreated, or not, with (G) the RIPK1 inhibitor Nec1s or (H) the protein translation inhibitor CHX before stimulation with 20 ng/ml mTNF. Cell death was measured in function of time by SG positivity. (**I**) *Hoip*$^{-/-}$ MEFs transduced with LentiCRISPRv2 constructs that targeted *Atg9a* or NT were pretreated with Nec1s before stimulation with 1 ng/ml mTNF. Cell death was measured in function of time by SG positivity. Cell-death experiments are presented as mean ± SEM of three independent experiments, and statistical significance was determined by using two-way analysis of variance (ANOVA) followed by a Tukey post hoc test. $^{*}P < 0.05$; $^{***}P < 0.001$; n.s., nonsignificant.

and autophagosome formation, respectively (*18*). ATG9A acts as a lipid scramblase that promotes phagophore expansion (*19*, *20*). The scramblase activity of ATG9A was required for its prosurvival function because reconstitution of *Atg9a*$^{-/-}$ MEFs with scramblase-deficient ATG9A mutants (*19*) also switched the TNF response to death (fig. S3A). These results suggested that autophagy, rather than the enzymatic-independent function of ATG9A in plasma membrane repair (*21*), was involved. Apart from ATG9A and FIP200, the autophagy machinery also includes many proteins grouped within distinct functional complexes (*18*). We inactivated components of each of these complexes with CRISPR-Cas9 and found that only a few of them shared a cytoprotective function. In the ATG9 complex, this was the case for the lipid transfer proteins ATG2A/B but not for the ATG9A paralogue ATG9B (Fig. 2A and fig. S3G). Within the unc-51-like autophagy activating kinase (ULK1) autophagy-initiation complex, ATG13 and ATG101 had similar cytoprotective functions, as previously reported (*22*), but the catalytic subunit ULK1 did not (Fig. 2B and fig. S3G). ULK1 independency was further confirmed in immortalized *Ulk1/2*$^{-/-}$ MEFs and by pharmacological inhibition of its kinase activity (ULK1i) (fig. S3, B and C). Accordingly, the main ULK1 phosphorylation site on ATG9A (Ser^{14}) (*23*) was also found to be dispensable for its ability to counteract TNF cytotoxicity (fig. S3D). In the subsequent vacuolar protein sorting-associated protein 34 (VPS34) nucleation complex, we identified a protective role for the lipid kinase VPS34 and for the adaptor ATG14, but not for BECLIN-1 or BECLIN-2 (Fig. 2C and fig. S3G). The use of a specific inhibitor (VPS34i) confirmed the requirement of VPS34 enzymatic activity for its cytoprotective function (fig. S3, E and F). Both the ATG12- and light chain 3 (LC3)–conjugation systems appeared dispensable for this checkpoint because inactivation of ATG5, ATG16L1, ATG7, or LC3 did not switch the TNF response from survival to death (Fig. 2D and fig. S3G). We confirmed that these prosurvival ATG proteins collaborate with ATG9A and FIP200 to the same cell-death checkpoint because they also prevented TNF-induced RIPK1-independent apoptosis, independent of gene activation but relying on M1-ubiquitination (fig. S3, E, F, and H to K). This systematic targeting approach revealed a clear discrepancy between proteins involved in autophagy initiation and those acting in the later phase of autophagosome maturation in their ability to counteract TNF cytotoxicity. Notably, mice deficient for the ATG proteins involved in this cell-death checkpoint died during embryogenesis, whereas mice deficient for the other ATGs only succumbed at or after birth (fig. S4A) (*22*–*32*). This observation indicates a crucial LC3-independent function of a subset of ATG proteins and suggests that these ATG proteins repress TNF cytotoxicity during embryogenesis. We confirmed that ATG9A

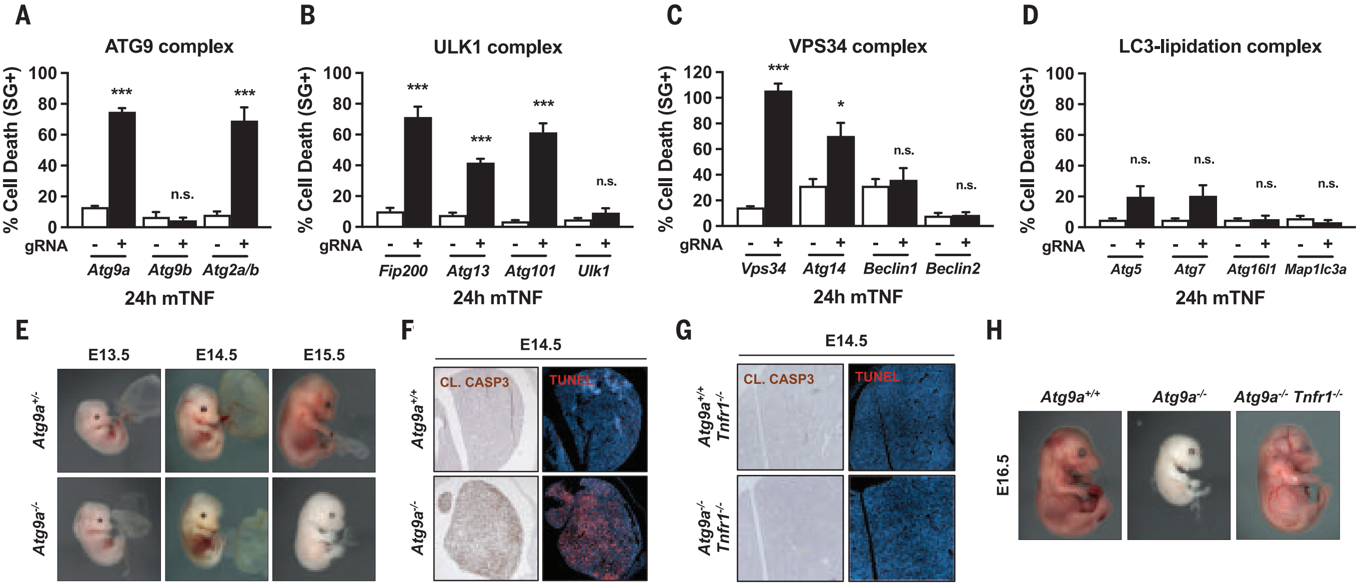

Fig. 2. The ATG9A-controlled cell-death checkpoint prevents TNF-mediated embryonic lethality independently of canonical autophagy. (**A** to **D**) MEFs that were transduced with LentiCRISPRv2 constructs or electroporated with Cas9-RNPs targeting the indicated genes or NT were stimulated with 20 ng/ml mTNF, and cell death was measured after 24 hours by SG positivity. (**E**) Representative images of $Atg9a^{+/-}$ and $Atg9a^{-/-}$ embryos taken at different stages during embryonic development. (**F** and **G**) Representative images of TUNEL (terminal deoxynucleotidyl transferase–mediated deoxyuridine triphosphate nick end labeling) and cleaved (CL.) CASP3 stainings on liver sections of E14.5 embryos of indicated genotype. (**H**) Representative images of $Atg9a^{+/+}$, $Atg9a^{-/-}$, and $Atg9a^{-/-}Tnfr1^{-/-}$ embryos at E16.5. Cell-death experiments are presented as mean ± SEM of at least three independent experiments, and statistical significance was determined by using unpaired two-sided *t* tests. *$P < 0.05$; ***$P < 0.001$; n.s. nonsignificant.

deficiency causes embryonic lethality at embryonic day 14.5 (E14.5) (Fig. 2E and fig. S4B) (*24*), which was associated with massive liver apoptosis (Fig. 2F and fig. S4C). The lethality was not caused by hepatocyte apoptosis because hepatocyte-specific ATG9A-deficient mice ($Atg9a^{AlfpCre}$) were born at normal rates (fig. S4D). By contrast, mice specifically lacking ATG9A in endothelial and fetal liver hematopoietic cells ($Atg9a^{Tie2Cre}$) also died at E14.5 (fig. S4E) (*33*). Vascular architecture appeared normal in the $Atg9a^{Tie2Cre}$ embryos, whereas clear signs of apoptosis were observed in the liver (fig. S4F). Thus, the death of fetal liver hematopoietic cells is responsible for lethality in $Atg9a^{-/-}$ mice. Furthermore, the additional deficiency of TNFR1 prevented excessive hematopoietic apoptosis in E14.5 ATG9A-deficient livers (Fig. 2G) and rescued the embryonic lethality to birth (Fig. 2H and fig. S4G). Thus, the embryonic lethality of the $Atg9a^{-/-}$ mice is exclusively caused by the release of a brake on TNF-mediated apoptosis, and not by a general defect in autophagy. Notably, NF-κB activation was not repressed in the liver of $Atg9a^{-/-}$ or $Atg9a^{Tie2Cre}$ embryos, which indicates that ATG9A also prevents TNF-mediated apoptosis independent of the NF-κB checkpoint in vivo (fig. S4, F and H).

ATG9A targets the CASP8-activating complex IIa for lysosomal degradation

In contrast to other death receptors, the induction of apoptosis by TNFR1 does not occur through recruitment of CASP8 to the receptor-associated complex I but occurs instead through a receptor-dissociated cytosolic complex II. Because autophagy promotes lysosomal degradation of cytosolic ubiquitinated cargoes, we hypothesized that the ATG9A-mediated unconventional autophagic process promotes cell survival by inducing the lysosomal degradation of complex IIa. We confirmed that single TNF stimulation leads to the assembly of complex IIa. Indeed, (activated) CASP8 did not coimmunoprecipitate with complex I (fig. S5A) and was equally isolated from lysates depleted, or not, of complex I (fig. S5B). Complex IIa contained ubiquitinated RIPK1, as previously reported (*4*, *34*, *35*). That TNF stimulation alone does not suffice to trigger apoptosis (fig. S5C) despite complex IIa being formed supports the existence of a protective mechanism that prevents its cytotoxic potential. Indeed, complex IIa disappeared within a few hours of its formation (fig. S5D). Pretreatment of the cells with the lysosomal inhibitors bafilomycin A1 (BafA1) and NH_4Cl or cathepsin inhibitors pepstatin A/E64D prevented its disappearance (Fig. 3A and fig. S5, E and F), indicating that complex IIa is a target for lysosomal degradation. This notion was strengthened by the presence of active CASP8 in purified lysosomes from TNF-stimulated cells (Fig. 3B and fig. S5G), by the TNF-dependent translocation of active CASP8 and ubiquitinated RIPK1 to the lysosome-containing membrane fraction (fig. S5, H to K), and by the localization of active CASP8 within lysosomal-associated membrane protein 1 (LAMP1)–positive lysosomes (fig. S5L). Furthermore, TNF also induced the presence of M1-ubiquitin chains in the lysosome-containing membrane fraction (fig. S5, I and K), which is in line with previous studies that reported M1-ubiquitinated RIPK1 in complex II (*34*, *35*). ATG9A deficiency did not affect the early assembly and activation of complex IIa (fig. S6A) but rather promoted the sequestration of complex IIa away from the cytosol in preparation for its subsequent lysosome-dependent clearance. To demonstrate this, we devised an approach to monitor the cytosolic versus vesicular localization of complex IIa. We immunoprecipitated CASP8 from mechanically lysed cells (to keep intracellular vesicles, such as autophagosomes and lysosomes, intact) in the absence or presence of detergent (to permeabilize and release the vesicles' content). By doing so, CASP8 could only be immunoprecipitated when cytosolic or when released from permeabilized vesicles (Fig. 3C). We included BafA1 in the experiment to prevent lysosomal turnover of complex IIa and to stabilize vesicular CASP8. This approach allowed us to confirm the TNF-dependent formation of complex IIa in the cytosol (early time point) and its subsequent transition to a vesicular compartment before its lysosomal degradation (late time point) (Fig. 3D and fig. S6B). Absence of ATG9A completely prevented the encapsulation of active CASP8, which consequently remained cytosolic at the later time point (Fig. 3E and fig. S6C). The defect in lysosomal

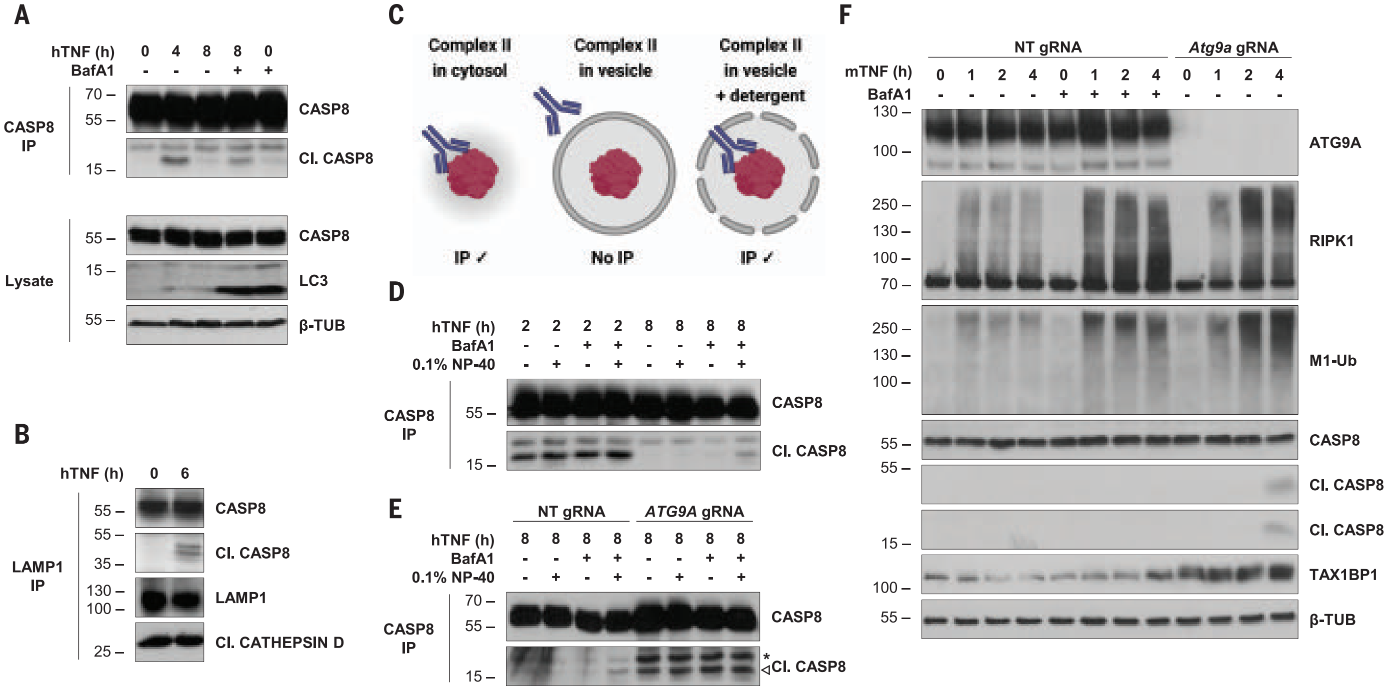

Fig. 3. ATG9A targets CASP8-activating complex IIa for lysosomal degradation. (**A**) HT1080 cells were pretreated, or not, with BafA1 before stimulation with 2 μg/ml human TNF (hTNF) for the indicated time points. CASP8 was subsequently immunoprecipitated, and protein levels were determined by immunoblot. IP, immunoprecipitation. (**B**) HT1080 cells were stimulated with 2 μg/ml hTNF, and lysosomes were immunoprecipitated from the postnuclear supernatant (PNS) by using an antibody to LAMP1. Protein levels were determined with immunoblot. (**C**) Graphical summary of CASP8 immunoprecipitation strategy from mechanical homogenates to determine vesicular or cytosolic localization of complex IIa. (**D** and **E**) WT HT1080 cells or HT1080 cells that were electroporated with Cas9-RNPs targeting *Atg9a* or NT were pretreated, or not, with BafA1 before stimulation with 2 μg/ml hTNF for the indicated time points. These cells were mechanically homogenized to obtain PNS, and CASP8 was immunoprecipitated from PNS in either the presence or absence of 0.1% NP-40. (**F**) *Atg9a*$^{-/-}$ MEFs or MEFs that were electroporated with NT Cas9-RNPs were pretreated, or not, with BafA1 before stimulation with 1 μg/ml mTNF for the indicated time points. These cells were lysed in radioimmunoprecipitation assay (RIPA) buffer, and protein levels were determined with immunoblot. Immunoblots are representative of two independent experiments. Specific (arrow) and aspecific (asterisk) bands are indicated for clarity. β-Tub, β-tubulin; M1-Ub, linear ubiquitin chains.

degradation of complex IIa caused by ATG9A deficiency was further illustrated by the TNF-dependent accumulation of ubiquitinated RIPK1, M1-ubiquitin chains, and activated CASP8, as also observed in WT cells that were treated with BafA1 (Fig. 3F). ATG9A deficiency, but not BafA1 treatment, switching the TNF response from survival to death supports a model in which ATG9A promotes the sequestration of complex IIa in an autophagosome before its fusion with the lysosome (fig. S6, D and E). BafA1 treatment inhibits lysosomal degradation of complex IIa, but not its exclusion from the cytosol. Once encapsulated, complex IIa loses its ability to transmit the lethal signal and therefore becomes unable to kill the cell. Because autophagic processes degrade specifically cytosolic (complex IIa) and not membrane-bound death-inducing signaling complex (DISC) cargoes, these results also explain why ATG9A is not cytoprotective in the TRAIL pathway (fig. S1R).

TAX1BP1 recruits the autophagy-initiation machinery to M1-ubiquitinated complex IIa

During selective autophagy, autophagy receptors escort the ubiquitinated cytosolic cargo to the growing phagophore, owing to the presence of two distinct protein interaction motifs. The ubiquitin-binding domain allows the interaction with the ubiquitin chains associated with the autophagic cargo, whereas the LC3-interacting region (LIR) associates with the LC3 moieties on the inner phagophore leaflet (*18*). Recent in vitro reports have, however, described the existence of an unconventional selective autophagic pathway that can bypass the LC3-conjugation machinery (*36*, *37*). In that case, the autophagy receptor directly binds and engages FIP200 to form an in situ phagophore around the cargo (*36*–*40*). To evaluate this possibility in the cell-death checkpoint, we first inactivated the best-characterized selective autophagy receptors by means of CRISPR-Cas9–mediated gene deletion and found that TAX1 binding protein 1 (TAX1BP1) was also required to protect cells from TNF-mediated RIPK1 kinase–independent apoptosis (Fig. 4A and fig. S7, A to C). Similar to the results obtained in ATG9A-deficient cells (Fig. 3F), the cell death observed in TAX1BP1-deficient MEFs was associated with a clear accumulation of ubiquitinated RIPK1, M1-ubiquitin chains, and active CASP8 (Fig. 4B). TAX1BP1 recognizes the cargo-associated ubiquitin chains by its dedicated ubiquitin-binding domains (UBZ1/2). The ubiquitin-binding capacity was required for TAX1BP1's prosurvival function because expressing a version of TAX1BP1 lacking its UBZ1/2 domain (ΔUBZ mutant) failed to rescue the TNF-dependent cell death in *Tax1bp1*$^{-/-}$ MEFs (fig. S7, D and E). In addition to the reported binding of UBZ1/2 to Lys^{63}-ubiquitin chains (fig. S7F) (*41*), TAX1BP1 also directly associated with M1-ubiquitin chains in a UBZ1/2-dependent manner (fig. S7G). RIPK1 was the major M1-ubiquitinated substrate that accumulates upon BafA1 treatment of TNF-stimulated cells (fig. S7H). Together with the fact that RIPK1 is ubiquitinated in complex IIa (fig. S5B), these results support a model in which TAX1BP1 recognizes M1-ubiquitinated RIPK1 within complex IIa to initiate its detoxification. Proximity ligation assays (PLAs) revealed a TNF-dependent decrease in the TAX1BP1-RIPK1 PLA signal that was completely prevented by treating the cells with BafA1 or by ATG9A deficiency (Fig. 4C and fig. S7I). RIPK1 deficiency was also sufficient to switch the TNF response from survival to RIPK1 kinase–independent apoptosis (fig. S7J). Removing the ubiquitinated

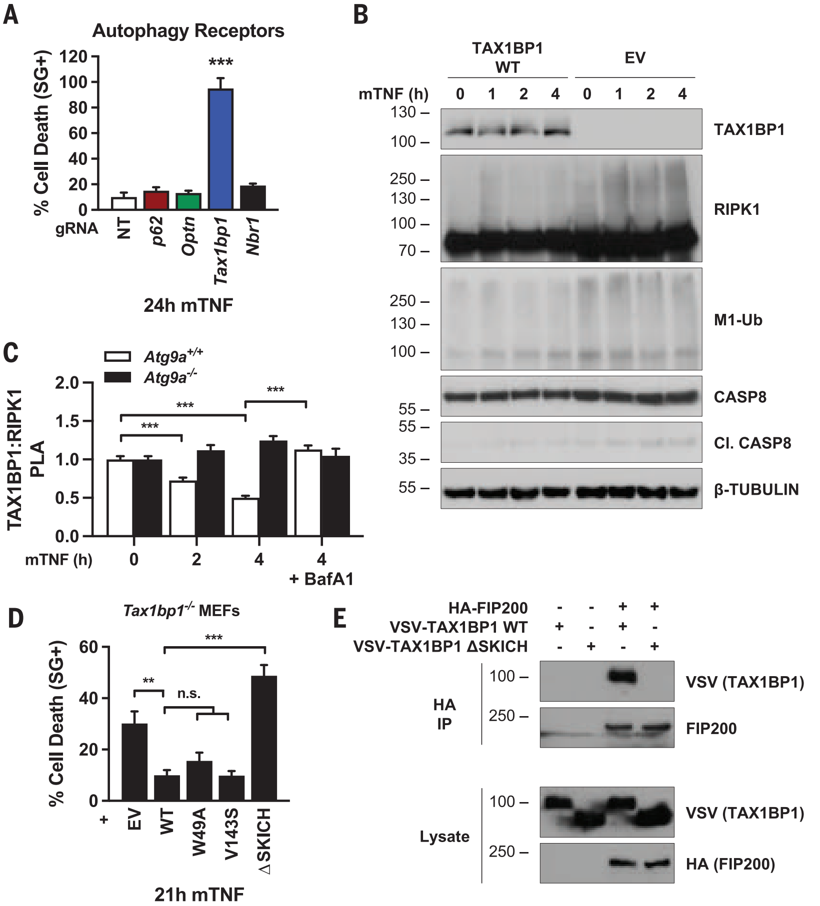

Fig. 4. TAX1BP1 recruits the autophagy-initiation machinery to M1-ubiquitinated complex IIa. (**A**) MEFs were electroporated with Cas9-RNPs targeting the indicated genes or NT. Cell death was measured by SG positivity after stimulating the cells for 24 hours with 20 ng/ml mTNF. (**B**) *Tax1bp1*$^{-/-}$ MEFs were reconstituted with inducible expression vectors encoding either WT TAX1BP1 or an empty vector (EV) and treated with 1 μg/ml doxycycline for 24 hours before stimulation. These cells were stimulated with 1 μg/ml mTNF for the indicated time points and lysed in RIPA buffer, and protein levels were determined with immunoblot. (**C**) *Atg9a*$^{+/+}$ and *Atg9a*$^{-/-}$ MEFs were pretreated with BafA1 as indicated before stimulation with 20 ng/ml mTNF for the indicated time points. PLA was performed to determine the interaction between TAX1BP1 and RIPK1. PLA puncta per cell relative to the untreated control were quantified. Representative data of two independent experiments are plotted. (**D**) *Tax1bp1*$^{-/-}$ MEFs were reconstituted with inducible expression vectors encoding either an EV, WT TAX1BP1, or indicated mutants and treated with 1 μg/ml doxycycline for 24 hours before stimulation. These cells were stimulated with 20 ng/ml mTNF for 21 hours, and cell death was measured by SG positivity. A, Ala; S, Ser; V, Val; W, Trp. (**E**) VSV-TAX1BP1 WT, VSV-TAX1BP1 ΔSKICH, and HA-FIP200 were expressed in human embryonic kidney–293 T cells, and TAX1BP1-FIP200 interaction was assessed through coimmunoprecipitation and subsequent immunoblotting. Immunoblots are representative of two independent experiments. HA, hemagglutinin; VSV, vesicular stomatitis virus. Cell death is presented as mean ± SEM of three independent experiments, and statistical significance was determined by using one-way ANOVA followed by a Tukey post hoc test. Statistical significance for the PLA experiment was determined by using two-way ANOVA followed by a Tukey post hoc test. $^{**}P < 0.01$; $^{***}P < 0.001$; n.s. nonsignificant.

component of complex IIa prevented its recognition by TAX1BP1 and subsequent lysosomal turnover. The prosurvival function of TAX1BP1 was independent of its LIR because reconstitution of *Tax1bp1*$^{-/-}$ cells with two defective LIR mutants of TAX1BP1 (W49A and V143S) (*41*) protected the cells from TNF cytotoxicity as efficiently as WT TAX1BP1 (Fig. 4D). By contrast, the protective role of TAX1BP1 relied on its N-terminal SKIP carboxyl homology (SKICH) domain (Fig. 4D), which is required for FIP200 binding (Fig. 4E) (*39*). We also observed accumulation of ubiquitinated RIPK1, M1-ubiquitin chains, and active CASP8 in cells expressing TAX1BP1 ΔSKICH, further indicating that the SKICH domain of TAX1BP1 was required to degrade these components (fig. S7K). A recent study further identified Ala^{114} of TAX1BP1 to be crucial for its interaction with FIP200 (*39*). Mutating this residue fully abrogated TAX1BP1's prosurvival function (fig. S7, L and M), indicating that TAX1BP1 needs to bind and recruit FIP200 to the autophagic cargo to prevent TNF cytotoxicity. Thus, TAX1BP1 recruits FIP200 and the upstream autophagy-initiation machinery to M1-ubiquitinated RIPK1 in complex IIa to initiate encapsulation of the cytosolic complex, which ultimately results in its lysosomal degradation (fig. S8).

The ATG9A-controlled cell-death checkpoint prevents inflammatory skin disease

Dysregulated TNFR1-mediated apoptosis drives inflammatory pathologies in the mouse skin (*42–45*). We thus evaluated the physiological role of the ATG9A cell-death checkpoint in skin homeostasis by generating mice harboring the keratinocyte-specific deletion of ATG9A (*Atg9a*^{EKO} mice) or ATG16L1 (*Atg16l1*^{EKO} mice). *Atg9a*^{EKO} mice spontaneously developed a severe inflammatory skin phenotype characterized by epidermal thickening and by the formation of inflammatory lesions on the back, which appeared at ~4 weeks of age and progressed over time (Fig. 5A and fig. S9A). *Atg16l1*^{EKO} mice did not develop such a phenotype (Fig. 5A and fig. S9, A and B), demonstrating that the anti-inflammatory role of ATG9A in the skin is not mediated by LC3-dependent canonical autophagy. *Atg9a*^{EKO} mice exhibited hyperplasia and a marked presence of pyknotic nuclei, both in lesional and nonlesional skin (fig. S9C), as well as a loss of barrier integrity measured by trans-epidermal water loss (TEWL) (Fig. 5B and fig. S9D). Moreover, keratinocyte-specific ATG9A deficiency led to systemic inflammation, as observed by the swollen skin-draining lymph nodes, increased spleen size, and elevated levels of circulating interleukin 6 (IL-6) (Fig. 5, C and D, and fig. S9E). *Atg9a*^{EKO} mice had similar levels of TNF in the blood serum compared with those in WT controls, indicating that the inflammatory phenotype does not originate from increased circulating TNF levels (fig. S9F). The increased inflammatory parameters observed in *Atg9a*^{EKO} mice corresponded with an elevated dermal influx of CD45^{+} macrophages, dendritic cells, neutrophils, and eosinophils but not in T cells (Fig. 5E and fig. S9G). In line with the prosurvival function of ATG9A in the TNF pathway, we observed an increased number of apoptotic cells in the thickened epidermal basal layer of *Atg9a*^{EKO} mice (Fig. 5F), which was greatly reduced in *Atg9a*^{EKO} *Tnfr1*$^{-/-}$ mice (Fig. 5G). The presence of dying cells in nonlesional skin sections of *Atg9a*^{EKO} mice indicates that cell death precedes lesion formation and suggests that aberrant keratinocyte apoptosis drives the inflammatory phenotype of these mice. *Atg9a*^{EKO} *Tnfr1*$^{-/-}$ mice did not develop inflammatory skin lesions or

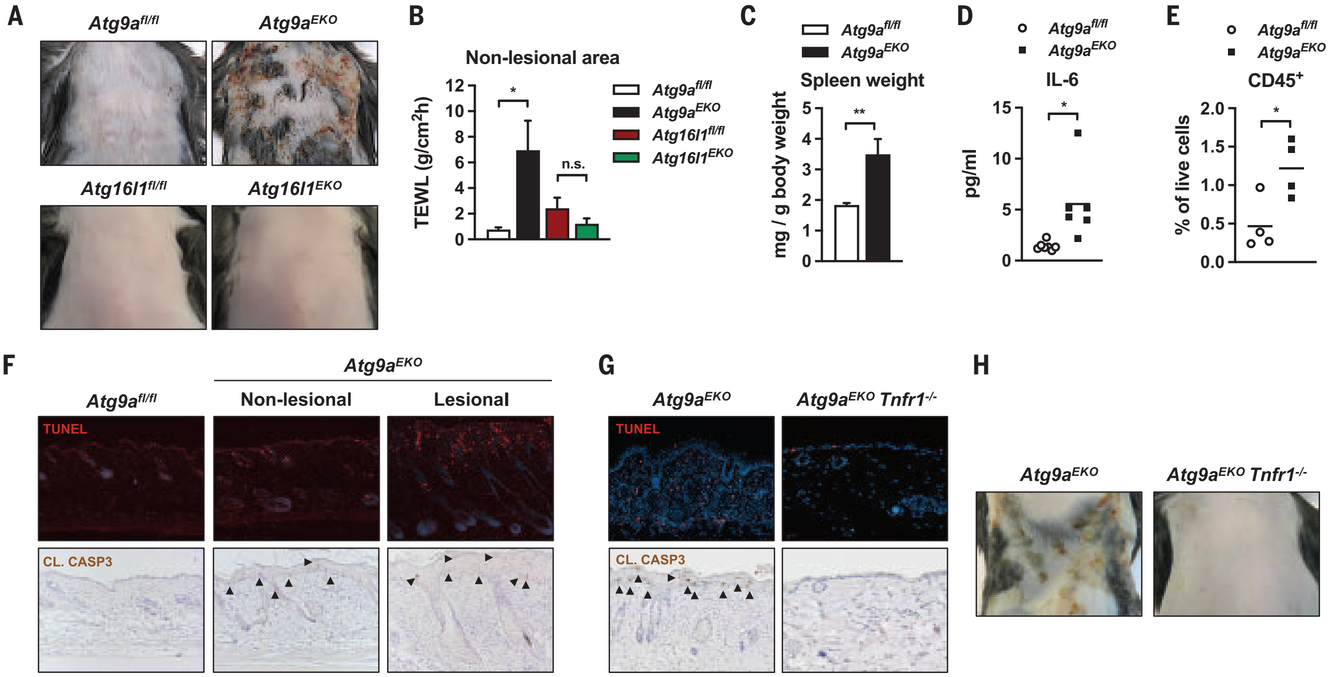

Fig. 5. The ATG9A-controlled cell-death checkpoint prevents inflammatory skin disease. (**A**) Representative images of 11-week-old *Atg9a*$^{fl/fl}$, *Atg9a*^{EKO}, *Atg16l1*$^{fl/fl}$, and *Atg16l1*^{EKO} mice. (**B**) TEWL measurements of nonlesional skin of 7-week-old mice of indicated genotype. (**C**) Spleen weight of 11-week-old mice of indicated genotypes. (**D**) Serum IL-6 levels of 11-week-old mice of indicated genotypes. (**E**) Percentage of CD45$^+$ immune cells isolated from the dermis of 9-week-old mice of indicated genotypes. (**F**) Representative images of TUNEL and cleaved CASP3 stainings on lesional and nonlesional skin sections of 7-week-old mice of indicated genotypes. (**G**) Representative images of TUNEL and cleaved CASP3 stainings on skin sections of 11-week-old mice of indicated genotypes. (**H**) Representative images of 11-week-old *Atg9a*^{EKO} and *Atg9a*^{EKO} *Tnfr1*$^{-/-}$ mice. TEWL (*Atg9a*$^{fl/fl}$$n$ = 3; *Atg9a*^{EKO}, *Atg16l1*$^{fl/fl}$, and *Atg16l1*^{EKO}n = 4) and spleen weight (*Atg9a*$^{fl/fl}$$n$ = 7; *Atg9a*^{EKO}n = 6) are presented as mean ± SEM. Individual observations of IL-6 levels and percentage of CD45$^+$ immune cells are plotted. Statistical significance for TEWL measurements was determined by using one-way ANOVA followed by a Tukey post hoc test. Statistical significance for spleen weight, IL-6 levels, and percentage of CD45$^+$ immune cells was determined by using unpaired two-sided t tests. *$P < 0.05$; **$P < 0.01$; n.s. nonsignificant.

show any signs of systemic inflammation (Fig. 5H and fig. S9, H to J). Thus, the ATG9A-dependent cell-death checkpoint is crucial to counteract TNFR1-mediated embryonic lethality and to maintain skin homeostasis by preventing cell death–driven inflammation.

Discussion

TNF-induced cell death is a major driver of inflammation (*46*), underlying several human inflammatory pathologies. The cell-death checkpoints that actively repress TNF cytotoxicity constitute crucial safeguards against these diseases. Here, we describe a fourth cell-death checkpoint in the TNF pathway that protects cells from RIPK1 kinase–independent apoptosis independently of NF-κB. We demonstrate its physiological importance by showing that its constitutive inactivation through ATG9A deletion leads to embryonic lethality. The death of *Atg9a*$^{-/-}$ embryos occurred at ~E14.5 because of uncontrolled TNF-mediated apoptosis of fetal liver hematopoietic cells, a phenotype shared with mice deficient in the NF-κB checkpoint that also represses RIPK1 kinase–independent apoptosis (*47*–*49*). The specific inactivation of this checkpoint in keratinocytes also caused epidermal apoptosis and inflammatory skin lesions, which led to severe systemic inflammation, a phenotype that resembles those previously reported in mice deficient for components of the other TNFR1 cell-death checkpoints (*42*–*45*). Mechanistically, this additional protective brake involved the ATG9A-dependent lysosomal degradation of the cytosolic CASP8-activating complex IIa that forms upon TNF sensing. We thus provide a molecular explanation for the nontoxic properties of the pool of CASP8 that is activated in response to TNFR1 activation. The similarity between the TNFR1-dependent embryonic lethality caused by a defect in NF-κB and in ATG9A can be explained by the excess of apoptosis that results from the same cytotoxic complex IIa. In NF-κB–deficient conditions, cytosolic CASP8 becomes pro-apoptotic, owing to the absence of repression by cFLIP. Deficiency in ATG9A instead prevents lysosomal degradation of complex IIa, leading to accumulation of activated cytosolic CASP8 that likely overcomes the repression by cFLIP. The lysosomal turnover of complex IIa was mediated not by classical macro-autophagy but instead by an alternative LC3-independent autophagic process that has so far only been reported in vitro for other types of cytosolic cargoes (*36*–*39*, *50*). Our work thus validates the physiological relevance of this alternative degradation process in an in vivo context and demonstrates its importance in preventing TNF cytotoxicity. Our results also provide an explanation for the discrepancy in phenotypes of mice deficient in different autophagy signaling mediators and clarify why only mice deficient in ATG proteins involved in this cell-death checkpoint die during embryonic development. We found that TAX1BP1 is required to bridge complex IIa to the upstream autophagy machinery for its encapsulation and subsequent lysosomal degradation. We present data that support a model in which TAX1BP1 uses its SKICH domain to bind the autophagy-initiation protein FIP200 and its UBZ domains to catch the M1-ubiquitin chains that are conjugated to RIPK1 in complex IIa. These results thus reveal an additional pro-survival role for LUBAC and identify M1-ubiquitination as a targeting signal for lysosomal turnover. Moreover, our results provide a molecular explanation for the scaffolding anti-apoptotic function of RIPK1. It will now be interesting to look for mutations in ATG9A or other components of the checkpoint in patients with inflammatory pathologies. Anti-TNF biologics would represent promising therapies for the patients who carry such mutations. Inactivating mutations in the genes that encode LUBAC and RIPK1 cause inflammatory pathologies in humans (*51–54*). Our results now indicate that the disease state of these individuals may involve the inactivation of complex IIa detoxification. Last, because TNF-induced cell death is believed to have evolved as a positive backup mechanism in response to the action of microbial effector proteins that interfere with the host immune signaling, it will be important to define the conditions in which sporadic inactivation of the checkpoint can be beneficial for the host.

REFERENCES AND NOTES

1. J. D. Webster, D. Vucic, *Front. Cell Dev. Biol.* **8**, 365 (2020).
2. A. Annibaldi, P. Meier, *Trends Mol. Med.* **24**, 49–65 (2018).
3. A. T. Ting, M. J. M. Bertrand, *Trends Immunol.* **37**, 535–545 (2016).
4. O. Micheau, J. Tschopp, *Cell* **114**, 181–190 (2003).
5. L. Wang, F. Du, X. Wang, *Cell* **133**, 693–703 (2008).
6. N. S. Wilson, V. Dixit, A. Ashkenazi, *Nat. Immunol.* **10**, 348–355 (2009).
7. D. J. Van Antwerp, S. J. Martin, T. Kafri, D. R. Green, I. M. Verma, *Science* **274**, 787–789 (1996).
8. Y. Dondelinger *et al.*, *Mol. Cell* **60**, 63–76 (2015).
9. E. Lafont *et al.*, *Nat. Cell Biol.* **20**, 1389–1399 (2018).
10. D. Xu *et al.*, *Cell* **174**, 1477–1491.e19 (2018).
11. T. Delanghe, Y. Dondelinger, M. J. M. Bertrand, *Trends Cell Biol.* **30**, 189–200 (2020).
12. S. Feng *et al.*, *Cell. Signal.* **19**, 2056–2067 (2007).
13. N. Lalaoui *et al.*, *Nature* **577**, 103–108 (2020).
14. Y. Lin, A. Devin, Y. Rodriguez, Z. G. Liu, *Genes Dev.* **13**, 2514–2526 (1999).
15. K. Newton *et al.*, *Nature* **574**, 428–431 (2019).
16. P. Tao *et al.*, *Nature* **577**, 109–114 (2020).
17. Y. Dondelinger, M. Darding, M. J. M. Bertrand, H. Walczak, *Cell. Mol. Life Sci.* **73**, 2165–2176 (2016).
18. I. Dikic, Z. Elazar, *Nat. Rev. Mol. Cell Biol.* **19**, 349–364 (2018).
19. S. Maeda *et al.*, *Nat. Struct. Mol. Biol.* **27**, 1194–1201 (2020).
20. K. Matoba *et al.*, *Nat. Struct. Mol. Biol.* **27**, 1185–1193 (2020).
21. A. Claude-Taupin *et al.*, *Nat. Cell Biol.* **23**, 846–858 (2021).
22. T. Kaizuka, N. Mizushima, *Mol. Cell. Biol.* **36**, 585–595 (2015).
23. C. Zhou *et al.*, *Cell Res.* **27**, 184–201 (2017).
24. T. Kojima *et al.*, *Reprod. Biol.* **15**, 131–138 (2015).
25. B. Gan *et al.*, *J. Cell Biol.* **175**, 121–133 (2006).
26. H. Morishita *et al.*, *Cell Rep.* **33**, 108477 (2020).
27. H. Cheong *et al.*, *Autophagy* **10**, 45–56 (2014).
28. S. R. Yoshii *et al.*, *Dev. Cell* **39**, 116–130 (2016).
29. M. Komatsu *et al.*, *J. Cell Biol.* **169**, 425–434 (2005).
30. T. Saitoh *et al.*, *Nature* **456**, 264–268 (2008).
31. G. M. Cann *et al.*, *Dev. Dyn.* **237**, 187–195 (2008).
32. M. Kundu *et al.*, *Blood* **112**, 1493–1502 (2008).
33. Y. Tang, A. Harrington, X. Yang, R. E. Friesel, L. Liaw, *Genesis* **48**, 563–567 (2010).
34. M. C. de Almagro, T. Goncharov, K. Newton, D. Vucic, *Cell Death Dis.* **6**, e1800 (2015).
35. M. C. de Almagro *et al.*, *Cell Death Differ.* **24**, 26–37 (2017).
36. J. N. S. Vargas *et al.*, *Mol. Cell* **74**, 347–362.e6 (2019).
37. E. Turco *et al.*, *Mol. Cell* **74**, 330–346.e11 (2019).
38. B. J. Ravenhill *et al.*, *Mol. Cell* **74**, 320–329.e6 (2019).
39. A. E. Ohnstad *et al.*, *EMBO J.* **39**, e104948 (2020).
40. X. Shi, C. Chang, A. L. Yokom, L. E. Jensen, J. H. Hurley, *eLife* **9**, e59099 (2020).
41. D. A. Tumbarello *et al.*, *PLOS Pathog.* **11**, e1005174 (2015).
42. A. Nenci *et al.*, *Hum. Mol. Genet.* **15**, 531–542 (2006).
43. S. Kumari *et al.*, *eLife* **3**, e03422 (2014).
44. J. A. Rickard *et al.*, *eLife* **3**, e03464 (2014).
45. L. Taraborrelli *et al.*, *Nat. Commun.* **9**, 3910 (2018).
46. K. Newton, V. M. Dixit, N. Kayagaki, *Science* **374**, 1076–1080 (2021).
47. A. A. Beg, W. C. Sha, R. T. Bronson, S. Ghosh, D. Baltimore, *Nature* **376**, 167–170 (1995).
48. Z. W. Li *et al.*, *J. Exp. Med.* **189**, 1839–1845 (1999).
49. M. Tanaka *et al.*, *Immunity* **10**, 421–429 (1999).
50. J. M. Goodwin *et al.*, *Cell Rep.* **20**, 2341–2356 (2017).
51. B. Boisson *et al.*, *Nat. Immunol.* **13**, 1178–1186 (2012).
52. B. Boisson *et al.*, *J. Exp. Med.* **212**, 939–951 (2015).
53. D. Cuchet-Lourenço *et al.*, *Science* **361**, 810–813 (2018).
54. H. Oda *et al.*, *Front. Immunol.* **10**, 479 (2019).

ACKNOWLEDGMENTS

We thank the VIB-UGent IRC Animal house for mouse husbandry and the VIB-UGent BioImaging Core for training, support, and access to the instrument park. The NEMO antibody was a kind gift from M. Pasparakis (University of Cologne, Cologne, Germany). The $Ulk1/2^{-/-}$ and $Hoip^{-/-}$ MEFs were kindly provided by S. Tooze (The Francis Crick Institute, London, UK) and H. Walczak (University of Cologne, Cologne, Germany), respectively. The mAPG9L1-EGFP plasmid was a kind gift from S. Scherer. Graphics were generated by using BioRender. **Funding:** Research in the group of M.J.M.B. is financially supported by Vlaams Instituut voor Biotechnologie (VIB); Ghent University (iBOF ATLANTIS); Fonds voor Wetenschappelijk Onderzoek Vlaanderen (FWO) (grants G035320N, G044518N, EOS G0G6618N, and EOS G0I5722N); and Flemish Government Methusalem (BOF16/MET_V/007, attributed to P. Vandenabeele). **Author contributions:** Conceptualization: J.H., D.P., and M.J.M.B. Formal analysis: J.H., D.P., and M.J.M.B. Funding acquisition: M.J.M.B. Investigation: J.H., D.P., M.J.M.B., L.V.H., B.G., J.F., and E.H. Project administration: M.J.M.B. Resources: Y.U., G.v.L., and M.J.M.B. Software: J.H. Supervision: M.J.M.B. Validation: J.H. and D.P. Visualization: J.H., D.P., and M.J.M.B. Writing—original draft: J.H., D.P., and M.J.M.B. Writing—review and editing: J.H., D.P., J.F., E.H., G.v.L., and M.J.M.B. **Competing interests:** The authors declare that they have no competing interests. **Data and materials availability:** All data needed to evaluate the conclusions in this paper are present either in the main text or in the supplementary materials. $Atg9a^{fl/fl}$ mice were obtained by means of a materials transfer agreement with the Juntendo University Graduate School of Medicine. Requests for resources, reagents, plasmids, and cell lines used in this study and additional information should be directed to corresponding author M.J.M.B. (mathieu.bertrand@irc.vib-ugent.be).

SUPPLEMENTARY MATERIALS

science.org/doi/10.1126/science.add6967
Materials and Methods
Figs. S1 to S9
References (*55–62*)
Table S1
MDAR Reproducibility Checklist

Submitted 29 June 2022; resubmitted 17 October 2022
Accepted 18 November 2022
10.1126/science.add6967

REPORTS

ORGANIC CHEMISTRY

Asymmetric intermolecular allylic C–H amination of alkenes with aliphatic amines

Kelvin Pak Shing Cheung[1], Jian Fang[1], Kallol Mukherjee[1], Andranik Mihranyan[1], Vladimir Gevorgyan[1,2]*

Aliphatic allylic amines are found in a great variety of complex and biorelevant molecules. The direct allylic C–H amination of alkenes serves as the most straightforward method toward these motifs. However, use of widely available internal alkenes with aliphatic amines in this transformation remains a synthetic challenge. In particular, palladium catalysis faces the twin challenges of inefficient coordination of Pd(II) to internal alkenes but excessively tight and therefore inhibitory coordination of Pd(II) by basic aliphatic amines. We report a general solution to these problems. The developed protocol, in contrast to a classical Pd(II/0) scenario, operates through a blue light–induced Pd(0/I/II) manifold with mild aryl bromide oxidant. This open-shell approach also enables enantio- and diastereoselective allylic C–H amination.

Aliphatic amines are prevalent motifs in natural products and pharmaceuticals. Allylic amines in particular are especially attractive synthetic targets as they possess diverse bioactivities and are also versatile synthons for downstream manipulations (Fig. 1A). One traditional approach toward aliphatic allylic amines is nucleophilic displacement using prefunctionalized alkenes (Fig. 1B, top left). Although this method is straightforward, it is usually accompanied by issues such as double allylation. Further, achieving high efficiency and selectivity in analogous substitution with secondary allyl electrophiles is often problematic. As a general solution, the Tsuji-Trost reaction represents the most versatile platform for allylic substitution (*1*), providing high regio-, diastereo-, and enantio-control (Fig. 1B, bottom left). Accessing complex allyl electrophiles, however, is no trivial task and consequently a direct oxidative allylic C–H amination approach that eliminates the need to prefunctionalize the alkene has become a rigorous field of study. Along these lines, considerable progress has been made since the seminal contributions of White and Liu on palladium-catalyzed allylic C–H amination (*2*, *3*). However, to date, most of the transition metal–catalyzed protocols employ nitrogen pronucleophiles

---

[1] Department of Chemistry and Biochemistry, The University of Texas at Dallas, Richardson, TX 75080, USA. [2] Department of Biochemistry, The University of Texas Southwestern Medical Center, Dallas, TX 75390, USA.
*Corresponding author. Email: vlad@utdallas.edu

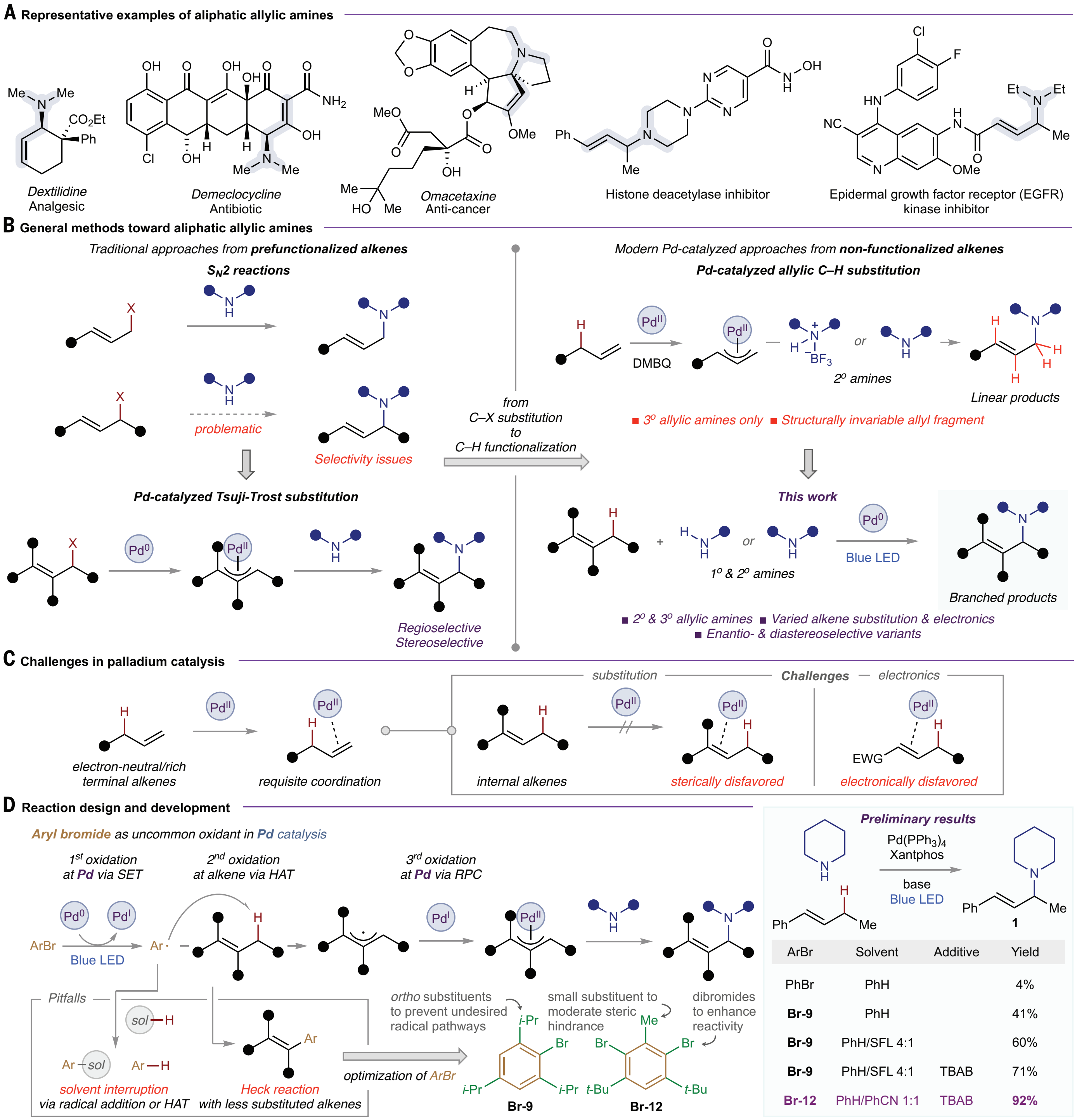

ArBr	Solvent	Additive	Yield
PhBr	PhH		4%
Br-9	PhH		41%
Br-9	PhH/SFL 4:1		60%
Br-9	PhH/SFL 4:1	TBAB	71%
Br-12	PhH/PhCN 1:1	TBAB	92%

Fig. 1. Background and reaction design. (**A**) Representative examples highlighting diverse bioactive aliphatic allylic amines. (**B**) General methods toward aliphatic allylic amines and this work. (**C**) Challenges in palladium catalysis. (**D**) Reaction design and development. DMBQ, dimethylbenzoquinone; SFL, sulfolane; TBAB, tetrabutylammonium bromide. HAT, hydrogen atom transfer; SET, single electron transfer; RPC, radical-polar crossover.

such as sulfonamides and carbamates (*4*–*10*) and are restricted to certain substitution patterns on alkenes, thus hampering the exploration of chemical space. Although there is a wealth of reports on alternative strategies proceeding through nitrene intermediates (*11*–*17*), the employment of prefunctionalized nitrogen sources such as tosyl azides and dioxazolones inevitably precludes the installation of an alkyl amine moiety. As such, the direct construction of aliphatic allylic amines using aliphatic amines, especially pharmaceutically valuable heterocycles such as piperidines and piperazines (*18*), remains a substantial challenge.

Recent advances in photocatalysis and electrochemistry have pushed forward the state of the art. In 2020, Ritter *et al.* used aminium radical addition (*19*) to establish the C–N bond

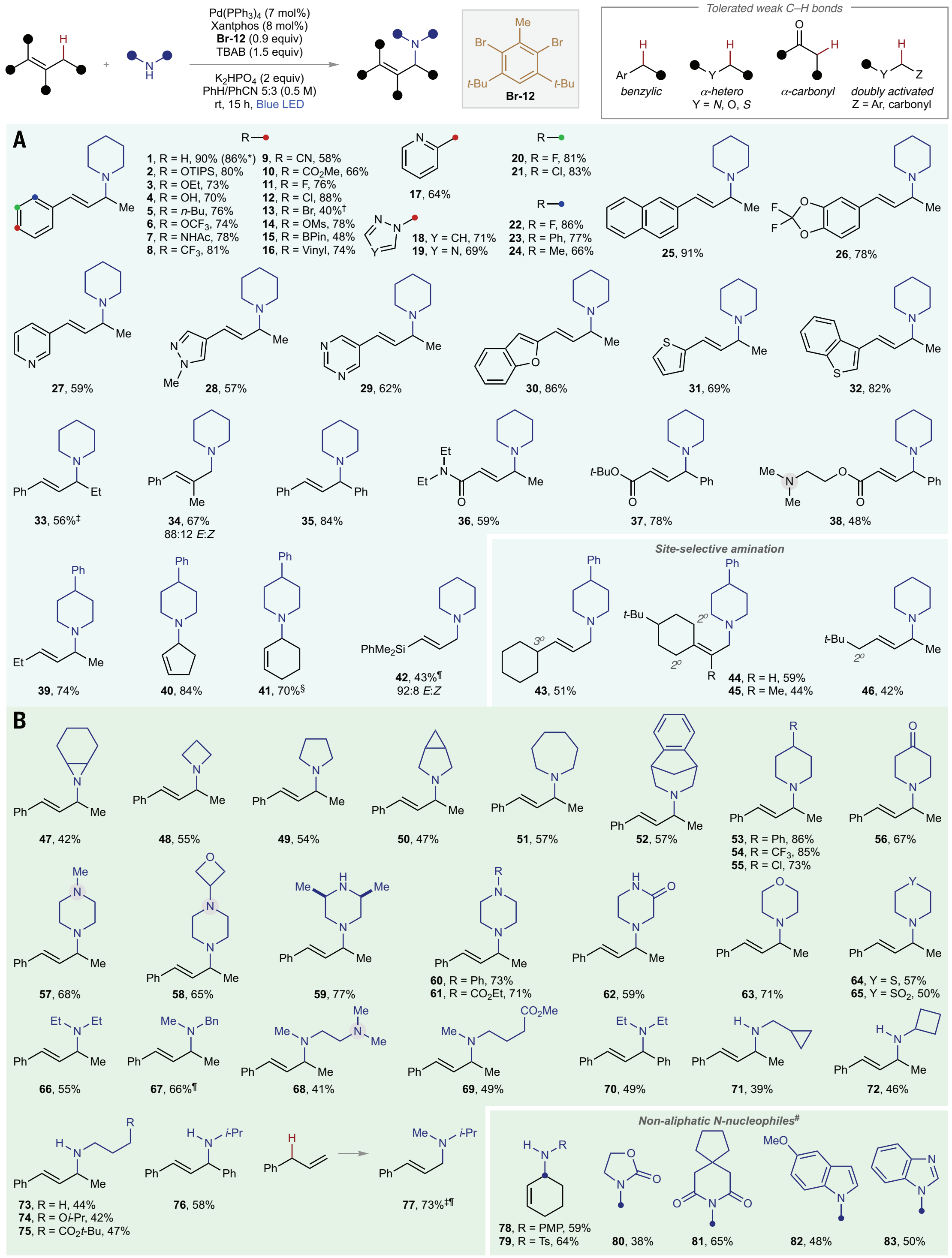

Fig. 2. Scope of the intermolecular allylic C–H amination. (**A**) Alkene scope. (**B**) Aliphatic amine scope. *, 0.5 equivalents of TBAB; †, 1.5 equivalents of **Br-12**; ‡, 10 mol% $Pd(PPh_3)_4$ and Xantphos; §, 0.7 equivalents of **Br-12**; ¶, 3.0 equivalents of alkene; #, see supplementary materials for detailed reaction conditions.

(*20*). This iminothianthrene-based method, however, requires extra synthetic effort and is intrinsically limited to synthesis of secondary allylic amines, as in the case of metal nitrenes. Complementary chemistry using secondary amines was recently achieved by Lei *et al.* (*21*), though this reaction typically requires more than 20 equivalents of alkene. Moreover, construction of the C–N bond in a stereoselective manner still remains elusive. Recently, Wickens *et al.* developed a one-pot two-step electrochemical *Z*-selective approach toward tertiary allylic amines (*22*). This protocol enables the direct use of secondary aliphatic amines but is incompatible with internal alkenes. Thus, despite these major breakthroughs a general platform that accommodates alkenes of different substitution paterns—as well as primary and secondary aliphatic amines—has not been realized.

To address these limitations, we revisited the well-established Pd II/0 mechanistic manifold, where the major challenge revolves around the use of a Pd(II) catalyst (Fig. 1C).

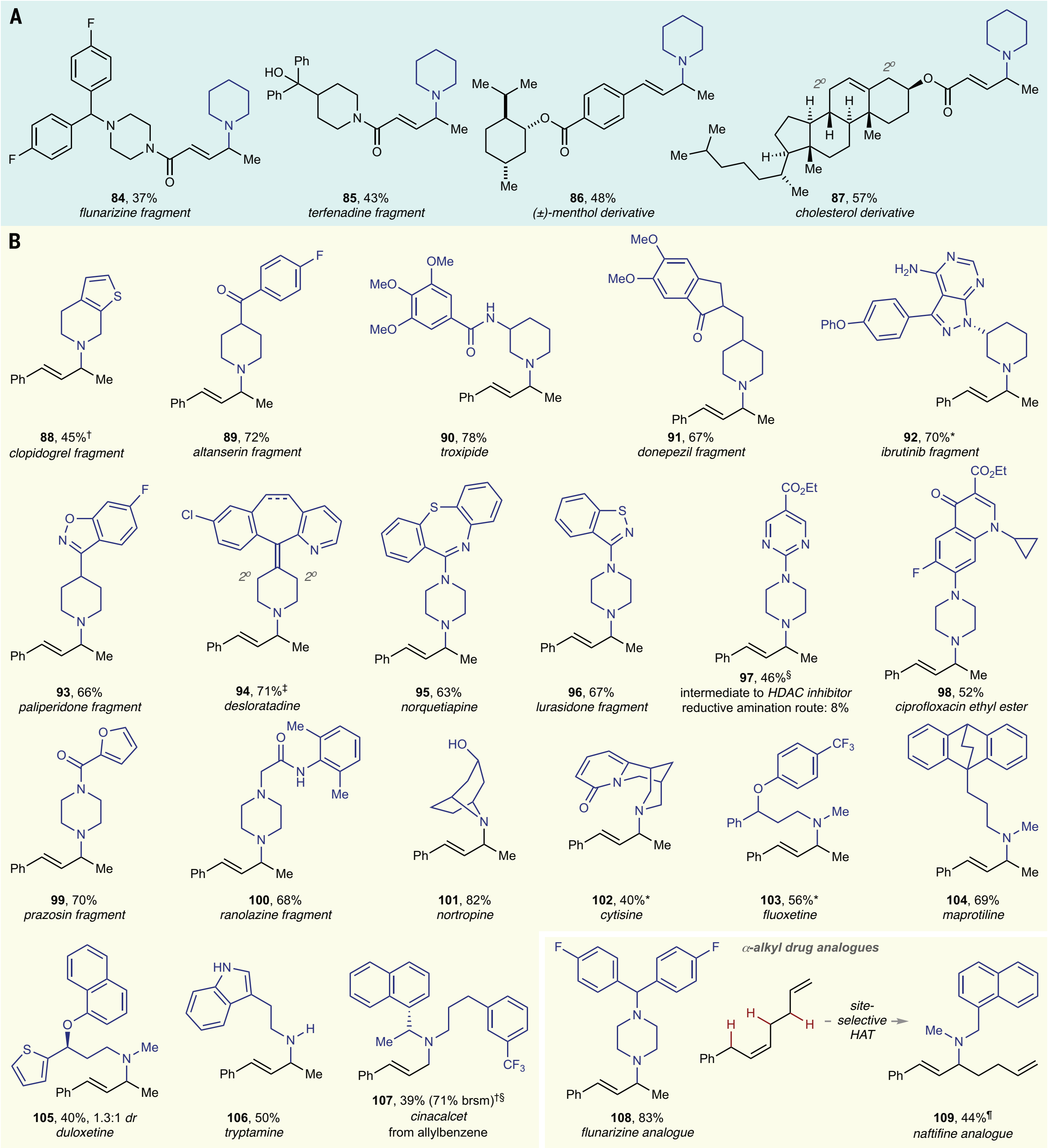

Fig. 3. Late-stage functionalization and synthesis of complex amines. (**A**) Scope of drug fragments and natural product derivatives. (**B**) Scope of complex aliphatic amines. *, 1:1 diastereomeric ratio; †, 3.0 equivalents of alkene; ‡, Product:desaturated product = 2.6:1, see supplementary materials for details; §, 10 mol% Pd(PPh$_3$)$_4$ and Xantphos; ¶, 2.5 equivalents of alkene.

First, the C–H cleavage step en route to the key π-allyl Pd(II) complex is preceded by Pd(II)–alkene coordination, which situates the metal center close to the C–H bond. Consequently, palladium catalysis is chiefly confined to the least congested, mono-substituted alkenes, and hence incorporation of the sterically more demanding internal congeners still remains elusive. These alkenes can also undergo undesired isomerization (*23*), which further complicates the reaction profile. Further, Pd(II) salts are prone to bind with Lewis basic aliphatic amines—particularly primary amines (*24*–*28*)—leading to, in this case, catalyst deactivation. Accordingly, using internal alkenes and aliphatic

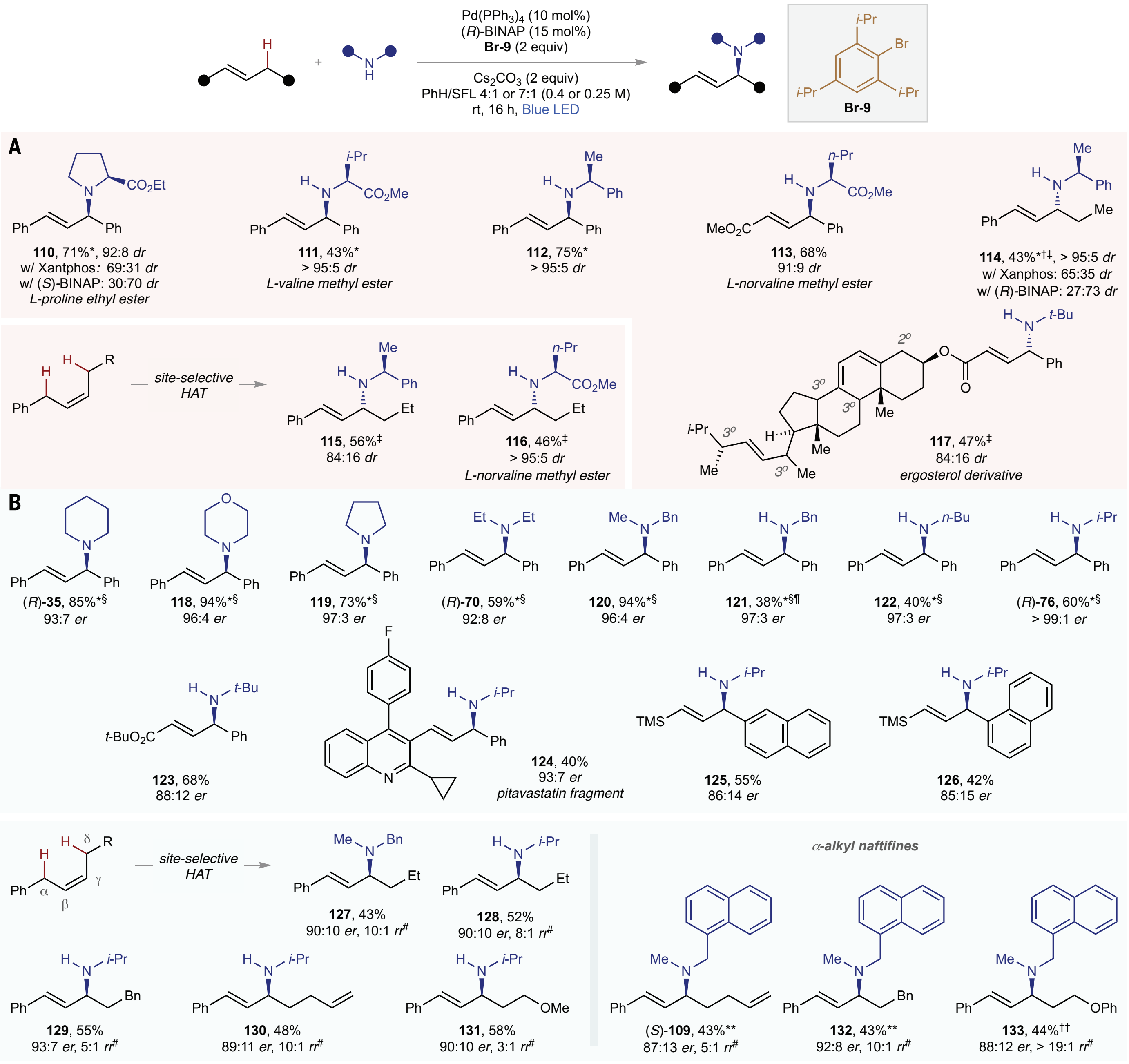

Fig. 4. Stereoselective allylic C–H amination. (**A**) Diastereoselective amination. (**B**) Enantioselective amination. *, Pd(OAc)$_2$/PPh$_3$ instead of Pd(PPh$_3$)$_4$ was used; †, without SFL; ‡, (*S*)-BINAP was used; §, 1.0 equivalent of TBAB was added; ¶, K$_2$CO$_3$ as base; #, regioselectivity of γ- to α-amination; **, 2.5 equivalents of alkene; ††, 3.0 equivalents of alkene.

amines concurrently in one transformation becomes much more arduous. Taken together, conventional palladium catalysis does not appear to be mechanistically viable for this process. White and Jiang independently showed very recently that linear tertiary allylic amines can be obtained from BF$_3$-complexed or simple secondary aliphatic amines (*29, 30*) (Fig. 1B, top right). However, employment of primary amines is still problematic as it leads to uncontrolled double allylation products (*29*). Moreover, substrates containing multiple sterically accessible amine moieties remain unexplored. In addition, the requisite coordination of alkenes with electrophilic Pd(II) catalysts still confines the scope to monosubstituted alkenes, thus offering minimal variations around the allylic amine motif and to electron-neutral and electron-rich alkenes only (Fig. 1C). We therefore wondered whether a complementary redox cycle could circumvent the involvement of the Pd(II) catalyst, thereby obviating the substrate-catalyst precoordination and substantially expanding the scope of alkenes.

In 2016, we reported a photocatalytically generated hybrid aryl Pd(I) radical capable of intramolecular hydrogen atom transfer (HAT) from aliphatic C(sp^3)–H sites (*31*). The large difference in bond dissociation enthalpy (BDE) between aryl and aliphatic C–H bonds (*32*) enders this elementary step thermodynamically favorable. This driving force is further augmented in the case of activated C–H bonds and has been exploited recently by several research groups using the respective aryl halides (*33–36*). We turned our attention to this homolytic mode of allylic C–H bond cleavage as an alternative to the heterolytic counterpart that operates through Pd(II)–alkene coordination. With this in mind, we hypothesized a reaction sequence relying on an uncommon role for aryl bromide as an oxidant in palladium catalysis, with the first oxidation occurring at the metal center through photoinduced single electron transfer, followed by a subsequent oxidation of an alkene by means of intermolecular HAT (*37*, *38*) (Fig. 1D). The formed hybrid allyl Pd(I) radical intermediate would collapse to a classical, closed-shell π-allyl Pd(II) complex upon the third formal oxidation at palladium through a radical-polar crossover (*39–41*) scenario. The latter could then be intercepted by an aliphatic amine to afford the desired C–H amination product, meanwhile returning the palladium catalyst to its original redox state to close the cycle. Under this mechanistic manifold, a Pd(0/I/II) cycle is operative, which is fundamentally distinct from the common Pd(II/0) paradigm. We reasoned that the Pd(I) intermediates, formed in this catalytic system, would have attenuated Lewis acidity, thereby minimizing isomerization of alkenes and interaction with aliphatic amines. Nevertheless, the use of an aryl radical introduces several pitfalls associated with its high reactivity, including interruption by solvent molecules through radical addition or HAT, as well as Heck reaction with the alkene substrate. Striking a balance between selectivity and reactivity of the aryl radical is thus crucial to an efficient transformation. Herein, we report a general photocatalytic platform for intermolecular allylic C–H amination of differently substituted alkenes with primary and secondary aliphatic amines to access branched allylic amine products (Fig. 1B, bottom right). We also describe the enantio- and diastereoselective variants of this protocol (*42–45*).

In line with our proposal, we first investigated the C–H amination of (*E*)-β-ethylstyrene with piperidine (Fig. 1D). A reaction system composed of catalytic Pd(PPh$_3$)$_4$/Xantphos, bromobenzene, and cesium carbonate upon irradiation with blue LED light for 15 hours at room temperature in benzene provided the desired allylic amine product **1** in 4% yield. In keeping with the aforementioned potential pitfalls (Fig. 1D), formation of substantial amounts of side products, stemming from radical addition to benzene and substrate to give biphenyl and Heck product, respectively, was observed. We therefore began the optimization by surveying a range of aryl bromides and found that **Br-9**, in which the isopropyl groups would inhibit radical addition by shielding the formed aryl radical, substantially enhanced the yield of **1** to 41% (table S1). Further evaluation of reaction parameters revealed the importance of a polar medium and the beneficial effect of tetrabutylammonium bromide (TBAB) as an additive, which collectively increased the yield to 71% (tables S2 and S5). To further capitalize on this result, we screened several other aryl bromides. Optimization studies identified **Br-12**, which can be obtained in multigram scale in one step through Friedel-Crafts bromination of commercially available 1,3-di-*tert*-butyl-5-methylbenzene, as the most effective aryl bromide (table S8). As outlined in Fig. 1D, we reasoned that **Br-12** exhibited better performance as one of the large alkyl substituents was replaced with a smaller methyl group to compensate for the lowered reactivity resulting from increased steric hindrance. The two bromine atoms in one arene core enhance reactivity as well as atom economy. After further fine tuning of the reaction parameters, we were able to obtain **1** in 90% isolated yield. Only two equivalents of the alkene partner are needed for this transformation, in comparison to previous reports on aryl radical-mediated reactions which require large excess (typically ≥5 equivalents) of substrate. A reaction using one equivalent of alkene afforded the product in 59% yield (table S9). Control experiments established that both palladium catalysts and visible light are essential components for this protocol. We also found that the reaction of isomeric β-ethylstyrene (2.8:1 *E*/*Z*) was almost as efficient, yielding **1** in a stereoconvergent manner. Besides, we observed no side products originating from α-C–H abstraction of piperidine, indicative of a chemoselective intermolecular HAT process. Other deleterious pathways such as alkene dimerization were also minimal, as reflected by the high material balance based on unreacted alkene (fig. S1).

We found that the optimized conditions were efficient with a wide range of alkenes (Fig. 2A). The scope was first evaluated by decorating the phenyl ring of the benchmark alkene with an array of substituents (**2** to **26**). A substrate containing a nucleophilic phenol moiety was chemoselectively aminated in good yield (**4**). Versatile latent coupling functionalities, such as aryl chlorides (**12** and **21**), bromides (**13**), mesylates (**14**), and boronates (**15**), were also compatible. Notably, the steric hindrance of **Br-12** prevents otherwise expected radical addition to a terminal double bond, thus allowing for the efficient preparation of synthetically useful styrene derivative **16**. We also found that both electron-rich and electron-deficient heteroaryl analogs could be employed, as exemplified by several *N*- (**27** to **29**), *O*- (**30**), and *S*-based (**31** and **32**) heterocycles. Other modifications of alkene, such as extending the alkyl chain (**33**) and shuffling the methyl group (**34**) and replacing it with a phenyl group (**35**), were also successful. Michael acceptors, which are not applicable in the traditional approach as a result of their electron-deficient nature (vide supra), efficiently underwent chemoselective C–H amination over 1,4-addition (**36** and **37**), further highlighting the generality of this methodology. We also found that a substrate bearing a pendant noncongested tertiary aliphatic amine moiety was compatible with our reaction conditions (**38**). In addition to activated alkenes, aliphatic alkenes were also compatible reaction partners (**39** to **42**). Lastly, in the case of aliphatic alkenes containing distinct allylic C–H sites, this aryl radical-based approach enabled the site-selective amination of stronger primary C–H bonds over weaker yet less accessible tertiary or secondary sites, in contrast to most intermolecular HAT reactions, which preferentially target weaker C–H bonds (**43** to **45**). Likewise, in the presence of multiple secondary C–H sites of different steric environments, a selective amination occurred at the less hindered position (**46**). In most cases where lower yields were obtained, presumably due to catalyst deactivation, we observed incomplete reactions even with prolonged reaction times.

We next examined the scope of aliphatic amines (Fig. 2B). Cyclic amines of different ring sizes, including aziridines, azetidines, pyrrolidines, and azepanes, proved to be viable nucleophiles, albeit with diminished yield compared with piperidine (**47** to **52**). A range of piperidine and piperazine derivatives were also prepared in good yields (**53** to **62**). Protecting one of the nitrogen atoms of piperazine with an electron-withdrawing group is not necessary, as illustrated by the efficient synthesis of **57** to **60**, including two *N*-alkyl piperazines. Other heterocyclic amines, such as morpholine and thiomorpholine, were also competent coupling partners (**63** to **65**). Acyclic secondary amines, though less effective, could also be used for this reaction (**66** to **70**). Notably, product **68** was obtained in respectable yield despite the strong chelating character of ethylenediamines. We also found that this protocol could be extended to primary amines (**71** to **76**), including pharmaceutically relevant cyclopropylmethyl and cyclobutyl amines **71** and **72**. This method is also efficient with terminal alkenes (**77**), which are the exclusive substrates for allylic C–H amination under the classical Pd(II/0) catalytic cycle. Likewise, various nonaliphatic nitrogen nucleophiles, such as anilines, sulfonamides, carbamates, imides, as well as aromatic *N*-heterocycles, are all competent nucleophiles in this transformation (**78** to **83**). As a general observation, substrates bearing α-hetero (**3**, **10**, **28**, **36**, **38**, **57** to **61**, **63** to **65**, **68**, **74**, **78**, **80**, and **82**) and α-carbonyl (**7**, **56**, **69**, **75**, and **81**) aliphatic C–H bonds were well tolerated. Notably, even benzylic (**5**, **24**, **52**, and **53**) and doubly activated (**62** and **67**) systems, which possess BDEs comparable to that of allylic C–H bonds, were found to be compatible, illustrating the robustness of the disclosed method.

We also evaluated the applicability of this photocatalytic process in a more complex setting (Fig. 3). As a demonstration of potential late-stage functionalization, drug fragments and natural product derivatives were successfully aminated (**84** to **87**). Given the medicinal significance of piperidine and piperazine cores, we tested a broad range of drugs (or their fragments) containing these motifs in this amination reaction, which led to the corresponding complex allylic amines in good yields (**88** to **100**). In particular, product **97**—a key intermediate to a histone deacetylase inhibitor (Fig. 1A)—was obtained in 46% yield, compared with 8% through traditional reductive amination routes (*42*). To further illustrate the utility of this protocol, we showed that various cyclic (**101** and **102**) and acyclic bioactive amines (**103** to **107**) also underwent smooth transformations. Notably, this method enables access to α-substituted analogs of known pharmaceutical agents, such as flunarizine (**108**) and naftifine (**109**), wherein the latter was obtained through a site-selective HAT of an alkene possessing three distinct secondary allylic C–H sites.

The construction of enantio-enriched aliphatic allylic amines through palladium-catalyzed allylic substitution of the respective prefunctionalized allyl electrophiles is well documented (*1*). Unfortunately, this valuable transformation has not been translated to the realm of C–H amination, mostly due to the limitations of the alkenes and invariably leading to linear products lacking stereogenic centers. Because our method delivers branched allylic amines with a new stereocenter, we aimed to develop this transformation in a stereocontrolled fashion.

First, diastereoselective reactions were examined (Fig. 4A). Amination of 1,3-diphenylpropene with proline ester, an abundant chiral amine, in the presence of achiral Xantphos ligand smoothly produced **110**, albeit with low diastereocontrol. The diastereoselectivity was substantially improved under a double stereodifferentiation scenario with the use of Pd/(*R*)-BINAP catalyst system. Employment of (*S*)-BINAP less selectively produced another diastereomer. Other chiral amines were equally efficient toward allylic amines (**111** and **112**). Good stereocontrol was also achieved in a more challenging case proceeding through unsymmetrical π-allyl Pd(II) intermediate (**113**). All these products (**110** to **113**) possess an aryl group α-to the *N*-atom. Analogous alkyl substituted product **114** was also accessible through this approach. As in the former case, employment of the achiral Pd/L catalyst system delivered the product in low diastereoselectivity. In this case, however, the *S*-enantiomer of BINAP was superior. This catalyst system was also successfully used for site- and diastereoselective amination of an alkene possessing multiple accessible allylic C–H bonds (**115** and **116**). Moreover, ergosterol derivative **117** could be selectively obtained through reaction of the respective chiral alkene and achiral amine.

Next, we examined the more challenging enantioselective version of our protocol. Notably, amination of the symmetrically substituted allylic system proceeded well, producing the respective amines with excellent enantiocontrol [(*R*)-**35**, (*R*)-**70**, (*R*)-**76**, **118** to **122**]. Good enantioselectivity was also observed with unsymmetrical allylic systems, possessing ester- (**123**), multisubstituted heteroaryl- (**124**), and silyl (**125** and **126**) groups. Finally, we embarked on the enantioselective amination of the most challenging substrates possessing multiple allylic C–H sites. Notably, a site-specific HAT occurred at the α-C–H site of the alkene to produce allylic amines **127** to **131**, as well as drug analogs (*S*)-**109**, **132**, and **133**, with high enantiocontrol and good regioselectivity. The latter reflects regiocontrol of the amination step. Overall, these results substantiate the feasibility of merging excited-state radical chemistry with ground state asymmetric processes with a single catalyst, which to date has not been achieved within photoexcited palladium catalysis (*43–46*).

REFERENCES AND NOTES

1. O. Pàmies *et al.*, *Chem. Rev.* **121**, 4373–4505 (2021).
2. S. A. Reed, M. C. White, *J. Am. Chem. Soc.* **130**, 3316–3318 (2008).
3. G. Liu, G. Yin, L. Wu, *Angew. Chem. Int. Ed.* **47**, 4733–4736 (2008).
4. S. A. Reed, A. R. Mazzotti, M. C. White, *J. Am. Chem. Soc.* **131**, 11701–11706 (2009).
5. G. Yin, Y. Wu, G. Liu, *J. Am. Chem. Soc.* **132**, 11978–11987 (2010).
6. C. C. Pattillo *et al.*, *J. Am. Chem. Soc.* **138**, 1265–1272 (2016).
7. R. Ma, M. C. White, *J. Am. Chem. Soc.* **140**, 3202–3205 (2018).
8. P.-S. Wang, L.-Z. Gong, *Acc. Chem. Res.* **53**, 2841–2854 (2020).
9. J. S. Burman, S. B. Blakey, *Angew. Chem. Int. Ed.* **56**, 13666–13669 (2017).
10. A. M. Kazerouni, Q. A. McKoy, S. B. Blakey, *Chem. Commun.* **56**, 13287–13300 (2020).
11. C. Liang *et al.*, *J. Am. Chem. Soc.* **130**, 343–350 (2008).
12. H. Lei, T. Rovis, *J. Am. Chem. Soc.* **141**, 2268–2273 (2019).
13. J. S. Burman, R. J. Harris, C. M. B. Farr, J. Bacsa, S. B. Blakey, *ACS Catal.* **9**, 5474–5479 (2019).
14. T. Knecht, S. Mondal, J. H. Ye, M. Das, F. Glorius, *Angew. Chem. Int. Ed.* **58**, 7117–7121 (2019).
15. H. Lei, T. Rovis, *Nat. Chem.* **12**, 725–731 (2020).
16. T. Ide *et al.*, *J. Am. Chem. Soc.* **143**, 14969–14975 (2021).
17. J. L. Roizen, M. E. Harvey, J. Du Bois, *Acc. Chem. Res.* **45**, 911–922 (2012).
18. E. Vitaku, D. T. Smith, J. T. Njardarson, *J. Med. Chem.* **57**, 10257–10274 (2014).
19. A. J. Musacchio *et al.*, *Science* **355**, 727–730 (2017).
20. Q. Cheng, J. Chen, S. Lin, T. Ritter, *J. Am. Chem. Soc.* **142**, 17287–17293 (2020).
21. S. Wang *et al.*, *Nat. Catal.* **5**, 642–651 (2022).
22. D. J. Wang, K. Targos, Z. K. Wickens, *J. Am. Chem. Soc.* **143**, 21503–21510 (2021).
23. X. Li, J. Jin, P. Chen, G. Liu, *Nat. Chem.* **14**, 425–432 (2022).
24. W. G. Whitehurst, J. H. Blackwell, G. N. Hermann, M. J. Gaunt, *Angew. Chem. Int. Ed.* **58**, 9054–9059 (2019).
25. Z. Zhuang, J.-Q. Yu, *J. Am. Chem. Soc.* **142**, 12015–12019 (2020).
26. J. Rodrigalvarez *et al.*, *Nat. Chem.* **12**, 76–81 (2020).
27. J. Rodrigalvarez, L. A. Reeve, J. Miró, M. J. Gaunt, *J. Am. Chem. Soc.* **144**, 3939–3948 (2022).
28. C. He, W. G. Whitehurst, M. J. Gaunt, *Chem* **5**, 1031–1058 (2019).
29. S. Z. Ali *et al.*, *Science* **376**, 276–283 (2022).
30. Y. Jin *et al.*, *Nat. Chem.* **14**, 1118–1125 (2022).
31. M. Parasram, P. Chuentragool, D. Sarkar, V. Gevorgyan, *J. Am. Chem. Soc.* **138**, 6340–6343 (2016).
32. Y.-R. Luo, *Handbook of Bond Dissociation Energies in Organic Compounds* (CRC Press, 2002).
33. B. Ye, J. Zhao, K. Zhao, J. M. McKenna, F. D. Toste, *J. Am. Chem. Soc.* **140**, 8350–8356 (2018).
34. Z. Liu *et al.*, *Chem. Sci.* **11**, 7619–7625 (2020).
35. J. Kang, H. S. Hwang, V. K. Soni, E. J. Cho, *Org. Lett.* **22**, 6112–6116 (2020).
36. T. Li *et al.*, *Chem. Sci.* **12**, 15655–15661 (2021).
37. The HAT step is likely to be the turnover-limiting step, as supported by a series of kinetic isotope effect (KIE) experiments. See supplementary materials for details.
38. K. A. Gardner, J. M. Mayer, *Science* **269**, 1849–1851 (1995).
39. H.-M. Huang *et al.*, *Nat. Catal.* **3**, 393–400 (2020).
40. K. P. Shing Cheung, D. Kurandina, T. Yata, V. Gevorgyan, *J. Am. Chem. Soc.* **142**, 9932–9937 (2020).
41. H.-M. Huang *et al.*, *J. Am. Chem. Soc.* **142**, 10173–10183 (2020).
42. P. Angibaud *et al.*, *Bioorg. Med. Chem. Lett.* **20**, 294–298 (2010).
43. M. Parasram, V. Gevorgyan, *Chem. Soc. Rev.* **46**, 6227–6240 (2017).
44. R. Kancherla, K. Muralirajan, A. Sagadevan, M. Rueping, *Trends Chem.* **1**, 510–523 (2019).
45. W. M. Cheng, R. Shang, *ACS Catal.* **10**, 9170–9196 (2020).
46. K. P. S. Cheung, S. Sarkar, V. Gevorgyan, *Chem. Rev.* **122**, 1543–1625 (2022).

ACKNOWLEDGMENTS

Funding: We acknowledge National Institute of Health (GM120281), National Science Foundation (CHE-1955663), and Welch Foundation (Chair, AT-0041) for financial support. K.P.S.C. acknowledges the support of UT Dallas Eugene McDermott Graduate Fellowship (202102). **Author contributions:** V.G. and K.P.S.C. conceived the project. K.P.S.C. developed the racemic reaction. K.P.S.C., A.M., and J.F. surveyed the scope of racemic reaction. K.P.S.C. and J.F. developed the stereoselective reaction. K.P.S.C., J.F., and K.M. surveyed the scope of stereoselective reaction. V.G. and K.P.S.C. wrote the manuscript. V.G. directed the project. **Competing interests:** Authors declare that they have no competing interests. **Data and materials availability:** Experimental procedures, optimization data, NMR spectra, mass spectrometry data, and HPLC traces are available in the supplementary materials.

SUPPLEMENTARY MATERIALS

science.org/doi/10.1126/science.abq1274
Materials and Methods
Figs. S1 to S8
Tables S1 to S10
NMR Spectra
HPLC Traces
References (*47–82*)

Submitted 19 March 2022; resubmitted 19 September 2022
Accepted 18 November 2022
10.1126/science.abq1274

EVOLUTIONARY ECOLOGY

The role of divergent ecological adaptation during allopatric speciation in vertebrates

Sean A. S. Anderson[1,2,3]* **and Jason T. Weir**[1,2,4]

After decades of debate, biologists today largely agree that most speciation events require an allopatric phase (that is, geographic separation), but the role of adaptive ecological divergence during this critical period is still unknown. Here, we show that relatively few allopatric pairs of birds, mammals, or amphibians exhibit trait differences consistent with models of divergent adaptation in each of many ecologically relevant traits. By fitting new evolutionary models to numerous sets of sister-pair trait differences, we find that speciating and recently speciated allopatric taxa seem to overwhelmingly evolve under similar rather than divergent macro–selective pressures. This contradicts the classical view of divergent adaptation as a prominent driver of the early stages of speciation and helps synthesize two historical controversies regarding the ecology and geography of species formation.

The geographic and ecological contexts in which new species arise are two subjects of historical controversy in evolution research. For much of the 20th century, biologists debated the geography of speciation and whether allopatry was required for the process to begin (*1*). By the turn of the 21st century, this debate shifted to whether speciation resulted from divergent adaptation to distinct ecological pressures (*2*, *3*), as had been classically hypothesized by Darwin and Wallace (*4*). Today, biologists largely agree that most speciation events require an allopatric phase (*1*, *5*), and it is clear that speciation can occur both in response to (*2*, *6*), and in the absence of (*3*, *7*, *8*), adaptive ecological divergence. Yet the effects of geographic separation and ecological divergence have been largely studied in isolation, and it is unclear whether and how they combine to generate new species. Most classic model systems of speciation ecology are in fact co-occurring lineage pairs [e.g., lake stickleback, Galápagos finches, rift-lake cichlids, host-switching insects (*9*–*12*)], and although diversification is increasingly studied in nonmodel and primarily allopatric taxa (*8*), the ecological context of their speciation has not been systematically characterized. It is thus unknown whether allopatric speciation typically involves divergent adaptation to distinct ecological pressures or whether lineages tend to adapt to similar pressures in allopatry, with most ecological divergence occurring later (e.g., during range expansion and the establishment of sympatry) (*3*) (Fig. 1). This distinction is important, because the two scenarios imply different limits to speciation rates (e.g., ecological opportunity versus time in allopatry) and thus different explanations for the buildup of biodiversity.

Addressing the general role of divergent adaptation in allopatry requires a broad-scale statistical approach. Here, we amass ecological trait data across a wide array of terrestrial vertebrates (birds, mammals, and amphibians) and create new statistical models to evaluate evidence for ecology-based divergent adaptation as a prominent evolutionary force during speciation's allopatric phase. Our approach is based on the prediction that if allopatric speciation is generally driven by divergent ecological adaptation, then speciating and recently speciated allopatric lineages (i.e., sister taxa) should tend to differ in ecologically relevant traits (e.g., body size, limb length, climate niche preferences) (Fig. 1A). However, some degree of trait differentiation between independently evolving lineages is inevitable over time and does not necessarily indicate adaptive divergence. We thus developed different evolutionary models of trait differentiation with and without divergent adaptation and compared the fit of these models to empirical distributions of trait differences in numerous sets of sister lineages.

We measured traits with well-established ecological importance in 129 allopatric sister pairs [i.e., speciating or recently speciated taxa, including taxonomic sister species and sister "phylogroups" (*13*) within species] of New World terrestrial birds from museum specimens and compiled an additional 14 published trait datasets for various groups of birds, mammals, and amphibians [see (*14*) for data criteria]. Each of the 15 datasets ultimately contained absolute trait differences and evolutionary age estimates for between 27 and 1001 allopatric sister pairs (median 87 allopatric pairs per dataset; Table 1). Most datasets contained measures of divergence for each sister pair in multiple ecologically relevant characters, including body size, feeding traits, appendage characteristics, and climate niche variables (Table 1 and table S1). We also included song data from birds, which is a social trait that is often strongly influenced by ecology (*15*). Some traits were not independent [e.g., limb length and principal component (PC) scores partly based on limb length], but they may yet have distinct functional relevance to the organisms (i.e., the interaction of several traits may have ecological relevance apart from that of any trait on its own). We therefore analyzed the statistical distributions of sister-pair divergence in each trait and composite trait from each of the 15 datasets (for a total of 130 separate analyses; Table 1 and table S1) to see how prevalent divergent adaptation appears to be among traits and across taxa [all data and code are deposited at (*16*)].

In our basic modeling design, differences in ecological traits begin to arise when a lineage splits into allopatric populations that start independently evolving. At this point, speciation has begun; if independent evolution continues long enough, reproductive isolation is inevitable. Trait differences develop over time as a stochastic process based on one of three underlying scenarios: (i) sister lineages adaptively diverge toward distinct trait optima [i.e., the divergent adaptation "DA" model (*17*), approximating the scenario shown in Fig. 1A]; (ii) lineages adapt about the same optimum as that of their allopatric sister (i.e., the shared optimum "SO" model, approximating the scenario shown in Fig. 1B); or (iii) both sisters in each pair evolve under phenotypic drift or fluctuating phenotypic selection (i.e., the Brownian motion "BM" model of trait differentiation). The three models differ in terms of the expected statistical distribution of trait differences through time (Fig. 2B); thus, in a given analysis, the models are each fit to an empirical distribution composed of the absolute differences in a particular trait for all of the sister pairs of a particular dataset. The relative fit of the different models to that empirical distribution is then judged using corrected Akaike information criterion (AICc).

In this basic framework, all sister pairs in a particular analysis are assumed to have diverged under the same evolutionary process, but our aim in this paper is to test alternative hypotheses for the relative contribution of divergent adaptation to allopatric divergence. We thus create two new mixture models that estimate the proportion of sister pairs in a dataset whose divergence in a given trait has occurred under alternative processes. These are the DA-SO mixture model, in which a proportion (P_{DA}) of sister pairs diverge under a DA process and the remaining proportion (P_{SO}) diverge under the SO process, and the SO-BM mixture model (Fig. 2, C to E). [A DA-BM model is also possible but was not used

---

[1]Department of Ecology and Evolutionary Biology, University of Toronto, Toronto, ON, Canada. [2]Department of Biological Sciences, University of Toronto at Scarborough, Toronto, ON, Canada. [3]Department of Biology, University of North Carolina at Chapel Hill, Chapel Hill, NC, USA. [4]Department of Natural History, Royal Ontario Museum, Toronto, ON, Canada.
*Corresponding author. Email: sean.as.anderson@gmail.com

Table 1. Support for divergent adaptation in various traits from 15 datasets. Rows are in descending order of the number of allopatric pairs in a dataset. "Number of traits supporting DA-SO" is the number of traits in a dataset for which DA-SO was supported over SO-BM by a minimum of two AICc. "Maximum P_{DA}" is the highest P_{DA} estimate from all traits for which DA-SO was supported in a given dataset and is a key basis for interpreting the role of DA in allopatric divergence. "PCA 2D" refers to two-dimensional Euclidean distances in the PC1-PC2 plane (PCA, principal components analysis). Results for individual analyses are shown in table S1. Sources for trait datasets and trees that were used to calculate divergence times are listed in table S3. Full results with additional parameter estimates are in the supplementary results files (*16*). Ma, million years; NA, not applicable.

Taxa	Number of allopatric pairs	Median pair age (Ma)	Traits measured	Number of traits supporting DA-SO/number of traits	Maximum P_{DA} (trait)
Birds general	1001	2.8	Morphology PC1-PC3; bill-only PC1-PC3; bill PCA 2D; morphology PCA 2D	5/8	0.133 (bill-only PC1)
Mammals general	500	2.1	Body mass	0/1	NA
Birds general	381	4.4	Bill length, width, and depth; hand-wing index; body mass; bill PC1-PC2; bill PCA 2D	6/8	0.145 (bill length)
Rodents	242	2.6	Appendage lengths; midpoint latitude; six climate variables; morphology PC1-PC3; climate PC1-PC3; morphology PCA 2D; climate PCA 2D	10/25	0.129 (climate PC3)
Frogs general	146	4.5	Six climate variables; climate PC1 and PC2; climate PCA 2D	5/9	0.147 (annual precipitation)
New World land birds	129	2.6	Body PC1-PC3; bill PC1-PC3; bill length, width, and depth; wing, tail, and tarsus length	0/12	NA
New World land birds	111	2.7	Climate PC1-PC3; body mass	2/4	0.321 (climate PC3)
Emberizoid birds	87	1.8	Bill specialization; bill shape; range area and perimeter; PC1-PC3 of bill geometric morphometrics; bill PCA 2D	3/8	1.00 (PCA 2D)*
Amazonian birds	86	2.3	Morphology PC1-PC7; song PC1-PC2	1/9	0.041 (song PC1)
New World land birds	74	2.7	Song pitch	1/1	1.00 (song pitch)*
New World land birds	69	5.4	Song length and syllable diversity	1/2	0.358 (song length)
Neotropical ovenbirds (Furnariidae)	37	2.0	Song PC1-PC4; bill PC1; tarsus length; song PCA 2D	0/6	NA
Salamanders	30	6.4	Eight linear morphometrics; morphology PC1 and PC2; morphology PCA 2D	2/11	0.171 (snout-vent length)
Plethodontid salamanders	29	6.5	Surface area (SA); volume (V), and SA/V ratio; seven linear morphometrics; seven climate variables; morphology PC1-PC2; Climate PC1-PC3; morphology PCA 2D; climate PCA 2D	1/16	0.072 (mean annual precipitation)
Plethodontid salamanders	27	5.0	Seven linear morphometrics; morphology PC1 and PC2; morphology PCA 2D	1/10	0.808 (body width)
Total				**38/130**	

*Support for DA-SO is contingent on an obvious outlier being removed (*14*).

because of performance testing issues; fig. S1 (*14*).] Our main analysis then consisted of fitting the two mixture models to each of the 130 empirical distributions of sister-pair trait differences, which allowed us to generally characterize model support and generate a distribution of P_{DA} estimates. With mixture models, we can address the central question of this paper: If divergent adaptation is generally the predominant process driving allopatric divergence, then (i) the DA-containing model (DA-SO) should be generally well supported over the SO-BM model and (ii) DA-like patterns of trait differences should predominate (i.e., $P_{DA} > 50\%$) in at least some eco- logically relevant traits in each of the 15 sets of sister pairs.

We find instead that only 38 of the 130 analyses strongly support the DA-SO model, and only a minor proportion of sister pairs from each dataset tend to show patterns of divergence consistent with DA in each trait (Fig. 3, Table 1, and table S1). The prevalence of DA was low and varied little across traits and datasets (Fig. 3A); the median P_{DA} from the 38 analyses in which DA-SO was well supported was 9.9% (bolded rows in table S1 show the trait-dataset combinations that support DA-SO). Critically, DA was well supported as the predominant driver of trait divergence (i.e., P_{DA} exceeded 50%) for just one trait each in just 3 of the 15 datasets in our study: a sample of Plethodontid salamanders (for the trait body weight), a sample of New World passerines (for the trait song pitch), and a sample of Emberizoid birds (for the trait bill shape) (Table 1). In other words, in 12 of the 15 groups of sister pairs that we analyzed, including global datasets of birds and mammals, DA was not supported as the prevailing driver of divergence in any of several ecologically relevant traits measured for those taxa (Fig. 3B and table S1). Instead, the SO process was consistently prominent; the median P_{SO} from the best-supported model in each of the 130 analyses was 93.2% (Fig. 3B). Thus, in each dataset, the vast majority of pairs have diverged under similar rather than divergent macro-selective pressures or drift-like processes in most or all ecological traits analyzed. These results are robust to alternative range

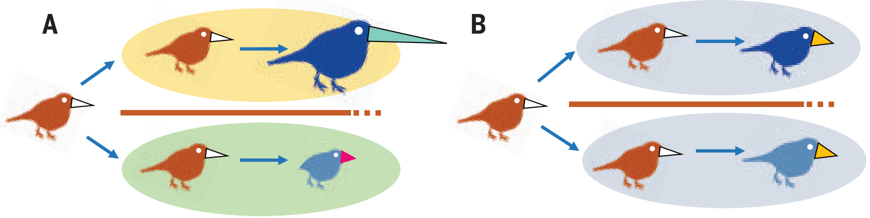

Fig. 1. Two modes of adaptation in allopatry. (**A** and **B**) A lineage splits into two allopatric populations separated by a geographic barrier. Over time, the populations evolve into new species. Body color differences symbolize that species are distinct. In (A), differently colored ovals represent allopatric habitats with distinct ecological characteristics. Speciation results as lineages adapt to these disparate environments, and divergent adaptation generates substantial differences in ecologically important traits (body size, beak size and shape, and tail length). In (B), same-colored ovals represent allopatric habitats that are ecologically alike. Lineages adapt in parallel to these like environments, and speciation results from factors unrelated to ecological divergence. Ecological traits may or may not evolve during this time, but if evolution occurs, it occurs in similar directions in the two lineages such that trait differences remain slight (beak shape). Taxa that speciate under the scenario shown in (A) may be better able to co-occur in sympatry once lineages expand their ranges and come into contact. Taxa from the scenario shown in (B) might competitively exclude one another or be forced to undergo character displacement. The two scenarios suggest different limiting factors in the build-up of biodiversity. Whether the scenario shown in (A) or (B) predominates in nature is unknown.

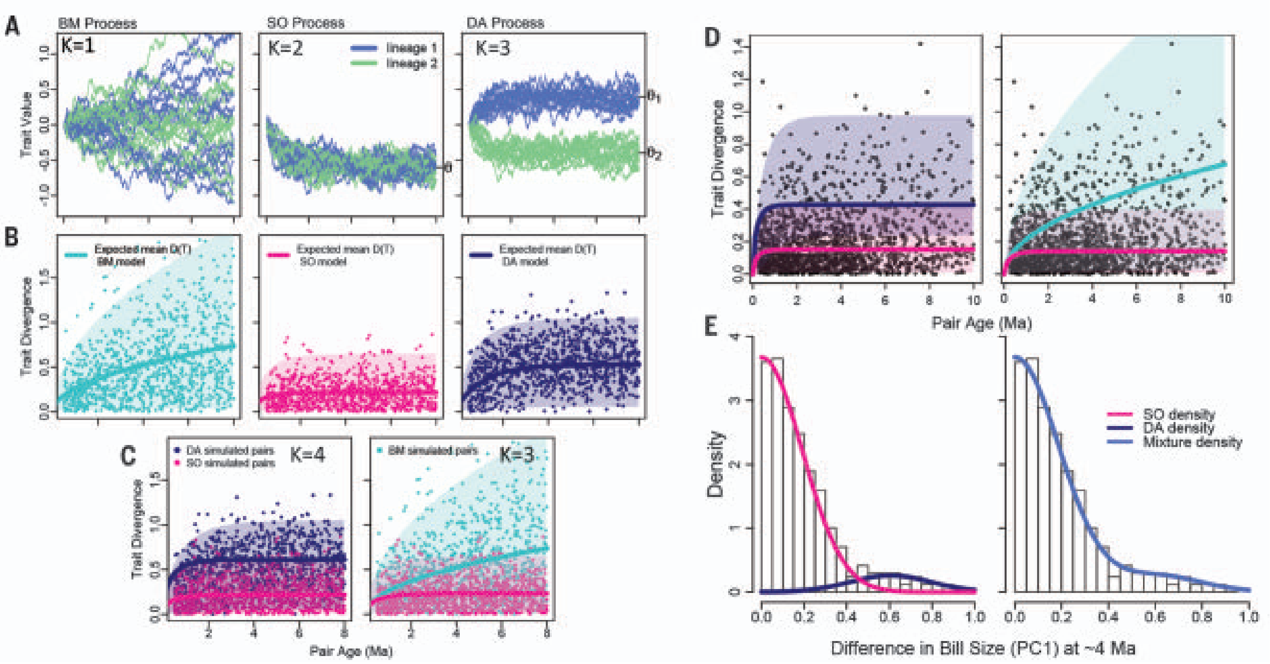

Fig. 2. Understanding trait differentiation models. Simulations are shown in (A) to (C), and real data are shown in (D) and (E); "K" denotes parameter count. (**A**) Replicate evolutionary walks (n = 15) of a continuous trait in sister lineages under BM, SO, and DA processes; θ_x is the trait optimum for lineage x. The SO model is agnostic as to whether the optimum shared between sisters differs from that of their common ancestor (as illustrated) or is the same. (**B**) Points are simulated trait differences for pairs of various ages. Models were fit to these simulated data, and their expectations were plotted. Model parameters determine the expected distribution of trait differences. In (B) to (D), colored lines show the mean and shaded areas show the 95% confidence intervals of this distribution. D(T) is the trait difference at time T. (**C**) DA-SO and SO-BM mixture models fit to simulated mixed datasets. (**D**) DA-SO and SO-BM mixture models fit to empirical bill-size differences from (*31*); DA-SO is the better-fit model from AICc (table S1). Figure S16 shows this style of graph for every dataset. In (B) to (D), colored lines show the mean, and shaded areas show the 95% confidence intervals of this distribution. (**E**) Model fits to data at a slice in time. Curves are proportion-weighted component densities (left) and the corresponding DA-SO mixture model density (right) expected at 4 million years. Histograms are bill size differences for pairs 3 million to 4.5 million years diverged (n = 339 pairs). Ma, million years.

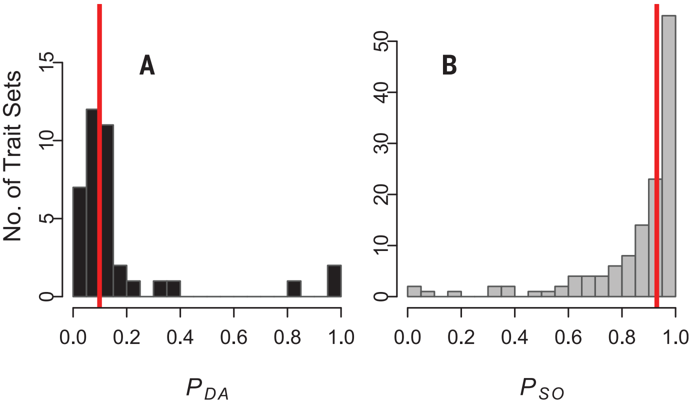

Fig. 3. Proportion of pairs diverging under alternative evolutionary processes. A "trait set" is a set of differences in a given trait for all of the sister pairs of a particular dataset (each row in table S1 is a trait set). Trait sets thus differed based on the trait and/or the set of sisters being analyzed. P_{DA} is the estimated proportion of sister pairs in a trait set whose divergence conforms to the DA component of a DA-SO mixture model; P_{SO} is the proportion that conforms to the SO component of either the DA-SO or SO-BM model. (**A**) P_{DA} estimates from the 38 trait sets for which DA-SO was well supported. (**B**) Frequency of P_{SO} estimates from the best-fit model for all 130 analyses. Red lines indicate median estimates of the proportion parameter [9.9 and 93.2% in (A) and (B), respectively]. The *y* axes have different scales. The histograms illustrate little variation across traits and datasets: DA was consistently a minor process and SO the major process driving trait divergence between speciating and recently speciated allopatric lineages.

overlap thresholds used for classifying lineages as allopatric (*14*) (fig. S2).

The consistently low prevalence of the DA process and high prevalence of the SO process are unlikely to be artifacts of model inadequacy or of assumption violations. Simulation-based model performance tests show that estimates of P_{DA} and P_{SO} are accurate over a wide and relevant range of parameter space and dataset sizes (*14*) (figs. S3 to S5). Moreover, when we intentionally violated model assumptions in our simulations, we were unable to generate errors that falsely recreated the empirical results (*14*) (figs. S6 to S10). We can also exclude "species sorting" [i.e., a bias in which sister pairs with more pronounced trait differences become sympatric at a higher rate (*18*)] as a key driver of our results, because simulations show that this process consistently generates a statistical artifact (a negative correlation between trait divergence and sister-pair age) that is largely absent from empirical datasets (*14*) (figs. S11 to S14). Also, although it is possible that a few of the sister pairs in our datasets were previously sympatric, the common pattern of exaggerated trait differences observed between sympatric close relatives (*18*, *19*) would suggest that unseen sympatry-to-allopatry state transitions would, if anything, tend to inflate rather than suppress support for the DA process. Similarly, although the assumption that trait differences accurately reflect ecological differences is violated when different traits have similar functions [i.e., "many-to-one mapping" (*20*)], such a violation causes functional divergence to be overestimated rather than underestimated and thus cannot account for the low P_{DA} values that we observed.

Does the ecology of allopatric speciation change with the ecological theater? Estimates of higher speciation rates at higher absolute latitudes (*21*, *22*) have inspired the hypothesis that temperate-zone speciation may be driven to a greater extent by adaptive ecological divergence than is speciation in the tropics (*23*) because of the greater availability of underexploited resources (i.e., "ecological opportunity") at temperate latitudes (*24*). To test this hypothesis, we compiled latitude data from digital range maps for each sister pair in each dataset and created new mixture models that permit the proportion of pairs evolving under a given process (i.e., P_{DA}, P_{SO}, or P_{BM} in DA-SO or SO-BM models) to vary with latitude (*14*) (fig. S15). Reanalyzing all sets of trait divergence from 14 of the 15 datasets [122 analyses total; we excluded one dataset because all pairs were Amazonian birds that together covered only a small latitudinal range (*14*)], we find that the estimated proportion of allopatric sister pairs evolving under a particular evolutionary process is, with few exceptions, latitudinally constant (table S2). Thus, although rates of trait evolution may change across latitudes, the underlying evolutionary process driving allopatric divergence appears to vary little. We speculate that reported estimates of faster evolutionary rates for high-latitude taxa are driven in some cases by "character displacement" [in the sense of (*25*)] in sympatry (i.e., geographic overlap), and it is the establishment of secondary sympatry rather than allopatric trait divergence that is generally faster at high latitudes (*26*). This dynamic was implicated for patterns of divergence in avian plumage coloration (*27*).

We note that ecological adaptation can drive evolution in a number of traits that were not included in our analysis. Adaptive differences in phenotypes such as behavior, cellular attributes, sensory complexes, and life history characteristics are generally not captured in trait datasets. It is therefore possible that adaptive ecological divergence has occurred on undetected trait axes in the sister-pair groups of our study. We also note, however, that most textbook examples of "ecological speciation" in vertebrates exhibit unambiguous adaptive differences in common aspects of adult external morphology (e.g., body size in most taxa, bill shape or size divergence in birds) (*2*, *28*), whereas we find only minor support for divergent adaptation as a prominent driver of divergence in these very same phenotypes and each of many additional traits. If adaptive ecological divergence is a major process during allopatric speciation in these pairs, then it is either much subtler than that observed in vertebrate model systems, there is greater variability in the trait axes on which different related pairs adaptively diverge, or it generally occurs on different and as-yet-unidentified trait axes for reasons that are unclear. The current most parsimonious interpretation is that our results reflect a genuine biological phenomenon: Allopatric divergence is most generally characterized by adaptive evolution to similar selective pressures.

Our study unites two historical controversies in evolution research—the roles of geographic and of ecological divergence in the evolution of new species. Using new models to analyze sister-pair trait differences, we find that adaptive ecological divergence in allopatry appears to be the exception rather than the rule in vertebrates. This result contradicts the classical idea that divergent adaptation initiates the earliest stages of speciation, and it supports an emerging picture in which new species commonly arise despite minimal ecological divergence (*8*). We suggest that it is notable that many textbook model systems of speciation ecology are sympatric taxa, because their pronounced ecological differences may have primarily evolved during or after the establishment of sympatry. Such differences may then be required more for ecological coexistence than for speciation per se. It is likewise possible that a previously reported correlation between ecological divergence and reproductive isolation in a diverse group of sister taxa (*29*) was mainly driven by sympatric pairs (sympatric and allopatric pairs were pooled in that analysis). This notion seems plausible because only premating (not postzygotic) isolation was correlated with ecological divergence in the study, and both ecological disparity and the strength of premating barriers are hypothesized to accelerate in sympatry [through character displacement and "reinforcement" (*30*), respectively]. A key implication of our result is that speciation in allopatry does not generally require lineages to exploit new resources or otherwise adapt to distinct ecological pressures but relies instead on their prolonged geographic separation. Our findings leave open the possibility that pronounced ecological divergence is generally important after allopatric speciation as lineages expand their ranges and begin to overlap (*3*, *18*).

REFERENCES AND NOTES

1. J. A. Coyne, H. A. Orr, *Speciation* (Sinauer, 2004).
2. D. Schluter, *Science* **323**, 737–741 (2009).
3. R. J. Rundell, T. D. Price, *Trends Ecol. Evol.* **24**, 394–399 (2009).
4. C. R. Darwin, A. R. Wallace, *J. Proc. Linn. Soc. Lond. Zool.* **3**, 45–62 (1858).
5. D. I. Bolnick, B. M. Fitzpatrick, *Annu. Rev. Ecol. Evol. Syst.* **38**, 459–487 (2007).
6. P. Nosil, *Ecological Speciation* (Oxford Univ. Press, 2012).
7. M. Simões *et al.*, *Trends Ecol. Evol.* **31**, 27–34 (2016).
8. J. E. Czekanski-Moir, R. J. Rundell, *Trends Ecol. Evol.* **34**, 400–415 (2019).
9. H. D. Rundle, L. Nagel, J. Wenrick Boughman, D. Schluter, *Science* **287**, 306–308 (2000).
10. L. M. Ratciliffe, P. R. Grant, *Anim. Behav.* **31**, 1139–1153 (1983).
11. O. Seehausen *et al.*, *Nature* **455**, 620–626 (2008).
12. K. E. Filchak, J. B. Roethele, J. L. Feder, *Nature* **407**, 739–742 (2000).
13. J. C. Avise, D. Walker, *Proc. Biol. Sci.* **265**, 457–463 (1998).
14. Materials and methods are available as supplementary materials.
15. J. T. Weir, D. J. Wheatcroft, T. D. Price, *Evolution* **66**, 2773–2783 (2012).
16. S. A. S. Anderson, J. T. Weir, Data for: The role of adaptive ecological divergence during allopatric speciation in vertebrates, Zenodo (2022); https://doi.org/10.5281/zenodo.7195944.
17. S. A. S. Anderson, J. T. Weir, *Am. Nat.* **196**, 429–442 (2020).
18. S. A. S. Anderson, J. T. Weir, *Proc. Natl. Acad. Sci. U.S.A.* **118**, e2021209118 (2021).
19. T. Dayan, D. Simberloff, *Ecol. Lett.* **8**, 875–894 (2005).
20. C. J. Thompson *et al.*, *Evolution* **71**, 2738–2749 (2017).
21. J. T. Weir, D. Schluter, *Science* **315**, 1574–1576 (2007).
22. D. L. Rabosky *et al.*, *Nature* **559**, 392–395 (2018).
23. A. D. Cutter, J. C. Gray, *Evolution* **70**, 2171–2185 (2016).
24. D. Schluter, *Am. Nat.* **187**, 1–18 (2016).
25. P. R. Grant, *Biol. J. Linn. Soc. London* **4**, 39–68 (1972).
26. J. T. Weir, T. D. Price, *Am. Nat.* **177**, 462–469 (2011).
27. P. R. Martin, R. Montgomerie, S. C. Lougheed, *Evolution* **64**, 336–347 (2010).
28. D. Schluter, *The Ecology of Adaptive Radiation* (Oxford Univ. Press, 2000).
29. D. J. Funk, P. Nosil, W. J. Etges, *Proc. Natl. Acad. Sci. U.S.A.* **103**, 3209–3213 (2006).
30. M. R. Servedio, M. A. F. Noor, *Annu. Rev. Ecol. Evol. Syst.* **34**, 339–364 (2003).
31. A. L. Pigot *et al.*, *Nat. Ecol. Evol.* **4**, 230–239 (2020).

ACKNOWLEDGMENTS

We thank D. Jackson for advice on data standardizations. L. Forsyth, J. Boyko, C. Boccia, and J. Santangelo answered questions about data availability. We thank T. Price, J. Bemmels, V. Luzuriaga-Aveiga, E. Mikkelson, and E. Nikelski for manuscript comments. We also thank the researchers who made their data publicly accessible or shared data when requested. M. Peck (Royal Ontario Museum), P. Sweet (American Museum of Natural History), and D. Willard (Field Museum of Natural History) assisted with access to museum collections. **Funding:** Funding was provided by a Natural Sciences and Engineering Research Council of Canada (NSERC) accelerator grant (492890; J.T.W.) and NSERC discovery grants (RGPIN-2016-0653 and RGPIN-2022-04817; J.T.W.). Development of the morphometric dataset was funded by an American Museum of Natural History Collection Study Grant and doctoral and postdoctoral fellowships from NSERC to J.T.W. and from supervisor grant support from the Canadian Foundation for Innovation (to D. Schluter) and the National Science Foundation (to T. Price). Simulation analyses were conducted on the Niagara supercomputer hosted by SciNet at the University of Toronto and the Cedar cluster at Simon Fraser University. Niagara and Cedar are assets of the Digital Research Alliance of Canada (formerly Compute Canada). SciNet is funded by the Canada Foundation for Innovation, the Government of Ontario, the Ontario Research Fund–Research Excellence, and the University of Toronto. **Author contributions:** S.A.S.A. and J.T.W. designed the study. J.T.W. generated New World avian trait data. S.A.S.A. encoded and tested the models, compiled and wrangled published datasets, ran analyses, and wrote the paper with input from J.T.W. **Competing interests:** The authors declare no competing interests. **Data and materials availability:** All data and code for reproducing the main empirical analysis, as well as final results files, are deposited at Zenodo (*16*). Data on trait divergence in New World avian sister pairs are provided in raw format and analysis-ready format. Data compiled from published sources are provided in the formats in which they were downloaded and in analysis-ready formats. Code for converting downloaded datasets to their analysis-ready formats is provided in deposited files.

SUPPLEMENTARY MATERIALS

science.org/doi/10.1126/science.abo7719
Materials and Methods
Figs. S1 to S16
Tables S1 to S3
References (*32–62*)
MDAR Reproducibility Checklist

Submitted 28 February 2022; accepted 15 November 2022
10.1126/science.abo7719

SPIN ICE

Dynamical fractal and anomalous noise in a clean magnetic crystal

Jonathan N. Hallén[1,2]*, Santiago A. Grigera[3], D. Alan Tennant[4,5], Claudio Castelnovo[1], Roderich Moessner[2]

Fractals—objects with noninteger dimensions—occur in manifold settings and length scales in nature. In this work, we identify an emergent dynamical fractal in a disorder-free, stoichiometric, and three-dimensional magnetic crystal in thermodynamic equilibrium. The phenomenon is born from constraints on the dynamics of the magnetic monopole excitations in spin ice, which restrict them to move on the fractal. This observation explains the anomalous exponent found in magnetic noise experiments in the spin ice compound $Dy_2Ti_2O_7$, and it resolves a long-standing puzzle about its rapidly diverging relaxation time. The capacity of spin ice to exhibit such notable phenomena suggests that there will be further unexpected discoveries in the cooperative dynamics of even simple topological many-body systems.

The current intense research efforts on the behavior of topological matter attempt to provide an understanding of these systems that is on the same level of both generality and detail as is available for conventional systems (*1*, *2*). One particular frontier concerns the dynamical properties, especially those of topological systems that host exotic, fractionalized excitations, such as Laughlin quasiparticles with anyonic statistics in the quantum Hall effect (*3*) or emergent magnetic monopoles in the topological spin liquid known as spin ice (*4*) (Fig. 1). The dynamical behavior of the latter has been an enigma since its discovery (*5*–*7*). Most recently, ultrasensitive, low-temperature superconducting quantum interference device (SQUID) experiments have identified another puzzle: The magnetic noise spectral density exhibits an anomalous power law as a function of frequency, with the low-temperature exponent $\alpha \approx 1.5$ deviating strongly from the well-known $\alpha = 2$ of a paramagnet (*8*, *9*) [see also (*10*–*12*)]. Within the generally successful framework of what we refer to as the standard model (SM) of spin ice dynamics (*13*, *14*), this behavior cannot be accounted for using broadly accepted model Hamiltonian parameters (*9*).

In this work, we identify the missing element: Besides the constraints imposed by the emergent gauge field in spin ice, there is a further dynamical bottleneck on account of the local (transverse) field distribution, which suppresses the dynamics of another quarter of the spins (*15*). Both restrictions reflect the random yet correlated orientation of the spins in the spin ice ground states and force the monopoles to move on an effectively disordered cluster in real space, even in the absence of quenched disorder.

Crucially, this cluster is close to a percolation transition. It therefore exhibits a well-developed fractal structure on short and intermediate length scales, which we characterize in detail. We show that it is through hosting effectively subdiffusive monopole motion that the fractal structure bequeaths anomalous exponents to the magnetic noise. Our numerical modeling of this process allows us to quantitatively reproduce the experimental noise curves, with only a single global fitting parameter for a

---

[1] TCM Group, Cavendish Laboratory, University of Cambridge, Cambridge CB3 0HE, UK. [2] Max Planck Institute for the Physics of Complex Systems, 01187 Dresden, Germany. [3] Instituto de Física de Líquidos y Sistemas Biológicos, UNLP-CONICET, 1900 La Plata, Argentina. [4] Department of Physics and Astronomy, University of Tennessee, Knoxville, TN 37996, USA. [5] Department of Materials Science and Engineering, University of Tennessee, Knoxville, TN 37996, USA.
*Corresponding author. Email: ejn41@cam.ac.uk

microscopic time scale. In the process, we also shed light onto a further, long-standing puzzle in spin ice—the steeper-than-expected rise of the macroscopic relaxation time upon cooling. Our theory explains this phenomenon naturally, in a clean (i.e., stoichiometric and uniform) system, as a reflection of the sparseness and structure of the dynamical fractal. The fractal geometry in spin ice thus influences the dynamics in a qualitative and experimentally observable way while leaving no signatures in the thermodynamics.

Spin ice is a topological magnet (*4*, *16*) with fractionalized quasiparticles in the form of mobile magnetic monopoles (*17*), as illustrated in Fig. 1. The low-temperature behavior of spin ice in and out of equilibrium can largely be recast in terms of the dynamics of a dilute gas of monopoles (*13*) and their interactions with the background spin configuration. Specifically, the widely used SM of incoherent spin ice dynamics forbids spin flips that create—rather than hop—monopoles (Fig. 1). For a monopole in a tetrahedron, this constraint systematically blocks one direction out of four (*14*).

This model has successfully described important features of the dynamics, especially the exponentially divergent relaxation time at low temperatures. However, it has failed to account for the large energy scale in the leading exponential growth of this time scale (*18*, *19*), and it has particularly been challenged by susceptibility (*20*–*22*) and anomalous magnetic noise experiments (*8*, *9*). These puzzles and their resolutions are discussed below.

The beyond the standard model (bSM) dynamics introduced here incorporate the observation that the internal field distribution on spins across which monopoles hop is peculiarly bimodal (*15*). In particular, one-third of the flippable spins experience a near-vanishing transverse field (*23*). We model these spins as flipping at a lower rate, $1/\tau_{\mathrm{slow}}$. By contrast, the other spins experience a finite transverse field and flip at some reference rate, $1/\tau_{\mathrm{fast}}$. (In the SM, all spins attempt to flip at a single rate, $1/\tau_0$.) We take τ_0, τ_{fast}, and τ_{slow} to be independent of temperature. The scale τ_{fast} defines our unit of time, and it is in fact the only fitting parameter in our analysis.

Regarding the interaction parameters, we use

$$\begin{aligned} H_{\mathrm{OP}} = Da^3 \sum_{i<j} \left[\frac{\vec{S}_i \cdot \vec{S}_j}{r_{ij}^3} - \frac{3\left(\vec{S}_i \cdot \vec{r}_{ij}\right)\left(\vec{S}_j \cdot \vec{r}_{ij}\right)}{r_{ij}^5} \right] \\ + J_1 \sum_{\langle i,j \rangle} \vec{S}_i \cdot \vec{S}_j + J_2 \sum_{\langle i,j \rangle_2} \vec{S}_i \cdot \vec{S}_j \\ + J_3 \sum_{\langle i,j \rangle_3} \vec{S}_i \cdot \vec{S}_j + J'_3 \sum_{\langle i,j \rangle'_3} \vec{S}_i \cdot \vec{S}_j \end{aligned} \qquad (1)$$

an extension of the conventional dipolar spin ice Hamiltonian that was previously obtained from a combined fit to neutron scattering, magnetic susceptibility, and specific heat measurements (*24*). It comprises long-range dipolar interactions and first, second, and third nearest-neighbor exchange terms with strengths

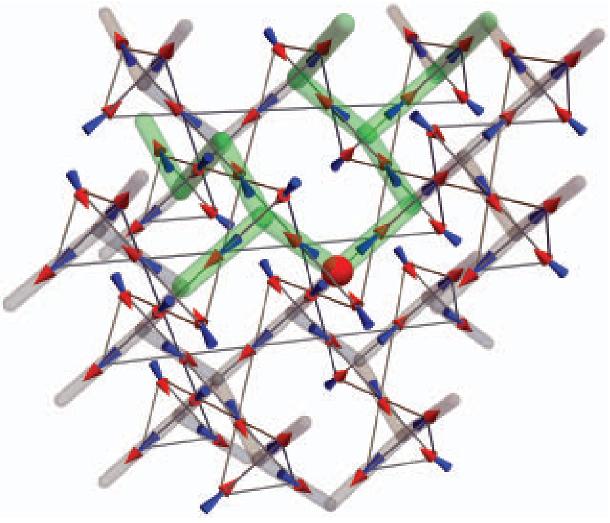

Fig. 1. The physics of spin ice. In spin ice, classical Ising-like moments reside on a pyrochlore lattice of corner-sharing tetrahedra. In each of the exponentially numerous ground states, two spins point into a tetrahedron and two point out. Violations of this ice rule take the form of magnetic monopoles (marked by the red sphere). These monopoles move on the diamond lattice formed by the centers of the tetrahedra. From a given position, monopoles can hop by flipping any one of the three majority spins (bonds highlighted in green and gray) but not the minority spin (unmarked bonds). Here, we show parts of a spin ice configuration, including all tetrahedra that this monopole could reach within three hops. Some spins experience a vanishing transverse field (*15*), and their dynamics are substantially suppressed. If moves through such spins are forbidden, the monopole is restricted to move on the paths highlighted in green—these form the emergent dynamical fractal.

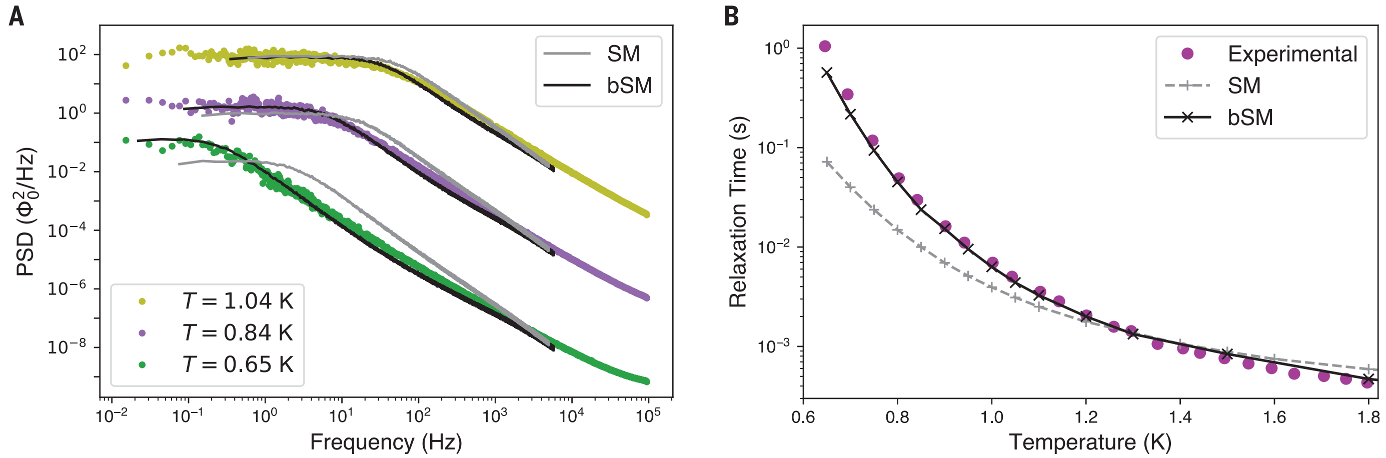

Fig. 2. Magnetization dynamics in $Dy_2Ti_2O_7$. (**A**) PSD of magnetization fluctuations extracted from SQUID measurements on $Dy_2Ti_2O_7$ (filled circles) (*9*). Monte Carlo results for H_{OP} with SM dynamics (gray) and bSM dynamics (black) are shown with solid lines. The curves have been shifted vertically (*23*). Overall time scale factors of τ_{fast} = 85 μs and τ_0 = 200 μs were applied for the bSM and SM results, respectively, to visually match the experimental data, with $\tau_{\mathrm{slow}} = \infty$ for simplicity. The deviation at high frequencies is a known feature of Monte Carlo dynamics, and other minor discrepancies are to be expected in a model with a necessarily sharper parameter distribution than the experimental system (*23*). (**B**) Relaxation times τ were extracted from fits of the PSD curves to the function $A[1+(2\pi\nu\tau)^{\alpha}]^{-1}$ for both experimental and numerical data.

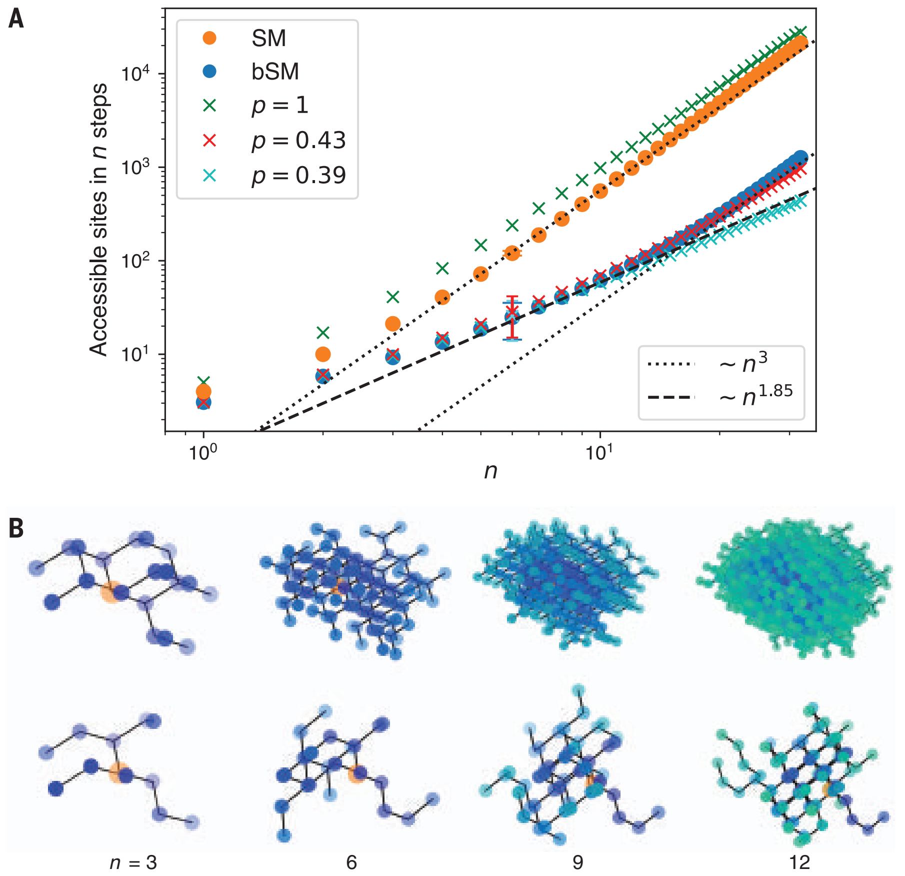

Fig. 3. Nature of the fractal clusters. (**A**) Number of sites that a monopole can visit within a given number of steps n, the so-called chemical distance, with SM (orange circles) and bSM (blue circles) dynamics. The corresponding results for a walker on the diamond lattice at various bond-filling fractions are shown by green, red, and cyan crosses. In the bSM case, there is a crossover between fractal ~$n^{1.85}$ and standard n^3 scaling occurring at $n_{cr} \approx 14$, when the monopole has traveled a distance of the order of the correlation length. Within the fractal regime, i.e., up to n_{cr}, the monopole can access ~130 sites. The error bars, shown only for $n = 6$ for simplicity, reflect the finite width of the distribution and are not the result of sampling (the statistical uncertainty is smaller than the size of the symbols). (**B**) Sites that a specific monopole, starting at the site marked in orange, can reach with SM dynamics (upper row) and bSM dynamics (lower row) within n steps. The color of the sites shifts from blue to green with the number of steps away from the starting site. The fractal cluster is much sparser, underpinning the rapidly diverging relaxation time (Fig. 2).

Da^3 = 1.3224 K, J_1 = 3.41 K, J_2 = 0.0 K, J_3 = −0.00466 K, and $J'_3 = 0.0439\text{K}$. For details, see (*23*), where a comparison is drawn to the maximally simple nearest-neighbor spin ice model.

Fig. 2A shows the magnetic noise measured using SQUID magnetometry on a single crystal of $Dy_2Ti_2O_7$ (*9*) in the temperature range $0.64\text{ K} \leq T \leq 1.04\text{ K}$, which is high enough to be above the freezing of spin ice (*7*) and low enough for monopoles to be sparse, weakly interacting quasiparticles. The noise is expressed in terms of the power spectral density (PSD), $S(\nu)$, defined as the temporal Fourier transform of the magnetization, $M(t)$, autocorrelation function: $S(\nu) = \mathcal{F}[\langle M(0)M(t)\rangle]$.

Comparison with our simulations using H_{OP} shows that bSM dynamics reproduce experiments over four orders of magnitude in frequency and six orders of magnitude in noise power (Fig. 2). The only fitting parameter is τ_{fast} = 85 μs [we estimate $\tau_{\text{slow}}/\tau_{\text{fast}} \gtrsim 10^3$ (*23*), indistinguishable from $\tau_{\text{slow}} = \infty$ in these plots]. By comparison, SM dynamics with fitting parameter τ_0 = 200 μs are unable to describe the experimental data at low temperature.

The extracted relaxation time from the bSM dynamics (Fig. 2B) also agrees well with the experiment (*9*), especially when compared with the SM, which yields much too short a relaxation time at low temperature. This has been a puzzle in the community for many years (*6*, *7*, *13*, *18*, *21*, *22*, *25*–*27*): In a gas of freely moving monopoles, the relaxation time of the magnetization scales with their inverse density (*14*), $1/\rho \sim \exp(\Delta_m/T)$, which is set by the energy cost Δ_m of an isolated monopole. Increasing the energy in the Arrhenius law to $\Delta_\tau > \Delta_m$ is largely precluded by basic statistical mechanics, whereas estimates suggest that a Δ_τ in excess of twice Δ_m is actually required to fit the experimental growth of the relaxation time (*25*). Previous theories of the steep rise of the relaxation time upon cooling invoked extrinsic contributions caused by open boundary effects, disorder, and an autonomously temperature-dependent microscopic time scale (*21*, *22*, *28*–*31*); the identification of an intrinsic mechanism leading to a parametrically faster growth of the relaxation time compared with $1/\rho$ has been lacking.

To explain the anomalous behavior in the magnetic noise and susceptibility and the corresponding strongly diverging relaxation time, we consider the motion of an isolated monopole in spin ice with bSM dynamics. This has between zero and three choices of sites to move to, with the statistical average being two. Linking the sites reachable by successive monopole hops, as in Fig. 3, yields a fractal cluster. Its fractal exponents are then picked up in the experimental anomalous noise signal, thus altering the relaxation properties of the system.

In more detail, to understand the fluctuations of the magnetization, we need to analyze the statistical properties of the monopole motion because (i) their motion proceeds through the flipping of spins and (ii) they are the natural (sparse, weakly interacting) quasiparticles in the regime $T \lesssim 1\,\text{K}$. The motion of the monopoles takes place on a dynamical cluster in real space, defined by excluding the spins that are not flippable energetically, or because of a small local transverse field.

For $\tau_{\text{slow}} = \infty$, this defines a percolation problem close to the critical point so that the fractal structure is visible on small and intermediate scales (Fig. 3). In this regime, the number of sites that the structure contains grows anomalously slowly with the chemical distance n—i.e., the minimum number of steps on the lattice needed to join two sites. We find that the growth agrees very well with $n^{1.85}$, the predicted exponent from critical percolation in $d = 3$ (*32*, *33*) (Fig. 3), in contrast to the conventional n^d. The sparseness of the fractal is notable: Up to $n_{cr} = 14$, it contains only ~130 of the 2071 sites available on the diamond lattice. Around n_{cr}, the system crosses over to conventional three-dimensional (3D) behavior at longer length scales. Although our dynamical rules yield a nonstandard correlated percolation problem, this does not affect its critical behavior, and the properties of the cluster are in fact accurately reproduced by a random walker on a random percolation cluster on the diamond lattice at filling fraction p = 0.43, which is only slightly above its critical value $p_c \approx 0.39$ (*23*, *34*).

Our discussion so far has largely been based on the behavior of a single monopole. Beyond this, the motion of other monopoles can change the local spin and transverse field configurations, thereby endowing the percolation cluster with slow dynamics of its own (*23*). A higher monopole density (alongside a finite τ_{slow}) therefore diminishes the crossover value n_{cr}.

It is the crossover in real space that terminates the anomalous regime in the PSD toward low frequencies in the time domain. At even lower frequencies, a plateau appears on account of the trajectories of different monopoles overlapping. From the theory of random walks on percolation clusters above the percolation threshold (*35*–*37*), the PSD of a monopole should show anomalous decay $S \sim \nu^{-(1+\sigma)}$ at high frequency and conventional decay $S \sim \nu^{-2}$ at low frequencies. Exact enumeration in the random percolation problem was previously used to obtain $\sigma = 0.50 \pm 0.01$ in $d = 3$ (*38*). This largely explains the experimentally observed anomalous power law, which hovers near $\nu^{-1.5}$ in the regime under consideration (*9*).

From the point of view of percolation, we have discovered a purely dynamically generated fractal object in a uniform, stoichiometric, and disorder-free bulk crystal. Its existence is predicated on the emergence of point-like mobile objects—the magnetic monopoles—in a 3D topological spin liquid that remains fluctuating down to low temperatures (*17*). The monopole motion is subject in turn to a twofold set of constraints. One, imposed by the emergent gauge field represented by the spin background, reflects the large-scale topological nature of the spin ice state. The other is purely microscopic in origin, resulting from an interplay of the geometric spin arrangement and the short-range statistical spin correlations imposed by the ice rules. It is the combination of these constraints that makes the monopoles move on a fractal structure. This in turn is the origin of the previously puzzling anomalous magnetic noise and rapidly diverging relaxation time. Conversely, this highly nontrivial phenomenology provides a validation of a concrete model of the microscopic dynamics, in particular the bimodal distribution of local transverse fields.

Notably, this is all accessible by probing magnetization response and fluctuations—specifically using ac susceptibility or noise measurements—whose frequency dependence reflects spatial information, linked by the (sub-)diffusive motion of the monopoles. The emergence of a dynamical fractal in a disorder-free crystal presents a distinct mechanism for the existence of anomalous noise—a subject studied in many other contexts within materials science (*39*–*42*) and elsewhere (*43*–*46*).

Some of the above elements can be manipulated in a controlled manner, all of which provide promising avenues for future experiments. Trivially, different spin ice compounds have different interaction parameters, resulting in broadly different transverse field distributions. Moreover, the microscopic dynamics can also be altered by applying uniaxial strain (*47*) or through the crystal field scheme by switching from (Kramers) Dy-based spin ice to, for example, (non-Kramers) Ho-based spin ice. For example, $Ho_2Ti_2O_7$ is predicted to have a smaller ratio $\tau_{\text{slow}}/\tau_{\text{fast}}$ (*15*).

Our effective percolation problem has turned out to be at a sweet spot near criticality—reducing constraints would eliminate the anomalous nature of the signal, whereas increasing them would likely eliminate equilibration. It will be interesting to see whether doing so (e.g., by the controlled introduction of some form of quenched or dynamical disorder) may shed light on the so-called glassy physics below 650 mK (*48*). Clearly the advent of highly tunable noisy intermediate-scale quantum (NISQ) platforms opens up a previously unexplored set of directions, especially in two dimensions (*49*, *50*), where anomalous noise has already been seen in the classical nanomagnetic artificial spin ice (*51*). This includes questions related to quantum diffusion of monopoles and the role of increasingly coherent many-body quantum dynamics (*49*). The latter could alter the noise in a characteristic way (*23*) and therefore be used as evidence for the presence of so-called ring-exchange processes in candidate quantum spin ice compounds.

REFERENCES AND NOTES

1. P. M. Chaikin, T. C. Lubensky, *Principles of Condensed Matter Physics* (Cambridge Univ. Press, 1995).
2. R. Moessner, J. E. Moore, *Topological Phases of Matter* (Cambridge Univ. Press, 2021).
3. A. Stern, *Ann. Phys.* **323**, 204–249 (2008).
4. M. Udagawa, L. Jaubert, *Spin Ice* (Springer, 2021).
5. J. Snyder, J. S. Slusky, R. J. Cava, P. Schiffer, *Nature* **413**, 48–51 (2001).
6. K. Matsuhira, Y. Hinatsu, T. Sakakibara, *J. Phys. Condens. Matter* **13**, L737–L746 (2001).
7. J. Snyder *et al*., *Phys. Rev. B* **69**, 064414 (2004).
8. R. Dusad *et al*., *Nature* **571**, 234–239 (2019).
9. A. M. Samarakoon *et al*., *Proc. Natl. Acad. Sci. U.S.A.* **119**, e2117453119 (2022).
10. C. A. Watson, I. Sochnikov, J. R. Kirtley, R. J. Cava, K. A. Moler, Real-space imaging and flux noise spectroscopy of magnetic dynamics in $Ho_2Ti_2O_7$. arXiv:1903.11465 [cond-mat.str-el] (2019).
11. F. K. K. Kirschner, F. Flicker, A. Yacoby, N. Y. Yao, S. J. Blundell, *Phys. Rev. B* **97**, 140402 (2018).
12. C. Nisoli, *Europhys. Lett.* **135**, 57002 (2021).
13. I. A. Ryzhkin, *Zh. Eksp. Teor. Fiz.* **128**, 559–566 (2005).
14. L. D. Jaubert, P. C. Holdsworth, *Nat. Phys.* **5**, 258–261 (2009).
15. B. Tomasello, C. Castelnovo, R. Moessner, J. Quintanilla, *Phys. Rev. Lett.* **123**, 067204 (2019).
16. C. Castelnovo, R. Moessner, S. Sondhi, *Annu. Rev. Condens. Matter Phys.* **3**, 35–55 (2012).
17. C. Castelnovo, R. Moessner, S. L. Sondhi, *Nature* **451**, 42–45 (2008).
18. K. Matsuhira *et al*., *J. Phys. Soc. Jpn.* **80**, 123711 (2011).
19. D. Pomaranski *et al*., *Nat. Phys.* **9**, 353–356 (2013).
20. J. A. Quilliam, L. R. Yaraskavitch, H. A. Dabkowska, B. D. Gaulin, J. B. Kycia, *Phys. Rev. B* **83**, 094424 (2011).
21. L. Yaraskavitch *et al*., *Phys. Rev. B* **85**, 020410 (2012).
22. H. Revell *et al*., *Nat. Phys.* **9**, 34–37 (2013).
23. See the supplementary materials.
24. A. M. Samarakoon *et al*., *Nat. Commun.* **11**, 892 (2020).
25. L. D. C. Jaubert, P. C. W. Holdsworth, *J. Phys. Condens. Matter* **23**, 164222 (2011).
26. S. T. Bramwell, *Phil. Trans. R. Soc. A* **370**, 5738–5766 (2012).
27. V. Raban, L. Berthier, P. C. Holdsworth, *Phys. Rev. B* **105**, 134431 (2022).
28. G. Sala *et al*., *Nat. Mater.* **13**, 488–493 (2014).
29. C. Paulsen *et al*., *Nat. Phys.* **10**, 135–139 (2014).
30. C. Paulsen *et al*., *Nat. Phys.* **12**, 661–666 (2016).
31. R. Edberg *et al*., Magnetic monopole relaxation effects probed by modulation calorimetry in small spin-ice samples. arXiv:2202.02801 [cond-mat.str-el] (2022).
32. S. Havlin, R. Nossal, *J. Phys. A Math. Gen.* **17**, L427–L432 (1984).
33. D. Stauffer, A. Aharony, *Introduction to Percolation Theory* (Taylor & Francis, 2018).
34. X. Xu, J. Wang, J.-P. Lv, Y. Deng, *Front. Phys.* **9**, 113–119 (2014).
35. P. G. de Gennes, *La Recherche* **7**, 919–927 (1976).
36. S. Havlin, D. Ben-Avraham, *Adv. Phys.* **36**, 695–798 (1987).
37. B. D. Hughes, in *Complex Media and Percolation Theory*, M. Sahimi, A. G. Hunt, Eds. (Springer, 2021), pp. 191–235.
38. H. Eduardo Roman, *J. Stat. Phys.* **58**, 375–382 (1990).
39. F. Aliev *et al*., *Appl. Phys. Lett.* **91**, 232504 (2007).
40. A. A. Balandin, *Nat. Nanotechnol.* **8**, 549–555 (2013).
41. M. Najafi, S. Tizdast, Z. Moghaddam, M. Samadpour, *Phys. Scr.* **96**, 125259 (2021).
42. B. N. Costanzi, E. D. Dahlberg, *Phys. Rev. Lett.* **119**, 097201 (2017).
43. R. F. Voss, J. Clarke, *Nature* **258**, 317–318 (1975).
44. W. H. Press, *Comment. Astrophys.* **7**, 103–119 (1978).
45. C. A. Varotsos, I. Melnikova, M. N. Efstathiou, C. Tzanis, *Theor. Appl. Climatol.* **111**, 641–648 (2013).
46. F. Vernotte, E. Lantz, *Metrologia* **52**, 222–237 (2015).
47. L. Pili *et al*., *Phys. Rev. B* **105**, 184422 (2022).
48. S. T. Bramwell, M. J. Gingras, *Science* **294**, 1495–1501 (2001).
49. A. D. King, C. Nisoli, E. D. Dahl, G. Poulin-Lamarre, A. Lopez-Bezanilla, *Science* **373**, 576–580 (2021).
50. M. Stern, C. Castelnovo, R. Moessner, V. Oganesyan, S. Gopalakrishnan, *Phys. Rev. B* **104**, 115114 (2021).
51. M. Goryca *et al*., *Phys. Rev. X* **11**, 011042 (2021).
52. J. Hallén, Dynamical fractal and anomalous noise in clean magnetic crystal, V3, *Edmond* (2022); https://doi.org/10.17617/3.JQHCJY.

ACKNOWLEDGMENTS

We express our gratitude to S. L. Sondhi and S. Zhang for useful discussions and to C. Nisoli and P. Schiffer for comments on the manuscript. **Funding:** This work was supported in part by Engineering and Physical Sciences Research Council (EPSRC) grants EP/P034616/1 and EP/T028580/1 (C.C. and J.N.H.), the Deutsche Forschungsgemeinschaft under grant SFB 1143 (project ID 247310070) (R.M. and J.N.H.), and the cluster of excellence ct.qmat (EXC 2147, project ID 390858490) (R.M. and J.N.H.). The work of D.A.T. was supported by the US Department of Energy, Office of Science, Office of Basic Energy Sciences, under award no. DE-SC0022311. Part of this work was carried out within the framework of a Max Planck independent research group on strongly correlated systems. **Author contributions:** Numerical simulations and analyses were carried out by J.N.H. under the joint supervision of C.C. and R.M. All authors were involved in discussing the results and writing the manuscript. **Competing interests:** The authors declare that they have no competing interests. **Data and materials availability:** All data and code are publicly available (*52*).

SUPPLEMENTARY MATERIALS

science.org/doi/10.1126/science.add1644
Materials and Methods
Supplementary Text
Figs. S1 to S8
References (*53*, *54*)

Submitted 24 May 2022; accepted 17 October 2022
10.1126/science.add1644

BIOMATERIALS

Soft strain-insensitive bioelectronics featuring brittle materials

Yichao Zhao[1,2]†, Bo Wang[1]†, Jiawei Tan[1,2]†, Hexing Yin[2], Ruyi Huang[3,4,5], Jialun Zhu[1], Shuyu Lin[1], Yan Zhou[3,4], David Jelinek[6,7], Zhengyang Sun[6], Kareem Youssef[2], Laurent Voisin[6], Abraham Horrillo[6], Kaiji Zhang[1,2], Benjamin M. Wu[2,8,9,10,11], Hilary A. Coller[6,7,12], Daniel C. Lu[3,4,5], Qibing Pei[2], Sam Emaminejad[1,10]*

Advancing electronics to interact with tissue necessitates meeting material constraints in electrochemical, electrical, and mechanical domains simultaneously. Clinical bioelectrodes with established electrochemical functionalities are rigid and mechanically mismatched with tissue. Whereas conductive materials with tissue-like softness and stretchability are demonstrated, when applied to electrochemically probe tissue, their performance is distorted by strain and corrosion. We devise a layered architectural composite design that couples strain-induced cracked films with a strain-isolated out-of-plane conductive pathway and in-plane nanowire networks to eliminate strain effects on device electrochemical performance. Accordingly, we developed a library of stretchable, highly conductive, and strain-insensitive bioelectrodes featuring clinically established brittle interfacial materials (iridium-oxide, gold, platinum, and carbon). We paired these bioelectrodes with different electrochemical probing methods (amperometry, voltammetry, and potentiometry) and demonstrated strain-insensitive sensing of multiple biomarkers and in vivo neuromodulation.

Interfacing electronics with biological tissues is the foundation of probing and actuating biological systems. Reliable interaction between biological tissues and electronics requires the use of materials that support underlying electrochemical and electrical processes and satisfy tissue-imposed mechanical constraints (*1*, *2*). The electrochemical process involves electron transfer and accumulation at the bioelectronics-tissue interface for in situ stimulation (for example, neuromodulation) and sensing (for example, biomarker molecules), necessitating the use of suitable interfacial materials. The electrical process involves electron transport for signal routing and setting intended operating points (for example, voltage), which requires the use of highly conductive materials (*3*). From the mechanics standpoint, materials that mimic tissue properties such as stretchability (~20 to 75%) and compliance (Young's modulus, *E*, on the order of kilopascals to megapascals) are needed to establish conformable contact with tissue for high fidelity sensing and stimulation. This requirement is critical for minimizing disruption of tissue function as well as the risk of implant complications that result from scar formation, lead fracture, and tissue injury (*1*). However, the electrochemical and electrical performance of these materials may be affected by the strain originating from the movement and complex topography of the tissue.

Clinically established interfacial materials with high electrochemical performance for bioelectronics-tissue interfaces (such as noble metal–based ones) are all rigid (E > 1 GPa) and brittle (fracture strain < 1%). Recent advances in soft and stretchable conductors have enabled the development of strain-resilient devices with tissue-like mechanical properties, which maintain their electrical connection despite being extensively stretched (~800%) (*4*, *5*). Although these strain-resilient devices are suitable for the construction and integration of soft, stretchable, solid-state electronics, when they are applied to electrochemically probe the tissue environment (involving ionic biofluid surrounding), their performance is distorted by strain- or corrosion-related issues. The former issue manifests in devices with relatively low intrinsic conductivity (such as graphene and PEDOT:PSS: 1 to 10^3 S/m), in which strain-induced changes to their resistance cause substantial deviation from the intended operating points (such as, activation voltage), subsequently corrupting the reactions at the interface (*6*–*8*). The latter issue is especially observed in devices with highly conductive materials that rapidly oxidize upon exposure to the surrounding solution (such as silver-based nanomaterials), despite the application of surface modification [prone to surface defects or pores (*9*)]. As such, this group of devices cannot sustain the wide voltage range required to perform electrochemical reactions (*5*, *10*).

We devised a layered architectural composite design that centers on decoupling the bioelectronic materials configuration into an interfacial element for electron transfer and an interconnection element for electron transport. This design allows for the exploiting and coupling of surface channel cracks (within the brittle interfacial element) and anisotropic out-of-plane/in-plane electron conduction (within the interconnection element) to eliminate strain effects on device performance. The design further allows for a broad selection for the interfacial materials, including brittle noble metal–based materials. Following this approach, we created a functionally diverse library of thin (~140 μm), soft (~10 MPa) (fig. S1), stretchable (>150%), highly conductive (~1 ohm/sq) and strain-insensitive bioelectrodes (SIBs).

Our fabrication strategy (Fig. 1A) is based on (i) constructing the tissue interfacing element as a thin film with favorable electron transfer characteristics, (ii) constructing the interconnection element by using intrinsically stretchable and highly conductive silver nanowire (AgNW)–based traces, which are inlaid in the surface layer of a soft rubbery matrix [poly(urethane acrylate), PUA], and (iii) seamlessly integrating the two elements by means of a thin adhesive and anisotropically conductive film (ACF), which features isolated conductive particles embedded in a stretchable matrix to facilitate anisotropic out-of-plane electrical conduction. A variety of thin-film materials, including those that are brittle but have high electrochemical performance [gold (Au) platinum (Pt), and iridium oxide (IrOx)], can be built atop the ACF-AgNW-PUA layers through standard thin-film deposition techniques (Fig. 1B).

Fundamentally, our SIB's strain insensitivity is controlled by three layer-specific strain energy dissipation mechanisms (Fig. 1, C and D, and fig. S2): (i) crack channeling of brittle interfacial thin film, (ii) strain isolation of the out-of-plane conductive pathway in the ACF layer, and (iii) realignment of in-plane AgNW networks. Interfacial channel cracks are exploited as means of tensile strain energy release. Each cracked fragment experiences minimal strain, while remaining electrically connected to the system, preserving the overall active surface area of the SIB. As the electrical bridge between the cracked interfacial thin film and the AgNW-PUA layer, the ACF renders strain-insensitive out-of-plane electrical conduction,

---

[1] Interconnected and Integrated Bioelectronics Lab (I^{2}BL), Department of Electrical and Computer Engineering, Samueli School of Engineering, University of California, Los Angeles, CA, USA. [2] Department of Materials Science and Engineering, Samueli School of Engineering, University of California, Los Angeles, CA, USA. [3] Department of Neurosurgery, David Geffen School of Medicine, University of California, Los Angeles, CA, USA. [4] Neuromotor Recovery and Rehabilitation Center, David Geffen School of Medicine, University of California, Los Angeles, CA, USA. [5] Brain Research Institute, University of California, Los Angeles, CA, USA. [6] Department of Molecular, Cell and Developmental Biology, University of California, Los Angeles, CA, USA. [7] Department of Biological Chemistry, David Geffen School of Medicine, University of California, Los Angeles, CA, USA. [8] Weintraub Center for Reconstructive Biotechnology, School of Dentistry, University of California, Los Angeles, CA, USA. [9] Division of Advanced Prosthodontics, School of Dentistry, University of California, Los Angeles, CA, USA. [10] Department of Bioengineering, Samueli School of Engineering, University of California, Los Angeles, CA, USA. [11] Department of Orthopaedic Surgery, David Geffen School of Medicine, University of California, Los Angeles, CA, USA. [12] Molecular Biology Institute, University of California, Los Angeles, CA, USA.
***Corresponding author. Email: emaminejad@ucla.edu**
†These authors contributed equally to this work.

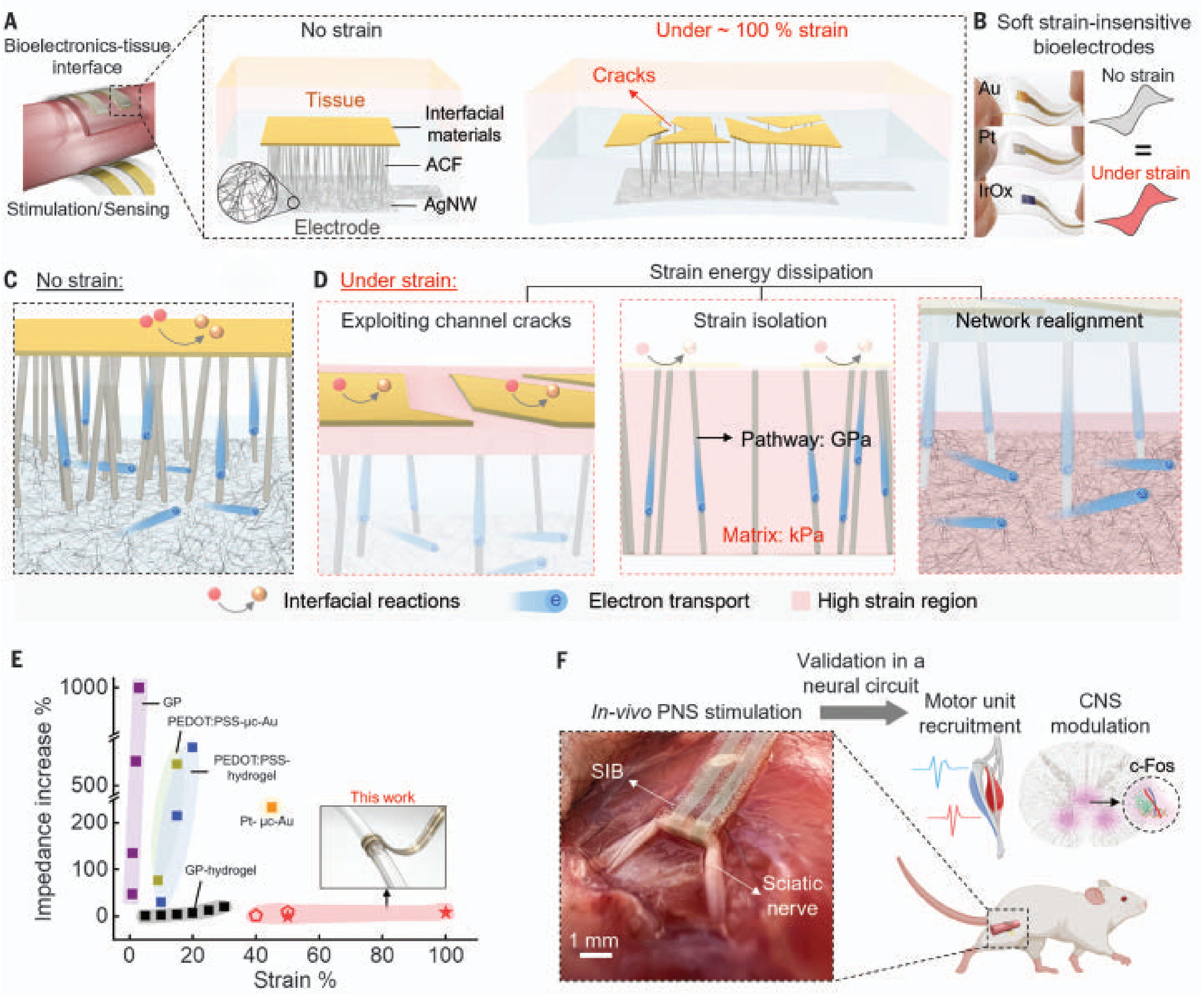

Fig. 1. Soft strain-insensitive bioelectrode (SIB): architecture, strain dissipation mechanisms, and applications. (**A**) Illustration of the SIB as a bioelectronics-tissue interface under strain. (**B**) Brittle noble metal–enabled SIBs for high fidelity stimulation and sensing under strain. (**C**) Schematic presentation of the SIB's underlying electron transfer and out-of-plane and in-plane electron transport processes. (**D**) Strain energy dissipation mechanisms within each layer of the SIB. (**E**) Ashby diagram of electrochemical impedance (at 1 kHz) increase versus tensile strain (*7*, *8*, *10*, *12*, *13*). Au-SIB and IrOx-SIB are indicated with star and pentagon markers, respectively. (**F**) A representative SIB interfacing the sciatic nerve of a mouse for nerve stimulation to achieve synchronized motor unit recruitment and CNS modulation, manifested as c-Fos expression.

because the rigid conductive microparticles (approximately gigapascals) are strain-isolated by the surrounding soft matrix (approximately kilopascals). The AgNWs in the bottom layer form in-plane conductive percolation networks that are strongly anchored onto the soft PUA substrate by means of in situ cross-linking. This strong binding enables network realignment to release strain energy (*11*).

The strain sensitivity of the electrical and electrochemical performances of the SIBs is compared with those obtained by the state-of-the-art stretchable bioelectrodes (Fig. 1E, fig. S3, and table S1) (*7*, *8*, *10*, *12*, *13*). We applied our SIBs to perform high-fidelity sensing of multiple biomarkers and neurostimulation under strain. We validated the in vivo operation of our SIBs in the context of a neural circuit. Specifically, we interfaced the bioelectrodes, featuring a brittle IrOx layer, with the sciatic nerve and verified the modulation of the bidirectional and interconnecting central nervous system (CNS) and motor unit (within the neural circuit) through peripheral nerve stimulation (PNS).

To visualize and quantitatively characterize the SIBs' strain insensitivity, we correspondingly used an electrochemical deposition–based staining method, electrical impedance spectroscopy (EIS), and cyclic voltammetry (CV). We characterized Au-deposited SIBs (Au-SIBs) as model test devices over a range of tensile strain conditions. The devised electrochemical staining method enables the spatial mapping of the electrical connection of the interfacial thin film. It uses a standard electrodeposition setup to deposit a conductive material (in this application, Pt) onto a test electrode under strain, in which only the electrode surface regions that remain electrically connected to the power source support electrodeposition (Fig. 2A). As a result, the electrochemically deposited regions

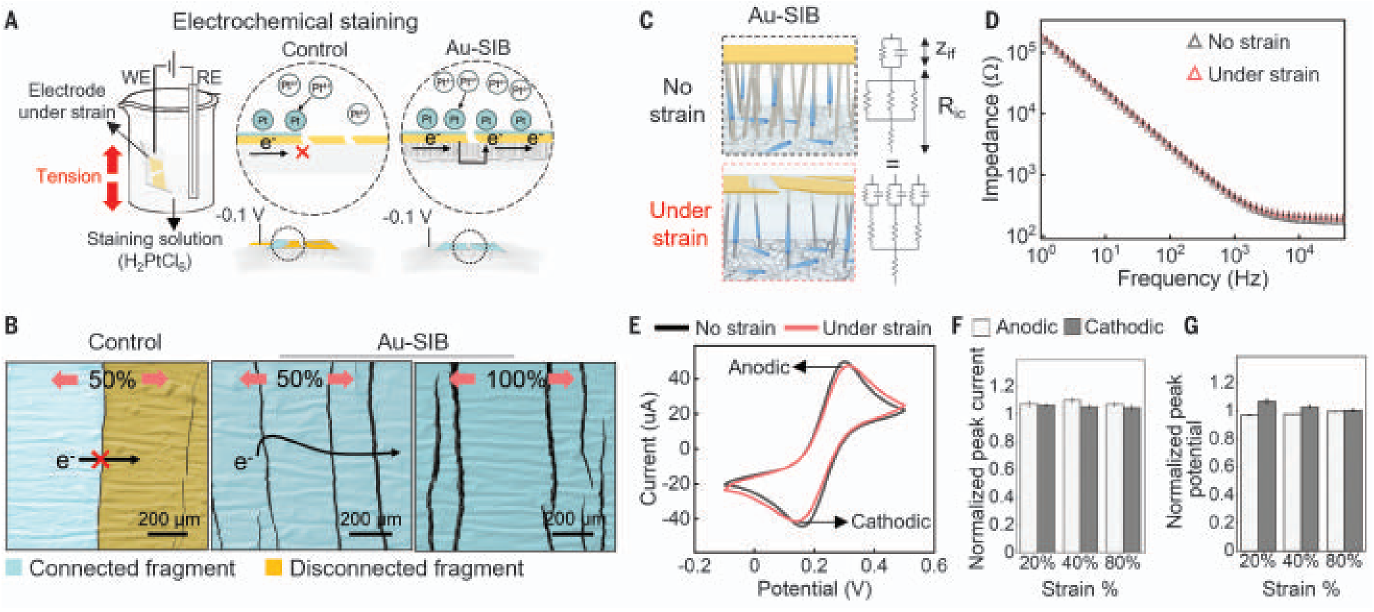

Fig. 2. Visualization and electrochemical characterization of Au-SIB performance under strain. (**A**) Schematic of the introduced electrochemical staining method. (**B**) Colored SEM images of the electrochemically stained control (Au, ACF, and PUA) electrode and Au-SIB under strain. They illustrate the electrical disconnection of a cracked fragment in the control electrode, whereas the Au-SIB's cracked fragments remained electrically connected. (**C**) Corresponding Randles model schematics of unstrained and strained or cracked SIBs. Interconnect resistance: R_{ic}. Interfacial impedance: Z_{if}. The SIB design enables the formation of parallel pathways for electron transfer and transport and maintenance of the active surface area under strain. (**D**) EIS comparison of Au-SIBs: unstrained versus 100% tensile-strained ($n = 3$ measurements by the same device for each strain condition). $P = 0.12$ comparing strained and unstrained measurement groups. Error bars indicate SEM. (**E**) CV comparison of Au-SIBs: unstrained versus 100% tensile-strained (in $K_3Fe(CN)_6$ solution). (**F** and **G**) The anodic and cathodic peak positions (F) and heights (G) of Au-SIBs under 20% through 80% strain (normalized to unstrained values; N = 3; p values 0.053 to 0.745; error bars indicate SEM).

("stained" regions) of the test electrodes exhibit a substantial imaging contrast under scanning electron microscopy (SEM) as compared with the nondeposited regions (fig. S4). As illustrated in Fig. 2B, the cracked fragments of a representative Au-SIB were fully "stained," indicating the preservation of their conductivity under varying large strain levels, in contrast to that of a control Au-elastomer electrode.

We characterized the cracked fragments by means of SEM imaging and analyzed the results with the aid of a dedicated statistical model (supplementary text S1). The results indicate that >99% of the brittle interfacial layer's surface area remains connected (fig. S5). Our cyclic stretching studies also demonstrate that the Au-SIB's crack density does not increase, despite repeated stretching (>10,000 cycles at 20% strain) (fig. S6A), and that the device's low resistance is minimally impacted during dynamic stretching (~2 ohm variation) (fig. S6B and C).

EIS and CV characterization results indicate that the changes to the SIB system's underlying electrochemical and electrical components (modeled in Fig. 2C) are negligible under strain. The impedance spectrum of representative 100% strained SIBs exhibited statistically identical curves in impedance magnitude (1 Hz to 100 kHz), as compared with their unstrained states (Fig. 2D and fig. S7). The SIB's electrochemical impedance has minimal change after 1000 cycles of tension (fig. S8). Furthermore, the CV plots of the unstrained and strained SIBs exhibit nearly identical features across 20 to 100% strain (Fig. 2, E to G). Without strain accommodation, tissue-induced strain causes a substantial increase in the interconnect resistance to the point of open circuit, which corrupts the electrode's electrical and electrochemical characteristics that manifest as as shifting and distortion of the EIS and CV curves, respectively (fig. S9).

Compared with bare AgNW-PUA, Au-SIB is more electrochemically stable (fig. S10). The underlying AgNW-PUA layer of the SIB does not experience galvanic corrosion in the presence of cracking. This contrasts with the case of Au-deposited AgNW-PUA electrodes, which galvanically corrode because of the crack-induced exposure of the AgNWs (fig. S11). The SIB's corrosion resistance indicates the protective role of the hydrophobic ACF in the prevention of AgNW oxidation and the release of cytotoxic Ag ions (useful for prolonged and biocompatible in vivo operations).

A diverse library of interfacial materials beyond Au can be simply incorporated into the SIB structure with standard thin film deposition techniques and paired with different application-specific electrochemical probing methods that involve wide ranging voltage and frequency conditions (Fig. 3A). We deposited Pt, carbon, and IrOx onto ACF as examples of commonly used brittle interfacial materials, leading to a series of SIBs with strain-insensitive interfacial electrochemical reaction features (validated with CV characterization) Fig. 3B). We applied these electrodes (exhibiting minimal device-to-device variation) (fig. S12) under large strain to carry out amperometry, voltammetry, and potentiometry, representing distinct electron transfer processes [Fig. 3, C (i, ii), D (i, ii), and E (i, ii)].

The choice of Pt as an interfacial material was motivated by its common use as a hydrogen peroxide (H_2O_2)–sensing layer in oxidase-based enzymatic biosensors. As shown in Fig. 3C, and figs. S13A and S14A, the corresponding amperometric responses of the Pt-SIB at its relaxed and tensile states were similar for different concentrations of H_2O_2. These results indicate that the faradaic current was minimally affected by the strain despite the occurrence of the cracks. We also observed strain-insensitive H_2O_2-sensing when using Au as an interfacial material (fig. S15).

The choice of carbon as an interfacial material was motivated by its common use in the quantification of low-concentration electroactive biomarkers. We investigated the effect of strain on the response of the carbon-SIB electrodes in the context of differential pulse

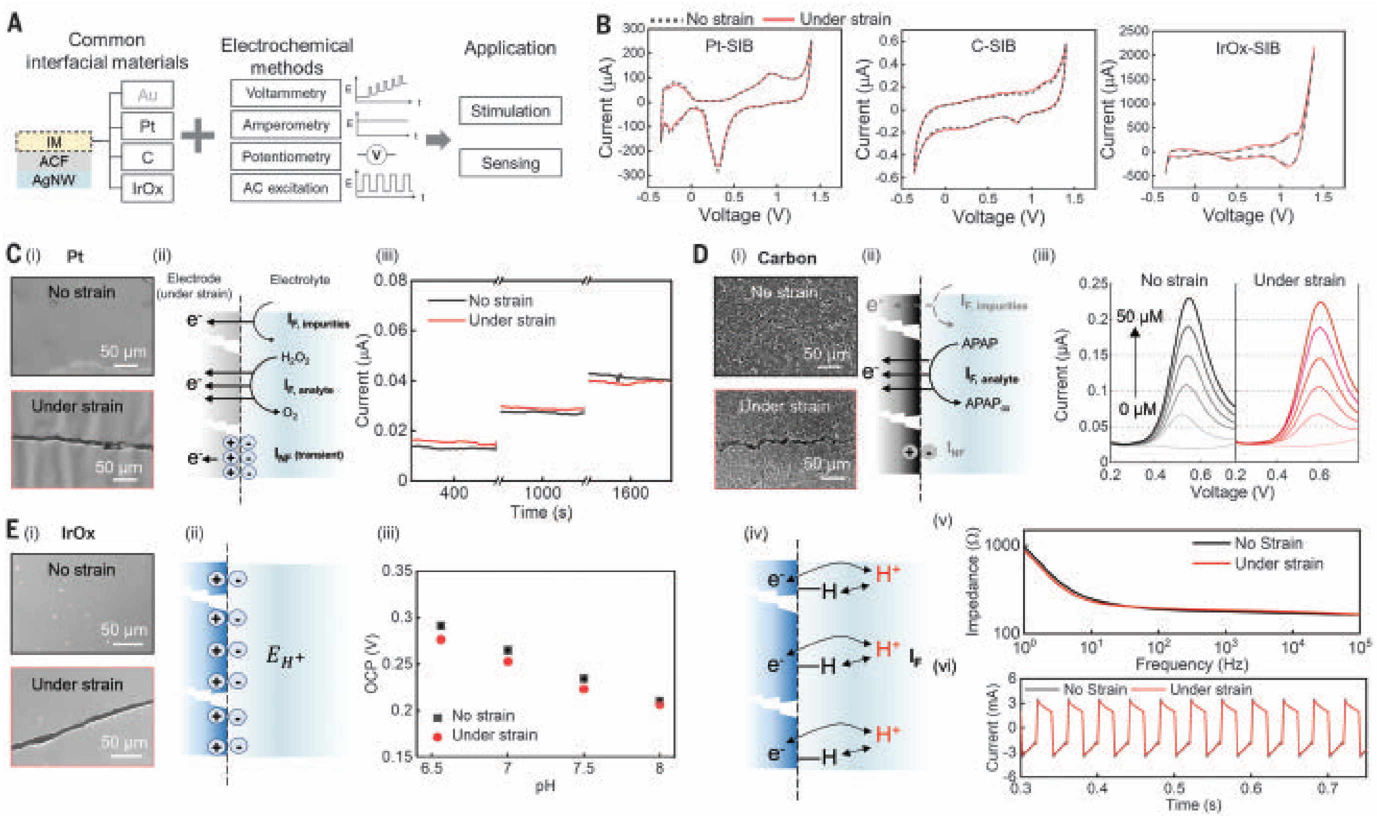

Fig. 3. A library of SIBs featuring brittle interfacial materials for electrochemical sensing and stimulation. (**A**) Pairing of SIBs with different electrochemical probing methods for diverse applications. IM represents the interfacial material layer. (**B**) CV characteristics of Pt-SIB, Carbon-SIB, and IrOx-SIB at 40% tensile strain versus unstrained state. (**C**) Pt-SIB characterization: (i) SEM images of the unstrained and 40% strained Pt-SIBs, (ii) schematic of the amperometric H_2O_2 sensing process, and (iii) Pt-SIB's H_2O_2 responses (0, 50, and 100 μM) at 40% tensile strain versus unstrained. (**D**) Carbon-SIB characterization: (i) SEM images of the unstrained and 100% strained carbon-SIBs, (ii) schematic of the DPV acetaminophen (APAP) sensing process, and (iii) carbon-SIB's APAP responses at 100% tensile strain versus unstrained. (**E**) IrOx-SIB characterization: (i) SEM images of the unstrained and 40% strained IrOx-SIBs, (ii) schematic of the pH sensing process, (iii) IrOx-SIB's pH open circuit potential (OCP) responses at 40% tensile strain versus unstrained, (iv) schematic of the faradaic process for neurostimulation, and (v, vi) corresponding EIS and ex vivo neurostimulation characterization of the IrOx-SIBs at 40% tensile strain versus unstrained.

voltammetry (DPV) for the detection of acetaminophen. As shown in Fig. 3D (iii) and fig. S13B, the corresponding DPV peak current measured by the electrode at its relaxed versus tensile states were similar for different concentrations of acetaminophen. The strain-induced shift in reduction-oxidation (redox) potential was minimal (~0.1 V).

The choice of IrOx as an interfacial material was motivated by its substantial yet unrealized full potential in bioelectronics. IrOx is not only biocompatible but also facilitates fast and reversible redox reactions with surrounding hydrogen ions (*14*), enabling large and reversible current injection. The latter point in particular supports IrOx's superiority over noble metals such as Au and Pt for tissue bioelectronics applications such as pH sensing and neural stimulation. However, because of its intrinsic brittleness, IrOx cannot be easily engineered as an inherently stretchable electrode. Our fabrication strategy enabled simple engineering of IrOx-SIBs where the tight bonding of the IrOx film (supporting electron transfer) to the underlying layer (supporting electron transport) ensured robust device operation despite IrOx's brittleness. The fabricated IrOx-SIB possesses a charge storage capacity of ~12 mC/cm^2 (fig. S16), which is similar to the charge storage capacity of standard clinical stimulation electrodes (*15*).

We investigated the IrOx-SIB for potentiometric pH sensing [Fig. 3E (ii)] and AC excitation in the form of biphasic pulses, for neurostimulation [Fig. 3E (iv)]. The open-circuit potential measurements indicate that the IrOx-SIB responses are correlated with the tested solution's pH levels, and that the electrode responses remain unperturbed under both static and dynamic tensile states [Fig. 3E (iii) and fig. S13C and fig. S14B]. As plotted in Fig. 3E (v) and fig. S17, the EIS measurements performed with our unstrained versus 40% strained IrOx-SIBs were similar, illustrating its strain insensitivity over a wide frequency range and informing its utility for both low- and high-frequency stimulation settings such as neuromodulation. Our studies in ex vivo neurostimulation characterization demonstrate the SIB's robustness in delivering stable current under both static and dynamic tensile conditions [Fig. 3E (vi) and fig. S14C].

As summarized in Fig. 4A, the IrOX-SIB presents electrochemical and electrical properties nearly identical to those of clinically used rigid cuff electrodes, while exhibiting tissue-like mechanical properties. The neural tissue–like mechanical characteristic of IrOx-SIB is advantageous over existing implantable electrodes that use rigid materials for neuromodulation because it potentially minimizes scar formation and immune response while rendering efficient stimulation even under deformation (*1*). To evaluate the performance of IrOx-SIBs during in vivo stimulation, we interfaced these bioelectrodes with the sciatic nerve to modulate the bidirectional and interconnecting spinal cord and muscles within the neural circuit (Fig. 4B). Accordingly, after validating its biocompatibility through cellular viability studies (fig. S18), the IrOx-SIB was applied in living mouse studies to deliver

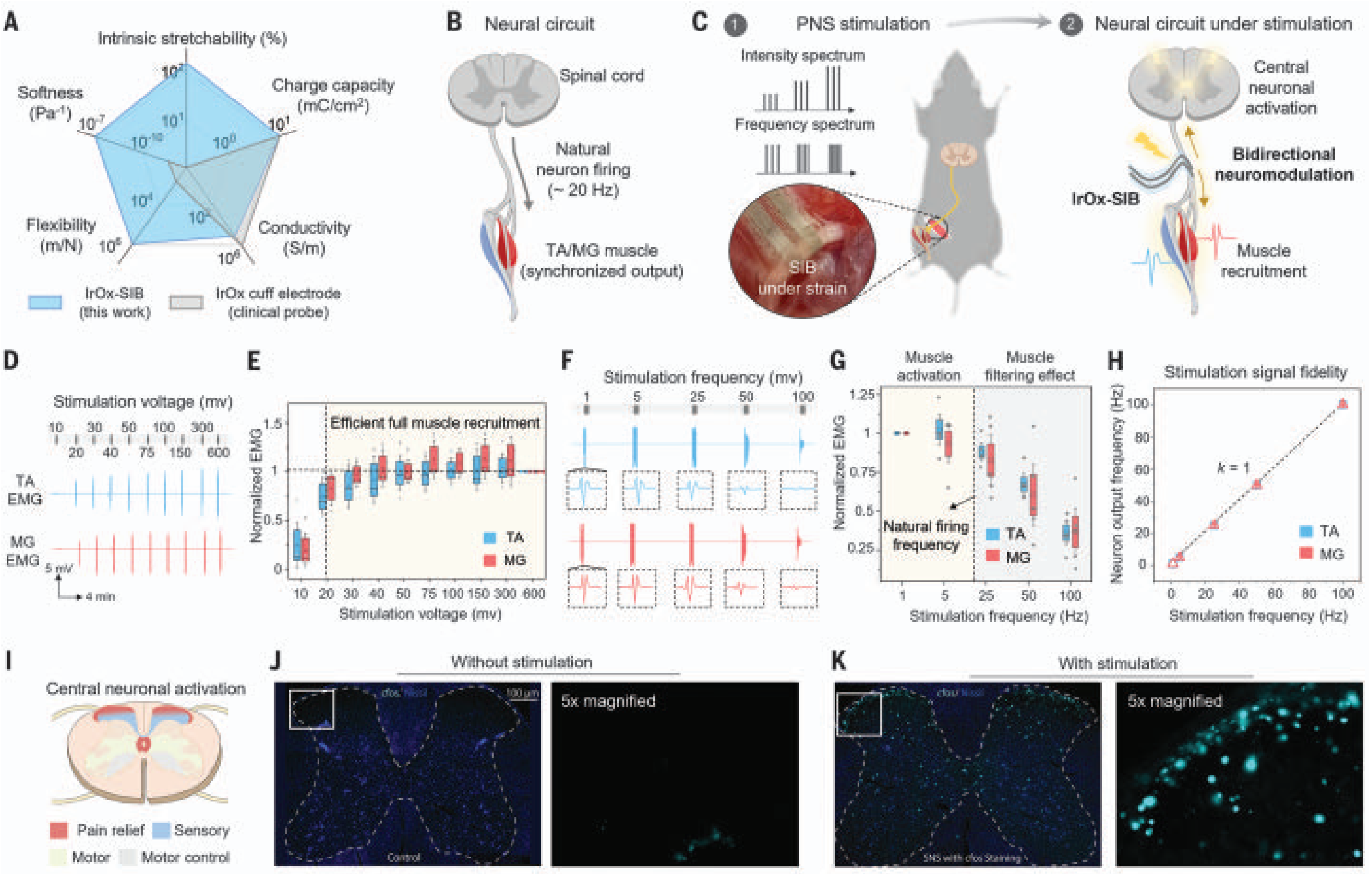

Fig. 4. In vivo neuromodulation through stimulation of the sciatic nerve by IrOx-SIB under deformation. (**A**) Radar chart of electrochemical, electrical, and mechanical properties of IrOx-SIB versus a standard IrOx cuff electrode. (**B**) Illustration of the neural circuit of a mouse. (**C**) In vivo evaluation of IrOx-SIB neuromodulation performance in an established neural circuit model. PNS responses were monitored through TA and MG recordings and CNS neuromodulation was evaluated through c-Fos staining of the lumbar spinal cord. (**D** to **G**) Sciatic nerve stimulation with different stimulation voltages at 1 Hz [(D) and (E)] and frequencies at 100 mV [(F) and (G)], and the correspondingly induced TA and MG muscle EMG recordings [(D) and (F)] and their respective normalized amplitudes [(E) and (G)]. (**H**) Comparison of the frequency of TA and MG neural signal outputs captured in G versus the stimulation frequency. (**I**) Schematics of regions determined by their neural functions within the spinal cord. (**J** and **K**) c-Fos expression patterns within lumbar spinal cord with (K) and without (J) sciatic nerve stimulation. Whole spinal cord staining (c-Fos single channel) images and zoomed-in views of the selected regions are shown. Dark blue color represents nissil staining and cyan color represents c-Fos staining.

clinically relevant voltage and frequency stimulation conditions.

We concurrently recorded the real-time electromyography (EMG) of the bilateral anterior tibialis (TA) and medial gastral (MG) muscles innervated by the sciatic nerve (Fig. 4C). To validate CNS neuromodulation, the subsequently expressed c-Fos protein levels (induced through sciatic nerve stimulation) in the lumbar spinal cord were labeled with immunofluorescent staining (Fig. 4C). Sciatic nerve stimulation with increasing voltage levels (at 1 Hz of frequency) led to the increase and following saturation of the TA and MG EMG intensities (Fig. 4, D and E). This trend indicates an increase in the synchronized recruitment of the available motor units, up to the point of full recruitment, which is achieved at potential levels as low as ~20 mV, thus illustrating efficient recruitment (*8*). As shown in Fig. 4, F and G, our studies involving sciatic nerve stimulation with excitation frequencies spanning from 1 to 100 Hz (at 100 mV) revealed the low-pass filtering characteristic (with cut-off frequency at ~20 Hz) of the muscle contraction (*16*). Despite being strained, our device induced TA and MG EMG with similar levels of signal-to-noise ratio (SNR; ~30 dB) as those produced by conventional electrodes (~10 to 38 dB at ~1 Hz) in unstrained settings (*17*, *18*).

As shown in fig. 4H, there is a one-to-one ratio between the applied stimulation frequencies and the recorded TA and MG muscle contraction frequencies. These results demonstrate the fidelity of the neural stimulation and the robustness of the strained SIB in supporting undistorted electron transfer and transport processes. From the standpoint of CNS neuromodulation (Fig. 4I), the c-Fos proteins are observably expressed in response to the sciatic nerve stimulation (Fig. 4K) (nonstimulated control shown in Fig. 4J). Furthermore, our staining results indicate the spatial concentration of the c-Fos expression in the dorsal horn of the spinal cord, which is related to the neural processing of sensory information such as pain.

We harnessed the superior electrochemical stability of diverse interfacial materials and the electrical conductivity of silver nanowire without being restricted by their inherent limitations in stretchable bioelectronic settings (interfacial materials' crack onset strain and silver nanowire's electrochemical instability). These materials were combined through the use of a strain-insensitive and anisotropic ultraconductive film. We simultaneously achieved strain insensitivity, high conductivity, and electrochemical stability with a diverse array of interfacial materials. On a broader level, by unlocking mechanical constraints, the design principle allows for the integration of materials in ways that may harness their superior properties in different domains. This allows for the attainment of maximum achievable performance offered across constituent materials.

REFERENCES AND NOTES

1. R. Feiner, T. Dvir, *Nat. Rev. Mater.* **3**, 17076 (2018).
2. S. P. Lacour, G. Courtine, J. Guck, *Nat. Rev. Mater.* **1**, 16063 (2016).
3. H. Yuk, B. Lu, X. Zhao, *Chem. Soc. Rev.* **48**, 1642–1667 (2019).
4. Y. Wang *et al.*, *ACS Nano* **12**, 9742–9749 (2018).
5. S. Choi *et al.*, *Nat. Nanotechnol.* **13**, 1048–1056 (2018).
6. Q. Zhai *et al.*, *Anal. Chem.* **90**, 13498–13505 (2018).
7. Y. Liu *et al.*, *Nat. Biomed. Eng.* **3**, 58–68 (2019).
8. J. Zhang *et al.*, *Nano Lett.* **18**, 2903–2911 (2018).
9. H. Lee *et al.*, *ACS Appl. Mater. Interfaces* **8**, 15449–15458 (2016).
10. F. Decataldo *et al.*, *Sci. Rep.* **9**, 10598 (2019).
11. J. Liang, L. Li, X. Niu, Z. Yu, Q. Pei, *Nat. Photonics* **7**, 817–824 (2013).
12. J. Deng *et al.*, *Nat. Mater.* **20**, 229–236 (2021).
13. I. R. Minev *et al.*, *Science* **347**, 159–163 (2015).
14. C. Boehler, S. Carli, L. Fadiga, T. Stieglitz, M. Asplund, *Nat. Protoc.* **15**, 3557–3578 (2020).
15. S. J. Wilks, S. M. Richardson-Burns, J. L. Hendricks, D. C. Martin, K. J. Otto, *Front. Neuroeng.* **2**, 7 (2009).
16. H. J. Freund, *Physiol. Rev.* **63**, 387–436 (1983).
17. S. Kim *et al.*, *ACS Appl. Mater. Interfaces* **10**, 33032–33042 (2018).
18. P. Sabetian, "Improved Peripheral Nerve Recording with a Small Form-factor Nerve Electrode; A Novel Bipolar Nerve Cuff Design," University of Toronto, Toronto, ON (2015).

ACKNOWLEDGMENTS

The authors appreciate the members of the UCLA nanoelectronics research facility (NRF) for their help in microfabrication/characterization. The authors extend their gratitude to L. Jin as well as to H. Lin, X. Cheng, H. Hojaiji and W. Yu for providing feedback on the presented work and insightful discussions. The authors also thank K. Sabet for statistical analysis; W. Yan for mechanical testing; and A. Vo, J. Park, and Y. Jinka for their assistance with device fabrication and BioRender.com for figures creation. **Funding:** This work was supported by National Science Foundation (CAREER Award 1847729) (S.E.); Startup package provided by the UCLA Henry Samueli School of Engineering and Applied Sciences (S.E.); National Institutes of Health (NIH) R21 DK128711-01 (S.E.); Innovation Award from the Broad Stem Cell Center (H.C.); NIH 1 R01 CA221296-01A1 (H.C.); NIH 1 R01 AR070245 (H.C.); DARPA HR0011-19-C-0043 (Q.P.); UCLA ECE Departmental Fellowship (Y.Z.). **Author contributions:** Conceptualization: Y.Z., B.W., and S.E. Methodology: Y.Z., B.W., J.T., H.Y., R.H., B.M.W., H.C., D.L., Q.P., and S.E. Investigation: Y.Z., B.W., J.T., H.Y., R.H., J.Z., S.L., Y.Z., D.J., Z.S., K.Y., L.V., A.H., K.Z., H.C., D.L., Q.P., and S.E. Visualization: Y.Z., B.W., J.T., R.H., J.Z., and S.L. Funding acquisition: H.C., D.L., Q.P., and S.E. Project administration: Y.Z. and B.W. Supervision: H.C., D.L., Q.P., and S.E. Writing – original draft: Y.Z., B.W., J.T., R.H., H.C., Q.P., and S.E. Writing – review and editing: Y.Z., B.W., J.T., H.Y., R.H., H.C., Q.P., and S.E. **Competing interests:** S.E., Y.Z., B.W., Q.P., E.A., and Y.S. are applying for patents related to the described work. **Data and materials availability:** All data are available in the main text or the supplementary materials. **License information:**

SUPPLEMENTARY MATERIALS

science.org/doi/10.1126/science.abn5142
Materials and Methods
Supplementary Text
Figs. S1 to S18
Table S1
References (*19–30*)

Submitted 31 December 2021; accepted 21 October 2022
10.1126/science.abn5142

SYNTHETIC BIOLOGY

Multidimensional control of therapeutic human cell function with synthetic gene circuits

Hui-Shan Li[1,2]†, Divya V. Israni[1,2]†, Keith A. Gagnon[1,2], Kok Ann Gan[1,3], Michael H. Raymond[1,2], Jeffry D. Sander[4,5,6], Kole T. Roybal[7,8,9,10], J. Keith Joung[4,5], Wilson W. Wong[1,2], Ahmad S. Khalil[1,2,3,11]*

Synthetic gene circuits that precisely control human cell function could expand the capabilities of gene- and cell-based therapies. However, platforms for developing circuits in primary human cells that drive robust functional changes in vivo and have compositions suitable for clinical use are lacking. Here, we developed synthetic zinc finger transcription regulators (synZiFTRs), which are compact and based largely on human-derived proteins. As a proof of principle, we engineered gene switches and circuits that allow precise, user-defined control over therapeutically relevant genes in primary T cells using orthogonal, US Food and Drug Administration–approved small-molecule inducers. Our circuits can instruct T cells to sequentially activate multiple cellular programs such as proliferation and antitumor activity to drive synergistic therapeutic responses. This platform should accelerate the development and clinical translation of synthetic gene circuits in diverse human cell types and contexts.

Cells use networks of interacting molecules to integrate and process signals into appropriate output responses. Synthetic biology aims to manipulate this process and drive the development of new biomedical technologies and therapies (*1–3*). For example, programming human cells with synthetic circuits that allow them to execute desired cellular functions in response to defined stimuli could enable new capabilities for gene- and cell-based therapies. One prominent example is chimeric antigen receptor (CAR) T cell immunotherapy, in which patient-derived T cells are redirected to attack tumors by genetically modifying them to express artificial antigen-targeting receptors. CAR-T cell therapy has shown clinical promise in treating certain cancers, leading to several approved cancer therapies (*4*). However, engineered T cells also display adverse, sometimes fatal side effects stemming from off-target toxicity and overactivation (*4–6*). Moreover, CAR-T cells have substantially limited clinical efficacy for most solid tumors (*7*), and the corresponding push to create more potent therapies has simultaneously heightened the risk of severe adverse side effects (*8*, *9*).

The challenge of balancing efficacy and toxicity to realize the full potential of these emerging therapeutic modalities has motivated recent efforts in mammalian synthetic biology aimed at developing methods for precise, temporal, and context-specific control of therapeutic cellular activity (*10–14*). Unfortunately, developing even simple synthetic circuits in primary human cells is challenging, particularly circuits capable of the strong outputs necessary to drive functional changes in vivo. Those that do exist harbor molecular components or formulations that are not suitable for clinical use. Therefore, existing methods are unlikely to scale to allow control over the different aspects of cell behavior such as localization, antitumor activity, and persistence, which collectively influence and dictate therapeutic outcomes (*15–20*). Overall, we lack versatile, scalable, and clinically viable gene circuit engineering platforms with which to reliably engineer relevant human cell types to address therapeutic challenges.

An established method for controlling mammalian cell behavior is by engineering transcriptional regulation. Efforts to control gene expression have primarily focused on a widely used set of artificial transcriptional regulators derived from microbial transcription factors (e.g., TetR and Gal4) and viral activators (e.g., VP16 and VP64) that exhibit robust functionality across many cell types and, in the case of TetR-based systems, are induced by a small-molecule antibiotic (*21*, *22*). However, there are not many of these regulators, thus restricting the number of genes that can be controlled in a circuit. They are also challenging to reprogram for new regulatory relationships, and

---

[1] Biological Design Center, Boston University, Boston, MA, USA. [2] Department of Biomedical Engineering, Boston University, Boston, MA, USA. [3] Program in Molecular Biology, Cell Biology, and Biochemistry, Boston University, Boston, MA, USA. [4] Molecular Pathology Unit, Center for Cancer Research, and Center for Computational and Integrative Biology, Massachusetts General Hospital, Boston, MA, USA. [5] Department of Pathology, Harvard Medical School, Boston, MA, USA. [6] Department of Genomics Technologies, Corteva Agriscience, Johnston, IA, USA. [7] Cell Design Institute and Department of Microbiology and Immunology, University of California, San Francisco, San Francisco, CA, USA. [8] Parker Institute for Cancer Immunotherapy, University of California, San Francisco, San Francisco, CA, USA. [9] Helen Diller Family Comprehensive Cancer Center, University of California, San Francisco, San Francisco, CA, USA. [10] Chan Zuckerberg Biohub, San Francisco, CA, USA. [11] Wyss Institute for Biologically Inspired Engineering, Harvard University, Boston, MA, USA.
***Corresponding author. Email: khalil@bu.edu (A.S.K.)**
†These authors contributed equally to this work.

their nonmammalian origins and chemical inducers present clinical hurdles for therapies that depend on persistent expression (*23*, *24*). Programmable DNA-targeting elements, such as the bacterial CRISPR-Cas9 system, have provided new methods for gene expression modulation and synthetic circuit design (*25*–*27*). However, the large size of Cas9 constrains what can be designed and delivered to primary human cells, and the high immunogenic potential of Cas9 is also well documented (*28*, *29*).

We outlined four basic properties for a toolkit that could support the rapid and scalable construction of gene expression circuits that are effective and potentially suitable for clinical use (Fig. 1A): (i) it should prioritize the use of human-derived proteins, when possible, to minimize immunogenic potential; (ii) it should be orthogonal to minimize cross-talk with native regulation; (iii) there should be safe regulation to ensure gene-regulatory activity that can be easily and safely controlled; and (iv) it should be compact, with minimized genetic footprints for efficient delivery into primary human cells and tissues. As a building block for our toolkit of synthetic regulators, we focused on Cys2His2 zinc fingers (ZFs), which balance clinical favorability and programmability. ZFs are small domains (~30 amino acids) that bind to ~3 base pairs (bp) of DNA (*30*). They are the most prevalent DNA binding domain found in human transcription factors (*31*), suggesting that they represent a flexible solution to DNA recognition with low immunogenicity potential. Indeed, a first-generation artificial ZF–based regulatory system showed multiyear functionality in nonhuman primates and had no apparent immunogenicity (*32*). Moreover, individual ZF domains can be reprogrammed to recognize new motifs and concatenated to generate proteins capable of specifically targeting longer DNA sequences (*33*–*36*). Although ZF engineering has been applied to generate endogenous genome editing and manipulation tools, we sought to create a collection of composable synthetic regulators with genome-orthogonal specificities.

We leveraged an archive of engineered two-finger (2F) units that explicitly account for context-dependent effects between adjacent fingers (*34*, *36*). By linking 2F units using flexible "disrupted" linkers (*37*), it is possible to construct functional 6F arrays capable of recognizing 18 bp, a length for which a random sequence has a high probability of being unique in the human genome (Fig. 1B and fig. S1B). We prioritized 6-bp subsites that are underrepresented in the human genome and selected arrays to minimize identity with the human genome. This yielded 11 targetable synthetic DNA binding motifs (DBMs) (Fig. 1C; fig. S1, C and D; and materials and methods). We next sought to engineer synthetic zinc finger transcription regulators (synZiFTRs) capable of strong

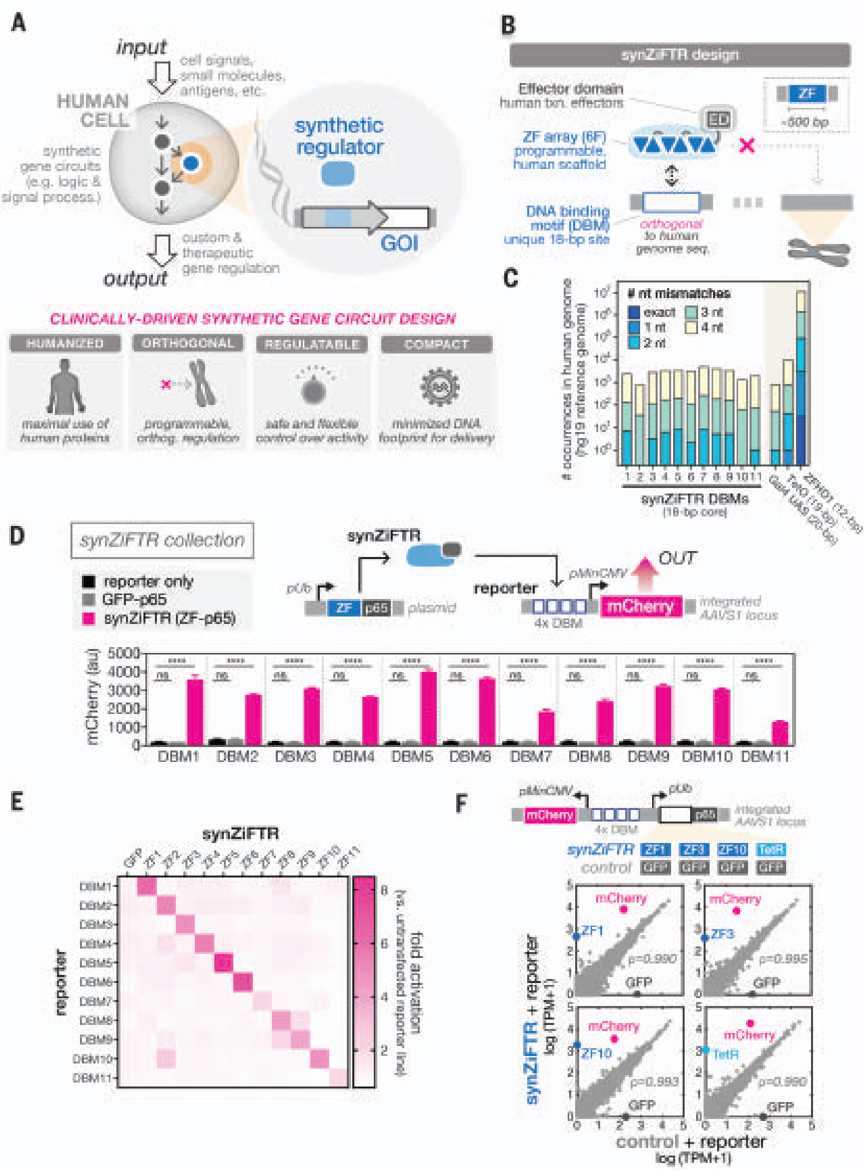

Fig. 1. Clinically driven design of compact, humanized, synthetic gene regulators (synZiFTRs) for mammalian cell engineering. (**A**) Top: Synthetic gene circuits are used to convert diverse input signals into the desired gene expression outputs to precisely control human cell function. Bottom: Criteria for clinically driven gene circuit design framework. (**B**) synZiFTR design. synZiFTRs have a modular design that is based on compact, human-derived protein domains. An engineered ZF array mediates interactions with a unique, human genome–orthogonal DBM, and human-derived effector domains (EDs) are used to modulate transcriptional activity. (**C**) Prevalence of synZiFTR recognition motifs in the human genome. Plotted are the occurences of exact and increasingly mismatched sequences for each synZiFTR DBM and response elements from common artificial regulators (Gal4 UAS, TetO, and ZFHD1). (**D**) synZiFTRs strongly activate gene expression at corresponding response promoters. Response element vectors were stably integrated into HEK293FT cells to generate reporter lines for each synZiFTR (ZF-p65 fusion). synZiFTR (or control) expression vectors were transfected into corresponding reporter lines, and mCherry was measured by flow cytometry after 2 days. Bars represent mean values for three measurements ± SD. Statistics represent one-way ANOVA with Dunnett's multiple comparisons; ns, not significant; $****P < 0.0001$. pUb, ubiquitin C promoter; pMinCMV, minimal CMV promoter; p65, amino acids 361 to 551. (**E**) synZiFTRs have mutually orthogonal regulatory specificities. Each synZiFTR expression vector was transfected into every reporter line, and mCherry was measured by flow cytometry after 2 days. Fold activation levels represent mean values for three biological replicates. (**F**) synZiFTRs exhibit specific and orthogonal transcriptional regulation profiles in human cells. Shown is the correlation of transcriptomes from RNA-sequencing measurements of HEK293FT cells stably expressing synZiFTR or TetR-p65 versus a GFP-p65 control. Points represent individual transcript levels normalized to transcripts per kilobase million (TPM), averaged between two technical replicates. The Pearson correlation coefficient was calculated for native (gray) transcripts. See fig. S3 for extended analyses.

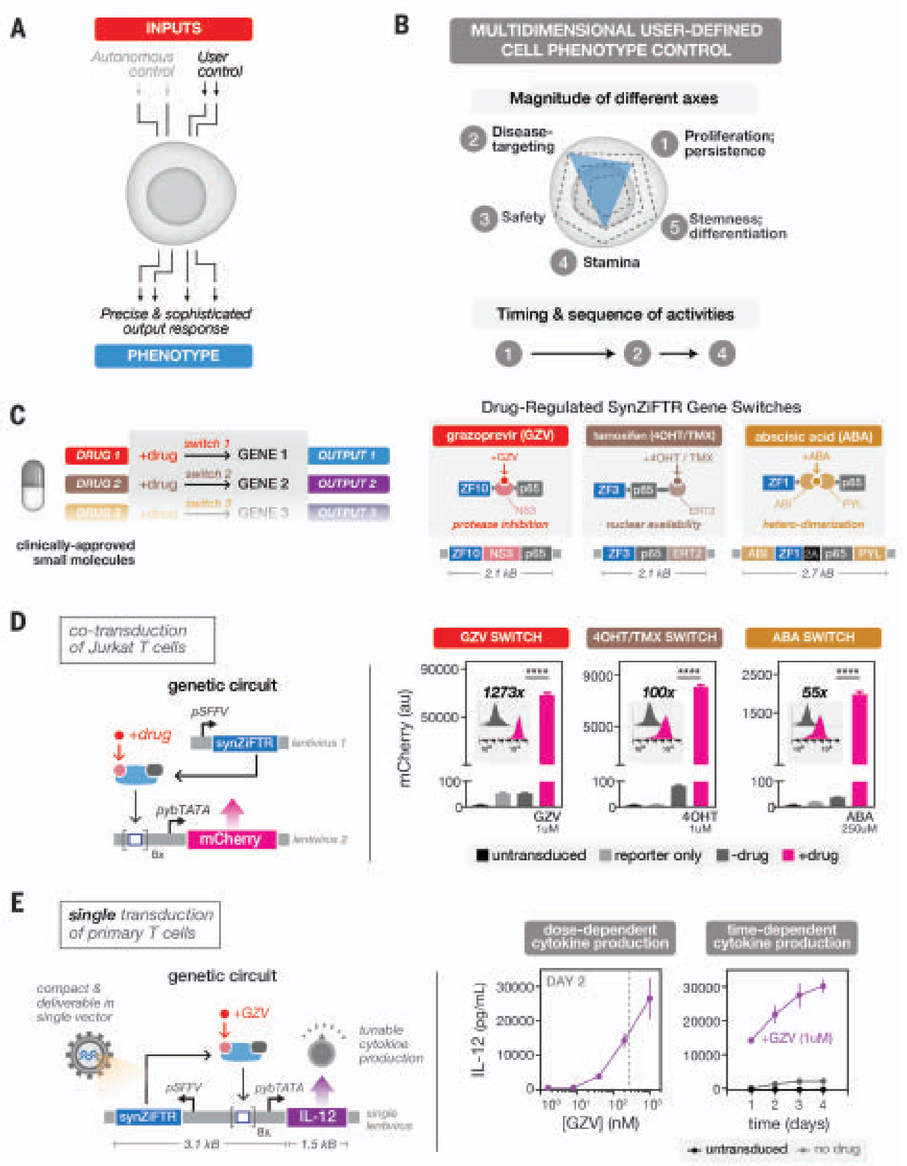

Fig. 2. synZiFTR gene switches allow precise, user-defined control over gene expression in human cells using clinically approved small molecules. (**A**) Two forms of cellular control: Circuits can be designed to enact cell-autonomous phenotype control (e.g., through recognition of disease-relevant cell surface molecules) or external, user-defined phenotype control (e.g., through administration of small molecules). (**B**) User-defined control over different axes of a cellular phenotype (top) and the chronology of cellular activities (bottom). (**C**) Implementing multigene user control with orthogonal gene switches that are regulated by clinically viable small molecules (right). Shown is the design of three distinct synZiFTR gene switches that are controlled by orthogonal small molecules: GZV, 4OHT/TMX, and ABA (right). NS3, hepatitis C virus NS3 protease domain; ERT2, human estrogen receptor T2 mutant domain; ABI, ABA-insensitive 1 domain (amino acids 126 to 423); PYL, PYR1-like 1 domain (amino acids 33 to 209). (**D**) Optimized synZiFTR switches enable strong inducible gene expression in Jurkat T cells. Jurkat T cells were cotransduced with reporter and synZiFTR expression lentiviral vectors in an equal ratio. mCherry fluorescence was measured by flow cytometry 4 days after induction by small molecules at the indicated concentrations. Bars represent mean values for three measurements ± SD. Statistics represent two-tailed Student's *t* test; $***P < 0.001$; $****P < 0.0001$. Histograms show absolute levels and mean fold activation for one representative measurement (insets). pSFFV, spleen focus-forming virus promoter; pybTATA, synthetic YB_TATA promoter. (**E**) Compact, single lentivirus–encoded synZiFTR switches enable titratable control over the expression of therapeutically relevant genes in primary human immune cells. Human primary T cells were transduced with a single lentiviral vector encoding GZV-regulated IL-12 (see the materials and methods). IL-12 production was measured by enzyme-linked immunosorbent assay (ELISA) at specified time points after induction (with or without 1 μM GZV). Points represent mean values for three measurements ± SD. Dashed line is the estimate of the C_{max} (maximum serum concentration) for traditional clinical dosing of GZV.

and specific regulation at these synthetic *cis* elements. We fused ZFs predicted to bind each DBM to the human p65 activation domain and screened for the most active candidates in human embryonic kidney 293FT (HEK293FT) reporter lines (fig. S2, A to C). Selected synZiFTRs strongly activated corresponding, but not noncognate, reporters (Fig. 1, D and E). To evaluate their impact on native regulation, we performed RNA-sequencing analysis on cell lines expressing three representative synZiFTRs, ZF1, ZF3, and ZF10, benchmarking these against a TetR-based activator. synZiFTR regulation profiles are highly specific, minimally affecting native transcript profiles, and compare favorably with the profile of TetR (Fig. 1F and fig. S3). These results establish a collection of compact, humanized, and genome-orthogonal synZiFTRs optimized for gene expression control and synthetic circuit design in human cells.

To achieve the goal of regulatable synZiFTR circuits, we considered methods for enacting gene regulation control in response to defined input stimuli (Fig. 2A). We focused our attention on user-defined regulation, which in principle allows total control over the timing, level, and context over which a therapeutic gene is expressed. Moreover, regulated circuits with user-defined control over multiple genes could be used to instruct engineered cells to dynamically activate different complementary cellular programs to achieve optimal phenotypes (Fig. 2B). One promising approach for user-defined control is using small molecules, which can be administered systemically or locally to switch ON a gene circuit and/or activate the production of a therapeutic gene product. We prioritized compounds that are already clinically approved or otherwise known to have favorable safety profiles. This resulted in three classes of small molecules that can regulate synZiFTR activity through distinct mechanisms, offering the potential for up to three orthogonal channels of gene expression control (Fig. 2C and fig. S4A). The first is grazoprevir (GZV), a US Food and Drug Administration (FDA)–approved antiviral drug from a family of protease-inhibiting compounds, which has an exceptional safety profile and is commonly taken at a high dose (100 mg/day) for up to 12 weeks (*38*). The addition of GZV stabilizes synZiFTRs incorporating the NS3 self-cleaving protease domain (from hepatitis C virus), driving gene transcription (*39*, *40*). The second compound is 4-hydroxytamoxifen/tamoxifen (4OHT/TMX), the FDA-approved and widely prescribed breast cancer drug that selectively modulates the nuclear availability of molecules fused to sensitized variants of the human estrogen receptor ERT2 (*41*, *42*). The third compound is abscisic acid (ABA), a plant hormone naturally present in many plant-based foods and classified as nontoxic to humans, which mediates conditional

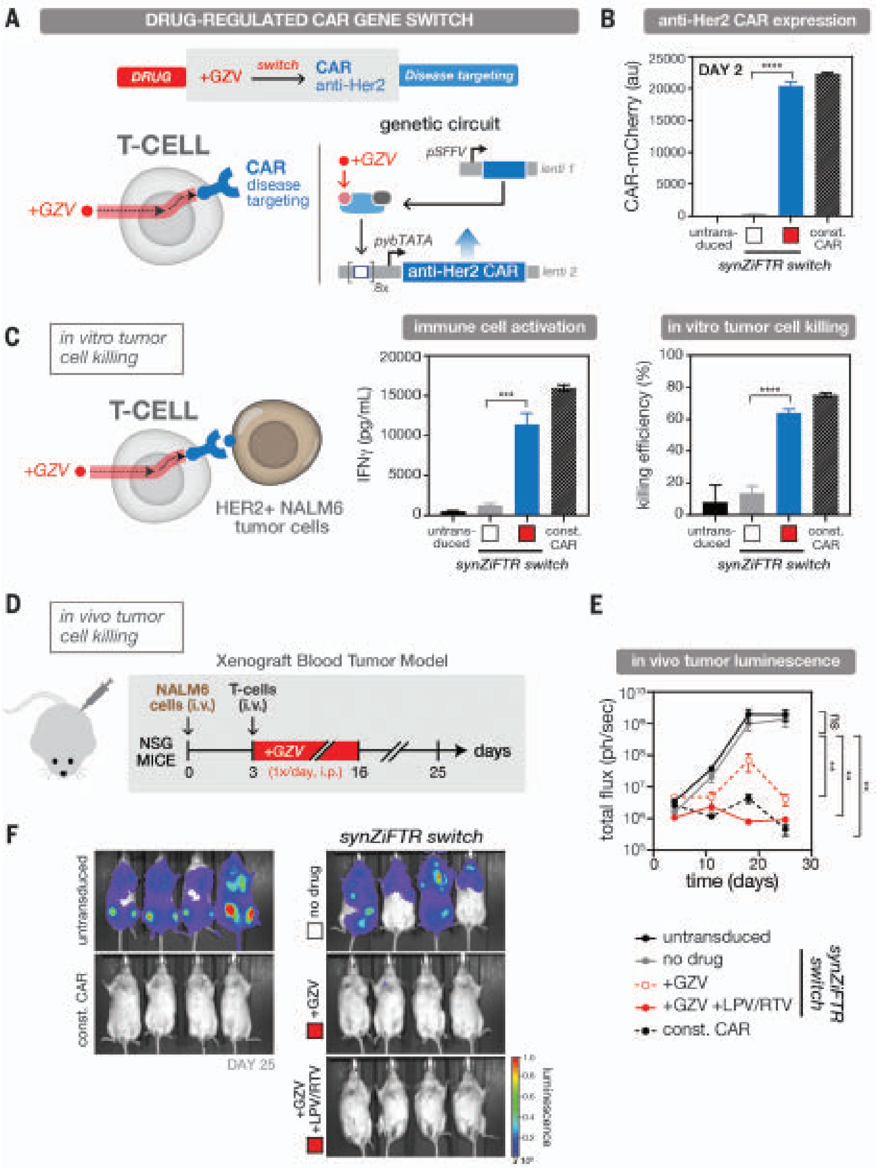

Fig. 3. synZiFTR gene circuit for drug-regulated postdelivery control over CAR expression and T cell killing in vivo. (**A**) Design of the synZiFTR gene circuit for GZV-dependent control over anti-Her2 CAR expression and tumor cell targeting and killing. (**B**) GZV-regulated CAR expression in primary T cells. Human primary T cells were cotransduced with equal ratios of lentiviral vectors encoding the synZiFTR CAR gene circuit (see the materials and methods). Expression of anti-Her2 CAR-mCherry was measured by flow cytometry 2 days after induction (with or without 1 μM GZV). White box, uninduced; red box, GZV induced. Const. CAR, constitutively expressed (pSFFV-CAR). Bars represent mean values for three measurements ± SD. Statistics represent two-tailed Student's *t* test; $^{***}P < 0.001$; $^{****}P < 0.0001$. (**C**) GZV-regulated immune cell activation and tumor cell killing in vitro. synZiFTR-controlled CAR T cells (preinduced with or without 1 μM GZV for 2 days) were cocultured with $HER2^{+}$ NALM6 target leukemia cells in a 1:1 ratio (left). Interferon-γ secretion from activated immune cells was measured by ELISA (center) and tumor cell killing by flow cytometry (right) 1 day after coculturing. White box, uninduced; red box, GZV induced. (**D**) Testing the in vivo efficacy of synZiFTR-regulated CAR T cells using a xenograft tumor mouse model. Shown is a timeline of an in vivo experiment in which NSG mice were injected intravenously with luciferase-labeled $HER2^{+}$ NALM6 cells to establish tumor xenografts, followed by treatment with T cells. GZV was formulated alone or in combination with LPV/RTV and administered intraperitoneally daily for 14 days. Mice were imaged weekly on days 4, 11, 18, and 25 to monitor tumor growth through luciferase activity. GZV was given at 25 mg/kg and LPV/RTV at 10 mg/kg. (**E**) Tumor burden over time, quantified as the total flux (photons/second) from the luciferase activity of each mouse using IVIS imaging. Points represent mean values ± SEM (*n* = 4 mice per condition). Statistics represent two-tailed, ratio-paired Student's *t* test; ns, not significant; $^{**}P < 0.01$. (**F**) IVIS imaging of mouse groups treated with untransduced cells, synZiFTR-regulated CAR T cells, synZiFTR-regulated CAR T cells with GZV, synZiFTR-regulated CAR T cells with GZV+LPV/RTV, or constitutive CAR cells (*n* = 4 mice per condition).

binding of complementary protein fragments (ABI and PYL) from the ABA stress response pathway to reconstitute an active synZiFTR (*43*). Note that there are trade-offs in priorities. For example, allowing the incorporation of minimal nonhuman-derived domains into the synZiFTR scaffold allows the use of drugs that minimally interfere with native cellular machinery (e.g., GZV) or of inexpensive nontoxic molecules (e.g., ABA).

We constructed GZV-, 4OHT/TMX-, and ABA-inducible gene switches using distinct ZFs (ZF1, ZF3, and ZF10) and tested their performance in Jurkat T cells (fig. S4, A and B). The three systems exhibited titratable control of reporter output, minimal leakage relative to reporter-only cells, strong dynamic ranges, and no cross-reactivity, and they returned to basal levels upon removal of inducer (fig. S4, C and D). Because of the orthogonality of the inducers and the modularity of the synZiFTR architecture, more elaborate gene switches can be readily designed for more complex forms of temporal control, including multiplexed ON/OFF switching (fig. S5).

To optimize synZiFTR circuit dynamics, we screened arrangements of DBM arrays and minimal promoters to identify combinations that reduced basal expression and improved dynamic range (*44*) (fig. S6A). This produced optimized designs for GZV-, 4OHT-, and ABA-inducible synZiFTR circuits that are encodable in either dual or single lentiviral vectors (Fig. 2D and fig. S6B) and can enable dose- and time-dependent control of therapeutically relevant payloads, such as the immunomodulatory factor interleukin-12 (IL-12), in therapeutically relevant primary human cells (Fig. 2E).

Do synZiFTR circuits enable in vivo, clinically relevant gene expression outputs? To investigate this, we turned to CAR T cell therapy as a proof of principle, initially choosing to develop a gene switch to control CAR expression and activate tumor-targeting functionality (Fig. 3A). This modality allows the rapid evaluation of whether small molecule–dependent synZiFTR activity is sufficient to elicit functional (i.e., disease-modifying) changes in vitro and in vivo, and recent work has established the value of controlling the timing of activation of CAR signaling for improved CAR T cell fitness and outcomes (*45*–*47*). We developed a GZV-regulated anti-Her2 CAR (Fig. 3A). Her2 is a receptor tyrosine kinase that is overexpressed in many tumors, including a small subset of leukemias (*48*). We previously demonstrated this anti-Her2 CAR in a xenograft liquid tumor model, thus providing a convenient platform with which to evaluate the efficacy of our synZiFTR circuits (*49*). Our gene switch exhibited GZV-dependent CAR expression in primary human T cells at levels comparable to that of a constitutively expressed CAR and

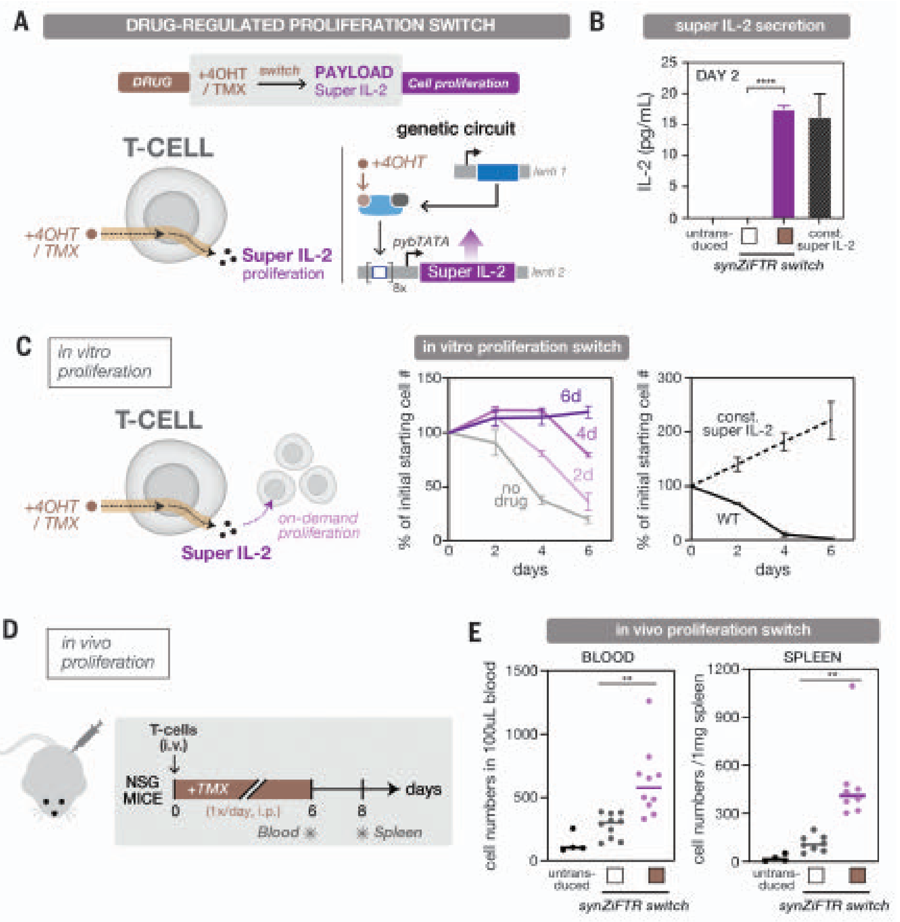

Fig. 4. synZiFTR gene circuit for drug-regulated, on-demand immune cell proliferation. (**A**) Design of the synZiFTR gene circuit for 4OHT/TMX-dependent control over super IL-2 expression and cell proliferation. (**B**) 4OHT-regulated super IL-2 production in primary T cells. Human primary T cells were cotransduced with equal ratios of lentiviral vectors encoding the synZiFTR-regulated proliferation gene circuit (see the materials and methods). Secretion of super IL-2 was measured by ELISA (for IL-2) 2 days after induction (with or without 1 μM 4OHT). White box, uninduced; brown box, 4OHT induced. Const. super IL-2, constitutively expressed (pSFFV-super IL-2). Bars represent mean values for three measurements ± SD. Statistics represent two-tailed Student's *t* test; $***P < 0.001$; $****P < 0.0001$. (**C**) 4OHT-regulated T cell proliferation in vitro. synZiFTR-regulated primary T cells were cultured in IL-2–free media, induced with 4OHT (1 μM) for different durations, and live-cell numbers were quantified by flow cytometry at the indicated days (center). Untransduced (wild-type) and constitutively expressing (const. super IL-2) T cells were cultured and quantified similarly (right). Lines represent mean values for three measurements ± SD. (**D**) Testing the in vivo efficacy of the drug-regulated, on-demand proliferation switch. Shown is a timeline of an in vivo experiment in which NSG mice were injected intravenously with primary T cells followed by daily treatment with TMX over 6 days. The blood and spleen were individually sampled on days 6 and 8, respectively, to quantify the change in T cell numbers. TMX was given at 75 mg/kg. (**E**) TMX-regulated T cell expansion in vivo. Human T cell numbers from blood and spleen samples were quantified by flow cytometry by gating for $hCD3^+/mCD45^-$ cells after staining for human CD3 (hCD3) and mouse CD45 (mCD45). Lines indicate the mean value; dots represent each mouse. Blood sample, $n = 10$; spleen sample, $n = 8$. White box, uninduced; brown box, TMX induced. Statistics represent two-tailed Student's *t* test; $**P < 0.01$.

with minimal output in the absence of inducer (Fig. 3B). When cocultured with Her2-overexpressing ($HER2^+$) NALM6 leukemia cells (fig. S7C), synZiFTR-regulated CAR cells were capable of drug-dependent activation and efficient tumor cell killing in vitro (Fig. 3C). These synZiFTR circuits are easily reconfigurable. By swapping the anti-Her2 CAR with an anti-CD19 CAR, we reproduced these in vitro results for a second CAR payload, demonstrating the generalizability of our platform (fig. S7).

Next, we tested the in vivo efficacy of synZiFTR-regulated CAR T cells using a simple xenograft blood tumor model (*49*) (Fig. 3D and materials and methods). Mice receiving synZiFTR-controlled CAR T cells were treated with GZV either alone or in combination with lopinavir/ritonavir (LPV/RTV), a cocktail known to increase drug bioavailability (*50*), and were able to clear the tumor. Conversely, those not treated with inducer developed high tumor burdens, as determined by IVIS imaging of luciferase-expressing $HER2^+$ tumors (Fig. 3, E and F, and fig. S8, A and B). Although both inducer conditions led to tumor eradication, clearance rates were faster with the cocktail, consistent with the constitutive CAR^+ control and with the ability of LPV/RTV to increase GZV bioavailability (Fig. 3E and fig. S8C). These results demonstrate that synZiFTR circuits can be used to program drug-dependent, post-delivery control over T cell antitumor activity in vivo.

In addition to controlling CAR-mediated tumor targeting, synZiFTRs are also suited to controlling the expression of other proteins such as IL-2 or IL-12, immunomodulatory cytokines that have long been considered to be potential anticancer agents because of their role in stimulating and regulating immune responses (*51*, *52*). Equipping engineered immune cells to produce cytokines is a compelling approach to improving their antitumor efficacy. However, high doses of IL-2 or IL-12 are known to cause severe side effects. Regulated expression represents a safer approach to leveraging the potential of these factors for augmenting immune cell efficacy. Moreover, as a T cell growth factor, user-regulated IL-2 production could serve as an exciting basis for achieving on-demand cellular proliferation.

To establish a proliferation gene switch, we used a TMX-inducible synZiFTR to regulate the expression of super IL-2, an enhanced version of IL-2 with stronger affinity to CD122 (*53*) (Fig. 4A). Our gene switch exhibited 4OHT/TMX–dependent super IL-2 production in vitro in primary T cells, once again to levels comparable to that of the constitutive control and with minimal output in the absence of inducer (Fig. 4B). Primary T cells require exogenous IL-2 to remain viable over long periods of time in culture, which provides a simple way to test the performance of the proliferation switch. We cultured equal numbers of engineered cells in media lacking IL-2 and induced them with 4OHT for different durations. Cells harboring the inducible super IL-2 switch exhibited duration-dependent proliferation (Fig. 4C). The synthetic system also exhibited dose-dependent control over super IL-2 production and cellular proliferation (fig. S9). Finally, to demonstrate the ability of the proliferation switch to control T cell growth in vivo, we injected engineered T cells into NSG mice intravenously and administered TMX

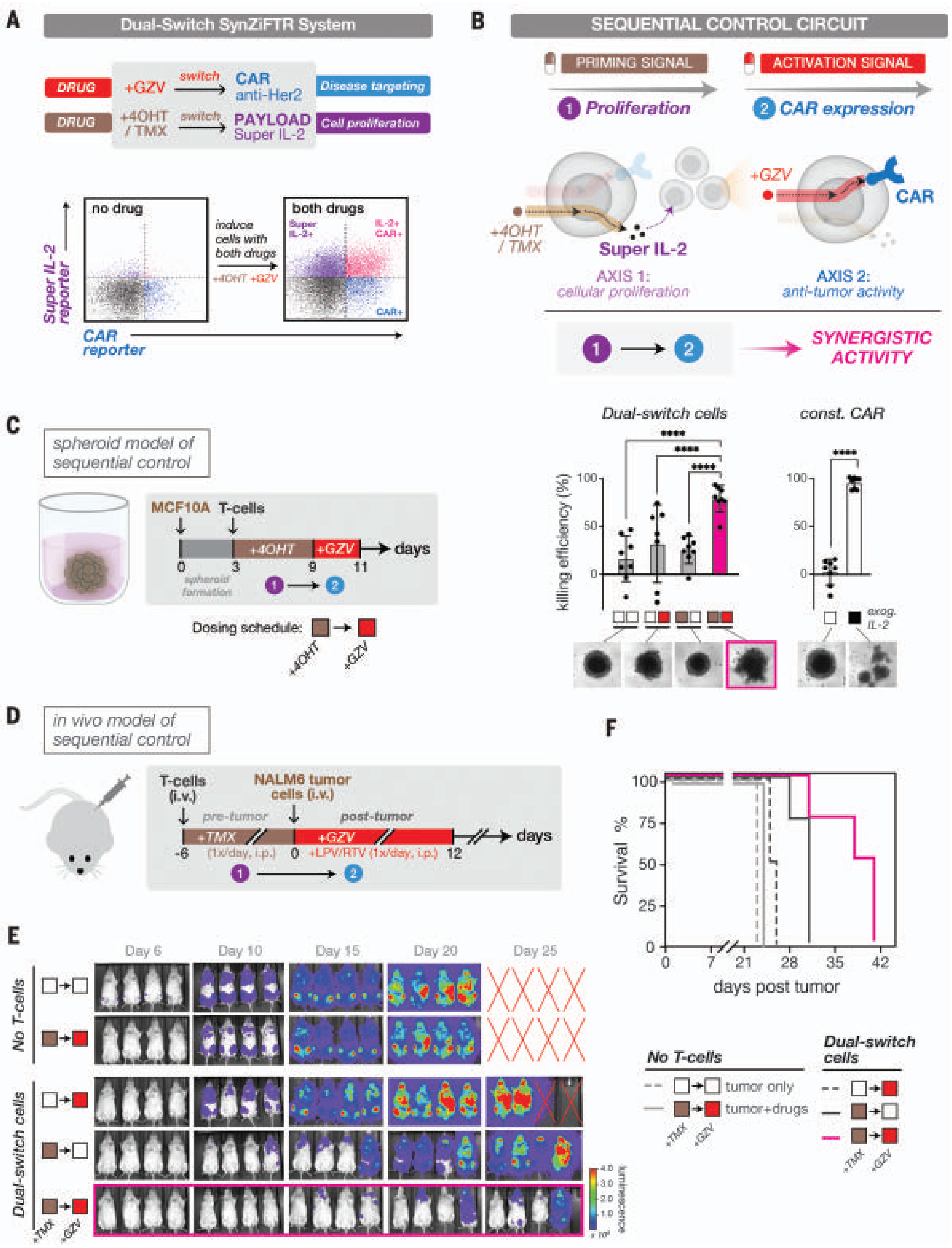

Fig. 5. Enacting sequential control of immune cell function to drive synergistic in vivo responses. (**A**) Dual-switch synZiFTR system for orthogonal, drug-inducible control over anti-Her2 CAR and super IL-2 expression (top). Circuit activation in primary T cells was assessed after induction with both drugs (1 μM GZV and 1 μM 4OHT) (bottom). Distinguishable reporters were used to measure gene activation for each channel with or without 1 day of induction: mCherry-fused anti-Her2 CAR and bicistronic super IL-2 reporter (super IL-2-2A-EGFP). See also fig. S10. (**B**) Schema for sequential control in which a priming signal (4OHT/TMX drug) was used to induce cellular proliferation of a small starting population of dual-switch cells through super IL-2 expression, followed by an activation signal (GZV) to induce cytotoxic activation through CAR expression. (**C**) In vitro spheroid model used to demonstrate the synergistic efficacy of sequential control over T cell proliferation (+4OHT) and activation (+GZV) behavior (left). T cell killing efficiency was measured by luminescence signals from spheroids, and representative morphology of spheroids at the end point is shown below (right). White box, uninduced; brown box, 4OHT induced; red box, GZV induced. Bars represent mean values ± SD. Const. CAR, constitutive CAR cells. (**D**) An in vivo model used to demonstrate the synergistic efficacy of sequential control over T cell proliferation (+TMX) and activation (+GZV) behavior. Shown is a timeline of an in vivo experiment in which NSG mice were injected intravenously with dual-switch T cells (1×10^6 cells) 6 days before the tumor challenge. TMX was administered intraperitoneally daily over 6 days to activate the proliferation switch before tumor challenge. $HER2^+$/$luciferase^+$ NALM6 cells (1×10^6 cells) were injected intravenously 6 days after injection of T cells, and the GZV-regulated CAR was switched ON by administering GZV in combination with LPV/RTV daily intraperitoneally over 12 days. TMX was given at 75 mg/kg, GZV at 25 mg/kg, and LPV/RTV at 10 mg/kg. (**E**) IVIS imaging of tumor burden over time of mouse groups treated with tumor alone (no T cells), tumor with both drugs in sequence (TMX → GZV), dual-switch T cells treated with GZV alone during the time window of day 0 → day 12 (∅ → GZV), dual-switch T cells treated with TMX alone during the time window of day 6 → day 0 (TMX → ∅), and dual-switch T cells treated with both drugs in sequence (TMX → GZV). (**F**) Kaplan-Meier survival curves for the various treatment groups for the in vivo sequential model study (*n* = 4 mice per condition). White box, uninduced; brown box, TMX induced; red box, GZV induced.

daily through intraperitoneal injection for 6 days. We observed enhanced T cell levels in the peripheral blood (day 6) and spleen (day 8) in mice receiving engineered T cells and exposed to TMX compared with mice receiving engineered T cells without TMX or untransduced cells only (Fig. 4, D and E). These results establish a synZiFTR gene switch for TMX-dependent control over super IL-2 production and in vivo, on-demand cell expansion.

The synZiFTR platform therefore enables the development of compact gene switches that are effective for dose- and time-dependent control of therapeutically relevant genes both in vitro and in vivo, setting the stage for genetic circuits that allow simultaneous and independent multigene control in the same cell. To investigate whether synZiFTRs can regulate two orthogonal gene programs, we transduced primary human T cells with vectors encoding GZV-regulated anti-Her2 CAR and TMX-regulated super IL-2 switches (Fig. 5A). Next, we induced cells with different combinations of the two drugs and used distinguishable reporters to measure gene activation for each channel. Engineered cells exhibited the desired orthogonal patterns of gene activation (fig. S10A). After induction with both drugs, >14% of cells simultaneously expressed high levels of both genes (Fig. 5A). Thus, our full dual-switch genetic circuit was delivered to a significant population of cells, and both switches were functional and orthogonal.

A capability afforded by dual-switch circuits is the possibility of enacting sequential control of cell function (Fig. 5B). Modulating cell functions on the basis of the timing and sequential order of signaling events is a critical regulatory mechanism in living systems (*54*, *55*), including in the immune system (*56*). Motivated by natural systems, engineered sequential control could dictate when and in what order distinct cellular programs are activated, potentially unlocking underexplored dimensions of cell therapy function. As a proof of principle, we envisioned a simple scenario in which a small starting population of engineered cells is first "primed" with one signal (4OHT/TMX, to drive cellular expansion and poise cells for activation) and subsequently "activated" by a second signal (GZV, to induce CAR expression and initiate antitumor activity) (Fig. 5B). We then set out to develop models to determine whether we could establish sequential control of immune cells in vitro and in vivo.

We began with a two-dimensional (2D) in vitro model that builds upon the cell proliferation experiments shown in Fig. 4. We cultured synZiFTR-controlled T cells for 6 days either with or without the priming signal (4OHT), activated CAR expression (with GZV), and subsequently challenged with HER2$^+$ NALM6 tumor cells 1 day after activation, comparing these cells with constitutive CAR-expressing cells (fig. S10B). Only cells harboring the dual-switch circuit exhibited expansion of cell numbers when induced with 4OHT (fig. S10C). Correspondingly, we found that only dual-switch cells that were 4OHT primed and subsequently GZV activated (4OHT → GZV) were capable of efficient tumor cell killing when challenged with fast-growing tumor cells 1 week (day 7) after initiating the culture (fig. S10D). Encouraged by these results, we sought to establish a 3D spheroid model of sequential control (Fig. 5C). Spheroids are an imperfect but useful model of in vivo solid tumors, sharing notable morphological and behavioral similarities, including the development of oxygen and nutrient gradients, the formation of a necrotic/apoptotic central core, and recapitulation of 3D cell-cell and cell-matrix interactions (*57*). We designed a 3D spheroid based on HER2$^+$ MCF10A breast mammary epithelial cells, which we used to test whether sequential control can drive functional changes to the spheroid targets (Fig. 5C and materials and methods). Spheroids cocultured with dual-switch cells and receiving the sequential 4OHT → GZV dose regimen exhibited synergistic responses, as measured by tumor cell killing and the corresponding morphological disruption of spheroids, including loss of their hallmark rounded shape and amorphous cell scattering throughout the well (Fig. 5C). These results provide evidence for engineered sequential control of T cell function in vitro.

Our next goal was to develop an in vivo model of sequential control. To look for conditions in which we could evaluate the control circuit, we modulated the infusion timing of constitutive CAR T cells in an NSG mouse leukemia model. Mice received either a preinfusion (at day –6) or a postinfusion (day 1) of a relatively low number of control constitutive CAR-expressing T cells (1×10^6 cells) (fig. S11A). At day 0, we injected the mice with HER2$^+$ Nalm6 tumor cells and tracked tumor burden. The preinfused CAR T cells were less effective at responding to the tumor challenge (fig. S11, B and C). The 6-day preinfusion tumor model offers a window of susceptibility to demonstrate the sequential control circuit. When we tested dual-switch T cells in this mouse model (Fig. 5D), we observed synergistic in vivo activity in reducing tumor burden in mice receiving the engineered T cells and the TMX → GZV dose regimen relative to other dosing schemes and non–T cell controls (Fig. 5, E and F, and fig. S11D). Mice that were not preconditioned with the TMX stimulus before the tumor cell challenge but were induced to activate CAR expression were significantly less effective at responding to the challenge, suggesting that the TMX phase was necessary for priming the population. These results provide evidence that we can engineer sequential control of T cell function in vivo using orthogonal FDA-approved drugs as stimuli. They also demonstrate the therapeutic potential of these circuits that can sequentially activate therapeutically relevant and synergistic genes to prime cells for antitumor activity.

In this work, we designed and tested in human cells a suite of clinically inspired synthetic gene regulators and circuits with demonstrated therapeutic potential. The synZiFTR platform features de novo–engineered ZFs that can be used to implement orthogonal and clinically viable drug-controlled genetic circuits with minimal genetic footprints. Using this platform, we demonstrated new capabilities for user-defined control over therapeutic cell function, including the creation of multi-input/-output circuits that enable sequential control of immune cell function to drive synergistic in vivo activity in reducing tumor burden.

We undertook the design of ZFs because of their hypercompact size, human origin, and demonstrated clinical viability. Moreover, we and others have demonstrated that ZF systems permit tunability at the level of DNA binding affinity and cooperativity, which is valuable in designing synthetic circuits with tunable and predictive input/output behaviors (*58*–*60*). Other programmable DNA-targeting systems use large proteins of nonhuman origin, which may pose issues with regard to immunogenicity. Analysis of our core synZiFTR architecture using an established immunogenicity prediction tool confirmed that our ZF peptides have lower predicted immunogenicity scores compared with those of TetR, Gal4, and *sp* dCas9 (fig. S12 and materials and methods). However, evaluating the true immunogenic potential of any synthetic system will ultimately require empirical measurements. Although the initial synZiFTR platform is based upon ZFs, alternative methods of gene activation, such as CRISPR-Cas systems engineered to have reduced size and immunogenic potential (*61*–*63*), may in the future complement the platform.

We outlined criteria to guide clinically driven gene circuit design processes. As we demonstrated with our gene switches, developing systems within this framework is a multidimensional optimization problem that will require prioritizing specific criteria depending on the application. Our GZV switch favors safe regulation, prioritizing the use of a clinically approved, pharmacokinetically favorable drug that does not target native cellular proteins. The TMX switch offers an entirely human-derived option. Overall, we believe that our synZiFTR systems offer superior options to existing drug-regulated systems because of the combination of drug safety, efficacy, regulatory orthogonality, and predicted low immunogenicity. In the future, efforts to predict potential immunogenic peptides (fig. S12), "de-immunize" synZiFTR domains, and perhaps incorporate new human-derived ligand-binding domains with biocompatible inducers could provide pathways to clinical translation. Finally, because of the modularity and orthogonality of the synZiFTR architecture, it should be relatively straightforward to incorporate other regulatory domains, including de novo–designed bioactive protein domains (*64*, *65*), and to use synZiFTRs as the basis for constructing cell-autonomous and multi-antigen recognition circuits (*11*, *12*, *66*).

The ability to encode temporal patterns using synZiFTR sequential control circuits could unlock an underexplored dimension of cell therapy function. For instance, the type 2 effector response is typically viewed as protumor; however, evidence is accumulating that it can also mediate antitumor immunity (*67*, *68*). One possible way to harness the type 2 response could be to activate it after an initial cytotoxic response by CAR T cells. Our synZiFTR platform would be ideally suited to perform such a complex therapeutic program safely and effectively.

We expect that our synZiFTR platform will translate widely to other clinically relevant cell types and contexts, enabling the future development of synthetic circuits for gene and cell therapies. Much more development remains and there are many other clinical considerations to address, but we hope these tools will begin to transform the rapid advances we are witnessing in mammalian synthetic biology into new solutions for safer, effective, and more powerful next-generation therapies.

REFERENCES AND NOTES

1. M. A. Fischbach, J. A. Bluestone, W. A. Lim, *Sci. Transl. Med.* **5**, 179ps7 (2013).
2. T. Kitada, B. DiAndreth, B. Teague, R. Weiss, *Science* **359**, eaad1067 (2018).
3. M. Xie, M. Fussenegger, *Nat. Rev. Mol. Cell Biol.* **19**, 507–525 (2018).
4. W. A. Lim, C. H. June, *Cell* **168**, 724–740 (2017).
5. K. A. Hay, *Br. J. Haematol.* **183**, 364–374 (2018).
6. R. A. Morgan *et al.*, *Mol. Ther.* **18**, 843–851 (2010).
7. G. Fucà, L. Reppel, E. Landoni, B. Savoldo, G. Dotti, *Clin. Cancer Res.* **26**, 2444–2451 (2020).
8. S. Rafiq, C. S. Hackett, R. J. Brentjens, *Nat. Rev. Clin. Oncol.* **17**, 147–167 (2020).
9. L. Zhang *et al.*, *Clin. Cancer Res.* **21**, 2278–2288 (2015).
10. X. J. Gao, L. S. Chong, M. S. Kim, M. B. Elowitz, *Science* **361**, 1252–1258 (2018).
11. K. T. Roybal *et al.*, *Cell* **164**, 770–779 (2016).
12. K. T. Roybal *et al.*, *Cell* **167**, 419–432.e16 (2016).
13. L. Schukur, B. Geering, G. Charpin-El Hamri, M. Fussenegger, *Sci. Transl. Med.* **7**, 318ra201 (2015).
14. M. Xie *et al.*, *Science* **354**, 1296–1301 (2016).
15. B. D. Choi *et al.*, *Nat. Biotechnol.* **37**, 1049–1058 (2019).
16. V. Golumba-Nagy, J. Kuehle, A. A. Hombach, H. Abken, *Mol. Ther.* **26**, 2218–2230 (2018).
17. B. Hu *et al.*, *Cell Rep.* **20**, 3025–3033 (2017).
18. E. Lanitis, G. Coukos, M. Irving, *Curr. Opin. Biotechnol.* **65**, 75–87 (2020).
19. S. Mardiana, B. J. Solomon, P. K. Darcy, P. A. Beavis, *Sci. Transl. Med.* **11**, eaaw2293 (2019).
20. M. Hong, J. D. Clubb, Y. Y. Chen, *Cancer Cell* **38**, 473–488 (2020).
21. S. Braselmann, P. Graninger, M. Busslinger, *Proc. Natl. Acad. Sci. U.S.A.* **90**, 1657–1661 (1993).
22. M. Gossen, H. Bujard, *Proc. Natl. Acad. Sci. U.S.A.* **89**, 5547–5551 (1992).
23. D. Favre *et al.*, *J. Virol.* **76**, 11605–11611 (2002).
24. A. M. Lena, P. Giannetti, E. Sporeno, G. Ciliberto, R. Savino, *J. Gene Med.* **7**, 1086–1096 (2005).
25. L. A. Gilbert *et al.*, *Cell* **154**, 442–451 (2013).
26. P. Perez-Pinera *et al.*, *Nat. Methods* **10**, 973–976 (2013).
27. J. G. Zalatan *et al.*, *Cell* **160**, 339–350 (2015).
28. C. T. Charlesworth *et al.*, *Nat. Med.* **25**, 249–254 (2019).
29. D. L. Wagner *et al.*, *Nat. Med.* **25**, 242–248 (2019).
30. N. P. Pavletich, C. O. Pabo, *Science* **252**, 809–817 (1991).
31. S. A. Lambert *et al.*, *Cell* **175**, 598–599 (2018).
32. V. M. Rivera *et al.*, *Blood* **105**, 1424–1430 (2005).
33. R. R. Beerli, C. F. Barbas3rd, *Nat. Biotechnol.* **20**, 135–141 (2002).
34. M. L. Maeder, S. Thibodeau-Beganny, J. D. Sander, D. F. Voytas, J. K. Joung, *Nat. Protoc.* **4**, 1471–1501 (2009).
35. C. O. Pabo, E. Peisach, R. A. Grant, *Annu. Rev. Biochem.* **70**, 313–340 (2001).
36. J. D. Sander *et al.*, *Nat. Methods* **8**, 67–69 (2011).
37. M. Moore, A. Klug, Y. Choo, *Proc. Natl. Acad. Sci. U.S.A.* **98**, 1437–1441 (2001).
38. J. K. Rockstroh *et al.*, *Lancet HIV* **2**, e319–e327 (2015).
39. C. L. Jacobs, R. K. Badiee, M. Z. Lin, *Nat. Methods* **15**, 523–526 (2018).
40. E. P. Tague, H. L. Dotson, S. N. Tunney, D. C. Sloas, J. T. Ngo, *Nat. Methods* **15**, 519–522 (2018).
41. R. Feil *et al.*, *Proc. Natl. Acad. Sci. U.S.A.* **93**, 10887–10890 (1996).
42. A. K. Indra *et al.*, *Nucleic Acids Res.* **27**, 4324–4327 (1999).
43. F. S. Liang, W. Q. Ho, G. R. Crabtree, *Sci. Signal.* **4**, rs2 (2011).
44. C. Ede, X. Chen, M. Y. Lin, Y. Y. Chen, *ACS Synth. Biol.* **5**, 395–404 (2016).
45. J. H. Choe *et al.*, *Sci. Transl. Med.* **13**, eabe7378 (2021).
46. A. Hyrenius-Wittsten *et al.*, *Sci. Transl. Med.* **13**, eabd8836 (2021).
47. E. W. Weber *et al.*, *Science* **372**, eaba1786 (2021).
48. P. Chevallier *et al.*, *Haematologica* **89**, 1399–1401 (2004).
49. J. H. Cho, J. J. Collins, W. W. Wong, *Cell* **173**, 1426–1438.e11 (2018).
50. H. P. Feng *et al.*, *Antimicrob. Agents Chemother.* **63**, e02142-18 (2019).
51. J. Cohen, *Science* **270**, 908 (1995).
52. J. P. Leonard *et al.*, *Blood* **90**, 2541–2548 (1997).
53. A. M. Levin *et al.*, *Nature* **484**, 529–533 (2012).
54. J. E. Purvis *et al.*, *Science* **336**, 1440–1444 (2012).
55. L. Cai, C. K. Dalal, M. B. Elowitz, *Nature* **455**, 485–490 (2008).
56. G. Napolitani, A. Rinaldi, F. Bertoni, F. Sallusto, A. Lanzavecchia, *Nat. Immunol.* **6**, 769–776 (2005).
57. F. Mittler *et al.*, *Front. Oncol.* **7**, 293 (2017).
58. C. J. Bashor *et al.*, *Science* **364**, 593–597 (2019).
59. P. S. Donahue *et al.*, *Nat. Commun.* **11**, 779 (2020).
60. A. S. Khalil *et al.*, *Cell* **150**, 647–658 (2012).
61. F. A. Ran *et al.*, *Nature* **520**, 186–191 (2015).
62. P. Pausch *et al.*, *Science* **369**, 333–337 (2020).
63. X. Xu *et al.*, *Mol. Cell* **81**, 4333–4345.e4 (2021).
64. R. A. Langan *et al.*, *Nature* **572**, 205–210 (2019).
65. Z. Chen *et al.*, *Nature* **565**, 106–111 (2019).
66. I. Zhu *et al.*, *Cell* **185**, 1431–1443.e16 (2022).
67. M. Liu *et al.*, *Nature* **587**, 115–120 (2020).
68. Z. Bai *et al.*, *Sci. Adv.* **8**, eabj2820 (2022).
69. Data for: H.-S. Li, D. V. Israni, K. A. Gagnon, K. A. Gan, M. H. Raymond, J. D. Sander, K. T. Roybal, J. K. Joung, W. W. Wong, A. S. Khalil, Multidimensional control of therapeutic human cell function with synthetic gene circuits, Dryad (2022); https://doi.org/10.5061/dryad.s7h44j19v.
70. Code for: H.-S. Li, D. V. Israni, K. A. Gagnon, K. A. Gan, M. H. Raymond, J. D. Sander, K. T. Roybal, J. K. Joung, W. W. Wong, A. S. Khalil, Multidimensional control of therapeutic human cell function with synthetic gene circuits, Zenodo (2022); https://doi.org/10.5281/zenodo.7216675.

ACKNOWLEDGMENTS

We thank M. Bobbin for technical assistance with the design of ZF arrays and C. Bashor, J. Ngo, and members of the Wong and Khalil laboratories for helpful discussions. **Funding:** This work was supported by the National Institutes of Health (NIH) (grant R01EB029483 to K.T.R., W.W.W., and A.S.K. and grant DP1 OD006862 to J.K.J.) and the National Science Foundation (NSF) (grant MCB-1713855 to A.S.K.). D.V.I. was supported by a NSF Graduate Research Fellowship (DGE-1247312). A.S.K. was supported by a DARPA Young Faculty Award (D16AP00142), an NIH Director's New Innovator Award (DP2AI131083), and a Department of Defense Vannevar Bush Faculty Fellowship (N00014-20-1-2825). **Author contributions:** D.V.I., J.D.S., and J.K.J. designed ZF proteins and target sequences. D.V.I. performed bioinformatic and sequencing analyses. D.V.I. designed genetic constructs and performed experiments related to Fig. 1. H.-S.L. and D.V.I. designed genetic constructs and performed experiments related to Fig. 2. H.-S.L. designed genetic constructs and performed experiments related to Figs. 3 to 5. K. A. Gagnon developed the 3D tumor spheroid model and performed spheroid experiments with H.-S.L. K. A. Gan and M.H.R. assisted with developing and testing genetic constructs for the dual-switch system. K.T.R., W.W.W., and A.S.K. oversaw the study. All authors analyzed the data. H.-S.L., D.V.I., M.H.R., W.W.W., and A.S.K. wrote the manuscript with input from all authors. **Competing interests:** D.V.I., J.D.S., J.K.J, and A.S.K. are inventors on a patent related to the synZiFTR technology. H.-S.L., D.V.I., K.T.R., W.W.W., and A.S.K. have filed patent applications related to drug-regulated synZiFTRs. J.K.J. is a coinventor on various patents and patent applications that describe gene editing and epigenetic editing technologies. K.T.R. is a cofounder of Arsenal Biosciences, was a founding scientist/consultant and stockholder in Cell Design Labs, now a Gilead Company, and holds stock in Gilead. J.K.J. has, or had during the course of this research, financial interests in several companies developing gene editing technology: Beam Therapeutics, Blink Therapeutics, Chroma Medicine, Editas Medicine, EpiLogic Therapeutics, Excelsior Genomics, Hera Biolabs, Monitor Biotechnologies, Nvelop Therapeutics (f/k/a ETx, Inc.), Pairwise Plants, Poseida Therapeutics, SeQure Dx, Inc., and Verve Therapeutics. J.K.J.'s financial interests in these companies include consulting fees and/or equity. J.K.J.'s interests were reviewed and are managed by Massachusetts General Hospital and Mass General Brigham in accordance with their conflict of interest policies. W.W.W. is a scientific cofounder of and holds equity in Senti Biosciences. A.S.K. is a scientific adviser for and holds equity in Senti Biosciences and Chroma Medicine and is a cofounder of Fynch Biosciences and K2 Biotechnologies. The remaining authors declare no competing interests. **Data and materials availability:** Plasmids encoding select synZiFTR constructs have been deposited at Addgene for distribution. All DNA constructs and cell lines are available from A.S.K. All sequencing data have been deposited in the Sequence Read Archive (SRA) under the BioProject accession code PRJNA714135. All other datasets have been deposited on Dryad (*69*). Computer code is available at https://github.com/khalillab/synZiFTR-analyses and is archived on Zenodo (*70*).

SUPPLEMENTARY MATERIALS

science.org/doi/10.1126/science.ade0156
Materials and Methods
Figs. S1 to S12
Tables S1 to S3
References (*71*–*81*)
MDAR Reproducibility Checklist

Submitted 19 July 2022; accepted 25 October 2022
10.1126/science.ade0156

QUANTUM MATERIALS

Hyperspectral imaging of exciton confinement within a moiré unit cell with a subnanometer electron probe

Sandhya Susarla[1,2]†‡, Mit H. Naik[1,3]†, Daria D. Blach[4], Jonas Zipfel[2]§, Takashi Taniguchi[5], Kenji Watanabe[6], Libai Huang[4], Ramamoorthy Ramesh[1,3,7], Felipe H. da Jornada[8,9], Steven G. Louie[1,3]*, Peter Ercius[2]*, Archana Raja[2]*

Electronic and optical excitations in two-dimensional systems are distinctly sensitive to the presence of a moiré superlattice. We used cryogenic transmission electron microscopy and spectroscopy to simultaneously image the structural reconstruction and associated localization of the lowest-energy intralayer exciton in a rotationally aligned WS_2-WSe_2 moiré superlattice. In conjunction with optical spectroscopy and ab initio calculations, we determined that the exciton center-of-mass wave function is confined to a radius of approximately 2 nanometers around the highest-energy stacking site in the moiré unit cell. Our results provide direct evidence that atomic reconstructions lead to the strongly confining moiré potentials and that engineering strain at the nanoscale will enable new types of excitonic lattices.

Moiré superlattices formed by stacking monolayers of van der Waals crystals are a burgeoning platform for discovery of fundamental physical phenomena (*1*). For example, the moiré superlattice of semiconducting transition-metal dichalcogenides (TMDCs) have been predicted to form a topologically protected lattice of bound electron-hole pairs or excitons that can act as a model system for quantum simulations and technologies (*2*–*4*). Recent optical spectroscopy studies have found signatures of interlayer and intralayer moiré excitons in TMDC heterostructures (*5*–*9*), investigated exciton diffusion in a superlattice potential (*10*), and found evidence for the cooperative nature of moiré excitons (*11*). An important parameter less well studied is the nature of the excitons at the nanoscale level. Nanoscale modulation or confinement of the center of mass of interlayer excitons has been recently probed in momentum space by using ultrafast angle-resolved photoemission electron spectroscopy (ARPES) (*12*). Similarly, the coupling and decoupling of interlayer excitons and phonons was probed by means of ultralow-frequency tip-enhanced Raman spectroscopy (*13*). A clear understanding of the degree of confinement of intralayer excitons as well as a measurement of the stacking at which the localization occurs has remained out of reach because of the diffraction limit of optical probes or the loss of phase information in ARPES. Such real-space visualization of the exciton localization is necessary to address the fundamental question of whether a moiré superlattice can support a periodic array of well-localized quantum excitations (*2*–*4*).

Electron microscopy can be used to measure structure and electronic transitions at high resolution. Using TMDC heterostructures as model systems, previous studies have measured either their atomic-scale structural reconstruction with annular dark-field scanning transmission electron microscopy (ADF-STEM) (*14*, *15*) or the excitonic signatures by using spatially averaged STEM low-loss electron energy-loss spectroscopy (STEM-EELS) (*16*–*18*). The advent of high-sensitivity direct electron detectors incorporated into EEL spectrometers along with cryogenic holders and monochromation provides an opportunity to simultaneously probe the weak exciton states and the structural reconstruction at the subnanometer scale.

We used simultaneous ADF-STEM and low-loss STEM-EELS mapping with hyperspectral analysis to directly image the in-plane structural reconstruction of a rotationally aligned (R-stacked) WS_2-WSe_2 moiré superlattice and the corresponding oscillator strength of the moiré exciton within the moiré unit cell.

We prepared an R-stacked heterostructure of WS_2 and WSe_2 monolayers encapsulated within ~16 nm and 10-nm-thick hexagonal boron nitride (hBN) on opposing sides. The sample was suspended over a 20- by 20-μm hole in a custom fabricated silicon TEM grid. hBN creates a uniform dielectric environment that narrows excitonic linewidths (*19*) and protects the sample from oxidation and beam damage. We verified the twist angle between the layers to be near-zero or R-stacked using second harmonic generation (SHG) (fig. S1) and position-averaged convergent beam electron diffraction (fig. S2), along with the emergence of strong emission from a lower-lying, interlayer exciton state in photoluminescence measurements (fig. S3). We then collected hyperspectral images from multiple regions under cryogenic conditions (100 K) using simultaneous ADF-STEM-EELS with a ~100-meV monochromated electron beam focused to less than a nanometer (Fig. 1A, supplementary text, and figs. S4 to S6). We implemented a custom data analysis routine based on unit cell averaging to improve the signal-to-noise ratio in the structural image and final EEL spectra and map (supplementary text and figs. S7 to S17).

The WS_2 and WSe_2 monolayers were direct band-gap semiconductors with a lattice parameter of 3.18 and 3.32 Å, respectively. The 4.4% lattice mismatch gave rise to a moiré periodicity of ~8 nm for near-zero relative twist. A schematic of the heterostructure is shown in Fig. 1B, with three high-symmetry stacking configurations: AA has metal and chalcogens vertically stacked, $B^{Se/W}$ has Se stacked on W, and $B^{W/S}$ has W stacked on S. The latter two are Bernal stacking regions. Because of steric effects, our density functional theory calculations show that stacking in the moiré superlattice affects the local energy landscape, and AA stacking has the highest energy (Fig. 1C) (*20*–*22*).

We obtained subnanoscale structural information by analyzing ADF-STEM images, in which intensity is proportional to the locally summed atomic number (Z) at each atomic column along the electron beam direction (materials and methods and supplementary text). Quantitative ADF-STEM has been used in the past to study in-plane reconstructions in large-period, lattice-matched moiré systems such as twisted bilayer MoS_2, WS_2, and MoS_2-WS_2 (*14*). To help interpret our experiments, we simulated ADF-STEM images of the theoretically predicted unrelaxed and relaxed moiré superlattice using multislice simulations (supplementary text) (*23*). The simulation of the unrelaxed moiré heterostructure in which circular regions of higher intensity correspond to the AA, $B^{Se/W}$, and $B^{W/S}$ stacking arrangements is shown in Fig. 1D. The AA region (Z_{eff} = 142) appears brighter than the $B^{Se/W}$ (Z_{eff} = 58) and $B^{W/S}$ (Z_{eff} = 54) regions. Without accounting for a structural reconstruction, all the stacking configurations have roughly the same area (fig. S18). However, the ADF-STEM simulation of the relaxed moiré heterostructure (Fig. 1E) shows clear differences among the sizes of the bright and dark regions. Driven by the stacking energy landscape (Fig. 1C), the effective

---

[1]Materials Science Division, Lawrence Berkeley National Laboratory, Berkeley, CA 94720, USA. [2]Molecular Foundry, Lawrence Berkeley National Laboratory, Berkeley, CA 94720, USA. [3]Department of Physics, University of California, Berkeley, CA 94720, USA. [4]Department of Chemistry, Purdue University, West Lafayette, IN 47907, USA. [5]International Center for Materials Nanoarchitectonics, National Institute for Materials Science, 1-1 Namiki, Tsukuba 305-0044, Japan. [6]Research Center for Functional Materials, National Institute for Materials Science, 1-1 Namiki, Tsukuba 305-0044, Japan. [7]Department of Materials Science and Engineering, University of California, Berkeley, CA 94720, USA. [8]Department of Materials Science and Engineering, Stanford University, Stanford, CA 94305, USA. [9]Stanford PULSE Institute, SLAC National Accelerator Laboratory, Menlo Park, CA 94025, USA.

***Corresponding author. Email: sglouie@berkeley.edu (S.G.L.); percius@lbl.gov (P.E.); araja@lbl.gov (A.R.)**

†These authors contributed equally to this work.

‡Present address: School for Engineering of Matter, Transport, and Energy, Arizona State University, Tempe, AZ, USA.

§Present address: ZEISS Semiconductor Manufacturing Technology, Oberkochen, Germany.

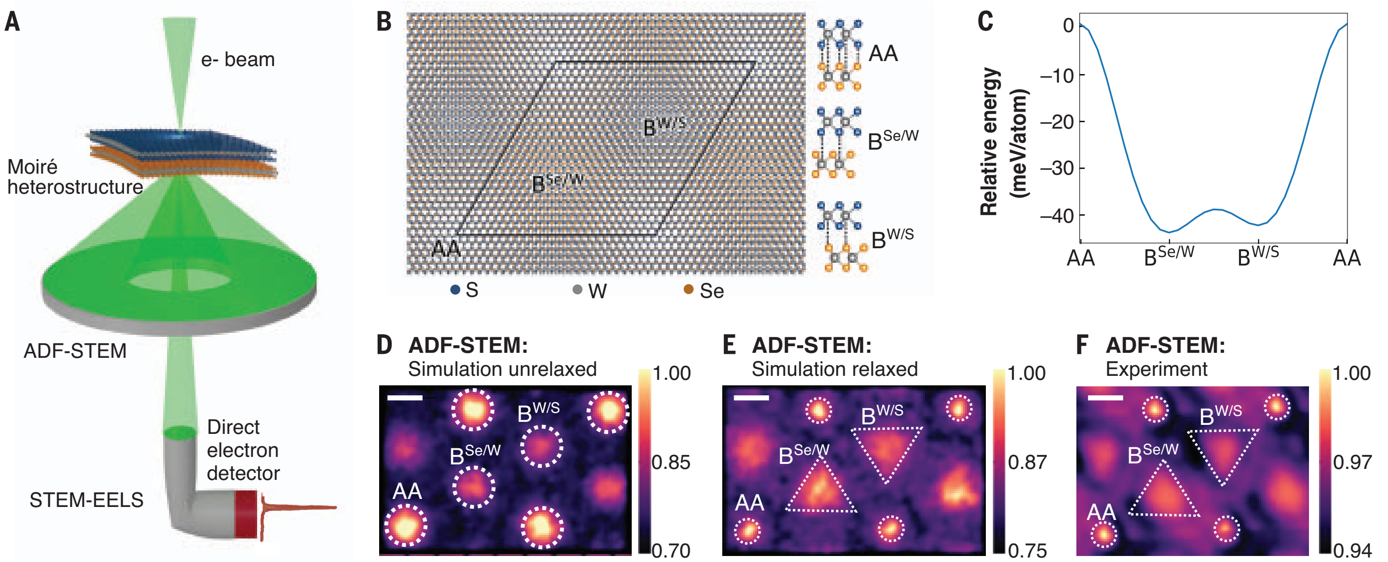

Fig. 1. Structural reconstruction of a WS_2-WSe_2 moiré heterostructure. (**A**) Schematic describing the simultaneous monochromated ADF-STEM-EELS experiment with a direct electron detector. (**B**) Structural model of reconstructed R-stacked WS_2-WSe_2 heterostructure showing different stacking configurations in a moiré unit cell. (**C**) Relative energy of the various stacking configurations in the moiré superlattice. (**D** and **E**) ADF-STEM multislice simulations of unrelaxed and relaxed heterostructures. (**F**) Experimental ADF-STEM unit cell periodically repeated to match the relaxed heterostructure in (D) and (E). Scale bars, (D) to (F) 2 nm. The color bars in (D) to (F) indicates the normalized intensity.

area corresponding to the high-energy AA configuration is reduced compared with the unrelaxed structure, and the $B^{Se/W}$ and $B^{W/S}$ regions form larger, triangular domains. Experimentally, we imaged an area of the sample that contained many moiré unit cells with a 5-Å probe step size. Although direct atomic resolution imaging was challenging because of the overlap of atoms with very small projected distances (fig. S19), our simulations allowed us to differentiate AA sites from B sites. We averaged the ADF-STEM intensities over 162 moiré unit cells (materials and methods and fig. S7) to obtain the final image shown in Fig. 1F. The experimental ADF-STEM unit cell is consistent across scans (fig. S8), not affected by hBN owing to incommensurate moire with respect to the TMDCs, and in agreement with the multislice simulation of the relaxed heterostructure (Fig. 1E, fig. S18, and table S1), providing the first direct evidence of in-plane structural reconstructions in a WS_2-WSe_2 moiré superlattice.

The structural transformation we observed (Fig. 1C) led to a strain redistribution over the whole moiré unit cell (with a maximum strain of ~1%) in the individual layers because of a fine balance between the strain energy cost and stacking energy gain (fig. S20) (*24*). The observed in-plane structural reconstruction in the present work is distinct from those in previous first-principle calculations (*22*, *25*) and ADF-STEM reports (*14*) in twisted lattice-matched systems, in which the strain was localized to the boundary between the lowest-energy stacking configurations. Usually, when a lattice-mismatched TMDC heterostructure is formed by use of thermodynamics-based growth techniques such as chemical vapor deposition, the heterostructure does not reconstruct (*10*). The unexpectedly large in-plane structural reconstruction we observed in the R-stacked van der Waals interfaces was recently predicted by theory, and the associated inhomogeneous strain in the individual layers is responsible for the formation of flat electronic bands (*24*) and spatially modulated excitonic states (*9*).

We studied the influence of the in-plane structural reconstruction on the moiré excitonic states through ensemble optical spectroscopy and localized low-loss STEM-EELS on the same sample, obtaining higher spectral resolution with the former technique and higher spatial resolution with the latter. The optical image of the R-stacked WS_2-WSe_2 heterostructure embedded within hBN is shown in Fig. 2A. A representative band-pass filtered ADF-STEM image of the heterostructure is shown in Fig. 2B, displaying a moiré pattern over a 100- by 100-nm region with 0.5-nm resolution. Shown in Fig. 2C are the average EEL spectra acquired from regions of monolayer WSe_2 (Fig. 2C, orange), monolayer WS_2 (Fig. 2C, blue), and WS_2-WSe_2 (Fig. 2C, green) compared with optical reflectivity spectra (Fig. 2C, gray). We performed EELS background subtraction using Gauss-Lorentz fitting in the pre- and postedge onset of the exciton peak (*26*) and smoothed with a Savitzsky-Golay algorithm (figs. S9 to S13). STEM-EELS measures the energy lost by incident electrons to electrons in the target atoms excited into empty states, and the EEL signal is proportional to the imaginary part of the dielectric constant of the material (*27*). Thus, we measured the local probability of creating an exciton, rather than the excitons themselves. The split A and B exciton peak positions arising from spin-orbit coupling of both WS_2 (A, 2.10 eV; B, 2.40 eV) and WSe_2 (A, 1.75 eV; B, 2.10 eV) monolayers in low-loss EELS match well with optical data, suggesting that the two spectroscopic techniques display a similar oscillator strength for the main exciton peaks. The zoomed-in moiré exciton peaks are shown in Fig. 2D. The lowest energy peak (1.65 eV) is slightly red-shifted compared with the WSe_2 monolayer A exciton peak (1.75 eV). The optical reflectivity measurement shows the three lowest-energy intralayer moiré exciton peaks (labeled I, II, and III). Although we could only resolve this fine structure of the moiré exciton peaks optically, subsequent broadening of the optical spectra by 100 meV yielded good agreement with the EEL spectra (Fig. 2D and table S2). The largest spectral contribution (58%) in the 1.6 to 1.7 eV range comes from the moiré exciton peak I (fig. S21), which is consistent with the largest oscillator strength predicted with ab initio *GW* plus Bethe-Salpeter equation (*GW*-BSE) calculations. The intralayer excitons can decay rapidly into lower-energy-state interlayer excitons; however, interlayer excitons were not observed in optical reflectance or EELS for this heterostructure system

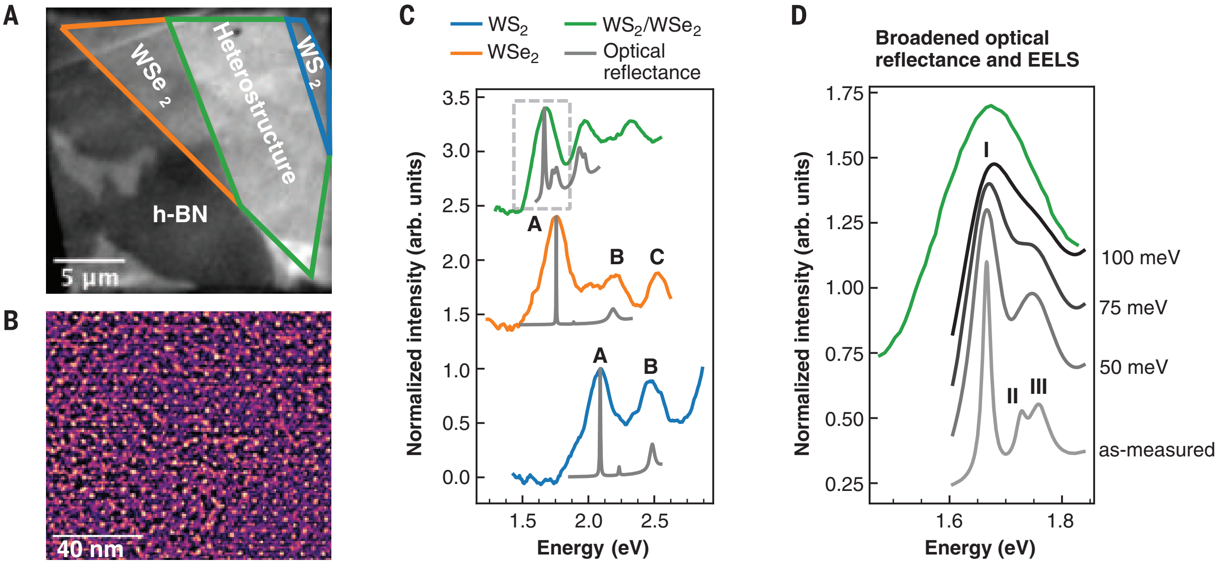

Fig. 2. Comparison of EELS with optical absorption. (**A**) Optical image of the R-stacked WS_2-WSe_2 heterostructure transferred on the TEM grid with hBN encapsulation. (**B**) False-colored band-pass filtered ADF-STEM image acquired during STEM-EELS showing a uniform moiré pattern over a 100- by 100-nm region. (**C**) Spatially averaged EEL spectra of the moiré heterostructure (green) compared with monolayer WSe_2 (orange) and WS_2 (blue), with reference optical reflectance spectra (gray). (**D**) Zoomed spectra of the moiré heterostructure showing the three distinct moiré exciton peaks resolvable with optics measurements. Gaussian broadening of 100 meV matches the EELS resolution.

because of their negligible (~1000× smaller) oscillator strength as compared with that of the intralayer excitations (*28*).

The splitting of the WSe_2 A exciton peak into three peaks in the WS_2-WSe_2 moiré superlattice is predicted (*9*) to be a result of the strong in-plane structural reconstruction observed in ADF-STEM measurements (Fig. 1), which is unlike other moiré systems in which layer hybridization can also contribute to the moiré-exciton fine structure (*7*). The in-plane structural reconstruction of the WSe_2 layer leads to flat electronic bands at the valence and conduction band edge. The wave functions corresponding to these flat band states are spatially modulated in the moiré superlattice (fig. S23). In the absence of the reconstruction, the flat bands were not observed (fig. S22), and the electronic states were delocalized in the moiré superlattice. Our first-principles *GW*-BSE calculations, which fully account for the spatial modulation of the valence and conduction band states owing to the structural reconstruction, reproduced the three peaks observed in the optical reflection contrast spectrum (fig. S24). The *GW*-BSE calculation for the large-area moiré superlattice was made possible by a recently developed pristine unit cell matrix projection (PUMP) method (*9*). The wave function that describes a moiré exciton state S is a linear combination of valence-to-conduction transitions in the Brillouin zone: $\psi^S(\boldsymbol{r}_\mathrm{e},\boldsymbol{r}_\mathrm{h}) = \sum_{vck} A^S_{vck}\phi_{ck}(\boldsymbol{r}_\mathrm{e})\phi^*_{vk}(\boldsymbol{r}_\mathrm{h})$, where $\boldsymbol{r}_\mathrm{e}$ and $\boldsymbol{r}_\mathrm{h}$ are the electron and hole coordinates, respectively; A^S_{vck} is the exciton envelope function; $\phi_{v\boldsymbol{k}}$ and $\phi_{c\boldsymbol{k}}$ are the single-particle Bloch states of the valence and conduction bands, respectively; $\boldsymbol{k}$ is the electron wave vector; and S is an exciton band index. Furthermore, our calculations show that the exciton associated with peak I forms a spatially modulated Wannier exciton with maximum charge density at the AA stacking in the moiré superlattice (Fig. 3A). In the absence of structural reconstructions, we expected only a single excitonic peak in this energy range, with no spatial modulation. We compared the oscillator strength of the moiré exciton, primarily peak I, with the experimental data by applying a 1.3-nm hard mask around the AA, $B^{Se/W}$, and $B^{W/S}$ positions determined from ADF-STEM structural images (supplementary text and figs. S14, S16, and S17). Although the electron beam was spatially confined to less than a nanometer in diameter, low-loss EELS delocalization limited the achievable spatial resolution to about 1 nm (*27*, *29*). We observed a clear difference in the peak intensities derived from the three stacking regions, indicating that the excitonic peak we observed in EELS (primarily peak I) has an inhomogeneous oscillator strength in the moiré unit cell, with the maximum intensity at AA stacking regions (Fig. 3B and figs. S16 and S17). This is in very good agreement with the results from our first-principles *GW*-BSE calculations that constrained the exciton-photon coupling matrix element $\langle S|\int d\boldsymbol{r}\psi^\dagger(\boldsymbol{r})\boldsymbol{A}(\boldsymbol{r})\cdot\mathbf{v}\psi(\boldsymbol{r})|0\rangle$ to a specific spatially resolved region by taking the vector potential $\boldsymbol{A}(\boldsymbol{r})$ to have a Gaussian profile, and where $\mathbf{v}$ is the velocity operator, $\psi(\boldsymbol{r})$ is a field operator, and $|0\rangle$ is the ground-state wave function (Fig. 3C and supplementary text). The oscillator strength of peak I has the largest contribution from around the AA stacking because the photoexcited electron and hole charge density are maximized in this region (Fig. 3A). For a Wannier-type exciton, the oscillator strength distribution is proportional to $\psi^S(\boldsymbol{r}_\mathrm{e} = \boldsymbol{x}, \boldsymbol{r}_\mathrm{h} = \boldsymbol{x})$, which corresponds to the wave function of the exciton center-of-mass coordinate, $\boldsymbol{R} = \frac{\boldsymbol{r}_\mathrm{e}+\boldsymbol{r}_\mathrm{h}}{2} = x$, and relative coordinate $\boldsymbol{r} = \frac{\boldsymbol{r}_\mathrm{e}-\boldsymbol{r}_\mathrm{h}}{2} = 0$—that is, $\psi^S(\boldsymbol{R} = \boldsymbol{x}, \boldsymbol{r} = 0)$.

To determine the spatial extent of the exciton modulation within a moiré unit cell, we generated a hyperspectral unit cell by shifting a 1.3-nm mask to different unit cell locations across a 100- by 100-nm scan, effectively creating a rolling average (supplementary text and figs. S14 and S15). Shown in Fig. 3D is the unit cell averaged and periodically repeated EELS intensity map generated by summing spectral intensity from 1.61 to 1.71 eV (figs. S15, S25, and S26). We observed that the intralayer exciton was constrained to the AA sites, which formed a triangular arrangement in the moiré pattern. Furthermore, the exciton intensity rapidly reduced beyond ~2 nm from the AA site, which is in good agreement with the corresponding *GW*-BSE–calculated oscillator strength map of the moiré exciton peak I (Fig. 3E).

The effect of structural reconstruction in moiré lattices has been predicted to generate

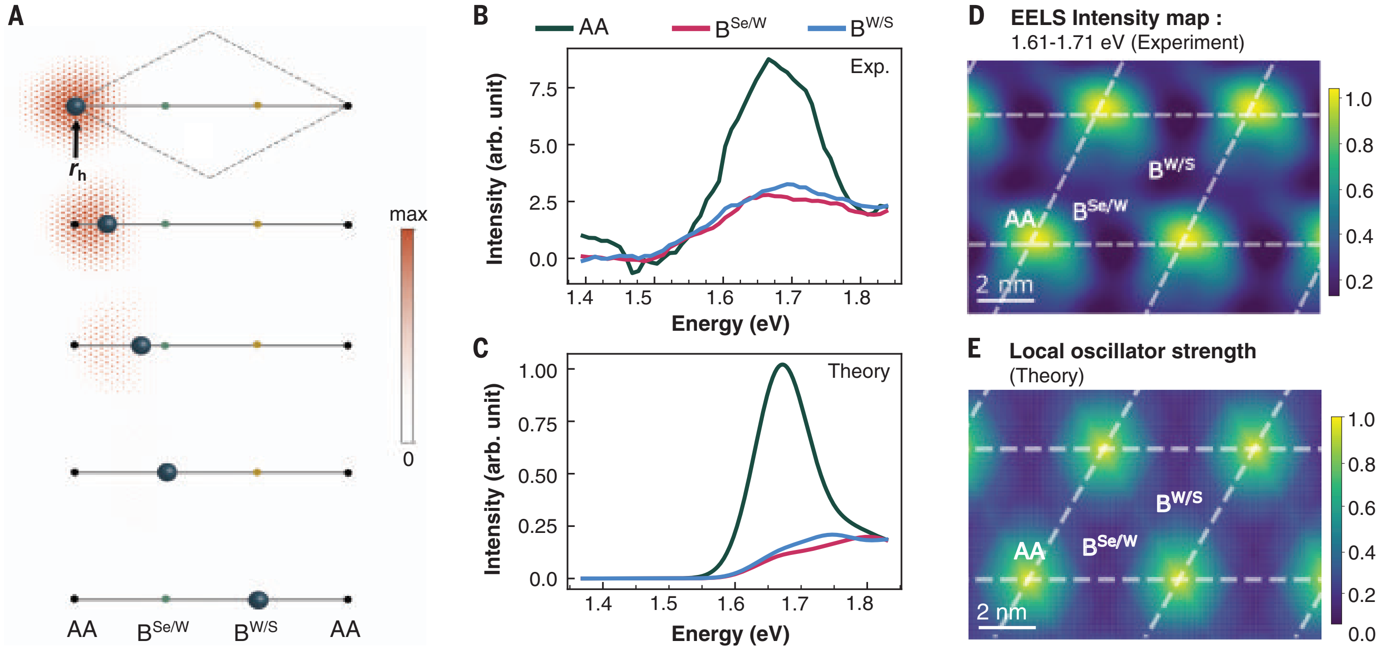

Fig. 3. Subnanoscale spatial mapping of moiré excitons: (**A**) Calculated electron charge density contributing to the peak I exciton, $\psi_S(\boldsymbol{r}_e, \boldsymbol{r}_h)$, for a fixed position of the hole, $\boldsymbol{r}_h$, in the moiré superlattice. The evolution of the electron charge density was plotted by moving the hole position across the longer diagonal of the superlattice, showing the spatially modulated character of the peak I exciton. (**B** and **C**) Comparison of spatially resolved experimental EELS and *GW*-BSE theory for different stacking configurations AA, $B^{Se/W}$, and $B^{W/S}$. (**D**) Experimental unit cell averaged and tiled EELS map, obtained by a rolling average with a 1.3-nm radius at different unit cell locations. Shown is the modulation of the EELS intensity, which is primarily composed of peak I at 1.65 eV. (**E**) Theoretically calculated oscillator strength distribution of the peak I exciton, with similar radial blurring as the experiment.

strong electronic and excitonic confinement (*9*, *24*). By taking advantage of the spatial and spectral resolution in cryogenic correlated ADF-STEM and STEM-EELS techniques, we directly captured the subnanometer scale in-plane structural reconstruction and the corresponding exciton localization without the limitations of diffractive optics. The structural reconstruction was not observed in thermodynamically grown heterostructures (*10*). We found that the structural reconstruction was robust over a submicrometer area of the sample, despite potential sources of disorder introduced by the multilayer mechanical stacking process. The in-plane structural reconstruction led to spatially modulated electronic bands (*24*, *30*) in this system, which was corroborated by the recent observations of strongly correlated Wigner crystal and Mott insulating phases (*31*, *32*).

The exciton wave function as a function of the center-of-mass coordinate (with small electron-hole relative coordinate) was localized to the AA site within a radius of ~2 nm. This suggests that the moiré potential was preserved over a large area of the sample and could support the formation of a triangular lattice of excitons. The diminished exciton intensity at the Bernal stacking regions (Fig. 3, D and E) is in agreement with the unexpected absence of trion formation upon hole doping of the same heterostructure system (supplementary text) (*5*, *9*). Unit cell averaging, which sampled across hundreds of square nanometers, greatly improved the signal-to-noise ratio of the EELS intensity map.

We discovered that the strong atomic relaxations within each moiré cell leads to confinement of excitons at a particular stacking site. This opens up the possibility of nanoscopic engineering of bosonic lattices in moiré heterostructures through external strain, twist-angle, and number of layers.

REFERENCES AND NOTES

1. D. M. Kennes *et al.*, *Nat. Phys.* **17**, 155–163 (2021).
2. E. Biolatti, R. C. Iotti, P. Zanardi, F. Rossi, *Phys. Rev. Lett.* **85**, 5647–5650 (2000).
3. S. H. Sung *et al.*, Torsional periodic lattice distortions and diffraction of twisted 2D materials. arXiv:2203.06510 [cond-mat.mtrl-sci] (2022).
4. F. Wu, T. Lovorn, A. H. MacDonald, *Phys. Rev. Lett.* **118**, 147401 (2017).
5. C. Jin *et al.*, *Nature* **567**, 76–80 (2019).
6. K. Tran *et al.*, *Nature* **567**, 71–75 (2019).
7. E. M. Alexeev *et al.*, *Nature* **567**, 81–86 (2019).
8. K. L. Seyler *et al.*, *Nature* **567**, 66–70 (2019).
9. M. H. Naik *et al.*, *Nature* **609**, 52–57 (2022).
10. L. Yuan *et al.*, *Nat. Mater.* **19**, 617–623 (2020).
11. L. Zhang *et al.*, *Nature* **591**, 61–65 (2021).
12. O. Karni *et al.*, *Nature* **603**, 247–252 (2022).
13. A. Rodriguez, A. Krayev, M. Velický, O. Frank, P. Z. El-Khoury, *J. Phys. Chem. Lett.* **13**, 5854–5859 (2022).
14. A. Weston *et al.*, *Nat. Nanotechnol.* **15**, 592–597 (2020).
15. A. Sushko *et al.*, High resolution imaging of reconstructed domains and moire patterns in functional van der Waals heterostructure devices. arXiv:1912.07446 [cond-mat.mes-hall] (2019).
16. L. H. G. Tizei *et al.*, *Phys. Rev. Lett.* **114**, 107601 (2015).
17. S. Susarla *et al.*, *Nano Lett.* **21**, 4071–4077 (2021).
18. P. K. Gogoi *et al.*, *ACS Nano* **13**, 9541–9550 (2019).
19. A. Raja *et al.*, *Nat. Nanotechnol.* **14**, 832–837 (2019).
20. M. H. Naik, I. Maity, P. K. Maiti, M. Jain, *J. Phys. Chem. C* **123**, 9770–9778 (2019).
21. M. H. Naik, M. Jain, *Phys. Rev. Lett.* **121**, 266401 (2018).
22. M. H. Naik, S. Kundu, I. Maity, M. Jain, *Phys. Rev. B* **102**, 075413 (2020).
23. L. Rangel DaCosta *et al.*, *Micron* **151**, 103141 (2021).
24. H. Li *et al.*, *Nat. Mater.* **20**, 945–950 (2021).
25. S. Carr *et al.*, *Phys. Rev. B* **98**, 224102 (2018).
26. J. Zhu, P. A. Crozier, P. Ercius, J. R. Anderson, *Microsc. Microanal.* **20**, 748–759 (2014).
27. R. F. Egerton, *Electron Energy-Loss Spectroscopy in the Electron Microscope* (Springer, ed. 3, 2011).
28. E. Barré *et al.*, *Science* **376**, 406–410 (2022).
29. R. F. Egerton, *Ultramicroscopy* **107**, 575–586 (2007).
30. C. H. Stansbury *et al.*, *Sci. Adv.* **7**, eabf4387 (2021).
31. H. Li *et al.*, *Nature* **597**, 650–654 (2021).
32. Y. Tang *et al.*, *Nature* **579**, 353–358 (2020).

ACKNOWLEDGMENTS

The authors thank M. Dandu and T. Heinz for thoughtful discussions on the results and J. Carlström for his inputs on sample fabrication. The authors also thank J. Ciston and C. Song for their support during the STEM-EELS experiments. We acknowledge P. A. Crozier for useful discussions about background subtraction in low-loss EELS. **Funding:** Support for sample fabrication and cryogenic optical spectroscopy was provided by the US Department of Energy (DOE) Office of Science, Basic Energy Sciences in Quantum Information Science under award DE-SC0022289. Electron microscopy and electron energy loss spectroscopy measurements, and corresponding simulations and analysis code development at the Molecular Foundry were supported by the (DOE) Office of Science, Office of Basic Energy Sciences, under contract DE-AC02-05CH11231. Electron microscopy and electron energy loss spectroscopy data analysis was supported by the DOE Office of Science, Basic Energy Sciences, Materials Sciences and Engineering Division under contract DE-AC02-05-CH11231 within the Quantum Materials program (KC2202). The theoretical calculations were primarily supported by the director, Office of Science, Office of Basic Energy Sciences, Materials Sciences and Engineering Division of the DOE under the van der Waals heterostructure program (KCWF16), contract DE-AC02-05CH11231, which provided the PUMP approach for the exciton properties of moiré systems. The work was also supported by the Center for Computational Study of Excited-State Phenomena in Energy Materials (C2SEPEM) at LBNL, funded by the DOE Office of Science, Basic Energy Sciences, Materials Sciences and Engineering Division under contract DE-AC02-05CH11231, as part of the Computational Materials Sciences Program which provided advanced codes and simulations, and supported by the Theory of Materials Program (KC2301) funded by the DOE Office of Science, Basic Energy Sciences, Materials Sciences and Engineering Division under contract DE-AC02-05CH11231, which provided conceptual analyses of the moiré excitons. Computational resources were provided by National Energy Research Scientific Computing Center (NERSC), which is supported by the DOE Office of Science under contract DE-AC02-05CH11231, Stampede2 at the Texas Advanced Computing Center (TACC), The University of Texas at Austin through Extreme Science and Engineering Discovery Environment (XSEDE), which is supported by National Science Foundation under grant ACI-1053575 and Frontera at TACC, which is supported by the National Science Foundation under grant OAC-1818253. K.W. and T.T. acknowledge support from JSPS KAKENHI (grants 19H05790, 20H00354, and 21H05233). L.H. acknowledges support from DOE Office of Basic Energy Sciences, through award DE-SC0016356 at Purdue University. J.Z. acknowledges fellowship support by the Deutsche Forschungsgemeinschaft (DFG, German Research Foundation) through the Walter-Benjamin Program 462503440. D.D.B. acknowledges fellowship support from the DOE Office of Science, Office of Workforce Development for Teachers and Scientists, Office of Science Graduate Student program through the SCGSR program administered by the Oak Ridge Institute for Science and Education (ORISE) for the DOE. ORISE is managed by ORAU under contract DE-SC0014664. **Author contributions:** Project supervision: A.R., P.E., R.R., F.H.J., and S.G.L. Conceptualization: A.R., P.E., S.S., and M.H.N. ADF-STEM-EELS experiments and data analysis: S.S. and P.E. *GW*-BSE theory: M.H.N., S.G.L., and F.H.J. Sample fabrication: D.D.B., T.T., and K.W. Optical reflectivity, second harmonic generation, and data analysis: J.Z. and D.D.B. Scientific discussion: A.R., R.R., S.G.L., F.H.J., L.H., P.E., S.S., and M.H.N. Writing – original draft: S.S., M.H.N., A.R., P.E., and F.H.J. Writing – review and editing: S.S., M.H.N., A.R., P.E., F.H.J., S.G.L., R.R., L.H., D.D.B., and J.Z. **Competing interests:** The authors declare that they have no competing interests. **Data and materials availability:** All data and code are available in the main text, the supplementary materials, and at DOI 10.5281/zenodo.7401985. The electronic structure codes used in this work—Quantum ESPRESSO, BerkeleyGW, and SIESTA—are open-source software.

SUPPLEMENTARY MATERIALS

science.org/doi/10.1126/science.add9294
Materials and Methods
Supplementary Text
Figs. S1 to S26
Table S1 and S2
References (*33*–*51*)

Submitted 19 July 2022; accepted 21 November 2022
10.1126/science.add9294

The 2023 Louisa Gross Horwitz Prize for Biology or Biochemistry

The Louisa Gross Horwitz Prize was established under the will of the late S. Gross Horwitz through a bequest to Columbia University and is named to honor the donor's mother. Louisa Gross Horwitz was the daughter of Dr. Samuel David Gross (1805–1889), a prominent surgeon of Philadelphia and author of the outstanding *Systems of Surgery* who served as president of the American Medical Association.

Each year since its inception in 1967, the Louisa Gross Horwitz Prize has been awarded by Columbia University for outstanding basic research in the fields of biology or biochemistry. The purpose of this award is to honor a scientific investigator or group of investigators whose contributions to knowledge in either of these fields are deemed worthy of special recognition.

The prize consists of an honorarium and a citation, which are awarded at a special presentation event. Unless otherwise recommended by the Prize Committee, the prize is awarded annually. Karl Deisseroth, MD, PhD, Stanford University; Peter Hegemann, PhD, Humboldt-Universität zu Berlin; and Gero Miesenböck, MD, University of Oxford, are the 2022 awardees.

QUALIFICATIONS FOR THE AWARD

The purpose of this prize is to reward scientists that have made recently transformative discoveries not yet recognized by high-visibility international awards. The Prize Committee recognizes no geographical limitations. The prize may be awarded to an individual or a group. When the prize is awarded to a group, the honorarium will be divided among the recipients, but each member will receive a citation.

NOMINATIONS

All materials must be written in the English language and submitted electronically at:
http://www.cumc.columbia.edu/research/horwitz-prize

Deadline date: Monday, January 30, 2023, 5:00 p.m. (EST)
Renominations are by invitation only.
Self-nominations are not permitted.

NOMINATIONS SHOULD INCLUDE:

1. A summary of the research on which this nomination is based (no more than 500 words).
2. A summary of the significance of this research in the fields of biology or biochemistry (no more than 500 words).
3. A brief biographical sketch of the nominee, including positions held and awards received by the nominee.
4. A copy of the nominee's curriculum vitae.
5. A key publication list of up to ten of the nominee's most significant publications relating to the research noted under item 1.

Columbia University
in the City of New York

KU The University of Kansas

Applications are invited for appointment as a tenured, **Distinguished Professor at the Full Professor** level in the Department of Pharmacology & Toxicology, School of Pharmacy at the University of Kansas. We are looking for an individual using a systems-based approach to understand mechanisms of disease and drug action, in order to advance disease prevention, diagnosis, and treatment for Alzheimer's disease or other neurological or neuropsychiatric disorder.

The successful candidate must hold a PhD, MD, or DVM, have an exceptional record of externally funded research and previous teaching experience at the undergraduate and/or graduate level. The person appointed to this position is expected to lead and participate in collaborative research projects.

The position comes with state-supported salary for nine-months and opportunity for grant-supported summer salary for an additional 3 months. Excellent University-shared core research facilities that houses specialized scientific instruments and provide expert consultation and services to investigators, a generous start-up package and endowed funds support the position.

For more information and to apply, go to: **https://employment.ku.edu/academic/23365BR** .

Review of applications will continue until the position is filled.

The University of Kansas is an EO/AAE, full policy at http://policy.ku.edu/IOA/nondiscrimination.

University of Minnesota

TENURE-TRACK ASSISTANT PROFESSOR POSITIONS IN SYNTHETIC BIOLOGY

The **Department of Biochemistry, Molecular Biology and Biophysics** (BMBB) and **the BioTechnology Institute** (BTI) in the College of Biological Sciences at the University of Minnesota are inviting applications for tenure-track Assistant Professor positions in Synthetic Biology.

Ideal candidates will develop a strong research program that establishes new research areas with a synthetic biology emphasis that complement current faculty research in synthetic biology and biotechnology within the BMBB department and the BTI. We seek to hire several candidates whose research aligns with impactful emerging areas in biotechnology and synthetic biology, including the following topic areas:

- Application of AI/machine learning to biological systems and genetic design, particularly in integrating 'omics-level datasets and high-throughput experimental systems; · Synthetic biology of eukaryotic systems, especially plants, animals, and mammalian cell lines;
- Cell-free systems, including applications in human or animal therapeutics or biomanufacturing;
- Genetically programmable materials, with a focus on platform systems whose physicochemical properties can be modified using synthetic biology.

The positions provide opportunity for collaboration across multiple disciplines in the life, physical and engineering disciplines, and access to students in multiple graduate programs. BMBB and BTI are centered in the Twin-Cities of Minneapolis and St. Paul that is a hub for biotech and biopharmaceutical companies and have close connections to industry. The U of M has been recognized for its excellence in technology commercialization and entrepreneurship of its faculty, and successful candidates can become part of this ecosystem. Candidates will be hired into BMBB as their academic tenure home and into the BTI.

The BMBB department and BTI are committed to increasing the diversity and inclusiveness of our faculty and are welcoming applications from candidates that will contribute to these goals.

To learn more about this opportunity and to apply, go to **https://hr.umn.edu/Jobs/Find-Job** and search for **Job # 352626**.

For additional information, contact the faculty search committee at:
BTIsearch@umn.edu.

HARVARD
UNIVERSITY

TENURED PROFESSOR IN TERRESTRIAL ECOLOGY

POSITION DESCRIPTION: The Department of Organismic and Evolutionary Biology (OEB) seeks to appoint a **tenured professor in terrestrial ecology** to serve as the next director of Harvard Forest. Terrestrial ecology is defined broadly, including studies at the physiological, population, community, or ecosystem level, and encompasses both above- and below-ground terrestrial ecosystems, and all biological kingdoms. We are especially interested in individuals who conduct rigorous observational and/or experimental work on how the structure, composition and functioning of eastern temperate forests are changing as a result of human activities. In addition, we are also interested in individuals who are advancing our understanding of how to conserve biodiversity in natural and human-dominated landscapes, the role of biodiversity in the maintenance of ecosystem services, and the dynamics of coupled human-natural systems.

Both OEB and Harvard Forest value diversity and are committed to building and sustaining culturally diverse intellectual communities on campus and at Harvard Forest. We especially welcome applications from members of groups historically under-represented in STEM and candidates with experience teaching and working with diverse communities and students. The professor will teach and advise at the undergraduate and graduate levels. Harvard Forest and the OEB Department have strong linkages to other allied departments and institutions, including: the Dept. of Earth and Planetary Science, the Arnold Arboretum, the Harvard University Herbaria, the Harvard Museum of Comparative Zoology, the Harvard Center for the Environment, the School of Engineering and Applied Sciences, Harvard's professional schools, and Harvard's new Salata Institute for Climate and Sustainability.

Harvard Forest (**https://harvardforest.fas.harvard.edu**), located in central Massachusetts, hosts integrated research, and educational and outreach programs investigating responses of forest dynamics to natural and human disturbances and environmental changes over broad spatial and temporal scales. It has more than 30 full-time staff, including six senior researchers. Its mission is to advance understanding of biological, physical, and social dimensions of terrestrial ecosystems in the forest landscapes of the eastern United States. Harvard Forest practices an open, inclusive, and collaborative approach to addressing local to global environmental challenges. The Forest's 4,000-acre land base hosts 100+ active research projects annually by PIs at more than two dozen institutions. Research includes deep engagement with regional stakeholders including conservation and forestry organizations, tribal nations, and state and federal agencies. Harvard Forest is one of the founding Long-Term Ecological Research (LTER) sites and plays a major role in LTER leadership, strategic planning, network-wide studies, and public engagement programs. It is also a National Ecological Observatory Network (NEON) site and member of the Ameriflux and ForestGEO research networks. Successful candidates will be expected to provide innovative leadership for Harvard Forest's mission in research and experiential education, particularly in the areas of ecology, ecosystem science, conservation biology, or global climate change. In addition, candidates will be expected to develop creative and impactful programs that leverage Harvard Forest's unique resources toward the benefit of research and education at the broader University.

The appointment is expected to begin on or after **July 1, 2023**.

BASIC QUALIFICATIONS: Candidates are required to have a doctorate in terrestrial ecology, ecosystem science, or related discipline.

ADDITIONAL QUALIFICATIONS: Demonstrated strong commitment to teaching, advising, and research is desired. Candidates should also evince intellectual leadership and impact on the field and potential for significant contributions to the department, University, and wider scholarly community. Also desired is a history of collaborative research and synthesis, student mentorship, and community engagement.

SPECIAL INSTRUCTIONS: Please submit the following materials through the ARIeS portal (**https://academicpositions.harvard.edu/postings/11821**). Review of applications will begin on **January 9th 2023**.

1. Cover letter
2. Curriculum Vitae
3. Teaching/advising statement (describing teaching philosophy and practices)
4. Research statement
5. Statement describing the candidate's vision for the future of inclusive leadership of a high-impact field station and center for experiential learning, including a history of collaborative research and synthesis, student mentorship, and engagement with broad stakeholders.
6. Statement describing efforts to encourage diversity, inclusion, and belonging. This can include a description of past and ongoing efforts, and anticipated future contributions.
7. Authorization form

Harvard University is committed to fostering a campus culture where everyone can thrive and experience a sense of inclusion and belonging. Community members are encouraged to model our values of integrity, responsible mentorship, equity, and excellence no matter where they are.

To support this commitment to our values of inclusion and excellence, the external finalist for this position will be required to complete a conduct questionnaire – specifically regarding findings of violation, on-going formal complaint investigations, or formal complaint investigations that did not conclude due to the external finalist's departure concerning: harassment or discrimination, retaliation, sexual misconduct, bullying or intimidating/abusive behavior, unprofessional relationship, or misconduct related to scholarship, research, teaching, service, or clinical/patient care.

Harvard will also make conduct inquiries to current and former employers of the external finalist regarding such misconduct. To facilitate these inquiries, Harvard requires all external applicants for this position to complete, sign, and upload the form entitled "Authorization to release information for external applicants" as part of their application. If an external applicant does not include the signed authorization with the application materials, the application will be considered incomplete, and, as with any incomplete application, will not receive further consideration.

Harvard University is committed to fostering a campus culture where everyone can thrive and experience a sense of inclusion and belonging. Community members are encouraged to model our values of integrity, responsible mentorship, equity, and excellence no matter where they are. To support this commitment, the external finalist for this position will be required to complete a questionnaire regarding misconduct and Harvard will make parallel inquiries to his/her/their current and former employers. View the definitions of misconduct and processes Harvard will use.

Harvard is an equal opportunity employer and all qualified applicants will receive consideration for employment without regard to race, color, sex, gender identity, sexual orientation, religion, creed, national origin, ancestry, age, protected veteran status, disability, genetic information, military service, pregnancy and pregnancy-related conditions, or other protected status.

CONTACT INFORMATION: Paul Moorcroft or Missy Holbrook, Search Committee, Department of Department of Organismic and Evolutionary Biology (**paul_moorcroft@harvard.edu, holbrook@oeb.harvard.edu**).

WORKING LIFE

By **Adrijana Crncec**

A series of fortunate events

My first stroke of luck came while I was sitting on the wooden stairwell in my childhood kitchen in Slovenia. My auntie was visiting from the United Kingdom, and we were talking about my plans for after I finished university. I had discovered a passion for molecular biology research, but there aren't many opportunities to do that type of work in Slovenia, and I thought I couldn't afford to move abroad. So, I was contemplating pursuing a master's in my undergraduate field of ecology at my local university, even though it wasn't what I was passionate about. To my surprise, my auntie encouraged me to think about international postgraduate studies, and even offered me my cousin's room while she was studying abroad for a year. It was the lucky break I needed—and I would have more in the years to come.

I was anxious about leaving my family, especially as my parents relied on my help around the farm. But with their support, I decided to apply for a master's program at a university near my auntie. When I was accepted, I was ecstatic. I was also nervous about moving to a foreign country and studying a new topic in a second language, as well as the financial toll. To save up for tuition fees, I worked part time at a shop and helped my father bale hay while also finishing my undergraduate degree. Despite my hard work, I was only able to save enough to cover one-third of the fees. Luckily a stipend from my country covered another third, and my parents were able to contribute the rest. I was as ready as I would ever be.

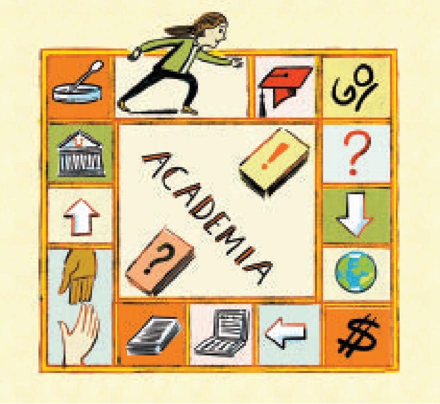

"I hope more PIs and graduate programs will give these students chances."

Once I arrived in the United Kingdom, amid culture shock and settling into my university program I found a part-time job at a grocery store. By working constantly and minimizing unnecessary daily costs, I was able to support myself, contribute my part of the household expenses with my auntie's family, and save for upcoming tuition fees while also navigating my academic work.

My relative good fortune didn't prevent me from nearing a breaking point after five exhausting months. On a lovely Saturday afternoon, after spending the morning at my part-time job, I headed to the lab. To my dismay, when I looked under the microscope, I realized I had washed away all my cells of interest. I broke into tears, went home, and spent the evening playing video games—a much-needed break after months of near-constant work. But I was too stubborn to give up. My brief reset helped me see that I could consider failed experiments a part of the learning process, always teaching you something—even if it's just what not to do.

Soon, my project began to yield interesting results, and discussing my ideas with others helped confirm that I love research and wanted to continue beyond my master's. To pursue a Ph.D., I had to find a funded position. After being rejected from several programs, one Friday evening in the computer lab I had a chance encounter with a principal investigator (PI) I vaguely remembered from two lectures he had given as part of my program's coursework. We were casually chatting while I was analyzing my data when he mentioned he was looking for a hardworking Ph.D. student and encouraged me to apply. I didn't think I stood a chance, but I figured I had nothing to lose.

To my surprise, that PI ended up offering me the position. He valued my motivation, work ethic, and ability to learn and was able to see past some of the shortcomings in my technical training and experience. I went on to complete my doctorate, and I'm now a postdoc in the United States, where I'm excited about the research opportunities that are available to me.

I never would have gotten here without luck. I worry about all the bright, passionate, capable students from underresourced countries and less privileged backgrounds who don't have the same family support and encouraging, open-minded mentors. I wish society would invest in the next generation of scientists by providing more funding opportunities for these talented students. And I hope more PIs and graduate programs will give these students chances like the ones I was lucky to get. ■

Adrijana Crncec is a postdoctoral fellow at the National Institutes of Health. Send your career story to SciCareerEditor@aaas.org.

ILLUSTRATION: ROBERT NEUBECKER

TRILLIONS OF MICROBES

ONE ESSAY

Jennifer Hill, Ph.D.
2022 Winner

The NOSTER *Science* Microbiome Prize is an international prize that rewards innovative research by investigators who have completed their terminal degree in the last 10 years and are working on the functional attributes of microbiota. The research can include any organism with the potential to contribute to our understanding of human or veterinary health and disease, or to guide therapeutic interventions. The winner and finalists will be chosen by a committee of independent scientists chaired by a senior editor of *Science*. The top prize includes a complimentary membership to AAAS, an online subscription to *Science*, and USD 25,000. Submit your research essay today.

NOSTER | Science
MICROBIOME
PRIZE

Apply by 24 January 2023 at www.science.org/noster

Sponsored by Noster, Inc